



Technische Universität München

Ingenieur fakultät Bau Geo Umwelt

Lehrstuhl für Methodik der Fernerkundung

Total and Tropospheric NO₂ Retrieval for GOME-2 and TROPOMI

Song Liu

Vollständiger Abdruck der von der Ingenieur fakultät Bau Geo Umwelt
der Technische Universität München zur Erlangung des akademischen Grades eines
Doktor-Ingenieurs (Dr.-Ing.) genehmigten Dissertation.

Vorsitzender: Prof. Dr. Urs Hugentobler

Prüfer der Dissertation:

1. Priv.-Doz. Dr.-Ing. Adrian Doicu
2. Prof. Dr.-Ing. habil. Richard Bamler
3. Prof. Dr. Mark Wenig
Ludwig-Maximilians-Universität München

Die Dissertation wurde am 04.07.2019 bei der Technischen Universität München eingereicht und durch die Ingenieur fakultät Bau Geo Umwelt am 22.10.2019 angenommen.

Erklärung

Ich erkläre an Eides statt, dass ich die bei der Ingenieur fakultät Bau Geo Umwelt der TUM zur Promotionsprüfung vorgelegte Arbeit mit dem Titel “Bestimmung von NO₂ Gesamtsäulen und troposphärischen Säulen aus GOME-2 und TROPOMI Daten” am Lehrstuhl für Methodik der Fernerkundung unter der Anleitung und Betreuung durch Dr. Adrian Doicu ohne sonstige Hilfe erstellt und bei Abfassung nur die gemäß § 6 Ab. 6 und 7 Satz 2 angebotenen Hilfsmittel benutzt habe.

Ich habe keine Organisation eingeschaltet, die gegen Entgelt Betreuerinnen und Betreuer für die Anfertigung von Dissertationen sucht, oder die mir obliegenden Pflichten hinsichtlich der Prüfungsleistungen für mich ganz oder teilweise erledigt.

Ich habe die Dissertation in dieser oder ähnlicher Form in keinem anderen Prüfungsverfahren als Prüfungsleistung vorgelegt.

Ich habe den angestrebten Doktorgrad noch nicht erworben und bin nicht in einem früheren Promotionsverfahren für den angestrebten Doktorgrad endgültig gescheitert.

Die öffentlich zugängliche Promotionsordnung der TUM ist mir bekannt, insbesondere habe ich die Bedeutung von § 28 (Nichtigkeit der Promotion) und § 29 (Entzug des Doktorgrades) zur Kenntnis genommen. Ich bin mir der Konsequenzen einer falschen Eidesstattlichen Erklärung bewusst.

München, 30. Juni 2019

Song Liu

Zusammenfassung

Stickstoffdioxid (NO_2) hat eine Schlüsselstellung in der Chemie der Atmosphäre. Obwohl Stickoxide ($\text{NO}_x = \text{NO}_2 + \text{NO}$) nur als Spurengase existieren, sind sie sowohl an dem Ozonabbau und den Halogenverbindungs-Reaktionen in der Stratosphäre als auch an der Bildung von Ozon und sekundären Aerosolen in der Troposphäre beteiligt. Eine große Menge von bodennahem NO_2 , das als Luftschadstoff die menschliche Gesundheit und das Ökosystem schädigt, wird bei der anthropogenen Verbrennung der fossilen Brennstoffe und der Biomasse erzeugt.

Um die räumlichen und zeitlichen Veränderungen der NO_2 -Konzentrationen global erfassen zu können, müssen Methoden der satellitengestützten Fernerkundung angewendet werden. Seit mehr als 10 Jahren stehen Beobachtungen des gesamten und troposphärischen NO_2 mit Hilfe vom Global Ozone Monitoring Experiment-2 (GOME-2) Instrument an Bord von Satelliten der MetOp-Reihe zur Verfügung. Im Oktober 2017 kam das fortgeschrittene TROPOspheric Monitoring Instrument (TROPOMI) an Bord von Sentinel-5 Precursor hinzu, das sich durch eine sehr gute räumliche Auflösung von $7 \text{ km} \times 3.5 \text{ km}$ auszeichnet. Sowohl GOME-2 als auch TROPOMI sind optische Absorptionsspektrometer, die im ultravioletten und sichtbaren Licht messen.

Diese Arbeit befasst sich mit der Bestimmung von NO_2 Gesamtsäulen und troposphärischen Säulen mit Hilfe der GOME-2 und TROPOMI Instrumente. Zur Bestimmung der Gesamtsäulen wird die Absorption aus den gemessenen Strahldichten mit der Methode der differentiellen optischen Absorptionsspektroskopie (DOAS) analysiert. Die Berechnung der troposphärischen NO_2 -Säulen beruht auf der Subtraktion des stratosphärischen Hintergrunds und der Simulation des Strahlungstransports. Die täglichen globalen Daten tragen wesentlich zu Untersuchungen der Atmosphärenphysik und -chemie bei.

In dieser Arbeit wird eine Reihe wichtiger Prozesse, die mit Atmosphärenphysik und -chemie in Zusammenhang stehen, mit besonderem Fokus auf NO_2 dargestellt. Sie verbindet eine ausführliche Beschreibung und eine Untersuchung über das DOAS-basierte Retrievalverfahren mit einer Übersicht über die vorhandenen Methoden. Darüber hinaus werden die Quellen von Hauptfehlern analysiert und besprochen, um die Messungen besser interpretieren zu können.

Danach wird ein verbessertes Retrievalverfahren auf kalibrierte Strahlungsmessungen von GOME-2 und TROPOMI angewendet, das auf qualitativ hochwertige und harmonisierte globale Beobachtungen abzielt. Die resultierenden NO_2 -Daten werden anhand der Messungen von verschiedenen satellitengetragenen NO_2 -Produkten sowie von bodengebundenen Instrumenten überprüft und validiert. Das Algorithmus-Framework kann für zukünftige ultraviolett-sichtbare Sensoren angepasst und als Referenz für die zukünftige Entwicklung des Algorithmus verwendet werden.

Abstract

Nitrogen dioxide (NO_2) is an important trace gas in the Earth's atmosphere. Nitrogen oxides ($\text{NO}_x = \text{NO}_2 + \text{NO}$) relate strongly to ozone destruction and halogen compound reactions in the stratosphere and serve as precursors of ozone and secondary aerosol in the troposphere. As a prominent air pollutant affecting human health and ecosystem, large amounts of NO_2 are produced in the boundary layer by anthropogenic combustion of fossil fuels and biomass over polluted hot spots.

Satellite-based remote sensing data has been applied to characterise the spatial and temporal variation of NO_2 concentrations. The Global Ozone Monitoring Experiment-2 (GOME-2) instruments, included on a series of MetOp satellites, have provided a consistent long-term NO_2 dataset for more than a decade. The NO_2 measurements have been extended by the new generation instrument TROPospheric Monitoring Instrument (TROPOMI) aboard the Sentinel-5 Precursor satellite with a high spatial resolution of $7 \text{ km} \times 3.5 \text{ km}$. Both GOME-2 and TROPOMI are ultraviolet-visible spectrometers providing NO_2 observations on global scale and daily basis.

The work presented in this thesis addresses the determination of total and tropospheric NO_2 columns using the GOME-2 and TROPOMI instruments. The NO_2 total columns are retrieved from the measured radiance spectra using the differential optical absorption spectroscopy (DOAS) method, based on which the tropospheric columns are determined with a subtraction of the stratospheric contribution and a simulation of the radiative transfer. The observations offer opportunities for the scientific community to make an extensive investigation into the atmospheric physics and chemistry.

In this work, a number of important processes related to the physics and chemistry of the atmosphere and specifically the NO_2 are introduced, followed by a detailed investigation of the DOAS-type NO_2 retrieval algorithm, including an overview of the satellite data heritage and state-of-the-art retrievals. In addition, the main error sources related to the retrieval uncertainty are analysed and discussed for each retrieval step, which play a critical role in the interpretation of the satellite NO_2 measurements.

To that end, a harmonized NO_2 retrieval algorithm is developed for GOME-2 and TROPOMI, aiming at high-quality global observations based on calibrated satellite data and state-of-the-science retrieval schemes. The retrieval algorithm is applied on measurements from GOME-2 and TROPOMI, and the resulting NO_2 data record is verified and validated using measurements from different satellite retrievals and correlative ground-based instruments. The proposed algorithm framework can be easily adapted for future ultraviolet-visible sensors and can be used as reference for future algorithm developments.

Acknowledgements

This thesis summarizes the work carried out during my Ph.D. study at German Aerospace Center (DLR) and Technical University of Munich (TUM) since 2015. I dedicate it to my supervisors and colleagues, to my family and friends, and to the years in Germany.

I would like to express my gratitude to my principle supervisor Dr. Adrian Doicu, who has supported me with his knowledge and trust since my study for the master's degree in 2012. The same gratitude goes to Prof. Dr. Richard Bamler and Prof. Dr. Mark Wenig for scientific discussions and professional comments.

I take this opportunity to acknowledge Dr. Pieter Valks, who has supported me over the past years with his knowledge, experience, and patience. This thesis would not have been completed without his supervision.

Many thanks go to Prof. Dr. Thomas Trautmann for offering me the opportunity to work on this thesis at DLR and the possibility to exchange the experience at conferences and during research visits. His feedback on the thesis is also acknowledged.

The work was jointly sponsored by the German Academic Exchange Service (DAAD) and the Remote Sensing Technology Institute (IMF) at DLR. With a long-term experience in retrieval methodologies and an enthusiastic work environment at the Atmospheric Processors (ATP) department, I am thankful for the Passive Sensing team led by Dr. Diego Loyola for academic discussions, the UPAS processor team for computer and programming help, and every member from the department for the delightful time with coffee, cake, lunch, and party.

The work is not possible without a close collaboration with colleagues at MPI-C in Maiz, IUB-UP in Bremen, KNMI in De Bilt, and particularly colleagues at BIRA-IASB in Brussels, who have provided me not only the up-to-date experience but also a warm atmosphere during my research stay in 2018.

I extend my deepest thanks to my parents and Wei for always standing by me during the challenging PhD journey. I also acknowledge all my friends from DLR and TUM, particularly from the master program ESPACE, and many more, who have made my sad times happy and my happy times unforgettable.

From the bottom of my heart, I appreciate each and every one of you for the time we shared, past and present, relaxed and passionate. Thank you all for being in my life.

Ich bedanke mich herzlich bei allen hervorragenden Menschen, denen ich in den letzten Jahren begegnet bin, dass sie in meinem Leben waren. Ganz, ganz lieben Dank!

感谢波澜不惊的时间，和时间长河里出现的你们。正因为有你们的理解和陪伴，
才有我一路的成长，尽可以去看，去做，去经历，去体会。
谨此以最真诚的心祝你们年年安康，事事顺遂。

List of Abbreviations

abbreviation	description
AC-SAF	Satellite Application Facility on Atmospheric Composition Monitoring
AMF	air mass factor
AERONET	AErosol RObotic NETwork
BIRA-IASB	Belgian Institute for Space Aeronomy
BRDF	bidirectional reflectance distribution function
CAL	Cloud-As-Layers
CAMELOT	Chemistry of the Atmosphere Mission concEpts and sentineL Observations Techniques
CAMS	Copernicus Atmosphere Monitoring Service
CRB	Clouds-as-Reflecting-Boundaries
DLER	directionally dependent Lambertian-equivalent reflectivity
DLR	German Aerospace Center
DOAS	differential optical absorption spectroscopy
DOMINO	Dutch OMI NO ₂ product
ECMWF	European Centre for Medium Range Weather Forecast
EUMETSAT	European Organisation for the Exploitation of Meteorological Satellites
FWHM	full width at half maximum
GDP	GOME Data Processor
GEMS	Geostationary Environmental Monitoring Spectrometer
GOME	Global Ozone Monitoring Experiment
GOME-2	Global Ozone Monitoring Experiment-2
H ₂ O _{vap}	water vapor
H ₂ O _{liq}	liquid water
IFS	Integrated Forecast System
IUP-UB	Institute of Environmental Physics at the University of Bremen
KNMI	Royal Netherlands Meteorological Institute
LER	Lambertian-equivalent reflectivity
LIDORT	Inearized Discrete Ordinate Radiative Transfer
MAXDOAS	multi-axis differential optical absorption spectroscopy
MODIS	MODerate resolution Imaging Spectroradiometer
MOZART	Model for OZone And Related chemical Tracers
MPI-C	Max Planck Institute for Chemistry
NO	nitrogen oxide
NO ₂	nitrogen dioxide
NO _x	nitrogen oxides
O ₃	ozone

O ₄	oxygen dimer
OCRA	Optical Cloud Recognition Algorithm
OMI	Ozone Monitoring Instrument
QA4ECV	Quality Assurance for Essential Climate Variables
RAA	relative azimuth angle
ROCINN	Retrieval Of Cloud Information using Neural Networks
SCIAMACHY	SCanning Imaging Absorption SpectroMeter for Atmospheric CHartographY
SCIATRAN	SCIAmachy radiative TRANsfer simulator
STREAM	STRatospheric Estimation Algorithm from Mainz
SZA	solar zenith angle
TEMPO	Tropospheric Emissions Monitoring of Pollution
TM5	Tracer Model 5
TOMS	Total Ozone Mapping Spectrometer
TROPOMI	TROPOspheric Monitoring Instrument
TUM	Technical University of Munich
VLIDORT	Vector-LInearized Discrete Ordinate Radiative Transfer
VZA	viewing zenith angle

List of Symbols

symbol	description
y	measurements
x	NO ₂ distribution
F	forward model
b	forward model parameters
x_a	a priori NO ₂ distribution
K	weighting function
R	retrieval method
\hat{b}	estimated forward model parameters
\hat{x}	estimated NO ₂ vertical column
G	gain factor
A	averaging kernel
S	slant column
M	air mass factor
I	earthshine radiation intensity
I_0	solar radiation intensity
τ	optical depth
L	light path length
λ	wavelength
k	absorption cross-section
n	absorber number density
g	absorber
P	polynomial
m	box-AMF
f	shape factor
f	vertical shape factor
z	altitude
l	layer
c	temperature correction coefficient
M^{cr}	clear-sky AMF
M^{cl}	cloudy-sky AMF
c_f	cloud fraction
S_{st}	stratospheric slant column
M_{tr}	tropospheric AMF
σ	uncertainty
A_s	surface albedo
ps	profile shape
c_p	cloud pressure

List of Figures

Chapter 1 Introduction	1
1.1 1976 US standard atmosphere.	2
1.2 Global NO _x emission trends in 1970-2008.	3
1.3 Scheme of interactions of solar radiation with the atmosphere and surface.	4
1.4 Spectral properties of sunlight.	4
Chapter 2 Atmospheric NO_x	7
2.1 Map of global NO _x emissions for the year 2012.	8
2.2 Vertical profile of the estimated lifetime of NO _x	9
2.3 MAXDOAS instrument and MAXDOAS measurement geometry.	12
2.4 Overview of European ultraviolet-visible backscatter satellite instruments.	12
2.5 Measurement principles for GOME-2 and TROPOMI.	13
Chapter 3 Atmospheric NO₂ retrieval	15
3.1 Illustration of applying the DOAS technique to the spectral analysis of NO ₂ from GOME-2 spectra at 425-497 nm.	19
3.2 Scheme of geometries for a geometric AMF and a scattering AMF.	21
3.3 Processing chain of the total and tropospheric NO ₂ retrieval for ultraviolet-visible backscatter satellite instruments.	24
3.4 Effect of the temperature-dependency of the NO ₂ absorption cross-sections on the DOAS retrieval.	25
3.5 Effect of the wavelength-dependency of the AMFs on the DOAS retrieval.	27
3.6 Illustration of estimating the slant column uncertainties using a statistic method.	28
Chapter 4 Analysis of NO₂ retrieval	31
4.1 Relative differences in NO ₂ slant columns simulated by VLIDORT and retrieved by DOAS using various fitting windows for basic scenarios.	32
4.2 A priori NO ₂ profiles for CAMELOT scenarios.	33
4.3 NO ₂ slant columns simulated by SCIATRAN and retrieved by DOAS using various fitting windows for CAMELOT scenarios.	34
4.4 Similar as Fig. 4.3 but for simulations without the temperature-dependency of the NO ₂ absorption cross-sections.	35

4.5	NO ₂ slant columns retrieved from noisy data using various fitting windows for CAMELOT scenarios.	36
4.6	A priori NO ₂ profiles simulated with TM5.	40
4.7	Effect of the wavelength on the box-AMFs.	41
4.8	Effect of the measurement geometry on the box-AMFs.	41
4.9	Effect of the surface albedo on the box-AMFs.	41
4.10	Effect of the surface pressure on the box-AMFs.	42
4.11	Effect of the cloud model on the cloudy-sky box-AMFs.	42
4.12	Effect of the single scattering albedo on the cloudy-sky box-AMFs.	42
4.13	Effect of the cloud optical depth on the cloudy-sky box-AMFs.	42
4.14	Effect of the cloud top height on the cloudy-sky box-AMFs.	42
4.15	Uncertainties in the tropospheric AMFs due to errors in the surface albedo, a priori profile shape, cloud fraction, and cloud pressure.	45
Chapter 5 NO₂ retrieval for GOME-2		47
5.1	Temporal evolution of the GOME-2 NO ₂ slant column errors from the operational product, the improved algorithm, and the QA4ECV dataset.	49
5.2	GOME-2 total NO ₂ columns and stratospheric NO ₂ columns retrieved from the STREAM algorithm and from the spatial filtering method.	51
5.3	Map of GOME-2 surface LER climatology, improved GOME-2 surface LER data taking into account the direction-dependency, and their differences over land and over water (figure continued on next page).	52
5.3	(figure continued from previous page)	53
5.4	Box-AMFs for clear and cloudy sky using the ROCINN_CAL and ROCINN_CRB cloud models over Italy.	54
5.5	Relative biases in GOME-2 tropospheric NO ₂ columns assuming implicit aerosol correction through the ROCINN_CRB and ROCINN_CAL cloud models in Xianghe.	55
5.6	Absolute and relative differences of GOME-2 and MAXDOAS tropospheric NO ₂ columns for the operational and improved algorithms in Xianghe.	56
Chapter 6 NO₂ retrieval for TROPOMI		57
6.1	Example of applying the DOAS technique to the spectral analysis of NO ₂ from TROPOMI spectra at 405-465 nm.	60
6.2	TROPOMI total NO ₂ distribution and stratospheric NO ₂ distribution obtained with the STREAM algorithm.	61
6.3	Tropospheric AMFs over Europe.	62
6.4	Yearly averaged TROPOMI tropospheric NO ₂ columns over Europe.	63
6.5	Seasonal variation of TROPOMI tropospheric NO ₂ columns over Germany and surrounding regions.	64
6.6	Weekday-weekend variation of TROPOMI tropospheric NO ₂ columns over Germany and surrounding regions.	65
6.7	Daily TROPOMI tropospheric NO ₂ columns over East Asia.	66
6.8	NO ₂ slant columns measured by TROPOMI, OMI and GOME-2 over the Pacific.	67

6.9	TROPOMI stratospheric NO ₂ columns derived using the STREAM algorithm and the operational data assimilation method over East China, Germany, and eastern US.	67
6.10	Daily and monthly mean time series and scatter plot of TROPOMI and MAXDOAS tropospheric NO ₂ columns in Xianghe.	68
6.11	Daily and monthly mean absolute and relative TROPOMI and MAXDOAS time series differences for the Xianghe station.	68

List of Tables

Chapter 3 Atmospheric NO₂ retrieval	15
3.1 Main settings of the NO ₂ retrieval for ultraviolet-visible satellite instruments.	17
Chapter 4 Analysis of NO₂ retrieval	31
4.1 Radiative transfer model and model parameters in calculating the synthetic spectra and AMFs.	32
4.2 Radiative transfer model and model parameters in calculating the tropospheric AMFs for clear sky and cloudy sky as reference.	38
4.3 Cloud properties in calculating the tropospheric AMFs for cloudy sky as reference.	38
4.4 Reference tropospheric AMFs for clear sky and cloudy sky.	39
4.5 Calculating the tropospheric AMFs for clear sky and cloudy sky by altering the model parameters.	39
4.6 Calculating the tropospheric AMFs for cloudy sky by altering the cloud properties.	39
4.7 Information on the input parameters for calculating the tropospheric AMFs.	44
4.8 Uncertainty estimates for surface albedo, a priori profile shape, cloud fraction, and cloud pressure.	45
Chapter 5 NO₂ retrieval for GOME-2	47
5.1 Main settings of GOME-2 DOAS retrieval of NO ₂ slant columns for the operational and improved algorithms.	48
5.2 Radiative transfer model and model parameters in deriving GOME-2 tropospheric NO ₂ columns for the operational and improved algorithms.	50
Chapter 6 NO₂ retrieval for TROPOMI	57
6.1 Main settings of the NO ₂ retrieval for TROPOMI from the KNMI operational product and the DLR development.	58
6.2 Overview over absorption cross-sections used in the TROPOMI NO ₂ retrieval.	59

Contents

Erklärung	i
Zusammenfassung	iii
Abstract	v
Acknowledgements	vii
List of Abbreviations	ix
List of Symbols	xi
List of Figures	xiii
List of Tables	xvii
1 Introduction	1
1.1 Background	1
1.2 Thesis objectives	5
1.3 Thesis outline	5
2 Atmospheric NO_x	7
2.1 Sources of NO _x	7
2.2 Sinks of NO _x	8
2.3 Reservoirs and lifetime of NO _x	8
2.4 Chemistry of NO _x	9
2.5 NO ₂ measurements	10
2.5.1 Ground-based measurements	11
2.5.2 Space-based measurements	11
3 Atmospheric NO₂ retrieval	15
3.1 Retrieval theory	15
3.2 DOAS slant column retrieval	16
3.3 Stratosphere-troposphere separation	20
3.4 AMF calculation	20
3.4.1 A priori NO ₂ profile	21
3.4.2 Box-AMF	22
3.4.3 Surface albedo	22
3.4.4 Clouds	23
3.4.5 Aerosols	23

3.5	Tropospheric vertical column computation	23
3.6	Error analysis	24
3.6.1	DOAS assumptions	25
3.6.2	Slant column uncertainties	26
3.6.3	Stratospheric column uncertainties	28
3.6.4	AMF uncertainties	28
3.6.5	Tropospheric column uncertainties	29
4	Analysis of NO₂ retrieval	31
4.1	DOAS fit using synthetic data	31
4.1.1	Basic scenarios	31
4.1.2	CAMELOT scenarios	33
4.1.3	Summary of synthetic studies	37
4.2	AMF sensitivities	37
4.2.1	Reference retrieval	38
4.2.2	Sensitivities of model parameters	39
4.2.3	Sensitivities of cloud properties	43
4.2.4	Summary of sensitivity tests	44
4.3	AMF uncertainties	44
5	NO₂ retrieval for GOME-2	47
5.1	GOME-2 NO ₂ product	47
5.2	Retrieval algorithm	48
5.2.1	DOAS slant column retrieval	48
5.2.2	Stratosphere-troposphere separation	49
5.2.3	AMF calculation	50
5.3	End-to-end validation	54
6	NO₂ retrieval for TROPOMI	57
6.1	TROPOMI NO ₂ product	57
6.2	Retrieval algorithm	58
6.2.1	DOAS slant column retrieval	58
6.2.2	Stratosphere-troposphere separation	59
6.2.3	AMF calculation	59
6.3	Examples of TROPOMI tropospheric NO ₂	62
6.4	Verification and validation	64
7	Conclusion and outlook	71
7.1	Conclusion	71
7.2	Outlook	72
	Bibliography	74
	Appendices	88
A	Inversion models for the retrieval of total and tropospheric NO₂ columns	89
B	The STRatospheric Estimation Algorithm from Mainz (STREAM): estimating stratospheric NO₂ from nadir-viewing satellites by weighted convolution	111

C	An improved total and tropospheric NO₂ column retrieval for GOME-2157	
D	An improved air mass factor calculation for NO₂ measurements from GOME-2	205
	Lebenslauf	248

Chapter 1

Introduction

1.1 Background

The *atmosphere* of Earth is a complex system of gases, known as air, separating the Earth's surface from space. Characterised by the temperature as a function of altitude, the atmosphere can be divided into a set of layers, as indicated in Fig. 1.1. Extended from the surface to 8-18 km altitude, the *troposphere* is the lowest layer of the atmosphere, which is critical for plants, animals, and humans on Earth, with $\sim 75\text{-}80\%$ of the mass of the atmosphere, most types of clouds, and almost all the weather. Within the troposphere, the lowest part up to 1-2 km is the boundary layer, separated from the free troposphere by a direct interaction of the atmosphere with the surface. Extended above the troposphere to ~ 50 km is the *stratosphere*, a relatively stable layer with little convection and mixing, due to the increasing temperature as increasing altitude. The boundary between the troposphere and the stratosphere is called the *tropopause*.

atmospheric constituents

The atmosphere contains several main gaseous constituents, such as nitrogen (N_2), oxygen (O_2), and argon (Ar). Gases like carbon dioxide (CO_2), nitrogen oxides (NO_x), methane (CH_4), and ozone (O_3) are *trace gases* that account for $\sim 0.1\%$ of the atmosphere. Despite the relative scarcity, various trace gases are involved in the greenhouse effect and related to global warming and climate change, referred to as *greenhouse gases*, including CO_2 , CH_4 , and water vapor. Water vapor typically accounts for less than 1% of the atmosphere in the dry areas and $\sim 4\%$ in the tropical regions. When the temperature of the gaseous water vapor in supersaturated air is reduced, water vapor forms *clouds* by condensing to liquid water droplets or (at lower temperatures) freezing to solid ice crystals. In addition, the atmosphere has a suspension of fine solid particles or liquid droplets in gases (usually air), known collectively as *aerosols*. Typical aerosols, such as plant pollen, mineral dust, sea salt, and smoke, generally have a smaller particle size than the cloud particles (Boucher et al., 2013).

As a prevalent form of NO_x , *nitrogen dioxide* (NO_2) is one of the most important chemical constituents in the Earth's atmosphere. In the stratosphere, NO_2 is strongly related to halogen compound reactions and ozone destruction (Solomon, 1999). In the troposphere, NO_2 is a prominent air pollutant affecting human respiratory system even with short exposures (Gamble et al., 1987; Kampa and Castanas, 2008). Additionally, NO_x serve as a precursor of ozone in the presence of volatile organic compounds and a precursor of secondary aerosols through gas-to-particle conversion (Seinfeld and Pandis, 2016). As a greenhouse gas, NO_2 contributes significantly to radiative forcing locally. The

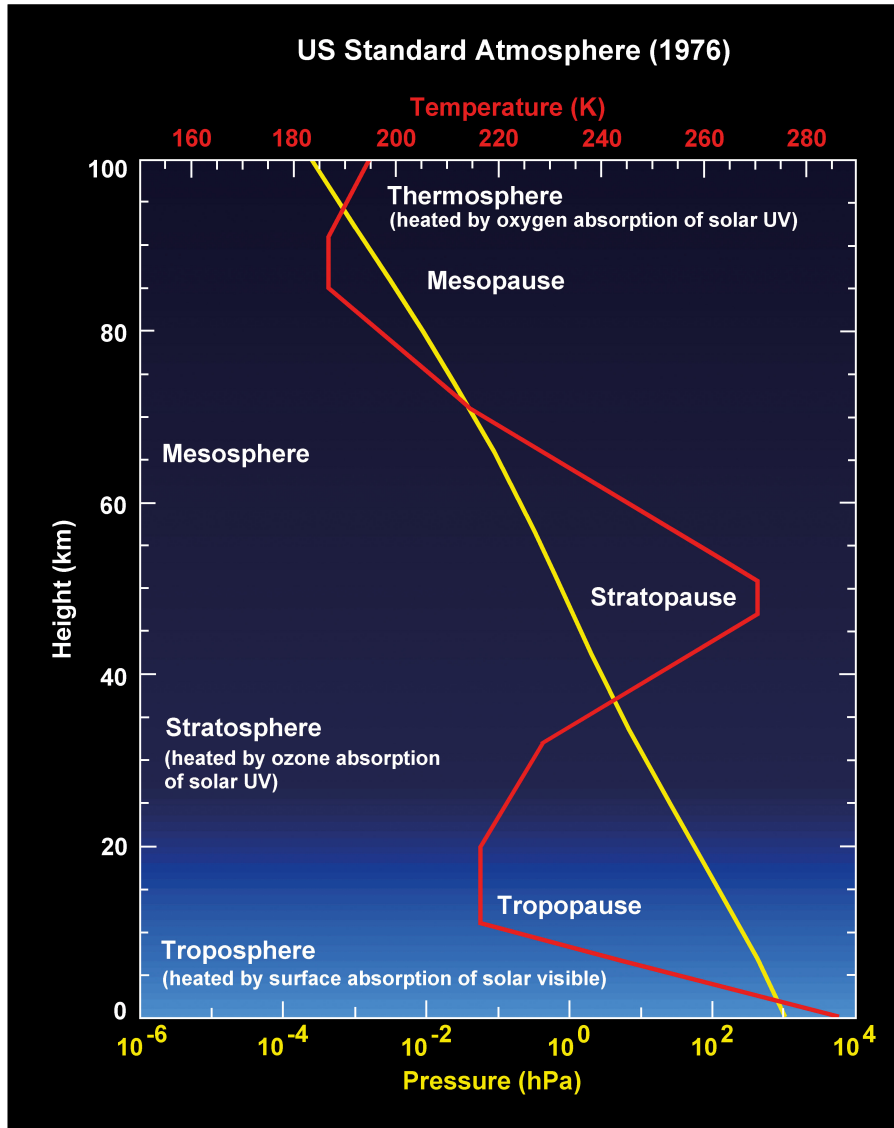


Figure 1.1: 1976 US standard atmosphere graph of atmospheric pressure and temperature profiles for mid latitudes. Adopted from Gottwald et al. (2006).

net effect of NO_x on climate forcing is modelled to be negative or cooling, with NO_x -driven aerosol screening dominating over tropospheric ozone warming (Shindell et al., 2009).

NO_x enter the atmosphere due to various *natural* processes, such as atmospheric lightning and biogenic activity in soil, and *anthropogenic* processes, such as fossil fuel combustion and biomass burning. According to the EDGAR version 4.2 emission dataset in Fig. 1.2, the anthropogenic emissions of NO_x have increased strongly during the past decades for Asian countries, primarily related to the energy consumption (Richter et al., 2005; Liu et al., 2017; Hilboll et al., 2017; Lee et al., 2019). Despite the reduced NO_x emissions in Europe, still around half of European Union member states exceed the air quality standards, mainly caused by the diesel car emissions (European Commission, 2017). The awareness of climate change and air pollution problems has been raised globally, and NO_x control and pollutant prevention techniques have been applied worldwide to reduce the NO_2 pollution.

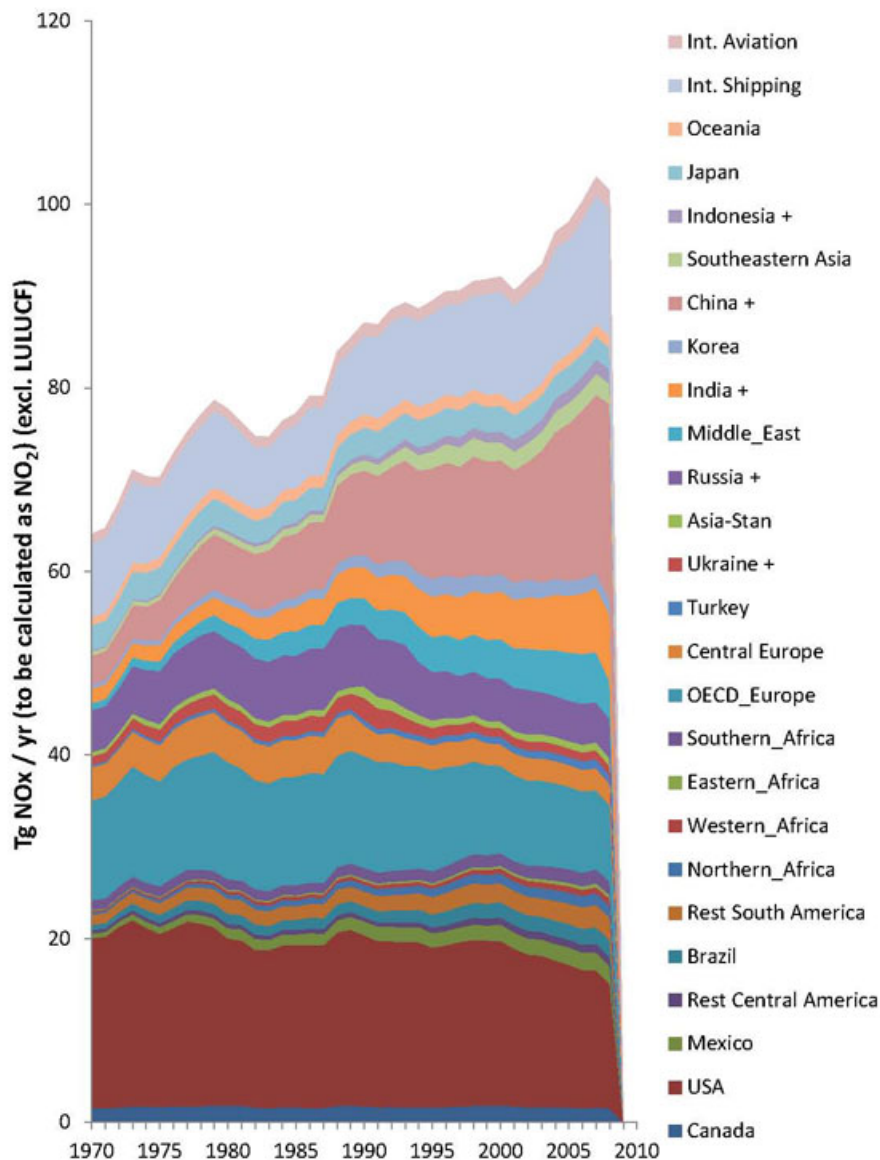


Figure 1.2: Global NO_x emission trends in 1970-2008 in Tg NO₂/yr. Adopted from EC-JRC/PBL. EDGAR version 4.2 emissions (<http://edgar.jrc.ec.europa.eu/>).

interactions in the atmosphere

The chemical composition of the atmosphere can be analysed due to a number of processes, in which solar radiation interacts with matter (gases, aerosols, and clouds), as illustrated in Fig. 1.3. When light travels through the Earth's atmosphere, the radiation can be removed by particles (aerosol and cloud) and molecules (such as oxygen, ozone, or NO₂) and converted to other forms of energy, a process termed as *absorption*. As the opposite to absorption, (thermal) *emission* is the process where an object emits radiation depending on its temperature. In addition, another fundamental process is the *scattering* of the incident radiation, during which the direction of a photon propagation is changed (elastic scattering) due to air molecules (Rayleigh scattering) or aerosol and cloud particles (Mie scattering). In contrast to elastic scattering, a photon can also be scattered inelastically by molecules (Raman scattering) with the molecules excited to high vibrational or rotational

energy levels. Furthermore, when sunlight penetrates the atmosphere, *reflection* takes place if the incident radiation “bounces” off the Earth’s surface diffusely (rough surface) or specularly (smooth surface).

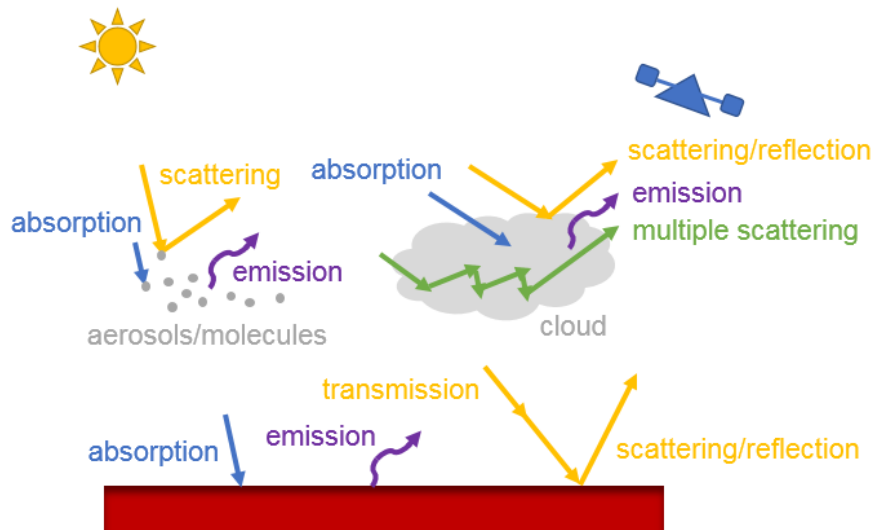


Figure 1.3: Scheme of interactions of solar radiation with the Earth’s atmosphere and surface.

Interactions of solar radiation with matter at different wavelengths yield different information about the atmosphere and surface. As shown in Fig. 1.4, $\sim 99\%$ of the solar power reaching the surface has a wavelength ranging from 300 nm to $2.5\ \mu\text{m}$, covering the *ultraviolet* region (below 380 nm), *visible* region (380-740 nm), and *infrared* region (above 740 nm). The visible range allows the penetration of radiation through the atmosphere to the surface, during which the atmospheric absorption and scattering as well as the surface reflectance directly affect the intensity of radiation.

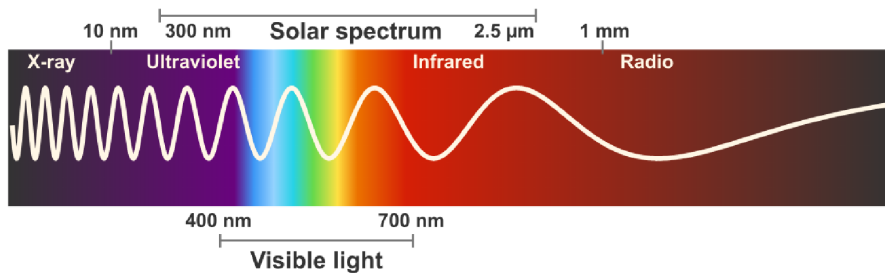


Figure 1.4: Spectral properties of sunlight. Adopted from <https://brilliant.org/practice/spectral-properties-sunlight/>.

atmospheric remote sensing

Measuring absorption spectra of molecules, remote sensing techniques have played an important role in the study of atmospheric chemistry and physics. As a commonly used method to measure trace gases in the atmosphere, the *differential optical absorption spectroscopy* (DOAS) technique (Solomon et al., 1987; Platt and Stutz, 2008) relies on the separation of highly structural absorption of traces gases and broad extinction features, e.g., the Rayleigh and Mie scattering. The DOAS method allows an accurate and fast retrieval of trace gas concentrations even for weak absorbers like NO_2 . Quantitative interpretation of the DOAS measurements, however, is not straightforward, as the observed

light follows complicated paths in the atmosphere, which requires detailed radiative transfer calculations based on a priori information on the state of the atmosphere and surface.

The contiguous wavelength coverage of recent satellite instruments enables the application of DOAS technique from space. As subjects of this study, Global Ozone Monitoring Experiment-2 (GOME-2) (Callies et al., 2000; Munro et al., 2016) on MetOp satellites and TROPospheric Monitoring Instrument (TROPOMI) (Veefkind et al., 2012) aboard the Sentinel-5 Precursor satellite are ultraviolet-visible spectrometers providing NO₂ observations on a global scale and daily basis. The GOME-2 instruments have been providing detailed global pictures of the atmospheric content since 2007 and will extend this unique dataset until 2023. The TROPOMI, with a strong focus on the troposphere, makes the regional monitoring possible with an unprecedented spatial resolution of 7 km × 3.5 km.

1.2 Thesis objectives

This thesis focuses on the retrieval of total and tropospheric NO₂ columns from the GOME-2 and TROPOMI observations with three main objectives:

- assessment of the quality of NO₂ retrievals using the DOAS method

As the DOAS-based method is widely applied in the NO₂ retrieval from satellite instruments, the accuracy of the method is evaluated based on synthetic measurements. Individual error sources related to the retrieval uncertainty are discussed, due to the importance for the interpretation of the satellite retrieval.

- development of harmonised NO₂ retrieval algorithms for GOME-2 and TROPOMI

A DOAS-based method is developed to retrieve the total and tropospheric NO₂ from the GOME-2 and TROPOMI measurements. Latest developments in the GOME-2 NO₂ retrieval algorithm are reported, and the improved algorithm is adapted and optimised for the TROPOMI instrument.

- verification and validation of the GOME-2 and TROPOMI NO₂ data

The overall quality of the retrieved GOME-2 and TROPOMI data is evaluated by comparing with NO₂ columns from different satellite retrievals and correlative ground-based instruments.

1.3 Thesis outline

This work is a *cumulative* dissertation comprising of four papers as presented in Appendices A-D. After a general introduction of atmospheric NO_x in Chap. 2, the DOAS-based retrieval of total and tropospheric NO₂ columns is presented with necessary basics and state-of-the-art in Chap. 3. Chapter 4 focuses on the theoretical studies addressing the overall quality of the DOAS-based retrieval (objective 1). Chapters 5 and 6 introduce the NO₂ retrieval algorithms using GOME-2 and TROPOMI measurements (objective 2), respectively, as well as the verification and validation of the NO₂ data (objective 3). Chapter 7 summarises the findings and provides directions for future research.

Chapter 2

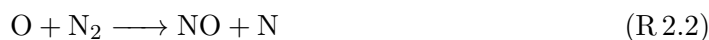
Atmospheric NO_x

NO₂ is an important trace gas in the Earth's stratosphere and troposphere. Since NO₂ and nitrogen oxide (NO) are rapidly converted into each other in the daytime atmosphere, they are commonly summed up to NO_x (NO_x=NO₂+NO). Over polluted hot spots, large amounts of NO_x are produced in the boundary layer by industrial processes, power generation, transportation, and biomass burning. In this chapter, the sources and sinks as well as the basic chemical reactions are described for atmospheric NO_x in the atmosphere, followed by an introduction of ground- and space-based measurements of NO₂ concentration.

2.1 Sources of NO_x

NO_x are produced in the atmosphere by both natural and anthropogenic processes. The natural sources of NO_x mainly include atmospheric lightning, natural fire, and microbial activity in soil. The main anthropogenic sources are fossil fuel combustion, surface and air transport, and biomass burning. Global NO_x emissions in the year 2012 are 122 Mt, as estimated by EDGAR version 4.3.2 (Fig. 2.1). The energy consumption emission is the predominant anthropogenic source of NO_x for Russia, China, India, and Oceania. The transport emission dominates the NO_x source for America, Europe, and Africa.

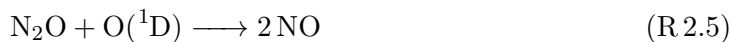
Most NO_x are primarily emitted in the form of NO. In connection with high temperatures above 2000 K (Zel'Dovich and Raizer, 1966) from *lightning* or *combustion activities* in furnaces, vehicle engines, and biomass burning, air molecules dissociate to form NO:



and NO can be rapidly converted to NO₂ by reaction with ozone:



In the stratosphere, NO_x are mainly formed from nitrous oxide (N₂O) transported from the troposphere, e.g., via the convective uplift from thunderstorms. N₂O is primarily produced by *soils* in the troposphere and photolyzed in the stratosphere (Brasseur and Solomon, 2005):



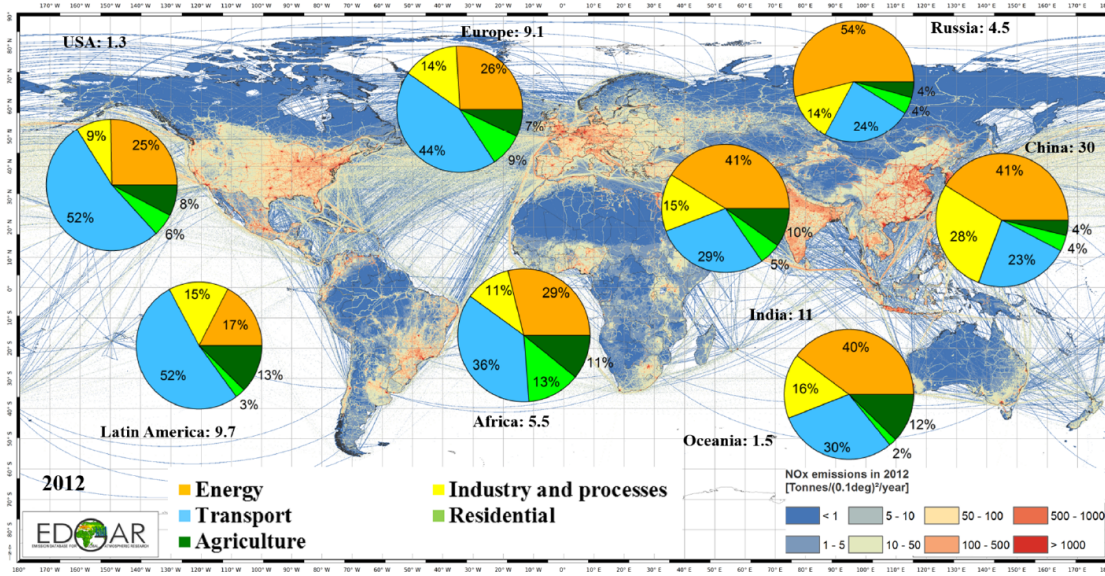


Figure 2.1: Map of global NO_x emissions and relative contributions of energy, industry, transport, residential, and agriculture for the year 2012. Total emissions (in Mt/yr) by region are reported next to each pie chart. Adopted from EDGAR version 4.3.2 emissions (Crippa et al., 2018).

2.2 Sinks of NO_x

With the exception of emissions by aircraft and lightning in Sect. 2.1, the NO_x produced by natural and anthropogenic processes are emitted into the boundary layer. Most of the generated NO_x are converted to nitric acid (HNO₃) and removed out of the atmosphere by precipitation, a process called *wet deposition* of HNO₃ (Jacob, 1999). During the daytime, HNO₃ is produced via the NO_x oxidation by the abundant hydroxyl radical (OH):



At nighttime, HNO₃ is generated via the combination product dinitrogen pentoxide (N₂O₅), which can react heterogeneously in the presence of aerosols (Dentener and Crutzen, 1993):



2.3 Reservoirs and lifetime of NO_x

Intermediate products of the NO_x oxidation in (R 2.6)-(R 2.9), including HNO₃, NO₃, and N₂O₅, are regarded as reservoirs for NO_x and summed up as total reactive nitrogen (NO_y) compounds (NO_y = NO_x + reservoir species). While HNO₃ is removed by precipitation in Sect. 2.2, the other NO_y species are eventually converted back to NO_x via photolysis in the sunlit atmosphere or reactions with radical species (Schultz et al., 1998).

Depending on the concentrations of species involved in (R 2.6)-(R 2.9), atmospheric pressure and temperature, and solar irradiation, the lifetime of NO_x varies from several

hours at the polluted surface to several days in the upper troposphere, as indicated in Fig. 2.2.

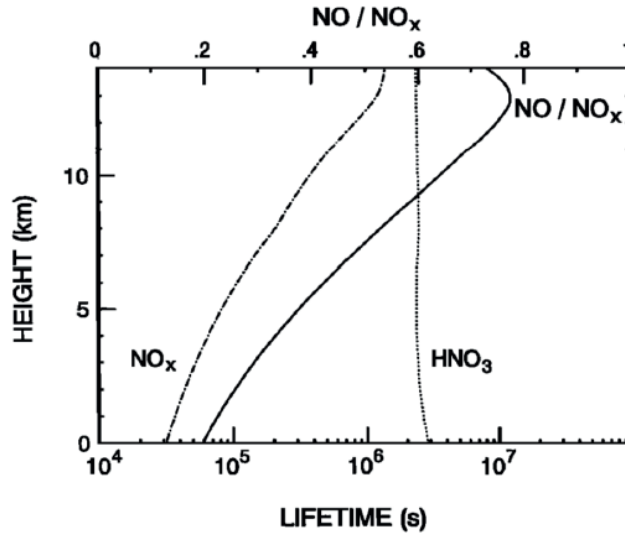


Figure 2.2: Vertical profiles of the estimated lifetime of NO_x and HNO₃. The calculated vertical profile of the NO/NO_x ratio is also shown. Adopted from Ehhalt et al. (1992).

2.4 Chemistry of NO_x

One main importance of NO_x in the atmospheric chemistry is their essential role in the determination of the Earth's ozone distribution.

cycle of NO_x and ozone

The cycling of NO₂ generally involves (R 2.4) and NO₂ photolysis (Nicolet, 1965) in the sunlit atmosphere:



The forward reactions (R 2.10) and (R 2.11) and the backward reaction (R 2.4) determine the local concentration of tropospheric ozone, depending on the NO_x concentration and the light intensity.

tropospheric ozone production

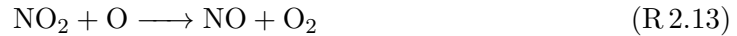
In addition to (R 2.4), NO can also react with organic peroxy radicals (RO₂) or hydroperoxy radicals (HO₂) to produce NO₂ (Stedman et al., 1970) without consuming ozone in the troposphere:



In air masses with high NO_x concentrations, RO₂ or HO₂ can efficiently convert NO into NO₂, resulting in tropospheric ozone production (Seinfeld and Pandis, 2016) with (R 2.10) and (R 2.11).

stratospheric ozone destruction

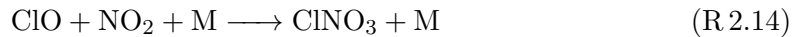
In the stratosphere, NO₂ reacts (alternatively to photolysis R 2.10) with atomic oxygen from oxygen photolysis:



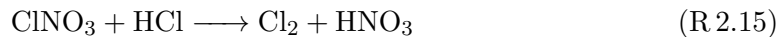
which leads to stratospheric ozone destruction (Solomon, 1999) with a catalytic cycle (Crutzen, 1970) in combination with (R 2.4).

polar ozone hole

Despite the involvement in the NO_x-catalysed stratospheric ozone destruction, NO₂ slows down the chlorine-induced ozone depletion by converting the active chlorine oxide (ClO) to the non-radical chlorine nitrate (ClNO₃) (Wennberg et al., 1994):



During polar winter with darkness, NO_x are transformed to longer lived reservoir species in Sect. 2.3, a process referred to as *denoxification* (Solomon, 1999). Furthermore, the formation of *polar vortex* separates the denoxified air masses with low NO_x from warm moist air masses of the mid-latitudes. In addition, the low temperatures cause the formation of persistent ice-like polar stratospheric clouds, providing the surfaces for the conversion of reservoirs ClNO₃ and hydrogen chloride (HCl) to molecular chlorine (Cl₂):



In winter, sedimentation of HNO₃-containing polar stratospheric clouds removes the NO_x reservoirs from the polar vortex, a process referred to as *denitrification* (Solomon, 1999). In spring with sufficient light, Cl₂ photolysis starts the catalytic ozone destruction cycles, and the efficiency of (R 2.14) is suppressed due to the missing NO_x within the polar vortex, leading to a significant stratospheric ozone destruction.

2.5 NO₂ measurements

To better understand the atmospheric environment, a number of different techniques have been developed to provide long-term NO₂ observations on local, regional, and global scales. Fundamentally, instruments are able to make *in-situ* or *remote sensing* measurements. The in-situ instruments are able to accurately determine the local NO₂ concentrations at a particular location with a high sensitivity for different atmospheric conditions. Remote sensing techniques, on the contrary, are principally spectroscopic methods sensing the radiation and allowing measurements remote from the instrument.

According to light source, remote sensing techniques can be broadly divided into *active* and *passive* methods. Active sensors emit an artificial light source and measure the reflected or scattered signal, while passive sensors detect the natural energy (from the Sun, Moon, or stars) that is reflected or emitted from the target. Active remote sensing techniques have a higher flexibility concerning the light path length and a wider spectral range due to the independence of daylight, but they normally require a sophisticated optical system and regular maintenance. In contrast, passive remote sensing techniques are more suitable for automated operation with a relatively simple experimental set-up.

According to platform, remote sensing observations of NO₂ concentrations are commonly obtained by *ground-based* and *space-based* instruments. Ground-based NO₂ measurements are beneficial to local or regional air pollution studies, especially for urban and suburban regions, while measurements from satellite instruments provide the possibility to measure the NO₂ concentrations globally, including rural or remote areas.

2.5.1 Ground-based measurements

Ground-based remote sensing measurements of atmospheric NO₂ have been applied since the development of the photon counting spectrophotometer (Dobson, 1957) in the mid-1920s (Kularni, 1975). The idea of the *Dobson* instrument and its successor Brewer spectrometer (Brewer et al., 1973) is to use the strong differential absorption of solar light by NO₂ at different wavelengths in the visible and near-ultraviolet region. Based on the measurement principle of absorption spectroscopy, the DOAS technique (Brewer et al., 1973; Noxon, 1975; Platt, 1994; Platt and Stutz, 2008) is one of the most commonly used spectroscopic methods to measure trace gases to date. DOAS uses the structured absorption of trace gases and removes the smooth extinction features like aerosol extinction or instrumental effects. Ground-based measurements can be accurately analysed by applying the passive DOAS technique for total (stratospheric plus tropospheric), stratospheric, and tropospheric column content, depending on the observed light source (direct solar irradiance, sky radiance in zenith direction, or sky radiance in multiple viewing directions).

direct Sun DOAS

Direct Sun DOAS has been applied to determine the total amount of NO₂ (e.g., Cede et al., 2006; Wenig et al., 2008). By pointing the instrument to the Sun, the spectral signature of NO₂ is captured straightforwardly in the direct light measurements, since all sunlight reaching the Earth's surface has to traverse the entire atmosphere. To date, automatic spectrometer systems using the direct Sun DOAS technique, like the Pandora instrument, are stable and reliable to provide measurements of NO₂ total columns with a high precision and a high sensitivity (Herman et al., 2009, 2018).

zenith sky DOAS

Zenith sky DOAS is mainly sensitive to stratospheric NO₂ and usually performed during twilight (sunrise and sunset) due to the long optical path in the stratosphere and relatively short vertical light path through the troposphere. Zenith sky DOAS instruments, such as the Système d'Analyse par Observations Zénithal (SAOZ) spectrometer (Pommereau and Goutail, 1988), have provided a high-quality monitoring of stratospheric NO₂ (e.g., Van Roozendaal et al., 1997; Liley et al., 2000; Hendrick et al., 2004, 2012).

MAXDOAS

Multi-axis DOAS (MAXDOAS), in contrast, allows the determination of vertically resolved abundances of atmospheric species in the lowermost troposphere (Hönninger et al., 2004; Wagner et al., 2004; Wittrock et al., 2004; Heckel et al., 2005; Frieß et al., 2006; Clémer et al., 2010; Hendrick et al., 2014; Ortega et al., 2015; Gielen et al., 2017). As shown in Fig. 2.3, the MAXDOAS instrument collects scattered sunlight in a series of line-of-sight angular directions from the horizon to the zenith. When the photons are collected simultaneously from different viewing elevations, a high sensitivity for tropospheric NO₂ is obtained by pointing the instrument to the horizon due to the long light path length, and measurements at higher elevations provide information on the rest of the column (Platt and Stutz, 2008).

2.5.2 Space-based measurements

Space-based measurements applying the DOAS technique have played an important role in monitoring and quantifying NO₂ concentrations with a global coverage. As indicated

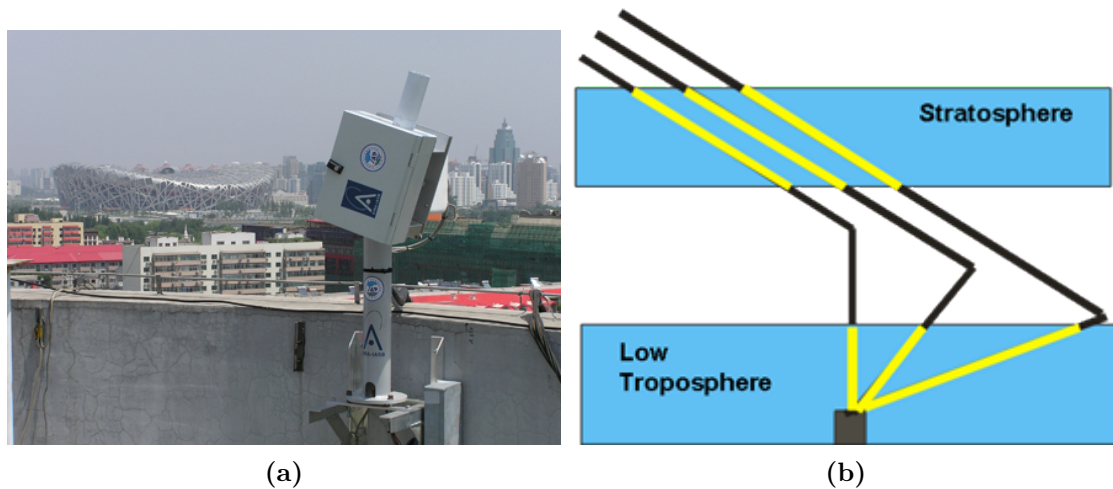


Figure 2.3: MAXDOAS instrument close to Beijing Olympic stadium in China (a) and MAXDOAS measurement geometry (b). Adopted from <http://www.aeronomie.be/en/topics/globalchange/airquality-china.htm>.

In Fig. 2.4, the first global NO₂ column measurements from satellite instrument were provided by Global Ozone Monitoring Experiment (GOME) on board ERS-2 with a spatial resolution of 320 km × 40 km and a global coverage within three days (Burrows et al., 1999). The NO₂ data record has been continued by SCanning Imaging Absorption SpectroMeter for Atmospheric CHartography (SCIAMACHY) (Bovensmann et al., 1999) aboard Envisat, Ozone Monitoring Instrument (OMI) (Levelt et al.) on EOS-Aura, GOME-2 (Callies et al., 2000; Munro et al., 2016) on MetOp satellites, and TROPOMI (Veefkind et al., 2012) aboard Sentinel-5 Precursor.

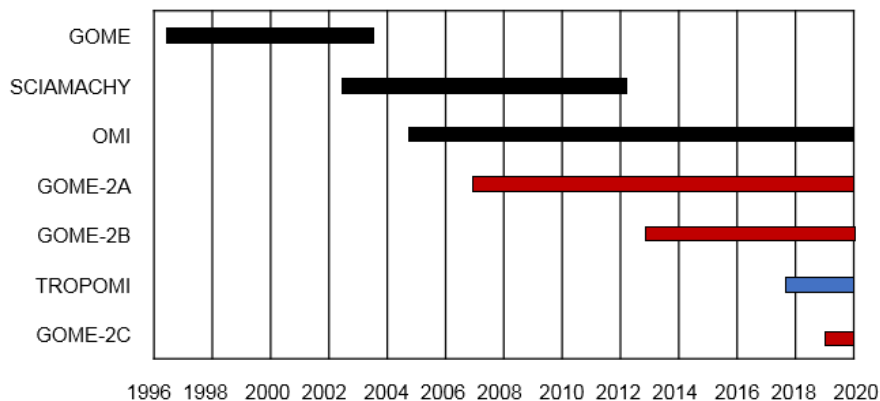


Figure 2.4: Overview of European ultraviolet-visible polar orbiting backscatter satellite instruments.

GOME-2

GOME-2 (Fig. 2.5a) is a nadir-scanning ultraviolet-visible spectrometer measuring the Earth's backscattered radiance and extra-terrestrial solar irradiance in the spectral range between 240 and 790 nm. The first GOME-2 was launched in October 2006 aboard the MetOp-A satellite, and a second GOME-2 was launched in September 2012 aboard

MetOp-B. The consistent long-term dataset will be further extended by the third GOME-2 on the MetOp-C platform (launched in November 2018). The Sun-synchronous polar orbit has an equator crossing time of 9:30 local time (descending node). The spectral resolution is 0.44-0.53 nm in the spectral window for the detection of NO₂. The default swath width of GOME-2 is 1920 km, enabling a global coverage in ~ 1.5 days. The default ground pixel size is 80 km \times 40 km in the forward scan, which remains almost constant over the full swath width. In a tandem operation of MetOp-A and MetOp-B from July 2013 onwards, a decreased swath of 960 km and an increased spatial resolution of 40 km \times 40 km are employed by GOME-2/MetOp-A.

TROPOMI

TROPOMI (Fig. 2.5b) is a push broom (non-scanning) imaging spectrometer covering wavelength bands between the ultraviolet and the shortwave infrared. Launched in October 2017, the 7-year-lifetime Sentinel-5 Precursor sensor TROPOMI provides NO₂ observations with a spatial resolution of 7 km \times 3.5 km (along \times across track) and a spectral resolution of 0.54 nm in the visible wavelength range. The swath width is ~ 2600 km in the direction across the track of the satellite that allows a daily global coverage. In combination with the morning observations from GOME-2, the early afternoon measurements (13:30 local time) from TROPOMI allow a better study of NO₂ diurnal variations.

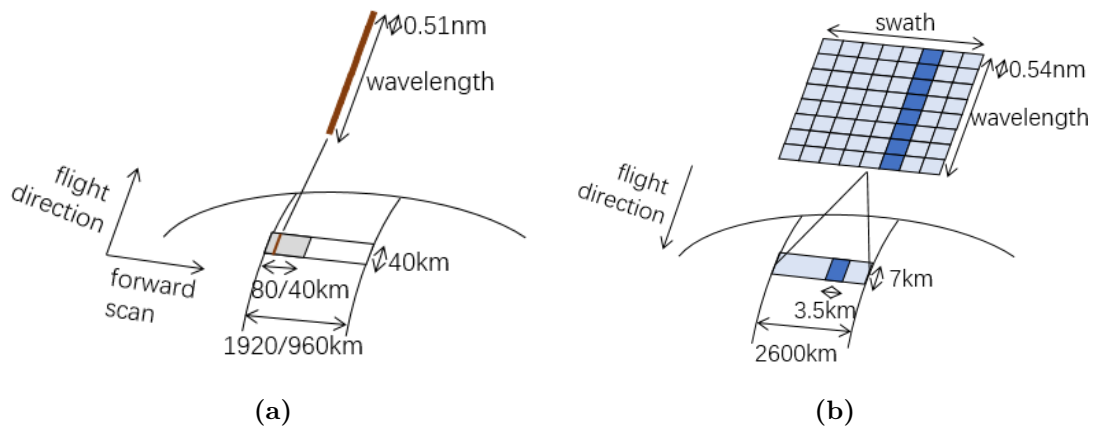


Figure 2.5: Measurement principles for GOME-2 (Callies et al., 2000; Munro et al., 2016)) in panel (a) and TROPOMI (adopted from Veeffkind et al. (2012)) in panel (b).

geostationary satellite constellation

In the future, the long-term satellite NO₂ observations will be further continued by forthcoming geostationary missions such as Sentinel-4 (Ingmann et al., 2012) over Europe, Geostationary Environmental Monitoring Spectrometer (GEMS) (Kim, 2012) over Asia, and Tropospheric Emissions Monitoring of Pollution (TEMPO) (Zoogman et al., 2017) over North America with a fast revisit time and a strong air quality focus.

Chapter 3

Atmospheric NO₂ retrieval

This chapter focuses on satellite remote sensing with solar backscatter measurements in the ultraviolet-visible wavelength range. The total NO₂ amount is derived from the spectral features using the commonly used DOAS retrieval method, based on which the tropospheric columns are determined with a subtraction of the stratospheric contributions and a numerical modelling of the atmospheric radiative transfer. In this chapter, the theoretical basis of the general retrieval algorithm is briefly introduced, relying on which the DOAS method is developed with simplifications and adaptations. A detailed theoretical analysis is referred to a journal article in Appendix A. Additionally, the DOAS-based algorithm and state-of-the-art retrievals are described for ultraviolet-visible backscatter satellite instruments, followed by a discussion of the main error sources and retrieval uncertainties.

3.1 Retrieval theory

In atmospheric remote sensing, a *forward* problem relates a given set of measurements \mathbf{y} (e.g., spectral radiances in the ultraviolet-visible wavelength range) to atmospheric parameters \mathbf{x} (e.g., the distribution of the trace gas) by applying a forward operator \mathbf{F} (Rodgers, 2000):

$$\mathbf{y} = \mathbf{F}(\mathbf{x}, \mathbf{b}) + \epsilon \quad (3.1)$$

where \mathbf{b} is a set of forward model parameters, including satellite viewing geometries, surface properties, and the presence of clouds and aerosols. ϵ denotes the error terms, such as the measurement noise, forward model errors, and the errors resulting from the uncertainties in the model parameters. For (weakly) non-linear forward models, \mathbf{F} can be linearised around the a priori trace gas distribution \mathbf{x}_a (Eskes and Boersma, 2003):

$$\mathbf{y} = \mathbf{F}(\mathbf{x}_a, \hat{\mathbf{b}}) + \mathbf{K}_x(\mathbf{x} - \mathbf{x}_a) + \epsilon. \quad (3.2)$$

Evaluated at $\mathbf{x} = \mathbf{x}_a$, the term $\mathbf{K}_x = \partial\mathbf{y}/\partial\mathbf{x}$ is called *weighting function* or Jacobian matrix, which describes the sensitivity of the measurements to changes in atmospheric parameters. $\hat{\mathbf{b}}$ is the best estimate of the forward model parameters.

The inverse or *retrieval* problem, or simply inversion, on the other hand, deals with the estimation of trace gas state $\hat{\mathbf{x}}$ from the observation vector \mathbf{y} with a retrieval procedure \mathbf{R} (Rodgers, 2000):

$$\hat{\mathbf{x}} = \mathbf{R}(\mathbf{y}, \mathbf{x}_a, \hat{\mathbf{b}}). \quad (3.3)$$

The linearisation of Eq. (3.3) around the a priori state $\mathbf{y}_a = \mathbf{F}(\mathbf{x}_a, \hat{\mathbf{b}})$ gives:

$$\hat{\mathbf{x}} = \mathbf{R}[\mathbf{F}(\mathbf{x}_a, \hat{\mathbf{b}}), \mathbf{x}_a, \hat{\mathbf{b}}] + \mathbf{G}_y[\mathbf{K}_x(\mathbf{x} - \mathbf{x}_a) + \epsilon] \quad (3.4)$$

with $\mathbf{G}_y = \partial\hat{\mathbf{x}}/\partial\mathbf{y}$ called *gain factor*. Here the vector $\mathbf{A} = \mathbf{G}_y\mathbf{K}_x = \partial\hat{\mathbf{x}}/\partial\mathbf{x}$ is referred to as *averaging kernel*, which describes the sensitivity of the retrieval to changes in atmospheric quantities and provides additional information for data interpretation and error analysis. The retrieval algorithm can be applied to obtain the vertical distribution for non-weak absorbers like ozone. For weak absorbers including NO₂, the estimated quantity \hat{x} is an integrated parameter, i.e., the vertical column density or *vertical column*. Note that the retrieved NO₂ state \hat{x} (vertical column) and the true NO₂ state \mathbf{x} (vertical distribution) have different dimensions.

For NO₂, the forward model \mathbf{F} can be linearised around $\mathbf{x}_a = 0$ (Eskes and Boersma, 2003):

$$\mathbf{y} = \mathbf{F}(0, \hat{\mathbf{b}}) + \mathbf{K}_x\mathbf{x} + \epsilon. \quad (3.5)$$

This linear relationship enables a practical separation of the retrieval in Eq. (3.3) into two steps. The absorption along an average photon path from the Sun through the atmosphere to the instrument, i.e., the slant column density or *slant column* $S(\mathbf{y})$, is first calculated, followed by a transfer of this absorption to the estimated vertical column \hat{x} as:

$$\hat{x} = \frac{S(\mathbf{y})}{M(\mathbf{x}_a, \hat{\mathbf{b}})}. \quad (3.6)$$

Referred to as *air mass factor* (AMF), M is derived by a geometric and radiative transfer calculation, depending on the a priori NO₂ distribution \mathbf{x}_a and the estimated forward model parameters $\hat{\mathbf{b}}$. Strictly speaking, $S(\mathbf{y})$ depends also on \mathbf{x}_a , but this dependency can be corrected for a posteriori during the calculation of M (see Sect. 3.4.2).

Appendix A shows a detailed derivation of the DOAS method in the context of general retrieval models with simplifications and approximations, providing a theoretical basis for applying the inversion theory and specifically the DOAS technique to retrieve the total and tropospheric NO₂ columns from satellite remote sensing data.

3.2 DOAS slant column retrieval

The basis of the absorption spectroscopy technique is the *Lambert-Beer's law*, namely the scattered radiation intensity I decreases exponentially with the light path length L in the case of homogeneous absorption:

$$I(\lambda) = I_0(\lambda)e^{-k(\lambda)nL}, \quad (3.7)$$

where I_0 denotes the initial intensity of a light beam, $k(\lambda)$ is the absorption reference spectrum or *absorption cross-section* at wavelength λ , and n is the number density of the absorber. Since k is a unique characteristic property of absorbers, the trace gas slant column S , defined as $\int_0^L n(l)dl$ in Eq. (3.6), can be determined from the ratio of reflectance spectra measurements with the absorbers (earthshine spectrum $I(\lambda)$) and without the absorbers (reference solar spectrum $I_0(\lambda)$) in the light beam:

$$\ln \left[\frac{I(\lambda)}{I_0(\lambda)} \right] = - \sum_g S_g k_g(\lambda) - P(\lambda) \quad (3.8)$$

with the left-hand side expression $\tau = -\ln[I(\lambda)/I_0(\lambda)]$ named as *optical depth*.

In Eq. (3.8), the spectral structures are separated into narrow-band absorption structures of trace gases g and broad-band contributions approximated by a low-order polynomial P , which is the foundation of the DOAS method (Platt and Stutz, 2008). Effectively,

Table 3.1: Main settings of the NO₂ retrieval for ultraviolet-visible satellite instruments.

	GOME v2 IUP-UB ^a	SCIAMACHY MPI-C ^b	OMI DOMINO v3.0 KNMI ^c	GOME-2 GDP 4.9 DLR ^d
fitting window	425-450 nm	430.8-459.5 nm	405-465 nm	425-497 nm
secondary trace gases	O ₃ , H ₂ O _{vap} , O ₄	O ₃ , H ₂ O _{vap} , O ₄ , H ₂ O _{liq} , CHOCHO	O ₃ , H ₂ O _{vap} , O ₄ , H ₂ O _{liq}	O ₃ , H ₂ O _{vap} , O ₄ , H ₂ O _{liq}
polynomial degree	3	5	5	5
reference spectrum	fixed solar reference on 28 February 1997	daily solar reference from the azimuthal scan mirror	annual mean solar ref- erence (2005)	daily solar reference
stratosphere-troposphere separation	data assimilation	limb-nadir matching	data assimilation	modified reference sec- tor method
radiative transfer model	SCIATRAN	McArtim	DAK	VLIDORT
surface albedo	GOME climatology	assumption	OMI climatology	GOME-2 dataset
a priori NO ₂ profile	MOZART	assumption	TM5	IFS(CB05BASCOE)
cloud parameters	FRESCO	FRESCO	OMCLDO2	OCRA/ROCINN

^aNüß (2005); Richter et al. (2005)^bBeirle et al. (2010)^cBoersma et al. (2011); van Geffen et al. (2015)^dValks et al. (2011); Chap. 5 of this work

the narrow-band components of the optical depth and the absorption cross-section, i.e., the differential optical depth and the differential absorption cross-section, respectively, are distinguished from the broad-band components, such as Rayleigh scattering, cloud and aerosol extinction, and surface reflection.

DOAS fit is a least-squares retrieval performed in a selected spectral window with slant column and polynomial coefficients as unknown parameters. Additionally, a number of effects also need to be considered in the fitting process:

$$\ln \left[\frac{I(\lambda + \Delta(\lambda)) - \delta(\lambda)}{I_0(\lambda)} \right] = - \sum_g S_g k_g(\lambda) - \alpha_R R(\lambda) - P(\lambda) \quad (3.9)$$

with $\Delta(\lambda)$ representing small wavelength shifts, $\delta(\lambda)$ an intensity offset correction, α_R a Ring scaling factor, and $R(\lambda)$ a Ring reference spectrum.

wavelength shift

The quality of DOAS strongly depends on a perfect alignment among the spectrum to analyse, the reference spectrum, and the absorption cross-sections. Small wavelength shifts in the order of a few percent can lead to strong systematic structures in the residual. To consider the possible misalignment, wavelength changes are corrected using shift and stretch parameters. It is necessary to mention that the shift and stretch as well as the offset parameters described below are included as non-linear terms in the fitting process, which can be numerically solved by the Marquardt-Levenberg algorithm (Marquardt, 1963; Levenberg, 1944).

intensity offset correction

Besides the radiances backscattered by the Earth's atmosphere, a number of both natural (i.e., the inelastic scattering in the atmosphere and the ocean) and instrumental (e.g., stray light in the spectrometer and change of detector's dark current) sources contribute to an additional "offset" to the scattering intensity. To correct for this drift, an intensity offset correction is modelled using a low-order polynomial with polynomial coefficients as fitting parameters.

Ring effect

Because the solar light is spectrally structured, the strong Fraunhofer lines (spectral absorption lines of the Sun) need to be accurately measured and corrected for passive DOAS applications. The so-called "filling-in" of Fraunhofer lines, referred to as *Ring effect* (Grainger and Ring, 1962), describes an intensity loss at the incident wavelength and a gain at the neighbouring wavelengths. The Ring effect is primarily caused by the inelastic rotational Raman scattering, during which the incident photons undergo a change of not only direction but also wavelength. The Ring effect results in a slight difference between the shape in the direct solar light and the earthshine radiance. In the DOAS analysis, the Ring effect is usually treated as a "pseudo absorber" by including in the DOAS fit a Ring reference spectrum, obtained by convolution of a solar spectrum (Chance and Spurr, 1997) with Raman cross-sections, and a scaling parameter to adjust the amplitude of the Ring reference spectrum.

Figure 3.1 shows an example of applying the DOAS technique to the spectral analysis of NO₂ from GOME-2 reflectance spectra at 425-497 nm. The wavelength range is selected considering prominent NO₂ absorption structures and controllable interferences from other absorbing species, e.g., water vapor (H₂O_{vap}), ozone (O₃), oxygen dimer (O₄),

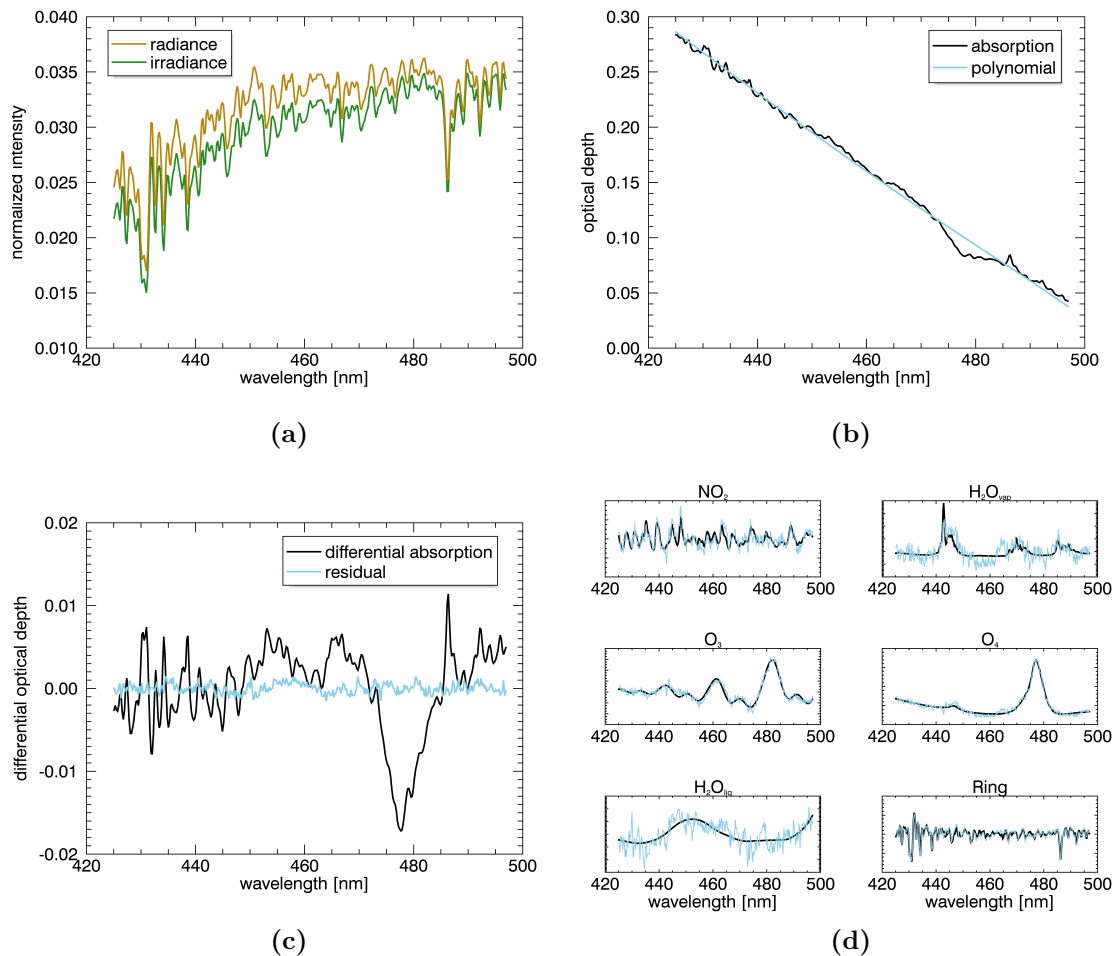


Figure 3.1: Illustration of applying the DOAS technique to the spectral analysis of NO₂ from GOME-2 spectra at 425-497 nm. (a) panel shows the normalised satellite spectrum with the absorbers (earthshine radiance $I(\lambda)$) and without the absorbers (reference solar irradiance $I_0(\lambda)$) in the light beam, (b) shows the separation of the optical depth into the narrow- and broad-band parts using a low-order polynomial, leaving the differential absorption spectrum in (c), and (d) shows the absorption spectra of the trace gases (black lines) scaled to the absorptions determined in the satellite spectrum (blue lines). In the same way as the trace gas absorption, the spectral reflection features of the Ring effect are also analysed.

and liquid water (H₂O_{liq}). In the same way as the trace gas absorption, the spectral reflection features of the Ring effect are also analysed.

Table 3.1 provides an overview of the DOAS fit settings used by different groups for ultraviolet-visible satellite instruments. Proper selection of the fit settings and accurate quantification of the possible resulting effects are essential for the measurement interpretation. For instance, the predefined fitting window 425-450 nm provides the best differential NO₂ absorption signal and the smallest interfering effect, while the 425-497 nm wavelength range improves the information content and increases the effective signal-to-noise ratio (Richter et al., 2011). In addition, the selection of fitting window is affected by instrumental parameters, such as the spectral coverage and calibration issues, which e.g. affect GOME and SCIAMACHY spectra from 460-500 nm. It is important to realize that the use of different fitting windows has critical implications on the interpretation of

the slant columns, mainly due to the wavelength-dependency of the Rayleigh scattering, particularly for polluted conditions with large tropospheric NO₂ columns (Richter et al., 2011). See Sect. 4.1 for further discussion on the fitting window.

3.3 Stratosphere-troposphere separation

Since DOAS yields NO₂ column integrated along the total light path from the Earth’s surface to the top of the atmosphere, the stratospheric contribution need to be estimated and removed to leave the information in the troposphere. This procedure is referred to as *stratosphere-troposphere separation* (Bucsela et al., 2006), after which both total and tropospheric slant columns are converted to vertical columns in Sect. 3.4. Table 3.1 categorizes the stratosphere-troposphere separation methods widely used for previous and current satellite instruments.

(modified) reference sector method

One of the first stratosphere-troposphere separation algorithm is the reference sector method (Richter and Burrows, 2002; Martin et al., 2002; Beirle et al., 2003), which estimates the stratospheric NO₂ columns from measurements over the remote Pacific. The reference sector method relies on the assumptions of longitudinally homogeneous stratospheric NO₂ and negligible tropospheric NO₂ over the Pacific, which may introduce systematic biases in the presence of large longitudinal variations at high latitudes (e.g., inside the polar vortex) or non-zero tropospheric background columns in the Pacific. To overcome the biases introduced by the longitudinal homogeneity assumption, a number of modified reference sector methods (e.g., Leue et al., 2001; Wenig et al., 2004; Valks et al., 2011; Bucsela et al., 2013) apply a masking approach to globally define the “clean” areas and an interpolation scheme over the masked regions. This group of modified reference sector methods is in general simple and robust, without dependency on additional data input (compared to the model-based methods below).

limb-nadir matching

The limb-nadir matching instrumental set-up is employed by SCIAMACHY for a direct stratospheric correction: the stratospheric air masses sensed in nadir were scanned in limb shortly before (Sioris et al., 2004; Sierk et al., 2006; Beirle et al., 2010; Hilboll et al., 2013b). However, such direct coincident measurements of total NO₂ columns (nadir) and stratospheric concentration profiles (limb) are not available for other instruments.

data assimilation

Another two approaches used for stratosphere-troposphere separation rely on the chemistry transport model. The modelled stratospheric NO₂ concentrations can be directly used to estimate the stratospheric columns after empirical corrections of offsets between satellite and model columns (Richter et al., 2005; Hilboll et al., 2013b). Alternatively, the model data can be incorporated by data assimilation (Eskes et al., 2003; Dirksen et al., 2011; van Geffen et al., 2019), in which the three-dimensional distributions of NO₂ are regularly updated such that the modelled stratospheric NO₂ concentrations are in close agreement with satellite measurements for low tropospheric contributions.

3.4 AMF calculation

The conversion between the slant column and the vertical column is implemented by division with an AMF in Eq. (3.6). In the absence of scattering, which is approximately

valid in the stratosphere, the AMF is a geometric factor (Fig. 3.2a) M_{geo} as a function of solar zenith angle (SZA) θ_0 and viewing zenith angle (VZA) θ :

$$M_{geo} = \frac{1}{\cos(\theta_0)} + \frac{1}{\cos(\theta)}. \quad (3.10)$$

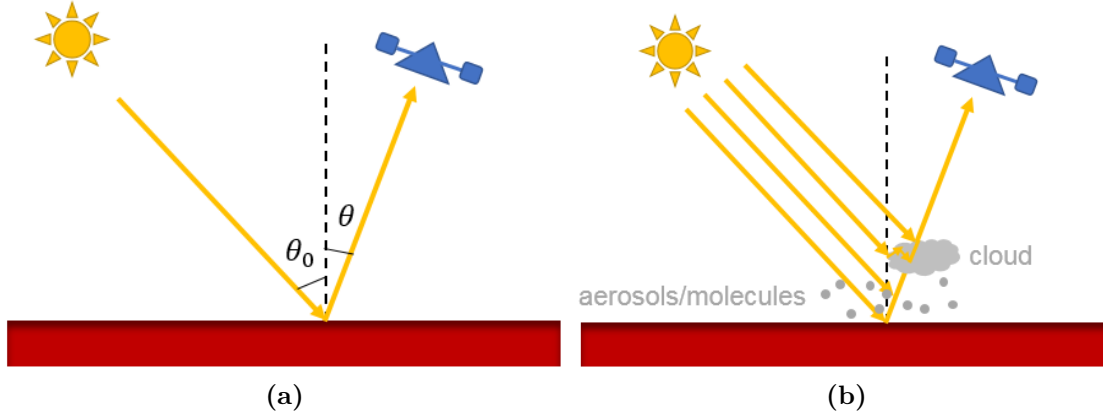


Figure 3.2: Scheme of geometries for a geometric AMF defined in a non-scattering atmosphere (a) and a scattering AMF influenced by the presence of air molecules, clouds, and aerosols (b).

The calculation of tropospheric AMF (Fig. 3.2b), however, is more complicated, since the light path is affected by the presence of air molecules as well as cloud and aerosol particles. For optically thin absorbers like NO_2 , the “scattering” AMF M is calculated by decoupling the altitude-dependent sensitivity of the backscattered spectrum I , defined as *box-AMF* $m(z)$, from the NO_2 abundance at altitude z , defined as *shape factor* $f(z)$ (Palmer et al., 2001):

$$M = \int_0^{\text{tropopause}} m(z)f(z)dz, \quad (3.11)$$

$$m(z) = -\frac{k(z)}{k_e} \frac{\partial \ln I}{\partial \tau}, \quad (3.12)$$

$$f(z) = \frac{n(z)}{\int_0^{\text{tropopause}} n(z)dz}, \quad (3.13)$$

where τ is the optical depth defined in Eq. (3.8), $n(z)$ is the number density, $k(z)$ is the absorption cross-section, and k_e is an average cross-section weighted by the NO_2 vertical distribution to account for the pressure- and temperature-dependency of $n(z)$. Since the pressure-dependency is generally small for NO_2 , the term $k(z)/k_e$ is practically replaced with a temperature correction factor in the AMF calculation (Boersma et al., 2004; Nüß et al., 2006; Bucsela et al., 2013).

3.4.1 A priori NO_2 profile

The number density $n(z)$ is usually obtained from a *chemistry transport model*. A global chemistry transport model generally includes both eulerian transport of aerosols and chemical species in the atmosphere and significant chemical and photochemical reactions of these atmospheric compositions. The continuing model upgrades (e.g., Horowitz et al., 2003; Müller and Stavrou, 2005; Huijnen et al., 2010, 2016; Williams et al., 2017) have

provided a priori NO₂ profiles with considerably improved horizontal, vertical, and temporal resolutions, which are essential to accurately capture the NO₂ variations, particularly for regions with large gradients of NO₂ emissions in space and time (Boersma et al., 2016).

3.4.2 Box-AMF

The box-AMF $m(z)$ is generally calculated with a *radiative transfer model*. The basic equation of radiative transfer model (Schwarzschild, 1914) describes the intensity attenuation due to absorption plus scattering and intensity enhancement due to emission plus multiple scattering:

$$\mu \frac{dI(\tau, \mu, \phi)}{d\tau} = I(\tau, \mu, \phi) - J(\tau, \mu, \phi) \quad (3.14)$$

with μ the cosine of inclination to the upward normal, ϕ the azimuth angle relative to a fixed direction, I the diffuse radiance, and J the source function. Modern treatments of the radiative transfer equation (e.g., Stammes, 2001; Mayer and Kylling, 2005; Spurr, 2008; Deutschmann et al., 2011; Rozanov et al., 2014) have provided useful information in retrieval problems involving least-squares minimization (Rodgers, 2000). Solutions of the forward radiative transfer model include the simulated top-of-atmosphere radiance and the radiance derivatives with respect to atmospheric and surface variables (i.e., weighting functions).

Implemented over the atmospheric layer l of the modelled a priori NO₂ profile, Eq. (3.11) can be written as:

$$M = \frac{\sum_l m_l(\mathbf{b}) x_{a,l} c_l}{\sum_l x_{a,l}}, \quad (3.15)$$

where $x_{a,l}$ is the partial column of the a priori NO₂ profile, and c_l is the temperature correction coefficient (Nüß et al., 2006). In the optically thin limits, the box-AMF m_l in Eq. (3.15) is independent of $x_{a,l}$ (with influences generally smaller than 1%) and thus can be determined with a tabulated calculation in practice. At a representative wavelength (typically the mid-point wavelength of the DOAS fitting window), the constructed box-AMF look-up table is a function of viewing geometries, surface albedo, surface pressure, and atmospheric pressure.

3.4.3 Surface albedo

The surface albedo is commonly described by a global Lambertian-equivalent reflectivity (LER) climatology in NO₂ retrieval, with the surface assumed as a Lambertian reflector with an isotropic diffuse reflection. Surface LER databases (e.g., Herman and Celarier, 1997; Koelemeijer et al., 2003; Kleipool et al., 2008; Tilstra et al., 2017) have been derived based on satellite reflectance data over cloud-free scenes. In addition, the surface reflectivity can be described more realistically by bidirectional reflectance distribution function (BRDF) (Nicodemus et al., 1992), an intrinsic geometry-dependent scattering characteristics containing a specular lobe (reflection by water in the forward scattering direction) and a retroreflection lobe (reflection by vegetation in the backward scattering direction). The surface BRDF has been implemented for the retrievals of both NO₂ and clouds (e.g., Zhou et al., 2010; Lin et al., 2014, 2015; Noguchi et al., 2014; Vasilkov et al., 2017; Lorente et al., 2018; Laughner et al., 2018; Qin et al., 2019), mainly based on external datasets e.g. from the MODerate resolution Imaging Spectroradiometer (MODIS) imaging sensor (Lucht et al., 2000).

3.4.4 Clouds

Depending on the geometrical and microphysical characteristics, clouds act as reflectors and absorbers, influencing the NO₂ retrieval mainly via the albedo effect with increased reflectivity, shielding effect with hidden NO₂ column below the cloud, and multiple scattering with enhanced absorption inside the cloud (Liu et al., 2004; Stammes et al., 2008; Kokhanovsky and Rozanov, 2008). In the presence of clouds, the AMF calculation adopts the *independent pixel approximation* (Cahalan et al., 1994):

$$M = \omega M^{cl} + (1 - \omega) M^{cr} \quad (3.16)$$

with M^{cl} representing the AMF for completely cloudy sky and M^{cr} for completely clear sky. M^{cl} and M^{cr} are derived with Eq. (3.15) with M^{cl} mainly relying on the cloud pressure (height) and the cloud albedo (optical depth). The cloud radiance fraction ω is derived from the radiometric or effective cloud fraction c_f :

$$\omega = \frac{c_f I^{cl}}{(1 - c_f) I^{cr} + c_f I^{cl}}, \quad (3.17)$$

where I^{cl} and I^{cr} are the radiances for cloudy and clear scenes, respectively, depending mostly on the viewing geometry, surface albedo and cloud albedo (optical depth).

Assuming that the clouds can be represented by homogeneous and (in horizontal direction) infinitely extended plane-parallel slabs, the three-dimensional radiative effects of clouds can be approximated by a one-dimensional radiative transfer model. Current cloud retrieval algorithms (e.g., Kokhanovsky et al., 2003; Grzegorski et al., 2006; Wang et al., 2008; Lelli et al., 2012; Veeffkind et al., 2016; Lutz et al., 2016; Loyola et al., 2018) derive radiometric cloud fraction, cloud pressure (height), and cloud albedo (optical depth) from the top-of-atmosphere reflectances, with the clouds treated as either opaque Lambertian reflectors or Mie scattering layers. The Mie scattering cloud model, which allows for the penetration of photons through the cloud, is more realistic than the Lambertian cloud model, which screens completely the atmosphere below the cloud (Rozanov and Kokhanovsky, 2004; Richter et al., 2015).

3.4.5 Aerosols

The aerosols and thin clouds are comparable in radiative effect, namely the albedo effect, shielding effect, and multiple scattering (Palmer et al., 2001; Leitão et al., 2010). Because cloud retrievals can hardly distinguish between clouds and aerosols, the aerosol effects on the AMF calculation are commonly corrected implicitly by assuming that the effective clouds partially account for the aerosol impacts (Boersma et al., 2004, 2011). In addition, an explicit aerosol correction is also possible if additional aerosol parameters (e.g., from chemistry transport models or external aerosol measurements) are available (e.g., Lin et al., 2014, 2015; Kuhlmann et al., 2015; Castellanos et al., 2015; Chimot et al., 2019; Liu et al., 2019).

3.5 Tropospheric vertical column computation

Figure 3.3 illustrates the processing chain of the total and tropospheric NO₂ retrieval for ultraviolet-visible backscatter satellite instruments. In the optically thin limit, the total slant column $S(\mathbf{y})$ can be regarded as a sum of the stratospheric and tropospheric

components, and the tropospheric vertical column \hat{x}_{tr} can be estimated from Eq. (3.6) as:

$$\hat{x}_{tr} = \frac{S(\mathbf{y}) - S_{st}}{M_{tr}(\mathbf{x}_{a,tr}, \hat{\mathbf{b}})}, \quad (3.18)$$

where S_{st} is the stratospheric slant column, and $M_{tr}(\mathbf{x}_{a,tr}, \hat{\mathbf{b}})$ is the tropospheric AMF.

The tropospheric NO₂ column computation is complicated in case of cloudy conditions. As a result of the shielding effect of optically thick clouds (see Sect. 3.4.4), a large fraction of the tropospheric NO₂ pollution below the clouds can not be detected by satellites. Therefore, satellite NO₂ measurements are typically filtered for cloud radiance fraction < 0.5 or radiometric cloud fraction < 0.2 to ensure a strong signal from the boundary layer. Note that the NO₂ column below the cloud, the so-called “ghost column”, is estimated implicitly using the cloudy-sky AMF M^{cl} in Eq. (3.16). Since this procedure relies on a clear-sky a priori NO₂ profile and neglects the difference of this profile in the clear-sky and cloudy-sky conditions, larger uncertainties are expected for the cloudy-sky AMF calculation (Valks et al., 2011).

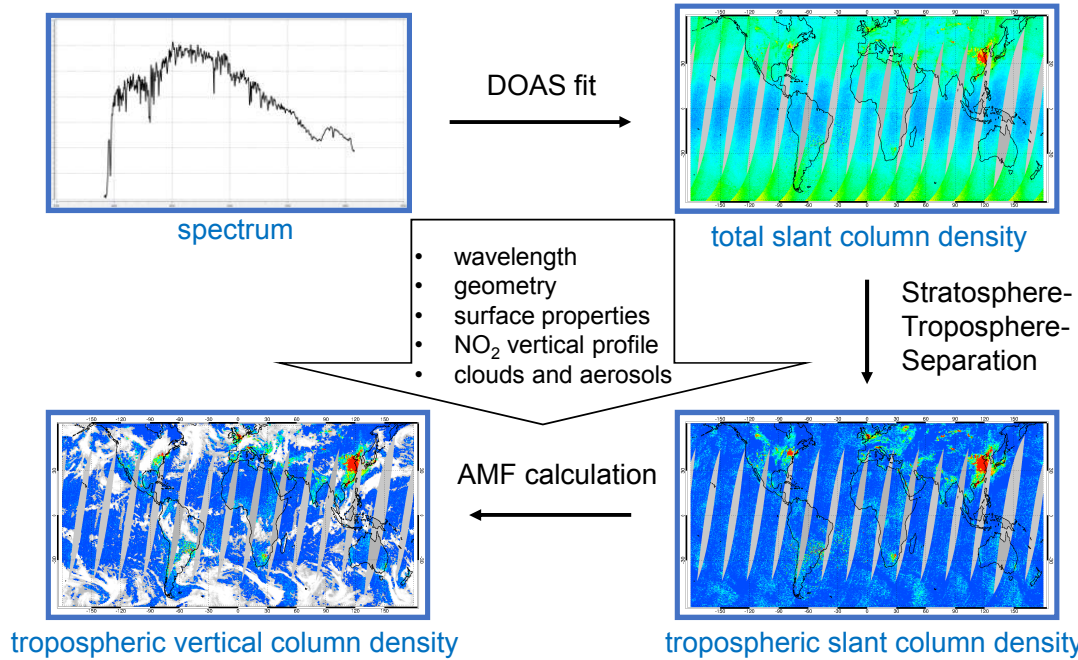


Figure 3.3: Processing chain of the total and tropospheric NO₂ retrieval for ultraviolet-visible backscatter satellite instruments.

3.6 Error analysis

The three components on the right-hand side of Eq. (3.18) are the main error sources in the computation of tropospheric NO₂ columns, which are in general uncorrelated, since they are obtained from independent steps as introduced above. In the following, the uncertainties involved in individual retrieval steps are introduced.

3.6.1 DOAS assumptions

For simplicity and efficiency reasons, a number of assumptions are made for the application of the DOAS least-squares fitting, which is described in this section to provide a better understanding of the data quality and retrieval uncertainty.

Influence of the instrumental spectral resolution can be neglected.

The resolution of the measured spectrum recording the high-resolution NO₂ absorption structures is limited by the spectrometer spectral resolution, which typically can not resolve the natural line widths of the absorptions. Accordingly, the laboratory absorption cross-sections need to be convolved on the spectrometer resolution using the instrumental spectral response function or *slit function*. However, as both $I(\lambda)$ and $I_0(\lambda)$ in Eq. (3.8) have been filtered by the slit function before the ratio, the Fraunhofer structures can not be totally removed, introducing an I_0 -effect (Johnston, 1996). The I_0 -effect can be corrected using modified absorption cross-sections for non-weak absorbers like ozone (Johnston, 1996) or can be simply neglected for most of the atmospheric absorbers including NO₂ (Wagner et al., 2001).

The absorption cross-sections are independent of pressure and temperature.

While the pressure-dependency of the absorption cross-sections can be generally neglected, the temperature-dependency is strong for NO₂ (Fig. 3.4) with an approximately linear effect. The temperature-dependency of NO₂ absorption cross-sections can be taken into account by including several cross-sections with different temperatures or by applying a single cross-section and implementing a posteriori temperature-correction in the AMF calculation in Eq. (3.15).

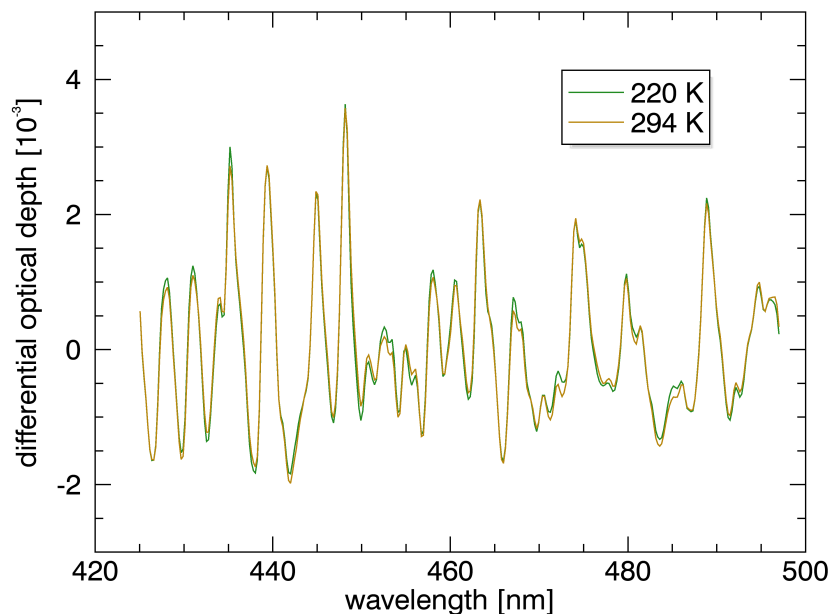


Figure 3.4: Absorption spectra of NO₂ fitted using absorption cross-sections at 220 K and 294 K.

The measured intensity can be represented by one effective light path.

One largest challenge in passive DOAS applications stems from the difficulty to determine the light path length, since the observed light follows complicated paths in the atmosphere, and each light beam travels on an individual path. For most situations, a most probable light path can be defined, and the length of this effective light path is determined in the radiative transfer calculation. However, due to the uncertainties in the information on the vertical distribution of NO₂, clouds, and aerosols as well as the optical properties of cloud and aerosol particles, the results of the radiative transfer calculation are inherently uncertain. See Sects. 4.2 and 4.3 for further discussion on the uncertainties introduced by the radiative transfer calculation.

The effective light path is independent of wavelength.

In DOAS, the light path is normally assumed to be independent of wavelength for weak absorbers. However, as shown in Fig. 3.5a, the sensitivity to NO₂ absorption increases with wavelength in the troposphere, for instance, by $\sim 40\%$ between 425-497 nm for a polluted boundary layer with 1×10^{16} molec/cm² NO₂, resulting mainly from the wavelength-dependency of the Rayleigh scattering and indicating the importance of selecting an appropriate wavelength for AMF calculation. For heavily polluted scenarios, the fitting residuals can be improved by including a pseudo cross-section in the DOAS fitting (Fig. 3.5b), which is a NO₂ cross-section scaled linearly by wavelength and orthogonalised to the actual NO₂ cross-section (Richter et al., 2015).

The effective light path is independent of NO₂ amount.

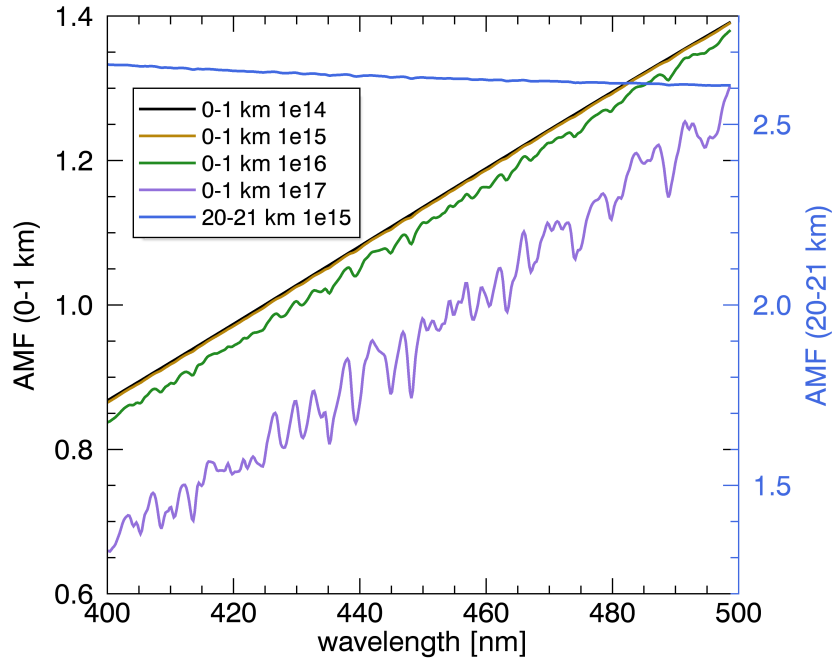
For optically thin absorbers like NO₂, the absorption effect on the overall radiations can be generally ignored. If, however, the NO₂ absorption is largely enhanced in the presence of heavily polluted scenarios, for instance, with a NO₂ column larger than 1×10^{16} molec/cm² in Fig. 3.5a, the calculated AMFs decrease by up to 25% and show spectral structures linked to NO₂ absorption bands. This effect can be taken into account by including a correction term based on tabulated factors between the NO₂ slant column and AMF in the DOAS fit (Richter et al., 2015).

The measurement errors of individual pixels are random and uncorrelated.

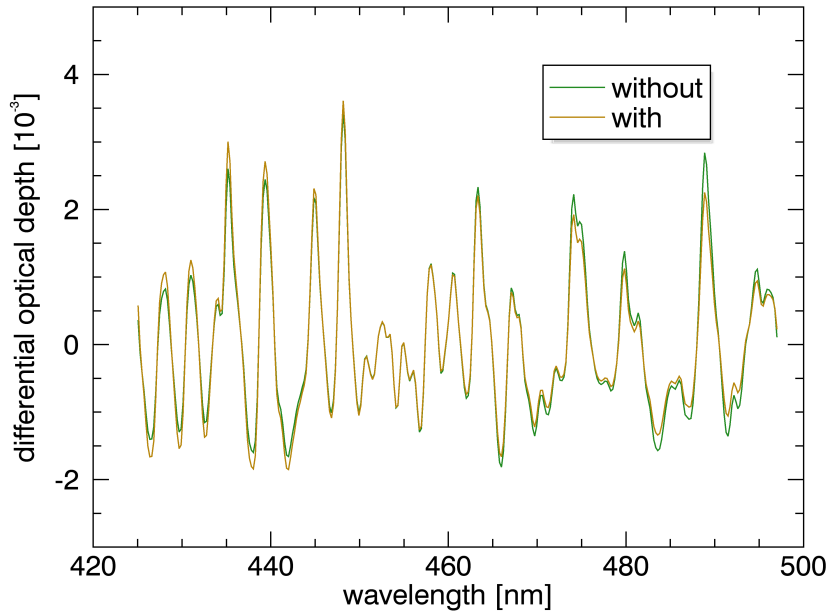
On one hand, the measurement error is normally dominated by photon noise and can be regarded as a source of random error. On the other hand, due to the limited instrumental spectral resolution, a single wavelength is imaged on a number of pixels, and thus the neighbouring pixels are not completely independent. Wavelength-dependent random changes in the instrument, consequently, will lead to systematic spectral structures, requiring a careful treatment of the DOAS residual structures other than pure noise, which can be related to the inaccurate reference spectra, the spectral misalignments, or instrumental issues.

3.6.2 Slant column uncertainties

The slant column uncertainties are commonly estimated using a statistic method (Wenig, 2001; Boersma et al., 2007), based on the spatial variability in the slant columns over confined pristine areas with known limited geophysical variability (the Pacific Ocean). For each spectral fit, the clean tropical Pacific region (20°S-20°N, 160°E-180°E) is divided into small boxes ($2^\circ \times 2^\circ$), and the variation of the NO₂ slant columns within each box is regarded as a good measure of random noise. Figure 3.6 shows an example of calculating the slant column error from the distribution of the slant column deviations. The Gaussian distribution has a full width at half maximum (FWHM) of 1.36×10^{15} molec/cm² for the



(a)



(b)

Figure 3.5: Effect of the wavelength-dependency of the AMFs on the DOAS retrieval for $\text{SZA}=50^\circ$, $\text{VZA}=0.25^\circ$, relative azimuth angle (RAA) $=90^\circ$, and surface albedo $=0.05$. (a) panel shows the wavelength-dependent AMFs for various pollution scenarios in the troposphere (0-1 km) and in the stratosphere (20-21 km). (b) panel shows the absorption spectra of NO₂ fitted with and without including the orthogonalised scaled NO₂ cross-section (NO₂ AMF proxy) for a surface layer with a NO₂ column of 1×10^{16} molec/cm².

425-450 nm fitting window and 1.04×10^{15} molec/cm² for the extended 425-497 nm wavelength range, which corresponds to a slant column error of $\sim 5.7 \times 10^{14}$ molec/cm² and $\sim 4.4 \times 10^{14}$ molec/cm², respectively.

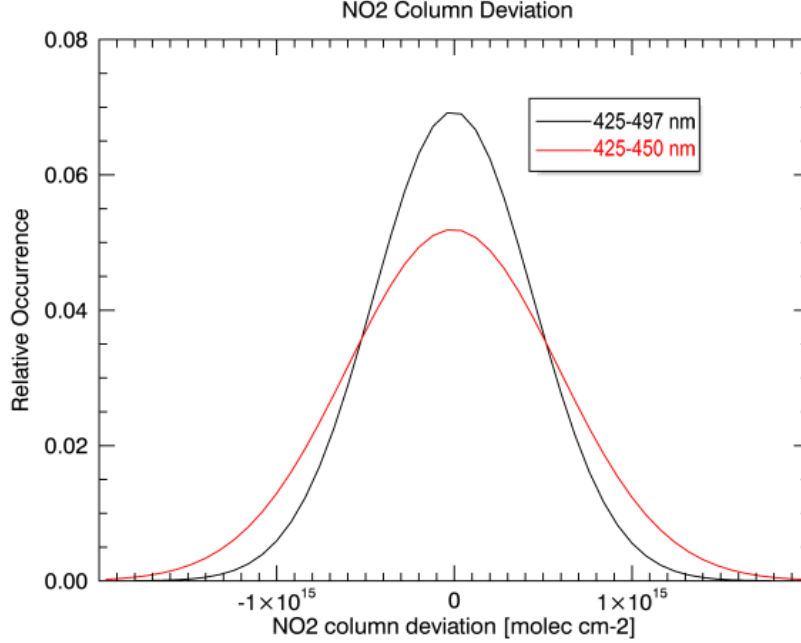


Figure 3.6: Illustration of estimating the slant column uncertainties from the spatial variability in the slant columns over the Pacific Ocean. Distribution of the derivations of GOME-2 NO₂ slant columns from corresponding $2^\circ \times 2^\circ$ box mean values in the tropical Pacific Ocean (20°S - 20°N , 160°E - 180°E) is shown for January 2008. The width of the Gaussian corresponds to a slant column error of $\sim 5.7 \times 10^{14}$ molec/cm² for the 425-450 nm fitting window and $\sim 4.4 \times 10^{14}$ molec/cm² for the extended 425-497 nm wavelength range. Curves are normalized to have unit area and centred on zero.

3.6.3 Stratospheric column uncertainties

The uncertainties in the stratospheric column calculation are estimated to be generally smaller than 3×10^{14} molec/cm² (Boersma et al., 2011; Valks et al., 2011; Bucsela et al., 2013), depending on the separation method. For the modified reference sector method, the assumption of the low longitudinal variability of stratospheric NO₂ increases the uncertainty for reference sector pixels with a strong spatio-temporal variability in stratospheric NO₂. On the contrary, the data assimilation method accounts for the dynamical features in stratospheric NO₂ due to the use of model forecast, but the stratosphere-troposphere-separation starts to quantitatively depend on a chemistry transport model.

3.6.4 AMF uncertainties

For the purpose of error analysis, the tropospheric AMF $M_{tr}(\hat{\mathbf{b}})$ in Eq. (3.18) ($\mathbf{x}_{a,tr}$ is dropped for simplicity) can be linearised around the true values of various a priori and model variables \mathbf{b} :

$$M_{tr}(\hat{\mathbf{b}}) = M_{tr}(\mathbf{b}) + \mathbf{K}_{\hat{\mathbf{b}}}(\hat{\mathbf{b}} - \mathbf{b}), \quad (3.19)$$

where $\mathbf{K}_{\hat{\mathbf{b}}} = \partial M_{tr} / \partial \hat{\mathbf{b}}$ denotes the local sensitivity of the AMF to the a priori and model parameters $\hat{\mathbf{b}}$. The AMF uncertainty or *error covariance* is calculated as:

$$\langle \epsilon_{M_{tr}}^2 \rangle = \left\langle \left(\sum_{\hat{b}} K_{\hat{b}} \epsilon_{\hat{b}} \right)^2 \right\rangle = \sum_{\hat{b}, \hat{b}'} K_{\hat{b}} K_{\hat{b}'} \langle \epsilon_{\hat{b}} \epsilon_{\hat{b}'} \rangle, \quad (3.20)$$

where $\sigma_b = \sqrt{\langle \epsilon_b^2 \rangle}$ with $\epsilon_b = \hat{b} - b$ is the best estimate of the uncertainty in b . If the uncertainties in the input variables are mutually uncorrelated, i.e., the error covariance terms $\langle \epsilon_{\hat{b}} \epsilon_{\hat{b}'} \rangle = 0$ for $\hat{b} \neq \hat{b}'$, the AMF uncertainty $\sigma_{M_{tr}} = \sqrt{\langle \epsilon_{M_{tr}}^2 \rangle}$ can be written as:

$$\sigma_{M_{tr}}^2 = \sum_{\hat{b}} (K_{\hat{b}} \sigma_{\hat{b}})^2. \quad (3.21)$$

See Sect. 4.3 for quantification of the AMF uncertainties.

3.6.5 Tropospheric column uncertainties

Referring to Eq. (3.18), the overall error $\sigma_{\hat{x}_{tr}}$ of the tropospheric column \hat{x}_{tr} can be expressed as:

$$\begin{aligned} \sigma_{\hat{x}_{tr}}^2 &= \left(\frac{\partial \hat{x}_{tr}}{\partial S} \right)^2 \sigma_S^2 + \left(\frac{\partial \hat{x}_{tr}}{\partial S_{st}} \right)^2 \sigma_{S_{st}}^2 + \left(\frac{\partial \hat{x}_{tr}}{\partial M_{tr}} \right)^2 \sigma_{M_{tr}}^2 \\ &= \left(\frac{1}{M_{tr}} \right)^2 \sigma_S^2 + \left(\frac{1}{M_{tr}} \right)^2 \sigma_{S_{st}}^2 + \left(\frac{S - S_{st}}{M_{tr}^2} \right)^2 \sigma_{M_{tr}}^2, \end{aligned} \quad (3.22)$$

which is a function of the error on the slant column S during the spectral fitting (see Sects. 3.6.1 and 3.6.2), the uncertainty in the stratospheric slant column S_{st} (see Sect. 3.6.3), and the uncertainty in the a priori and ancillary data required for the calculation of the tropospheric AMF M_{tr} (see Sect. 3.6.4). For clean scenarios with small amounts of NO_2 , the retrieval uncertainty is dominated by the errors in S and S_{st} , while for polluted cases, the retrieval uncertainty is mainly driven by the uncertainties in M_{tr} (Boersma et al., 2004, 2018).

Chapter 4

Analysis of NO₂ retrieval

The total and tropospheric NO₂ retrieval algorithm comprises three steps: the slant column fitting with the DOAS method from the measured (ir)radiance, the separation of the stratospheric contribution, and the conversion of the slant column to the vertical column through division by the AMF, as detailed in Chap. 3. In this chapter, the systematic and random errors introduced by applying the DOAS slant column retrieval are estimated by applying the retrieval scheme to synthetic spectra. Sensitivity studies are made to explain to which extent the AMF calculation is affected by individual atmospheric and surface parameters, based on which the AMF uncertainties are estimated quantitatively.

4.1 DOAS fit using synthetic data

One important task of the DOAS analysis is the accurate determination of the uncertainties in the retrieved parameters (see Sect. 3.6.1 for simplifications adopted by the DOAS fit). To evaluate the DOAS method, the fitting technique is applied to synthetic satellite measurements from both basic atmospheric scenarios with NO₂ absorption at different altitude regimes (Sect. 4.1.1) and realistic atmospheric scenarios with various pollution conditions (Sect. 4.1.2). The DOAS retrievals are implemented for three commonly used fitting windows (see Table 3.1): the narrow 425-450 nm window with smallest interferences by other species, the wider 405-465 nm window to improve the effective signal-to-noise ratio, and the widest 425-497 nm window with extension to longer wavelengths. The 425-497 nm window has a stronger sensitivity to the NO₂ columns in boundary layer due to the decreasing Rayleigh scattering with wavelength (see Fig. 3.5a). However, the spectral interfering effect (e.g., from liquid water and soil) also increases (Richter et al., 2011).

4.1.1 Basic scenarios

Table 4.1 describes the set-up of the radiative transfer simulations for an idealized atmosphere with only Rayleigh scattering and NO₂ absorption. Based on the radiative transfer model VLIDORT version 2.7 (Spurr, 2006), the clear-sky top-of-atmosphere radiance spectra and slant columns are simulated to yield input data and reference data for the DOAS retrieval, respectively. Covering a wide range of measurement geometries and surface albedo values, a total of 300 simulated spectra between 405-497 nm are computed with a 0.22 nm step (spectral sampling of GOME-2 and TROPOMI) for the mid-latitude summer atmosphere (Anderson et al., 1986). One single NO₂ absorption cross-section (Vandaele et al., 1998) at 220 K, convolved with a Gaussian line shape with a FWHM of 0.54 nm (spectral resolution of GOME-2 and TROPOMI), is included in the radia-

Table 4.1: Radiative transfer model and model parameters in calculating the synthetic spectra and AMFs.

radiative transfer model	VLIDORT v2.7
atmospheric profile	mid-latitude summer atmosphere
SZA	10°, 30°, 50°, 70°, 88°
VZA	75°, 50°, 30°, 10°, 0°
RAA	0°, 90°, 180°
surface albedo	0.05, 0.2, 0.5, 0.8
surface pressure	1010 hPa
NO ₂ vertical profile	constant volume mixing ratio within a 1 km layer

tive transfer simulations. The simulations are implemented for several NO₂ scenarios at different altitude regimes (boundary layer, free troposphere, and stratosphere) and with various total column amounts (from 1×10^{14} to 1×10^{17} molec/cm²). The influences from other gases, the Ring effect, measurement noise, clouds, and aerosols are not considered for the basic scenarios.

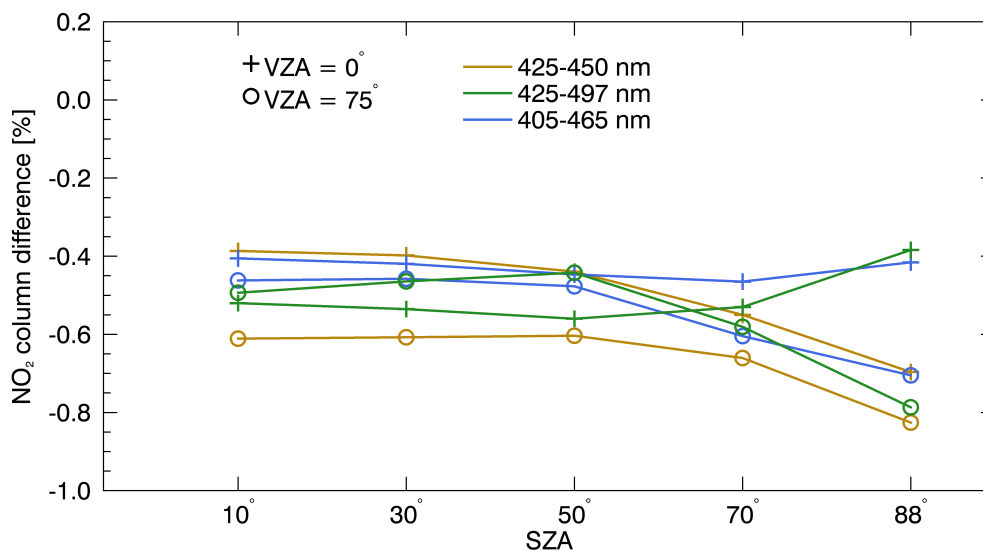


Figure 4.1: Relative differences in NO₂ slant columns simulated by VLIDORT and retrieved by DOAS for a tropospheric layer at 0-1 km with a total NO₂ column of 1×10^{15} molec/cm². The DOAS retrievals are implemented for three fitting windows (see Sect. 4.1). The set of considered geophysical parameters is given in Table 4.1, and here measurements are shown for RAA = 0° and surface albedo = 0.05.

Figure 4.1 shows the relative differences in the simulated and retrieved slant columns for a boundary layer at 0-1 km with a total NO₂ vertical column of 1×10^{15} molec/cm². The DOAS retrievals are implemented using the QDOAS software (Danckaert et al., 2015) developed at the Belgian Institute for Space Aeronomy (BIRA-IASB). For all the three fitting windows, the calculated NO₂ slant columns are close to the a priori truth (based on AMFs near the mid-point wavelength of the given fitting window). Differences are within 1% for the tropospheric NO₂ layer and 0.15% for the stratospheric NO₂ layer (not shown). Slightly larger biases are found for high SZAs and high VZAs, due to the small amount of

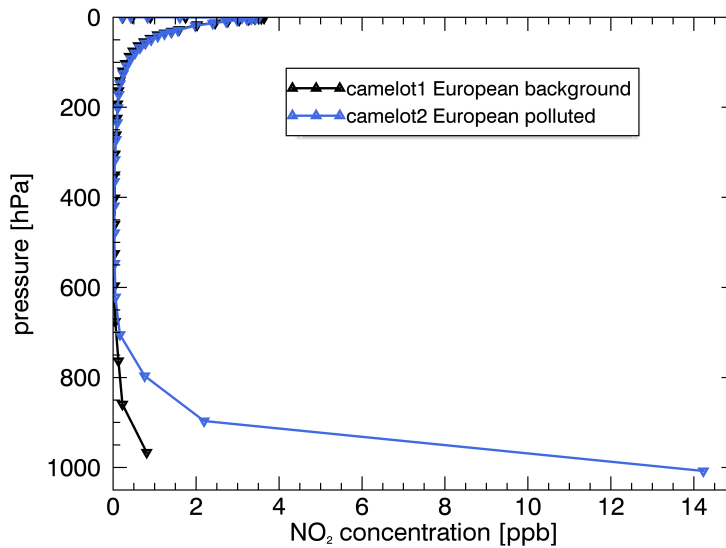


Figure 4.2: A priori NO_2 profiles for CAMELOT European background scenario and European polluted scenario.

radiation reaching the NO_2 layer or incomplete sphericity correction in VILDORT, which corrects for the curved atmosphere in the solar and single scattered beam but applies a plane-parallel assumption for the multiple scattered photons (Spurr, 2008).

4.1.2 CAMELOT scenarios

Within the verification activities for the TROPOMI instrument, a common set of scenarios and synthetic data are used to analyse the DOAS-based retrieval algorithms (Richter et al., 2015). Performed at the Institute of Environmental Physics (IUP-UB) at the University of Bremen (Germany) using SCIATRAN version 3.2.5 (Rozanov et al., 2014), the radiative transfer simulations include temperature-dependent absorption cross-sections, the Ring effect, and realistic NO_2 vertical profiles as defined within the Chemistry of the Atmosphere Mission concEpts and sentinel Observations Techniques (CAMELOT) project (Veefkind, 2009).

CAMELOT aims at the definition of the air quality and climate protocol monitoring parts of GEMS, Sentinel-4, and Sentinel-5 missions (see Sect. 2.5.2). In CAMELOT, a series of geophysical scenarios is defined for representative areas, such as polluted regions in Europe, Asia, and North America. Figure 4.2 shows the a priori NO_2 vertical profiles for the CAMELOT European background scenario (southern France) and European polluted scenario (the Benelux region) as examples. For each CAMELOT atmospheric scenario, 28 viewing geometries are defined in the radiative transfer simulations to cover the full swath width of TROPOMI with VZA varying from -54° to $+54^\circ$ (defined at the satellite). See Richter et al. (2015) for detailed set-up of the synthetic data.

Figure 4.3 shows the comparisons of the simulated and retrieved slant columns for the CAMELOT European background scenario and European polluted scenario. The retrieved NO_2 slant columns are lower than the simulated numbers by up to 9% for the background scenario and up to 20% for the polluted scenario. Differences within 8% are found between different fitting windows for both simulated and retrieved results.

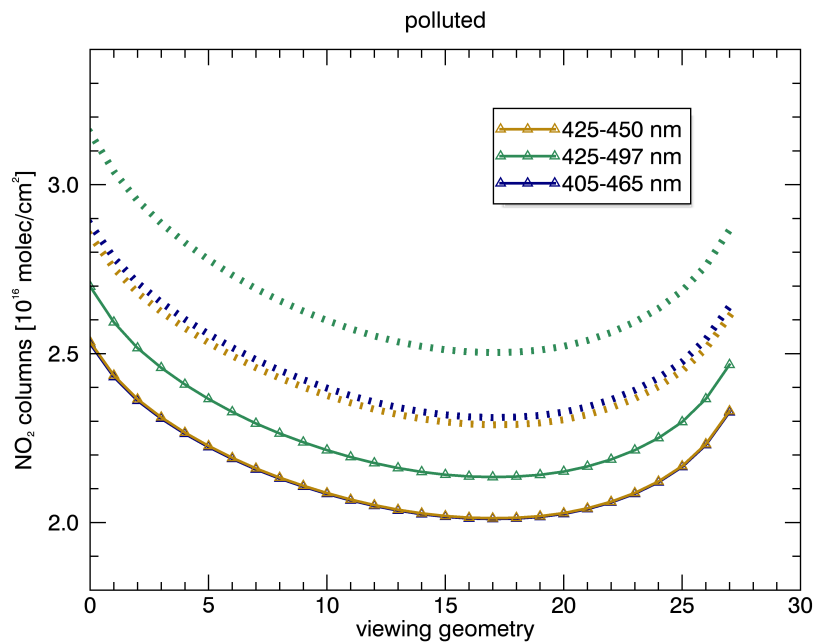
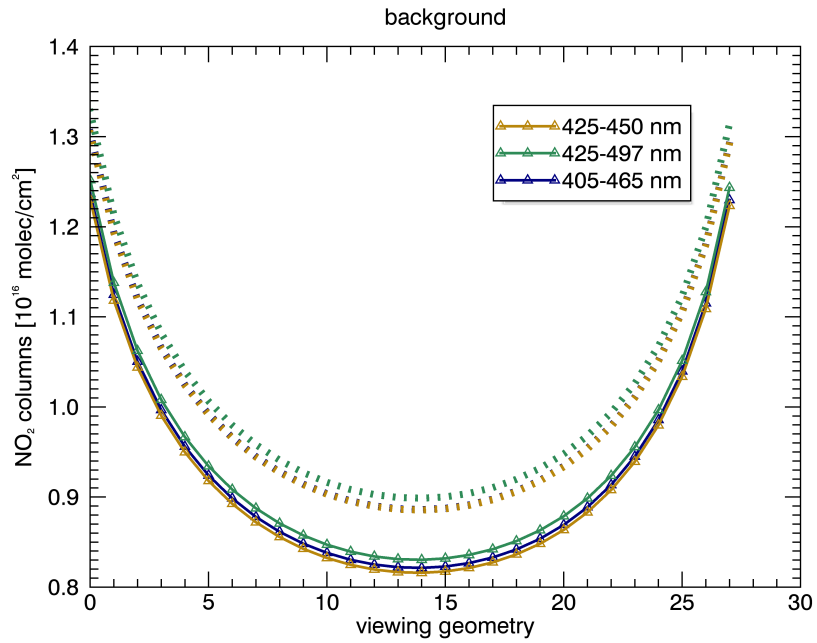


Figure 4.3: NO₂ slant columns simulated by SCIATRAN (dotted lines) and retrieved by DOAS (solid lines) using various fitting windows for CAMELOT European background scenario (a) and European polluted scenario (b). The comparisons are shown for 28 viewing geometries covering a full swath width of TROPOMI with VZA varying from -54° to $+54^\circ$.

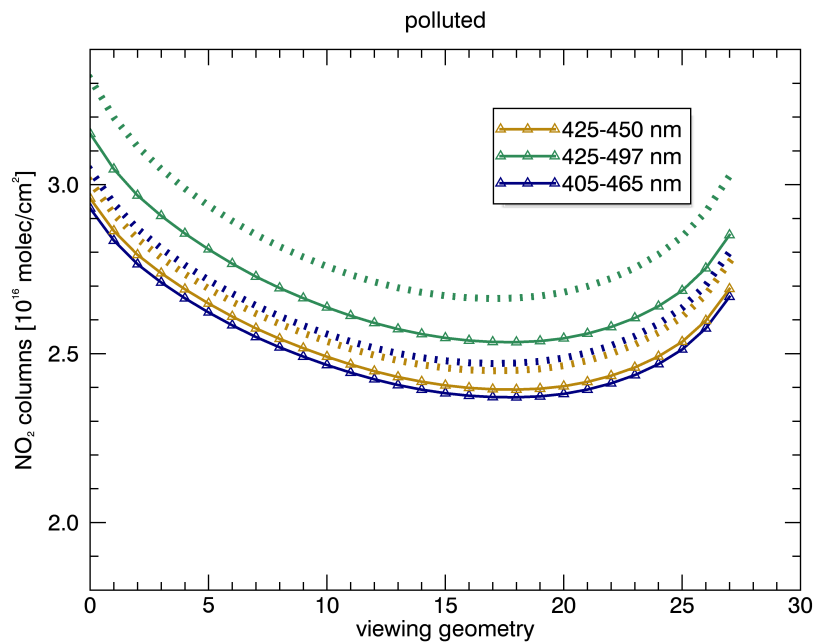
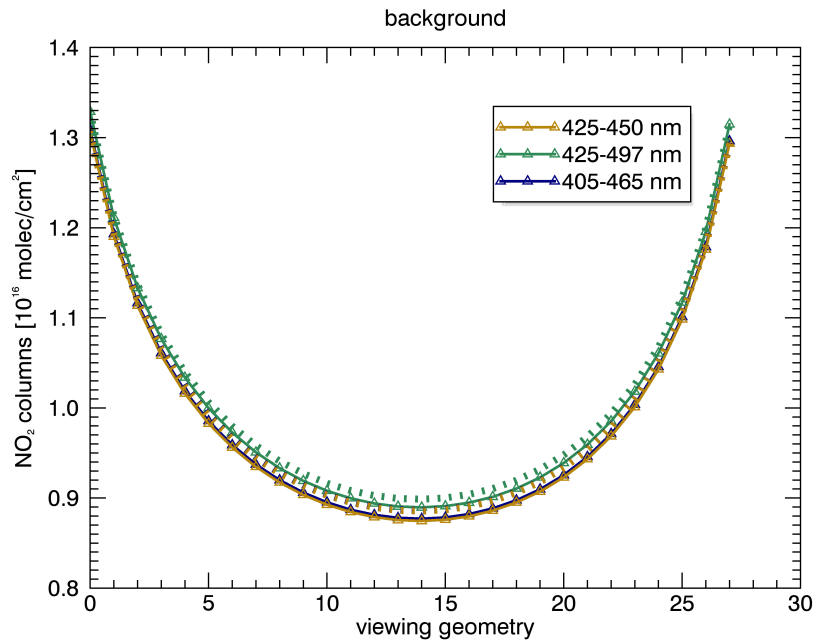


Figure 4.4: Similar as Fig. 4.3 but for simulations without the temperature-dependency of the NO_2 absorption cross-sections (only one NO_2 cross-section measured at 220 K is included in the SCIATRAN simulations).

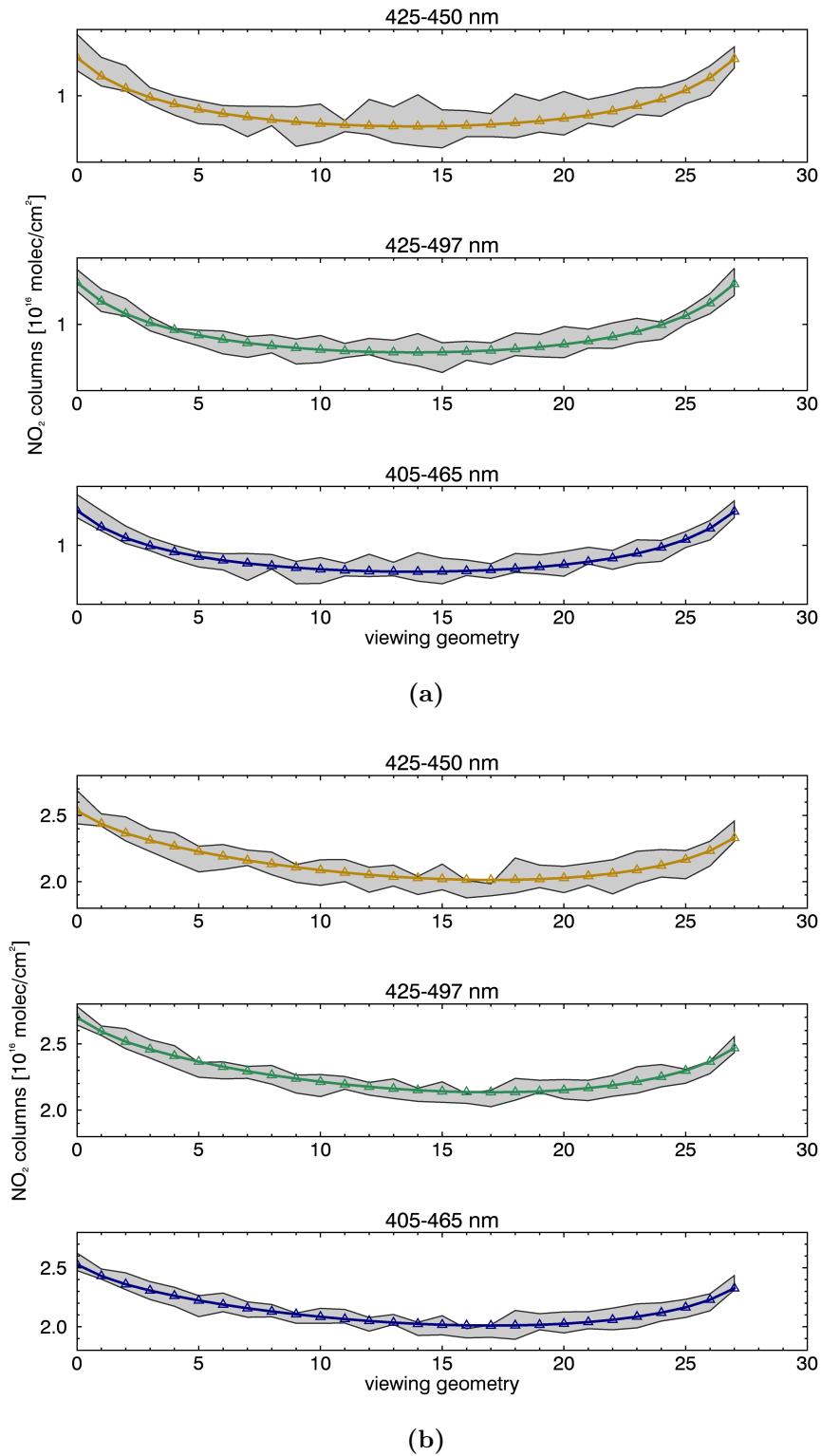


Figure 4.5: NO₂ slant columns retrieved using various fitting windows for CAMELOT European background scenario (a) and European polluted scenario (b). Solid lines show the results retrieved from the simulated spectra without noise in Fig. 4.3. Grey shadow indicates the standard deviations of the fitting results from noisy spectra.

Possible explanations for these differences include the temperature-dependency of the NO₂ absorption cross-sections (see Fig. 3.4) and the wavelength-dependency of the AMFs (see Fig. 3.5a).

To further analyse the impact of the temperature-dependency of the NO₂ absorption cross-sections, results from a dedicated run of SCIATRAN without temperature-dependency (only one NO₂ cross-section measured at 220 K is included in the radiative transfer simulations) are shown in Fig. 4.4. Compared to Fig. 4.3, largely reduced differences are noticed for both scenarios, with remaining differences lower than 1% for the background case and 5% for the polluted case, mainly attributed to the wavelength-dependency of the AMFs. Note that the temperature-dependency of the NO₂ absorption cross-sections are considered for the vertical column calculation with a posteriori correction in Eq. (3.15), and the wavelength-dependency of the AMFs are considered by selecting an appropriate wavelength in Sect. 3.4.2.

For each viewing geometry, nine noisy spectra with normally distributed uncorrelated noise (signal-to-noise ratio = 1000) are simulated in addition to the noise-free spectrum used in Fig. 4.3. Figure 4.5 shows the statistics of the fitting results of noisy spectra for the CAMELOT European background and polluted scenario. Variations in the standard deviations between different viewing geometries are resulted from the different noisy spectra. Taking the background scenario as an example, the standard deviations vary between 0.03-0.15 for the 425-450 nm fitting window and 0.04-0.09 for 425-497 nm and 405-465 nm. The lower standard deviations for the 425-497 nm and 405-465 nm fitting windows benefit from the inclusion of more NO₂ absorption structures from the wider wavelength ranges.

4.1.3 Summary of synthetic studies

For the idealized scenarios with only Rayleigh scattering and NO₂ absorption, the slant columns retrieved with three fitting windows are close to the simulations with biases lower than 1% for NO₂ in the tropospheric layer and 0.15% for stratospheric layer. For the realistic CAMELOT scenarios, the slant columns are underestimated by up to 9% for the background case and 20% for the polluted case, mainly related to the temperature-dependency of the NO₂ absorption cross-sections and the wavelength-dependency of the AMFs, both of which will be taken into account in the vertical column calculation. When the synthetic data without the temperature-dependency of the NO₂ absorption cross-sections are applied in the DOAS fit, the biases are reduced to 1% for the background case and 5% for the polluted case. Performed on the noisy data, the extended 405-465 nm and 425-497 nm fitting windows show a better performance, beneficial from the inclusion of more spectral points and hence the improvement of the effective signal-to-noise ratio. The 425-497 nm wavelength range is more advantageous due to a stronger sensitivity to NO₂ in boundary layer.

4.2 AMF sensitivities

The AMF is used to convert the slant column to the vertical column and closely related to the accuracy of the tropospheric column retrieval (see Sect. 3.6.5). Based on Eqs. (3.15) and (3.16), the tropospheric AMF is determined with the altitude-dependent box-AMF (calculated with a radiative transfer model) and the a priori NO₂ vertical profile shape, relying on a number of model parameters and cloud properties. In this section, the importance of each input parameter is addressed for the tropospheric AMF calculation

Table 4.2: Radiative transfer model and model parameters in calculating the tropospheric AMFs for clear sky (M_{tr}^{cr}) and cloudy sky (M_{tr}^{cl}) as reference.

radiative transfer model	VLIDORT v2.7
atmospheric profile	mid-latitude summer atmosphere
wavelength	437.5 nm
measurement geometry	SZA=40°, VZA=20°, RAA=135°
surface albedo	0.05
surface pressure	1010 hPa

Table 4.3: Cloud properties in calculating the tropospheric AMFs for cloudy sky (M_{tr}^{cl}) as reference.

cloud model	Mie scattering cloud
single scattering albedo	1
phase function	Henyeey-Greenstein (asymmetry parameter=0.85)
cloud optical thickness	20
cloud top height	6 km
geometric thickness	1 km

with sensitivity tests perturbing the parameters upon a “reference retrieval” (Sect. 4.2.1). The effects of model parameters (Sect. 4.2.2) and cloud properties (Sect. 4.2.3) are illustrated for the box-AMF calculation, and their effects on the determined tropospheric AMFs are quantified based on assumed a priori NO₂ profiles.

4.2.1 Reference retrieval

The reference retrievals are implemented according to Tables 4.2 and 4.3 for completely clear sky and completely cloudy sky, respectively. The reference retrievals apply typical a priori NO₂ profiles simulated with the chemistry transport model TM5 (Huijnen et al., 2010; Williams et al., 2017) for a clean scenario, with most of NO₂ columns located in the stratosphere, and for a polluted scenario, with a pronounced peak in the boundary layer, as shown in Fig. 4.6.

Figure 4.7 (black lines) shows the reference box-AMFs for clear sky and cloudy sky, which are independent of the assumed a priori profile (see Sect. 3.4.2). The clear-sky box-AMFs decrease exponentially towards the surface due to the stronger Rayleigh scattering that reduces the light path by scattering a part of photons before they reach the surface. The fully-cloudy box-AMFs show strong gradients around the cloud with higher values above the cloud layer (albedo effect) and lower values below the cloud layer (shielding effect). Largest numbers are displayed close to the top the cloud, mainly explained by the multiple scattering, above which the values decrease to the stratospheric limit.

Based on the box-AMFs in Fig. 4.7 (black lines), the reference tropospheric AMFs are calculated via Eq. (3.15) and summarised in Table 4.4. For both clean and polluted scenarios, smaller tropospheric AMFs are obtained for cloudy sky than clear sky, indicating the dominating screening effect of NO₂ by high cloud (6 km or 450 hPa). Since smallest box-AMFs are located close to the surface, especially for cloudy sky, the use of the polluted profile reduces the tropospheric AMFs by more than 50% compared to the unpolluted profile. For individual satellite measurements, the NO₂ profile shape, coming from an external database, has the potential of significantly biasing the retrieved tropo-

spheric column. For instance, the vertical transport modelled for stable meteorological regimes may result in large errors in profile shape in the case of strong meteorological activity (Boersma et al., 2004).

Table 4.4: Reference tropospheric AMFs for clear sky (M_{tr}^{cr}) and cloudy sky (M_{tr}^{cl}). Results are shown for the clean and polluted scenario, respectively.

M_{tr}^{cr}		M_{tr}^{cl}	
(clean)	(polluted)	(clean)	(polluted)
1.66	0.79	1.27	0.05

Table 4.5: Calculating the tropospheric AMFs for clear sky (M_{tr}^{cr}) and cloudy sky (M_{tr}^{cl}) by altering the model parameters. Reference values of M_{tr}^{cr} and M_{tr}^{cl} are reported in Table 4.4. Results are shown for the clean and polluted scenario, respectively.

Fig.	varied parameter	difference from the reference	ΔM_{tr}^{cr}		ΔM_{tr}^{cl}	
			(clean)	(polluted)	(clean)	(polluted)
4.7	wavelength	461 nm	+0.05	+0.11	-0.02	+0.002
4.8	measurement geometry	SZA = 80°	+1.29	-0.15	+1.16	-0.02
4.9	surface albedo	0.8	+1.31	+2.41	+1.51	+2.50
4.10	surface pressure	990 hPa	+0.03	+0.01	+0.04	+0.001

Table 4.6: Calculating the tropospheric AMFs for cloudy sky (M_{tr}^{cl}) by altering the cloud properties. Reference values of M_{tr}^{cl} are reported in Table 4.4. Results are shown for the clean and polluted scenario, respectively.

Fig.	varied parameter	difference from the reference	ΔM_{tr}^{cl}	
			(clean)	(polluted)
4.11	cloud model	Lambertian reflector	-0.24	-0.04
4.12	single scattering albedo	0.8	+0.03	+0.01
4.13	cloud optical depth	5	+0.43	+0.35
4.14	cloud top height	1 km	+1.07	+0.41

4.2.2 Sensitivities of model parameters

In this section, the sensitivity tests are implemented for four model parameters specified in Table 4.5. The impacts of the model parameters on the altitude-dependent box-AMF calculation are shown in Figs. 4.7-4.10, and the impacts on the determined tropospheric AMFs are reported in Table 4.5.

wavelength (Fig. 4.7)

The AMFs are typically calculated at the mid-point wavelength of the DOAS fitting window. For a clear atmosphere, the Rayleigh scattering is dependent on wavelength with a stronger effect at shorter wavelengths. Therefore, the box-AMFs increase by up to 20% in the boundary layer when increasing the wavelength from 437.5 nm (mid-point wavelength of the 425-450 nm window) to 461 nm (mid-point wavelength of the 425-497 nm window), which is particularly important for the polluted scenario with an enhanced tropospheric AMF by 0.11 (14%). The differences are less pronounced in the presence of clouds due to the much weaker wavelength-dependency of the Mie scattering. It is

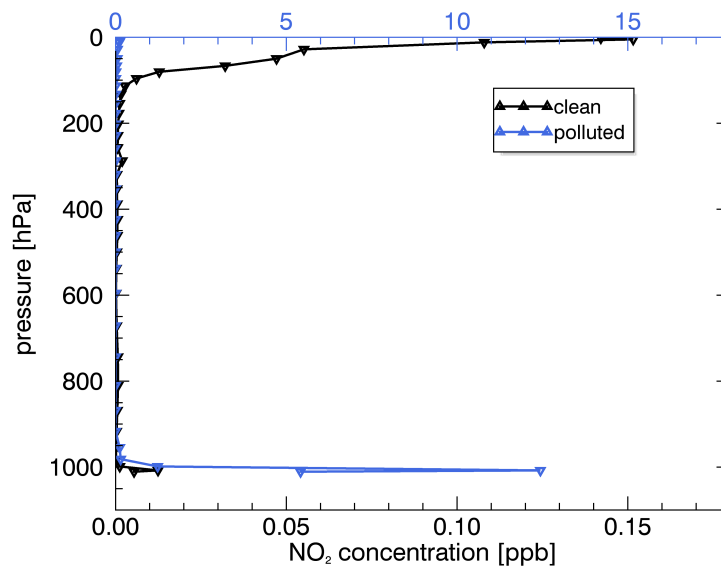


Figure 4.6: A priori NO₂ profiles simulated with TM5 at 9:30 local time for a clean and polluted scenario. Profiles with pressure > 150 hPa (tropopause) are used in the tropospheric AMF calculation.

important that the wavelength-dependency of the AMFs is considered when applying the different DOAS fitting windows (see Sect. 4.1), but the uncertainty is generally small.

measurement geometry (Fig. 4.8)

For clear sky, the box-AMFs in the free troposphere increase significantly for a SZA of 80° (typical for satellite measurements in polar winter) due to the enhancement in the overall light path length. The SZA-dependency is weaker in the boundary layer because of the larger impact of scattering, where smaller box-AMFs are found for the 80° SZA, since more photons are scattered before they reach the layer. Consequently, the tropospheric AMF increases to 2.95 for the clean scenario and decreases to 0.64 for the polluted scenario. For cloudy sky, the box-AMFs above the cloud are increased, and the values below are decreased. Note that the AMF calculation depends also on VZA and RAA, but these measurement geometries are typically known with high accuracy and do not contribute significantly to the retrieval uncertainty.

surface albedo (Fig. 4.9)

The clear-sky box-AMFs decrease toward the surface for a dark surface (such as water and vegetation with a typical surface albedo smaller than 0.1) due to the increasing scattering. The effect is opposite for a bright surface (such as snow and ice with a typical surface albedo of ~0.8) due to a stronger reflection of light at the surface. As higher albedo values lead to larger box-AMFs, especially for the boundary layer, the determined tropospheric AMFs are enhanced, especially for the polluted scenario with most of the NO₂ amounts located near the surface. For cloudy-sky box-AMFs, larger values are noticeable between the surface and cloud, where the light path is enhanced by multiple scattering, influencing more significantly the tropospheric AMF for the polluted scenario.

surface pressure (Fig. 4.10)

For an atmospheric layer at a fixed altitude, shifting the surface to a lower surface pressure

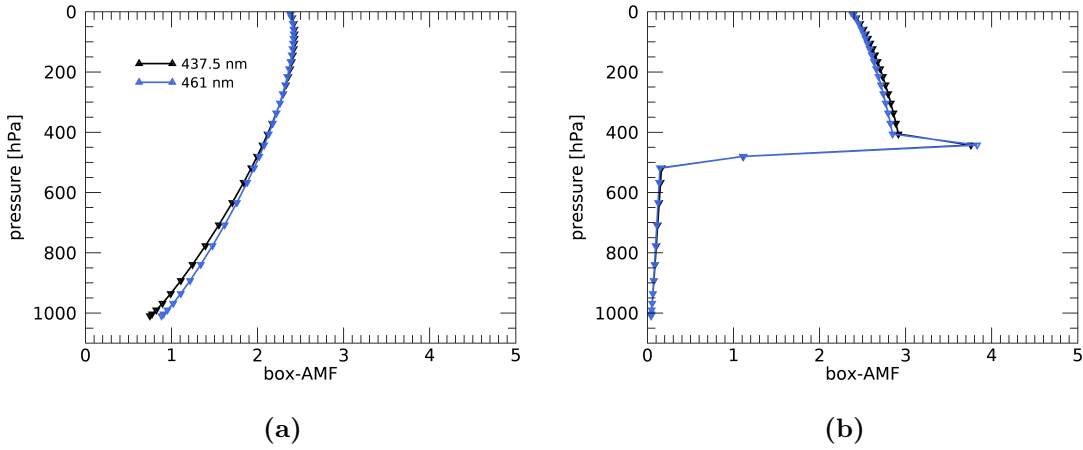


Figure 4.7: Effect of the wavelength on the NO₂ box-AMFs for clear-sky pixel (a) and fully-cloudy pixel (b). Black lines indicate the reference retrievals in Tables 4.2 and 4.3. Differences in the calculated tropospheric AMFs with respect to the references are listed in Table 4.5. Box-AMFs with pressure > 150 hPa (tropopause) are used in the tropospheric AMF calculation.

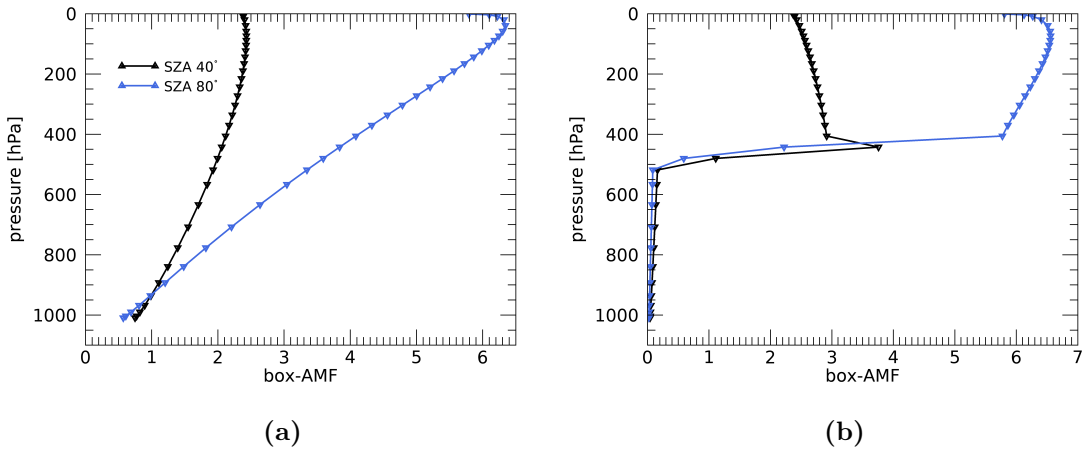


Figure 4.8: Similar as Fig. 4.7 but for effect of the measurement geometry (SZA).

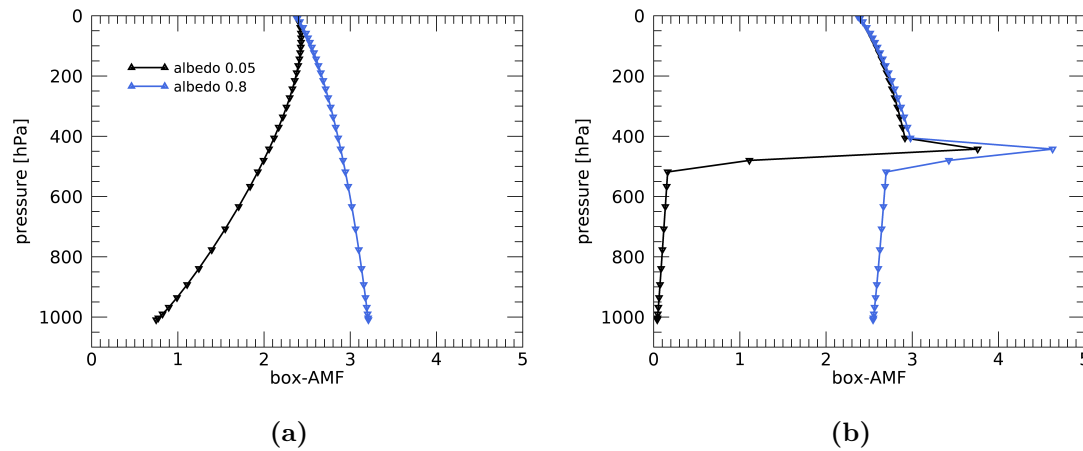


Figure 4.9: Similar as Fig. 4.7 but for effect of the surface albedo.

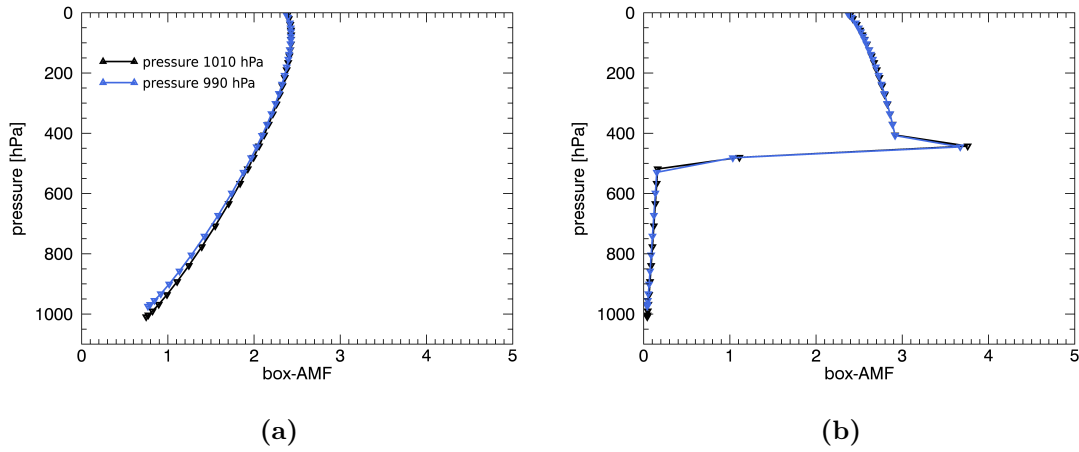


Figure 4.10: Similar as Fig. 4.7 but for effect of the surface pressure.

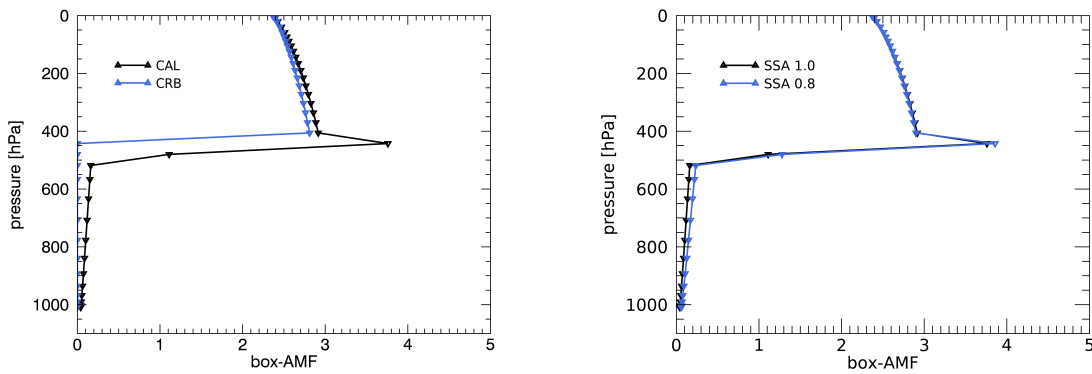


Figure 4.11: Similar as Fig. 4.7b but for effect of the cloud model.

Figure 4.12: Similar as Fig. 4.7b but for effect of the single scattering albedo.

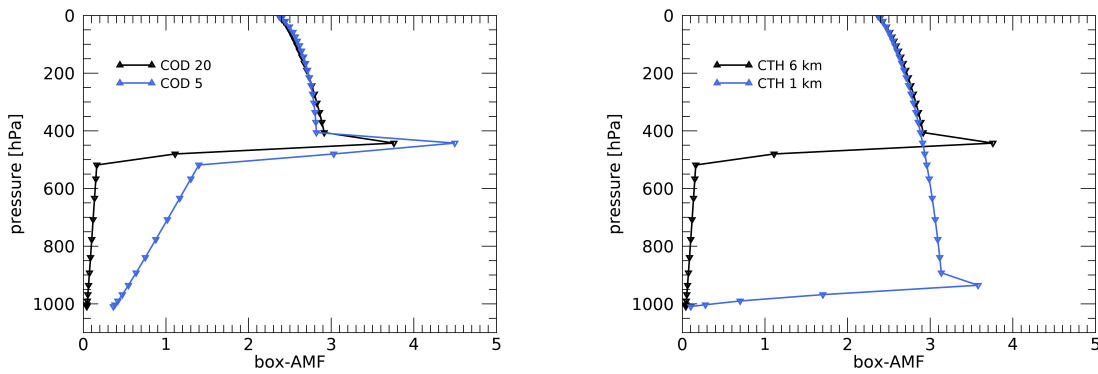


Figure 4.13: Similar as Fig. 4.7b but for effect of the cloud optical depth.

Figure 4.14: Similar as Fig. 4.7b but for effect of the cloud top height.

reduces the clear-sky box-AMF by reducing the amount of light scattered below. On the contrary, for an atmospheric layer at an altitude relative to the surface, e.g., 0-100 m above the surface, the box-AMF increases due to the reduced amount of light scattered above and effectively the enhanced light reaching the layer (Zhou et al., 2009), resulting in an increased clear-sky tropospheric AMF. For the cloudy-sky case, reducing the surface pressure decreases the number of shielded layers and hence increases the calculated cloudy-sky tropospheric AMF. In general, the effect of the surface pressure on the AMF calculation is lower than 3%.

4.2.3 Sensitivities of cloud properties

In this section, the sensitivity tests are analysed for the cloud properties specified in Table 4.6. Their influences on the cloudy-sky box-AMFs are shown in Figs 4.11-4.14, and the influences on the cloudy-sky tropospheric AMFs are reported in Table 4.6.

cloud model (Fig. 4.11)

Instead of considering the physical properties of the Mie scattering cloud in the AMF calculation, the cloud can also be idealized as a perfect Lambertian reflector with a high cloud albedo, calculated to be 0.7 based on a simple approximation (Kokhanovsky, 2006) and the reference cloud properties in Table 4.3. Neglecting the scattering and absorption inside and below the cloud, the use of a Lambertian cloud generates zero values for box-AMFs below the top of the opaque cloud, leading to an underestimation of the cloudy-sky tropospheric AMF by more than 19%, particularly for the polluted scenario. More realistic results are obtained with the Mie scattering cloud, which takes the multiple scattering of light inside the cloud and the contributions of atmospheric layers between the cloud bottom and the ground into account (see Sect. 3.4.4).

single scattering albedo (Fig. 4.12)

The single scattering albedo, the ratio of scattering efficiency to total extinction efficiency, is a key optical characteristic of the cloud and aerosol particles. When the single scattering albedo decreases, namely the absorbing ability of cloud increases, the effective light path is enhanced due to the reduced amount of light scattered above the cloud layer, producing a positive effect on the box-AMFs within and below the cloud layer. Compared to the choice of cloud model above, however, the assumed cloud optical properties play a less important role in the AMF calculation.

cloud optical depth (Fig. 4.13)

In the presence of optically thin cloud with a cloud optical depth of 5, the box-AMFs below the cloud are enhanced compared to the thick cloud, indicating a reduced screening of NO₂. Increased values are also found inside the cloud layer as a result of increased multiple scattering. Therefore, the resulting tropospheric AMFs are increased, particularly for the polluted scenario. It is worth noting that the radiative effect of aerosols and thin clouds are comparable to each other (see Sect. 3.4.5), therefore similar effects for thin clouds can be expected for aerosols.

cloud top height (Fig. 4.14)

When the cloud is shifted to the surface, below the NO₂ bulk in the clean scenario, the absorption of light by NO₂ molecules is enhanced due to the illumination from below. Therefore, the cloudy-sky tropospheric AMF increases to 2.34, higher than the clear-sky value (1.66), indicating the dominating albedo effect and multiple scattering effect by low

Table 4.7: Information on the input parameters for calculating the tropospheric AMFs.

input parameter	impact on uncertainty	source of information
wavelength	low	selection based on fitting window
measurement geometry	low	measurement description
surface albedo	high	climatology
surface pressure	medium	database
NO ₂ vertical profile	high	chemistry transport model
cloud model	high	reflecting or scattering cloud assumption
cloud parameters	high	simultaneous measurement

cloud (1 km or 900 hPa), in contrast to the dominating screening effect of NO₂ by high cloud in the reference retrieval (see Sect. 4.2.1). For the polluted scenario, the impact of the cloud top height on the cloudy-sky tropospheric AMF is significant, for which a large uncertainty in the NO₂ ghost column is expected for the low cloud (see Sect. 3.5).

4.2.4 Summary of sensitivity tests

Table 4.7 summarise the information for the various input parameters presented in Sects. 4.2.1-4.2.3. Despite the large sensitivities on the tropospheric AMF calculation in Table 4.5, the uncertainties related to the wavelength selection (Fig. 4.7) and measurement geometries (Fig. 4.8) are much smaller than the uncertainties introduced by the ancillary surface parameters and the a priori NO₂ profile. The surface albedo (Fig. 4.9) generally has a larger influence on the tropospheric AMF calculation than the surface pressure (Fig. 4.10). For cloudy sky in Table 4.6, the tropospheric AMF calculation is also significantly affected by the cloud model (Fig. 4.11) and the cloud parameters, including the cloud optical depth (Fig. 4.13), the cloud top height (Fig. 4.14), and additionally the radiometric cloud fraction, which determines the combination of the clear-sky and cloud-sky AMFs in Eq. (3.16). The assumed cloud optical properties (Fig. 4.12) are less important for the tropospheric AMF calculation and uncertainty estimation.

4.3 AMF uncertainties

The overall tropospheric AMF uncertainty is mainly driven by the uncertainties in the surface albedo A_s , a priori profile shape ps , cloud fraction c_f , and cloud pressure c_p , as introduced in Sect. 4.2. Referring to Eq. (3.21), the uncertainty in the tropospheric AMF $\sigma_{M_{tr}}$ can be calculated through the uncertainty propagation as:

$$\sigma_{M_{tr}}^2 = \left(\frac{\partial M_{tr}}{\partial A_s} \sigma_{A_s} \right)^2 + \left(\frac{\partial M_{tr}}{\partial ps} \sigma_{ps} \right)^2 + \left(\frac{\partial M_{tr}}{\partial c_f} \sigma_{c_f} \right)^2 + \left(\frac{\partial M_{tr}}{\partial c_p} \sigma_{c_p} \right)^2. \quad (4.1)$$

$\partial M_{tr}/\partial A_s$ denotes the local sensitivity of the tropospheric AMF to the surface albedo, and σ_{A_s} is the best estimate of the uncertainty in the surface albedo, and so on. The estimated values σ_{A_s} , σ_{ps} , σ_{c_f} , and σ_{c_p} are reported in Table 4.8. Here the NO₂ profile shape ps is practically described by a so-called ‘‘profile height’’, the altitude (pressure) below which 75% of the NO₂ vertical column resides (De Smedt et al., 2018), with lower altitudes (higher pressures) indicating stronger pollutions, as a larger fraction of NO₂ amounts are located near the surface.

Figure 4.15 shows the uncertainties in the tropospheric AMFs at 461 nm due to errors in the surface albedo and a priori profile shape for clear sky and errors in the cloud

Table 4.8: Uncertainty estimates for surface albedo A_s , a priori profile shape ps , cloud fraction c_f , and cloud pressure c_p in Eq. (4.1).

σ_{A_s}	0.02	(Kleipool et al., 2008)
σ_{ps}	75 hPa	(De Smedt et al., 2018)
σ_{c_f}	0.05	(Veefkind et al., 2016)
σ_{c_p}	50 hPa	(Veefkind et al., 2016)

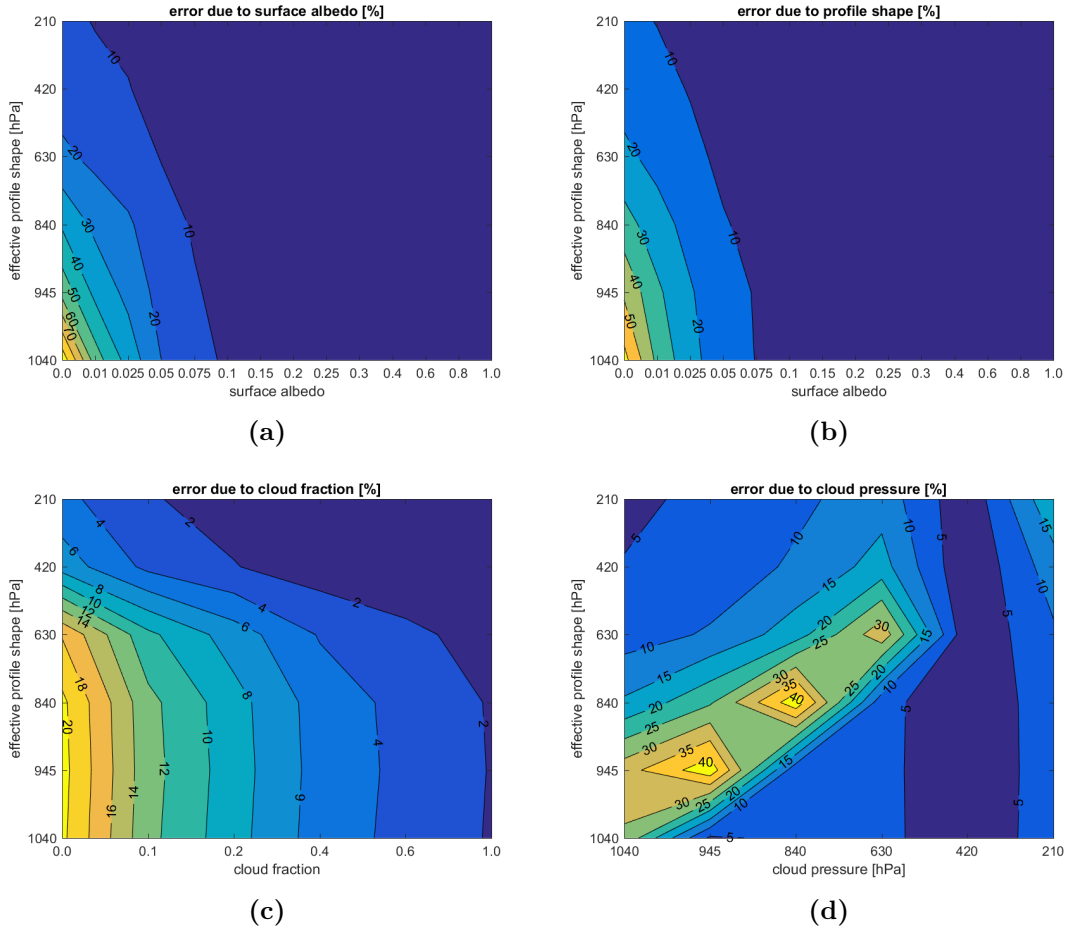


Figure 4.15: Uncertainties in the tropospheric AMFs at 461 nm due to errors in the surface albedo (a), a priori profile shape (b), cloud fraction (c), and cloud pressure (d). Values are shown for $\text{SZA}=40^\circ$, $\text{VZA}=20^\circ$, $\text{RAA}=135^\circ$, and surface pressure = 1050 hPa. The y-axis indicates the atmospheric pressure, below which 75% of the NO_2 vertical column resides, with higher pressures meaning stronger pollutions. (a) and (b) are illustrated for clear sky. (c) and (d) are calculated for surface albedo = 0.05 and cloud albedo = 0.8 with (c) for cloud pressure = 630 hPa and (d) for cloud fraction = 0.2.

fraction and cloud pressure for cloudy sky. Results are shown for a typical GOME-2 and TROPOMI viewing geometry. In Fig. 4.15a, the uncertainty contributions due to errors in the surface albedo are largest for small albedo values and polluted situations. The uncertainties are in the level of 20%-30% for polluted continents with a typical surface albedo in the 0.03-0.05 range. In Fig. 4.15b, a similar effect is observed for the a priori profile shape errors with uncertainties up to 20%. It is worth mentioning that the application of the averaging kernel (see Sect. 3.1) can remove the uncertainties resulting

from the errors in the a priori profile shape for applications such as data assimilation and validation study (Eskes and Boersma, 2003).

In Fig. 4.15c, as the satellite measurements are normally filtered for cloud radiance fraction < 0.5 or cloud fraction < 0.2 (see Sect. 3.5), the tropospheric AMF uncertainties related to the cloud fraction are in the 10%-20% range. Larger errors are found for small cloud fractions and profiles with most NO₂ concentrations below the cloud (cloud pressure = 630 hPa). In Fig. 4.15d, errors in the cloud pressure introduce an tropospheric AMF uncertainty ranging from 5% to 40%, with large numbers for clouds close to the NO₂ bulk, especially for polluted situations with low clouds, in line with Sect. 3.5.

To conclude, the tropospheric AMF uncertainties introduced by the errors in the surface albedo and a priori NO₂ profile are about 20% respectively for typical polluted scenarios with small surface albedo values and high surface NO₂ concentrations. The uncertainties related to the cloud fraction are 10%-20%, and the cloud pressure-related uncertainties are in the 5%-40% range. Consequently, the total uncertainty in the tropospheric AMF is estimated to range from 15% to 50%, and the total uncertainty in the tropospheric NO₂ column is likely in the 40%-80% range. The findings agree well with previous uncertainty studies (e.g., Boersma et al., 2004; Lorente et al., 2017; Boersma et al., 2018) and indicate the necessities of accurate surface albedo database, up-to-date a priori NO₂ profiles, and realistic cloud correction procedures.

Chapter 5

NO₂ retrieval for GOME-2

The GOME-2 instruments (see Sect. 2.5.2) aboard the MetOp-A and MetOp-B platforms have been providing a unique NO₂ dataset since the year 2007. In this chapter, the latest developments in the NO₂ retrieval algorithm for GOME-2 are reported, with illustrations for the algorithm refinement with respect to previous versions, the algorithm application on GOME-2 NO₂ measurements, and an end-to-end validation using correlative ground-based MAXDOAS (see Sect. 2.5.1) dataset. This chapter gives a brief summary of three journal articles gathered in Appendices B-D.

5.1 GOME-2 NO₂ product

The operational GOME-2 NO₂ product processing chain starts with the level 0 to 1b processing at the European Organisation for the Exploitation of Meteorological Satellites (EUMETSAT) in Darmstadt (Germany), where the raw instrument (level 0) data is converted into geolocated and calibrated (level 1b) (ir)radiances. The level 1b (ir)radiances are disseminated to the German Aerospace Center (DLR) in Oberpfaffenhofen (Germany) and further processed using the Universal Processor for UV/VIS Atmospheric Spectrometers (UPAS) system. The resulting level 2 near-real-time total column products including NO₂ columns can be received by user communities two hours after sensing. Offline and reprocessed GOME-2 level 2 and consolidated products are also provided within one day by DLR, which can be ordered via FTP-server and the EUMETSAT Data Centre (<https://acsaf.org/>).

The GOME-2 total and tropospheric NO₂ products are generated using the GOME Data Processor (GDP) algorithm at DLR in the framework of EUMETSAT's Satellite Application Facility on Atmospheric Composition Monitoring (AC-SAF). The GDP algorithm applies the DOAS technique (see Sect. 3.2) to determine the slant columns from calibrated GOME-2 (ir)radiance data in the visible wavelength range. The stratospheric NO₂ component is obtained by the modified reference sector method (see Sect. 3.3). The tropospheric vertical columns are determined using AMFs (see Sect. 3.4) based on cloud information from the Optical Cloud Recognition Algorithm (OCRA) and Retrieval Of Cloud Information using Neural Networks (ROCINN) algorithms (Loyola et al., 2007, 2011; Lutz et al., 2016; Loyola et al., 2018).

Table 5.1: Main settings of GOME-2 DOAS retrieval of NO₂ slant columns.

	operational retrieval (Valks et al., 2011, 2017)	improved algorithm (this work)
fitting window	425-450 nm	425-497 nm
absorption cross-sections	NO ₂ , O ₃ , H ₂ O _{vap} , O ₄ , Ring	NO ₂ , O ₃ , H ₂ O _{vap} , O ₄ , Ring, H ₂ O _{liq} , resolution correction
polynomial degree	3	5
intensity offset correction	constant	linear
slit function	preflight	stretched preflight

5.2 Retrieval algorithm

Following the classical three-step-retrieval in Chap. 3, the current operational retrieval algorithm (GDP 4.8) for total and tropospheric NO₂ from GOME-2 was first introduced by Valks et al. (2011, 2017) and has been successfully applied in studies of NO₂ concentration detection, satellite dataset intercomparison, and NO₂ emission estimation (e.g., Mijling et al., 2013; Hilboll et al., 2013a, 2017; Krotkov et al., 2017; Irie et al., 2012; Gu et al., 2014; Miyazaki et al., 2017; Ding et al., 2017). An improved algorithm is described in this section and will be implemented in a future release (GDP 4.9).

5.2.1 DOAS slant column retrieval

Appendix C (Sect. 4 therein) describes an improved DOAS slant column retrieval using a larger 425-497 nm wavelength fitting window (Richter et al., 2011) to increase the signal-to-noise ratio (see Sect. 3.6.2 for uncertainty analysis and Sect. 4.1 for performance of different fitting windows.). Table 5.1 compares the DOAS settings for the operational and improved algorithms. In the improved retrieval, absorption cross-sections are updated, and a linear intensity offset correction is applied. The long-term and in-orbit variations of GOME-2 slit function are corrected by deriving effective slit functions with a stretched preflight GOME-2 slit function and by including a “resolution correction function” (Azam et al., 2015) as a pseudo absorber cross-section in the DOAS fit, respectively. In addition, the application of a new version (6.1) of the GOME-2 level 1b data (EUMETSAT, 2015) largely reduces the offset between GOME-2/MetOp-A and GOME-2/MetOp-B NO₂ columns by removing calibration artefacts in the GOME-2/MetOp-B irradiances (EUMETSAT, 2015). Compared to the operational algorithm, the improved NO₂ columns are higher by $\sim 1\text{-}3 \times 10^{14}$ molec/cm² (up to 27%).

The quality of the improved slant column retrieval is evaluated using the GOME-2 NO₂ dataset from the Quality Assurance for Essential Climate Variables (QA4ECV, www.qa4ecv.eu) project. QA4ECV (Lorente et al., 2017; Zara et al., 2018; Boersma et al., 2018) aims at quality-assured satellite products using a retrieval algorithm harmonised for GOME, SCIAMACHY, OMI and GOME-2. Figure 5.1 presents the time series of the calculated GOME-2 slant column errors from the operational, improved, and QA4ECV datasets, following the statistical method in Sect. 3.6.2. Compared to the operational algorithm, the improved NO₂ slant column errors are lower by $\sim 24\%$. Compared to the QA4ECV product, the improved NO₂ slant columns show good consistency (not shown), and the NO₂ slant column errors are $\sim 14\%$ - 28% smaller, indicating a good overall quality of the improved DOAS retrieval.

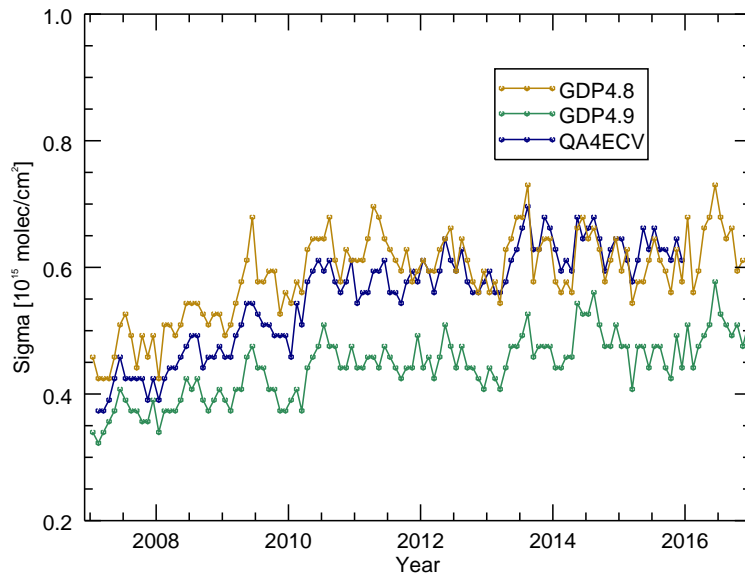


Figure 5.1: Temporal evolution of the GOME-2 NO₂ slant column errors from the operational GDP 4.8 product (January 2007-December 2016), the improved GDP 4.9 algorithm (January 2007-December 2016), and the QA4ECV dataset (February 2007-December 2015) using deviations of NO₂ slant columns from box ($2^\circ \times 2^\circ$) mean values over the tropical Pacific (20°S - 20°N , 160°E - 180°E).

5.2.2 Stratosphere-troposphere separation

Appendix B presents the STRatospheric Estimation Algorithm from Mainz (STREAM) for the determination of the stratospheric NO₂ columns. Belonging to the modified reference sector method (see Sect. 3.3), STREAM applies the total column measurements over clean and remote regions as well as over clouded scenes where the tropospheric columns are effectively shielded. STREAM calculates weighting factors for each satellite pixel to define the contribution of total columns to the stratospheric estimation: potentially polluted pixels are weighted low, cloudy observations (with medium cloud heights) are weighted high, and the weights are further adjusted in a second iteration if pixels suffer from large biases in the tropospheric residues. Depending on these weighting factors, stratospheric NO₂ fields are derived by a weighted convolution on the total columns using convolution kernels, which are wider at lower latitudes due to the low longitudinal variability assumption of stratospheric NO₂ and narrower at higher latitudes to reflect the stronger natural variations.

Appendix C (Sect. 5 therein) describes the optimization of STREAM for the GOME-2 instrument, as STREAM was originally designed for TROPOMI. For the adaption to GOME-2 measurements, the performance of STREAM is analysed by applying it to GOME-2 synthetic data and by comparing the differences between estimated and original stratospheric fields. The synthetic data are calculated using simulated NO₂ fields from the IFS(CB05BASCOE) experiment (Huijnen et al., 2016), which a combination of tropospheric chemistry module in the Integrated Forecast System (IFS, current version based on the CB05 scheme) and stratospheric chemistry from the Belgian Assimilation System for Chemical Observations (BASCOE) system. Applied to the synthetic data, the estimated stratospheric NO₂ columns from STREAM show good consistency with the a priori truth. A slight overestimation by $\sim 1\text{-}2 \times 10^{14}$ molec/cm² is found for low latitudes, and larger differences by up to $\sim 5 \times 10^{14}$ molec/cm² are found at higher latitudes. To re-

Table 5.2: Radiative transfer model and model parameters in deriving GOME-2 tropospheric NO₂ columns.

	operational retrieval (Valks et al., 2011, 2017)	improved algorithm (this work)
radiative transfer model	LIDORT v2.2	VLIDORT v2.7
surface albedo	TOMS/GOME LER	direction-dependent GOME-2 LER
a priori NO ₂ profile	monthly MOZART-2 (1.875°×1.875°)	daily IFS(CB05BASCOE) (0.7°×0.7°)
cloud parameter	OCRA/ROCINN_CRB	OCRA/ROCINN_CAL

duce the biases over the subtropical regions in winter, an improved latitudinal correction is introduced in STREAM.

Figure 5.2 presents the total columns from GOME-2 and the stratospheric NO₂ calculated with STREAM and with the spatial filtering method used in the GDP 4.8 algorithm in February and August 2009. The spatial filtering algorithm belongs to the modified reference sector method and relies on a pollution mask and a low-pass filtering in zonal direction. Compared to this method, the application of STREAM decreases the stratospheric NO₂ columns by $\sim 1 \times 10^{14}$ molec/cm² in general and reduces largely the overestimation over polluted areas.

As the spatial filtering method and also other modified reference sector methods in Sect. 3.3 generally define a strict pollution mask of regions with potential tropospheric pollution, information over most continents is hardly used for the stratospheric estimation, which can lead to large errors during interpolation. STREAM overcomes these artifacts with an improved treatment of polluted and cloudy pixels by defining weighting factors for each satellite pixel.

5.2.3 AMF calculation

Appendix C (Sect. 6 therein) and Appendix D describe an improved AMF calculation based on a new box-AMF look-up table and realistic model parameters, as summarised in Table 5.2. See Sects. 4.2 and 4.3 for importance of individual model parameters.

box-AMF

The box-AMF look-up table (see Sect. 3.4.2) is generated using the latest version 2.7 of VLIDORT radiative transfer model (Spurr, 2006) with an increased number of reference points and vertical layers to reduce interpolation errors. Compared to the scalar (intensity-only) LIDORT code, the vector VLIDORT provides more realistic modelling results with a treatment of light polarisation.

surface albedo

The surface albedo (see Sect. 3.4.3) is described by a GOME-2 surface LER climatology (Tilstra et al., 2017), derived with a higher resolution, newer observations, and an improved LER algorithm, compared to the TOMS/GOME LER climatology (Boersma et al., 2004). Additionally, the surface BRDF effect is taken into account by improving the GOME-2 surface LER climatology with a GOME-2 directionally dependent LER (DLER) dataset (Tilstra et al., 2019) over land and an ocean surface albedo parametrization (Jin et al., 2004, 2011) over water.

Figure 5.3 shows the original and improved GOME-2 LER dataset and their differences on 3 February and 5 August 2010. Over land, the use of the DLER dataset improves

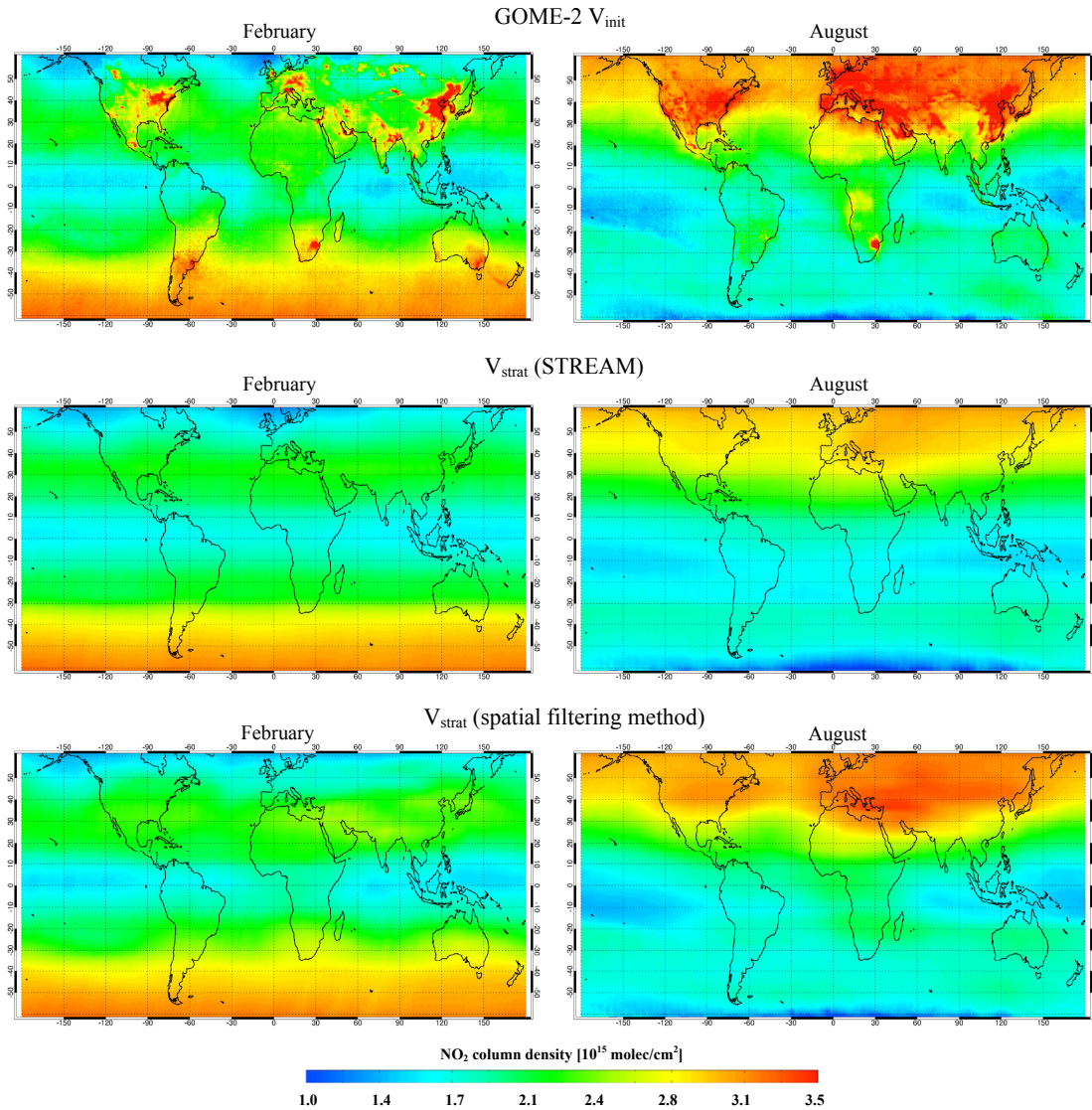


Figure 5.2: GOME-2 total NO_2 columns and stratospheric NO_2 columns retrieved from the STREAM algorithm and from the spatial filtering method used in GDP 4.8 in February and August 2009.

the underestimation of the surface albedo at the west side of the GOME-2 orbit (backward scattering geometry) and increases the AMFs by up to 15% for polluted regions (not shown). Over water, the updated surface albedo increases over sun glint areas (forward scattering geometry) and coastal regions with large SZAs and VZAs, for which the tropospheric NO_2 columns are reduced by up to 10% (not shown).

Compared to other state-of-the-science BRDF studies based on the MODIS measurements in Sect. 3.4.3, the proposed method relies on the GOME-2 LER data, which is consistent with the GOME-2 NO_2 observations, considering the illumination conditions, observation geometries, and instrumental characteristics. In addition, since most of the current NO_2 and cloud retrievals (e.g., Boersma et al., 2018; van Geffen et al., 2019; Loyola et al., 2018; Desmons et al., 2019) are still based on the Lambertian surface input, this method is advanced by providing a consistent Lambertian input with a proper treatment of angular dependency.

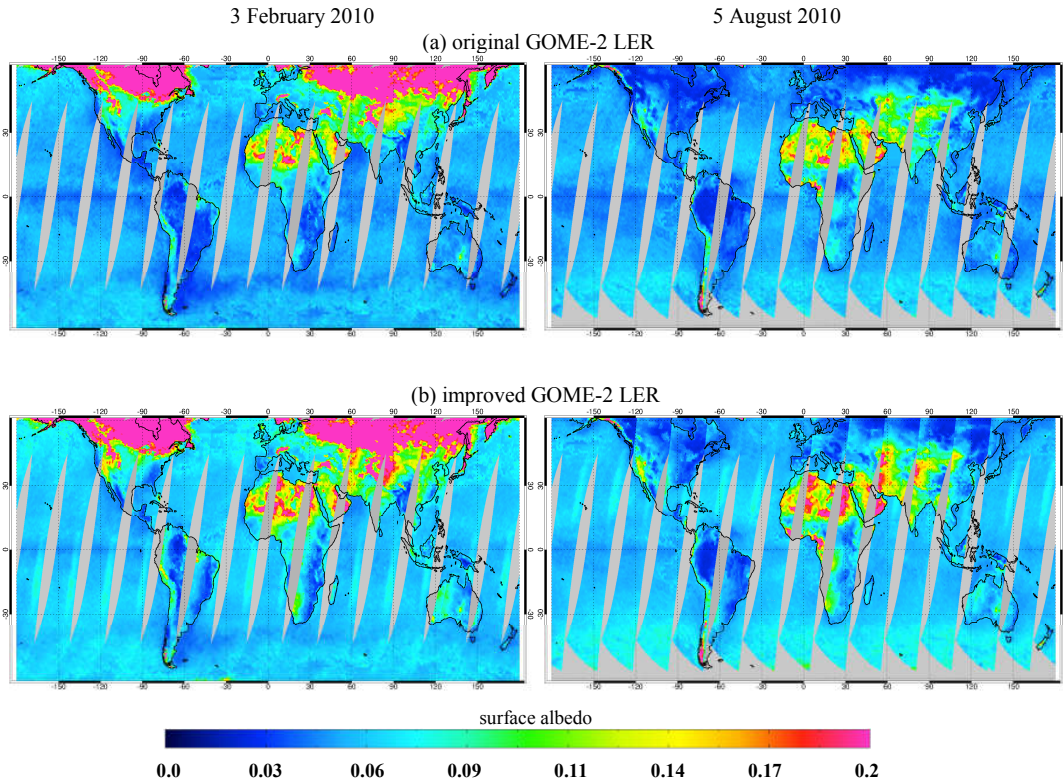


Figure 5.3: Map of GOME-2 surface LER climatology (Tilstra et al., 2017) in February and August (a), improved GOME-2 surface LER data taking into account the direction-dependency on 3 February and 5 August 2010 (b), and their differences over land (c) and over water (d) (figure continued on next page).

a priori NO₂ profile

Daily a priori NO₂ profiles (see Sect. 3.4.1) with higher resolutions are obtained from the chemistry transport model IFS(CB05BASCOE) (Huijnen et al., 2016) based on the recent emission inventory CAMS_GLOB_ANT v2.1 (Granier et al., 2019). IFS(CB05BASCOE), an advanced version of IFS system (Flemming et al., 2017), was developed by the European Centre for Medium Range Weather Forecast (ECMWF) and has been running fully operationally in the Copernicus Atmosphere Monitoring Service (CAMS, <http://atmosphere.copernicus.eu>). Profile forecasts from CAMS will be applied in the prototype and operational NO₂ retrieval algorithm for the Sentinel-4 (Sanders et al., 2018) and Sentinel-5 (van Geffen et al., 2018) missions with the advantage of operational implementation and high resolution.

Compared to the currently used MOZART-2 profiles (Horowitz et al., 2003), improvement in the spatial resolution gives a more accurate description of the NO₂ gradient and transport. The use of daily profiles provides a better description of the temporal NO₂ variation, especially for regions dominated by emission and transport. In general, the application of IFS(CB05BASCOE) vertical profiles affects the tropospheric NO₂ columns by more than 1×10^{15} molec/cm² for polluted regions.

clouds

More realistic ROCINN cloud parameters are provided by a Cloud-As-Layers (CAL) cloud product (Loyola et al., 2018), which treats the clouds as uniform layers of water droplets, instead of the current Clouds-as-Reflecting-Boundaries (CRB) cloud model, which as-

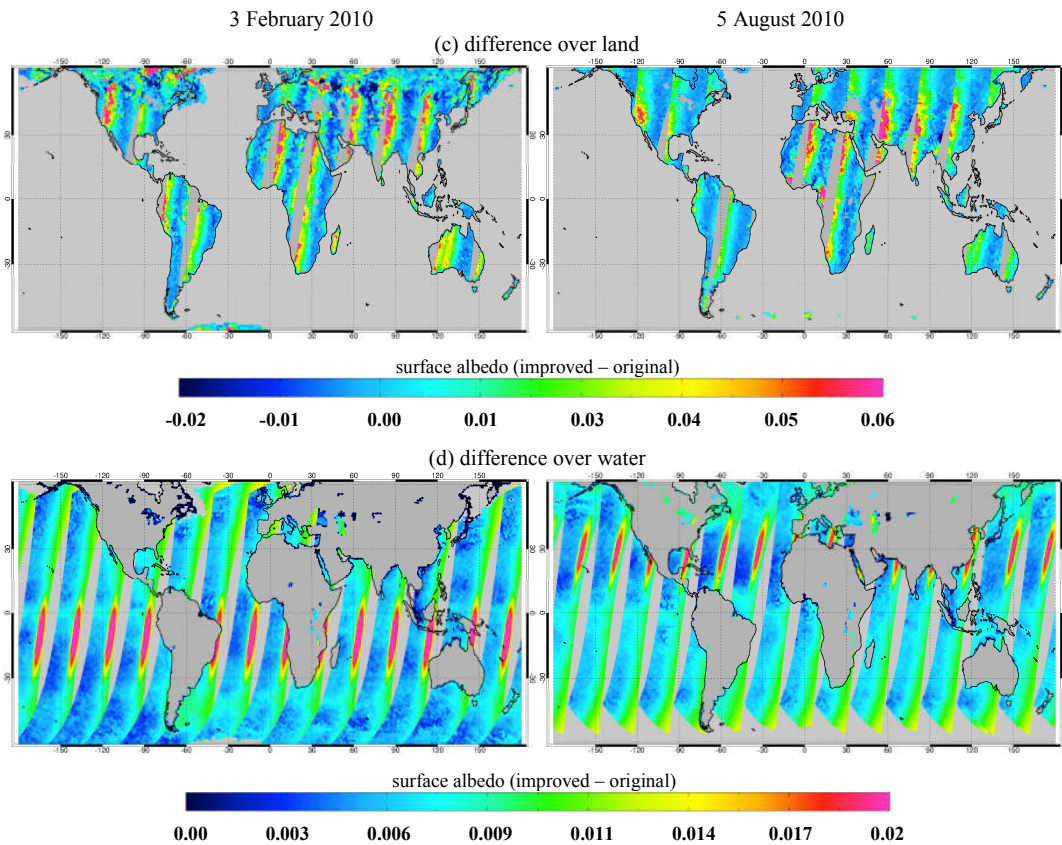


Figure 5.3: (figure continued from previous page)

sumes the clouds as Lambertian reflectors (see Sect. 3.4.4).

Figure 5.4 shows an example of the derived box-AMFs for clear sky and cloudy sky using the CRB and CAL model over Italy (45.3° N, 11.2° E) on 1 February 2010. The cloud information and the calculated tropospheric AMFs are also reported. Compared to the clear-sky box-AMFs, the CAL-based cloudy-sky box-AMFs increase above the cloud layer (albedo effect) and decrease below the cloud layer (shielding effect), consistent with the theoretical study in Fig. 4.11. Compared to the CRB model, the use of the CAL model takes account of the sensitivities inside and below the cloud layer and increases the cloudy-sky AMF by 0.3. Consequently, the retrieved tropospheric NO_2 column decreases by 2.5×10^{15} molec/cm² (12%), based on a polluted NO_2 profile with most of the NO_2 concentration located near the surface.

aerosols

The impact of aerosols (see Sect. 3.4.5) on the tropospheric NO_2 retrieval is investigated by comparing the concurrent retrievals based on ground-based aerosol measurements (explicit aerosol correction) and aerosol-induced cloud parameters (implicit aerosol correction). The explicit modelling of aerosol scattering and absorption is implemented for the AMF calculation by introducing the AERONET aerosol optical properties (Holben et al., 1998; Giles et al., 2019) and MAXDOAS aerosol extinction profiles (Cl  mer et al., 2010; Gielen et al., 2017) in the radiative transfer calculation.

Figure 5.5 presents the relative biases in tropospheric NO_2 columns retrieved assuming implicit aerosol correction via the CRB and CAL cloud model for Xianghe (39.75° N, 116.96° E, a typical suburban site ~ 60 km from Beijing in China) in March 2010–December

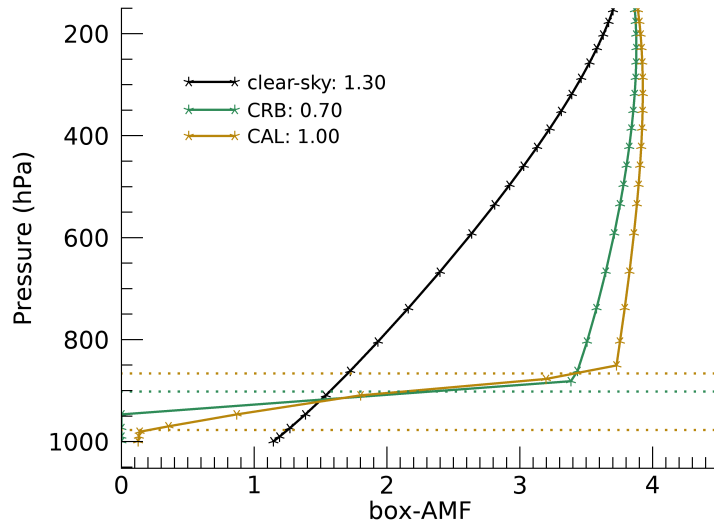


Figure 5.4: Box-AMFs for clear and cloudy sky using the ROCINN_CAL and ROCINN_CRB cloud models over Italy (45.3° N, 11.2° E) on 1 February 2010. The tropospheric AMF is given next to each label. The ROCINN_CRB cloud top pressure is shown as a horizontal green line, and the ROCINN_CAL cloud top and base pressure are shown as horizontal brown lines. Cloud radiance fraction = 0.47, cloud optical depth = 6.85, SZA = 69°, VZA = 3°, and RAA = 42°.

2016. Resulted from the overestimated shielding effect, the tropospheric NO₂ columns retrieved using the CRB-based implicit aerosol correction are on average 33% larger than using the explicit aerosol correction. The differences are largely reduced by applying the CAL cloud model (9%).

To summarize, the use of above new features affects the tropospheric NO₂ columns on average within $\pm 20\%$ in winter and $\pm 5\%$ in summer over polluted regions. The total uncertainty in the tropospheric AMF for polluted conditions is estimated to decrease from 15%-50% in the operational product to 10%-35% in this work.

5.3 End-to-end validation

Appendix C (Sect. 7 therein) and Appendix D (Sect. 5 therein) introduce the validation of the NO₂ data derived from the improved GOME-2 algorithm using correlative ground-based MAXDOAS observations (Pinardi et al., 2014, 2015). The MAXDOAS measurements are analysed and performed by BIRA-IASB in Brussels (Belgium) in the AC-SAF context (Hassinen et al., 2016) for six MAXDOAS stations (Beijing, Bujumbura, OHP, Reunion, Uccle, and Xianghe) covering urban, suburban, and background situations. Taking the suburban Xianghe station as an example, the improved GOME-2 dataset shows a similar seasonal variation in the tropospheric NO₂ columns as the MAXDOAS measurements with a relative difference of -5.8% (-2.7×10^{15} molec/cm² in absolute) and a correlation coefficient of 0.91.

Figure 5.6 reports the monthly mean absolute and relative differences for the operational and improved algorithms for the Xianghe station. The daily differences are also reported through the histogram panel. Compared to the current operational product,

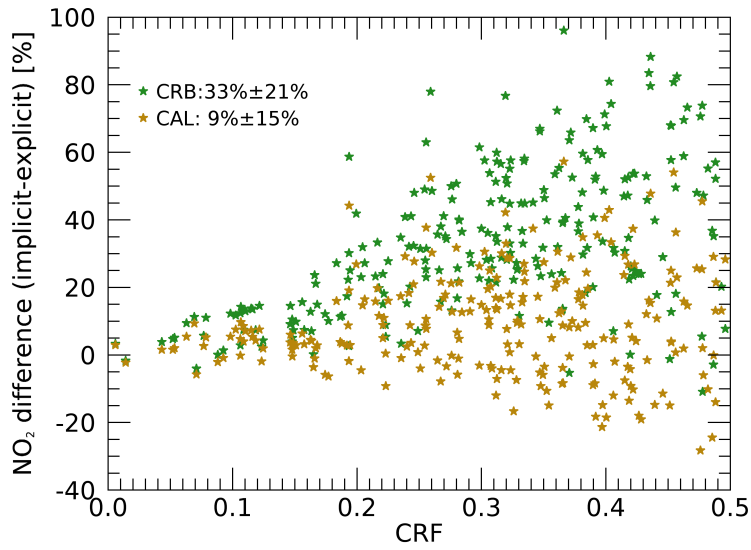


Figure 5.5: Relative biases in GOME-2 tropospheric NO₂ columns assuming implicit aerosol correction through the ROCINN_CRB and ROCINN_CAL cloud models in Xianghe (39.75°N, 116.96°E) in March 2010-December 2016. Only measurements with cloud radiance fraction < 0.5, cloud optical depth < 5, and cloud top height < 3 km are included. Cloud observations with fitting RMS > 1×10^{-4} or number of iterations > 20 are filtered out. The mean value and standard deviation are given next to each label.

the improved dataset is a significant improvement, considering the reduction of the absolute and relative monthly mean bias as well as the reduction in the spread of the daily comparison points. Similar large improvements are found for all the MAXDOAS stations.

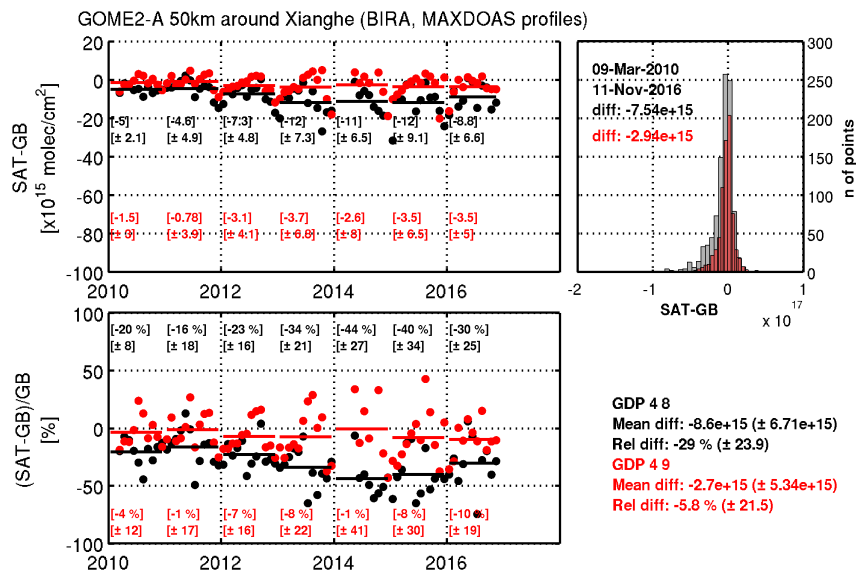


Figure 5.6: Absolute and relative differences of GOME-2 and MAXDOAS tropospheric NO₂ columns. The time series presents the monthly mean differences for the operational GDP 4.8 (black) and the improved GDP 4.9 (red). The total mean differences values and standard deviations are given, as well as the yearly values. The histogram presents the daily differences over the whole time series for the two products (grey for GDP 4.8 and red for GDP 4.9).

Chapter 6

NO₂ retrieval for TROPOMI

Launched in October 2017, the TROPOMI instrument (see Sect. 2.5.2) aboard Sentinel-5 Precursor provides the potential to monitor air quality over large point sources across the globe with a spatial resolution as high as 7 km×3.5 km. In this chapter, the algorithm for the retrieval of total and tropospheric NO₂ columns from the GOME-2 measurements in Sect. 5.2 is adapted for TROPOMI. Examples of applying the retrieval algorithm on TROPOMI measurements are shown. The overall quality of the dataset is evaluated by a comparison with additional satellite datasets and a validation using ground-based MAXDOAS measurements.

6.1 TROPOMI NO₂ product

The operational TROPOMI retrieval of NO₂ columns is based on the Dutch OMI NO₂ product (DOMINO) system (Boersma et al., 2007, 2011) with developments within the QA4ECV project (Lorente et al., 2017; Zara et al., 2018; Boersma et al., 2018) and improvements related to the specific TROPOMI aspects. The DOMINO processor is a retrieval-assimilation-modelling system based on a DOAS analysis, an AMF calculation, and a data assimilation for the separation of the stratospheric and tropospheric contributions to the NO₂ column (see Sect. 3.3).

The TROPOMI NO₂ processing is operationally performed in two locations. The DOAS retrieval takes place at the official level 2 processing site at DLR in Oberpfaffenhofen (Germany). The data assimilation system providing stratosphere-troposphere-separation information as well as NO₂ profile data is running at the Royal Netherlands Meteorological Institute (KNMI) in De Bilt (the Netherlands). Finally, the conversion of the slant column into the tropospheric and stratospheric NO₂ columns will take place in the near-real-time processing mode at DLR and in offline or reprocessing mode at KNMI.

The near-real-time TROPOMI NO₂ data are available within three hours after data acquisition based on a forecast of the chemistry transport model data. The offline processing data are available after a few days, and the reprocessing of Sentinel-5 Precursor products will be performed when major product upgrades are considered necessary. All TROPOMI data can be obtained from the Copernicus Open Access Hub (<https://scihub.copernicus.eu/>) and the TEMIS website (<http://www.temis.nl/airpollution/no2.html>).

Table 6.1: Main settings of the NO₂ retrieval for TROPOMI.

	KNMI operational product (van Geffen et al., 2019)	DLR development (this work)
fitting window	405-465 nm	425-497 ¹ nm
secondary trace gases	O ₃ , H ₂ O _{vap} , O ₄ , H ₂ O _{liq}	O ₃ , H ₂ O _{vap} , O ₄ , H ₂ O _{liq}
polynomial degree	5	5
reference spectrum	daily solar reference	daily solar reference
stratosphere-troposphere separation	data assimilation (TM5-MP)	modified reference sector method (STREAM)
radiative transfer model	DAK	VLIDORT
surface albedo	OMI climatology	OMI climatology
a priori NO ₂ profile	TM5-MP	TM5-MP
cloud parameters	FRESCO	OCRA/ROCINN

¹ The wavelength range 405-465 nm is chosen at the moment due to the saturation issue around 490 nm during the E1 commissioning phase in the first six months after launch (Kleipool et al., 2018).

6.2 Retrieval algorithm

The operational total and tropospheric NO₂ retrieval algorithm at KNMI is summarized in Table 6.1 and described in detail by van Geffen et al. (2019). In the following, the retrieval algorithm in Sect. 5.2, which was originally designed for the GOME-2 instrument at DLR, is adapted and optimised for TROPOMI measurements.

6.2.1 DOAS slant column retrieval

The current fitting window in the DOAS fit for TROPOMI is 405-465 nm as a heritage of OMI retrieval (see Table 3.1 for introduction of the OMI retrieval and Sect. 4.1 for performance of the 405-465 nm fitting window), due to the possible pixel saturation at ~490 nm during the commissioning phase (Kleipool et al., 2018). Saturated pixels (with a high signal flux) can cause the so-called “blooming”, when the multiple pixels (with a lower signal flux) neighbouring the saturated pixels are also affected by saturation. The blooming pixels will be flagged in a future update of the TROPOMI level 0-1b processor (Rozemeijer and Kleipool, 2018) and will be excluded from the retrieval when applying the 425-497 nm fitting window.

Consistent with Sect. 5.2.1, a fifth-order polynomial is applied to account for the spectrally smooth features from molecular scattering and absorption. The closest-in-time daily irradiance measured with TROPOMI is used for the reference spectrum. The absorption cross-sections of NO₂, O₃, H₂O_{vap}, O₄, and H₂O_{liq} are convolved with the preflight TROPOMI slit function and included in the DOAS fit to describe the spectral effect of each species, as detailed in Table 6.2. The Ring effect is treated as a pseudo absorber, by means of an additive Ring reference spectrum and a scaling coefficient as fitting parameter. A linear intensity offset correction is fitted as another effective cross-section to correct for the stray light in the spectrometer, the inelastic scattering in the ocean, and remaining calibration issues in the level 1 data. Shift and stretch parameters are applied to cross-section wavelength grids to improve the wavelength registration and compensate for inaccuracy in the wavelength calibration. The TROPOMI spectra are analysed using the QDOAS software developed at BIRA-IASB (Danckaert et al., 2015).

Table 6.2: Overview over absorption cross-sections used in the TROPOMI NO₂ retrieval.

NO ₂ (220 K)	Vandaele et al. (2002)
O ₃ (228 K)	Brion et al. (1998)
H ₂ O _{vap} (293 K)	Rothman et al. (2010), rescaled as in Lampel et al. (2015)
O ₄ (293 K)	Thalman and Volkamer (2013)
H ₂ O _{liq} (297 K)	Pope and Fry (1997), smoothed as in Peters et al. (2014)

Figure 6.1 presents a fitting example for TROPOMI orbit 3272 on 1 June 2018.

6.2.2 Stratosphere-troposphere separation

The stratosphere-troposphere separation algorithm STREAM (Appendix B) was developed as a verification algorithm for the TROPOMI instrument, as a complement to the operational stratospheric correction based on data assimilation of slant columns in the TM5-MP chemistry transport model (Huijnen et al., 2010; Williams et al., 2017). STREAM has been successfully applied to the NO₂ measurements from GOME-2 (see Sect. 5.2.2) and OMI (see Appendix B) with the advantage of requiring no model input (see Sect. 3.6.3). To reduce the biases over the subtropical regions in winter, an improved latitudinal correction (see Sect. 5.2.2) is introduced in STREAM for the application of TROPOMI measurements.

Figure 6.2 plots an example of the total and stratospheric NO₂ columns from TROPOMI on 1 January 2018. Based on the operational TROPOMI OCRA/ROCINN cloud product (Lutz et al., 2016; Loyola et al., 2018), the updated STREAM successfully separates the stratospheric and tropospheric contributions over polluted regions. The stratospheric NO₂ presents an overall smooth pattern with a strong dependency on latitude and season, related to the photochemical changes and dynamic variabilities. At high latitudes in the southern hemisphere, the conversions of reservoir species to NO_x are enhanced due to the increased number of sunlit hours (see Sect. 2.3), and the NO_x loss reactions are suppressed due to the reduced humidity (see Sect. 2.2), resulting in high stratospheric NO₂ columns. Low values are found for the northern polar vortex, because of the denoxification and denitrification processes (see Sec 2.4). An increase of stratospheric NO₂ concentration with latitude is resulted from the poleward transport of air masses, during which the NO_x are produced via reaction (R 2.5).

6.2.3 AMF calculation

The AMFs are calculated via the pre-calculated look-up table to transfer the stratospheric and tropospheric slant columns to vertical columns, depending on the TROPOMI measurement geometries, surface albedo, surface pressure, a priori NO₂ profiles, clouds, and aerosols. The look-up table is calculated at 437.5 nm (near the mid-point wavelength of fitting window), as recommended by Boersma et al. (2018), using the linearised vector code VLIDORT (Spurr, 2006) version 2.7 with a treatment of light polarisation included. VLIDORT applies the discrete ordinates method to generate simulated intensity and analytic intensity derivatives with respect to atmospheric and surface parameters (weighting functions).

The surface albedo is described by a climatology based on three years of OMI LER measurements at 440 nm (Kleipool et al., 2008), which is advantageous due to the similar overpass time (13:30 local time) and viewing conditions with TROPOMI. The surface albedo for each TROPOMI pixel is calculated by an area-weighted tessellation of the

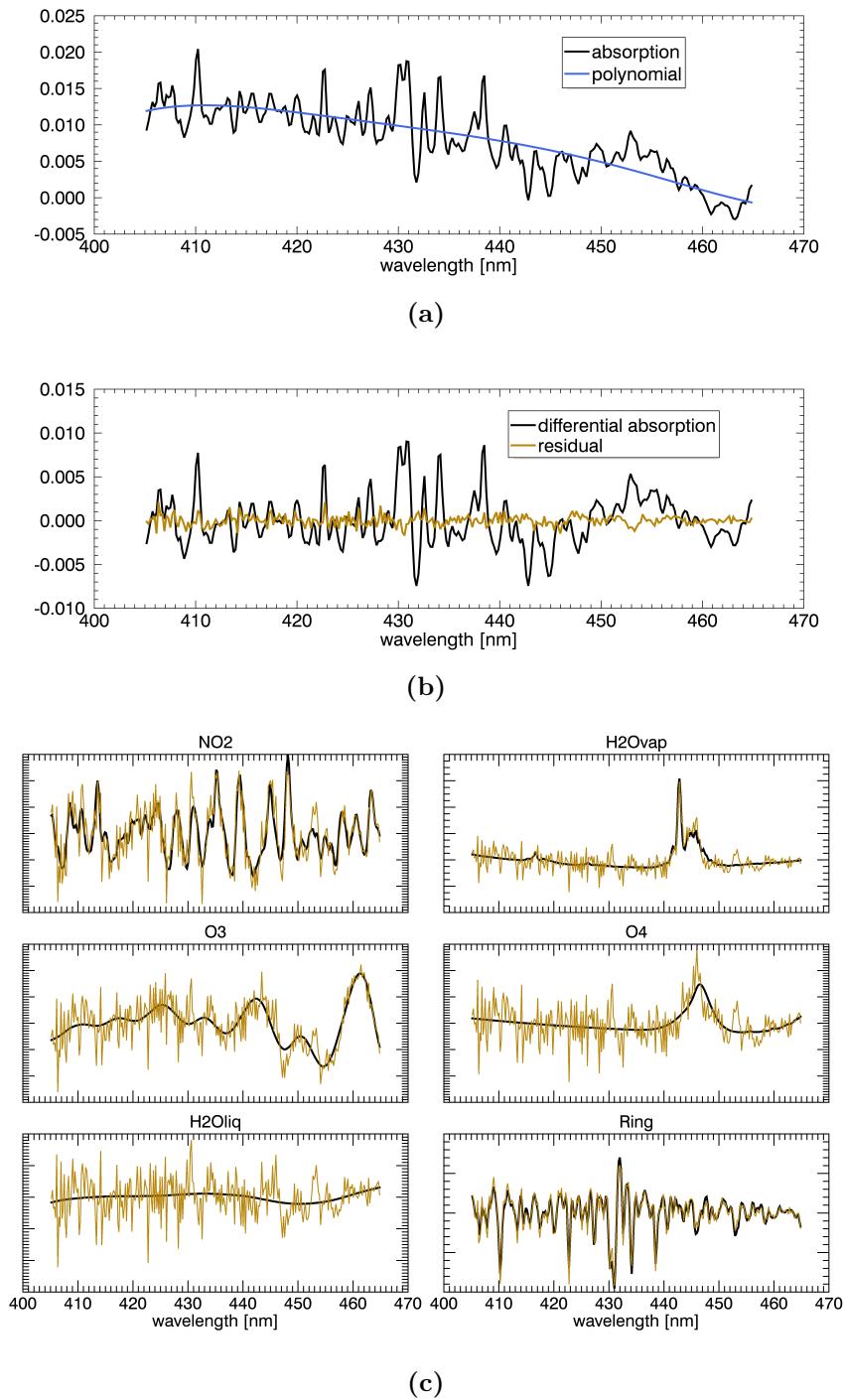


Figure 6.1: Example of applying the DOAS technique to the spectral analysis of NO_2 from TROPOMI spectra at 405–465 nm for orbit 3272 on 1 June 2018. The absorption is separated into the narrow and broad-band part using a fifth-order polynomial in panel (a), yielding the differential absorption spectrum and fitting residuals in panel (b). The differential absorption cross-sections of the trace gases and the Ring effect (black lines) are scaled to the differential absorption determined in the satellite spectrum (blue lines) in panel (c).

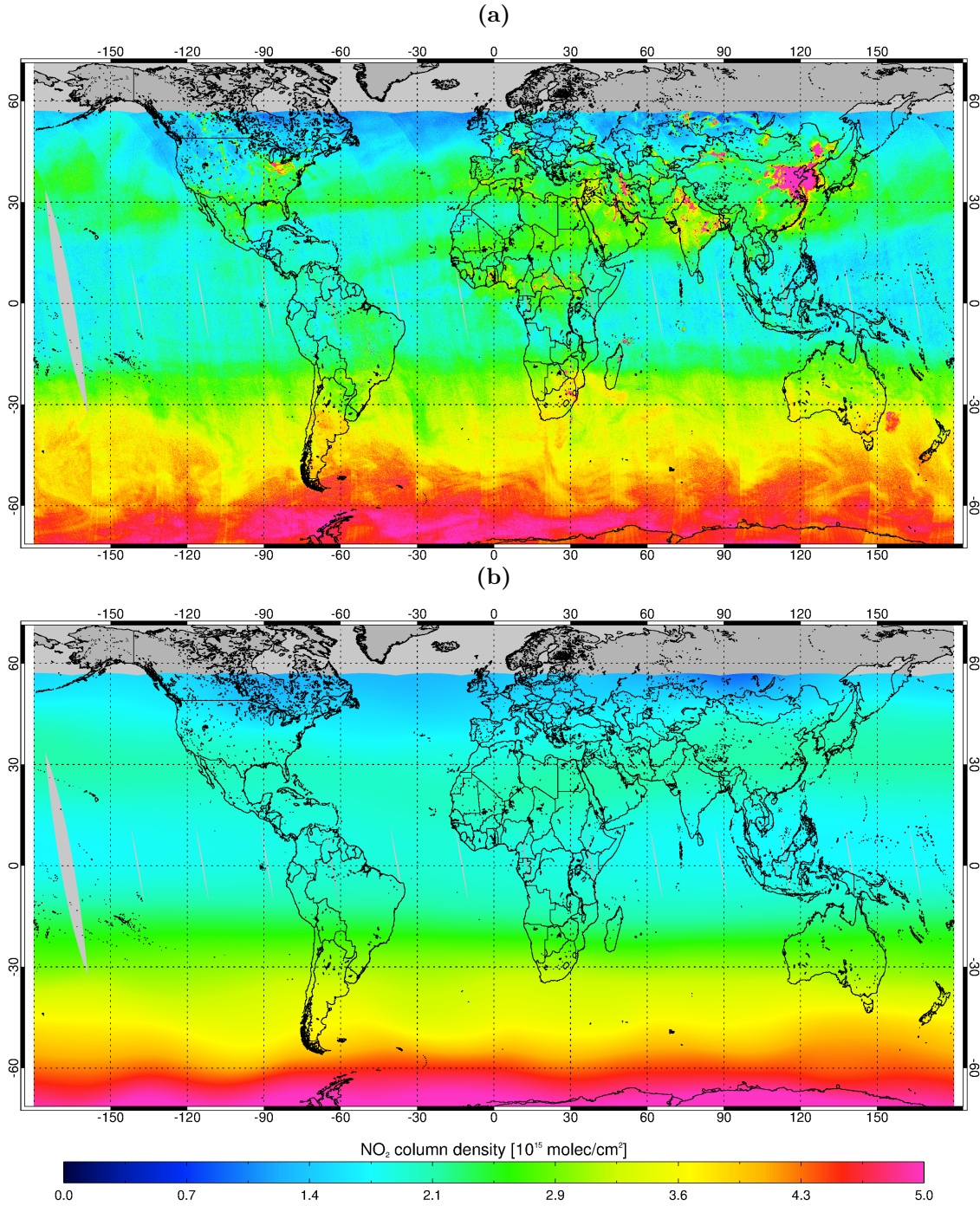


Figure 6.2: TROPOMI total NO₂ distribution (a) and corresponding stratospheric NO₂ distribution as obtained with the STREAM algorithm (b) on 1 January 2018.

OMI monthly averaged surface albedo maps and a linear interpolation in time to the measurement day. The surface pressure is taken from the ECMWF operational model. The daily TM5-MP vertical NO₂ profiles (Williams et al., 2017) simulated at a global $1^\circ \times 1^\circ$ resolution are used as a priori NO₂ vertical profiles due to the operational advantage. The a priori profiles are determined for the satellite overpass time and interpolated to the center of the TROPOMI pixel based on four nearest neighbour TM5-MP cell centers.

In the presence of clouds, the operational TROPOMI cloud parameters from the

OCRA/ROCINN algorithms (Lutz et al., 2016; Loyola et al., 2018) are used in the independent pixel approximation, with clouds treated as opaque Lambertian surfaces for computational efficiency sake. The cloud fraction is determined with OCRA by separating a spectral scene into cloudy contribution and cloud-free background, and the cloud pressure and cloud albedo are derived using the ROCINN algorithm by comparing simulated and measured radiance in and near the O₂ A-band. The aerosol effect is not explicitly corrected, assuming that the effective clouds from OCRA/ROCINN have partly accounted for the effect of aerosols on the light paths.

Figure 6.3 presents the variability in the tropospheric AMFs for pixels with cloud radiance fraction < 0.5 (see Sect. 3.5) over Europe for orbit 3704 on 1 July 2018. Small values between 0.5 and 1.0 are mainly found over polluted regions, such as the UK, the Benelux, and Germany. Higher values by more than 2.0 are found over clean regions, such as the oceans, the mountains, and the snow coverages, especially at extreme geometries. These values are in agreement with theoretical studies in Sect. 4.2.2.

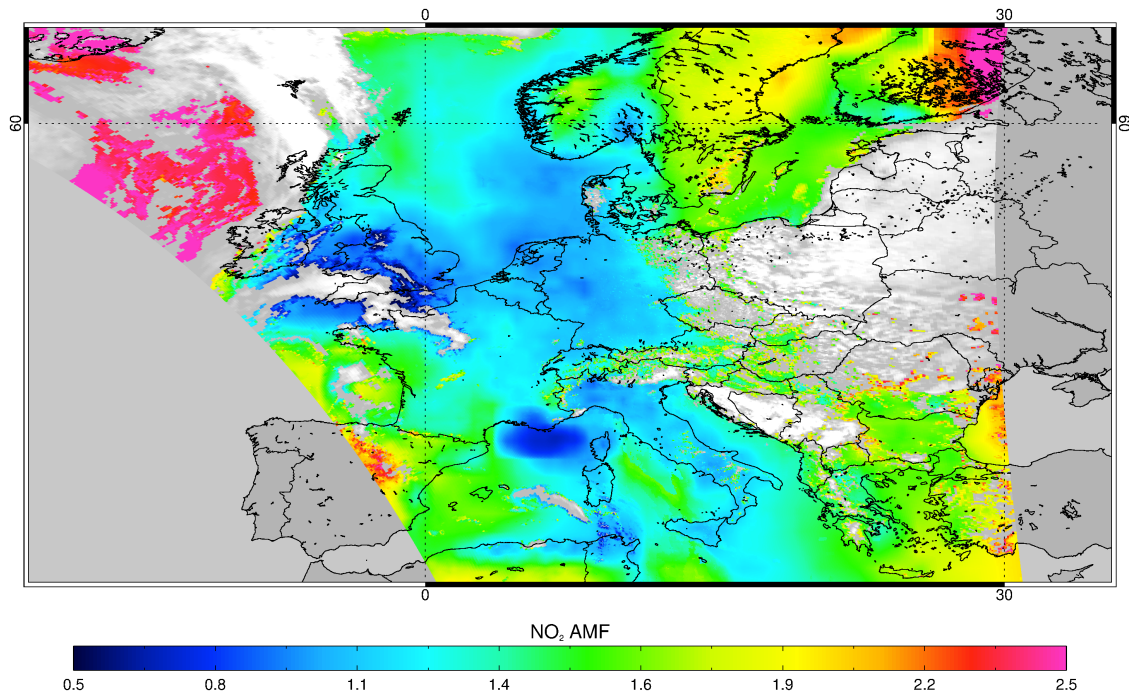


Figure 6.3: Tropospheric AMFs for pixels with cloud radiance fraction < 0.5 over Europe for orbit 3704 on 1 July 2018.

6.3 Examples of TROPOMI tropospheric NO₂

Figure 6.4 shows the yearly averaged tropospheric NO₂ columns from TROPOMI for pixels with cloud radiance fraction < 0.5 over Europe in 2018. High tropospheric NO₂ concentrations by more than 5×10^{15} molec/cm² are found over urban and industrial areas, such as the Po Valley, Germany’s Ruhr region, the Benelux, South-East England, and Turkey’s Marmara region. A number of “city-size” polluted regions, e.g., around Paris, Madrid, Rome, Athens, and Moscow, are clearly captured by the TROPOMI NO₂ measurements. Additionally, NO₂ emissions over the shipping routes, e.g., the maritime connection between the Iberian Peninsula and North Africa, as well as over the highways, e.g., the main East-West thoroughfare in Austria, are also detected. These large tropo-

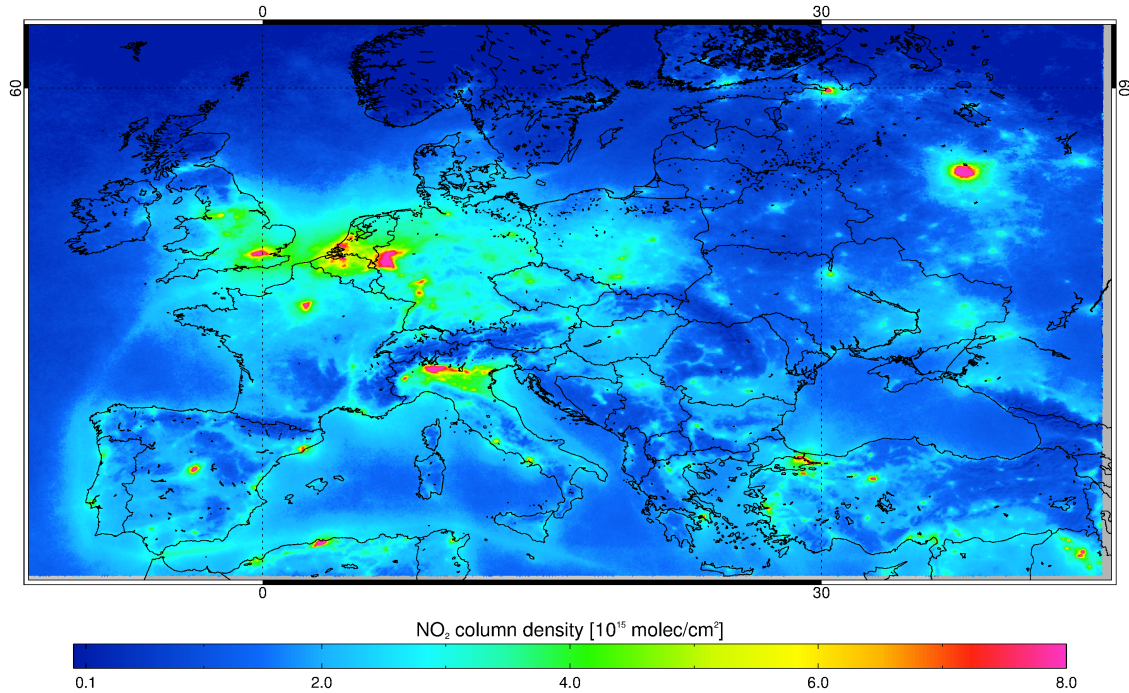


Figure 6.4: Yearly averaged TROPOMI tropospheric NO₂ columns for pixels with cloud radiance fraction < 0.5 over Europe in 2018.

spheric NO₂ concentrations are mainly caused by anthropogenic combustion activities via reactions (R 2.1)-(R 2.4) and consistent with the global NO_x emissions in Fig. 2.1.

Figure 6.5 presents the seasonal variation of TROPOMI tropospheric NO₂ columns for pixels with cloud radiance fraction < 0.5 over Germany and surrounding regions in 2017-2018. The highest tropospheric NO₂ level is found during winter, probably resulted from the increased emissions from heating processes and the increased lifetime of NO₂ due to the low temperature (see Sect. 2.3). The NO₂ values are generally lower by more than 1×10^{15} molec/cm² in summer.

Figure 6.6 presents the weekday-weekend variation of TROPOMI tropospheric NO₂ columns for pixels with cloud radiance fraction < 0.5 over Germany and surrounding regions on 21-28 July 2018. The high values of TROPOMI tropospheric NO₂ columns over the Po Valley, the Ruhr region, and the Benelux are significantly reduced on Sunday (27 July 2018), likely due to the reduced traffic- and industrial-related NO₂ emissions corresponding to the weekend pattern, in agreement with previous studies (e.g., Wickert, 2001; Beirle et al., 2003)

Figure 6.7 presents the daily tropospheric NO₂ columns for pixels with cloud radiance fraction < 0.5 over East Asia on 11 March 2018. With a spatial resolution of 7 km × 3.5 km and a swath width of ~2600 km, the TROPOMI measurements are able to detect regionally the high NO₂ concentrations, for instance, over the economical zones in East China and industrial regions in Korea and Japan, at the power plants in North India, as well as at the highways in Northwest China and the shipping lanes in the Strait of Malacca.

Benefited from the fine spatial resolution and the high signal-to-noise ratio, the daily global NO₂ measurements from TROPOMI have opened a new era for air quality and climate change monitoring, particularly for studies such as regional NO₂ distribution and transport, air quality forecast and analyses, NO_x lifetime and emission estimate, and

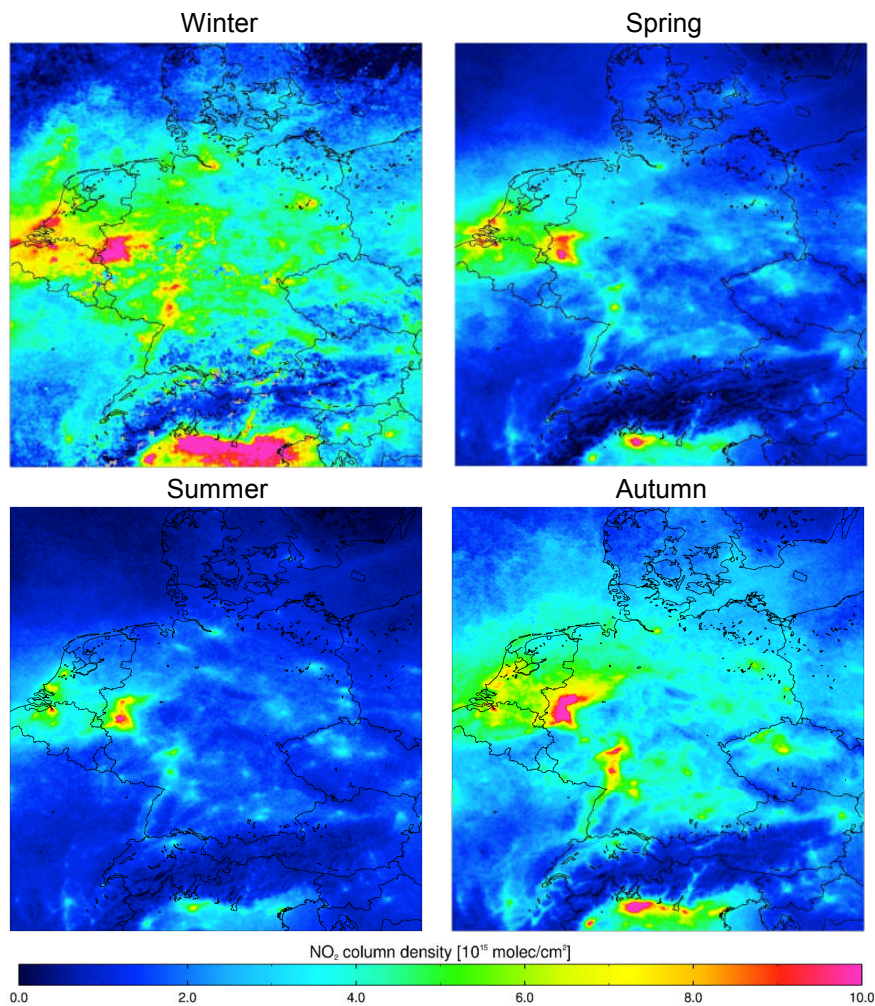


Figure 6.5: Seasonal variation of TROPOMI tropospheric NO₂ columns for pixels with cloud radiance fraction < 0.5 over Germany and surrounding regions in winter (December 2017-February 2018), spring (March-May 2018), summer (June-August 2018), and autumn (September-November 2018).

interpretation of volatile organic compound levels, ozone variations, or aerosol loading.

6.4 Verification and validation

A verification and validation approach usually includes several steps. First, the DOAS analysis results, cloud property retrievals, and AMF calculations are compared with other independent retrievals. Second, the stratospheric reference is evaluated by comparison with correlative observations from ground-based zenith-looking DOAS spectrometers and from other established nadir-looking satellite retrievals. Third, the total and tropospheric NO₂ column data are compared with correlative observations from ground-based direct Sun DOAS and MAXDOAS spectrometers, respectively (Pinardi et al., 2014, 2015). See Sect. 2.5.1 for introduction of the ground-based measurements.

slant columns

The overall quality of TROPOMI total NO₂ columns is evaluated by comparing to OMI

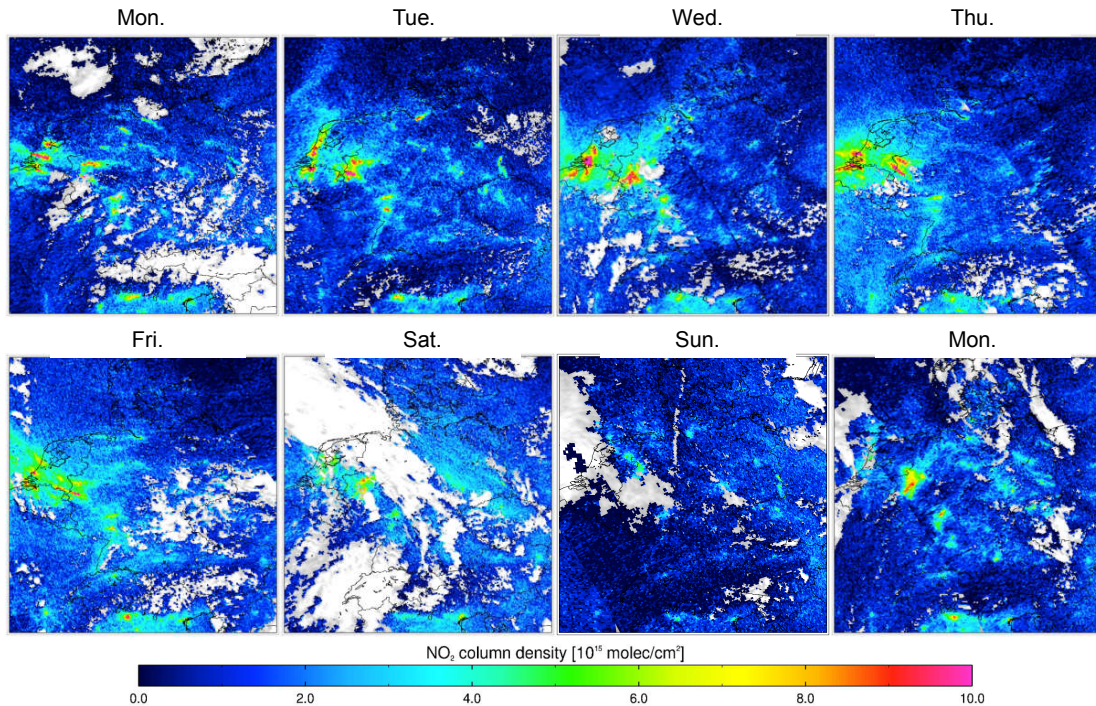


Figure 6.6: Weekday-weekend variation of TROPOMI tropospheric NO_2 columns for pixels with cloud radiance fraction < 0.5 over Germany and surrounding regions on 21-28 July 2018.

and GOME-2 data. Figure 6.8 shows time series of TROPOMI, OMI and GOME-2 NO_2 over the Pacific region (160°E - 180°E) for 20° latitude bands in the northern hemisphere in 2018. Over this area, the impact of tropospheric pollution is assumed to be negligible. The slant columns are normalised by their geometric AMFs to consider the angular dependencies. The TROPOMI and OMI datasets show overall good agreement with consistent daily, seasonal, and latitudinal variations, due to the strong similarities in the illumination conditions, observation geometries, and instrumental characteristics between the two spectrometers. The TROPOMI and GOME-2 measurements differ systematically by $\sim 5 \times 10^{14}$ molec/ cm^2 , mainly related to the different overpass time (13:30 local time for TROPOMI and 9:30 local time for GOME-2) and the strong diurnal variation in the stratospheric NO_2 (Belmonte Rivas et al., 2014).

stratospheric columns

The stratospheric NO_2 columns are compared with the operational TROPOMI product version 1.0.2 derived by KNMI. Due to the use of same level 1 measurements and consistent DOAS settings, differences in the slant columns from the two NO_2 datasets are generally small. Therefore, the different stratospheric columns are attributed to the use of different stratosphere-troposphere separation algorithms (data assimilation for KNMI product and STREAM for this work). Figure 6.9 shows the TROPOMI stratospheric NO_2 columns derived using the STREAM algorithm and using the data assimilation method over East China, Germany, and eastern US in July 2018. The stratospheric NO_2 columns obtained from the two methods are similar in general with daily differences within $\pm 5 \times 10^{14}$ molec/ cm^2 and monthly mean differences up to $\sim 2 \times 10^{14}$ molec/ cm^2 . See Sect. 3.6.3 for uncertainty analysis of the two methods.

tropospheric columns

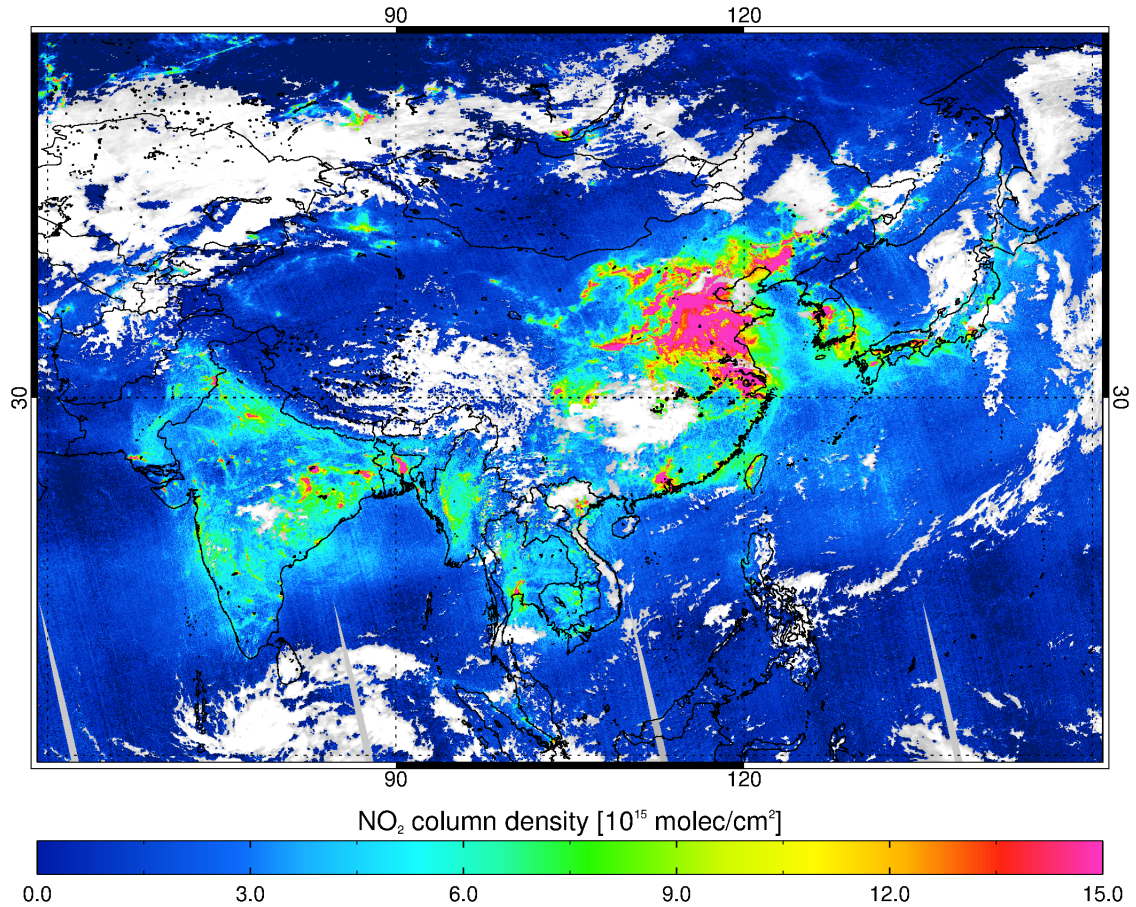


Figure 6.7: Tropospheric NO₂ columns from TROPOMI for pixels with cloud radiance fraction < 0.5 over East Asia on 11 March 2018.

The TROPOMI tropospheric NO₂ columns are validated by comparison with ground-based MAXDOAS measurements (see Sect. 5.3) in Xianghe (39.75°N, 116.96°E) in January–July 2018. The BIRA-IASB Xianghe site is a suburban station surrounded by industrialized areas in North China (Cl mer et al., 2010; Hendrick et al., 2014; Vlemmix et al., 2015). For the validation of TROPOMI measurements, comparison datasets are selected by averaging daily the TROPOMI measurements (cloud radiance fraction < 0.5) within 20 km around Xianghe and by interpolating the ground-based data at the satellite overpass time (13:30 local time).

Figure 6.10 shows the time series and scatter plots of the TROPOMI and MAXDOAS tropospheric NO₂ columns in Xianghe, including the statistical information on the number of points, correlation coefficient, as well as slope and intercept of orthogonal regression analysis. The TROPOMI and MAXDOAS measurements show good agreement with similar variations in the tropospheric NO₂ columns. The monthly mean values range between 0.5×10^{16} and 3×10^{16} molec/cm², depending mainly on the solar radiation, emission sources, and meteorological conditions. A correlation coefficient of 0.96, a regression slope of 1.12 (± 0.12), and an intercept of $-0.38 (\pm 0.17) \times 10^{16}$ molec/cm² are derived for the comparison of monthly mean values. These results are qualitatively consistent with previous validation exercises (e.g., Celarier et al., 2008; Kramer et al., 2008; Chen et al., 2009; Irie et al., 2012; Ma et al., 2013; Wu et al., 2013; Kanaya et al., 2014; Wang et al., 2017; Drosoglou et al., 2017, 2018).

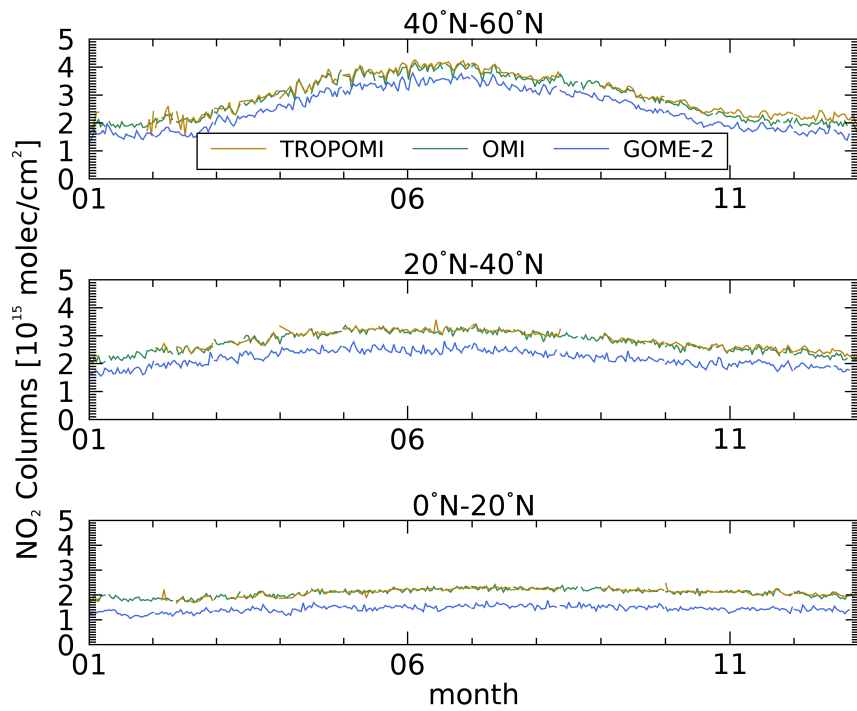


Figure 6.8: NO_2 slant columns measured by TROPOMI, OMI and GOME-2 over the Pacific (160°E - 180°E) for 20° latitude bands in the northern hemisphere in 2018. Geometric AMFs have been applied to consider the different angular dependencies.

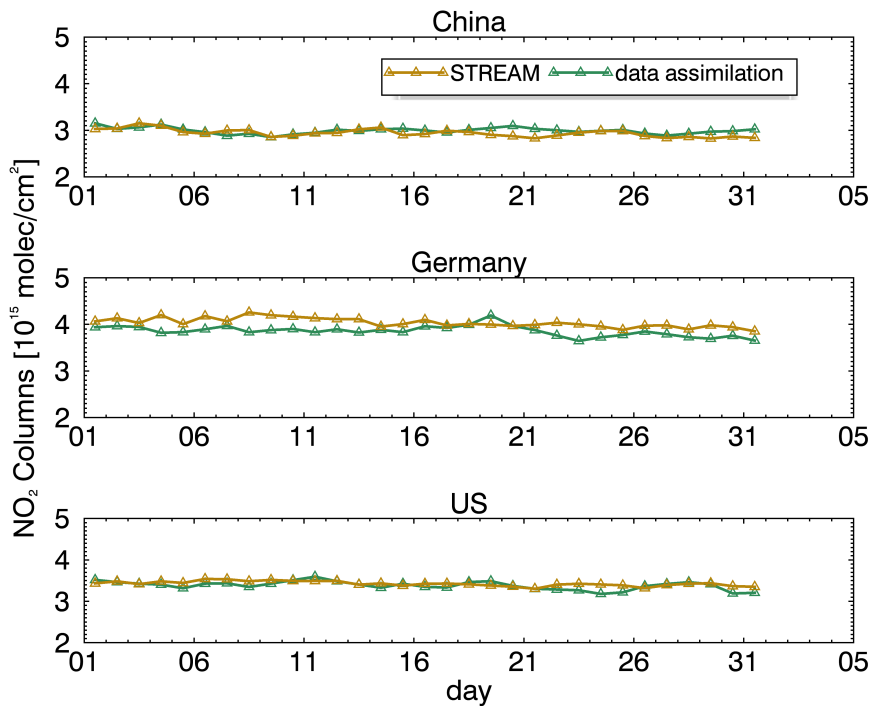


Figure 6.9: TROPOMI stratospheric NO_2 columns derived using the STREAM algorithm and the operational data assimilation method over East China (21°N - 41°N , 110°E - 122°E), Germany (45°N - 57°N , 3°E - 17°E), and eastern US (30°N - 45°N , 70°W - 90°W) in July 2018.

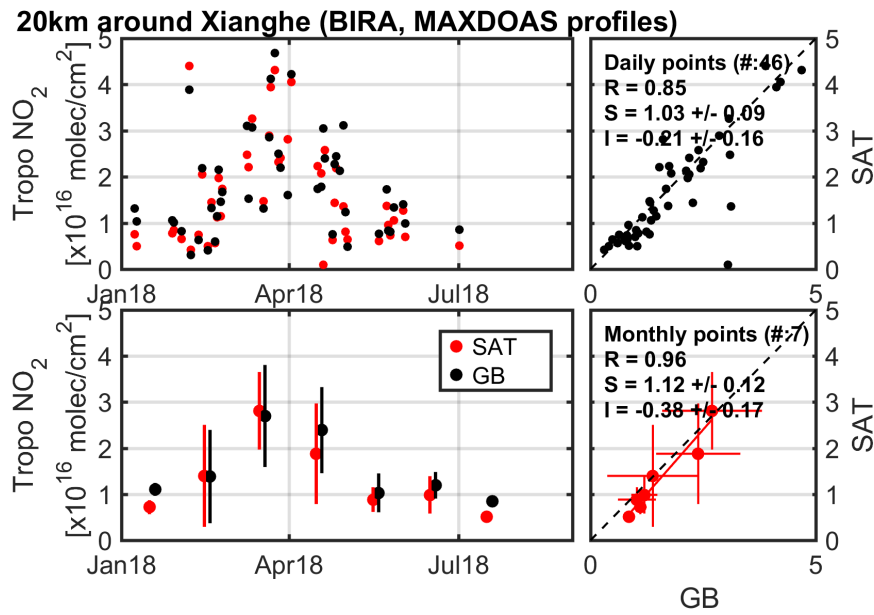


Figure 6.10: Daily and monthly mean time series and scatter plot of TROPOMI and MAXDOAS tropospheric NO₂ columns (mean value of all the pixels within 20 km around Xianghe, 39.75°N, 116.96°E).

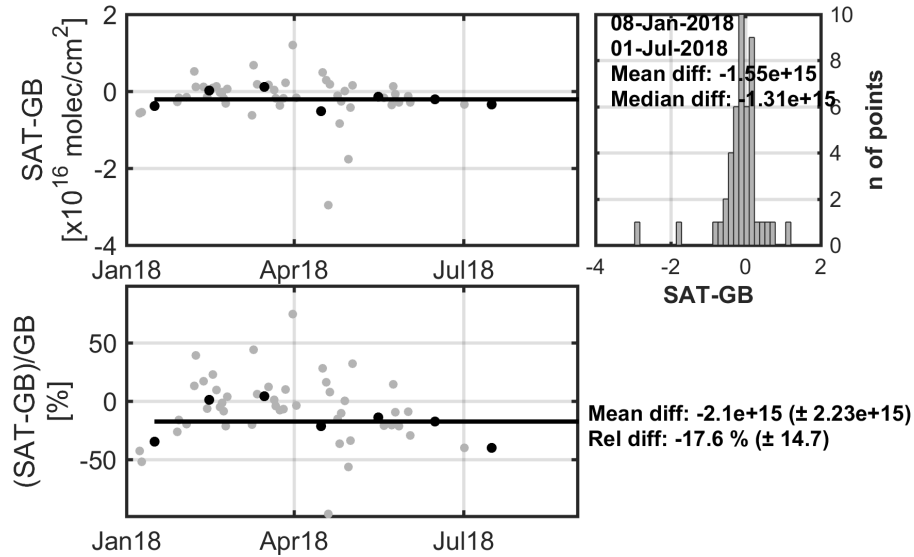


Figure 6.11: Daily (grey dots) and monthly mean (black dots) absolute and relative TROPOMI and MAXDOAS time series differences for the Xianghe station. The histogram of the daily differences is also given, along with the mean and median difference. The total time-series absolute and relative monthly differences are reported outside the panels.

Figure 6.11 presents the absolute and relative differences of TROPOMI and MAXDOAS measurements. As described in the histogram, the daily differences are on average

within $\pm 5 \times 10^{15}$ molec/cm² with a median value of -1.3×10^{15} molec/cm². The monthly NO₂ levels are underestimated by 17.6% by TROPOMI with a standard deviation of $\pm 14.7\%$, mostly explained by the relatively low sensitivity of space-borne measurements near the surface, the gradient-smoothing effect, and the aerosol shielding effect. These effects are often inherent to the different measurement types, the specific conditions of the validation sites, and the remaining impact of structural uncertainties (Boersma et al., 2016), such as the impact of the choices of the albedo database and the a priori NO₂ profiles for the satellite AMF calculation (see Sects. 4.2 and 4.3).

To conclude, the TROPOMI data show consistent total and stratospheric columns with other nadir-looking satellite measurements and other independent satellite retrievals with differences lower than 5×10^{14} molec/cm². The TROPOMI tropospheric NO₂ columns agree well with the ground-based MAXDOAS measurements with a correlation coefficient of 0.96 for monthly points and a median difference -1.3×10^{15} molec/cm² for daily points. The Xianghe site, by its suburban nature, is the best site for validation, since NO₂ concentrations from urban stations are generally underestimated by the satellite instruments due to the averaging of a local source over a pixel size, and difficulties arise for remote stations when small local sources are present (Pinardi et al., 2015). In the future, the data quality of the TROPOMI measurements will be further evaluated using data from other sites (see Sect. 7.2).

Chapter 7

Conclusion and outlook

7.1 Conclusion

This work has described the application of the GOME-2 and TROPOMI satellite instruments for monitoring the NO₂ pollution patterns. The GOME-2 sensors on the Sun-synchronous polar orbiting MetOp satellites have been providing a continuous NO₂ dataset since 2007 with a global coverage on a daily basis. This long-term NO₂ data record has been extended by the TROPOMI instrument aboard the Sentinel-5 Precursor with an unprecedented resolution of 7 km × 3.5 km. Based on the satellite (ir)radiances, the abundance of NO₂ is retrieved from the narrow-band absorption structures of NO₂ in the backscattered radiation in the visible spectral region.

retrieval method

In Chap. 3, the classical three-step-retrieval of total and tropospheric NO₂ columns for ultraviolet-visible backscatter satellite instruments is introduced. The NO₂ slant columns are determined using the DOAS technique, based on which the tropospheric NO₂ vertical columns are retrieved with a subtraction of the stratospheric contributions and an AMF calculation with a radiative transfer model. State-of-the-art retrievals for specific instrument and thorough uncertainty estimations for each algorithm step are essential for good data quality. The theoretical basis for applying the DOAS-based technique is discussed in the context of general retrieval theory in a paper in Appendix A.

theoretical analysis

In Chap. 4, the reliability of the DOAS-based algorithm for retrieving NO₂ is discussed. The performance of the DOAS slant column retrieval is evaluated by applying it to the simulated radiances, with biases lower than 1% for basic scenarios with NO₂ absorption at different altitude regimes and up to 20% for realistic scenarios with various pollution conditions. These biases are corrected for the vertical columns during the AMF calculation. Error sources in the AMF calculation are assessed by analysing the influences of individual input parameters, such as surface properties, a priori NO₂ profile, and cloud parameters. Errors in these parameters introduce an overall AMF uncertainty of 15%-50% for polluted conditions, indicating the necessity of appropriate retrieval settings and accurate a priori and ancillary data.

retrieval for GOME-2

In Chap. 5, the application of the retrieval algorithm to GOME-2 measurements is described, focusing on the latest developments in the operational algorithm at DLR based on three papers in Appendices B-D. Compared to the previous NO₂ retrieval schemes,

the developed algorithm applies an extended 425-497 nm wavelength fitting window and an improved (ir)radiance calibration for the DOAS retrieval, showing a better data quality and consistency with state-of-the-science datasets. The stratospheric estimation is implemented using the STREAM scheme, which largely reduces the overestimation of stratospheric NO₂ columns over polluted regions. The calculation of AMF applies an improved description of the radiative transfer, a direction-dependent surface albedo dataset, advanced high-resolution a priori NO₂ profiles, and realistic cloud parameters with clouds treated as scattering layers of water droplets. The use of these new features has an impact of more than 10% on the retrieved tropospheric NO₂ columns over polluted regions. To evaluate the data quality of GOME-2 tropospheric NO₂ columns, an end-to-end validation is performed using the MAXDOAS measurements from BIRA-IASB stations covering urban, suburban, and background situations. The new dataset shows a globally improved agreement with the MAXDOAS measurements, with a reduction of the absolute and relative monthly mean bias as well as a reduction in the spread of the daily comparison points.

retrieval for TROPOMI

In Chap. 6, the improved GOME-2 algorithm is adapted and optimised for the TROPOMI instrument. The TROPOMI retrieval algorithm relies on a fitting window of 405-465 nm as a heritage of OMI DOAS fit, an updated STREAM algorithm to estimate the stratospheric contribution, and an AMF calculation based on the operational TROPOMI cloud products. Example applications of the TROPOMI tropospheric NO₂ columns show kilometer-scale spatial details, such as power plants, shipping routes, and major highways, which have not been possible on daily basis for previous space-borne spectrometers, beneficial from the high spatial resolution and the good data quality for TROPOMI. The verification and validation of the TROPOMI measurements are implemented by comparing the slant columns to the OMI and GOME-2 dataset, comparing the stratospheric columns to the operational KNMI TROPOMI product, and comparing the tropospheric NO₂ measurements to the ground-based MAXDOAS observations at the BIRA-IASB Xianghe station. The retrieved slant and stratospheric columns agree well with the correlative satellite datasets with differences within $\pm 5 \times 10^{14}$ molec/cm². The tropospheric columns from the TROPOMI and MAXDOAS measurements show similar variations with a correlation coefficient of 0.96 and a median difference -1.3×10^{15} molec/cm², indicating a good data quality.

7.2 Outlook

The algorithm framework proposed in this work can be easily adapted for future ultraviolet-visible sensors and can be used as reference for future algorithm developments.

new instruments and missions

In the future, the NO₂ retrieval algorithm can be adapted for new instruments and missions to monitor the NO₂ concentrations. With the new GOME-2 instrument launched on MetOp-C in November 2018, the operations of three MetOp platforms ensure a continuous long-term dataset until 2023, providing a better understanding of NO₂ diurnal variation in combination with afternoon observations from OMI and TROPOMI. Future missions such as geostationary Sentinel-4 and polar-orbiting Sentinel-5 offer new perspectives for monitoring NO₂ with a fast revisiting time and a high spatial resolution, providing information on atmospheric variables in support of European policies.

TROPOMI algorithm refinement

Future versions of the NO₂ retrieval algorithm for the Sentinel-5 Precursor sensor TROPOMI will focus on the use of the extended 425-497 nm fitting window, when the detector saturation and blooming are correctly flagged in the level 1b data. Further benefits come from an improved STREAM by taking the across-track diurnal variation of stratospheric NO₂ into account. The use of improved a priori and ancillary information, such as TROPOMI-based surface albedo dataset in combination with the snow or ice cover information from the Near-real-time Ice and Snow Extent (NISE) dataset (Nolin et al., 1998), high-resolution NO₂ profiles from the CAMS regional air quality ensemble (METEO-FRANCE et al., 2016), and global aerosol vertical distributions from the space-borne Cloud-Aerosol Lidar and Infrared Pathfinder Satellite Observation (CALIPSO) lidar (Tackett et al., 2018) will additionally improve the AMF calculation. The OCRA/ROCINN cloud parameters will be updated with an improved spatial misalignment correction between the ultraviolet-visible band (used for NO₂ retrieval) and near-infrared band (used for ROCINN cloud retrieval). In addition, the quantitative interpretation of the OCRA/ROCINN cloud product for aerosol-dominated scenes and the impact on NO₂ retrieval algorithm will be further investigated.

TROPOMI validation

The data quality of the TROPOMI tropospheric NO₂ measurements will be further analysed using data from additional BIRA-IASB MAXDOAS stations, such as Uccle (urban polluted site in Belgium), Bujumbura (remote site in Burundi in tropical Africa), and OHP (background site in southern France). Dedicated measurements from recent and future validation campaigns, such as the Cabauw Intercomparison of Nitrogen Dioxide Measuring Instruments 2 (CINDI-2) campaign (Kreher et al., 2019) and TROPOMI validation eXperiment 2019 (TROLIX'19) at the KNMI Cabauw site, provide a good chance for TROPOMI validation with independent instruments. The validation of total and stratospheric NO₂ columns will benefit from network-based direct Sun instruments, e.g., the Pandora systems, and zenith sky instruments, e.g., spectrometers affiliated with the Network for the Detection of Atmospheric Composition Change (NDACC), respectively (Pinardi et al., 2018).

Bibliography

- Anderson, G. P., Clough, S. A., Kneizys, F., Chetwynd, J. H., and Shettle, E. P.: AFGL atmospheric constituent profiles (0.120 km), Tech. rep., AIR FORCE GEOPHYSICS LAB HANSCOM AFB MA, 1986.
- Azam, F., Richter, A., Weber, M., Noë, S., and Burrows, J.: GOME-2 on MetOp-B Follow-on analysis of GOME2 in orbit degradation, Tech. rep., EUM/CO/09/4600000696/RM, Final Report, IUP University of Bremen, 2015.
- Beirle, S., Platt, U., Wenig, M., and Wagner, T.: Weekly cycle of NO₂ by GOME measurements: a signature of anthropogenic sources, *Atmos. Chem. Phys.*, **3**, 2225–2232, 2003.
- Beirle, S., Kühl, S., Pukite, J., and Wagner, T.: Retrieval of tropospheric column densities of NO₂ from combined SCIAMACHY nadir/limb measurements, *Atmos. Meas. Tech.*, **3**, 283–299, 2010.
- Belmonte Rivas, M., Veefkind, P., Boersma, F., Levelt, P., Eskes, H., and Gille, J.: Intercomparison of daytime stratospheric NO₂ satellite retrievals and model simulations, *Atmos. Meas. Tech.*, **7**, 2203–2225, 2014.
- Boersma, K., Eskes, H., and Brinksma, E.: Error analysis for tropospheric NO₂ retrieval from space, *J. Geophys. Res. Atmos.*, **109**, 2004.
- Boersma, K., Vinken, G., and Eskes, H.: Representativeness errors in comparing chemistry transport and chemistry climate models with satellite UV–Vis tropospheric column retrievals, *Geosci. Model Dev.*, **9**, 875, 2016.
- Boersma, K. F., Eskes, H. J., Veefkind, J. P., Brinksma, E. J., van der A, R. J., Sneep, M., van den Oord, G. H. J., Levelt, P. F., Stammes, P., Gleason, J. F., and Bucsela, E. J.: Near-real time retrieval of tropospheric NO₂ from OMI, *Atmos. Chem. Phys.*, **7**, 2103–2118, 2007.
- Boersma, K. F., Eskes, H. J., Dirksen, R. J., van der A, R. J., Veefkind, J. P., Stammes, P., Huijnen, V., Kleipool, Q. L., Sneep, M., Claas, J., Leitão, J., Richter, A., Zhou, Y., and Brunner, D.: An improved tropospheric NO₂ column retrieval algorithm for the Ozone Monitoring Instrument, *Atmos. Meas. Tech.*, **4**, 1905, 2011.
- Boersma, K. F., Eskes, H. J., Richter, A., De Smedt, I., Lorente, A., Beirle, S., van Geffen, J. H. G. M., Zara, M., Peters, E., Van Roozendaal, M., Wagner, T., Maasackers, J. D., van der A, R. J., Nightingale, J., De Rudder, A., Irie, H., Pinardi, G., Lambert, J.-C., and Compornolle, S. C.: Improving algorithms and uncertainty estimates for satellite NO₂ retrievals: results from the quality assurance for the essential climate variables (QA4ECV) project, *Atmos. Meas. Tech.*, **11**, 6651–6678, 2018.
- Boucher, O., Randall, D., Artaxo, P., Bretherton, C., Feingold, G., Forster, P., Kerminen, V.-M., Kondo, Y., Liao, H., Lohmann, U., Rasch, P., Satheesh, S., Sherwood, S., Stevens, B., and Zhang, X.: Clouds and aerosols, in: *Climate change 2013: the physical science basis. Contribution of Working Group I to the Fifth Assessment Report of the Intergovernmental Panel on Climate Change*, pp. 571–657, Cambridge University Press, 2013.

- Bovensmann, H., Burrows, J., Buchwitz, M., Frerick, J., Rozanov, V., Chance, K., and Goede, A.: SCIAMACHY: Mission objectives and measurement modes, *J. Atmos. Sci.*, 56, 1999.
- Brasseur, G. P. and Solomon, S.: *Aeronomy of the middle atmosphere: chemistry and physics of the stratosphere and mesosphere*, 3rd ed., Springer Science & Business Media, 2005.
- Brewer, A., McElroy, C., and Kerr, J.: Nitrogen dioxide concentrations in the atmosphere, *Nature*, 246, 129, 1973.
- Brion, J., Chakir, A., Charbonnier, J., Daumont, D., Parisse, C., and Malicet, J.: Absorption spectra measurements for the ozone molecule in the 350–830 nm region, *J. Atmos. Chem.*, 30, 291–299, 1998.
- Bucsela, E., Krotkov, N., Celarier, E., Lamsal, L., Swartz, W., Bhartia, P., Boersma, K., Veefkind, J., Gleason, J., and Pickering, K.: A new stratospheric and tropospheric NO₂ retrieval algorithm for nadir-viewing satellite instruments: applications to OMI, *Atmos. Meas. Tech.*, 6, 2607, 2013.
- Bucsela, E. J., Celarier, E. A., Wenig, M. O., Gleason, J. F., Veefkind, J. P., Boersma, K. F., and Brinksma, E. J.: Algorithm for NO₂ vertical column retrieval from the ozone monitoring instrument, *IEEE Trans. Geosci. Remote Sens.*, 44, 1245–1258, 2006.
- Burrows, J. P., Weber, M., Buchwitz, M., Rozanov, V., Ladstätter-Weissenmayer, A., Richter, A., DeBeek, R., Hoogen, R., Bramstedt, K., Eichmann, K.-U., Eisinger, M., and Perner, D.: The global ozone monitoring experiment (GOME): Mission concept and first scientific results, *J. Atmos. Sci.*, 56, 151–175, 1999.
- Cahalan, R. F., Ridgway, W., Wiscombe, W. J., Bell, T. L., and Snider, J. B.: The albedo of fractal stratocumulus clouds, *J. Atmos. Sci.*, 51, 2434–2455, 1994.
- Callies, J., Corpaccioli, E., Eisinger, M., Hahne, A., and Lefebvre, A.: GOME-2-Metop’s second-generation sensor for operational ozone monitoring, *ESA bulletin*, 102, 28–36, 2000.
- Castellanos, P., Boersma, K., Torres, O., and De Haan, J.: OMI tropospheric NO₂ air mass factors over South America: effects of biomass burning aerosols, *Atmos. Meas. Tech.*, 8, 3831–3849, 2015.
- Cede, A., Herman, J., Richter, A., Krotkov, N., and Burrows, J.: Measurements of nitrogen dioxide total column amounts using a Brewer double spectrophotometer in direct Sun mode, *J. Geophys. Res. Atmos.*, 111, 2006.
- Celarier, E. A., Brinksma, E. J., Gleason, J. F., Veefkind, J. P., Cede, A., Herman, J. R., Ionov, D., Goutail, F., Pommereau, J.-P., Lambert, J.-C., van Roozendael, M., Pinardi, G., Wittrock, F., Schönhardt, A., Richter, A., Ibrahim, O. W., Wagner, T., Bojkov, B., Mount, G., Spinei, E., Chen, C. M., Pongetti, T. J., Sander, S. P., Bucsela, E. J., Wenig, M. O., Swart, D. P. J., Volten, H., Kroon, M., and Levelt, P. F.: Validation of Ozone Monitoring Instrument nitrogen dioxide columns, *J. Geophys. Res. Atmos.*, 113, 2008.
- Chance, K. V. and Spurr, R. J.: Ring effect studies: Rayleigh scattering, including molecular parameters for rotational Raman scattering, and the Fraunhofer spectrum, *Appl. Opt.*, 36, 5224–5230, 1997.
- Chen, D., Zhou, B., Beirle, S., Chen, L., and Wagner, T.: Tropospheric NO₂ column densities deduced from zenith-sky DOAS measurements in Shanghai, China, and their application to satellite validation, *Atmos. Chem. Phys.*, 9, 3641–3662, 2009.
- Chimot, J., Veefkind, J. P., Haan, J. F. d., Stammes, P., and Levelt, P. F.: Minimizing aerosol effects on the OMI tropospheric NO₂ retrieval—An improved use of the 477 nm O₂-O₂ band and an estimation of the aerosol correction uncertainty, *Atmos. Meas. Tech.*, 12, 491–516, 2019.

- Clémer, K., Van Roozendael, M., Fayt, C., Hendrick, F., Hermans, C., Pinardi, G., Spurr, R., Wang, P., and De Mazière, M.: Multiple wavelength retrieval of tropospheric aerosol optical properties from MAXDOAS measurements in Beijing, *Atmos. Meas. Tech.*, 3, 863, 2010.
- Crippa, M., Guizzardi, D., Muntean, M., Schaaf, E., Dentener, F., van Aardenne, J. A., Monni, S., Doering, U., Olivier, J. G. J., Pagliari, V., and Janssens-Maenhout, G.: Gridded emissions of air pollutants for the period 1970-2012 within EDGAR v4. 3.2, *Earth Syst. Sci. Data*, 10, 1987–2013, 2018.
- Crutzen, P. J.: The influence of nitrogen oxides on the atmospheric ozone content, *Q. J. R. Meteorol. Soc.*, 96, 320–325, 1970.
- Danckaert, T., Fayt, C., Van Roozendael, M., De Smedt, I., Letocart, V., Merlaud, A., and Pinardi, G.: QDOAS software user manual 2.109, 2015.
- De Smedt, I., Theys, N., Yu, H., Danckaert, T., Lerot, C., Compernelle, S., Van Roozendael, M., Richter, A., Hilboll, A., Peters, E., Pedergnana, M., Loyola, D., Beirle, S., Wagner, T., Eskes, H., van Geffen, J., Boersma, K. F., and Veeckind, P.: Algorithm theoretical baseline for formaldehyde retrievals from S5P TROPOMI and from the QA4ECV project, *Atmos. Meas. Tech.*, 11, 2395–2426, 2018.
- Dentener, F. J. and Crutzen, P. J.: Reaction of N_2O_5 on tropospheric aerosols: Impact on the global distributions of NO_x , O_3 , and OH , *J. Geophys. Res. Atmos.*, 98, 7149–7163, 1993.
- Desmons, M., Wang, P., Stammes, P., and Tilstra, L. G.: FRESCO-B: a fast cloud retrieval algorithm using oxygen B-band measurements from GOME-2, *Atmos. Meas. Tech.*, 12, 2485–2498, 2019.
- Deutschmann, T., Beirle, S., Frieß, U., Grzegorski, M., Kern, C., Kritten, L., Platt, U., Prados-Román, C., Pułki, J., Wagner, T., Werner, B., and Pfeilsticker, K.: The Monte Carlo atmospheric radiative transfer model McArtim: Introduction and validation of Jacobians and 3D features, *J. Quant. Spectrosc. Radiat. Transf.*, 112, 1119–1137, 2011.
- Ding, J., Miyazaki, K., van der A, R. J., Mijling, B., Kurokawa, J.-I., Cho, S., Janssens-Maenhout, G., Zhang, Q., Liu, F., and Levelt, P. F.: Intercomparison of NO_x emission inventories over East Asia, *Atmos. Chem. Phys.*, 17, 10 125, 2017.
- Dirksen, R. J., Boersma, K. F., Eskes, H. J., Ionov, D. V., Bucsela, E. J., Levelt, P. F., and Kelder, H. M.: Evaluation of stratospheric NO_2 retrieved from the Ozone Monitoring Instrument: Intercomparison, diurnal cycle, and trending, *J. Geophys. Res. Atmos.*, 116, 2011.
- Dobson, G.: Observers' handbook for the ozone spectrophotometer, *Ann. Int. Geophys. Year*, 5, 46–89, 1957.
- Drosoglou, T., Bais, A. F., Zyrichidou, I., Kouremeti, N., Poupkou, A., Liora, N., Giannaros, C., Koukouli, M. E., Balis, D., and Melas, D.: Comparisons of ground-based tropospheric NO_2 MAX-DOAS measurements to satellite observations with the aid of an air quality model over the Thessaloniki area, Greece, *Atmos. Chem. Phys.*, 17, 5829–5849, 2017.
- Drosoglou, T., Koukouli, M. E., Kouremeti, N., Bais, A. F., Zyrichidou, I., Balis, D., Xu, J., and Li, A.: MAX-DOAS NO_2 observations over Guangzhou, China; ground-based and satellite comparisons, *Atmos. Meas. Tech.*, 11, 2239–2255, 2018.
- Ehhalt, D. H., Rohrer, F., and Wahner, A.: Sources and distribution of NO_x in the upper troposphere at northern mid-latitudes, *J. Geophys. Res. Atmos.*, 97, 3725–3738, 1992.
- Eskes, H. and Boersma, K.: Averaging kernels for DOAS total-column satellite retrievals, *Atmos. Chem. Phys.*, 3, 1285–1291, 2003.

- Eskes, H., Van Velthoven, P., Valks, P., and Kelder, H.: Assimilation of GOME total-ozone satellite observations in a three-dimensional tracer-transport model, *Q. J. R. Meteorol. Soc.*, 129, 1663–1681, 2003.
- EUMETSAT: GOME-2 Newsletter Archive, Tech. rep., EUM/OPS-EPS/TEN/09/0552, 2015.
- European Commission: The EU Environmental Implementation Review: Common challenges and how to combine efforts to deliver better results, Tech. rep., Ref.: SWD(2017)33-60 fina, 2017.
- Flemming, J., Benedetti, A., Inness, A., Engelen, R. J., Jones, L., Huijnen, V., Remy, S., Parrington, M., Suttie, M., Bozzo, A., Peuch, V.-H., Akritidis, D., and Katragkou, E.: The CAMS interim reanalysis of carbon monoxide, ozone and aerosol for 2003–2015, *Atmos. Chem. Phys.*, 17, 1945–1983, 2017.
- Frieß, U., Monks, P., Remedios, J., Rozanov, A., Sinreich, R., Wagner, T., and Platt, U.: MAX-DOAS O₄ measurements: A new technique to derive information on atmospheric aerosols: 2. Modeling studies, *J. Geophys. Res. Atmos.*, 111, 2006.
- Gamble, J., Jones, W., and Minshall, S.: Epidemiological-environmental study of diesel bus garage workers: acute effects of NO₂ and respirable particulate on the respiratory system, *Environ. Res.*, 42, 201–214, 1987.
- Gielen, C., Hendrick, F., Pinardi, G., De Smedt, I., Fayt, C., Hermans, C., Stavrakou, T., Bauwens, M., Müller, J.-F., Ndenzako, E., Nzohabonayo, P., Akimana, R., Niyonzima, S., Van Roozendael, M., and De Mazière, M.: Characterisation of Central-African aerosol and trace-gas emissions based on MAX-DOAS measurements and model simulations over Bujumbura, Burundi., *Atmos. Chem. Phys. Discuss.*, pp. 1–41, 2017.
- Giles, D. M., Sinyuk, A., Sorokin, M. G., Schafer, J. S., Smirnov, A., Slutsker, I., Eck, T. F., Holben, B. N., Lewis, J. R., Campbell, J. R., Welton, E. J., Korkin, S. V., and Lyapustin, A. I.: Advancements in the Aerosol Robotic Network (AERONET) Version 3 database—automated near-real-time quality control algorithm with improved cloud screening for Sun photometer aerosol optical depth (AOD) measurements, *Atmos. Meas. Tech.*, 12, 169–209, 2019.
- Gottwald, M., Bovensmann, H., Lichtenberg, G., Noel, S., von Barga, A., Slijkhuis, S., Pitters, A., Hoogeveen, R., von Savigny, C., Buchwitz, M., Kokhanovsky, A., Richter, A., Rozanov, A., Holzer-Popp, T., Bramstedt, K., Lambert, J.-C., Skupin, J., Wittrock, F., Schrijver, H., and Burrows, J.: Sciamachy, Monitoring the Changing Earth’s Atmosphere, DLR, 2006.
- Grainger, J. and Ring, J.: Anomalous Fraunhofer line profiles, *Nature*, 193, 762, 1962.
- Granier, C., Darras, S., Denier van der Gon, H., Doubalova, J., Elguindi, N., Galle, B., Gauss, M., Guevara, M., Jalkanen, J.-P., Kuenen, J., Liousse, C., Quack, B., Simpson, D., and Sindelarova, K.: The Copernicus Atmosphere Monitoring Service global and regional emissions, Tech. rep., Copernicus Atmosphere Monitoring Service (CAMS) report, 2019.
- Grzegorski, M., Wenig, M., Platt, U., Stammes, P., Fournier, N., and Wagner, T.: The Heidelberg iterative cloud retrieval utilities (HICRU) and its application to GOME data, *Atmos. Chem. Phys.*, 6, 4461–4476, 2006.
- Gu, D., Wang, Y., Smeltzer, C., and Boersma, K. F.: Anthropogenic emissions of NO_x over China: Reconciling the difference of inverse modeling results using GOME-2 and OMI measurements, *J. Geophys. Res. Atmos.*, 119, 7732–7740, 2014.
- Hassinen, S., Balis, D., Bauer, H., Begoin, M., Delcloo, A., Eleftheratos, K., Gimeno Garcia, S., Granville, J., Grossi, M., Hao, N., Hedelt, P., Hendrick, F., Hess, M., Heue, K.-P., Hovila, J., Jønch-Sørensen, H., Kalakoski, N., Kauppi, A., Kiemle, S., Kins, L., Koukouli, M. E., Kujanpää, J., Lambert, J.-C., Lang, R., Lerot, C., Loyola, D., Pedernana, M., Pinardi, G., Romahn, F., van Roozendael, M., Lutz, R., De Smedt, I., Stammes, P., Steinbrecht, W., Tamminen, J.,

- Theys, N., Tilstra, L. G., Tuinder, O. N. E., Valks, P., Zerefos, C., Zimmer, W., and Zyrichidou, I.: Overview of the O3M SAF GOME-2 operational atmospheric composition and UV radiation data products and data availability, *Atmos. Meas. Tech.*, 9, 383, 2016.
- Heckel, A., Richter, A., Tarsu, T., Wittrock, F., Hak, C., Pundt, I., Junkermann, W., and Burrows, J.: MAX-DOAS measurements of formaldehyde in the Po-Valley, *Atmos. Chem. Phys.*, 5, 909–918, 2005.
- Hendrick, F., Barret, B., Van Roozendael, M., Boesch, H., Butz, A., De Mazière, M., Goutail, F., Hermans, C., Lambert, J.-C., Pfeilsticker, K., and Pommereau, J.-P.: Retrieval of nitrogen dioxide stratospheric profiles from ground-based zenith-sky UV-visible observations: validation of the technique through correlative comparisons, *Atmos. Chem. Phys.*, 4, 2091–2106, 2004.
- Hendrick, F., Mahieu, E., Bodeker, G. E., Boersma, K. F., Chipperfield, M. P., De Mazière, M., De Smedt, I., Demoulin, P., Fayt, C., Hermans, C., Kreher, K., Lejeune, B., Pinardi, G., Servais, C., Stübi, R., van der A, R., Vernier, J.-P., and Van Roozendael, M.: Analysis of stratospheric NO₂ trends above Jungfraujoch using ground-based UV-visible, FTIR, and satellite nadir observations, *Atmos. Chem. Phys.*, 12, 8851–8864, 2012.
- Hendrick, F., Müller, J.-F., Clémer, K., Wang, P., De Mazière, M., Fayt, C., Gielen, C., Hermans, C., Ma, J. Z., Pinardi, G., Stavrou, T., Vlemmix, T., and Van Roozendael, M.: Four years of ground-based MAX-DOAS observations of HONO and NO₂ in the Beijing area, *Atmos. Chem. Phys.*, 14, 765–781, 2014.
- Herman, J. and Celarier, E.: Earth surface reflectivity climatology at 340–380 nm from TOMS data, *J. Geophys. Res. Atmos.*, 102, 28 003–28 011, 1997.
- Herman, J., Cede, A., Spinei, E., Mount, G., Tzortziou, M., and Abuhassan, N.: NO₂ column amounts from ground-based Pandora and MFDOAS spectrometers using the direct-Sun DOAS technique: Intercomparisons and application to OMI validation, *J. Geophys. Res. Atmos.*, 114, 2009.
- Herman, J., Spinei, E., Fried, A., Kim, J., Kim, J., Kim, W., Cede, A., Abuhassan, N., and Segal-Rozenhaimer, M.: NO₂ and HCHO measurements in Korea from 2012 to 2016 from Pandora spectrometer instruments compared with OMI retrievals and with aircraft measurements during the KORUS-AQ campaign., *Atmos. Meas. Tech.*, 11, 2018.
- Hilboll, A., Richter, A., and Burrows, J.: Long-term changes of tropospheric NO₂ over megacities derived from multiple satellite instruments, *Atmos. Chem. Phys.*, 13, 4145–4169, 2013a.
- Hilboll, A., Richter, A., Rozanov, A., Hodnebrog, Ø., Heckel, A., Solberg, S., Stordal, F., and Burrows, J.: Improvements to the retrieval of tropospheric NO₂ from satellite-stratospheric correction using SCIAMACHY limb/nadir matching and comparison to Oslo CTM2 simulations, *Atmos. Meas. Tech.*, 6, 565–584, 2013b.
- Hilboll, A., Richter, A., and Burrows, J. P.: NO₂ pollution over India observed from space—The impact of rapid economic growth, and a recent decline, *Atmos. Chem. Phys. Discuss.*, 2017.
- Holben, B., Eck, T., Slutsker, I., Tanré, D., Buis, J., Setzer, A., Vermote, E., Reagan, J., Kaufman, Y., Nakajima, T., Lavenue, F., Jankowiak, I., and Smirnov, A.: AERONET—A federated instrument network and data archive for aerosol characterization, 66, 1–16, 1998.
- Hönninger, G., Friedeburg, C. v., and Platt, U.: Multi axis differential optical absorption spectroscopy (MAX-DOAS), *Atmos. Chem. Phys.*, 4, 231–254, 2004.
- Horowitz, L. W., Walters, S., Mauzerall, D. L., Emmons, L. K., Rasch, P. J., Granier, C., Tie, X., Lamarque, J.-F., Schultz, M. G., Tyndall, G. S., Orlando, J. J., and Brasseur, G. P.: A global simulation of tropospheric ozone and related tracers: Description and evaluation of MOZART, version 2, *J. Geophys. Res. Atmos.*, 108, 2003.

- Huijnen, V., Williams, J., van Weele, M., van Noije, T., Krol, M., Dentener, F., Segers, A., Houweling, S., Peters, W., de Laat, J., Boersma, F., Bergamaschi, P., van Velthoven, P., Le Sager, P., Eskes, H., Alkemade, F., Scheele, R., Nédélec, P., and Pätz, H.-W.: The global chemistry transport model TM5: description and evaluation of the tropospheric chemistry version 3.0, *Geosci. Model Dev.*, 3, 445–473, 2010.
- Huijnen, V., Flemming, J., Chabrilat, S., Errera, Q., Christophe, Y., Blechschmidt, A.-M., Richter, A., and Eskes, H.: C-IFS-CB05-BASCOE: stratospheric chemistry in the Integrated Forecasting System of ECMWF, *Geosci. Model Dev.*, 9, 3071–3091, 2016.
- Ingmann, P., Veihelmann, B., Langen, J., Lamarre, D., Stark, H., and Courrèges-Lacoste, G. B.: Requirements for the GMES Atmosphere Service and ESA’s implementation concept: Sentinels-4/-5 and-5p, *Remote Sens. Environ.*, 120, 58–69, 2012.
- Irie, H., Boersma, K., Kanaya, Y., Takashima, H., Pan, X., and Wang, Z.: Quantitative bias estimates for tropospheric NO₂ columns retrieved from SCIAMACHY, OMI, and GOME-2 using a common standard for East Asia, *Atmos. Meas. Tech.*, 5, 2403–2411, 2012.
- Jacob, D.: Introduction to atmospheric chemistry, Princeton University Press, 1999.
- Jin, Z., Charlock, T. P., Smith Jr, W. L., and Rutledge, K.: A parameterization of ocean surface albedo, *Geophys. Res. Lett.*, 31, 2004.
- Jin, Z., Qiao, Y., Wang, Y., Fang, Y., and Yi, W.: A new parameterization of spectral and broadband ocean surface albedo, *Opt. Express*, 19, 26 429–26 443, 2011.
- Johnston, P.: Making UV/Vis Cross sections, reference Fraunhofer and synthetic spectra, Unpublished Manuscript, NIWA, Lauder, 1996.
- Kampa, M. and Castanas, E.: Human health effects of air pollution, *Environ. Pollut.* 151, 362–367, 2008.
- Kanaya, Y., Irie, H., Takashima, H., Iwabuchi, H., Akimoto, H., Sudo, K., Gu, M., Chong, J., Kim, Y. J., Lee, H., Li, A., Si, F., Xu, J., Xie, P.-H., Liu, W.-Q., Dzhola, A., Postylyakov, O., Ivanov, V., Grechko, E., Terpugova, S., and Panchenko, M.: Long-term MAX-DOAS network observations of NO₂ in Russia and Asia (MADRAS) during the period 2007–2012: instrumentation, elucidation of climatology, and comparisons with OMI satellite observations and global model simulations., *Atmos. Chem. Phys.*, 14, 2014.
- Kim, J.: GEMS (Geostationary Environment Monitoring Spectrometer) onboard the GeoKOMPSAT to monitor air quality in high temporal and spatial resolution over Asia-Pacific Region, in: EGU General Assembly Conference Abstracts, vol. 14, p. 4051, 2012.
- Kleipool, Q., Dobber, M., de Haan, J., and Levelt, P.: Earth surface reflectance climatology from 3 years of OMI data, *J. Geophys. Res. Atmos.*, 113, 2008.
- Kleipool, Q., Ludewig, A., Babić, L., Bartstra, R., Braak, R., Dierssen, W., Dewitte, P.-J., Kenter, P., Landzaat, R., Leloux, J., Loots, E., Meijering, P., van der Plas, E., Rozemeijer, N., Schepers, D., Schiavini, D., Smeets, J., Vacanti, G., Vonk, F., and Veeffkind, P.: Pre-launch calibration results of the TROPOMI payload on-board the Sentinel-5 Precursor satellite, *Atmos. Meas. Tech.*, pp. 6439–6479, 2018.
- Koelemeijer, R., De Haan, J., and Stammes, P.: A database of spectral surface reflectivity in the range 335–772 nm derived from 5.5 years of GOME observations, *J. Geophys. Res. Atmos.*, 108, 2003.
- Kokhanovsky, A.: Cloud Optics, Springer, 2006.
- Kokhanovsky, A. and Rozanov, V.: The uncertainties of satellite DOAS total ozone retrieval for a cloudy sky, *Atmospheric Res.*, 87, 27–36, 2008.

- Kokhanovsky, A., Rozanov, V., Zege, E., Bovensmann, H., and Burrows, J.: A semianalytical cloud retrieval algorithm using backscattered radiation in 0.4–2.4 μm spectral region, *J. Geophys. Res. Atmos.*, 108, 2003.
- Kramer, L. J., Leigh, R. J., Remedios, J. J., and Monks, P. S.: Comparison of OMI and ground-based in situ and MAX-DOAS measurements of tropospheric nitrogen dioxide in an urban area, *J. Geophys. Res. Atmos.*, 113, 2008.
- Kreher, K., Van Roozendaal, M., Hendrick, F., Apituley, A., Dimitropoulou, E., Frieß, U., Richter, A., Wagner, T., Abuhassan, N., Ang, L., Anguas, M., Bais, A., Benavent, N., Bösch, T., Bogner, K., Borovski, A., Bruchkouski, I., Cede, A., Chan, K. L., Donner, S., Drosoglou, T., Fayt, C., Finkenzeller, H., Garcia-Nieto, D., Gielen, C., Gómez-Martín, L., Hao, N., Herman, J. R., Hermans, C., Hoque, S., Irie, H., Jin, J., Johnston, P., Khayyam Butt, J., Khokhar, F., Koenig, T. K., Kuhn, J., Kumar, V., Lampel, J., Liu, C., Ma, J., Merlaud, A., Mishra, A. K., Müller, M., Navarro-Comas, M., Ostendorf, M., Pazmino, A., Peters, E., Pinardi, G., Pinharanda, M., Piters, A., Platt, U., Postlyakov, O., Prados-Roman, C., Puentedura, O., Querel, R., Saiz-Lopez, A., Schönhardt, A., Schreier, S. F., Seyler, A., Sinha, V., Spinei, E., Strong, K., Tack, F., Tian, X., Tiefengraber, M., Tirpitz, J.-L., van Gent, J., Volkamer, R., Vrekoussis, M., Wang, S., Wang, Z., Wenig, M., Wittrock, F., Xie, P. H., Xu, J., Yela, M., Zhang, C., and Zhao, X.: Intercomparison of NO_2 , O_4 , O_3 and HCHO slant column measurements by MAX-DOAS and zenith-sky UV-Visible spectrometers during the CINDI-2 campaign, *Atmos. Meas. Tech. Discuss.*, 2019, 1–58, 2019.
- Krotkov, N. A., Lamsal, L. N., Celarier, E. A., Swartz, W. H., Marchenko, S. V., Bucsele, E. J., Chan, K. L., Wenig, M., and Zara, M.: The version 3 OMI NO_2 standard product, *Atmos. Meas. Tech.*, 10, 3133–3149, 2017.
- Kuhlmann, G., Lam, Y., Cheung, H., Hartl, A., Fung, J. C. H., Chan, P., and Wenig, M. O.: Development of a custom OMI NO_2 data product for evaluating biases in a regional chemistry transport model, *Atmos. Chem. Phys.*, 15, 5627–5644, 2015.
- Kularni, R.: Measurements of NO_2 using the Dobson spectrophotometer, *J. Atmos. Sci.*, 32, 1641–1643, 1975.
- Lampel, J., Pöhler, D., Tschritter, J., Frieß, U., and Platt, U.: On the relative absorption strengths of water vapour in the blue wavelength range, *Atmos. Meas. Tech.*, 8, 4329–4346, 2015.
- Laughner, J. L., Zhu, Q., and Cohen, R. C.: The Berkeley High Resolution Tropospheric NO_2 product, *Earth Syst. Sci. Data*, 10, 2069–2095, 2018.
- Lee, H.-H., Iraqui, O., and Wang, C.: The Impact of Future Fuel Consumption on Regional Air Quality in Southeast Asia, *Sci. Rep.*, 9, 2648, 2019.
- Leitão, J., Richter, A., Vrekoussis, M., Kokhanovsky, A., Zhang, Q., Beekmann, M., and Burrows, J.: On the improvement of NO_2 satellite retrievals— aerosol impact on the airmass factors, *Atmos. Meas. Tech.*, 3, 475–493, 2010.
- Lelli, L., Kokhanovsky, A., Rozanov, V., Vountas, M., Sayer, A., and Burrows, J.: Seven years of global retrieval of cloud properties using space-borne data of GOME, *Atmos. Meas. Tech.*, 5, 1551, 2012.
- Leue, C., Wenig, M., Wagner, T., Klimm, O., Platt, U., and Jähne, B.: Quantitative analysis of NO_x emissions from Global Ozone Monitoring Experiment satellite image sequences, *J. Geophys. Res. Atmos.*, 106, 5493–5505, 2001.
- Levelt, P. F., van den Oord, G. H., Dobber, M. R., Malkki, A., Visser, H., de Vries, J., Stammes, P., Lundell, J. O., and Saari, H.: The ozone monitoring instrument, *IEEE Trans. Geosci. Remote Sens.*

- Levenberg, K.: A method for the solution of certain non-linear problems in least squares, *Quart. Appl. Math.*, 2, 164–168, 1944.
- Liley, J., Johnston, P., McKenzie, R., Thomas, A., and Boyd, I.: Stratospheric NO₂ variations from at Lauder, New Zealand a long time series, *J. Geophys. Res. Atmos.*, 105, 11–633, 2000.
- Lin, J., Martin, R., Boersma, K., Sneep, M., Stammes, P., Spurr, R., Wang, P., Van Roozendael, M., Clémer, K., and Irie, H.: Retrieving tropospheric nitrogen dioxide from the Ozone Monitoring Instrument: effects of aerosols, surface reflectance anisotropy, and vertical profile of nitrogen dioxide, *Atmos. Chem. Phys.*, 14, 1441–1461, 2014.
- Lin, J., Liu, M., Xin, J., Boersma, K., Spurr, R., Martin, R., and Zhang, Q.: Influence of aerosols and surface reflectance on satellite NO₂ retrieval: seasonal and spatial characteristics and implications for NO_x emission constraints, *Atmos. Chem. Phys.*, 15, 11 217, 2015.
- Liu, F., Beirle, S., Zhang, Q., van der A, R. J., Zheng, B., Tong, D., and He, K.: NO_x emission trends over Chinese cities estimated from OMI observations during 2005 to 2015, *Atmos. Chem. Phys.*, 17, 9261–9275, 2017.
- Liu, M., Lin, J., Boersma, K. F., Pinardi, G., Wang, Y., Chimot, J., Wagner, T., Xie, P., Eskes, H., Van Roozendael, M., Hendrick, F., Wang, P., Wang, T., Yan, Y., Chen, L., and Ni, R.: Improved aerosol correction for OMI tropospheric NO₂ retrieval over East Asia: constraint from CALIOP aerosol vertical profile, *Atmos. Meas. Tech.*, 12, 1–21, 2019.
- Liu, X., Newchurch, M., Loughman, R., and Bhartia, P.: Errors resulting from assuming opaque Lambertian clouds in TOMS ozone retrieval, *J. Quant. Spectrosc. Radiat. Transf.*, 85, 337–365, 2004.
- Lorente, A., Folkert Boersma, K., Yu, H., Dörner, S., Hilboll, A., Richter, A., Liu, M., Lamsal, L. N., Barkley, M., De Smedt, I., Van Roozendael, M., Wang, Y., Wagner, T., Beirle, S., Lin, J.-T., Krotkov, N., Stammes, P., Wang, P., Eskes, H. J., and Krol, M.: Structural uncertainty in air mass factor calculation for NO₂ and HCHO satellite retrievals, *Atmos. Meas. Tech.*, 10, 759, 2017.
- Lorente, A., Boersma, K. F., Stammes, P., Tilstra, L. G., Richter, A., Yu, H., Kharbouche, S., and Muller, J.-P.: The importance of surface reflectance anisotropy for cloud and NO₂ retrievals from GOME-2 and OMI, *Atmos. Meas. Tech.*, 11, 4509–4529, 2018.
- Loyola, D., Thomas, W., Livschitz, Y., Ruppert, T., Albert, P., and Hollmann, R.: Cloud properties derived from GOME/ERS-2 backscatter data for trace gas retrieval, *IEEE Trans. Geosci. Remote Sens.*, 45, 2747–2758, 2007.
- Loyola, D., García, S. G., Lutz, R., Argyrouli, A., Romahn, F., Spurr, R. J., Pedernana, M., Doicu, A., García, V. M., and Schüssler, O.: The operational cloud retrieval algorithms from TROPOMI on board Sentinel-5 Precursor, *Atmos. Meas. Tech.*, 11, 409, 2018.
- Loyola, D. G., Koukouli, M. E., Valks, P., Balis, D. S., Hao, N., Van Roozendael, M., Spurr, R. J. D., Zimmer, W., Kiemle, S., Lerot, C., and Lambert, J.-C.: The GOME-2 total column ozone product: Retrieval algorithm and ground-based validation, *J. Geophys. Res. Atmos.*, 116, 2011.
- Lucht, W., Schaaf, C. B., and Strahler, A. H.: An algorithm for the retrieval of albedo from space using semiempirical BRDF models, *IEEE Trans. Geosci. Remote Sens.*, 38, 977–998, 2000.
- Lutz, R., Loyola, D., Gimeno García, S., and Romahn, F.: OCRA radiometric cloud fractions for GOME-2 on MetOp-A/B, *Atmos. Meas. Tech.*, 9, 2357–2379, 2016.
- Ma, J., Beirle, S., Jin, J., Shaiganfar, R., Yan, P., and Wagner, T.: Tropospheric NO₂ vertical column densities over Beijing: results of the first three years of ground-based MAX-DOAS measurements (2008–2011) and satellite validation, *Atmos. Chem. Phys.*, 13, 1547–1567, 2013.

- Marquardt, D. W.: An algorithm for least-squares estimation of nonlinear parameters, *J. Soc. Ind. Appl. Math.*, 11, 431–441, 1963.
- Martin, R. V., Chance, K., Jacob, D. J., Kurosu, T. P., Spurr, R. J., Bucsela, E., Gleason, J. F., Palmer, P. I., Bey, I., Fiore, A. M., Li, Q., Yantosca, R. M., and Koelemeijer, R.: An improved retrieval of tropospheric nitrogen dioxide from GOME, *J. Geophys. Res. Atmos.*, 107, 2002.
- Mayer, B. and Kylling, A.: The libRadtran software package for radiative transfer calculations—description and examples of use, *Atmos. Chem. Phys.*, 5, 1855–1877, 2005.
- METEO-FRANCE et al.: Regional Production, Description of the operational models and of the ENSEMBLE system, Tech. rep., CAMS_50.2015SC1_Models_Factsheets.201610_v2, 2016.
- Mijling, B., van der A, R., and Zhang, Q.: Regional nitrogen oxides emission trends in East Asia observed from space, *Atmos. Chem. Phys.*, 13, 12 003–12 012, 2013.
- Miyazaki, K., Eskes, H., Sudo, K., Boersma, K. F., Bowman, K., and Kanaya, Y.: Decadal changes in global surface NO_x emissions from multi-constituent satellite data assimilation, *Atmos. Chem. Phys.*, 17, 807–837, 2017.
- Müller, J.-F. and Stavrakou, T.: Inversion of CO and NO_x emissions using the adjoint of the IMAGES model, *Atmos. Chem. Phys.*, 5, 1157–1186, 2005.
- Munro, R., Lang, R., Klaes, D., Poli, G., Retscher, C., Lindstrot, R., Huckle, R., Lacan, A., Grzegorski, M., Holdak, A., Kokhanovsky, A., Livschitz, J., and Eisinger, M.: The GOME-2 instrument on the Metop series of satellites: instrument design, calibration, and level 1 data processing—an overview, *Atmos. Meas. Tech.*, 9, 1279–1301, 2016.
- Nicodemus, F. E., Richmond, J., Hsia, J., Ginsberg, I., and Limperis, T.: Geometrical considerations and nomenclature for reflectance, in: *Radiometry*, pp. 94–145, Jones and Bartlett Publishers, Inc., 1992.
- Nicolet, M.: Nitrogen oxides in the chemosphere, *J. Geophys. Res. Atmos.*, 70, 679–689, 1965.
- Noguchi, K., Richter, A., Rozanov, V., Rozanov, A., Burrows, J., Irie, H., and Kita, K.: Effect of surface BRDF of various land cover types on geostationary observations of tropospheric NO₂, *Atmos. Meas. Tech.*, 7, 3497–3508, 2014.
- Nolin, A., Armstrong, R., and Maslanik, J.: Near Real-Time SSM/I EASE-Grid Daily Global Ice Concentration and Snow Extent, updated daily, Boulder, CO, USA: National Snow and Ice Data Center, Digital media, 1998.
- Noxon, J.: Nitrogen dioxide in the stratosphere and troposphere measured by ground-based absorption spectroscopy, *Science*, 189, 547–549, 1975.
- Nüß, H.: Verbesserungen des troposphärischen NO₂-Retrievals aus GOME- und SCIAMACHY-Daten, Doktorarbeit, Universität Bremen, 2005.
- Nüß, H., Richter, A., Valks, P., and Burrows, J.: Improvement of the NO₂ total column retrieval for GOME-2, 2006.
- Ortega, I., Koenig, T., Sinreich, R., Thomson, D., and Volkamer, R.: The CU 2-D-MAX-DOAS instrument—Part 1: Retrieval of 3-D distributions of NO₂ and azimuth-dependent OVOC ratios, *Atmos. Meas. Tech.*, 8, 2371, 2015.
- Palmer, P. I., Jacob, D. J., Chance, K., Martin, R. V., Spurr, R. J., Kurosu, T. P., Bey, I., Yantosca, R., Fiore, A., and Li, Q.: Air mass factor formulation for spectroscopic measurements from satellites: Application to formaldehyde retrievals from the Global Ozone Monitoring Experiment, *J. Geophys. Res. Atmos.*, 106, 14 539–14 550, 2001.

- Peters, E., Wittrock, F., Richter, A., Alvarado, L., Rozanov, V., and Burrows, J.: Liquid water absorption and scattering effects in DOAS retrievals over oceans, *Atmos. Meas. Tech.*, 7, 4203–4221, 2014.
- Pinardi, G., Van Roozendael, M., Lambert, J.-C., Granville, J., Hendrick, F., Tack, F., Yu, H., Cede, A., Kanaya, Y., Irie, I., Goutail, F., Pommereau, J.-P., Pazmino, A., Wittrock, F., Richter, A., Wagner, T., Gu, M., Remmers, J., Friess, U., Vlemmix, T., PETERS, A., Hao, N., Tiefengraber, M., Herman, J., Abuhassan, N., Bais, A., Kouremeti, N., Hovila, J., Holla, R., Chong, J., Postylyakov, O., and Ma, J.: GOME-2 total and tropospheric NO₂ validation based on zenith-sky, direct-sun and multi-axis DOAS network observations, in: *Proc. of the 2014 EUMETSAT Meteorological Satellite Conference*, Geneva, Switzerland, EUMETSAT, 2014.
- Pinardi, G., Lambert, J.-C., Granville, J., Yu, H., De Smedt, I., van Roozendael, M., and Valks, P.: O3M-SAF validation report, *Tech. rep.*, SAF/O3M/IASB/VR/NO2/TN-IASB-GOME2-O3MSAF-NO2-2015, Issue 1/1, 2015.
- Pinardi, G., Vigouroux, C., Langerock, B., De Mazière, M., Granville, J., Lambert, J.-C., Hendrick, F., and Van Roozendael, M.: Validation of TROPOMI NO₂ and HCHO vertical columns with UV-Vis DOAS and FTIR instruments, in: *ESA ATMOS conference*, Salzburg, Austria, 2018.
- Platt, U.: *Differential Optical Absorption Spectroscopy (DOAS) in Air Monitoring by Spectroscopic Techniques*, Ed. Markus W. Sigrist, 1994.
- Platt, U. and Stutz, J.: *Differential Optical Absorption Spectroscopy*, Springer, 2008.
- Pommereau, J. P. and Goutail, F.: O₃ and NO₂ ground-based measurements by visible spectrometry during Arctic winter and spring 1988, *Geophys. Res. Lett.*, 15, 891–894, 1988.
- Pope, R. M. and Fry, E. S.: Absorption spectrum (380–700 nm) of pure water. II. Integrating cavity measurements, *Appl. Opt.*, 36, 8710–8723, 1997.
- Qin, W., Fasnacht, Z., Haffner, D., Vasilkov, A., Joiner, J., Krotkov, N., Fisher, B., and Spurr, R.: A geometry-dependent surface Lambertian-equivalent reflectivity product at 466 nm for UV/Vis retrievals: Part I. Evaluation over land surfaces using measurements from OMI, *Atmos. Meas. Tech. Discuss.*, pp. 1–31, 2019.
- Richter, A. and Burrows, J.: Tropospheric NO₂ from GOME measurements, *Adv. Space Res.*, 29, 1673–1683, 2002.
- Richter, A., Burrows, J. P., Nüß, H., Granier, C., and Niemeier, U.: Increase in tropospheric nitrogen dioxide over China observed from space, *Nature*, 437, 129, 2005.
- Richter, A., Begoin, M., Hilboll, A., and Burrows, J.: An improved NO₂ retrieval for the GOME-2 satellite instrument, *Atmos. Meas. Tech.*, 4, 1147–1159, 2011.
- Richter, A. et al.: S5P/TROPOMI Science Verification Report, *Tech. rep.*, S5P-IUP-L2-ScVR-RP issue 2.1, 2015.
- Rodgers, C. D.: *Inverse methods for atmospheric sounding: theory and practice*, vol. 2, World scientific, 2000.
- Rothman, L., Gordon, I., Barber, R., Dothe, H., Gamache, R., Goldman, A., Perevalov, V., Tashkun, S., and Tennyson, J.: HITRAN, the high-temperature molecular spectroscopic database, *J. Quant. Spectrosc. Radiat. Transf.*, 111, 2139–2150, 2010.
- Rozanov, V., Rozanov, A., Kokhanovsky, A., and Burrows, J.: Radiative transfer through terrestrial atmosphere and ocean: software package SCIATRAN, *J. Quant. Spectrosc. Radiat. Transf.*, 133, 13–71, 2014.

- Rozanov, V. V. and Kokhanovsky, A. A.: Semianalytical cloud retrieval algorithm as applied to the cloud top altitude and the cloud geometrical thickness determination from top-of-atmosphere reflectance measurements in the oxygen A band, *J. Geophys. Res. Atmos.*, 109, 2004.
- Rozemeijer, N. C. and Kleipool, Q.: S5P Mission Performance Centre Level 1b Readme, Tech. rep., S5P-MPC-KNMI-PRF-L1B issue 1.0.0 version V01.00.00., 2018.
- Sanders, A., Richter, A., and Eskes, H.: Sentinel-4 Level-2 ATBD Total and Tropospheric NO₂, Tech. rep., S4-L2-IUP_KNMI-ATBD-2004 issue 2.0, 2018.
- Schultz, M., Schmitt, R., Thomas, K., and Volz-Thomas, A.: Photochemical box modeling of long-range transport from North America to Tenerife during the North Atlantic Regional Experiment (NARE) 1993, *J. Geophys. Res. Atmos.*, 103, 13 477–13 488, 1998.
- Schwarzschild, K.: Über Diffusion und Absorption in der Sonnenatmosphäre, *Sitz. K. Preuss. Akad. Wiss.*, p. 1183, 1914.
- Seinfeld, J. and Pandis, S.: *Atmospheric chemistry and physics: from air pollution to climate change*, 3rd ed., 2016.
- Shindell, D. T., Faluvegi, G., Koch, D. M., Schmidt, G. A., Unger, N., and Bauer, S. E.: Improved attribution of climate forcing to emissions, *Science*, 326, 716–718, 2009.
- Sierk, B., Richter, A., Rozanov, A., Von Savigny, C., Schmoltner, A., Buchwitz, M., Bovensmann, H., and Burrows, J.: Retrieval and monitoring of atmospheric trace gas concentrations in nadir and limb geometry using the space-borne SCIAMACHY instrument, *Environ. Monit. Assess.*, 120, 65–77, 2006.
- Sioris, C., Kurosu, T., Martin, R., and Chance, K.: Stratospheric and tropospheric NO₂ observed by SCIAMACHY: first results, *Adv. Space Res.*, 34, 780–785, 2004.
- Solomon, S.: Stratospheric ozone depletion: A review of concepts and history, *Rev. Geophys.*, 37, 275–316, 1999.
- Solomon, S., Schmeltekopf, A. L., and Sanders, R. W.: On the interpretation of zenith sky absorption measurements, *J. Geophys. Res. Atmos.*, 92, 8311–8319, 1987.
- Spurr, R.: LIDORT and VLIDORT: Linearized pseudo-spherical scalar and vector discrete ordinate radiative transfer models for use in remote sensing retrieval problems, in: *Light Scattering Reviews 3*, pp. 229–275, Springer, 2008.
- Spurr, R. J.: VLIDORT: A linearized pseudo-spherical vector discrete ordinate radiative transfer code for forward model and retrieval studies in multilayer multiple scattering media, *J. Quant. Spectrosc. Radiat. Transf.*, 102, 316–342, 2006.
- Stammes, P.: Spectral radiance modelling in the UV-visible range, in: *IRS 2000: Current problems in atmospheric radiation*, pp. 385–388, 2001.
- Stammes, P., Sneep, M., De Haan, J., Veefkind, J., Wang, P., and Levelt, P.: Effective cloud fractions from the Ozone Monitoring Instrument: Theoretical framework and validation, *J. Geophys. Res. Atmos.*, 113, 2008.
- Stedman, D., Morris, E., Daby, E., Niki, H., and Weinstock, B.: The role of OH radicals in photochemical smog reactions, in: *160th National ACS Meeting*, 13–18 September 1970, Chicago, IL, 1970.
- Tackett, J. L., Winker, D. M., Getzewich, B. J., Vaughan, M. A., Young, S. A., and Kar, J.: CALIPSO lidar level 3 aerosol profile product: version 3 algorithm design, *Atmos. Meas. Tech.*, 11, 4129–4152, 2018.

- Thalman, R. and Volkamer, R.: Temperature dependent absorption cross-sections of O₂-O₂ collision pairs between 340 and 630 nm and at atmospherically relevant pressure, *Phys. Chem. Chem. Phys.*, 15, 15 371–15 381, 2013.
- Tilstra, L., Tuinder, O., Wang, P., and Stammes, P.: Surface reflectivity climatologies from UV to NIR determined from Earth observations by GOME-2 and SCIAMACHY, *J. Geophys. Res. Atmos.*, 122, 4084–4111, 2017.
- Tilstra, L., Tuinder, O., and Stammes, P.: GOME-2 surface LER product - Algorithm Theoretical Basis Document, Tech. rep., KNMI Report SAF/AC/KNMI/ATBD/003, Issue 3.1, 2019.
- Valks, P., Pinardi, G., Richter, A., Lambert, J.-C., Hao, N., Loyola, D., Van Roozendael, M., and Emmadi, S.: Operational total and tropospheric NO₂ column retrieval for GOME-2, *Atmos. Meas. Tech.*, 4, 1491, 2011.
- Valks, P., Loyola, D., Hao, N., Hedelt, P., Slijkhuis, S., Grossi, M., Begoin, M., Gimeno Garcia, S., and Lutz, R.: Algorithm Theoretical Basis Document for GOME-2 Total Column Products of Ozone, NO₂, BrO, SO₂, H₂O, HCHO and Cloud Properties (GDP 4.8 for AC SAF OTO and NTO), Tech. rep., SAF/AC/DLR/ATBD/01, Iss./Rev.: 3/A/2, 2017.
- van Geffen, J., Boersma, K., Van Roozendael, M., Hendrick, F., Mahieu, E., De Smedt, I., Sneep, M., and Veefkind, J.: Improved spectral fitting of nitrogen dioxide from OMI in the 405–465 nm window, *Atmos. Meas. Tech.*, 8, 1685–1699, 2015.
- van Geffen, J., Boersma, K., Eskes, H., Maasackers, J., and Veefkind, J.: TROPOMI ATBD of the total and tropospheric NO₂ data products, Tech. rep., S5P-KNMI-L2-0005-RP issue 1.4.0. KNMI, De Bilt, the Netherlands, 2019.
- van Geffen, J. H. G. M., Eskes, H. J., Boersma, K. F., and Veefkind, J. P.: ATBD for NO₂ in Sentinel-5 L2 Prototype Processors, Tech. rep., KNMI-ESA-S5L2PP-ATBD-001 version 3.0., 2018.
- Van Roozendael, M., De Mazière, M., Hermans, C., Simon, P., Pommereau, J.-P., Goutail, F., Tie, X., Brasseur, G., and Granier, C.: Ground-based observations of stratospheric NO₂ at high and midlatitudes in Europe after the Mount Pinatubo eruption, *J. Geophys. Res. Atmos.*, 102, 19 171–19 176, 1997.
- Vandaele, A. C., Hermans, C., Simon, P. C., Carleer, M., Colin, R., Fally, S., Merienne, M.-F., Jenouvrier, A., and Coquart, B.: Measurements of the NO₂ absorption cross-section from 42 000 cm⁻¹ to 10 000 cm⁻¹ (238–1000 nm) at 220 K and 294 K, *J. Quant. Spectrosc. Radiat. Transf.*, 59, 171–184, 1998.
- Vandaele, A. C., Hermans, C., Fally, S., Carleer, M., Colin, R., Merienne, M.-F., Jenouvrier, A., and Coquart, B.: High-resolution Fourier transform measurement of the NO₂ visible and near-infrared absorption cross sections: Temperature and pressure effects, *J. Geophys. Res. Atmos.*, 107, 2002.
- Vasilkov, A., Qin, W., Krotkov, N., Lamsal, L., Spurr, R., Haffner, D., Joiner, J., Eun-Su, Y., and Marchenko, S.: Accounting for the effects of surface BRDF on satellite cloud and trace-gas retrievals: a new approach based on geometry-dependent Lambertian equivalent reflectivity applied to OMI algorithms, *Atmos. Meas. Tech.*, 10, 333, 2017.
- Veefkind, J.: CAMELOT Final Report, Tech. rep., RP-CAM-KNMI-050, Issue 1, 2009.
- Veefkind, J., Aben, I., McMullan, K., Förster, H., De Vries, J., Otter, G., Claas, J., Eskes, H., De Haan, J., Kleipool, Q., van Weele, M., Hasekamp, O., Hoogeveen, R., Landgraf, J., Snel, R., Tol, P., Ingmann, P., Voors, R., Kruizinga, B., Vink, R., Visser, H., and Levelt, P.: TROPOMI on the ESA Sentinel-5 Precursor: A GMES mission for global observations of the atmospheric composition for climate, air quality and ozone layer applications, *Remote Sens. Environ.*, 120, 70–83, 2012.

- Veefkind, J. P., De Haan, J. F., Sneep, M., and Levelt, P. F.: Improvements to the OMI O₂-O₂ operational cloud algorithm and comparisons with ground-based radar-lidar observations, *Atmos. Meas. Tech.*, 9, 2016.
- Vlemmix, T., Hendrick, F., Pinardi, G., De Smedt, I., Fayt, C., Hermans, C., Piters, A., Wang, P., Levelt, P., and Van Roozendael, M.: MAX-DOAS observations of aerosols, formaldehyde and nitrogen dioxide in the Beijing area: comparison of two profile retrieval approaches, *Atmos. Meas. Tech.*, 8, 941, 2015.
- Wagner, T., Chance, K., Frieß, U., Gil, M., Goutail, F., Hönninger, G., Johnston, P., Karlsen-Tørnkvist, K., Kostadinov, I., Leser, H., Petritoli, A., Richter, A., Van Roozendael, M., and Platt, U.: Correction of the Ring effect and I0-effect for DOAS observations of scattered sunlight, in: 1st DOAS Workshop, Heidelberg, Germany, pp. 13–14, 2001.
- Wagner, T., Dix, B. v., Friedeburg, C. v., Frieß, U., Sanghavi, S., Sinreich, R., and Platt, U.: MAX-DOAS O₄ measurements: A new technique to derive information on atmospheric aerosols—Principles and information content, *J. Geophys. Res. Atmos.*, 109, 2004.
- Wang, P., Stammes, P., van der A, R., Pinardi, G., and van Roozendael, M.: FRESCO+: an improved O₂ A-band cloud retrieval algorithm for tropospheric trace gas retrievals, *Atmos. Chem. Phys.*, 8, 6565–6576, 2008.
- Wang, Y., Beirle, S., Lampel, J., Koukouli, M., De Smedt, I., Theys, N., Li, A., Wu, D., Xie, P., Liu, C., Van Roozendael, M., Stavrou, T., Müller, J.-F., and Wagner, T.: Validation of OMI, GOME-2A and GOME-2B tropospheric NO₂, SO₂ and HCHO products using MAX-DOAS observations from 2011 to 2014 in Wuxi, China: investigation of the effects of priori profiles and aerosols on the satellite products, *Atmos. Chem. Phys.*, 17, 5007, 2017.
- Wenig, M.: Satellite Measurement of Long-term Global Tropospheric Trace Gas Distributions and Source Strengths: Algorithm Development and Data Analysis, Ph.D. Thesis, Heidelberg University, 2001.
- Wenig, M., Kühl, S., Beirle, S., Bucsela, E., Jähne, B., Platt, U., Gleason, J., and Wagner, T.: Retrieval and analysis of stratospheric NO₂ from the Global Ozone Monitoring Experiment, *J. Geophys. Res. Atmos.*, 109, 2004.
- Wenig, M. O., Cede, A., Bucsela, E., Celarier, E., Boersma, K., Veefkind, J., Brinksma, E., Gleason, J., and Herman, J.: Validation of OMI tropospheric NO₂ column densities using direct-Sun mode Brewer measurements at NASA Goddard Space Flight Center, *J. Geophys. Res. Atmos.*, 113, 2008.
- Wennberg, P. O., Cohen, R. C., Stimpfle, R. M., Koplow, J. P., Anderson, J. G., Salawitch, R. J., Fahey, D. W., Woodbridge, E. L., Keim, E. R., Gao, R. S., Webster, C. R., May, R. D., Toohey, D. W., Avallone, L. M., Proffitt, M. H., Loewenstein, M., Podolske, J. R., Chan, K. R., and Wofsy, S. C.: Removal of stratospheric O₃ by radicals: In situ measurements of OH, HO₂, NO, NO₂, ClO, and BrO, *Science*, 266, 398–404, 1994.
- Wickert, B.: Berechnung anthropogener Emissionen in Deutschland für Ozonsimulationen, Doktorarbeit, Universität Stuttgart, 2001.
- Williams, J. E., Boersma, K. F., Le Sager, P., and Verstraeten, W. W.: The high-resolution version of TM5-MP for optimized satellite retrievals: description and validation, *Geosci. Model Dev.*, 10, 721, 2017.
- Wittrock, F., Oetjen, H., Richter, A., Fietkau, S., Medeke, T., Rozanov, A., and Burrows, J.: MAX-DOAS measurements of atmospheric trace gases in Ny-Ålesund-Radiative transfer studies and their application, *Atmos. Chem. Phys.*, 4, 955–966, 2004.

- Wu, F. C., Xie, P. H., Li, A., Chan, K. L., Hartl, A., Wang, Y., Si, F. Q., Zeng, Y., Qin, M., Xu, J., Liu, J. G., Liu, W. Q., and Wenig, M.: Observations of SO₂ and NO₂ by mobile DOAS in the Guangzhou eastern area during the Asian Games 2010, *Atmos. Meas. Tech.*, 6, 2277–2292, 2013.
- Zara, M., Boersma, K. F., De Smedt, I., Richter, A., Peters, E., van Geffen, J. H. G. M., Beirle, S., Wagner, T., Van Roozendael, M., Marchenko, S., Lamsal, L. N., and Eskes, H. J.: Improved slant column density retrieval of nitrogen dioxide and formaldehyde for OMI and GOME-2A from QA4ECV: intercomparison, uncertainty characterisation, and trends, *Atmos. Meas. Tech.*, 11, 4033–4058, 2018.
- Zel'Dovich, Y. B. and Raizer, Y. P.: *Physics of Shock Waves and High-Temperature Hydrodynamic Phenomena*, 1966.
- Zhou, Y., Brunner, D., Boersma, K., Dirksen, R., and Wang, P.: An improved tropospheric NO₂ retrieval for OMI observations in the vicinity of mountainous terrain, *Atmos. Meas. Tech.*, 2, 401–416, 2009.
- Zhou, Y., Brunner, D., Spurr, R., Boersma, K., Sneep, M., Popp, C., and Buchmann, B.: Accounting for surface reflectance anisotropy in satellite retrievals of tropospheric NO₂, *Atmos. Meas. Tech.*, 3, 1185–1203, 2010.
- Zoogman, P., Liu, X., Suleiman, R., Pennington, W., Flittner, D., Al-Saadi, J., Hilton, B.B. and Nicks, D., Newchurch, M., Carr, J., Janz, S., Andraschko, M., Arola, A., Baker, B., Canova, B., Chan Miller, C., Cohen, R., Davis, J., Dussault, M., Edwards, D., Fishman, J., Ghulam, A., González Abad, G., Grutter, M., Herman, J., Houck, J., Jacob, D., Joiner, J., Kerridge, B., Kim, J., Krotkov, N., Lamsal, L., Li, C., Lindfors, A., Martin, R., McElroy, C., McLinden, C., Natraj, V., Neil, D., Nowlan, C., O'Sullivan, E., Palmer, P., Pierce, R., Pippin, M., Saiz-Lopez, A., Spurr, R., Szykman, J., Torres, O., Veefkind, J., Veihelmann, B., Wang, H., Wang, J., and Chance, K.: Tropospheric emissions: Monitoring of pollution (TEMPO), *J. Quant. Spectrosc. Radiat. Transf.*, 186, 17–39, 2017.

Appendix A

Inversion models for the retrieval of total and tropospheric NO₂ columns

Liu, S.: Inversion Models for the Retrieval of Total and Tropospheric NO₂ Columns, *Atmosphere*, 10, 607, <https://doi.org/10.3390/atmos10100607>, 2019.

Article

Inversion Models for the Retrieval of Total and Tropospheric NO₂ Columns

Song Liu

Deutsches Zentrum für Luft- und Raumfahrt (DLR), Institut für Methodik der Fernerkundung (IMF),
82234 Oberpfaffenhofen, Germany; song.liu@dlr.de

Received: 4 September 2019; Accepted: 2 October 2019; Published: 9 October 2019



Abstract: Inversion models for retrieving the total and tropospheric nitrogen dioxide (NO₂) columns from spaceborne remote sensing data are presented. For total column retrieval, we propose the so-called differential radiance models with internal and external closure and solve the underlying nonlinear equations by using the method of Tikhonov regularization and the iteratively regularized Gauss–Newton method. For tropospheric column retrieval, we design a nonlinear and a linear model by using the results of the total column retrieval and the value of the stratospheric NO₂ column delivered by a stratosphere–troposphere separation method. We also analyze the fundamentals of the commonly used differential optical absorption spectroscopy (DOAS) model and outline its relationship to the proposed inversion models. By a numerical analysis, we analyze the accuracy of the inversion models to retrieve total and tropospheric NO₂ columns.

Keywords: inversion model; regularization; NO₂ retrieval; DOAS

1. Introduction

Nitrogen dioxide (NO₂) is an important trace gas in the Earth’s stratosphere and troposphere. The stratospheric NO₂ is strongly related to halogen compound reactions and ozone destruction [1]. In the troposphere, nitrogen oxides (NO_x = NO₂ + NO) serve as a precursor of ozone in the presence of volatile organic compounds and a precursor of secondary aerosols through gas-to-particle conversion [2]. As a greenhouse gas, NO₂ contributes significantly to radiative forcing locally [3]. As a prominent air pollutant affecting human health and ecosystems, substantial amounts of NO₂ are produced in the boundary layer by industrial processes, power generation, transportation, and biomass burning.

Atmospheric remote sensing measurements in the UV and visible region, for instance, from nadir-viewing satellite instruments such as the Ozone Monitoring Instrument (OMI) [4] and Global Ozone Monitoring Experiment-2 (GOME-2) [5,6], have been monitoring global NO₂ on a long-term scale. A new generation of instruments like the Tropospheric Monitoring Instrument (TROPOMI) [7] aboard the Sentinel-5 Precursor satellite, with high spatial resolution, and geostationary missions like Sentinel-4 [8], with a fast revisit time, enable the continuous monitoring of NO₂ concentrations for the following years. NO₂ measurements from satellite instruments have been thoroughly validated using correlative ground-based measurements [9–11] and have been widely used to characterize the distribution, evolution, or transport of NO₂ [12–14], to estimate NO_x emission [15,16], and to interpret ozone variation [17,18].

Based on a linearity assumption of the log of the radiances on the total column, the differential optical absorption spectroscopy (DOAS) model [19] is commonly used to derive the NO₂ columns [20–25]. In DOAS, the spectral structure of a measured spectrum is separated into a narrowband absorption structure of trace gases and a broadband contribution approximated by a low-order polynomial. Effectively, the differential spectrum, used to obtain the trace gas information,

is distinguished from the smooth background, such as Rayleigh scattering, cloud and aerosol extinction, and surface reflection.

In this paper, we aim to design inversion models that are more general than the DOAS model, for the retrieval of total and tropospheric NO₂ columns. The underlying nonlinear equations of the inversion models are solved by using classical regularization methods. The paper is organized as follows. In Section 2, we describe the regularization methods for stably solving nonlinear ill-posed problems. In Section 3, we present two nonlinear inversion models for total NO₂ column retrieval, while in Section 4, we design a nonlinear and a linear inversion model for tropospheric NO₂ column retrieval. In Section 5, we analyze the theoretical basis of the DOAS model and outline its relationship to the general inversion models. The numerical accuracy of the proposed inversion models is investigated in Section 6.

2. Regularization Methods

In our analysis, we consider the nonlinear data model [26]

$$\mathbf{y}^\delta = \mathbf{F}(\mathbf{x}) + \delta, \tag{1}$$

where $\mathbf{F} : \mathbb{R}^n \rightarrow \mathbb{R}^m$ is the forward model, $\mathbf{x} \in \mathbb{R}^n$ is the state vector, $\mathbf{y}^\delta \in \mathbb{R}^m$ is the noisy data vector, and $\delta \in \mathbb{R}^m$ is the measurement error vector. In a deterministic setting, the measurement error vector δ is characterized by the noise level Δ (defined as an upper bound for δ , i.e., $\|\delta\| \leq \Delta$), the state vector \mathbf{x} is a deterministic vector, and we are faced with the solution of the nonlinear equation

$$\mathbf{y}^\delta = \mathbf{F}(\mathbf{x}). \tag{2}$$

In a stochastic setting, δ and \mathbf{x} are random vectors, and the data Model (1) is solved by means of a Bayesian approach.

Because the nonlinear Equation (2) is usually ill-posed, a regularization method should be used to compute a solution with physical meaning. In classical regularization theory, two widely used methods are the method of Tikhonov regularization and the iteratively regularized Gauss–Newton method.

2.1. Tikhonov Regularization

In the framework of Tikhonov regularization [27], a regularized solution to the nonlinear Equation (2) is computed as the minimizer of the Tikhonov function

$$\mathcal{F}_\alpha(\mathbf{x}) = \|\mathbf{y}^\delta - \mathbf{F}(\mathbf{x})\|^2 + \alpha \|\mathbf{L}(\mathbf{x} - \mathbf{x}_a)\|^2, \tag{3}$$

where α is the regularization parameter, \mathbf{L} is the regularization matrix, and \mathbf{x}_a is the a priori state vector, the best beforehand estimate of the solution. The regularization matrix \mathbf{L} , controlling the magnitude or the smoothness of the solution, can be chosen as the identity matrix, a diagonal matrix, the discrete approximations to the first- and second-order derivative operators, or as the Cholesky factor of the inverse of an a priori covariance matrix.

The minimization of the Tikhonov function in Equation (3) can be formulated as a least-squares problem, and the regularized solution can be computed by using optimization methods, such as step-length and trust-region methods [28,29]. These nonlinear optimization methods are iterative methods, which compute the new iterate by approximating the objective function around the actual iterate by a quadratic model.

Belonging to the category of step-length methods, the Gauss–Newton method for least-squares problems has an important practical interpretation. At the iteration step i , considering a linearization of $\mathbf{F}(\mathbf{x})$ around the current iterate \mathbf{x}_{ai}^δ ,

$$\mathbf{F}(\mathbf{x}) \approx \mathbf{F}(\mathbf{x}_{ai}^\delta) + \mathbf{K}_{ai}(\mathbf{x} - \mathbf{x}_{ai}^\delta), \tag{4}$$

where

$$\mathbf{K}_{\alpha i} = \mathbf{K}(\mathbf{x}_{\alpha i}^\delta) = \frac{\partial \mathbf{F}}{\partial \mathbf{x}}(\mathbf{x}_{\alpha i}^\delta) \in \mathbb{R}^{m \times n} \tag{5}$$

is the Jacobian matrix evaluated at $\mathbf{x}_{\alpha i}^\delta$, and replacing $\mathbf{F}(\mathbf{x})$ in Equation (2) by its linearization (4), the result is

$$\mathbf{K}_{\alpha i}(\mathbf{x} - \mathbf{x}_a) = \mathbf{y}_i^\delta, \tag{6}$$

where

$$\mathbf{y}_i^\delta = \mathbf{y}^\delta - \mathbf{F}(\mathbf{x}_{\alpha i}^\delta) + \mathbf{K}_{\alpha i}(\mathbf{x}_{\alpha i}^\delta - \mathbf{x}_a) \tag{7}$$

is the linearized data vector at iteration step i . Since the nonlinear problem is ill-posed, its linearization is also ill-posed. Thus, we solve the linearized Equation (6) by means of Tikhonov regularization with the penalty term $\alpha \|\mathbf{L}(\mathbf{x} - \mathbf{x}_a)\|^2$.

The Tikhonov function for the linearized equation takes the form

$$\mathcal{F}_{l\alpha i}(\mathbf{x}) = \|\mathbf{y}_i^\delta - \mathbf{K}_{\alpha i}(\mathbf{x} - \mathbf{x}_a)\|^2 + \alpha \|\mathbf{L}(\mathbf{x} - \mathbf{x}_a)\|^2, \tag{8}$$

and its minimizer, i.e., the new iterate $\mathbf{x}_{\alpha i+1}^\delta$, is given by

$$\mathbf{x}_{\alpha i+1}^\delta = \mathbf{x}_a + \mathbf{K}_{\alpha i}^\dagger \mathbf{y}_i^\delta, \tag{9}$$

where

$$\mathbf{K}_{\alpha i}^\dagger = (\mathbf{K}_{\alpha i}^T \mathbf{K}_{\alpha i} + \alpha \mathbf{L}^T \mathbf{L})^{-1} \mathbf{K}_{\alpha i}^T \tag{10}$$

is the regularized generalized inverse, also known as the gain matrix [30], at iteration step i . The iterative process is stopped according to

1. the relative X-convergence test [28], when the iterates $\mathbf{x}_{\alpha i}^\delta$ converge, and/or
2. the relative function convergence test [30,31], when the residuals $\|\mathbf{y}^\delta - \mathbf{F}(\mathbf{x}_{\alpha i}^\delta)\|$ converge.

Therefore, the solution of a nonlinear ill-posed problem by means of Tikhonov regularization is equivalent to the solution of a sequence of ill-posed linearizations of the forward model about the current iterate.

The selection of the optimal value of the regularization parameter α_{opt} is a crucial issue of Tikhonov regularization. With too little regularization, reconstructions deviate significantly from the a priori, and the solution is said to be underregularized. With too much regularization, the reconstructions are too close to the a priori, and the solution is said to be over-regularized. Several regularization parameter choice methods have been discussed in [26,32], including the expected error estimation method, the maximum likelihood estimation, generalized cross-validation [33], and the nonlinear L-curve method [34].

The idea of the expected error estimation method is to perform a random exploration of a domain, in which the exact solution \mathbf{x}^\dagger is supposed to lie, and for each state vector realization \mathbf{x}_i^\dagger , to compute the optimal regularization parameter for error estimation as $\alpha_{opti} = \arg \min_\alpha \mathcal{E} \{ \|\mathbf{e}_\alpha^\delta(\mathbf{x}_i^\dagger)\|^2 \}$, where

$$\mathcal{E} \{ \|\mathbf{e}_\alpha^\delta(\mathbf{x}^\dagger)\|^2 \} = \|\mathbf{e}_{s\alpha}(\mathbf{x}^\dagger)\|^2 + \mathcal{E} \{ \|\mathbf{e}_{n\alpha}^\delta\|^2 \} \tag{11}$$

is the expected value of the total error vector $\mathbf{e}_\alpha^\delta(\mathbf{x}^\dagger) = \mathbf{x}^\dagger - \mathbf{x}_\alpha^\delta$, $\mathbf{e}_{s\alpha}(\mathbf{x}^\dagger) = (\mathbf{I}_n - \mathbf{A}_\alpha)(\mathbf{x}^\dagger - \mathbf{x}_a)$ is the smoothing error vector, $\mathbf{e}_{n\alpha}^\delta = -\mathbf{K}_\alpha^\dagger \delta$ is the noise error vector, \mathbf{x}_α^δ is the regularized solution, and $\mathbf{A}_\alpha = \mathbf{K}_\alpha^\dagger \mathbf{K}_\alpha$ is the averaging kernel matrix at the solution \mathbf{x}_α^δ . Under the assumption that δ is white noise with variance σ^2 , we compute the exponent $p_i = \log \alpha_{opti} / \log \sigma$ and choose the optimal regularization parameter as $\alpha_{opt} = \sigma^{\bar{p}}$, where $\bar{p} = (1/N_x) \sum_{i=1}^{N_x} p_i$ is the sample mean exponent, and N_x is the sample size.

2.2. Iteratively Regularized Gauss–Newton Method

Unfortunately, at the present time, there is no fail-safe regularization parameter choice method that guarantees small solution errors in any circumstance, that is, for any noisy data vector. An amelioration of the problems associated with regularization parameter selection is achieved in the framework of the so-called iterative regularization methods, of which the iteratively regularized Gauss–Newton method [35] is a relevant representative. These approaches, in which the amount of regularization is gradually decreased during the iterative process, are less sensitive to overestimations of the regularization parameter but require more iteration steps to achieve convergence.

Essentially, the iteratively regularized Gauss–Newton method relies on the solution of the linearized equation (cf. Equation (6)) $\mathbf{K}_i(\mathbf{x} - \mathbf{x}_a) = \mathbf{y}_i^\delta$ by means of Tikhonov regularization with the penalty term $\alpha_i \|\mathbf{L}(\mathbf{x} - \mathbf{x}_a)\|^2$. The new iterate minimizing the function

$$\mathcal{F}_{i_i}(\mathbf{x}) = \|\mathbf{y}_i^\delta - \mathbf{K}_i(\mathbf{x} - \mathbf{x}_a)\|^2 + \alpha_i \|\mathbf{L}(\mathbf{x} - \mathbf{x}_a)\|^2 \tag{12}$$

is given by

$$\mathbf{x}_{i+1}^\delta = \mathbf{x}_a + \mathbf{K}_i^\dagger \mathbf{y}_i^\delta, \tag{13}$$

where

$$\mathbf{K}_i^\dagger = (\mathbf{K}_i^T \mathbf{K}_i + \alpha_i \mathbf{L}^T \mathbf{L})^{-1} \mathbf{K}_i^T. \tag{14}$$

For iterative regularization methods, the number of iteration steps i plays the role of the regularization parameter, and the iterative process is stopped after an appropriate number of steps i^* in order to avoid an uncontrolled expansion of the errors in the data. In fact, a mere minimization of the residual $\|\mathbf{r}_i^\delta\|$, where

$$\mathbf{r}_i^\delta = \mathbf{y}^\delta - \mathbf{F}(\mathbf{x}_i^\delta)$$

is the residual vector at \mathbf{x}_i^δ , leads to a semi-convergent behavior of the iterated solution: while the error in the residual decreases as the number of iteration steps increases, the error in the solution starts to increase after an initial decay.

A widely used a posteriori choice for the stopping index i^* in dependence of the noise level Δ is the discrepancy principle [36]. According to this stopping rule, the iterative process is terminated after i^* steps such that

$$\|\mathbf{r}_{i^*}^\delta\|^2 \leq \tau \Delta^2 < \|\mathbf{r}_i^\delta\|^2, \quad 0 \leq i < i^*, \tag{15}$$

with $\tau > 1$. Hence, the regularized solution of the iteratively regularized Gauss–Newton method is $\mathbf{x}_{i^*}^\delta$. As in many practical problems arising in atmospheric remote sensing, the noise level cannot be a priori estimated, so we adopt a practical approach. This is based on the observation that the square residual $\|\mathbf{r}_i^\delta\|^2$ decreases during the iterative process and attains a plateau at approximately Δ^2 . Thus, if the nonlinear residuals $\|\mathbf{r}_i^\delta\|$ converge to $\|\mathbf{r}_\infty^\delta\|$ within a prescribed tolerance, we use the estimate

$$\Delta^2 = \|\mathbf{r}_\infty^\delta\|^2.$$

The above heuristic stopping rule does not have any mathematical justification but works sufficiently well in practice.

At first glance, this method seems to be identical to the method of Tikhonov regularization, but the following differences exist:

1. the regularization parameters are the terms of a decreasing (geometric) sequence, i.e., $\alpha_i = q\alpha_{i-1}$, with $q < 1$;
2. the iterative process is stopped according to the discrepancy principle (15) instead of requiring the convergence of iterates.

The numerical experiments performed in [26] showed that at the solution $\mathbf{x}_{k^*}^\delta$, α_{k^*} is close to α_{opt} and so that $\mathbf{x}_{k^*}^\delta$ is close to the Tikhonov solution corresponding to the optimal value of the regularization

parameter $\mathbf{x}_{\alpha_{\text{opt}}}^\delta$. Another positive feature of the method is that by decreasing the regularization parameter at each iteration step, problems that do not require regularization (or a small amount of regularization) can be handled.

In the following, the method of Tikhonov regularization and the iteratively regularized Gauss–Newton method will be used to solve the nonlinear equations corresponding to different inversion models for total and tropospheric column retrievals.

3. Total NO₂ Column Retrieval

Consider a discretization of the atmosphere in N_{lay} layers, and let the stratosphere extend from layer 1 to layer $N_t - 1$ and the troposphere extend from layer N_t to layer N_{lay} . The total column of a gas g is defined by

$$X_g = \sum_{j=1}^{N_{\text{lay}}} x_{g,j}, \tag{16}$$

while the stratospheric and tropospheric total columns are given respectively by

$$X_{\text{sg}} = \sum_{j=1}^{N_t-1} x_{g,j}, \tag{17}$$

and

$$X_{\text{tg}} = \sum_{j=N_t}^{N_{\text{lay}}} x_{g,j}, \tag{18}$$

where $x_{g,j}$ is the partial column of gas g on later j . Obviously, we have $X_g = X_{\text{tg}} + X_{\text{sg}}$.

An important task of the retrieval is the computation of the partial derivative of the radiance I with respect to the total column X_g of gas g . In a radiative transfer model, I is a function of $x_{g,j}$, i.e., $I = I(x_{g,1}, \dots, x_{g,N_{\text{lay}}})$, and the partial derivatives $\partial I / \partial x_{g,j}$, $j = 1, \dots, N_{\text{lay}}$ are computable quantities (delivered by a linearized radiative transfer model). Under the assumptions that the profile $\{x_{g,1}, \dots, x_{g,N_{\text{lay}}}\}$ is a scaled version of an a priori profile $\{x_{\text{ag},1}, \dots, x_{\text{ag},N_{\text{lay}}}\}$ and that s_g is the scale factor of gas g , i.e., $x_{g,j} = s_g x_{\text{ag},j}$, for all $j = 1, \dots, N_{\text{lay}}$, we have $s_g = X_g / X_{\text{ag}}$ and hence the one-to-one correspondence $x_{g,j} = (X_g / X_{\text{ag}}) x_{\text{ag},j}$. Consequently, the partial derivative of I with respect to X_g can be computed as

$$D_g = \sum_{j=1}^{N_{\text{lay}}} \frac{\partial I}{\partial x_{g,j}} \frac{\partial x_{g,j}}{\partial X_g} = \sum_{j=1}^{N_{\text{lay}}} \frac{x_{\text{ag},j}}{X_{\text{ag}}} \frac{\partial I}{\partial x_{g,j}}.$$

For the retrieval of the total columns X_g of N_g gases, we regard the radiance I as a function of $\mathbf{X} = [X_1, \dots, X_{N_g}]$, i.e., $I = I(\mathbf{X})$. In principle, the retrieval can be performed by considering the radiance model

$$\ln I_{\text{mes}}^\delta(\lambda_k) = \ln I_{\text{sim}}(\lambda_k, \mathbf{X}) + \sum_{j=1}^{N_s} b_j S_j(\lambda_k), \quad k = 1, \dots, N_\lambda, \tag{19}$$

where $I_{\text{mes}}^\delta(\lambda_k)$ is the Sun-normalized spectral radiance measured by the instrument at wavelength λ_k with $k = 1, \dots, N_\lambda$, $I_{\text{sim}}(\lambda_k, \mathbf{X})$ is the radiance computed by a radiative transfer model, $S_j(\lambda_k)$ with $j = 1, \dots, N_s$ are the correction spectra describing different kinds of instrumental effects, such as the polarization correction spectrum, undersampling spectrum, offset correction spectrum, and more complex physical phenomena (e.g., Ring spectrum), and finally, the wavelength-independent coefficients b_j , encapsulated in the row vector $\mathbf{b} = [b_1, \dots, b_{N_s}]$, are the amplitudes of the correction spectra. Another option, which is adopted in our analysis, is to consider the following two differential radiance models:

1. the differential radiance model with internal closure (DRMI), relying on the solution of the nonlinear equation

$$R_{\text{mes}}^{\delta}(\lambda_k) = R_{\text{sim}}(\lambda_k, \mathbf{X}) + \sum_{j=1}^{N_g} b_j S_j(\lambda_k), \quad k = 1, \dots, N_{\lambda}, \quad (20)$$

for the state vector $\mathbf{x} = [\mathbf{X}, \mathbf{b}]^T$, where

$$R_{\text{mes}}^{\delta}(\lambda_k) = \ln I_{\text{mes}}^{\delta}(\lambda_k) - P_{\text{mes}}(\lambda_k, \mathbf{c}_{\text{mes}}) \quad (21)$$

is the differential measured spectrum and

$$R_{\text{sim}}(\lambda_k, \mathbf{X}) = \ln I_{\text{sim}}(\lambda_k, \mathbf{X}) - P_{\text{sim}}(\lambda_k, \mathbf{c}_{\text{sim}}(\mathbf{X})) \quad (22)$$

is the differential simulated spectrum, and

2. the differential radiance model with external closure (DRME), relying on the solution of the nonlinear equation

$$R_{\text{mes}}^{\delta}(\lambda_k) = \ln I_{\text{sim}}(\lambda_k, \mathbf{X}) + \sum_{j=1}^{N_g} b_j S_j(\lambda_k) - P(\lambda_k, \mathbf{c}), \quad k = 1, \dots, N_{\lambda}, \quad (23)$$

for the state vector $\mathbf{x} = [\mathbf{X}, \mathbf{b}, \mathbf{c}]^T$.

In Equations (21)–(23), the polynomials $P_{\text{mes}}(\lambda, \mathbf{c}_{\text{mes}})$, $P_{\text{sim}}(\lambda, \mathbf{c}_{\text{sim}}(\mathbf{X}))$, and $P(\lambda, \mathbf{c})$ are intended to account for the low-order frequency structure due to scattering mechanisms, e.g., by clouds and aerosols. The coefficients $\mathbf{c}_{\text{mes}} = [c_{\text{mes}1}, \dots, c_{\text{mes}N}]$ and $\mathbf{c}_{\text{sim}}(\mathbf{X}) = [c_{\text{sim}1}(\mathbf{X}), \dots, c_{\text{sim}N}(\mathbf{X})]$ of the smoothing polynomials $P_{\text{mes}}(\lambda, \mathbf{c}_{\text{mes}})$ and $P_{\text{sim}}(\lambda, \mathbf{c}_{\text{sim}}(\mathbf{X}))$ with degree $N - 1$, respectively, are the solutions of the least-squares problems

$$\mathbf{c}_{\text{mes}} = \arg \min_{\mathbf{c}} \sum_{k=1}^{N_{\lambda}} [\ln I_{\text{mes}}^{\delta}(\lambda_k) - P_{\text{mes}}(\lambda_k, \mathbf{c})]^2 \quad (24)$$

and

$$\mathbf{c}_{\text{sim}}(\mathbf{X}) = \arg \min_{\mathbf{c}} \sum_{k=1}^{N_{\lambda}} [\ln I_{\text{sim}}(\lambda_k, \mathbf{X}) - P_{\text{sim}}(\lambda_k, \mathbf{c})]^2, \quad (25)$$

respectively. These coefficients are uniquely determined by $\ln I_{\text{mes}}^{\delta}(\lambda_k)$ and $\ln I_{\text{sim}}(\lambda_k, \mathbf{X})$, and thus they are not included in the state vector \mathbf{x} . In contrast, the coefficients $\mathbf{c} = [c_1, \dots, c_N]$ of the smoothing polynomial $P(\lambda, \mathbf{c})$ with degree $N - 1$ in Equation (23) are included in the state vector \mathbf{x} .

Comparing the inversion models relying on Equations (20) and (23), we note the following differences:

1. in DRMI, we fit the differential measured and simulated spectra, while in DRME we fit the differential measured spectrum with a simulated spectrum from which we extract its smooth component;
2. in DRMI, the dimension of the state vector \mathbf{x} is smaller, and possible correlations between the components of the state vector can be avoided; however, the computational complexity is higher because the partial derivative of $\mathbf{c}_{\text{sim}}(\mathbf{X})$ with respect to \mathbf{X} needs to be computed.

The regularization matrix is chosen as a diagonal matrix. Specifically, the penalty term $\alpha \|\mathbf{L}(\mathbf{x} - \mathbf{x}_a)\|^2$ is taken as

$$\alpha \left[\sum_{g=1}^{N_g} \frac{w_g}{X_{ag}} (X_g - X_{ag})^2 + \sum_{j=1}^{N_s} \frac{w_{bj}}{b_{aj}} (b_j - b_{aj})^2 \right] \tag{26}$$

for DRMI and

$$\alpha \left[\sum_{g=1}^{N_g} \frac{w_g}{X_{ag}} (X_g - X_{ag})^2 + \sum_{j=1}^{N_s} \frac{w_{bj}}{b_{aj}} (b_j - b_{aj})^2 + \sum_{p=1}^N \frac{w_{cp}}{c_{ap}} (c_p - c_{ap})^2 \right] \tag{27}$$

for DRME. Here, the scalars $\{w_g\}_{g=1}^{N_g}$, $\{w_{bj}\}_{j=1}^{N_s}$, and $\{w_{cp}\}_{p=1}^N$ give the weight of each component of the state vector into the regularization matrix. Note that if a weighting factor is very large, the component is close to the a priori, while for a very small weighting factor, the component is practically unconstrained.

In the above inversion models, the wavelength shift $\Delta\lambda$ is not included in the retrieval. To take the wavelength shift into account, we replace $R_{mes}^\delta(\lambda_k)$ in the left-hand sides of Equations (20) and (23) by $R_{mes}^\delta(\lambda_k + \Delta\lambda)$ and consider $\Delta\lambda$ as a component of the state vector \mathbf{x} . Therefore, Equations (20) and (23) are nonlinear with respect to the total column \mathbf{X} and the wavelength shift $\Delta\lambda$ but linear with respect to the amplitudes \mathbf{b} of the correction spectra and the coefficients \mathbf{c} of the smoothing polynomial (in the case of DRME).

4. Tropospheric NO₂ Column Retrieval

The UV-visible NO₂ columns measured by satellite instruments consist of stratospheric and tropospheric contributions, which show comparable magnitudes and contribute to the signal with different weights, particularly for polluted scenarios. As the nadir-viewing measurements do not contain information on the vertical distribution, the a priori vertical NO₂ profiles are typically obtained from chemistry transfer models. The models are usually characterized by considerable differences [37], and currently, there is no consensus in the models on what the vertical profile of NO₂ over a given area is. Therefore a direct retrieval of tropospheric NO₂ columns is practically impossible, and a careful estimation and removal of stratospheric contribution is essential for the determination of tropospheric NO₂ columns.

The retrieval of the tropospheric column of gas \bar{g} (specifically, NO₂) is performed under the assumption that we have some a priori knowledge about the stratospheric column. More precisely, we assume that $X_{s\bar{g}}$ can be approximated by

$$X_{s\bar{g}} \approx X_{s\bar{g}}^* \tag{28}$$

where $X_{s\bar{g}}^*$ is delivered by the reference sector method [38–40] or from data assimilation [41,42], a procedure we refer to as stratosphere–troposphere separation [43].

For tropospheric column retrieval, we propose a nonlinear and a linear model.

4.1. Nonlinear Model

In principle, considering the approximation

$$I = I(\mathbf{X}) = I(X_{t\bar{g}}, X_{s\bar{g}}, \mathbf{X}_{-\bar{g}}) \approx I(X_{t\bar{g}}, X_{s\bar{g}}^*, \mathbf{X}_{-\bar{g}}), \tag{29}$$

where $\mathbf{X}_{-\bar{g}}$ is the set of all total columns excepting $X_{\bar{g}}$, i.e., $\mathbf{X} = \{X_{\bar{g}}\} \cup \mathbf{X}_{-\bar{g}}$, the tropospheric column can be retrieved by solving the nonlinear Equations (20) and (23) with

$$I_{sim}(\lambda_k, \mathbf{X}) \rightarrow I_{sim}(\lambda_k, X_{t\bar{g}}, X_{s\bar{g}}^*, \mathbf{X}_{-\bar{g}}) \tag{30}$$

for the state vector $\mathbf{x} = [X_{t\bar{g}}, \mathbf{X}_{-\bar{g}}, \mathbf{b}]^T$ and $\mathbf{x} = [X_t, \mathbf{X}_{-\bar{g}}, \mathbf{b}, \mathbf{c}]^T$, respectively. However, our numerical experiments showed that the accuracy in retrieving $X_{t\bar{g}}$ is higher if we fix the columns $\mathbf{X}_{-\bar{g}}$ and the amplitudes \mathbf{b} of the correction spectra to the values computed by a total column retrieval; following [44], we refer to this inversion step as pre-processing step. In this regard, we compute $X_{t\bar{g}}$ by solving

1. the nonlinear equation of DRMI

$$R_{\text{mes}}^\delta(\lambda_k) = R_{\text{sim}}^\delta(\lambda_k, X_{t\bar{g}}, X_{s\bar{g}}^*, \mathbf{X}_{-\bar{g}}) + \sum_{j=1}^{N_s} b_j S_j(\lambda_k), \quad k = 1, \dots, N_\lambda, \quad (31)$$

2. for the state vector $\mathbf{x} = [X_{t\bar{g}}]$, and the nonlinear equation of DRME

$$R_{\text{mes}}^\delta(\lambda_k) = \ln I_{\text{sim}}(\lambda_k, X_{t\bar{g}}, X_{s\bar{g}}^*, \mathbf{X}_{-\bar{g}}) + \sum_{j=1}^{N_s} b_j S_j(\lambda_k) - P(\lambda_k, \mathbf{c}), \quad k = 1, \dots, N_\lambda, \quad (32)$$

for the state vector $\mathbf{x} = [X_{t\bar{g}}, \mathbf{c}]^T$.

In summary, this approach involves the following steps.

- Step 1.** Solve the nonlinear Equation (20) of DRMI for $\mathbf{x} = [\mathbf{X}, \mathbf{b}]^T$ or the nonlinear Equation (23) of DRME for $\mathbf{x} = [\mathbf{X}, \mathbf{b}, \mathbf{c}]^T$.
- Step 2.** With $X_{s\bar{g}}^*$ delivered by a stratosphere–troposphere separation method and $\mathbf{X}_{-\bar{g}}$ and \mathbf{b} determined at Step 1, solve the nonlinear Equation (31) of DRMI for $\mathbf{x} = [X_{t\bar{g}}]$ or the nonlinear Equation (32) of DRME for $\mathbf{x} = [X_{t\bar{g}}, \mathbf{c}]^T$.

4.2. Linear Model

Recalling that $\mathbf{X} = \{X_{\bar{g}}\} \cup \mathbf{X}_{-\bar{g}} = \{X_{t\bar{g}}, X_{s\bar{g}}\} \cup \mathbf{X}_{-\bar{g}}$, we consider the following linearizations around the a priori:

$$\begin{aligned} \ln I_{\text{sim}}(\lambda_k, \mathbf{X}) &\approx \ln I_{\text{sim}}(\lambda_k, \mathbf{X}_a) + (X_{\bar{g}} - X_{a\bar{g}})W_{\bar{g}}(\lambda_k, \mathbf{X}_a) \\ &\quad + \sum_{g=1, g \neq \bar{g}}^{N_g} (X_g - X_{ag})W_g(\lambda_k, \mathbf{X}_a) \end{aligned} \quad (33)$$

and

$$\begin{aligned} \ln I_{\text{sim}}(\lambda_k, \mathbf{X}) &\approx \ln I_{\text{sim}}(\lambda_k, \mathbf{X}_a) + (X_{t\bar{g}} - X_{at\bar{g}})W_{t\bar{g}}(\lambda_k, \mathbf{X}_a) \\ &\quad + (X_{s\bar{g}} - X_{as\bar{g}})W_{s\bar{g}}(\lambda_k, \mathbf{X}_a) \\ &\quad + \sum_{g=1, g \neq \bar{g}}^{N_g} (X_g - X_{ag})W_g(\lambda_k, \mathbf{X}_a) \end{aligned} \quad (34)$$

to obtain

$$\begin{aligned} (X_{\bar{g}} - X_{a\bar{g}})W_{\bar{g}}(\lambda_k, \mathbf{X}_a) &= (X_{t\bar{g}} - X_{at\bar{g}})W_{t\bar{g}}(\lambda_k, \mathbf{X}_a) \\ &\quad + (X_{s\bar{g}} - X_{as\bar{g}})W_{s\bar{g}}(\lambda_k, \mathbf{X}_a) \end{aligned} \quad (35)$$

with

$$W_g(\lambda_k, \mathbf{X}_a) = \sum_{j=1}^{N_{\text{lay}}} \frac{x_{ag,j}}{X_{ag}} \frac{\partial \ln I_{\text{sim}}}{\partial x_{g,j}}(\lambda_k, \mathbf{X}_a), \quad (36)$$

$$W_{sg}(\lambda_k, \mathbf{X}_a) = \sum_{j=1}^{N_t-1} \frac{x_{ag,j}}{X_{ag}} \frac{\partial \ln I_{sim}}{\partial x_{g,j}}(\lambda_k, \mathbf{X}_a), \tag{37}$$

and

$$W_{tg}(\lambda_k, \mathbf{X}_a) = \sum_{j=N_t}^{N_{lay}} \frac{x_{ag,j}}{X_{ag}} \frac{\partial \ln I_{sim}}{\partial x_{g,j}}(\lambda_k, \mathbf{X}_a). \tag{38}$$

For scaled profiles, it can be shown that similar to Equation (35), we have

$$X_{\bar{g}}W_{\bar{g}}(\lambda_k, \mathbf{X}_a) = X_{t\bar{g}}W_{t\bar{g}}(\lambda_k, \mathbf{X}_a) + X_{s\bar{g}}W_{s\bar{g}}(\lambda_k, \mathbf{X}_a). \tag{39}$$

Now, if $X_{\bar{g}}$ is known from the total column retrieval and $X_{s\bar{g}} = X_{s\bar{g}}^*$, we may compute $X_{t\bar{g}}$ from Equation (39) at a reference wavelength $\lambda_0 = \lambda_{k_0}$ for some $k_0 \in \{1, \dots, N_\lambda\}$, i.e.,

$$X_{t\bar{g}} = \frac{X_{\bar{g}}W_{\bar{g}}(\lambda_0, \mathbf{X}_a) - X_{s\bar{g}}^*W_{s\bar{g}}(\lambda_0, \mathbf{X}_a)}{W_{t\bar{g}}(\lambda_0, \mathbf{X}_a)}, \tag{40}$$

or as the solution of a least-squares problem in the spectral domain, i.e.,

$$X_{t\bar{g}} = \arg \min_{X_{t\bar{g}}} \sum_{k=1}^{N_\lambda} \left[X_{t\bar{g}}W_{t\bar{g}}(\lambda_k, \mathbf{X}_a) + X_{s\bar{g}}^*W_{s\bar{g}}(\lambda_k, \mathbf{X}_a) - X_{\bar{g}}W_{\bar{g}}(\lambda_k, \mathbf{X}_a) \right]^2. \tag{41}$$

This approach involves the following computational steps.

- Step 1.** Solve the nonlinear Equation (20) of DRMI for $\mathbf{x} = [\mathbf{X}, \mathbf{b}]^T$ or the nonlinear Equation (23) of DRME for $\mathbf{x} = [\mathbf{X}, \mathbf{b}, \mathbf{c}]^T$.
- Step 2.** With $X_{s\bar{g}}^*$ delivered by a stratosphere–troposphere separation method and $X_{\bar{g}}$ determined at Step 1, compute $X_{t\bar{g}}$ by means of Equation (40) or as the solution of the least-squares problem (41).

Comparing the two inversion models, the following conclusions can be drawn.

1. In both models, we compute in the pre-processing step the total columns of all gases \mathbf{X} and the amplitudes \mathbf{b} of the correction spectra by means of DRMI or DRME.
2. In the nonlinear model, we compute the tropospheric column $X_{t\bar{g}}$ of gas \bar{g} by using $\mathbf{X}_{-\bar{g}}$ and \mathbf{b} determined in the pre-processing step and by solving a nonlinear equation corresponding to DRMI or DRME. The accuracy in computing $X_{t\bar{g}}$ is affected by the accuracy in computing $\mathbf{X}_{-\bar{g}}$ and \mathbf{b} .
3. In the linear model, we compute the tropospheric column $X_{t\bar{g}}$ of gas \bar{g} by using $X_{\bar{g}}$ determined in the pre-processing step and by solving a linear equation. The accuracy in computing $X_{t\bar{g}}$ is affected by the accuracy in computing $X_{\bar{g}}$ and the linearity assumptions (33) and (34).

5. DOAS Model

In this section, we describe the standard DOAS inversion model [19] for total and tropospheric NO₂ column retrievals.

5.1. Total NO₂ Column Retrieval

In the DOAS model, the equation

$$\begin{aligned} \ln I_{mes}^\delta(\lambda_k) = & - \sum_{g=1}^{N_g} S_g C_{absg}(\lambda_k) + \sum_{j=1}^{N_s} b_j S_j(\lambda_k) \\ & + P_D(\lambda_k, \mathbf{c}_D), \quad k = 1, \dots, N_\lambda, \end{aligned} \tag{42}$$

is solved for the state vector $\mathbf{x} = [\mathbf{S}, \mathbf{b}, \mathbf{c}_D]^T$, where $\mathbf{S} = [S_1, \dots, S_{N_g}]$, S_g is the slant column of gas g , and $C_{\text{abs}g}(\lambda_k)$ is the differential absorption cross section of gas g at wavelength λ_k . The total column X_g is then computed from the slant column S_g by means of the relation

$$S_g = A(X_{\text{ag}})X_g, \tag{43}$$

where $A(X_{\text{ag}})$ is the air-mass factor of gas g . Note that the slant column and the air-mass factor are assumed to be wavelength-independent and that the air-mass factor is defined with respect to the a priori. Also note that in the DOAS model, the measured spectrum is fitted by the sum of a differential component (the first two terms on the right-hand side of Equation (42)) and a smooth component (the last term in Equation (42)).

In the framework of the DOAS model, the main problem that has to be solved is the computation of the air-mass factor. Inserting Equation (43) in Equation (42) and comparing the resulting equation with Equation (19), we deduce that $\ln I_{\text{sim}}(\lambda_k, \mathbf{X})$ is of the form

$$\ln I_{\text{sim}}(\lambda_k, \mathbf{X}) = - \sum_{g=1}^{N_g} A(X_{\text{ag}})C_{\text{abs}g}(\lambda_k)X_g + \tilde{P}_D(\lambda_k, \tilde{\mathbf{c}}_D), \quad k = 1, \dots, N_\lambda, \tag{44}$$

where the polynomial $\tilde{P}_D(\lambda_k, \tilde{\mathbf{c}}_D)$, extracting the smooth component of $\ln I_{\text{sim}}(\lambda_k, \mathbf{X})$, is close but not identical with the smoothing polynomial $P_D(\lambda_k, \mathbf{c}_D)$, matching the smooth component of $\ln I_{\text{mes}}^\delta(\lambda_k)$ in Equation (42). The above equation gives recipes for computing the air-mass factor. Two frequently used methods are described below.

1. Setting $\mathbf{X} = \mathbf{X}_a$ in Equation (44) gives

$$\ln I_{\text{sim}}(\lambda_k, \mathbf{X}_a) = - \sum_{g=1}^{N_g} A(X_{\text{ag}})C_{\text{abs}g}(\lambda_k)X_{\text{ag}} + \tilde{P}_D(\lambda_k, \tilde{\mathbf{c}}_D). \tag{45}$$

From Equations (44) and (45), we obtain

$$\ln I_{\text{sim}}(\lambda_k, \mathbf{X}) = \ln I_{\text{sim}}(\lambda_k, \mathbf{X}_a) - \sum_{g=1}^{N_g} A(X_{\text{ag}})C_{\text{abs}g}(\lambda_k)(X_g - X_{\text{ag}}). \tag{46}$$

Consequently, by means of the linearization

$$\ln I_{\text{sim}}(\lambda_k, \mathbf{X}) = \ln I_{\text{sim}}(\lambda_k, \mathbf{X}_a) + \sum_{g=1}^{N_g} (X_g - X_{\text{ag}})W_g(\lambda_k, \mathbf{X}_a) \tag{47}$$

and Equation (46), we find

$$A(X_{\text{ag}}) = - \frac{1}{C_{\text{abs}g}(\lambda_k)} W_g(\lambda_k, \mathbf{X}_a), \tag{48}$$

for any $k = 1, \dots, N_\lambda$.

2. Let $I_{\text{sim}}(\lambda_k, \mathbf{X}_a)$ be the radiance for a complete atmosphere with N_g gases and $I_{\text{sim}}(\lambda_k, \mathbf{X}_{a-\bar{g}})$ for an atmosphere without the gas \bar{g} . In view of Equation (45), we can write

$$\ln I_{\text{sim}}(\lambda_k, \mathbf{X}_{a-\bar{g}}) = - \sum_{g=1, g \neq \bar{g}}^{N_g} A(X_{\text{ag}})C_{\text{abs}g}(\lambda_k)X_{\text{ag}} + \tilde{P}_D(\lambda_k, \tilde{\mathbf{c}}_D), \tag{49}$$

provided that the smoothing polynomial remains the same. As a result, from Equations (45) and (49), we get

$$A(X_{a\bar{g}}) = -\frac{1}{C_{\text{abs}\bar{g}}(\lambda_k)X_{a\bar{g}}} \ln \left[\frac{I_{\text{sim}}(\lambda_k, \mathbf{X}_a)}{I_{\text{sim}}(\lambda_k, \mathbf{X}_{a-\bar{g}})} \right] \quad (50)$$

for any $k = 1, \dots, N_\lambda$.

Several comments are in order.

1. Equation (48) is computed with the scaling approximation for the NO₂ vertical profile. This assumption is not employed in the second method, but it is apparent that Equation (50) can be interpreted as a finite-difference approximation of Equation (48).
2. Because the right-hand sides of Equations (48) and (50) are wavelength-dependent, we can compute the air-mass factor at a reference wavelength λ_0 or by averaging in the spectral domain. For example, the computational formulas corresponding to Equation (48) read as

$$A(X_{a\bar{g}}) = -\frac{1}{C_{\text{abs}\bar{g}}(\lambda_0)} W_g(\lambda_0, \mathbf{X}_a) \quad (51)$$

and

$$A(X_{a\bar{g}}) = -\frac{1}{N_\lambda} \sum_{k=1}^{N_\lambda} \frac{1}{C_{\text{abs}\bar{g}}(\lambda_k)} W_g(\lambda_k, \mathbf{X}_a). \quad (52)$$

3. It is not hard to see that the DOAS model with the $A(X_{a\bar{g}})$ as in Equation (48) is in some sense equivalent with the first iteration step of DRME. Indeed, in this case, we consider a linearization of $\ln I_{\text{sim}}(\lambda_k, \mathbf{X})$ around the a priori \mathbf{X}_a as in Equation (47). Hence, from Equations (21) and (23), we get

$$\begin{aligned} \ln I_{\text{mes}}^\delta(\lambda_k) &= \ln I_{\text{sim}}(\lambda_k, \mathbf{X}_a) + \sum_{g=1}^{N_g} (X_g - X_{a\bar{g}}) W_g(\lambda_k, \mathbf{X}_a) \\ &+ \sum_{j=1}^{N_s} b_j S_j(\lambda_k) + P_{\text{mes}}(\lambda_k, \mathbf{c}_{\text{mes}}) - P(\lambda_k, \mathbf{c}) \end{aligned} \quad (53)$$

$$\stackrel{(45)}{=} - \sum_{g=1}^{N_g} A(X_{a\bar{g}}) C_{\text{abs}\bar{g}}(\lambda_k) X_{a\bar{g}}$$

$$\begin{aligned} &+ \sum_{g=1}^{N_g} (X_g - X_{a\bar{g}}) W_g(\lambda_k, \mathbf{X}_a) \\ &+ \sum_{j=1}^{N_s} b_j S_j(\lambda_k) + P_{\text{mes}}(\lambda_k, \mathbf{c}_{\text{mes}}) - P(\lambda_k, \mathbf{c}) + \tilde{P}_D(\lambda_k, \tilde{\mathbf{c}}_D) \end{aligned}$$

$$\stackrel{(48)}{=} - \sum_{g=1}^{N_g} A(X_{a\bar{g}}) C_{\text{abs}\bar{g}}(\lambda_k) X_g$$

$$\begin{aligned} &+ \sum_{j=1}^{N_s} b_j S_j(\lambda_k) + P_{\text{mes}}(\lambda_k, \mathbf{c}_{\text{mes}}) - P(\lambda_k, \mathbf{c}) + \tilde{P}_D(\lambda_k, \tilde{\mathbf{c}}_D) \end{aligned}$$

$$\stackrel{(43)}{=} - \sum_{g=1}^{N_g} S_g C_{\text{abs}\bar{g}}(\lambda_k) + \sum_{j=1}^{N_s} b_j S_j(\lambda_k) + P_D(\lambda_k, \mathbf{c}_D), \quad (54)$$

where

$$P_D(\lambda_k, \mathbf{c}_D) = \tilde{P}_D(\lambda_k, \tilde{\mathbf{c}}_D) + P_{\text{mes}}(\lambda_k, \mathbf{c}_{\text{mes}}) - P(\lambda_k, \mathbf{c}).$$

Thus, the solution of the linearized Equation (53) for $\mathbf{x} = [\mathbf{X}, \mathbf{b}, \mathbf{c}]^T$ is equivalent with the solution of the DOAS Equation (54) for $\mathbf{x} = [\mathbf{S}, \mathbf{b}, \mathbf{c}_D]^T$. Note that because $P_{\text{mes}}(\lambda_k, \mathbf{c}_{\text{mes}})$ is close to $P(\lambda_k, \mathbf{c})$, $P_D(\lambda_k, \mathbf{c}_D)$ is also close to $\tilde{P}_D(\lambda_k, \tilde{\mathbf{c}}_D)$.

5.2. Tropospheric NO₂ Column Retrieval

Coming to the tropospheric column retrieval, we use Equation (48) to express Equation (39) in terms of air-mass factors as

$$X_{\bar{g}} A(X_{\bar{a}\bar{g}}) = X_{\bar{t}\bar{g}} A_t(X_{\bar{a}\bar{g}}) + X_{\bar{s}\bar{g}} A_s(X_{\bar{a}\bar{g}}) \tag{55}$$

with

$$A_t(X_{\bar{a}\bar{g}}) = -\frac{1}{C_{\text{abs}\bar{g}}(\lambda_k)} W_{\bar{t}\bar{g}}(\lambda_k, \mathbf{X}_a) \tag{56}$$

and

$$A_s(X_{\bar{a}\bar{g}}) = -\frac{1}{C_{\text{abs}\bar{g}}(\lambda_k)} W_{\bar{s}\bar{g}}(\lambda_k, \mathbf{X}_a) \tag{57}$$

for any $k = 1, \dots, N_\lambda$. If $S_{\bar{g}}$ is the solution of Equation (42), then from Equations (43) and (55), we obtain

$$S_{\bar{g}} = X_{\bar{t}\bar{g}} A_t(X_{\bar{a}\bar{g}}) + X_{\bar{s}\bar{g}} A_s(X_{\bar{a}\bar{g}}), \tag{58}$$

and for $X_{\bar{s}\bar{g}} = X_{\bar{s}\bar{g}}^*$, we end up with

$$X_{\bar{t}\bar{g}} = \frac{S_{\bar{g}} - X_{\bar{s}\bar{g}}^* A_s(X_{\bar{a}\bar{g}})}{A_t(X_{\bar{a}\bar{g}})}. \tag{59}$$

If $A_t(X_{\bar{a}\bar{g}})$ and $A_s(X_{\bar{a}\bar{g}})$ are computed from Equations (56) and (57) at a reference wavelength λ_0 , then Equation (59) is the counterpart of Equation (40).

In conclusion, the standard DOAS inversion model for total and tropospheric column retrieval is entirely based on the linearity assumption of the forward model with respect to the total and tropospheric columns. More precisely, the model is equivalent to

1. the first iteration step of DRME for computing the total column (see Section 3) and
2. the linear model for computing the tropospheric column (see Section 4).

6. Numerical Analysis

In this section, we analyze the numerical accuracy of the proposed inversion models. The radiances and the Jacobian matrices are computed by a radiative transfer model based on the discrete ordinate method with matrix exponential [45,46]. The spectral range is between 425 and 497 nm, the number of spectral points is $N_\lambda = 345$, and the average spectral resolution is $\Delta\lambda_0 = 0.2$ nm. The calculations are performed for a mid-latitude summer atmosphere [47] with a solar zenith angle of 30°, a relative azimuth angle of 180°, and a Lambertian surface with albedo of 0.05. The atmosphere between 0 and 50 km is discretized with a step of 0.5 km between 0 and 2 km, 1 km between 2 and 20 km, 5 km between 20 and 30 km, and 10 km between 30 and 50 km. The troposphere extends to an altitude of 15 km.

The simulations include the absorption of NO₂, ozone (O₃), oxygen dimer (O₄), and water vapor, the Ring correction spectrum $S_1(\lambda_k) = S_R(\lambda_k)$, the offset correction spectrum $S_2(\lambda_k) = S_O(\lambda_k)$, and the wavelength shift $\Delta\lambda$. The scattering by clouds and aerosols is not taken into account. Vertical NO₂ volume mixing ratio profiles for a clean scenario, which typically shows a larger concentration at higher altitudes, and a polluted scenario, which typically shows a larger concentration near the surface, are illustrated in Figure 1. These profiles are taken as a priori partial column profiles and used to generate the true (exact) partial column profiles.

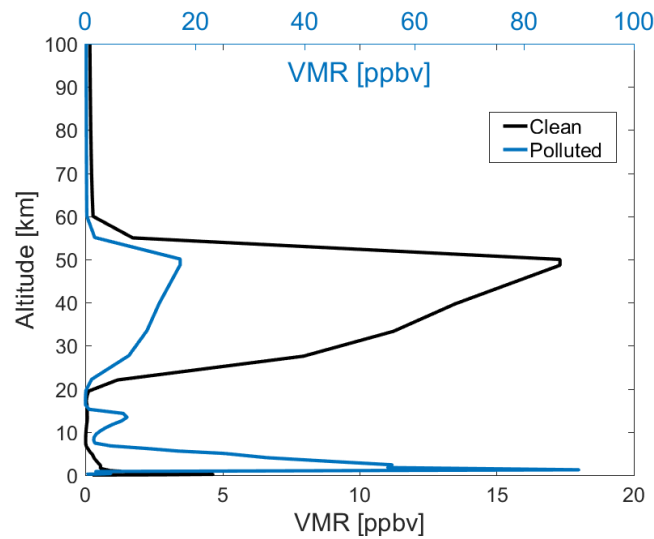


Figure 1. Vertical NO₂ volume mixing ratio (VMR) profiles for the clean and polluted scenarios. Note that both profiles have the same stratospheric NO₂ column.

Denoting the a priori partial columns of gas g by $x_{ag,j}$, $j = 1, \dots, N_{lay}$ and choosing cubic smoothing polynomials ($N = 4$) and the amplitudes of the correction spectra as $b_1 = b_{aR} = 5 \times 10^{-2}$ and $b_2 = b_{aO} = 10^{-2}$, we generate synthetic measurement spectra as follows:

1. we choose $x_{g,j}^\dagger = s_g x_{ag,j}$ with $j = 1, \dots, N_{lay}$ and $s_g = 1.5$ (if not stated otherwise) and compute $X_g^\dagger = \sum_{j=1}^{N_{lay}} x_{g,j}^\dagger = s_g X_{ag}$, $X_{sNO_2}^\dagger = \sum_{j=1}^{N_t-1} x_{NO_2,j}^\dagger$ and $X_{tNO_2}^\dagger = \sum_{j=N_t}^{N_{lay}} x_{NO_2,j}^\dagger$; thus, the exact total NO₂ column to be retrieved is $X_{NO_2}^\dagger = 1.5 X_{aNO_2}$;
2. for $\mathbf{X}^\dagger = [X_{NO_2}^\dagger, X_{O_3}^\dagger, X_{O_4}^\dagger, X_{H_2O}^\dagger]$, we compute $I_{sim}(\lambda_k, \mathbf{X}^\dagger)$ by the radiative transfer model;
3. we determine the coefficients $\mathbf{c}_{sim}(\mathbf{X}^\dagger)$ of the smoothing polynomial $P_{sim}(\lambda_k, \mathbf{c}_{sim}(\mathbf{X}^\dagger))$ by solving the least-squares problem (25);
4. we compute $I_{sim}^\delta(\lambda_k, \mathbf{X}^\dagger) = I_{sim}(\lambda_k, \mathbf{X}^\dagger) + \delta_k$, where δ_k are independent Gaussian random variables with zero mean and standard deviation

$$\sigma_k = \frac{I_{sim}(\lambda_k, \mathbf{X}^\dagger)}{SNR},$$

and SNR is the signal-to-noise ratio;

5. we choose $b_1^\dagger = b_R^\dagger = 2b_{aR}$, $b_2^\dagger = b_O^\dagger = 2b_{aO}$, and $\Delta\lambda^\dagger = 0.2\Delta\lambda_0$;
6. for DRMI, we compute the k th component of the noisy data vector as

$$R_{mes}^\delta(\lambda_k) = [\ln I_{sim}^\delta(\lambda_k + \Delta\lambda^\dagger, \mathbf{X}^\dagger) - P_{sim}(\lambda_k, \mathbf{c}_{sim}(\mathbf{X}^\dagger))] + \sum_{j=1}^{N_s} b_j^\dagger S_j(\lambda_k);$$

7. for DRME, we choose $\mathbf{c}^\dagger = 0.5 \mathbf{c}_{sim}(\mathbf{X}^\dagger)$ and compute the k th component of the noisy data vector as

$$R_{mes}^\delta(\lambda_k) = \ln I_{sim}^\delta(\lambda_k + \Delta\lambda^\dagger, \mathbf{X}^\dagger) + \sum_{j=1}^{N_s} b_j^\dagger S_j(\lambda_k) - P(\lambda_k, \mathbf{c}^\dagger).$$

Note that in view of the approximation

$$\begin{aligned} & \ln I_{sim}^\delta(\lambda_k, \mathbf{X}^\dagger) \\ & \approx \ln I_{sim}(\lambda_k, \mathbf{X}^\dagger) + \frac{\delta_k}{I_{sim}(\lambda_k, \mathbf{X}^\dagger)}, \end{aligned}$$

the error in $\ln I_{\text{sim}}^{\delta}(\lambda_k, \mathbf{X}^{\dagger})$ is $\delta_{\ln k} = \delta_k / I_{\text{sim}}(\lambda_k, \mathbf{X}^{\dagger})$, implying $\sigma_{\ln k} = 1/\text{SNR}$ for all k . Thus, the error vector δ_{\ln} is white noise with covariance matrix $\sigma_{\ln k}^2 \mathbf{I}_m$, where \mathbf{I}_m is the identity matrix.

Some parameters characterizing the regularization algorithms are chosen as follows.

1. As usual, the initial guess is taken to be equal to the a priori, i.e., $\mathbf{x}_0 = \mathbf{x}_a$.
2. If not stated otherwise, the regularization parameter of the method of Tikhonov regularization is chosen as $\alpha = \sigma_{\ln k}^2$, while for the iteratively regularized Gauss–Newton method, the initial value of the regularization parameter is $\alpha_0 = \sigma_{\ln k}$ and the regularization strength is gradually decreased during the iterative process with a constant ratio $q = 0.2$. Because the iteratively regularized Gauss–Newton method is less sensitive to the overestimation of the regularization parameter, the choice of $\alpha_0 \gg \alpha$ should guarantee that the method is able to capture the optimal value of the regularization parameter, i.e., $\alpha_{k^*} \approx \alpha_{\text{opt}}$.
3. The weighting factors of the state vector in (26) and (27) are given by standard deviations for $\{w_g\}_{g=1}^{N_g}$ and empirical values for $\{w_{bj}\}_{j=1}^{N_s}$ and $\{w_{cp}\}_{p=1}^N$.
4. The control parameter in the discrepancy principle Equation (15) is $\tau = 1.2$.

Figure 2 shows the radiances $\ln I_{\text{sim}}(\lambda, \mathbf{X}_a)$ and the differential radiances $\ln I_{\text{sim}}(\lambda, \mathbf{X}_a) - P_{\text{sim}}(\lambda_k, \mathbf{c}_{\text{sim}}(\mathbf{X}_a))$ for the clean and polluted NO_2 profiles. For optically thin absorbers in the visible wavelength range, such as the clean NO_2 profile, the absorption effect on the overall radiances is small. In contrast, for the polluted NO_2 profile, the absorption is largely enhanced; the radiances decrease by more than 15% and show a spectral structure linked to the NO_2 absorption bands. Due to the lack of a differential structure, we expect that the inversion models based on the analysis of differential spectra will have difficulties in handling the clean scenario, and in particular when the signal-to-noise ratio is small.

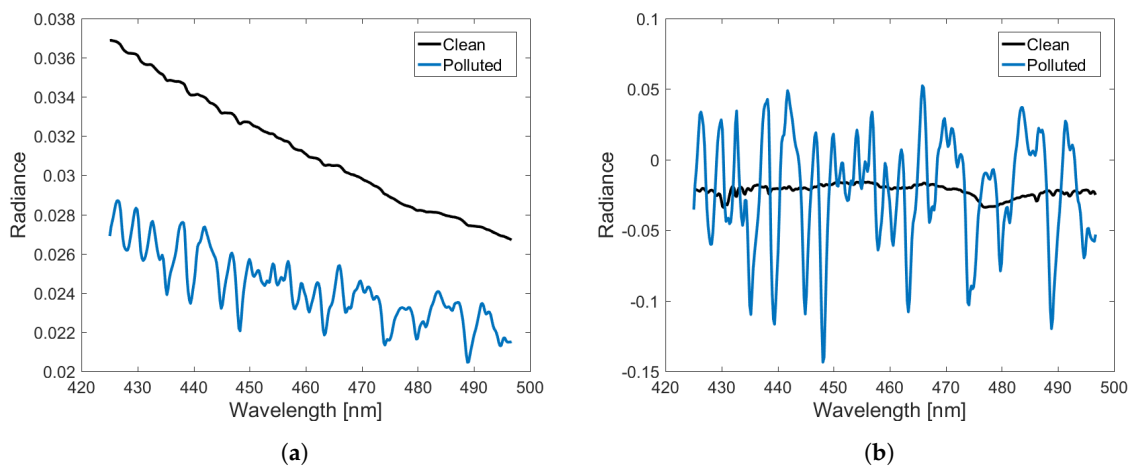


Figure 2. (a) Radiances and (b) differential radiances for the clean and polluted scenarios.

6.1. Total NO_2 Column Retrieval

In Figure 3, we illustrate the relative errors in the total NO_2 column versus the signal-to-noise ratio for the clean scenario. The results correspond to DRMI and DRME and the two regularization methods (Tikhonov regularization and the iteratively regularized Gauss–Newton method). The following conclusions can be drawn.

1. The relative errors decrease with the increasing signal-to-noise ratio.
2. In general, for small values of the signal-to-noise ratio ($\text{SNR} < 10^3$), the relative errors obtained by the iteratively regularized Gauss–Newton method are smaller than those delivered by the method of Tikhonov regularization. Note that for the clean scenario with $\text{SNR} < 10^3$ (where the NO_2 signal is very low and the noise level is relatively high), the retrieval error is dominated by the noise error rather than the smoothing error.

- For small values of the signal-to-noise ratio ($\text{SNR} < 10^3$), DRMI equipped with the method of Tikhonov regularization delivers more reliable results than DRME; when the iteratively regularized Gauss–Newton method is used as regularization method, the reverse situation occurs.
- For large values of the signal-to-noise ratio ($\text{SNR} \geq 10^3$), the relative errors are within $\pm 0.5\%$ for all inversion models and regularization methods.

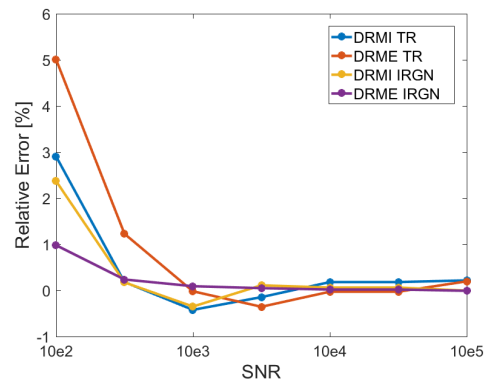


Figure 3. Relative errors in the total NO_2 column as a function of signal-to-noise ratio (SNR). The results correspond to the clean scenario and are computed by means of the differential radiance model with internal closure (DRMI) and differential radiance model with external closure (DRME) models using the method of Tikhonov regularization (TR) and the iteratively regularized Gauss–Newton (IRGN) method.

Figure 4 shows the variation of the square residuals, corresponding to DRMI and DRME in combination with the iteratively regularized Gauss–Newton method, versus the iteration step for the clean scenario. In Figure 4b, the variation of the regularization parameter α_k in the case of $\text{SNR} = 10^3$ is also shown. The results demonstrate the basic features of the iterative regularization method.

- The residuals attain a plateau, which is used for estimating the noise level. This plateau is more pronounced for small values of the signal-to-noise ratio and decreases when the signal-to-noise ratio increases.
- At the initial guess, the residual corresponding to the DRMI model is much smaller than that corresponding to the DRME. The reason is that the discrepancies between the differential spectra are usually small. However, at the end of the iterative processes, the residuals are comparable.
- In DRMI, the residual decreases very fast at the first iteration step, while in DRME, there is a period of stagnation after which the residual decreases very rapidly.
- For small values of the signal-to-noise ratio ($\text{SNR} \leq 10^3$), the iterative process in DRMI terminates after 3–4 iterations, while 10 iteration steps are required in DRME. However, the final residual in DRMI is slightly larger than in DRME; this result explains the larger relative errors provided by DRMI.
- In DRME and for $\text{SNR} = 10^3$, the initial value of the regularization parameter is $\alpha_0 = 10^{-3}$, while the final value, which is an estimate of the optimal value, is approximately equal to 10^{-6} . Thus, the amount of regularization is small, and the solution coincides practically with the ordinary least-squares solution.

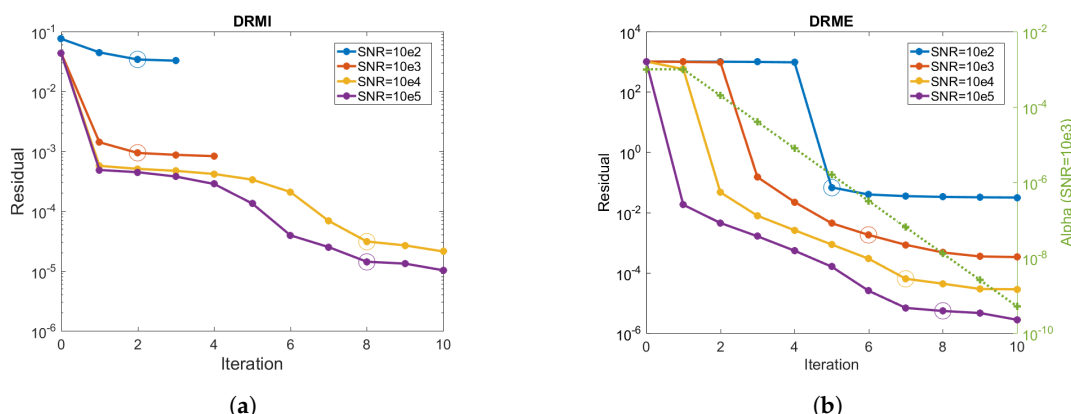


Figure 4. Square residuals computed by means of the (a) DRMI and (b) DRME models as a function of iteration number. The iteratively regularized Gauss–Newton (IRGN) method is applied, and the results correspond to the clean scenario. The iteration steps with the estimated optimal regularization parameter are marked (circles). For DRME and $SNR = 10^3$, the history of the regularization parameter is also shown (green line).

In Figure 5, we plot the absolute errors in the total NO_2 column for the polluted scenario. The results correspond to DRME and the signal-to-noise ratio $SNR = 10^3$. In this case, the regularization parameter of Tikhonov regularization corresponds to the optimal value predicted by the iteratively regularized Gauss–Newton method. The following observations can be noticed.

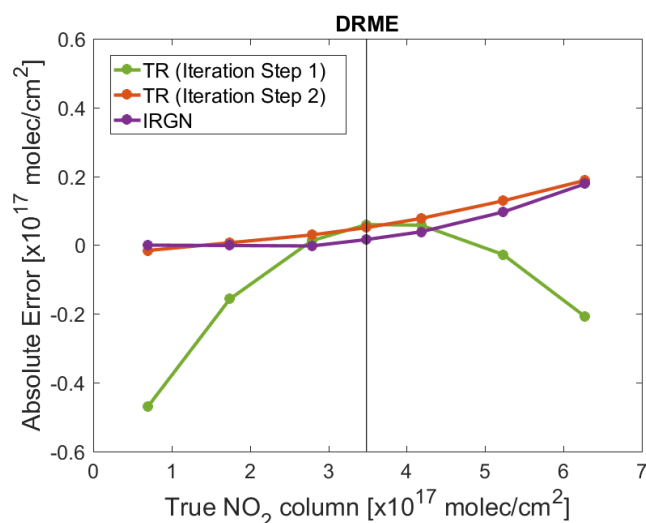


Figure 5. Absolute errors in the total NO_2 column for different values of the true total column. The results correspond to the polluted scenario and are computed by means of DRME using the method of Tikhonov regularization (TR) and the iteratively regularized Gauss–Newton (IRGN) method. The signal-to-noise ratio is $SNR = 10^3$, and the vertical line shows the initial value of the total column.

1. The errors, obtained after one iteration step by the method of Tikhonov regularization, are large, and in particular when (i) the discrepancies between the values of the true and initial (a priori) total columns are significant, and (ii) the true values are lower than the initial values. However, the errors decrease significantly at the second iteration step, when they become comparable with the errors obtained by the iteratively regularized Gauss–Newton method. Recalling that the standard DOAS model is equivalent with the first iteration step of the DRME model (see Section 5), we conclude that the DOAS model can be used when the problem is not too nonlinear.

- An error up to 4% is found for large values of the true total column, likely due to the stronger interference between the NO₂ and Ring effect signatures [48] for polluted cases with deeper spectral structures (see Figure 2).

6.2. Tropospheric NO₂ Column Retrieval

Figure 6 shows the relative errors in the tropospheric NO₂ column versus the signal-to-noise ratio for the clean scenario. The results are computed with (i) the nonlinear model, in which $\mathbf{X}_{-\bar{g}} = [X_{\text{O}_3}, X_{\text{O}_4}, X_{\text{H}_2\text{O}}]$ and \mathbf{b} are determined in the pre-processing step by using DRMI and DRME, and (ii) the linear model, in which X_{NO_2} is again determined in the pre-processing step by means of DRMI and DRME. The regularization methods used in DRMI and DRME are the method of Tikhonov regularization and the iteratively regularized Gauss–Newton method. The following conclusions can be drawn.

- The relative errors of the linear model are smaller than those of the nonlinear model. This means that in the pre-processing step, the columns $\mathbf{X}_{-\bar{g}}$ of the auxiliary gases and the amplitudes \mathbf{b} of the correction spectra are not accurately retrieved, while the total NO₂ column X_{NO_2} is.
- For the linear model, the relative errors corresponding to the total column X_{NO_2} delivered by the iteratively regularized Gauss–Newton method are smaller than those delivered by the method of Tikhonov regularization. This result is not surprising because the first method yields more accurate total NO₂ column retrievals than the second one (see Figure 3).
- The linear model using DRME in the pre-processing step in conjunction with the iteratively regularized Gauss–Newton method has the best retrieval performance; the relative errors are less than 5% for $\text{SNR} = 10^2$ and less than 2% for $\text{SNR} \geq 10^3$.

The plots in Figure 7 illustrate the absolute errors in the tropospheric NO₂ column for the polluted scenario. In the pre-processing step, only DRME is used to determine $\mathbf{X}_{-\bar{g}} = [X_{\text{O}_3}, X_{\text{O}_4}, X_{\text{H}_2\text{O}}]$ and \mathbf{b} for the nonlinear model and X_{NO_2} for the linear model. The signal-to-noise ratio is $\text{SNR} = 10^3$. The results lead to the following conclusions.

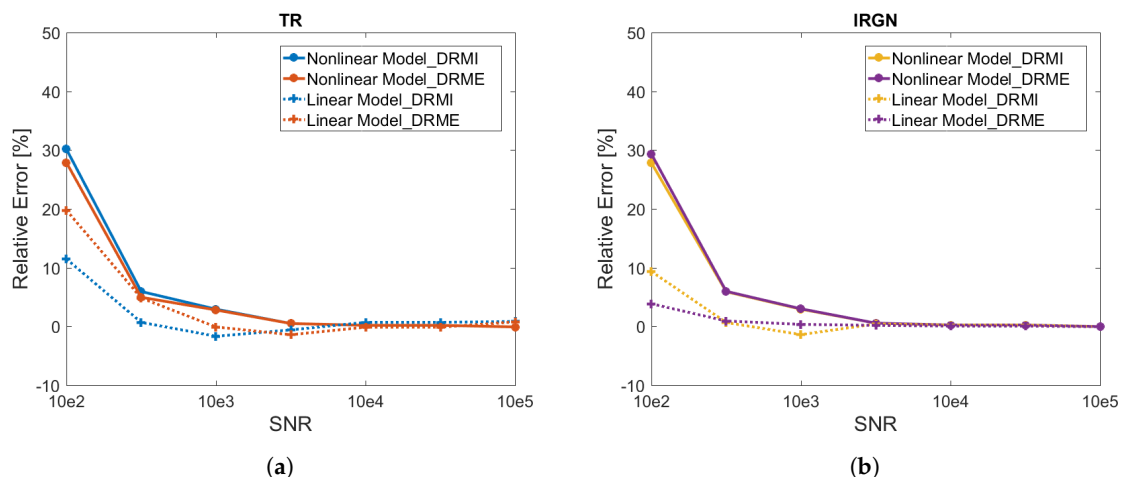


Figure 6. Relative errors in the tropospheric NO₂ column as a function of SNR. The results are computed by means of linear and nonlinear models using in the pre-processing step the DRMI and DRME models in conjunction with (a) the method of Tikhonov regularization (TR) and (b) the iteratively regularized Gauss–Newton (IRGN) method.

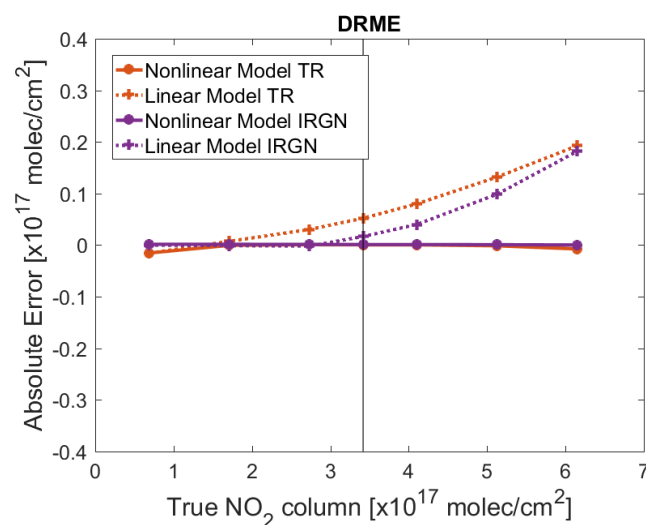


Figure 7. Absolute errors in the tropospheric NO₂ column for different values of the true tropospheric columns. The results correspond to the polluted scenario and are computed by means of linear and nonlinear models and using in the pre-processing step the DRME model in conjunction with Tikhonov regularization (TR) and the iteratively regularized Gauss–Newton (IRGN) method. The signal-to-noise ratio is $SNR = 10^3$, and the vertical line shows the initial value of the tropospheric column.

1. In contrast to the clean scenario, the errors of the nonlinear model are smaller than those of the linear model. This means that the problem is nonlinear and that the linearizations (33) and (34) around the a priori do not describe the forward model accurately. Remember that the same conclusion has been drawn for the total NO₂ column retrieval (see Figure 5).
2. The corresponding errors of the nonlinear model are less than 0.3%, regardless of the regularization method used in the pre-processing step.

7. Conclusions

NO₂ columns retrieved from satellite remote sensing measurements have been successfully applied in many studies. The NO₂ abundance is retrieved from the absorption structures of NO₂ by analyzing the backscattered radiation in the visible spectral region. In this study, we have presented several inversion models for retrieving the total and tropospheric NO₂ columns, which can be applied on spaceborne remote sensing data from current and upcoming hyperspectral instruments to characterize the spatial and temporal variation of NO₂ concentrations.

For total column retrieval, we proposed the differential radiance models with internal and external closure, DRMI and DRME, respectively. The underlying nonlinear equations, involving, in addition to the total NO₂ column, the total columns of the auxiliary gases, the amplitudes of the correction spectra, the coefficients of the smoothing polynomial, and the wavelength shift, are solved by means of regularization, that is, by using the method of Tikhonov regularization and the iteratively regularized Gauss–Newton method. Our numerical analysis showed that (i) for small values of the signal-to-noise ratio, DRMI along with the method of Tikhonov regularization yields more accurate results than DRME and that the reverse situation occurs when the iteratively regularized Gauss–Newton method is used as a regularization method, (ii) the iteratively regularized Gauss–Newton method is superior to the method of Tikhonov regularization because it is less sensitive to overestimations of the regularization parameter and can handle problems that actually do not require regularization, and finally, (iii) the best inversion model is DRME equipped with the iteratively regularized Gauss–Newton method.

The tropospheric column is retrieved in the framework of a nonlinear and a linear model by using (i) the results of the total column retrieval and (ii) the value of the stratospheric NO₂ column delivered by a stratosphere–troposphere separation method. Specifically, in the nonlinear model, the nonlinear

equations corresponding to DRMI or DRME are solved, while in the linear model, a linear equation that is the result of two linearity assumptions around the a priori is solved. Our numerical analysis revealed that for the clean scenario, when the problem is nearly linear, the linear model is superior to the nonlinear model, while for the polluted scenario, when the linearity assumption does not hold, the nonlinear model is better.

In our analysis, we also discussed the standard DOAS inversion model for total and tropospheric column retrieval and showed that this model is equivalent with the first iteration step of DRME for computing the total column and the linear model for computing the tropospheric column.

Funding: This work is funded by the DLR-DAAD Research Fellowships 2015 (57186656) programme with reference number 91585186.

Acknowledgments: Many thanks go to Adrian Doicu, Jian Xu, and Pieter Valks for discussions.

Conflicts of Interest: The author declares no conflict of interest. The funders had no role in the design of the study; in the collection, analyses, or interpretation of data; in the writing of the manuscript, or in the decision to publish the results.

References

- Solomon, S. Stratospheric ozone depletion: A review of concepts and history. *Rev. Geophys.* **1999**, *37*, 275–316. [[CrossRef](#)]
- Seinfeld, J.; Pandis, S. *Atmospheric Chemistry and Physics: From Air Pollution to Climate Change*, 3rd ed.; Wiley: Hoboken, NJ, USA, 2016.
- Shindell, D.T.; Faluvegi, G.; Koch, D.M.; Schmidt, G.A.; Unger, N.; Bauer, S.E. Improved attribution of climate forcing to emissions. *Science* **2009**, *326*, 716–718. [[CrossRef](#)] [[PubMed](#)]
- Levelt, P.; Van den Oord, G.; Dobber, M.; Malkki, A.; Visser, H.; de Vries, J.; Stammes, P.; Lundell, J.; Saari, H. The Ozone Monitoring Instrument. *IEEE Trans. Geosci. Remote Sens.* **2006**, *44*, 1093–1101. [[CrossRef](#)]
- Callies, J.; Corpaccioli, E.; Eisinger, M.; Hahne, A.; Lefebvre, A. GOME-2-Metop's second-generation sensor for operational ozone monitoring. *ESA Bull.* **2000**, *102*, 28–36.
- Munro, R.; Lang, R.; Klaes, D.; Poli, G.; Retscher, C.; Lindstrot, R.; Huckle, R.; Lacan, A.; Grzegorski, M.; Holdak, A.; et al. The GOME-2 instrument on the Metop series of satellites: instrument design, calibration, and level 1 data processing—An overview. *Atmos. Meas. Tech.* **2016**, *9*, 1279–1301. [[CrossRef](#)]
- Veefkind, J.; Aben, I.; McMullan, K.; Förster, H.; De Vries, J.; Otter, G.; Claas, J.; Eskes, H.; De Haan, J.; Kleipool, Q.; et al. TROPOMI on the ESA Sentinel-5 Precursor: A GMES mission for global observations of the atmospheric composition for climate, air quality and ozone layer applications. *Remote Sens. Environ.* **2012**, *120*, 70–83. [[CrossRef](#)]
- Ingmann, P.; Veihelmann, B.; Langen, J.; Lamarre, D.; Stark, H.; Courrèges-Lacoste, G.B. Requirements for the GMES Atmosphere Service and ESA's implementation concept: Sentinels-4/-5 and-5p. *Remote Sens. Environ.* **2012**, *120*, 58–69. [[CrossRef](#)]
- Lambert, J.; Granville, J.; Allaart, M.; Blumenstock, T.; Coosemans, T.; De Maziere, M.; Friess, U.; Gil, M.; Goutail, F.; Ionov, D.; et al. Ground-Based Comparisons of Early SCIAMACHY O₃ and NO₂ Columns. In *ESA Special Publication*; European Space Agency: Paris, France, 2003; Volume 531.
- Pinardi, G.; Van Roozendaal, M.; Lambert, J.C.; Granville, J.; Hendrick, F.; Tack, F.; Yu, H.; Cede, A.; Kanaya, Y.; Irie, I.; et al. GOME-2 total and tropospheric NO₂ validation based on zenith-sky, direct-sun and multi-axis DOAS network observations. In Proceedings of the 2014 EUMETSAT Meteorological Satellite Conference (EUMETSAT), Geneva, Switzerland, 22–26 September 2014.
- Pinardi, G.; Lambert, J.C.; Granville, J.; Yu, H.; De Smedt, I.; van Roozendaal, M.; Valks, P. *O3M-SAF Validation Report*; Technical Report, SAF/O3M/IASB/VR/NO2/TN-IASB-GOME2-O3MSAF-NO2-2015; EUMETSAT: Darmstadt, Germany, 2015.
- Hilboll, A.; Richter, A.; Burrows, J. Long-term changes of tropospheric NO₂ over megacities derived from multiple satellite instruments. *Atmos. Chem. Phys.* **2013**, *13*, 4145–4169. [[CrossRef](#)]
- Hilboll, A.; Richter, A.; Burrows, J.P. NO₂ pollution over India observed from space—The impact of rapid economic growth, and a recent decline. *Atmos. Chem. Phys. Discuss.* **2017**. [[CrossRef](#)]

14. Zien, A.; Richter, A.; Hilboll, A.; Blechschmidt, A.M.; Burrows, J. Systematic analysis of tropospheric NO₂ long-range transport events detected in GOME-2 satellite data. *Atmos. Chem. Phys.* **2014**, *14*, 7367–7396. [[CrossRef](#)]
15. Ding, J.; Miyazaki, K.; van der A, R.J.; Mijling, B.; Kurokawa, J.I.; Cho, S.; Janssens-Maenhout, G.; Zhang, Q.; Liu, F.; Levelt, P.F. Intercomparison of NO_x emission inventories over East Asia. *Atmos. Chem. Phys.* **2017**, *17*, 10125. [[CrossRef](#)]
16. Visser, A.J.; Boersma, K.F.; Ganzeveld, L.N.; Krol, M.C. European NO_x emissions in WRF-Chem derived from OMI: impacts on summertime surface ozone. *Atmos. Chem. Phys.* **2019**, *19*, 11821–11841. [[CrossRef](#)]
17. Safieddine, S.; Clerbaux, C.; George, M.; Hadji-Lazaro, J.; Hurtmans, D.; Coheur, P.F.; Wespes, C.; Loyola, D.; Valks, P.; Hao, N. Tropospheric ozone and nitrogen dioxide measurements in urban and rural regions as seen by IASI and GOME-2. *J. Geophys. Res. Atmos.* **2013**, *118*. [[CrossRef](#)]
18. Varotsos, C.; Christodoulakis, J.; Tzani, C.; Cracknell, A. Signature of tropospheric ozone and nitrogen dioxide from space: A case study for Athens, Greece. *Atmos. Environ.* **2014**, *89*, 721–730. [[CrossRef](#)]
19. Platt, U.; Stutz, J. *Differential Optical Absorption Spectroscopy*; Springer: Berlin/Heidelberg, Germany, 2008.
20. Burrows, J.P.; Weber, M.; Buchwitz, M.; Rozanov, V.; Ladstätter-Weissenmayer, A.; Richter, A.; DeBeek, R.; Hoogen, R.; Bramstedt, K.; Eichmann, K.U.; et al. The global ozone monitoring experiment (GOME): Mission concept and first scientific results. *J. Atmos. Sci.* **1999**, *56*, 151–175. [[CrossRef](#)]
21. Richter, A.; Burrows, J.P.; Nüß, H.; Granier, C.; Niemeier, U. Increase in tropospheric nitrogen dioxide over China observed from space. *Nature* **2005**, *437*, 129. [[CrossRef](#)]
22. Valks, P.; Pinardi, G.; Richter, A.; Lambert, J.C.; Hao, N.; Loyola, D.; Van Roozendaal, M.; Emmadi, S. Operational total and tropospheric NO₂ column retrieval for GOME-2. *Atmos. Meas. Tech.* **2011**, *4*, 1491. [[CrossRef](#)]
23. Van Geffen, J.; Boersma, K.; Van Roozendaal, M.; Hendrick, F.; Mahieu, E.; De Smedt, I.; Snee, M.; Veefkind, J. Improved spectral fitting of nitrogen dioxide from OMI in the 405–465 nm window. *Atmos. Meas. Tech.* **2015**, *8*, 1685–1699. [[CrossRef](#)]
24. Van Geffen, J.; Boersma, K.; Eskes, H.; Maasackers, J.; Veefkind, J. *TROPOMI ATBD of the Total and Tropospheric NO₂ Data Products*; Technical Report, S5P-KNMI-L2-0005-RP issue 1.4.0; KNMI: De Bilt, The Netherlands, 2019.
25. Liu, S.; Valks, P.; Pinardi, G.; De Smedt, I.; Yu, H.; Beirle, S.; Richter, A. An Improved Total and Tropospheric NO₂ Column Retrieval for GOME-2. *Atmos. Meas. Tech.* **2019**, *12*, 1029–1057. [[CrossRef](#)]
26. Doicu, A.; Trautmann, T.; Schreier, F. *Numerical Regularization for Atmospheric Inverse Problems*; Springer Science & Business Media: Berlin/Heidelberg, Germany, 2010.
27. Tikhonov, A.N. On the solution of ill-posed problems and the method of regularization. *Dokl. Akad. Nauk SSSR* **1963**, *151*, 501–504.
28. Dennis, J.E., Jr.; Schnabel, R.B. *Numerical Methods for Unconstrained Optimization and Nonlinear Equations*; Society for Industrial and Applied Mathematics (SIAM): Philadelphia, PA, USA, 1996; Volume 16.
29. Gill, P.E.; Murray, W.; Wright, M.H. *Practical Optimization*; Academic Press: Cambridge, MA, USA, 1981.
30. Rodgers, C.D. *Inverse Methods for Atmospheric Sounding: Theory and Practice*; World Scientific: Singapore, 2000; Volume 2.
31. Carissimo, A.; De Feis, I.; Serio, C. The physical retrieval methodology for IASI: The δ -IASI code. *Environ. Model. Softw.* **2005**, *20*, 1111–1126. [[CrossRef](#)]
32. Xu, J.; Schreier, F.; Doicu, A.; Trautmann, T. Assessment of Tikhonov-type regularization methods for solving atmospheric inverse problems. *J. Quant. Spectrosc. Radiat. Transf.* **2016**, *184*, 274–286. [[CrossRef](#)]
33. Wahba, G. Practical approximate solutions to linear operator equations when the data are noisy. *SIAM J. Numer. Anal.* **1977**, *14*, 651–667. [[CrossRef](#)]
34. Hansen, P.C. Analysis of discrete ill-posed problems by means of the L-curve. *SIAM Rev.* **1992**, *34*, 561–580. [[CrossRef](#)]
35. Bakushinskii, A.B. The problem of the convergence of the iteratively regularized Gauss–Newton method. *Zhurnal Vychislitel'noi Mat. Mat. Fiz.* **1992**, *32*, 1503–1509.
36. Morozov, V.A. On the solution of functional equations by the method of regularization. *Dokl. Akad. Nauk SSSR* **1966**, *167*, 510–512.

37. Huijnen, V.; Eskes, H.J.; Poupkou, A.; Elbern, H.; Boersma, K.F.; Foret, G.; Sofiev, M.; Valdebenito, A.; Flemming, J.; Stein, O.; et al. Comparison of OMI NO₂ tropospheric columns with an ensemble of global and European regional air quality models. *Atmos. Chem. Phys.* **2010**, *10*, 3273–3296. [[CrossRef](#)]
38. Richter, A.; Burrows, J. Tropospheric NO₂ from GOME measurements. *Adv. Space Res.* **2002**, *29*, 1673–1683. [[CrossRef](#)]
39. Bucsela, E.; Krotkov, N.; Celarier, E.; Lamsal, L.; Swartz, W.; Bhartia, P.; Boersma, K.; Veefkind, J.; Gleason, J.; Pickering, K. A new stratospheric and tropospheric NO₂ retrieval algorithm for nadir-viewing satellite instruments: Applications to OMI. *Atmos. Meas. Tech.* **2013**, *6*, 2607. [[CrossRef](#)]
40. Beirle, S.; Hörmann, C.; Jöckel, P.; Liu, S.; Penning de Vries, M.; Pozzer, A.; Sihler, H.; Valks, P.; Wagner, T. The STRatospheric Estimation Algorithm from Mainz (STREAM): Estimating stratospheric NO₂ from nadir-viewing satellites by weighted convolution. *Atmos. Meas. Tech.* **2016**, *9*, 2753–2779. [[CrossRef](#)]
41. Eskes, H.; Van Velthoven, P.; Valks, P.; Kelder, H. Assimilation of GOME total-ozone satellite observations in a three-dimensional tracer-transport model. *Q. J. R. Meteorol. Soc.* **2003**, *129*, 1663–1681. [[CrossRef](#)]
42. Dirksen, R.J.; Boersma, K.F.; Eskes, H.J.; Ionov, D.V.; Bucsela, E.J.; Levelt, P.F.; Kelder, H.M. Evaluation of stratospheric NO₂ retrieved from the Ozone Monitoring Instrument: Intercomparison, diurnal cycle, and trending. *J. Geophys. Res. Atmos.* **2011**, *116*, D08305. [[CrossRef](#)]
43. Bucsela, E.J.; Celarier, E.A.; Wenig, M.O.; Gleason, J.F.; Veefkind, J.P.; Boersma, K.F.; Brinksma, E.J. Algorithm for NO₂ vertical column retrieval from the ozone monitoring instrument. *IEEE Trans. Geosci. Remote Sens.* **2006**, *44*, 1245–1258. [[CrossRef](#)]
44. Rozanov, A.; Rozanov, V.; Buchwitz, M.; Kokhanovsky, A.; Burrows, J. SCIATRAN 2.0—A new radiative transfer model for geophysical applications in the 175–2400 nm spectral region. *Adv. Space Res.* **2005**, *36*, 1015–1019. [[CrossRef](#)]
45. Doicu, A.; Trautmann, T. Discrete-ordinate method with matrix exponential for a pseudo-spherical atmosphere: Scalar case. *J. Quant. Spectrosc. Radiat. Transf.* **2009**, *110*, 146–158. [[CrossRef](#)]
46. Doicu, A.; Trautmann, T. Discrete-ordinate method with matrix exponential for a pseudo-spherical atmosphere: Vector case. *J. Quant. Spectrosc. Radiat. Transf.* **2009**, *110*, 159–172. [[CrossRef](#)]
47. Anderson, G.P.; Clough, S.A.; Kneizys, F.; Chetwynd, J.H.; Shettle, E.P. *AFGL Atmospheric Constituent Profiles (0.120 km)*; Technical Report; Air Force Geophysics Lab.: Hanscom AFB, MA, USA, 1986.
48. Marchenko, S.; Krotkov, N.; Lamsal, L.; Celarier, E.; Swartz, W.; Bucsela, E. Revising the slant column density retrieval of nitrogen dioxide observed by the Ozone Monitoring Instrument. *J. Geophys. Res. Atmos.* **2015**, *120*, 5670–5692. [[CrossRef](#)]



© 2019 by the author. Licensee MDPI, Basel, Switzerland. This article is an open access article distributed under the terms and conditions of the Creative Commons Attribution (CC BY) license (<http://creativecommons.org/licenses/by/4.0/>).

Appendix B

The STRatospheric Estimation Algorithm from Mainz (STREAM): estimating stratospheric NO₂ from nadir-viewing satellites by weighted convolution

Beirle, S., Hörmann, C., Jöckel, P., Liu, S., Penning de Vries, M., Pozzer, A., Sihler, H., Valks, P., and Wagner, T.: The STRatospheric Estimation Algorithm from Mainz (STREAM): estimating stratospheric NO₂ from nadir-viewing satellites by weighted convolution, *Atmos. Meas. Tech.*, 9, 2753-2779, <https://doi.org/10.5194/amt-9-2753-2016>, 2016.



The STRatospheric Estimation Algorithm from Mainz (STREAM): estimating stratospheric NO₂ from nadir-viewing satellites by weighted convolution

Steffen Beirle¹, Christoph Hörmann¹, Patrick Jöckel², Song Liu³, Marloes Penning de Vries¹, Andrea Pozzer¹,
Holger Sihler¹, Pieter Valks³, and Thomas Wagner¹

¹Max Planck Institute for Chemistry, Mainz, Germany

²Deutsches Zentrum für Luft- und Raumfahrt (DLR), Institut für Physik der Atmosphäre,
Oberpfaffenhofen, Germany

³Deutsches Zentrum für Luft- und Raumfahrt (DLR), Institut für Methodik der Fernerkundung (IMF),
Oberpfaffenhofen, Germany

Correspondence to: Steffen Beirle (steffen.beirle@mpic.de)

Received: 23 December 2015 – Published in Atmos. Meas. Tech. Discuss.: 18 January 2016

Revised: 20 May 2016 – Accepted: 1 June 2016 – Published: 4 July 2016

Abstract. The STRatospheric Estimation Algorithm from Mainz (STREAM) determines stratospheric columns of NO₂ which are needed for the retrieval of tropospheric columns from satellite observations. It is based on the total column measurements over clean, remote regions as well as over clouded scenes where the tropospheric column is effectively shielded. The contribution of individual satellite measurements to the stratospheric estimate is controlled by various weighting factors. STREAM is a flexible and robust algorithm and does not require input from chemical transport models. It was developed as a verification algorithm for the upcoming satellite instrument TROPOMI, as a complement to the operational stratospheric correction based on data assimilation. STREAM was successfully applied to the UV/vis satellite instruments GOME 1/2, SCIAMACHY, and OMI. It overcomes some of the artifacts of previous algorithms, as it is capable of reproducing gradients of stratospheric NO₂, e.g., related to the polar vortex, and reduces interpolation errors over continents. Based on synthetic input data, the uncertainty of STREAM was quantified as about $0.1\text{--}0.2 \times 10^{15}$ molecules cm⁻², in accordance with the typical deviations between stratospheric estimates from different algorithms compared in this study.

1 Introduction

Beginning with the launch of the Global Ozone Monitoring Experiment (GOME) on the ERS-2 satellite in 1995 (Burrows et al., 1999), several instruments (SCIAMACHY, OMI, GOME-2; see Table 1 for acronyms and references) perform spectrally resolved measurements of sunlight reflected by the Earth's surface and atmosphere. With differential absorption spectroscopy (DOAS) (Platt and Stutz, 2008), the column densities (denoted as “columns” henceforth) of numerous important atmospheric absorbers can be determined by their characteristic spectral “fingerprints”, amongst others nitrogen dioxide (NO₂).

Nitrogen oxides (NO_x = NO₂ + NO) play a key role in the chemistry of both the stratosphere and the troposphere. Stratospheric NO_x has been a research topic for several decades due in particular to its role in ozone and halogen chemistry.

Satellite measurements provide long-term global information on spatiotemporal patterns of stratospheric NO₂ (e.g., Wenig et al., 2004; Dirksen et al., 2011). During the last decades, the analysis of tropospheric trace gases from nadir-viewing satellite instruments moved more and more into focus, supported by the availability of longer time series and improved spatial resolution. Tropospheric NO₂ columns derived from satellite are nowadays widely used by the scientific community to deduce spatial patterns, source type

Table 1. UV/vis satellite instruments compared or discussed in this study

Acronym	Instrument	Launch	Footprint (km ²)	Earth coverage per day	Instrument reference	Data product used in this study	Data reference
GOME	Global Ozone Monitoring Experiment	1995	40 × 320	1/3	Burrows et al. (1999)	TEMIS	Boersma and Eskes (2004)
SCIAMACHY	SCanning Imaging Absorption spectroMeter for Atmospheric CHartographY	2002	30 × 60	1/6	Bovensmann et al. (1999)	MPI-C Mainz	Beirle and Wagner (2012)
GOME-2	Global Ozone Monitoring Experiment-2	2006 ^a	40 × 80 ^b	2/3	Callies et al. (2000)	O3M SAF	Valks et al. (2015)
OMI	Ozone Monitoring Instrument	2004	13 × 26 ^c	1 ^d	Levelt et al. (2006)	NASA v003 / SP2 DOMINO v2	Bucsela et al. (2013) Boersma et al. (2011)
TROPOMI	TROPOspheric Monitoring Instrument	2016	7 × 7 ^c	1	Veeffkind et al. (2012)		
Sentinel 4		2021	7 × 7	– ^e	Ingmann et al. (2012)		

^a On Metop-A. A second GOME-2 instrument was launched 2012 on Metop-B, and a third is planned to be launched on Metop-C in 2018.

^b Switched to 40 × 40 km² for GOME-2/Metop-A in Metop-A and Metop-B tandem operation.

^c At nadir.

^d Reduced coverage after row anomaly in 2007; see <http://projects.knmi.nl/omi/research/product/rowanomaly-background.php>.

^e Geostationary orbit: hourly coverage over Europe.

and strength, and trends of NO_x emissions from fossil fuel combustion, biomass burning, soil emissions, and lightning. Overviews over the wide range of scientific applications of satellite-based tropospheric NO₂ products are given in, e.g., Martin (2008) or Monks and Beirle (2011).

The retrieval of tropospheric NO₂ columns from total column measurements requires the estimation and removal of the stratospheric column, a procedure we refer to as “stratosphere–troposphere separation” (STS) as in Bucsela et al. (2006).

One of the first STS algorithms is the reference sector method (RSM), which estimates the global stratospheric NO₂ fields from measurements over the remote Pacific (Richter and Burrows, 2002; Martin et al., 2002; Beirle et al., 2003), based on the assumptions of (a) longitudinal homogeneity of stratospheric NO₂ and (b) negligible tropospheric contribution over the reference region in the Pacific. This procedure is quite simple, transparent, and robust. A further side effect is that any systematic bias in the NO₂ columns, which might be introduced by the instrument (e.g., degradation or spectral interference caused by the diffusor plate used for measurements of the solar reference; Richter and Burrows, 2002) or sub-optimal spectral analysis (van Geffen et al., 2015; Marchenko et al., 2015), is classified as stratospheric signal and thereby removed from the tropospheric column.

The RSM was applied by different groups to different satellite instruments and generally performs well. However, the resulting tropospheric NO₂ columns are affected by systematic biases caused by the following simplifying assumptions.

- The tropospheric background column in the Pacific is very low (compared to columns over regions exposed to significant NO_x sources) but not 0. Neglecting the tropospheric background results in tropospheric columns that are biased low by about some 10¹⁴ molec cm^{−2} (Martin et al., 2002; Valks et al., 2011; Hilboll et al., 2013). Some algorithms explicitly correct for this tropospheric background: Martin et al. (2002) perform a correction based on GEOS-CHEM, while Valks et al. (2011) assume a constant background of 0.1 × 10¹⁵ molec cm^{−2}. Other algorithms prefer to stick to the tropospheric “excess” columns, which are slightly biased low but do not need any model input (Richter and Burrows, 2002; Bucsela et al., 2006).
- The assumption of longitudinal homogeneity is generally reasonable, at least in temporal means when small-scale stratospheric dynamic features cancel out. However, large longitudinal variations can occur in particular close to the polar vortex, as already discussed by Richter and Burrows (2002), Martin et al. (2002), and Boersma et al. (2004). Thus, tropospheric columns derived by RSM can be off by more than 10¹⁵ molec cm^{−2} in winter at latitudes from 50° polewards, thereby affecting scientific interpretations of tropospheric columns over North America or northern Europe. Note that also at low latitudes, systematic artifacts show up in tropospheric columns resulting from RSM, in particular over the Indian ocean, which are related to longitudinal inhomogeneities.

To overcome the artifacts caused by the assumption of longitudinal homogeneity, several modifications of the RSM have been proposed in recent years, while the basic approach of

using nadir measurements over clean regions for STS has been retained. We refer to this group of algorithms as “modified RSM” (MRSM). MRSMs generally define a “pollution mask” of regions with potentially non-negligible tropospheric columns. Measurements over these regions are skipped within the stratospheric estimation. Thus, in order to define stratospheric columns over the masked areas, interpolation is required. For this purpose, Leue et al. (2001) and Wenig et al. (2004) applied “normalized convolution” (Knutsson and Westin, 1993), an efficient algorithm which combines interpolation and smoothing. Bucselá et al. (2006) realized interpolation by fitting harmonics (wave-2) over the “clean” areas. Valks et al. (2011) applied a zonal boxcar filter of 30° width.

All of these algorithms applied a rather conservative masking approach for potentially polluted pixels. Continents were masked out almost completely. At northern midlatitudes, the masked area is often even larger than the area used for the stratospheric estimation, and over the Eurasian continent the MRSM algorithms miss any supporting measurement points over about 10 000 km. This can lead to significant errors during interpolation. In particular the wave fitting approach can lead to large biases (Dirksen et al., 2011).

Leue et al. (2001) estimated the stratospheric fields based on clouded measurements over the ocean and subsequent interpolation. The focus on clouded observations provides a direct stratospheric measurement, as the tropospheric column is mostly shielded; thus, no further correction of the tropospheric background should be needed. However, clouded pixels possibly contain NO_x produced by lightning (e.g., Beirle et al., 2006). Therefore, Wenig et al. (2004) changed the Heidelberg STS algorithm (Leue et al., 2001) by switching from clouded to cloud-free observations as input for the stratospheric estimate¹.

Recently, Bucselá et al. (2013) proposed an MRSM which defines “unpolluted” pixels not with a fixed mask but according to the a priori expected tropospheric contribution to the total column for each individual satellite observation. This is determined from radiative transfer calculations based on a monthly mean NO₂ profile from a chemical transport model (CTM) and the actual cloud conditions. This procedure results in additional supporting points over continents in cases of clouds shielding the tropospheric column and thereby largely reduces potential interpolation artifacts.

Apart from (modified) reference sector methods, there are two further completely different approaches used for STS, which are based on (a) independent measurements or (b) CTMs.

- a. Coincident, but independent, stratospheric measurements are available for SCIAMACHY (Bovensmann et al., 1999). It was operated in alternating nadir/limb geometry, such that the stratospheric air masses sensed in

nadir were scanned in limb shortly before (“limb–nadir matching”, LNM). This unique instrumental setup allowed for a direct stratospheric correction, although systematic offsets between limb and nadir measurements still had to be corrected empirically. STS by LNM was successfully applied for NO₂ (Sioris et al., 2004; Sierk et al., 2006; Beirle et al., 2010a; Hilboll et al., 2013) and ozone (Ebojie et al., 2014). However, such direct coincident measurements of total columns (nadir) and stratospheric concentration profiles (limb) are not available for other satellite instruments, and merging measurements from different sensors always faces the problem of spatiotemporal mismatching, requiring interpolation and photochemical corrections (compare Belmonte Rivas et al., 2014), and thus cannot be easily used for consistent long-term operational retrievals.

- b. Stratospheric NO₂ concentrations provided by CTMs can be used directly for STS after empirical correction of systematic offsets between satellite and model columns, e.g., by matching both over the Pacific (Richter et al., 2005; Hilboll et al., 2013). A more sophisticated way to incorporate CTMs in STS is data assimilation (Eskes et al., 2003; Dirksen et al., 2011), in which modeled 3-D distributions of NO₂ are regularly updated such that the modeled stratospheric column is in close agreement with the satellite measurement when the tropospheric contribution (as forecasted by the CTM) is low.

In 2016, the ESA’s Sentinel 5 precursor (S5p) satellite (Ingmann et al., 2012) will be launched, carrying the Tropospheric Monitoring Instrument (TROPOMI) (Veefkind et al., 2012). The operational (“prototype”) tropospheric column product of NO₂ from TROPOMI will be derived by a STS using data assimilation (van Geffen et al., 2014), based on the expertise of the Koninklijk Nederlands Meteorologisch Instituut (KNMI) as demonstrated by a 20-year record of tropospheric columns from different satellite sensors provided by the Tropospheric Emission Monitoring Internet Service (TEMIS, www.temis.nl; Boersma and Eskes, 2004; Boersma et al., 2011).

Within the S5p level 2 project, for each prototype product a “verification” product was developed in order to verify the prototype algorithms, detect possible shortcomings, and reveal potential improvements. The TROPOMI verification algorithm for NO₂ STS, the STRatospheric Estimation Algorithm from Mainz (STREAM), was developed at the Max Planck Institute for Chemistry (MPI-C), Mainz. It is an MRSM, requiring no further model input, and can thus be considered as a complementary approach to data assimilation.

STREAM does not apply a strict discrimination of “clean” vs. “polluted” satellite pixels. Instead, weighting factors are defined for each satellite pixel determining its impact on the

¹This aspect will be discussed in detail in Sect. 5.4.

stratospheric estimate (similar to data assimilation). In particular, clouded observations are weighted high, as they provide direct measurements of the stratospheric field. This approach dampens the small but systematically high bias of stratospheric columns estimated from total column measurements and the resulting low bias of tropospheric columns.

The paper is organized in the following way. In Sect. 2, the STREAM algorithm is described in detail. Section 3 provides information on the satellite and model data sets used in this study. Section 4 analyses the performance of STREAM and its sensitivity to input parameters based on both actual satellite measurements and synthetic data. In Sect. 5, the STREAM results are discussed in comparison to other STS algorithms, including the TROPOMI prototype algorithm. A general discussion on the challenges and uncertainties of STREAM in particular, and STS in general, is given, followed by conclusions (Sect. 6). Several additional images and tables are provided in the Supplement and referenced by a prefix “S”.

2 Methods

STREAM is in the tradition of MRSM algorithms that estimate the stratospheric field directly from satellite measurements for which the tropospheric contribution is considered to be negligible. For this purpose, measurements over remote regions with negligible tropospheric sources, as well as cloudy measurements, are used. In contrast to other MRSMs, however, no strict pollution mask is applied. Instead, weighting factors are used.

STREAM consists basically of two steps:

1. A set of weighting factors is calculated for each satellite pixel: a “pollution weight” that reduces the contribution of potentially polluted pixels, a “cloud weight” that increases the contribution of cloudy observations, and the “tropospheric residue (TR) weight” that adjusts the total weight in case of exceptionally large or negative TRs. The product of these weighting factors determines to what extent the associated NO₂ total columns contribute to the estimated stratospheric field (Sect. 2.2).
2. Global maps of stratospheric NO₂ are determined by applying weighted convolution (Sect. 2.3).

Before describing the details of the STREAM algorithm, however, we first define the investigated quantities and abbreviations used hereafter, as summarized in Table 2.

2.1 Terminology

2.1.1 NO₂ column densities and units

With differential optical absorption spectroscopy (DOAS; Platt and Stutz, 2008), so-called slant column densities (SCDs) S , i.e., concentrations integrated along the mean light

path, are derived. SCDs are converted into VCDs (vertical column densities, i.e., vertically integrated concentrations) V via the air-mass factor (AMF) A : $V = S/A$. The AMF A depends on radiative transfer (determined by wavelength, atmospheric absorbers, viewing geometry, surface albedo, clouds, and aerosols) and the trace gas profile. For the stratospheric column of NO₂, A is basically determined by viewing geometry.

In this study, all column densities are given in column density units (CDU) to increase readability:

$$1 \text{ CDU} := 1 \times 10^{15} \text{ molecules cm}^{-2}. \quad (1)$$

2.1.2 Total vertical column V^*

We define V^* as “total” vertical column, given by the SCD S divided by the stratospheric AMF A_{strat} :

$$V^* = S/A_{\text{strat}}. \quad (2)$$

The application of the stratospheric AMF basically removes the dependencies of S on viewing angles. Over clean regions with negligible tropospheric columns, V^* represents the actual total VCD and can be used for the estimation of stratospheric fields. In case of tropospheric pollution, however, V^* underestimates the actual total VCD, as the AMF is generally smaller in the troposphere than in the stratosphere (see also next section). These situations are, to the best of our knowledge, excluded from the stratospheric estimate by the definition of appropriate weighting factors (see Sect. 2.2).

2.1.3 Stratospheric vertical column and tropospheric residue

STREAM yields an estimate for the stratospheric VCD V_{strat} based on the assumption that V^* can be considered as proxy for V_{strat} in “clean” regions and over cloudy scenes.

In order to evaluate the performance of the stratospheric estimation, we define the TR as the difference of total and stratospheric VCDs (based on a stratospheric AMF):

$$T^* = V^* - V_{\text{strat}}. \quad (3)$$

Tropospheric VCDs (TVCDs), which are the final product of NO₂ retrievals used for further tropospheric research, are connected to T^* via the ratio of stratospheric and tropospheric AMF:

$$V_{\text{trop}} = T^* \times \frac{A_{\text{strat}}}{A_{\text{trop}}}. \quad (4)$$

For cloud-free satellite pixels, the ratio $A_{\text{strat}}/A_{\text{trop}}$ typically ranges from about 1 above clean oceans at low and midlatitudes to ≈ 2 – 3 above moderately polluted regions and up to > 4 at high latitudes and over strong NO_x sources, where NO₂ profiles peak close to the ground, causing low A_{trop} . Figure S1 in the Supplement displays monthly mean ratios

Table 2. Terms and abbreviations related to STREAM used in this study.

Symbol	Abbrev.	Term	Description
A	AMF	Air-mass factor	Factor relating vertical to slant column density
	CDU	Column density unit	Unit of column densities: 1×10^{15} molecules cm^{-2}
G	CK	Convolution kernel	Kernel used for weighted convolution; here 2-D Gaussian
p_{cld} c	CP	Cloud pressure	
	CRF	Cloud radiance fraction	
	LNM	Limb–nadir matching	Stratospheric correction based on coincident stratospheric measurements in limb geometry (SCIAMACHY).
P	MRSM	Modified reference sector method	An STS estimating stratospheric columns based on the total columns over “clean” regions, but allowing for longitudinal variations
	RSM	Reference sector method	see Sect. S2.2 An STS estimating stratospheric columns based on the total columns over a reference sector (here 180 to 140° W), assuming longitudinal homogeneity
S	SCD	Slant column density	Concentration integrated along mean light path
	STS	Stratosphere–troposphere separation	The procedure of separating the total column into stratospheric and tropospheric fractions
T^*	TR	Tropospheric residue	Difference of total and stratospheric column*, Eq. (3)
w		Weighting factor	
V_{trop}	TVCD	Tropospheric vertical column density	See Eq. (4)
V	VCD	Vertical column density	Vertically integrated concentration
V^*			Total VCD*
V_{strat}			Stratospheric VCD
ϑ	lat	Latitude	
φ	long	Longitude	

* based on stratospheric AMF

$A_{\text{strat}}/A_{\text{trop}}$ for cloud-free scenes based on AMFs provided in the NASA OMNO2 product.

In this study, we focus on the tropospheric residue T^* instead of V_{trop} for several reasons.

1. As only stratospheric AMFs are applied, biases in the stratospheric estimation can directly be related (factor -1) to the respective biases in T^* .
2. The comparison of TRs among different algorithms instead of TVCDs isolates the effect of the different STS and excludes differences in tropospheric AMFs (which are beyond the scope of this study).
3. T^* can be determined and is of high interest for the evaluation of STS performance also for clouded scenes with very low tropospheric AMFs.

2.1.4 Version

The description given in this paper and the definition of a priori settings refer to STREAM version v0.92.

2.2 Definition of weighting factors

MRSMs usually flag satellite pixels as either clean or (potentially) polluted and skip the latter for the stratospheric esti-

mation. In STREAM, instead, weighting factors for individual satellite pixels determine how strongly they are considered in the stratospheric estimation. Satellite measurements which are expected to have low/high tropospheric contribution are assigned a high/low weighting factor, respectively.

2.2.1 Pollution weight

In order to estimate the stratospheric NO₂ field from total column measurements, only “clean” measurements where the tropospheric column is negligible should be considered. In cases of very high total columns ($V^* > 10$ CDU), which clearly exceed the domain of stratospheric columns, a tropospheric contribution is obvious, and these measurements are excluded by assigning them a weighting factor of 0.

In most cases, however, the tropospheric contribution to the total column is not that easy to determine. We thus define a pollution weight w_{pol} based on our a priori knowledge about the mean spatial distribution of tropospheric NO₂, reflecting potentially polluted regions. For this purpose, we make use of the multiannual mean tropospheric NO₂ column as derived from SCIAMACHY (Beirle and Wagner, 2012). Based on this climatology, a “pollution proxy” P is defined as function of latitude ϑ and longitude φ . P indicates the regions affected by tropospheric pollution plus a “safety margin” in order to account for possible advection, while it is

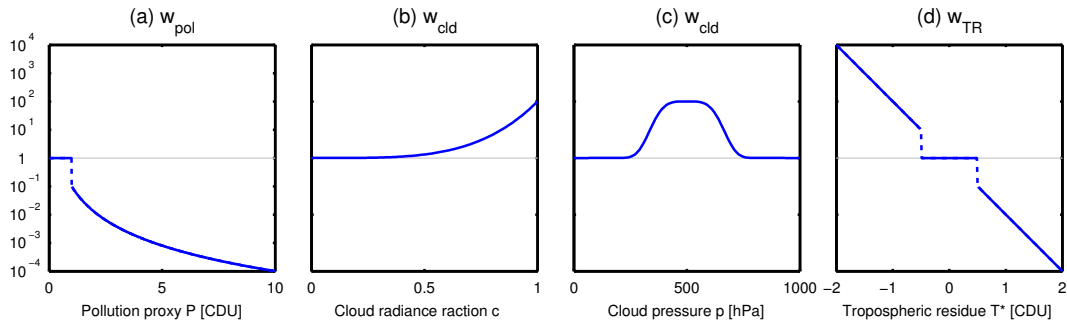


Figure 1. Definition of weighting factors (a) w_{pol} as a function of the pollution proxy P (Eq. 5), (b) w_{cld} as a function of the cloud radiance fraction (Eq. 6) for a cloud pressure of 500 hPa, (c) w_{cld} as a function of the cloud pressure (Eq. 6) for a cloud radiance fraction of 1, and (d) w_{TR} as a function of the tropospheric residue (Eq. 7).

undefined for remote unpolluted regions. Details on the definition of P are given in the Supplement (Sect. S2.2.1), and P is displayed in Fig. S2d.

The pollution weight w_{pol} is then defined as

$$w_{\text{pol}} = 0.1/P(\vartheta, \varphi)^3, \quad (5)$$

where P is defined, and $w_{\text{pol}} = 1$ elsewhere. Hence, the higher the pollution proxy P , the lower the weighting factor and the less the measurement contributes to the stratospheric estimate. Equation (5) is displayed in Fig. 1a, and the resulting map for w_{pol} is shown in Fig. 2a. Large continental regions are assigned with a weight ≤ 0.1 . Strongly polluted regions like the USA, Europe, or China have weights of 0.01 down to below 0.001. Note that the additional application of the tropospheric residue weight (Sect. 2.2.3) further decreases the weight of satellite measurements containing high tropospheric pollution.

2.2.2 Cloud weight

In addition to measurements over remote regions free of tropospheric sources, clouded satellite measurements, where the tropospheric column is shielded, also provide a good proxy for the stratospheric column. Thus, the factor w_{cld} is used to increase the weight of clouded satellite pixels. This is achieved by the following definition:

$$w_{\text{cld}} := 10^{2 \times w_c \times w_p} \quad (6a)$$

$$\text{with } w_c := c^4 \quad (6b)$$

$$\text{and } w_p := e^{-\frac{1}{2} \left(\frac{p_{\text{cld}} - p_{\text{ref}}}{\zeta p} \right)^2}. \quad (6c)$$

w_c reflects the dependency on the cloud radiance fraction (CRF) c . Due to the exponent of 4, only pixels with large cloud radiance fraction obtain a high weighting factor and contribute strongly to the stratospheric estimation.

w_p describes the dependency on cloud pressure (CP) p_{cld} . It is defined as a modified Gaussian (with exponent 4 instead of 2, making it flat-topped) centered at $p_{\text{ref}} = 500$ hPa

with a width $\zeta = 150$ hPa; i.e., only cloudy measurements at medium altitudes are assigned a high weighting factor, while high clouds (potentially contaminated by lightning NO_x) as well as low clouds (where tropospheric pollution might still be visible) are excluded.

As both w_c and w_p yield values in the range from 0 to 1, the factor of 2 in the exponent of Eq. (6a) sets the maximum value of w_{cld} to 10^2 , which would compensate for pollution weights down to 10^{-2} .

The dependencies of w_{cld} on CRF and CP, as defined in Eq. (6), are displayed in Fig. 1b and c, respectively. The spatial pattern of w_{cld} is shown exemplarily for OMI CP and CRF on 1 January 2005 in Fig. 2b. w_{cld} reaches values up to 100 in several parts of the world, including regions which were pre-classified as potentially polluted, thus competing with a low w_{pol} (Fig. 2a).

2.2.3 Tropospheric residue weight

STREAM yields global fields of stratospheric VCDs V_{strat} , explained in detail below (Sect. 2.3), which allow us to calculate tropospheric residues T^* according to Eq. (3). While the “true” tropospheric fields are not known, the resulting T^* can still be used in order to evaluate the STS performance and improve the stratospheric estimate in a second iteration, whenever T^* clearly indicates an under- or overestimation of V_{strat} .

- A high value of T^* likely indicates tropospheric pollution, in particular over potentially polluted regions. The respective satellite pixels should not be used for the stratospheric estimation.
- As negative columns are nonphysical, $T^* < 0$ indicates that the stratospheric field has been overestimated. This happens when the weighted convolution with neighboring pixels with high total columns causes the estimated stratosphere to be even higher than the local total columns. In order to avoid this effect, consequently, the respective local total columns should be assigned a

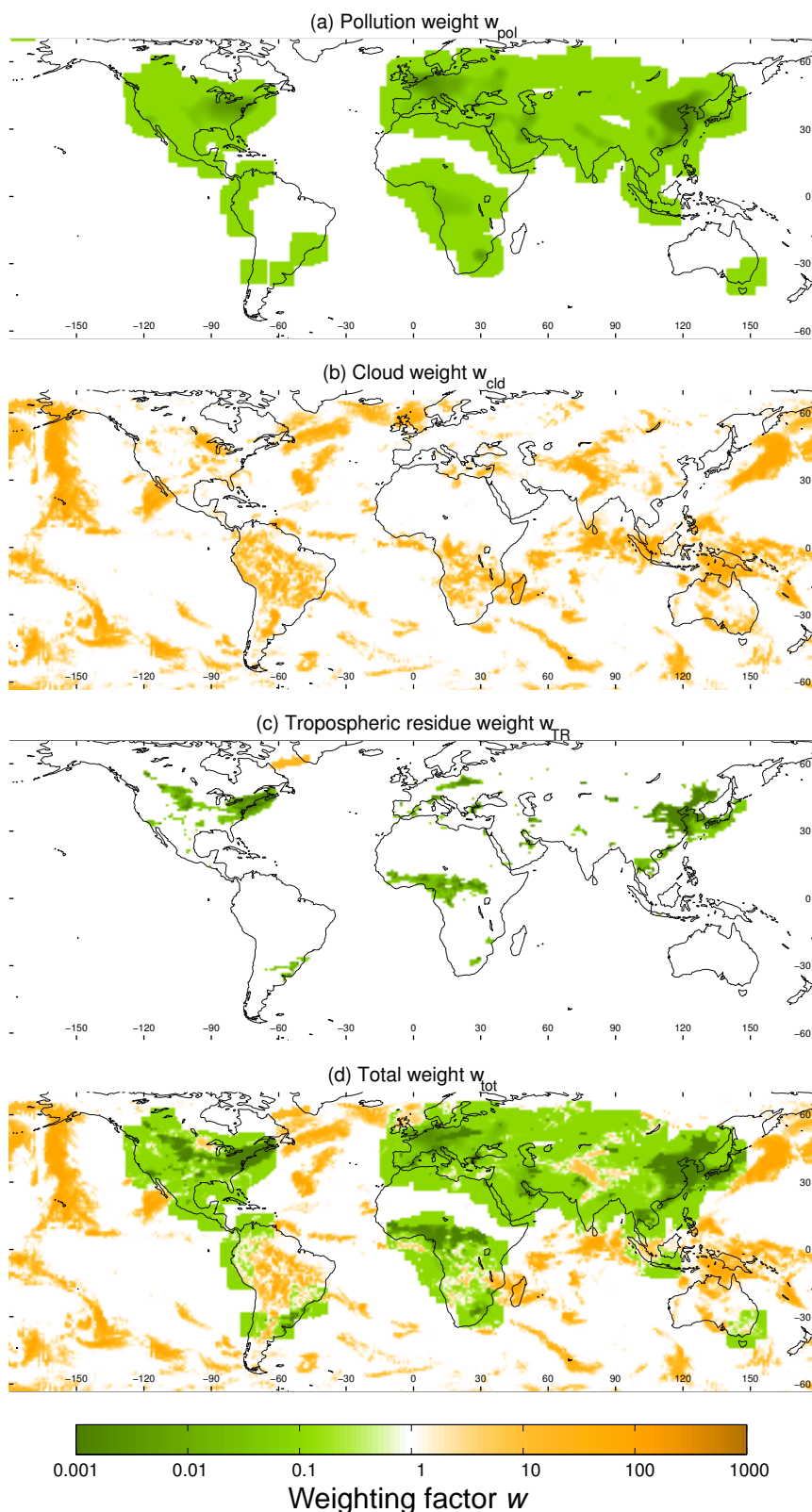


Figure 2. Maps of the weighting factors for 1 January 2005 for OMI: (a) pollution weight w_{pol} , (b) cloud weight w_{cld} , (c) tropospheric residue weight w_{TR} , and (d) product of all weighting factors (Eq. 8).

higher weighting factor such that they contribute more strongly to the stratospheric estimate.

We thus define a further weighting factor w_{TR} , which weights down/up the pixels associated with a large positive/negative TR, respectively. It turned out, however, that the stratospheric estimate is very sensitive to the definition of w_{TR} , and a simple definition based on the TR of individual satellite pixels can easily result in systematic artifacts. This results from T^* being defined as the difference of V^* and V_{strat} (Eq. 3), i.e., two quantities of the same order of magnitude with non-negligible errors. Thus, the resulting statistical distribution of T^* inevitably includes negative values. These negative values caused by statistical fluctuations must not be excluded from the probability density function in order to keep the mean unbiased, but they should also not be used as a trigger for weighting up the respective measurement within the stratospheric estimation. Thus, w_{TR} should be only applied to significant and systematic deviations of T^* from 0. This is achieved by the following settings.

1. In contrast to w_{cld} , which is defined for each individual satellite measurement, w_{TR} is defined based on the TRs averaged over $1^\circ \times 1^\circ$ grid pixels; i.e., first the values of T^* within one grid pixel are averaged, reducing statistical noise, before w_{TR} is calculated, and the resulting weight is then assigned to all satellite measurements within the grid pixel.
2. w_{TR} is only applied when the absolute value of the mean grid box T^* exceeds a threshold of 0.5 CDU, which is typically larger than the spectral fitting error:

$$w_{\text{TR}} := \begin{cases} 10^{-2 \times T^*} & \text{if } |T^*| > 0.5 \text{ CDU} \\ 1, & \text{else.} \end{cases} \quad (7)$$

3. w_{TR} is only applied for grid pixels where the adjacent grid pixels exceed the threshold as well. By this additional condition it is guaranteed that a single outlier in the satellite measurements cannot trigger w_{TR} , as every satellite measurement is assigned to exactly one grid pixel (see Sect. 2.3).
4. $w_{\text{TR}} < 1$, which is meant to decrease the weight of polluted pixels, is only applied over potentially polluted regions with $w_{\text{pol}} < 1$. Without this additional condition, patterns of erroneously enhanced TR caused by stratospheric dynamics would even be amplified by w_{TR} .

w_{TR} could in principle be tuned in multiple iterations. In STREAM v0.92, only one iteration is performed, as a second iteration turned out to have marginal effect (see Sect. S4.2.5).

The dependency of w_{TR} on TR (grid pixel average), as defined in Eq. 7, is displayed in Fig. 1d, and the resulting map for w_{TR} on 1 January 2005 is shown in Fig. 2c. After the initial stratospheric estimate, STREAM yields high values for

T^* over parts of the USA, Europe, central Africa, and China, resulting in low w_{TR} . Observations over these regions are already associated with a low pollution weight. However, due to the additional application of w_{TR} , the net weight is lowered further by orders of magnitude, and the respective satellite pixels will hardly contribute to the stratospheric estimate in the next iteration, even in the case of high w_{cld} .

In the initial STREAM run, the resulting TR is systematically < 0 over east Canada and Greenland, caused by the asymmetric polar vortex. Over the Labrador Sea, initial values for T^* are systematically below the threshold of 0.5 CDU and thus trigger a high w_{TR} , and the respective observations of low total VCDs contribute strongly to the stratospheric estimate in the next iteration.

Note that, due to the threshold of 0.5 CDU (criterion 2), w_{TR} cannot correct small biases such as the expected low bias in TR caused by estimating the stratospheric column from total column measurements.

2.2.4 Total weight

The total weight of each satellite pixel is defined as the product of the individual weighting factors:

$$w_{\text{tot}} := w_{\text{pol}} \times w_{\text{cld}} \times w_{\text{TR}} \quad (8)$$

(i.e., the logarithms as shown in Fig. 2a–c are simply added, resulting in Fig. 2d). The a priori pollution weight can still be recognized in the global pattern but is significantly modified by w_{TR} (further reducing the overall weight over, e.g., the USA and China) and w_{cld} , which competes with the pollution weights < 1 . In some regions (e.g., west of the Great Lakes, Scotland, or the Himalayas) the cloud weight shifts the initially low w_{pol} to a net weight > 1 .

The concept of the combination of different weighting factors is easily extendible by further weights, e.g., based on fire or flash counts in order to account for NO_x emissions from biomass burning or lightning.

2.3 Weighted convolution

Global daily maps of the stratospheric column are derived by applying “weighted convolution”, i.e., a spatial convolution which takes the individual weights for each satellite pixel into account. This approach is an extension of the “normalized convolution” presented in Knutsson and Westin (1993). Weighted convolution at the same time smoothes and interpolates the stratospheric field. A similar approach was used by Leue et al. (2001), who applied the fitting errors of NO₂ SCDs as single weights.

The algorithm is implemented as follows.

- A lat/long grid is defined with 1° resolution. Each satellite pixel is sorted into the matching grid pixel according to its center coordinates. At the j th latitudinal/ i th longitudinal grid position, there are K satellite pixels

with the total columns V_{ijk} ($k = 1 \dots K$) and the weights w_{ijk} . We define

$$C_{ij} := \sum w_{ijk} \times V_{ijk} \quad (9)$$

and

$$W_{ij} := \sum w_{ijk}. \quad (10)$$

In the case of measurement gaps (i.e., $K = 0$), both C_{ij} and W_{ij} are set to 0.

The weighted mean VCD for each grid pixel is then given as

$$V_{ij} = \frac{C_{ij}}{W_{ij}} \quad (11)$$

for $K > 0$ and undefined for $K = 0$ (gaps).

- A convolution kernel (CK) G is defined (see below). Spatial convolution is applied to both C and W (taking the dateline into account appropriately, i.e., $i = 1$ and $i = 360$ are adjacent grid pixels):

$$\overline{C} := G \otimes C, \quad (12)$$

$$\overline{W} := G \otimes W. \quad (13)$$

- The smoothed stratospheric VCD for each grid pixel as derived from weighted convolution is then given as

$$\overline{V}_{ij} := \frac{\overline{C}_{ij}}{\overline{W}_{ij}}. \quad (14)$$

We illustrate this procedure for a simple 1-D example in the Supplement (Sect. S2.3 and Fig. S3).

The degree of smoothing is determined by the definition of the CK G , which is defined as a 2-D Gaussian in STREAM v0.92 with the longitudinal/latitudinal variances σ_φ^2 and σ_ϑ^2 , respectively. Generally, information on the stratospheric column over polluted regions should be taken from clean measurements at the same latitude. Thus, σ_φ has to be sufficiently large, while σ_ϑ has to be low as gradients in latitudinal dimension should be mostly conserved. For high latitudes, however, the longitudinal extent of the CK has to be small enough as well in order to be able to resolve the strong gradients caused by the polar vortex.

In order to meet these requirements, we implement the convolution in the following way:

1. Two CKs are defined in order to meet the different requirements for polar vs. equatorial regions (see Fig. S4):

$$\begin{aligned} G^{\text{pol}} &:= G(\sigma_\varphi = 10^\circ, \sigma_\vartheta = 5^\circ) \\ G^{\text{eq}} &:= G(\sigma_\varphi = 50^\circ, \sigma_\vartheta = 10^\circ). \end{aligned} \quad (15)$$

Note that the difference of the CKs, which are defined on a regular degree grid, is even more drastic in kilometer space.

2. Stratospheric VCDs $V_{\text{strat}}^{\text{eq}}$ and $V_{\text{strat}}^{\text{pol}}$ are derived for both CK according to Eqs. (12)–(14).

3. The final stratospheric VCD is defined as the weighted mean of both, depending on latitude ϑ :

$$V_{\text{strat}} := \cos^2(\vartheta) V_{\text{strat}}^{\text{eq}} + \sin^2(\vartheta) V_{\text{strat}}^{\text{pol}}. \quad (16)$$

By this method, spatial smoothing is wide enough at the equator (needed to interpolate, e.g., the stratosphere over central Africa) but small enough at the polar vortex.

In latitudinal direction, this procedure can cause small, but systematic, biases when stratospheric NO₂ shows significant latitudinal gradients on scales of σ_{lat} or smaller. To overcome this, STREAM provides the (default) option to run the weighted convolution on “latitude-corrected” VCDs; i.e., the mean dependency of V^* on latitude is (1) determined (again over the Pacific), (2) subtracted from all individual V_{ijk} , and (3) added again to the stratospheric estimate from weighted convolution. By this procedure, latitudinal gradients are largely removed for the convolution (but not from the final stratospheric fields), and the systematic biases vanish (as shown in Sect. S2.3).

2.4 Data processing

STREAM estimates stratospheric fields and tropospheric residues for individual orbits, using NO₂ measurements of the dayside of the orbit. Note that the effect of changes of local time on stratospheric NO₂ across orbit is generally low (see Sect. S2.4) and is thus neglected within STREAM. For each orbit under investigation, the orbit itself plus the seven previous and subsequent orbits (corresponding to about ± 12 h in time, or $\pm 180^\circ$ in space (longitude), for the investigated satellite instruments in polar sun-synchronous orbits) are used for the calculation of V^* , weighting factors, and thus V_{strat} via weighted convolution. For the daily means presented in this study, all orbits where the orbit start date matches the day of interest are averaged.

Alternatively, STREAM can be run in “near-real time” (NRT) mode, in which the 14 past, but no future, orbits are included in the weighted convolution. We discuss the performance of STREAM NRT for the example of GOME-2 in Sect. 5.2.

STREAM v0.92, implemented as a MATLAB script at MPI-C, requires about 10 s for processing one orbit of OMI data on a normal desktop computer (3.4 GHz). Time-consuming steps are, at about equal parts, the sorting of the satellite pixels on the global grid V_{ijk} and the convolution process, while the time needed for the calculation of weighting factors is negligible.

3 Data sets

3.1 Satellite data sets

Several UV/vis satellite instruments provide column measurements of atmospheric NO₂. Table 1 summarizes the characteristics of the instruments and provides references to the data products used in this study, from which the total NO₂ SCD, the stratospheric AMF, and the cloud fraction/cloud top height are taken as input for STREAM. Below we provide details on the satellite characteristics and the data sets used in this study, starting with OMI (as STREAM was optimized for OMI within TROPOMI verification) and GOME-2, followed by older instruments with particular challenges such as poor spatial coverage (SCIAMACHY) or resolution (GOME).

3.1.1 OMI

In this study we mainly focus on OMI for two reasons.

1. OMI provides daily coverage with small ground pixels. While this already results in a high number of available satellite pixels per day ($> 10^6$), the number of clouded pixels matching the requirements to cause a high w_{cld} is also high (more than 10^5 pixels have a $w_{\text{cld}} > 5$).
2. STREAM is the STS verification algorithm for TROPOMI. Algorithm testing within TROPOMI verification and comparisons to the TROPOMI prototype algorithm are performed based on actual OMI measurements.

STREAM basically requires V^* ($=S/A_{\text{strat}}$) as input. For OMI, we use the level 2 “OMNO2” data product (version 3) provided by NASA (Bucsela et al., 2013) and labeled as “Standard Product 2” (SP2) therein, which provides de-striped NO₂ SCDs and stratospheric AMFs². In addition, quality proxies are used to exclude dubious measurements (like those affected by the “row anomaly”³). Also information on CRF and CP, which is needed for the calculation of w_{cld} , is provided by the OMNO2 v003 hdf files, based on the “improved OMI O₂–O₂ cloud algorithm” (Bucsela et al., 2013) OMCLDO2.

The NASA v003 product involves a STS algorithm based on an MRSM as well. The resulting tropospheric residues of STREAM and NASA v003 are compared and discussed in detail in Sect. 5.1.2.

In addition to the NASA product, we also extract the DOMINO (version 2) level 2 data as provided by TEMIS, for two purposes.

²In the DOMINO v2 product, total SCDs are not de-striped, and stratospheric AMFs are only provided up to a solar zenith angle (SZA) of 80°

³<http://projects.knmi.nl/omi/research/product/rowanomaly-background.php#overview>

1. The TROPOMI “prototype algorithm” (van Geffen et al., 2014) is developed by KNMI based on model assimilation similar to the DOMINO v2 algorithm. Due to the high computational effort of data assimilation, no dedicated TROPOMI verification data set is available for verification. Instead, we compare the results of STREAM directly to DOMINO v2 (Sect. 5.1.1).
2. DOMINO provides TM4 model profiles of NO₂ (needed for the calculation of DOMINO tropospheric AMFs). Here, we use the TM4 data in order to construct synthetic total columns of NO₂ for performance tests of STREAM (see Sect. 3.3).

Both OMI products are based on the same spectroscopic analysis; i.e., both start with the same NO₂ SCD. Note that this SCD is biased high by about 1 CDU due to shortcomings in the spectral retrieval (see van Geffen et al. (2015) and references therein). Recent algorithm refinements have removed this bias (van Geffen et al., 2015; Marchenko et al., 2015), but updated NASA or TEMIS products are not available yet. However, such an overall bias will be interpreted as stratospheric feature by STREAM and thus does not affect its performance (the same holds for the operational NASA and TEMIS STS algorithms). Still, the resulting TRs are expected to decrease slightly as the bias decreases for larger SCDs (Marchenko et al., 2015, Fig. 3 therein).

3.1.2 GOME-2

The GOME-2 instruments on the Metop-A and B satellites provide a time series of almost 10 years with the perspective of continuation until 2025 due to the upcoming instrument on Metop-C. GOME-2 provides a good spatial coverage with moderate satellite ground pixel size.

We applied STREAM to total NO₂ columns from the operational product (GDP 4.7), as provided by DLR in the framework of the Ozone Satellite Application Facilities (O3M SAF), for Metop-A.

The operational product uses an MRSM for STS (Valks et al., 2011, 2015) as well. We compare the results of STREAM and the GDP 4.7 algorithm in Sect. 5.2.

3.1.3 SCIAMACHY

STREAM was applied to the SCIAMACHY VCDs retrieved at MPIC Mainz (Beirle et al., 2010a; Beirle and Wagner, 2012). While OMI provides daily global coverage, the coverage of SCIAMACHY is rather poor (only about one-sixth of the Earth per day), and ground pixels are larger than for OMI (except for swath edges). Consequently, also the number of total (about 60 000) and cloudy (about 4000) pixels per day is much lower than for OMI. Thus, SCIAMACHY can be considered as extreme test case for the performance of STREAM.

One reason for the poor spatial coverage of SCIAMACHY is the measurement mode alternating between nadir and limb geometry. This, however, provides the unique SCIAMACHY feature of a direct measurement of the stratospheric column. We thus compare the TR resulting from STREAM to the MPI-C SCIAMACHY product based on LNM (Beirle et al., 2010a), using the MPI-C retrieval scheme for NO₂ concentration profiles from limb measurements (Kühl et al., 2008) (Sect. 5.3).

3.1.4 GOME

GOME was the first nadir-viewing spectrometer in the UV/vis spectral range with a spectral resolution enabling DOAS analyses. Due to large ground pixel size (320 km across track), only a low number of (total as well as clouded) satellite pixels per day is available. We nevertheless included GOME in this analysis in order to investigate to what extent STREAM can be applied within homogenized retrievals for multiple satellite instruments, as planned within the QA4ECV (Quality Assurance for Essential Climate Variables) project⁴. We apply STREAM to the VCDs provided by TEMIS (Boersma and Eskes, 2004) and compare the resulting TRs to a simple RSM (Sect. 5.4).

3.2 Model data

For comparisons, and for the calculation of synthetic total columns for performance tests of STREAM, we make use of stratospheric NO₂ as provided by the ECHAM5/MESy Atmospheric Chemistry (EMAC) model, which is a modular global climate and chemistry simulation system (Jöckel et al., 2006, 2010, 2016).

We use the results from simulation *RCISD-base-10a* of the ESCiMo (Earth System Chemistry integrated Modelling) project as detailed by Jöckel et al. (2016). Here, only basic information on this specific simulation is summarized.

The model results were obtained with ECHAM5 version 5.3.02 (Roeckner et al., 2006) and MESy version 2.51 at T42L90MA resolution, i.e., with a spherical truncation of T42, corresponding to a quadratic Gaussian grid of approx. 2.8° by 2.8° in latitude and longitude, and 90 vertical hybrid pressure levels up to 0.01 hPa. The dynamics of the general circulation model was nudged by Newtonian relaxation towards ERA-Interim reanalysis data (Dee et al., 2011).

Simulation *RCISD-base-10a* was selected from among the various ESCiMo simulations for several reasons:

- a. it has been nudged to reproduce the “observed” synoptic situations;
- b. its stratospheric resolution is, with $\simeq 65$ levels, finer compared to other simulations from the ESCiMo project;

- c. the simulated total column and tropospheric partial column ozone compare well with observations (Jöckel et al., 2016); and
- d. the precursor emissions from the land transport sector are most realistic in comparison to other simulations.

In conclusion, this simulation represents the state-of-the-art in terms of numerical simulation of the atmospheric chemistry. Moreover, the applied nudging technique allows a direct comparison with observational data, since the simulated meteorological situation corresponds to the observed.

Specifically for this study, the submodel SORBIT (Jöckel et al., 2010) was used to extract NO₂ mixing ratios along the sun-synchronous orbit of the Aura satellite, thus matching the local time of OMI observations. Stratospheric VCDs were calculated by vertical integration of the modeled NO₂ mixing ratios between the tropopause height (as diagnosed according to the WMO definition based on lapse rate equatorwards of 30° north/south and as iso-surface of 3.5 PVU potential vorticity poleward of 30° latitude) and the top of the atmosphere.

In this study, we make use of the modeled stratospheric columns for two purposes.

1. We perform a simple model-based STS for comparison. To remove systematic biases between satellite measurements and EMAC, a latitude dependent offset is determined in the Pacific and corrected for globally, similar as in Richter et al. (2005) and Hilboll et al. (2013). We refer to this EMAC-based STS as STS_{EMAC} and applied it to OMI data (Sect. 5.1.3).
2. Stratospheric VCDs from EMAC are used to construct a synthetic data set of total NO₂ VCDs for performance tests of STREAM (see next section).

3.3 Synthetic VCD

We test the performance of STREAM on synthetic VCDs, which allows a quantitative comparison of the estimated TR to the a priori “truth”. The input to STREAM, i.e., synthetic total columns of NO₂, should realistically represent (a) stratospheric chemistry and dynamics, (b) tropospheric emissions, transport, and chemistry, (c) cloud fields, and (d) the satellite sampling. For these purposes, we construct synthetic NO₂ column densities V^* based on

- a. stratospheric VCDs from EMAC⁵ at AURA overpass time (Sect. 3.2),
- b. modeled tropospheric VCDs from TM4 (Sect. 3.1.1), and

⁵Stratospheric columns are taken from EMAC rather than TM4, as the latter does not represent a free model run of stratospheric chemistry and dynamics but uses the satellite measurements for assimilation.

⁴<http://www.qa4ecv.eu/>

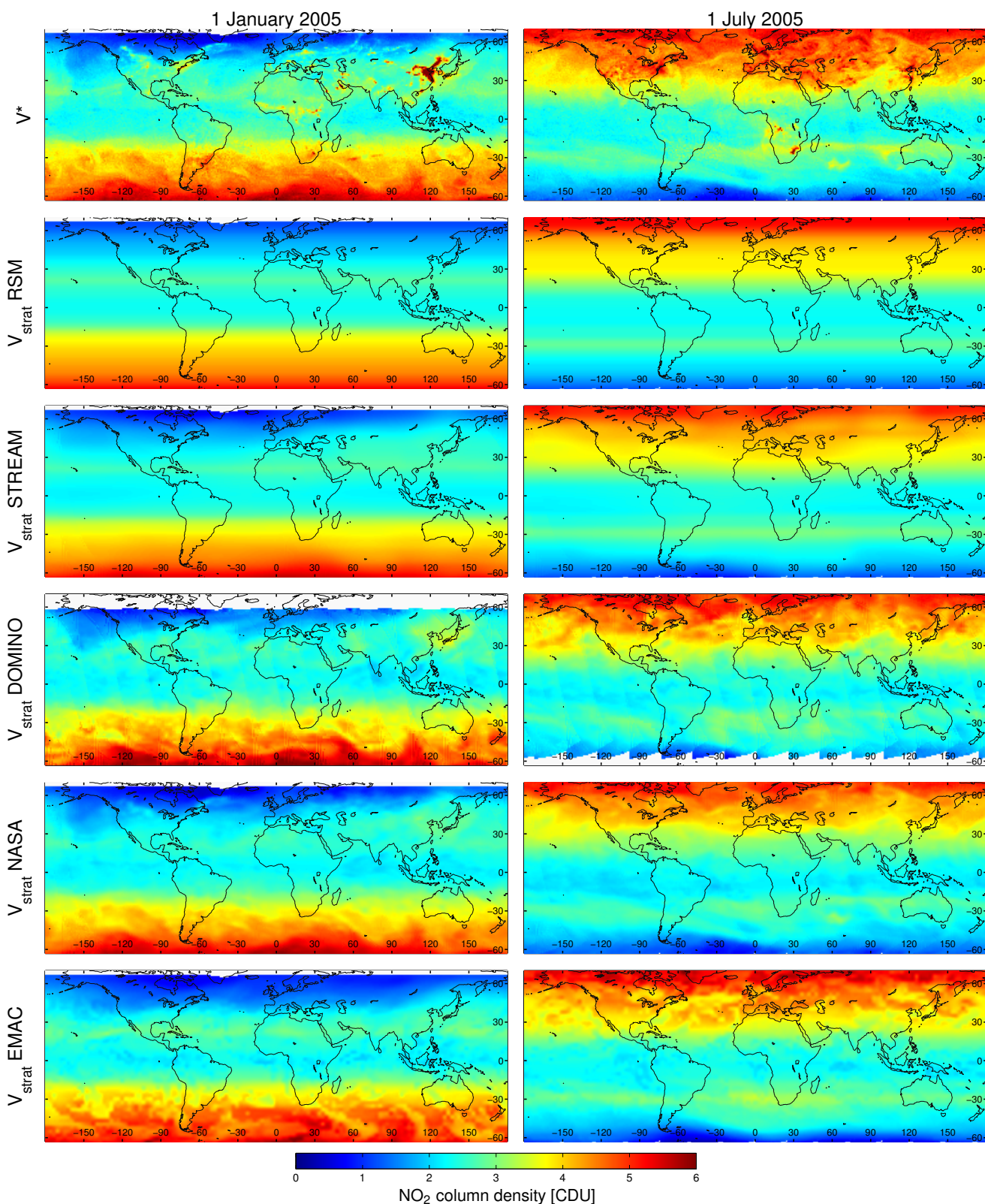


Figure 3. Total OMI VCD V^* (top) and the resulting stratospheric estimate V_{strat} from RSM (second row) and STREAM (third row) for 1 January (left) and 1 July (right) 2005. Resulting V_{strat} from other algorithms are included as well for comparison (see Sect. 5).

- c. measured cloud properties and the respective tropospheric AMFs from OMI as provided in the DOMINO NO₂ product.

Synthetic TRs are given as $T^* = V_{\text{trop}} \times A_{\text{trop}} / A_{\text{strat}}$ (compare Eq. 4). Synthetic total columns V^* are then calculated as $V_{\text{strat}} + T^*$ (Eq. 3) and fed into STREAM. The resulting fields of stratospheric VCDs and the respective TRs can then be compared to the a priori “truth”. Synthetic V_{strat} , TVCD, and T^* are displayed in Fig. S7 for 2 selected days.

4 Algorithm performance

In this section we analyze the performance of STREAM. As the true stratospheric VCD is not known, the error of any STS algorithm is not easily accessible. Still, the STS performance can be evaluated based on the properties of the resulting TR: in remote regions without substantial NO_x emissions, T^* should generally be low but still positive (about 0.1 CDU; Valks et al., 2011). Also the variability of T^* over both space and time should be low in regions free of tropospheric sources.

Below, we investigate the characteristics of T^* from STREAM (Sect. 4.1) and its dependency on a priori settings (Sect. 4.2) for OMI measurements. In addition, the error of T^* is quantified based on synthetic data (Sect. 4.3). Application of STREAM to other satellite instruments and the comparisons between STREAM and other STS algorithms are provided in Sect. 5.

4.1 Performance of STREAM for OMI compared to RSM

Figure 3 displays the OMI daily mean VCD V^* (top) as well as the respective stratospheric field from RSM (second row) and STREAM (third row) for 1 January (left) and 1 July 2005 (right), respectively. The overall latitudinal as well as longitudinal dependencies are clearly reflected in the stratospheric fields, while small-scale stratospheric features are lost by the spatial convolution. Figures 4 and 5 display the resulting TRs, respectively, for both daily (top) and monthly (bottom) means. Figure 6 summarizes the daily and monthly statistical properties of TR, i.e., the median as well as 10th/90th and 25th/75th percentiles (light/dark bars) for different regions (see Fig. S8 for an illustrative sketch of the meaning of the percentile bars, as well as the definition of regions).

Overall, spatial patterns of TR are similar for RSM and STREAM, in particular the enhanced values reflecting tropospheric pollution over, e.g., the USA, central Africa, or China. However, RSM reveals several artifacts of both enhanced as well as systematically negative TR as a consequence of the simple assumption of zonal invariability of stratospheric NO₂. For instance, on 1 January 2005, VCDs over northern Canada are lowered due to the polar vortex (Fig. 3 top left). Consequently, the simple RSM results in

negative T_{RSM}^* down to -0.7 CDU (Fig. 4). In contrast, T_{RSM}^* over northeastern Russia is quite high (>0.5 CDU). This pattern is slightly reduced but still present in the monthly mean (see the statistics of T_{RSM}^* for high latitudes in Fig. 6).

This artifact is largely reduced by STREAM (Fig. 5 top left). The spread of T^* at high latitudes is more than 3 times lower than that of T_{RSM}^* (Fig. 6). Also for July, systematic structures showing up in T_{RSM}^* (in polar regions, but also in the Indian ocean at $30\text{--}60^\circ\text{S}$) are largely reduced in STREAM.

Over the Pacific, T_{RSM}^* is, by construction, 0 on average. T^* is systematically higher by about 0.1 CDU (Fig. 6). This results from the emphasis of clouded pixels used for STREAM, which directly reflect the stratospheric rather than the total VCD. This additional advantage of STREAM over RSM is further discussed below (Sect. 5.6).

As both RSM and STREAM generally assume stratospheric patterns of NO₂ to be smooth, i.e., do not resolve longitudinal variations at all (RSM) or on scales $< \sigma_\varphi$ (STREAM), the small-scale variations in daily total VCDs (Fig. 3 top) are transferred to the TR, resulting in “patchy” daily TRs ranging from about -0.1 up to $+0.4$ CDU in remote regions (10th–90th percentiles). In the monthly means, however, these patchy structures have mostly vanished (both for RSM and STREAM), as the spatial patterns of different days at variable locations cancel each other out. The remaining systematic patterns in monthly mean T^* have generally larger spatial scales and are within 0 up to $+0.25$ CDU in remote regions.

On 1 July, a band of enhanced V^* shows up around $20\text{--}30^\circ\text{S}$, where (a) V^* is higher in the Indian Ocean compared to the Pacific and (b) the structure of enhanced V^* is “tilted” in the Pacific (see Fig. 3 top right); i.e., the RSM assumption of zonal invariance is not fulfilled. Consequently, the RSM results in extended horizontal structures (“stripes”) of low/high-biased T^* over South America and the Indian Ocean, respectively, ranging from -0.5 up to almost 1.0 CDU (Fig. 4 top right). Again, temporal averaging reduces the amplitude, but systematic patterns of about ± 0.4 CDU remain in the monthly mean (Fig. 4 bottom right). As STREAM also assumes a weak variation of V_{strat} with longitude, in particular at low latitudes, the artifacts in T^* are very similar to those of T_{RSM}^* at $20\text{--}30^\circ\text{S}$. Note that this artifact is particularly strong in July 2005 (as compared to 2010; see Sect. 5.1.4).

In Sect. 5, TRs from STREAM are investigated for other satellite instruments and compared to other STS algorithms, and the advantages and limitations of STREAM are discussed further.

4.2 Impact of a priori settings

STREAM determines the stratospheric NO₂ VCD V_{strat} based on weighting factors as described in Sect. 2. The resulting TRs thus depend on the weighting factor

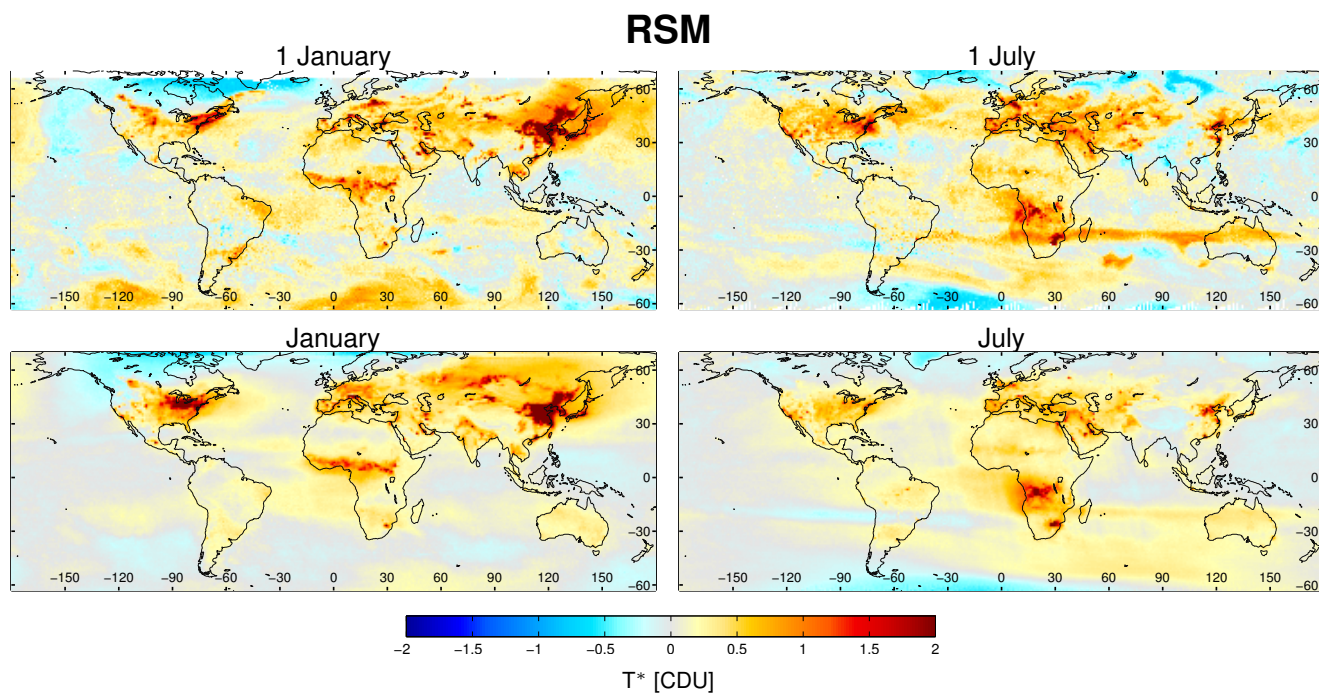


Figure 4. OMI tropospheric residues T^* based on RSM for January (left) and July (right) 2005 for the first day of the month (top) and the monthly mean (bottom).

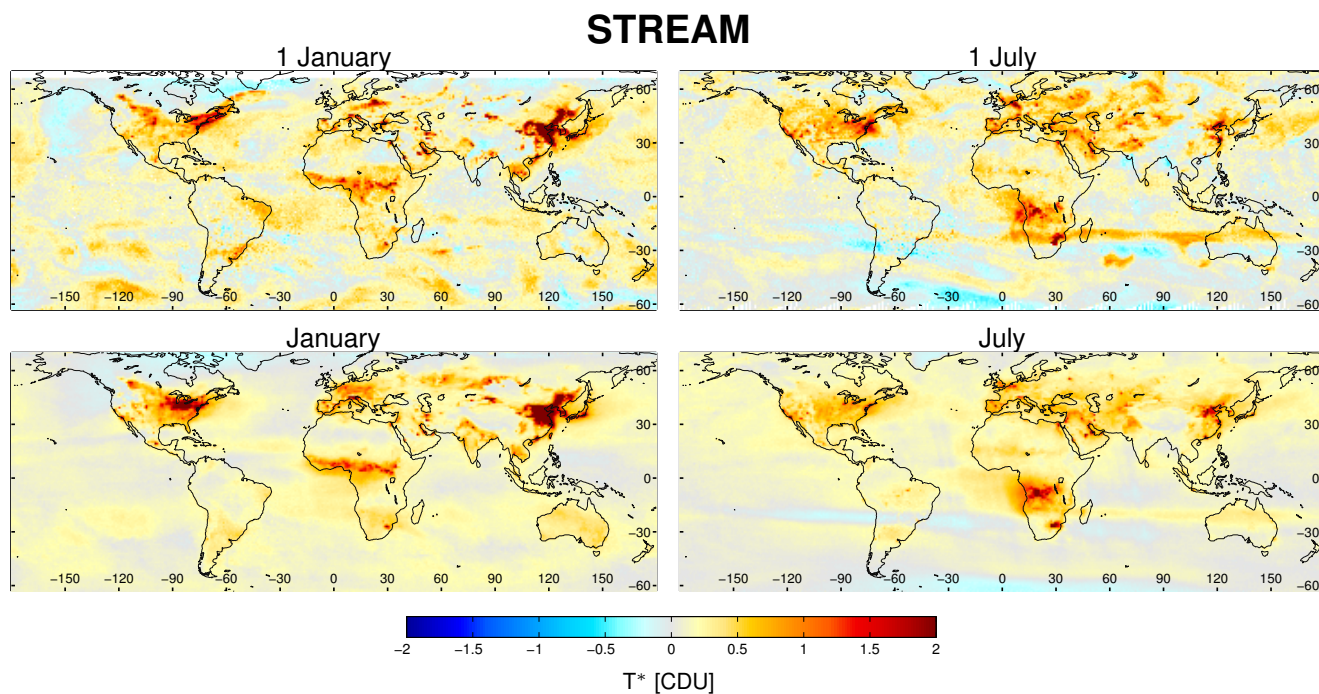


Figure 5. OMI tropospheric residues T^* based on STREAM for January (left) and July (right) 2005 for the first day of the month (top) and the monthly mean (bottom).

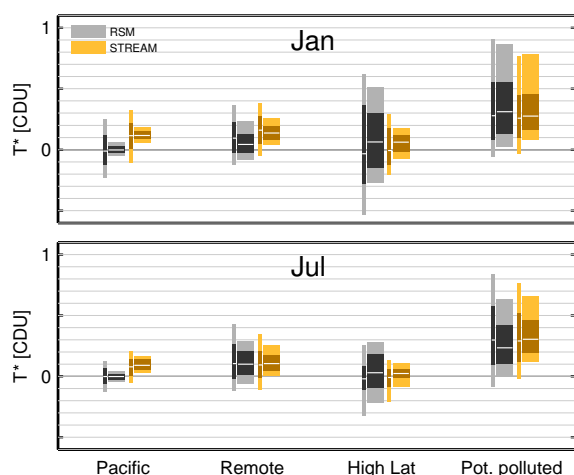


Figure 6. Regional statistics of OMI tropospheric residues T^* from RSM and STREAM for January (top) and July (bottom) 2005. Light and dark bars reflect the 10–90th and 25–75th percentiles, respectively. The median is indicated in white. Narrow bars show the statistics for the first day of the month, wide bars those of the monthly means (see also Fig. S8 left for illustration). The regions are defined in Fig. S8 right. “High latitudes” refer to the respective hemispheric winter only.

definition and convolution settings. We performed runs of STREAM with one-by-one modifications of each parameter and compared the results to the baseline setting. Overall, the effects of a priori settings on T^* have been found to be rather small (of the order of 0.1 CDU), and the STREAM results are thus robust with respect to the parameters chosen in v0.92.

Below, we summarize the main findings of the performed sensitivity studies. Figures and details are provided in the Supplement.

4.2.1 Impact of cloud weight

The cloud weight w_{cld} was varied (a) by setting it to 1 (i.e., not accounting for cloud properties at all), (b) increasing w_{cld} by a factor of 10 for clouded pixels, (c) including high-altitude clouds in the calculation of w_{cld} , and (d) including low-altitude clouds in the calculation of w_{cld} .

- When no w_{cld} is applied, the tropospheric estimate over the Pacific is ≈ 0 , as for the classical RSM, instead of about 0.1 CDU for the baseline. This difference corresponds to the order of the tropospheric background of NO₂. Over potentially polluted regions, however, the difference to the baseline is larger (0.2 CDU). Here, the stratospheric estimate is additionally biased high due to missing supporting points over continents.
- The “high w_{cld} ” scenario is achieved by modifying Eq. (6a) from $w_{\text{cld}} := 10^{2 \times w_c \times w_p}$ to $w_{\text{cld}} := 10^{3 \times w_c \times w_p}$; i.e., w_{cld} is increased by a factor of 10

for cloudy pixels of mid-altitude but stays unchanged for cloud-free pixels. In this scenario, measurements over clouds by far dominate the stratospheric estimate, yielding lower V_{strat} , and thus higher T^* , compared to the baseline. However, the difference is very small (< 0.05 CDU). In addition, the variability of T^* is generally slightly higher in case of a 10 fold increased w_{cld} .

- When high-altitude clouds are included in the calculation of w_{cld} , the resulting TR hardly changes at all, indicating that the impact of lightning NO_x on NO₂ satellite observations is generally small.
- The inclusion of low-altitude clouds has almost no effect as well, as expected over clean regions. Over potentially polluted regions, however, it is expected that low-altitude clouds result in increased total columns V^* as soon as there is significant NO₂ above or within the cloud, causing high tropospheric AMFs. Consequently, V_{strat} is expected to be biased high, and T^* biased low over potentially polluted regions, when low clouds are included in the calculation of w_{cld} . This effect was indeed found, but the absolute change is rather small (< 0.1 CDU in winter, almost 0 in summer). This weak dependency on the inclusion of low-altitude clouds probably results from the conservative definition of w_{pol} , which is already very low over regularly polluted regions.

Following the argument that cloudy observations provide a direct measurement of the stratospheric column, a higher cloud weight would be expected to be more favorable and to result in higher tropospheric background over the Pacific. This is indeed observed for OMI. For other satellite instruments, however, results are somewhat contradictory (see Sects. 5.3, 5.4, and 6). Thus, the definition of w_{cld} in Eq. (6) is kept as a compromise in order to have common algorithm settings across different satellite platforms.

4.2.2 Impact of convolution

In STREAM, two different CK are applied, yielding two stratospheric estimates, and the final V_{strat} is calculated as weighted mean of both (see Sect. 2.3 and Eqs. 15 and 16). We tested the impact of the choice for CK by applying both the polar (“narrow”) and equatorial (“wide”) CK globally. The narrow CK, and thus the potential range of influence of satellite pixels with high weights, is limited to about $2 \times \sigma_\varphi = 20^\circ$ in longitude. This potentially leads to biases over continents caused by spatial interpolation. Thus, the resulting T^* is (too) low over central Africa. Overall, median T^* over potentially polluted regions is lower compared to the baseline settings by about 0.1 CDU.

For wide CK, however, the longitudinal gradients at high latitudes are not resolved anymore. Consequently, the spatial variability of daily T^* at high latitudes is increased by a factor of 2. We conclude that our choice of the combined CK

for high and low latitudes is a good compromise for realizing weighted convolution.

4.2.3 Impact of latitude correction

When the initial correction of the latitudinal dependency of V^* over the Pacific is omitted, the resulting TR reveals global stripes with negative values around the equator and maxima (≈ 0.5 CDU) at about 30° N/S, both in winter and summer.

4.2.4 Impact of the number of considered orbits

In STREAM baseline settings, for each orbit, stratospheric estimation is based on the previous and subsequent seven orbits, corresponding to full global coverage for OMI. Switching this parameter to either ± 14 or ± 3 orbits has almost no impact on the resulting TR.

In case of NRT application of STREAM, no subsequent orbits are available, and the previous 14 orbits have to be considered. This setup also results in essentially the same T^* statistics (compare Sect. 5.2).

4.2.5 Impact of tropospheric residue weight

In STREAM v0.92, one iteration for w_{TR} is applied. When w_{TR} is omitted, the spread of T^* slightly increases for high latitudes. A second iteration does not yield a further improvement. Lowering the threshold in Eq. (7) from 0.5 to 0.3 CDU results in a slightly lower spread of T^* at high latitudes in summer.

4.2.6 Impact of pollution weight

The impact of pollution weight is investigated by multiplying w_{pol} (where different from 1, compare Fig. 2a) by 0.1 (“low w_{pol} ”) or 10 (“high w_{pol} ”). In the first case, the resulting pollution weight over most continents is below 0.01, while in the second case it is increased to 1 (meaning that w_{pol} is switched off) except for industrialized pollution hotspots.

In remote regions, the change of pollution weight has almost no impact. In potentially polluted regions, the impact is only moderate as well. Low w_{pol} does not differ much from the baseline, as the latter already assigns rather low weighting factors to potentially polluted pixels; a further decrease by factor 0.1 thus does not change much.

Only for high w_{pol} can a significant change of TR be seen; in this case, the inclusion of more partly polluted observations causes a high bias in the stratospheric estimate and the resulting TRs are biased low by almost 0.1 CDU in winter.

4.3 Performance for synthetic data

In order to estimate the uncertainties of the STREAM stratospheric estimate (and thus tropospheric residues), we apply the algorithm to synthetic input data, as defined in Sect. 3.3, for which the “true” stratospheric fields and TR are known. Again, a simple RSM is applied as well for comparison.

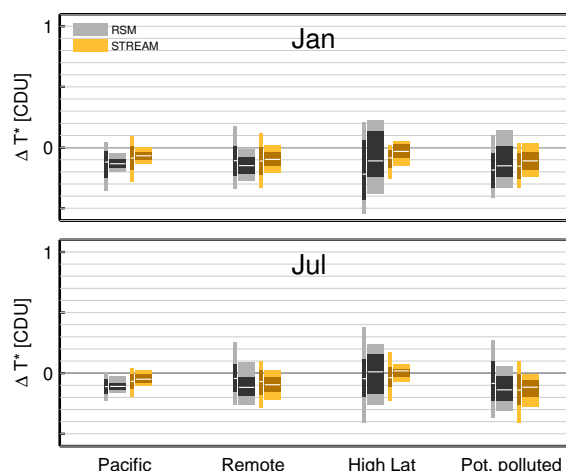


Figure 7. Regional statistics of the error of T^* from STREAM, i.e., the difference of estimated and a priori TR (based on synthetic total columns as defined in Sect. 3.3).

Figure 7 displays the statistics of the error of T^* , i.e., the difference ΔT^* of estimated and a priori TR, which equals the difference between the true and the estimated stratospheric VCD, for different regions. The spatial patterns of ΔT^* are shown in the Supplement (Fig. S20).

Over the Pacific, RSM results in TR biased low by 0.1 CDU. With STREAM, the bias is reduced (0.05 CDU) but not completely removed. On 1 January 2005, ΔT^* shows a variability of almost 0.4 CDU (10th to 90th percentile) for both algorithms. This is mainly caused by the small-scale structures of stratospheric NO₂ in EMAC over the Pacific, in particular at southern latitudes (see Fig. S7), which are resolved by neither STREAM nor RSM. The respective spatial variability of the monthly mean, however, is much lower (about 0.1 CDU).

Again, the simple RSM results in large biases and high variability of ΔT^* at high latitudes, which are largely reduced by STREAM.

Overall, the agreement of a priori and estimated T^* from STREAM is very good, in particular for monthly means. Remaining systematic biases are about -0.1 CDU over potentially polluted regions; i.e., resulting TRs are slightly underestimated, as expected due to the general approach of using total column measurements as proxy for the stratospheric estimation.

The application of STREAM to synthetic data thus provides a valuable estimate of the algorithm’s accuracy. One might think that using the synthetic data for optimizing the definition of weighting factors is the next step forward. However, we refrain from doing so due to some contradictory results for different instruments. Concretely, the remaining bias in TR for synthetic data of about 0.1 CDU could be further reduced by increasing w_{cld} . This, however, has adverse ef-

fects on SCIAMACHY and GOME results (see Sects. 5.3 and 5.4).

5 Comparison to other algorithms and discussion

In this section, we apply STREAM to different satellite instruments, compare the results to various existing STS algorithms, and discuss the challenges, limitations, and uncertainties of STS in general and STREAM in detail.

5.1 OMI

As shown in the previous section, STREAM as applied to OMI data generally shows a good performance (Figs. 5 and 6). The systematic artifacts of a simple RSM, such as the large variability of T^* at high latitudes, are largely removed by STREAM. In addition, the application of w_{cld} emphasizes cloudy observations which directly reflect the stratospheric column. Mean T^* over the Pacific is thus not 0 anymore as in RSM, and an additional correction for the tropospheric background is not required in STREAM.

The sensitivity of STREAM on a priori parameters has been found to be small. Remaining monthly mean TRs in clean regions and their variability are of the order of 0.1 CDU.

Below, we compare the OMI results for 2005 to other algorithms, i.e., the operational DOMINO (Sect. 5.1.1) and NASA (Sect. 5.1.2) data products as well as a simple model-based correction using EMAC (Sect. 5.1.3). Figure 8 summarizes the statistics of regional T^* from the different algorithms. Note that only coincident measurements where all four data products exist are included in Fig. 8 in order to allow for a meaningful comparison; in particular, high latitudes in hemispheric winter are skipped, as DOMINO data are not provided for $\text{SZA} > 80^\circ$. Thus, the statistics for STREAM slightly differ from those shown in Fig. 6.

5.1.1 Comparison to DOMINO

STREAM is part of the TROPOMI verification activities. The operational TROPOMI (“prototype”) algorithm for STS of NO₂ (van Geffen et al., 2014) was developed by KNMI, based on the DOMINO data processor for OMI (Boersma et al., 2007, 2011) (Boersma et al., 2011). The STS therein is done by assimilating the satellite measurements in the CTM TM4 (Dirksen et al., 2011).

For TROPOMI verification, we compare STREAM results for OMI to the respective DOMINO product as shown in Fig. S21. On a daily basis, “patchy” patterns of enhanced as well as negative TR show up over remote regions (Fig. S21), which result from the dynamical features already present in total VCDs (Fig. 3) combined with the respective dynamics prognosed by the model; spatial mismatch of these patterns can easily cause biases of the estimated TRs in both directions. Interestingly, some patterns look even reversed as

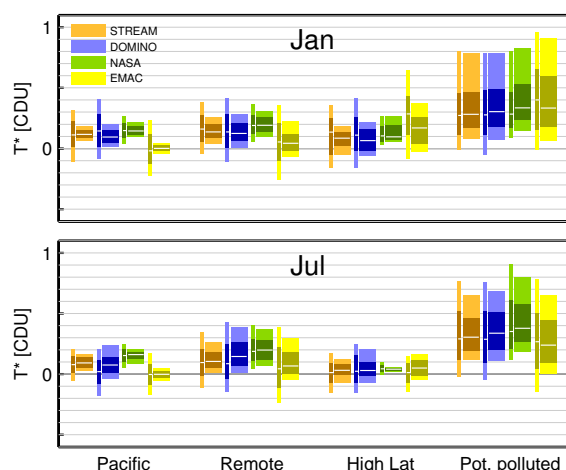


Figure 8. Regional statistics of OMI tropospheric residues T^* from different STS algorithms for January (top) and July (bottom) 2005. Note that the values for STREAM slightly differ from Fig. 6, as here only coincident satellite pixels of STREAM, DOMINO, and NASA are included.

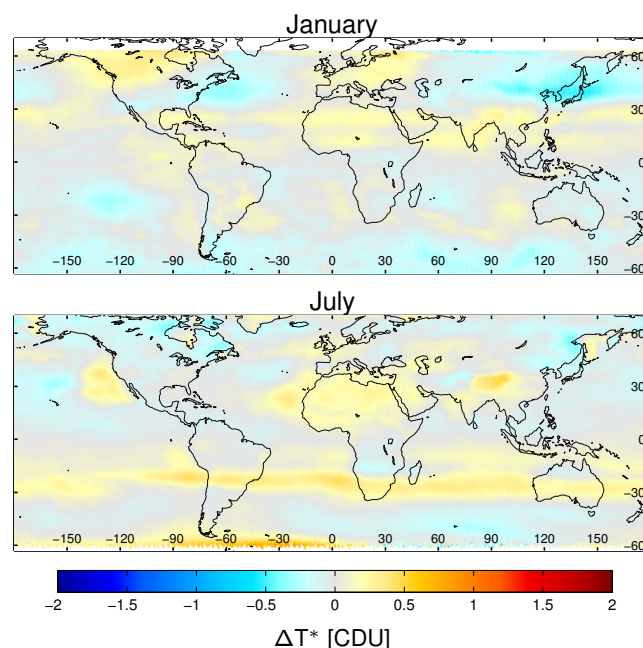


Figure 9. Monthly mean difference of tropospheric residues T^* from DOMINO and STREAM for OMI measurements in January (top) and July (bottom) 2005.

compared to STREAM (Fig. 5), for instance southeast from South Africa (around 50°S , 50°E). In the monthly means, these patches again are mostly canceled out.

Mean regional TRs (Fig. 8) are very similar between STREAM and DOMINO. However, the variability of T^* is slightly higher for DOMINO, in particular at high latitudes, as well as in the Pacific and in remote regions in July.

Figure 9 displays the differences of the monthly mean TR between STS_EMAC and STREAM for January and July 2005. Overall, the differences are quite small (below ± 0.1 CDU for 65 % of the world between 60° S and 60° N). Nonetheless, the monthly means reveal systematic regional deviations of more than ± 0.3 CDU (for less than 3 % of the world).

In January, TRs over East Asia at high latitudes are systematically higher for STREAM. This is probably related to an underestimation by DOMINO, as the DOMINO TRs are very low and partly negative in this region. Over North America, TRs from STREAM are higher than from DOMINO at the east coast but vice versa over western Canada. In both cases, the lower TR is slightly negative, indicating an overestimation of V_{strat} from DOMINO/STREAM at the east/west coast, respectively.

In July, the TR reveals a “stripe”-like structure at about 30° S, as already discussed in Sect. 4.1. In DOMINO, similar bands of enhanced tropospheric residue are found around 30° S, in particular in the Indian ocean. As the amplitude and width of these bands is different for STREAM and DOMINO, this feature is most striking in the difference map; TRs around 30° S are generally higher for DOMINO.

DOMINO reveals some patches of systematically enhanced TRs that are not observed by STREAM and thus show up in the difference map as well (west of the USA, west of the Sahara, Himalaya). Reasons for these regionally enhanced TRs (and thus low-biased stratosphere) have to be investigated in future studies.

5.1.2 Comparison to NASA

The official OMI NO₂ product provided by NASA uses an MRSM for STS as well, as described in Bucsele et al. (2013). Daily and monthly maps of TR from NASA (OMNO2 v003/SP2) are shown in Fig. S22.

The NASA STS corrects for the tropospheric background based on a “fixed model estimate” (Bucsele et al., 2013). Consequently, TRs are about 0.1 to 0.3 CDU over clean regions throughout the world.

TRs from NASA are impressively smooth even on a daily basis. This results from the STS algorithm which, over clean regions, interprets the difference between the total column and the (small) modeled tropospheric column as stratospheric column whenever the quotient of the modeled tropospheric slant column and stratospheric AMF (matching our definition of T^*) goes below a threshold of 0.3 CDU. Thus, at southern high latitudes in July (completely classified as unpolluted in the NASA algorithm), the TR is almost 0 ± 0 , i.e., shows no variability at all (compare Fig. 8) just by construction, as all the variability present in the total column was assigned to the stratospheric column (compare Fig. 3).

While this is probably a reasonable procedure over completely clean regions, we would like to point out the following.

1. The smoothness of NASA TR over oceans is not surprising, as it is reached by construction. In particular, the smooth patterns of TR over oceans allow no conclusion on the NASA STS performance over polluted continental regions, where TRs are based on interpolated stratospheric fields, just as in STREAM.
2. The NASA procedure of assigning the total column variability in clean regions completely to the stratospheric estimate also removes any cloud dependency of the TR, which affects applications such as profile retrievals by cloud slicing (e.g., Belmonte Rivas et al., 2014).
3. The NASA procedure runs the risk of labeling episodic NO₂ transport events over oceans (Zien et al., 2014) as stratospheric pattern. Bucsele et al. (2013) perform an automatic “hotspot” identification and elimination scheme to avoid this. Nonetheless, on 1 January, a NO₂ transport event can be seen in the total VCD east of Canada (Fig. 3 top left) which is similar to the “meteorological bomb” described in Stohl et al. (2003). This event is clearly visible in T^* from STREAM (Fig. 5 top left) but only weakly in T^* from NASA (Fig. S22 top left). The reason for this discrepancy is that the local enhancement of NO₂ is partly classified as a stratospheric feature in the NASA product, as illustrated in Fig. S23 (left).

Figure 10 displays the differences of the monthly mean TR for January and July 2005. Again, overall agreement is very good: in January, both products agree within 0.1 CDU for 69 % of the Earth and within 0.3 CDU anywhere. In July, agreement within 0.1/0.3 CDU is found for 64 %/94 % of the Earth (for latitudes below 60°), respectively. Again, the band at 30° S sticks out in the difference map as discussed above. Highest deviations of up to 0.5 CDU, however, are observed over the Sahara. Within the NASA STS, the Sahara is masked out completely, as the high albedo and low cloud fractions result in high tropospheric AMFs, such that even low tropospheric VCDs could contribute significantly to the total column. In STREAM, however, large parts of the Sahara are treated as unpolluted and are assigned with $w = 1$. A close check of the stratospheric estimates from STREAM and NASA over the Sahara reveals that the large deviation probably results from both a high-biased V_{strat} by STREAM and a low-biased V_{strat} by NASA (see Fig. S23 right).

5.1.3 Comparison to STS_{EMAC}

We have used the stratospheric 3-D mixing ratios provided by EMAC in order to perform a simple model-based STS, similar to Hilboll et al. (2013). First, the latitude-dependent offset between EMAC and OMI VCDs is estimated over the Pacific (when a multiplicative adjustment is performed,

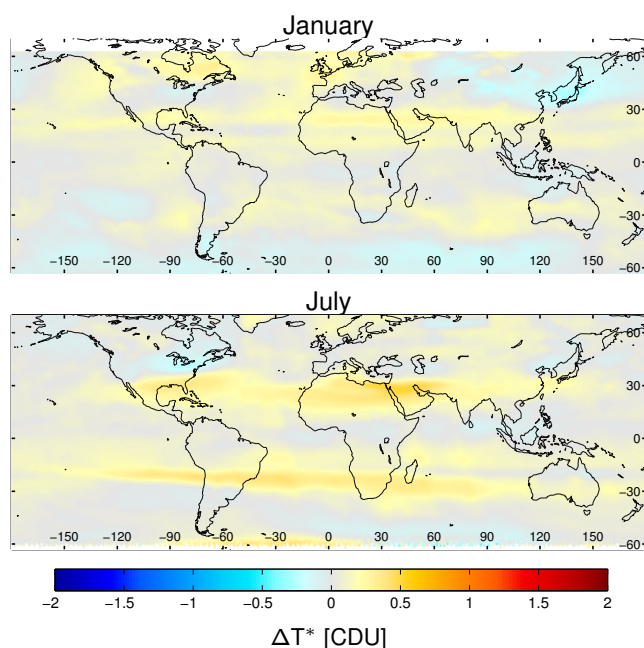


Figure 10. Monthly mean difference of tropospheric residues T^* from NASA and STREAM for OMI measurements in January (top) and July (bottom) 2005.

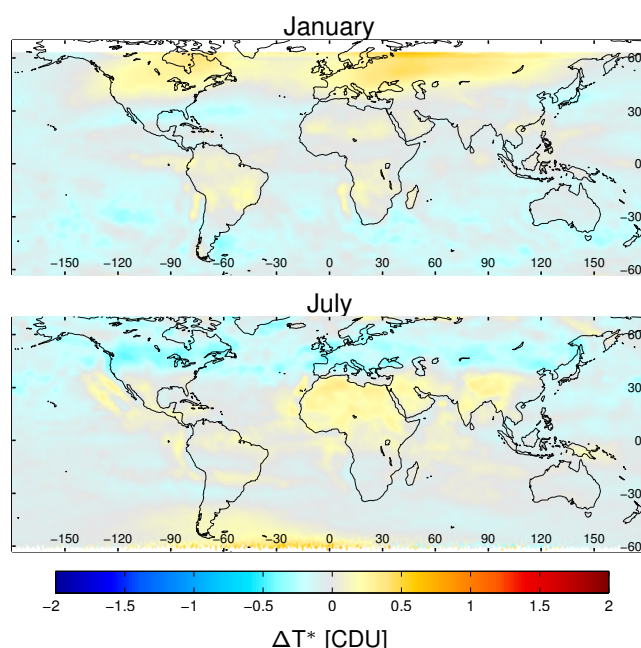


Figure 11. Monthly mean difference of tropospheric residues T^* from STSEMAC and STREAM for OMI measurements in January (top) and July (bottom) 2005.

results hardly change). Second, the offset-corrected stratospheric NO₂ VCDs is used for global STS. No additional correction for the tropospheric background is performed, such that the mean TR over the Pacific is 0 by construction.

Daily and monthly maps of TR from STSEMAC are shown in Fig. S24. Daily maps reveal patches of TR from -0.3 CDU up to 0.4 CDU resulting from mismatches in actual and modeled stratospheric dynamics. In the monthly mean, these fluctuations largely cancel out. Overall, variability (10th–90th percentiles) of T^* in remote regions was found to be about 0.3 – 0.4 , similar to that for DOMINO.

Figure 11 displays the differences of the monthly mean TR for January and July 2005. The overall negative values over ocean are a result of the neglect of the tropospheric background in STSEMAC. Besides this, the most striking features are

1. positive deviations (i.e., TR from STSEMAC being higher than from STREAM) over North America and Eurasia in January (up to 0.45 CDU, north from 35° N),
2. negative deviations over North America and Eurasia in July (down to -0.45 CDU, north from 35° N), and
3. positive deviations over the Sahara, Middle East, India, and western China in July (up to 0.38 CDU).

The systematic deviations north from 35° N (1 and 2) are caused by the longitudinal dependency of stratospheric NO₂ from EMAC which differs from the pattern in total column (see Fig. 3). In detail, stratospheric NO₂ over Siberia is quite

low in EMAC, resulting in high-biased TR (similar as for RSM) and indicating that the mean longitudinal dependency of stratospheric NO₂ is not fully reproduced by EMAC. Deviations in July over Sahara and southern Asia (3), however, are at least partly caused by a low bias of T^* from STREAM as discussed in the previous section.

Overall, deviations are moderate, and STSEMAC still improves the statistics of TR for high latitudes as compared to a simple RSM. It thus might be considered as a simple alternative STS with the advantage that it can be expected to work with the same performance for any satellite instrument, independent of spatiotemporal coverage.

5.1.4 OMI after row anomaly

In 2005, OMI measurements were performed with good instrumental performance, providing daily global coverage. This has changed since summer 2007, when radiance measurements of poor quality regularly occurred at particular cross-track positions (“row anomaly”). We thus also tested STREAM on OMI data after the onset of the row anomaly: Figs. S25 and S26 show T^* for 2010. While the daily maps reveal gaps due to the exclusion of measurements affected by the row anomaly, the monthly mean patterns as well as the statistical properties are comparable to the results for 2005. The row anomaly thus does not impact the performance of STREAM (or DOMINO or NASA retrievals).

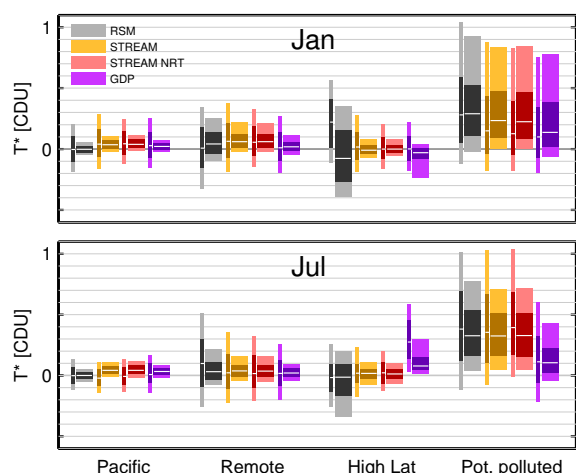


Figure 12. Regional statistics of GOME-2 tropospheric residues T^* from different algorithms for January (top) and July (bottom) 2010. Conventions as in Fig. 6.

5.2 GOME-2

STREAM has been applied to GOME-2 (Metop-A) data for the year 2010. The resulting daily and monthly mean maps are shown in Fig. S27. Again, statistical properties are summarized in Fig. 12.

The overall performance of STREAM, i.e., median and variability range of TR, is generally similar to that found of OMI. However, while OMI TRs are about 0.1 CDU over the Pacific, lower values (0.05 CDU) are found for GOME-2. This might be related to differences of cloud statistics due to pixel size, in particular a lower number of fully clouded pixels for GOME-2, as well as differences in local time, cloud products, or systematic spectral interferences caused by clouds in either retrieval algorithm.

On 1 July 2010, GOME-2 is operated in narrow swath mode, causing poor global coverage. This, however, does not affect STREAM performance.

On 15 January 2010, STREAM results in extraordinarily high TR over the ocean (Fig. S28), which turned out to be caused by a solar eclipse (Espenak and Anderson, 2008). Removing the affected orbit results in normal performance for this day. We recommend that screening of solar eclipses be done automatically (as done for OMI) before running any STS algorithm.

5.2.1 Comparison to NRT mode

STREAM is foreseen to be implemented in an update of the operational GOME-2 data processor as operated in the framework of the O3M SAF. This requires a slight modification of STREAM in order to work on NRT data.

In STREAM v0.92, the stratospheric fields are estimated for each orbit based on the total column measurements, including seven previous and seven subsequent orbits. In

NRT, however, no subsequent orbits are available. Thus, STREAM has to be operated on the current plus 14 previous orbits instead.

We ran STREAM in NRT mode. The resulting maps are shown in Fig. S28, and the statistics of TR are included in Fig. 12. The deviations between baseline and NRT are marginal. Thus, STREAM can be operated in NRT with stable performance.

5.2.2 Comparison to operational product (GDP 4.7)

In the current operational data processor (GDP 4.7), STS for NO₂ is done by an MRSM as described in Valks et al. (2011, 2015). Basically, polluted regions (defined by monthly mean TVCDs from the MOZART-2 model being larger than 1 CDU) are masked out. Global stratospheric fields are derived by low-pass filtering in zonal direction by a 30° boxcar filter.

Figure S30 displays daily and monthly mean maps of T^* in January and July 2010. The respective regional statistics are included in Fig. 12.

Overall, TRs from GDP are relatively low. Over the Pacific, mean T^* is close to 0 in January, despite the applied tropospheric background correction of 0.1 CDU. Over potentially polluted regions, median TR from GDP is systematically lower (by 0.2 CDU in July) than from STREAM, and almost a quarter of all TRs are even negative.

Figure 13 displays the differences of the monthly mean TR from GDP 4.7 and STREAM for January and July 2010, again pointing out the systematically lower values of GDP TR over continents in July. The systematic low bias of GDP TR probably results from moderately polluted pixels over regions labeled as “unpolluted”, which still might imply MOZART-2 TVCDs of up to 1 CDU. These measurements cause a high bias of the estimated stratospheric field around polluted regions; by the subsequent low-pass filtering, this high bias is passed over the polluted regions and results in low-biased TR. Further investigations are needed to find out why this effect is stronger in July than in January.

5.3 SCIAMACHY

We have applied STREAM to SCIAMACHY VCDs from the MPI-C NO₂ retrieval (Beirle et al., 2010a). The resulting daily and monthly mean maps for 2010 are shown in Fig. S31. Regional statistics are provided in Fig. 14, compared again to the simple RSM and, additionally, to the results of LNM.

Though SCIAMACHY provides poorer daily spatial coverage, STREAM overall still works well. Again, a clear reduction of the variability of T^* is found at high latitudes as compared to RSM. Over the Pacific, mean TR from STREAM is higher than for the RSM (= 0) but, similar to GOME-2, not as high as for OMI. Again, this could be related to the low number of cloudy satellite pixels and spec-

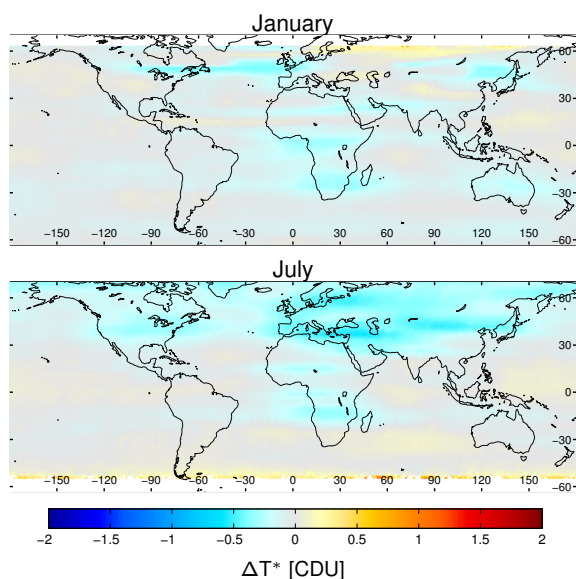


Figure 13. Monthly mean difference of tropospheric residues T^* from GDP 4.7 and STREAM for GOME-2 measurements in January (top) and July (bottom) 2010.

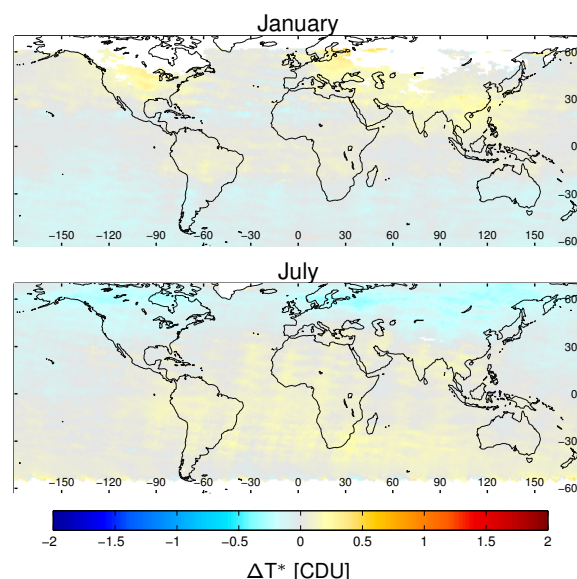


Figure 15. Monthly mean difference of tropospheric residues T^* from LNM and STREAM for SCIAMACHY measurements in January (top) and July (bottom) 2010. Gaps at high latitudes in January are caused by respective gaps in the FRESCO cloud product.

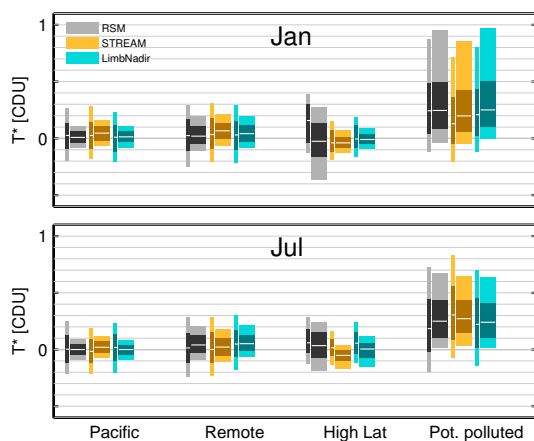


Figure 14. Regional statistics of SCIAMACHY tropospheric residues T^* from different algorithms for January (top) and July (bottom) 2010. Conventions as in Fig. 6.

tral interferences, affecting the DOAS analysis, related to clouds. Overall, regional statistics of T^* are similar to OMI or GOME-2. However, a systematic latitudinal dependency of T^* remains, showing positive values in hemispheric summer and negative values in hemispheric winter. This results from the latitudinal dependencies of V^* being different for clouded and cloud-free observations, as shown in Fig. S33, for reasons not yet understood.

5.3.1 Comparison to LNM

Within the SCIAMACHY MPIC NO₂ retrieval (Beirle et al., 2010a), STS is performed based on LNM. This can be

considered as a completely different STS approach, based on actual measurements but not involving CTMs or large-scale interpolation, and thus provide a valuable information on STREAM performance. Figure S32 displays the daily and monthly mean TR from LNM in 2010.

In the LNM STS, the latitude-dependent offset between nadir and limb is determined over the Pacific and corrected for globally; i.e., mean TR in the Pacific is 0 by construction. Overall, regional statistics of T^* from LNM are very similar to those from STREAM. Figure 15 displays the monthly mean difference of both algorithms. The deviation is dominated by the latitudinal dependency of T^* from STREAM (see above); when this is removed, both algorithms agree within 0.2 CDU for most parts of the globe.

5.4 GOME

GOME was the first instrument of the investigated series of UV/vis spectrometers suited for DOAS analyses of tropospheric trace gases. The comparably small number of GOME pixels and the large across-track footprint (320 km) required a modification of STREAM: we have switched the resolution of the global grid used for weighted convolution from 1 to 5°, i.e., wider than the GOME across-track width at moderate latitudes. Thereby it is ensured that a grid pixel usually contains multiple satellite pixels and that also adjacent grid pixels are not empty (as would be the case for a 1° grid), which is the prerequisite for the calculation of w_{TR} .

We have applied STREAM to GOME data as provided by TEMIS. The resulting TRs are again compared to the sim-

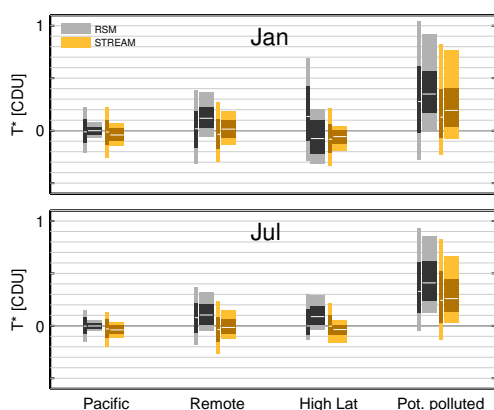


Figure 16. Regional statistics of GOME tropospheric residues T^* from different algorithms for January (top) and July (bottom) 1999. Conventions as in Fig. 6.

ple RSM. Figure 16 displays the regional TR statistics for GOME in January and July 1999. The respective maps are provided in the Supplement (Fig. S34).

Overall, STREAM yields reasonable results for GOME as well. However, some systematic biases are observed:

- over the Pacific, TRs from STREAM were found to be negative, which can only be explained when the measured columns for cloudy pixels are higher than for cloud-free pixels;
- over potentially polluted regions, T^* from STREAM is systematically lower than from RSM (by 0.2 CDU in July). This might be a consequence of the applied cloud weight, which has obviously different effects on GOME than on OMI.

This explanation would be consistent with previous findings: while Leue et al. (2001) base the STS on cloudy pixels, Wenig et al. (2004) switched the Heidelberg STS to cloud-free pixels after noticing that GOME columns are higher instead of lower over clouds. Wenig et al. (2004) relate this to the contribution of lightning NO_x. However, as (a) the impact of lightning NO_x on satellite observations is generally small (Beirle et al., 2010b) and (b) lightning activity over the remote Pacific used for the RSM is very weak, we rather suspect that a different effect is responsible for this finding, most probably related to the specific instrumental features of GOME (Burrows et al., 1999), in particular the dichroic mirrors causing polarization dependent spectral structures. It might thus be worth re-checking the DOAS analysis of NO₂ for GOME for spectral interferences related to clouds. A second possible effect, which might in particular contribute to the large discrepancy over polluted regions, is that cloud properties are averaged over the large GOME ground pixel; i.e., in an extreme case, low and high cloud layers, which would both be skipped in w_{cld} if resolved by the satellite pixel, might yield, on average, an effective cloud height

with a high w_{cld} . Any tropospheric pollution within (or directly above) the low cloud layer would then bias high the stratospheric estimate and bias low the TR.

5.5 Future instruments

5.5.1 TROPOMI

TROPOMI (Veefkind et al., 2012) on S5p will be launched in 2016. Instrumental setup and spatial coverage are similar to OMI, but TROPOMI will provide a better spatial resolution of $7 \times 7 \text{ km}^2$ at nadir.

STREAM was developed as a verification algorithm for TROPOMI STS and was tested and compared to the TROPOMI prototype algorithm based on OMI measurements (see above). Though no TROPOMI measurements are available yet, it can be expected that the performance of STREAM on TROPOMI will be even better than for OMI, because, due to the better spatial resolution, more individual satellite pixels are available and among them a higher fraction of clouded pixels. Thus, more sampling points over potentially polluted regions will be available, further decreasing interpolation errors.

5.5.2 Sentinel 4 (S4)

The satellite instruments investigated so far are all operated in low, sun-synchronous orbits, providing global coverage at fixed local time. In the near future, a new generation of spectrometers on geostationary orbits will be launched by different space agencies. Over Europe, S4 (Ingmann et al., 2012) will be the first mission providing a spectral resolving UV/vis instrument on a geostationary satellite. The spatial coverage is focussed on Europe. Thus, no “clean” reference regions are regularly available. STREAM might overcome this problem by using clouded observations where the tropospheric pollution is effectively shielded.

We simply evaluate the expected performance of STREAM on S4 measurements by clipping OMI measurements to the area covered by S4 (as given in Courrèges-Lacoste et al., 2010). The STREAM settings are identical to v0.92, except for the a priori removal of the overall latitude dependency in the reference sector, as no Pacific measurements are available for S4. Figure 17 displays the resulting TR (top) and the difference of TR between clipped and global OMI data (bottom) for January 2005.

Though tropospheric pollution over Europe and the Middle East is evident, i.e., an extended clean reference region is actually not available, STREAM is still capable of yielding an accurate stratospheric estimate. Only at the northern and southern borders are systematic biases observed, which can be caused by the overall latitudinal dependency of the stratospheric VCD and border effects of the weighted convolution and can probably be reduced by dedicated optimization of the algorithm for S4.

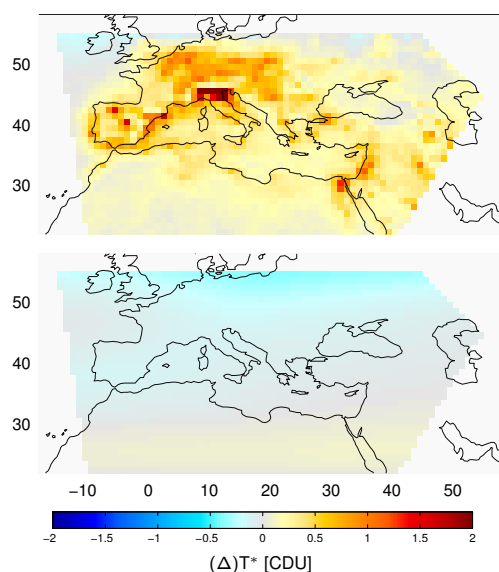


Figure 17. Performance of STREAM on “S4 data” (i.e., OMI measurements clipped to the area covered by S4) for January 2005. The top panel displays the resulting TR, the bottom panel shows the difference to the TR resulting from full OMI data as shown in Fig. 5. The area covered by S4 in winter has been taken from Courrèges-Lacoste et al. (2010).

Situation will probably be improved for real S4 measurements due to the higher number of clouded pixels in S4 compared to OMI. Thus, this first check is highly encouraging to further investigate the applicability of STREAM to S4 and possible improvements.

5.6 Advantages and limitations of STREAM

STREAM was successfully applied to various satellite measurements with a wide range of spatial resolution and coverage. STREAM is an MRSM and does not need any model input. It can thus be considered as a complementary approach to data assimilation, as chosen for the TROPOMI prototype algorithm.

As (M)RSMs usually estimate the stratospheric column based on total column measurements over clean regions, they generally miss the (small) tropospheric background of the order of some 0.1 CDU. Several (M)RSMs explicitly correct for this effect based on a priori tropospheric background columns (Martin et al., 2002; Valks et al., 2011; Bucseles et al., 2013). In case of STREAM, however, cloudy pixels, which allow a direct measurement of the actual stratospheric column (except for the small tropospheric column above the cloud), are emphasized. Thus, an additional tropospheric background correction should be unnecessary. Accordingly, in case of OMI, TRs from STREAM are about 0.1 CDU over clean regions, similar as for TRs from DOMINO and NASA. This is close to the a priori value chosen by Valks et al. (2011) but below the values given in Martin et al. (2002)

(about 0.15–0.3 CDU, assuming a tropospheric AMF of 2) and Hilboll et al. (2013) (0.1 up to >0.6 CDU⁶).

In case of other satellite instruments, however, the TR over the Pacific was found to be lower (GOME-2 and SCIAMACHY) or even negative (GOME-1). The latter can only be explained by cloudy measurements being systematically higher than cloud-free measurements. Further investigations are needed to infer this discrepancy between OMI and GOME-1/2/SCIAMACHY and find how it is related to differences in the cloud products and/or the spectral analysis of NO₂.

STREAM assumes stratospheric NO₂ fields having low zonal variability, in particular at low latitudes. This is reflected by the choice of a wide convolution kernel at the equator. STREAM is thus not capable of resolving diurnal small-scale patterns caused by stratospheric dynamics. These patterns, however, largely cancel out in monthly means.

Whenever actual stratospheric fields do not match the a priori assumption of zonal smoothness, e.g., in case of “tilted” structures or actual large-scale zonal gradients like differences in the stratospheric column over Pacific and Indian ocean, the TR resulting from STREAM can show artificial “stripes”. Further investigations might lead to additional sophisticated algorithm steps to remove these artifacts. However, it has to be taken care that the benefit really outbalances the drawbacks (added complexity) and that no other artifacts/biases are introduced.

The dependencies of TR on STREAM parameter settings have been found to be low ($\lesssim 0.1$ CDU). The application of STREAM on synthetic data results in deviations to the a priori truth of the same order. These deviations are systematic, i.e., the stratospheric patterns estimated by STREAM are slightly biased high, which can be expected, as they are based on total column measurements, which are always higher than the stratospheric column.

Overall, STREAM uncertainty is well within the general uncertainties of STS (see next section). Note that systematic changes of the NO₂ columns of the same order of 0.1 CDU can also result from changes of the settings for the DOAS analysis, like fit interval, inclusion of additional absorbers in the analysis, or the treatment of rotational and vibrational Raman scattering, creating overall biases as well as spatial patterns, e.g., over oligotrophic oceans (E. Peters, personal communication, 2016).

5.7 General uncertainties and challenges of stratosphere–troposphere separation

The uncertainty of STS can often not be directly quantified, as the “true” stratospheric 4-D concentration fields are not known. One approach to assess the STS performance is the

⁶Note, however, that the high values are only reported at higher latitudes in winter, when the ratio $A_{\text{strat}}/A_{\text{trop}}$ is almost 2 (Fig. S1); thus the large discrepancy is at least partly resolved when the TR is transferred in a TVCD via Eq. (4).

usage of synthetic data, as in Sect. 4.3. In addition, the TR can be used to evaluate the plausibility of the stratospheric estimate and to derive realistic uncertainties:

- Negative TRs are nonphysical. Thus, the occurrence of on average negative T^* (exceeding the values/frequencies explainable by noise) clearly indicates a positive bias of the estimated stratosphere.
- Tropospheric background columns over regions free of NO_x sources are expected to have low spatiotemporal variability. Thus, the observed variability of T^* over clean regions serves as proxy of the uncertainty (precision) of the STS. From different algorithms (MRSMs as well as model-based methods), typical variabilities of T^* over remote regions are about 0.5 CDU for daily means and about 0.2–0.3 CDU for monthly means. For a simple RSM, much higher values (≈ 1 CDU) are found at high latitudes.

Systematic biases (accuracy) of STS can be estimated from the intercomparison of TRs from different algorithms. Figure 18 displays the standard deviation of monthly mean TR from the algorithms shown in Fig. 8 and discussed in Sect. 5.1, i.e., two different, independent MRSM approaches (STREAM and NASA) as well as two STS based on models, a simple one (STSEMAC) and a complex data assimilation setup (DOMINO). Note that the upper range of the color bar was lowered to 0.3 CDU.

Overall, the standard deviation of TR from different STS is low (typically <0.1 CDU and below <0.2 CDU for most parts of the world). It is thus consistent with the uncertainty estimates of stratospheric columns given in literature (Boersma et al. (2011): 0.15–0.25 CDU (SCD); Valks et al. (2011): 0.15–0.3 CDU (VCD); Bucsela et al. (2013): 0.2 CDU (VCD)) and with the magnitude of systematic deviations found in the study on synthetic data (Sect. 4.3).

With respect to the final NO₂ TVCD product, which is higher than TR by the ratio of stratospheric and tropospheric AMFs (Eq. 4), uncertainties of this order are completely negligible over polluted regions such as the US east coast, central Europe, or eastern China. Nonetheless, a regional bias >0.2 CDU (e.g., over Russia in January) can contribute significantly to the relative uncertainty of TVCDs aside the pollution hotspots. Thus, the uncertainty of STS has to be kept in mind in studies focusing on NO_x emissions from, e.g., biomass burning or soil emissions over regions like Siberia, the Sahel, or Australia.

5.8 Other trace gases

STREAM was developed as STS algorithm for NO₂. However, several other trace gas satellite retrievals face problems which are similar to STS from an algorithmic point of view, i.e., that a small-scale tropospheric signal has to be separated from a smooth background (e.g., caused by stratospheric

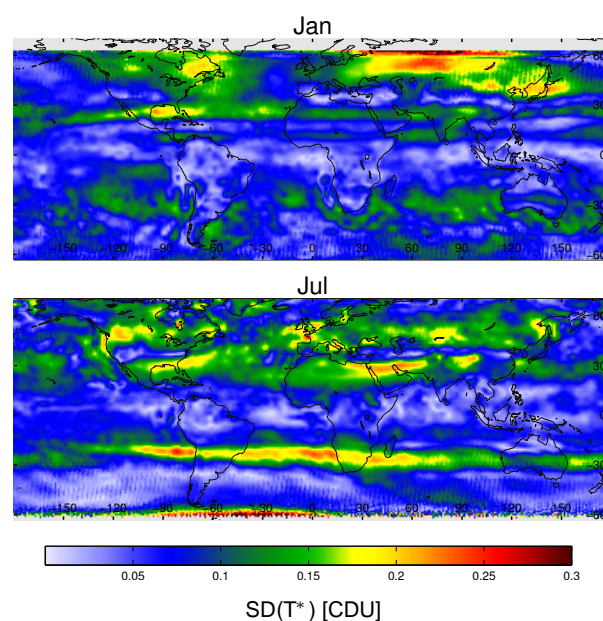


Figure 18. Standard deviation of monthly mean T^* from different algorithms (STREAM, DOMINO, NASA, and STSEMAC) for January (top) and July (bottom) 2005 (OMI).

columns or, in particular in case of trace gases with low optical depth, shortcomings of the spectral analysis, introducing artificial dependencies on, for example, SZA or ozone columns). Thus, the concept of weighted convolution could be used within the satellite retrievals of, for example, SO₂, BrO, HCHO, or CHOCHO, with appropriately chosen and optimized weighting factors.

6 Conclusions

The separation of the stratospheric and tropospheric column is a key step in the retrieval of NO₂ TVCDs from total column satellite measurements. As coincident direct measurements of the stratospheric column are usually not available (except for SCIAMACHY), current STS algorithms either use CTMs (directly or via data assimilation) or follow a modified reference sector method (MRSM) approach, where the stratospheric columns are basically estimated from total column measurements over clean regions.

We have developed the MRSM STREAM. Weighting factors determine how far individual satellite pixels contribute to the stratospheric estimate. Over potentially polluted regions (according to an NO₂ climatology), weights are lowered, whereas measurements over mid-altitude clouds are assigned with a high weighting factor. Global stratospheric fields are derived by weighted convolution and subtracted from total columns to yield tropospheric residues (TRs). In a second iteration, weighting factors are modified based on the TR: high TR indicates tropospheric pollution, and the respective satel-

lite pixels are assigned with a lower weight. For systematically negative TR, however, weighting factors are increased. The concept of multiplicative weights can easily be extended by additional factors, e.g., based on fire counts in order to explicitly exclude biomass burning events.

STREAM results are robust with respect to variations of the algorithm settings and parameters. With the baseline settings, the errors of STREAM on a synthetic data set have been found to be below 0.1 CDU on average.

STREAM was successfully applied to satellite measurements from GOME 1/2, SCIAMACHY, and OMI. The resulting TRs over clean regions and their variability have been found to be low. However, systematic “stripes” can appear in STREAM TR when the basic assumption that the stratospheric column varies smoothly with longitude is not fulfilled, e.g., in case of “tilted” stratospheric patterns.

The emphasis of clouded observations, which provide a direct measurement of the stratospheric rather than the total column, should supersede an additional correction for the tropospheric background, which successfully worked for OMI but less so for GOME and SCIAMACHY. This might be related to differences in pixel size or local overpass time, both potentially affecting cloud statistics, or differences in the cloud algorithms. However, the detailed reasons are not yet fully understood and require further investigations.

STREAM, which was developed as TROPOMI verification algorithm, was optimized for OMI measurements. Within an O3M SAF visiting scientist project, it was also applied to GOME-2, and STREAM is foreseen to be implemented in an upcoming GDP update.

Results from STREAM were compared to the TROPOMI prototype algorithm, as represented by the DOMINO v2 product, in which STS is implemented by data assimilation. Differences between monthly mean TRs from STREAM and DOMINO are found to be low (almost 0 on average with regional patterns up to about ± 0.1 – 0.2 CDU). A comparison to other state-of-the-art STS schemes yields deviations of similar order.

The impact of STS is thus generally negligible for TVCDs over heavily polluted regions. However, the remaining uncertainties still contribute significantly to the total error of TVCDs over moderately polluted regions and have to be kept in mind for emission estimates of area sources of NO_x such as soil emissions or biomass burning.

7 Data availability

STREAM has been tested on NO₂ retrievals from different satellite instruments as listed in Table 1. The input data sets are publicly accessible; the respective links to the data sets are included in the references provided in Table 1.

Information about the Supplement

Additional images, tables, and text are provided in the Supplement. All references to tables and figures in the Supplement are indicated by a prefix “S”. For readability, the Supplement is structured analogously to the paper; i.e., additional material to Sect. 2.3 can be found in Sect. S2.3 of the Supplement.

The Supplement related to this article is available online at doi:10.5194/amt-9-2753-2016-supplement.

Acknowledgements. We would like to thank the agencies providing the satellite data: The OMI OMNO2 product is archived and distributed from the Goddard Earth Sciences Data & Information Services center (NASA). We acknowledge the free use of GOME and OMI (DOMINO) level 2 data from www.temis.nl. GOME-2 GDP 4.7 level 2 data is provided by DLR within the framework of EUMETSAT’s O3M SAF. SCIAMACHY level1 data is provided by ESA.

This study was supported by the following projects: Within TROPOMI verification, funding was provided by DLR Bonn under contract 50EE1247 for the development of STREAM and the comparison to the TROPOMI prototype algorithm. Within an O3M SAF visiting scientist project, STREAM was adopted to GOME-2 and compared to the current GDP 4.7 data product. Steffen Beirle acknowledges funding from the FP7 Project Quality Assurance for Essential Climate Variables (QA4ECV), no. 607405.

We acknowledge fruitful discussions with and valuable feedback from many colleagues, in particular during the TROPOMI verification and QA4ECV meetings, especially Andreas Richter, Andreas Hilboll (both IUP Bremen, Germany), Folkert Boersma, and Henk Eskes (both KNMI De Bilt, the Netherlands). Andreas Stohl (NILU, Kjeller, Norway) is acknowledged for discussions on NO₂ transport.

The article processing charges for this open-access publication were covered by the Max Planck Society.

Edited by: B. Veihelmann

References

- Beirle, S., Platt, U., Wenig, M., and Wagner, T.: Weekly cycle of NO₂ by GOME measurements: a signature of anthropogenic sources, *Atmos. Chem. Phys.*, 3, 2225–2232, doi:10.5194/acp-3-2225-2003, 2003.
- Beirle, S., Spichtinger, N., Stohl, A., Cummins, K. L., Turner, T., Boccippio, D., Cooper, O. R., Wenig, M., Grzegorski, M., Platt, U., and Wagner, T.: Estimating the NO_x produced by lightning from GOME and NLDN data: a case study in the Gulf of Mexico, *Atmos. Chem. Phys.*, 6, 1075–1089, doi:10.5194/acp-6-1075-2006, 2006.

- Beirle, S., Köhl, S., Pukite, J., and Wagner, T.: Retrieval of tropospheric column densities of NO₂ from combined SCIAMACHY nadir/limb measurements, *Atmos. Meas. Tech.*, 3, 283–299, doi:10.5194/amt-3-283-2010, 2010a.
- Beirle, S., Huntrieser, H., and Wagner, T.: Direct satellite observation of lightning-produced NO_x, *Atmos. Chem. Phys.*, 10, 10965–10986, doi:10.5194/acp-10-10965-2010, 2010b.
- Beirle, S. and Wagner, T.: Tropospheric vertical column densities of NO₂ from SCIAMACHY, available at: http://www.sciamachy.org/products/NO2/NO2tc_v1_0_MPL_AD.pdf (last access: 17 June 2016), 2012 (data available at: <http://www.sciamachy.org/products/index.php?species=NO2>).
- Belmonte Rivas, M., Veefkind, P., Boersma, F., Levelt, P., Eskes, H., and Gille, J.: Intercomparison of daytime stratospheric NO₂ satellite retrievals and model simulations, *Atmos. Meas. Tech.*, 7, 2203–2225, doi:10.5194/amt-7-2203-2014, 2014.
- Boersma, K., Eskes, H., and Brinksma, E.: Error analysis for tropospheric NO₂ retrieval from space, *J. Geophys. Res.-Atmos.*, 109, D04311, doi:10.1029/2003JD003962, 2004.
- Boersma, K. and Eskes, H.: Assimilated SCIAMACHY NO₂ fields: HDF data file user manual, available at: http://www.temis.nl/airpollution/no2col/papers/no2col_hdf_docu.pdf (last access: 17 June 2016), 2004 (data available at: <http://www.temis.nl/airpollution/no2col/no2colgome.php>).
- Boersma, K. F., Eskes, H. J., Veefkind, J. P., Brinksma, E. J., van der A, R. J., Sneep, M., van den Oord, G. H. J., Levelt, P. F., Stammes, P., Gleason, J. F., and Bucsela, E. J.: Near-real time retrieval of tropospheric NO₂ from OMI, *Atmos. Chem. Phys.*, 7, 2103–2118, doi:10.5194/acp-7-2103-2007, 2007.
- Boersma, K. F., Eskes, H. J., Dirksen, R. J., van der A, R. J., Veefkind, J. P., Stammes, P., Huijnen, V., Kleipool, Q. L., Sneep, M., Claas, J., Leitão, J., Richter, A., Zhou, Y., and Brunner, D.: An improved tropospheric NO₂ column retrieval algorithm for the Ozone Monitoring Instrument, *Atmos. Meas. Tech.*, 4, 1905–1928, doi:10.5194/amt-4-1905-2011, 2011 (data available at: http://www.temis.nl/airpollution/no2col/no2regioomi_v2.php).
- Bovensmann, H., Burrows, J., Buchwitz, M., Frerick, J., Noel, S., Rozanov, V., Chance, K., and Goede, A.: SCIAMACHY: Mission objectives and measurement modes, *J. Atmos. Sci.*, 56, 127–150, 1999.
- Bucsela, E. J., Celarier, E. A., Wenig, M. O., Gleason, J. F., Veefkind, J. P., Boersma, K. F., and Brinksma, E. J.: Algorithm for NO₂ vertical column retrieval from the ozone monitoring instrument, *IEEE T. Geosci. Remote*, 44(5), 1245–1258, doi:10.1109/TGRS.2005.863715, 2006.
- Bucsela, E. J., Krotkov, N. A., Celarier, E. A., Lamsal, L. N., Swartz, W. H., Bhartia, P. K., Boersma, K. F., Veefkind, J. P., Gleason, J. F., and Pickering, K. E.: A new stratospheric and tropospheric NO₂ retrieval algorithm for nadir-viewing satellite instruments: applications to OMI, *Atmos. Meas. Tech.*, 6, 2607–2626, doi:10.5194/amt-6-2607-2013, 2013 (data available at: http://mirador.gsfc.nasa.gov/collections/OMNO2_003.shtml).
- Burrows, J. P., Weber, M., Buchwitz, M., Rozanov, V., Ladstätter-Weißmayer, A., Richter, A., DeBeek, R., Hoogen, R., Bramstedt, K., Eichmann, K. U., and Eisinger, M.: The global ozone monitoring experiment (GOME): Mission concept and first scientific results, *J. Atmos. Sci.*, 56, 151–175, doi:10.1175/1520-0469(1999)056<0151:TGOMEG>2.0.CO;2, 1999.
- Callies, J., Corpaccioli, E., Eisinger, M., Hahne, A., and Lefebvre, A.: GOME-2 - Metop's second-generation sensor for operational ozone monitoring, *ESA Bull.-Eur. Space Agency*, 102, 28–36, 2000.
- Courrèges-Lacoste, G. B., Ahlers, B., Guldemann, B., Short, A., Veihelmann, B., Stark, H.: The Sentinel-4/UVN instrument on-board MTG-S, available at: https://www.eumetsat.int/cs/idcplg?IdcService=GET_FILE&dDocName=pdf_conf_p59_s1_01_bazalget_p&allowInterrupt=1&noSaveAs=1&RevisionSelectionMethod=LatestReleased (last access: 17 June 2016), 2010.
- Dee, D. P., Uppala, S. M., Simmons, A. J., Berrisford, P., Poli, P., Kobayashi, S., Andrae, U., Balmaseda, M. A., Balsamo, G., Bauer, P., Bechtold, P., Beljaars, A. C. M., van de Berg, L., Bidlot, J., Bormann, N., Delsol, C., Dragani, R., Fuentes, M., Geer, A. J., Haimberger, L., Healy, S. B., Hersbach, H., Hólm, E. V., Isaksen, I., Kållberg, P., Köhler, M., Matricardi, M., McNally, A. P., Monge-Sanz, B. M., Morcrette, J.-J., Park, B.-K., Peubey, C., de Rosnay, P., Tavolato, C., Thépaut, J.-N., and Vitart, F.: The ERA-Interim reanalysis: configuration and performance of the data assimilation system, *Q. J. Roy. Meteor. Soc.*, 137, 553–597, doi:10.1002/qj.828, 2011.
- Dirksen, R. J., Boersma, K. F., Eskes, H. J., Ionov, D. V., Bucsela, E. J., Levelt, P. F., and Kelder, H. M.: Evaluation of stratospheric NO₂ retrieved from the Ozone Monitoring Instrument: Intercomparison, diurnal cycle, and trending, *J. Geophys. Res.-Atmos.*, 116, D08305, doi:10.1029/2010JD014943, 2011.
- Ebojje, F., von Savigny, C., Ladstätter-Weißmayer, A., Rozanov, A., Weber, M., Eichmann, K.-U., Bötzel, S., Rahpoe, N., Bovensmann, H., and Burrows, J. P.: Tropospheric column amount of ozone retrieved from SCIAMACHY limb-nadir-matching observations, *Atmos. Meas. Tech.*, 7, 2073–2096, doi:10.5194/amt-7-2073-2014, 2014.
- Eskes, H. J., Velthoven, P. F. J. V., Valks, P. J. M., and Kelder, H. M.: Assimilation of GOME total-ozone satellite observations in a three-dimensional tracer-transport model, *Q. J. Roy. Meteor. Soc.*, 129, 1663–1681, doi:10.1256/qj.02.14, 2003.
- Espanak, F., and Anderson, J.: Annular and Total Solar Eclipses of 2010, NASA/TP-2008-214171, available at: <http://eclipse.gsfc.nasa.gov/SEpubs/2010/TP214171a.pdf> (last access: 17 June 2016), 2008.
- Hilboll, A., Richter, A., Rozanov, A., Hodnebrog, Ø., Heckel, A., Solberg, S., Stordal, F., and Burrows, J. P.: Improvements to the retrieval of tropospheric NO₂ from satellite – stratospheric correction using SCIAMACHY limb/nadir matching and comparison to Oslo CTM2 simulations, *Atmos. Meas. Tech.*, 6, 565–584, doi:10.5194/amt-6-565-2013, 2013.
- Ingmann, P., B. Veihelmann, A.G. Straume, Y. Meijer, The status of implementation of the atmospheric composition related GMES missions Sentinel-4/Sentinel-5 and Sentinel-5p, Proceedings of the 2012 EUMETSAT Meteorological Satellite Conference, Sopot, Poland, 3–7 September 2012.
- Jöckel, P., Tost, H., Pozzer, A., Brühl, C., Buchholz, J., Ganzeveld, L., Hoor, P., Kerkweg, A., Lawrence, M. G., Sander, R., Steil, B., Stiller, G., Tanarhte, M., Taraborrelli, D., van Aardenne, J., and Lelieveld, J.: The atmospheric chemistry general circulation model ECHAM5/MESy1: consistent simulation of ozone from the surface to the mesosphere, *Atmos. Chem. Phys.*, 6, 5067–5104, doi:10.5194/acp-6-5067-2006, 2006.

- Jöckel, P., Kerkweg, A., Pozzer, A., Sander, R., Tost, H., Riede, H., Baumgaertner, A., Gromov, S., and Kern, B.: Development cycle 2 of the Modular Earth Submodel System (MESSy2), *Geosci. Model Dev.*, 3, 717–752, doi:10.5194/gmd-3-717-2010, 2010.
- Jöckel, P., Tost, H., Pozzer, A., Kunze, M., Kirner, O., Brenninkmeijer, C. A. M., Brinkop, S., Cai, D. S., Dyroff, C., Eckstein, J., Frank, F., Garny, H., Gottschaldt, K.-D., Graf, P., Grewe, V., Kerkweg, A., Kern, B., Matthes, S., Mertens, M., Meul, S., Neu-maier, M., Nützel, M., Oberländer-Hayn, S., Ruhnke, R., Runde, T., Sander, R., Scharffe, D., and Zahn, A.: Earth System Chemistry integrated Modelling (ESCI-Mo) with the Modular Earth Submodel System (MESSy) version 2.51, *Geosci. Model Dev.*, 9, 1153–1200, doi:10.5194/gmd-9-1153-2016, 2016.
- Knutsson, H., and Westin, C.-F.: Normalized and differential convolution, in Proceedings of Computer Society Conference on Computer Vision and Pattern Recognition (CVPR), IEEE, 515–523, doi:10.1109/CVPR.1993.341081, 1993.
- Kühl, S., J. Pukite, T. Deutschmann, U. Platt, and T. Wagner: SCIAMACHY limb measurements of NO₂, BrO and OClO. Retrieval of vertical profiles: Algorithm, first results, sensitivity and comparison studies, *Adv. Space Res.*, 42, 1747–1764, 2008.
- Leue, C., Wenig, M., Wagner, T., Klimm, O., Platt, U., and Jähne, B.: Quantitative analysis of NO_x emissions from Global Ozone Monitoring Experiment satellite image sequences, *J. Geophys. Res.*, 106, 5493–5505, 2001.
- Levelt, P., Van den Oord, G., Dobber, M., Malkki, A., Visser, H., de Vries, J., Stammes, P., Lundell, J., and Saari, H.: The Ozone Monitoring Instrument, *IEEE T. Geosci. Remote*, 44, 1093–1101, doi:10.1109/TGRS.2006.872333, 2006.
- Marchenko, S., Krotkov, N. A., Lamsal, L. N., Celarier, E. A., Swartz, W. H., and Bucsel, E. J.: Revising the slant column density retrieval of nitrogen dioxide observed by the Ozone Monitoring Instrument, *J. Geophys. Res.-Atmos.*, 120, 5670–5692, doi:10.1002/2014JD022913, 2015.
- Martin, R., Chance, K., Jacob, D., Kurosu, T., Spurr, R., Bucsel, E., Gleason, J., Palmer, P., Bey, I., Fiore, A., Li, Q., Yantosca, R., and Koelemeijer, R.: An improved retrieval of tropospheric nitrogen dioxide from GOME, *J. Geophys. Res.-Atmos.*, 107, 4437, doi:10.1029/2001JD001027, 2002.
- Martin, R. V.: Satellite remote sensing of surface air quality, *Atmos. Environ.*, 42, 7823–7843, 2008.
- Monks, P. S. and Beirle, S.: Applications of Satellite Observations of Tropospheric Composition, in *The Remote Sensing of Tropospheric Composition from Space*, 365–449, Springer-Verlag Berlin Heidelberg, 2011.
- Platt, U. and Stutz, J.: *Differential Optical Absorption Spectroscopy*, Springer-Verlag Berlin Heidelberg, ISBN-13: 978-3-540-21193-8, 2008.
- Richter, A. and Burrows, J. P.: Tropospheric NO₂ from GOME Measurements, *Adv. Space Res.*, 29, 1673–1683, 2002.
- Richter, A., Burrows, J. P., Nusz, H., Granier, C., and Niemeier, U.: Increase in tropospheric nitrogen dioxide over China observed from space, *Nature*, 437, 129–132, doi:10.1038/nature04092, 2005.
- Roeckner, E., Brokopf, R., Esch, M., Giorgetta, M., Hagemann, S., Kornbluh, L., Manzini, E., Schlese, U., and Schulzweida, U.: Sensitivity of simulated climate to horizontal and vertical resolution in the ECHAM5 atmosphere model, *J. Clim.*, 19, 3771–3791, doi:10.1175/JCLI3824.1, 2006.
- Sierk, B., Richter, A., Rozanov, A., von Savigny, Ch., Schmoltner, A. M., Buchwitz, M., Bovensmann, H., and Burrows, J. P.: Retrieval and monitoring of atmospheric trace gas concentrations in nadir and limb geometry using the space-borne SCIAMACHY instrument, *Environ. Monit. Assess.*, 120, 65–77, doi:10.1007/s10661-005-9049-9, 2006.
- Sioris, C. E., Kurosu, T. P., Martin, R. V., and Chance, K.: Stratospheric and tropospheric NO₂ observed by SCIAMACHY: first results, *Adv. Space Res.*, 34, 780–785, 2004.
- Stohl, A., Huntrieser, H., Richter, A., Beirle, S., Cooper, O. R., Eckhardt, S., Forster, C., James, P., Spichtinger, N., Wenig, M., Wagner, T., Burrows, J. P., and Platt, U.: Rapid intercontinental air pollution transport associated with a meteorological bomb, *Atmos. Chem. Phys.*, 3, 969–985, doi:10.5194/acp-3-969-2003, 2003.
- Valks, P., Pinardi, G., Richter, A., Lambert, J.-C., Hao, N., Loyola, D., Van Roozendaal, M., and Emmadi, S.: Operational total and tropospheric NO₂ column retrieval for GOME-2, *Atmos. Meas. Tech.*, 4, 1491–1514, doi:10.5194/amt-4-1491-2011, 2011.
- Valks, P., Loyola, D., Hao, N., Hedelt, P., Slijkhuys, S., and Grossi, M.: Algorithm Theoretical Basis Document for GOME-2 Total Column Products of Ozone, NO₂, BrO, SO₂, H₂O, HCHO, and Cloud Properties, DLR/GOME-2/ATBD/01, Issue 3/A, available at: <https://atmos.eoc.dlr.de/gome2/documentation.html> (last access: 17 June 2016), 2015 (data available at: <http://atmos.eoc.dlr.de/gome/product.html>).
- van Geffen, J. H. G. M., Boersma K. F., Eskes, H. J., Maasackers, J. D., and Veefkind, J.P.: TROPOMI ATBD of the total and tropospheric NO₂ data products, Reports S5P-KNMI-L2-0005-RP version 0.11.0, 2 October 2014, KNMI, De Bilt, the Netherlands, 2014.
- van Geffen, J. H. G. M., Boersma, K. F., Van Roozendaal, M., Hendrick, F., Mahieu, E., De Smedt, I., Sneep, M., and Veefkind, J. P.: Improved spectral fitting of nitrogen dioxide from OMI in the 405–465 nm window, *Atmos. Meas. Tech.*, 8, 1685–1699, doi:10.5194/amt-8-1685-2015, 2015.
- Veefkind, J. P., Aben, I., McMullan, K., Förster, H., de Vries, J., Otter, G., Claas, J., Eskes, H. J., de Haan, J. F., Kleipool, Q., van Weele, M., Hasekamp, O., Hoogeveen, R., Landgraf, J., Snel, R., Tol, P., Ingmann, P., Voors, R., Kruizinga, B., Vink, R., Visser, H., and Levelt, P. F.: TROPOMI on the ESA Sentinel-5 Precursor: A GMES mission for global observations of the atmospheric composition for climate, air quality and ozone layer applications, *Remote Sens. Environ.*, 120, 70–83, doi:10.1016/j.rse.2011.09.027, 2012.
- Wenig, M., Kühl, S., Beirle, S., Bucsel, E., Jähne, B., Platt, U., Gleason, J., and Wagner, T.: Retrieval and analysis of stratospheric NO₂ from the Global Ozone Monitoring Experiment, *J. Geophys. Res.*, 109, D04315, doi:10.1029/2003JD003652, 2004.
- Zien, A. W., Richter, A., Hilboll, A., Blechschmidt, A.-M., and Burrows, J. P.: Systematic analysis of tropospheric NO₂ long-range transport events detected in GOME-2 satellite data, *Atmos. Chem. Phys.*, 14, 7367–7396, doi:10.5194/acp-14-7367-2014, 2014.

Supplement of Atmos. Meas. Tech., 9, 2753–2779, 2016
<http://www.atmos-meas-tech.net/9/2753/2016/>
doi:10.5194/amt-9-2753-2016-supplement
© Author(s) 2016. CC Attribution 3.0 License.



Atmospheric
Measurement
Techniques

Open Access



Supplement of

**The STRatospheric Estimation Algorithm from Mainz (STREAM):
estimating stratospheric NO₂ from nadir-viewing satellites
by weighted convolution**

S. Beirle et al.

Correspondence to: Steffen Beirle (steffen.beirle@mpic.de)

The copyright of individual parts of the supplement might differ from the CC-BY 3.0 licence.

S1. Supplementary material

This document provides additional images, tables, and text. All references to tables and figures in the main manuscript are given in plain numbers, while tables and figures in the supplement are indicated by a prefix “S”. The supplement is structured analogously to the manuscript. I.e., additional material to section 2.3 can be found in section S2.3 of the supplement.

S2. Methods

S2.1 Terminology

Abbreviations are defined in the main manuscript (Table 2). All column densities are given in column density units of 1 CDU=10¹⁵ molec cm⁻².

STS performance is analyzed based on tropospheric residues (TR) (Eq. 1); tropospheric VCDs are generally higher than TR by the ratio $A_{\text{strat}}/A_{\text{trop}}$. Figure S1 displays the monthly mean of this ratio of AMFs, as provided in the NASA product, for cloud free conditions.

Within the discussion of the MPI-C STS for SCIAMACHY based on LNM (Beirle et al., 2010), tropospheric SCDs (TSCDs) have been analyzed. For OMI, however, viewing angle dependencies would dominate daily maps of TSCDs due to the far larger range of viewing angles of OMI compared to SCIAMACHY. In this study, we thus focus on TR, i.e. we applied stratospheric AMFs in order to eliminate the viewing angle dependencies of TSCDs.

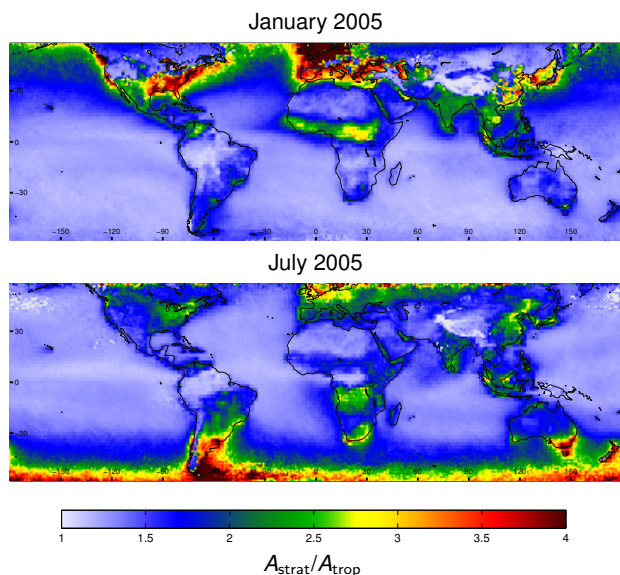


Fig. S 1. Ratio of monthly mean stratospheric and tropospheric AMFs as provided by NASA for cloud free observations (CRF<0.3) for January (top) and July (bottom) 2005. On average, cloud free TVCDs are higher than TRs by this ratio (Eq. 2).

S2.2 Weighting factors

S2.2.1 Pollution weight

If the stratospheric NO₂ is estimated from total column density measurements, regions with tropospheric pollution have to be excluded. Thus, we assign potentially polluted satellite pixels a pollution weight $w_{\text{pol}} < 1$ based on our a-priori knowledge of tropospheric NO₂. For this purpose we use a climatology of tropospheric NO₂ column densities from SCIAMACHY measurements 2003-2011 (Beirle and Wagner, 2012) shown in Fig. S2a. So far, no seasonality of NO₂ is considered in the definition of P . This could be added to a future version, but the impact on STREAM is expected to be low (compare section 4.2.6).

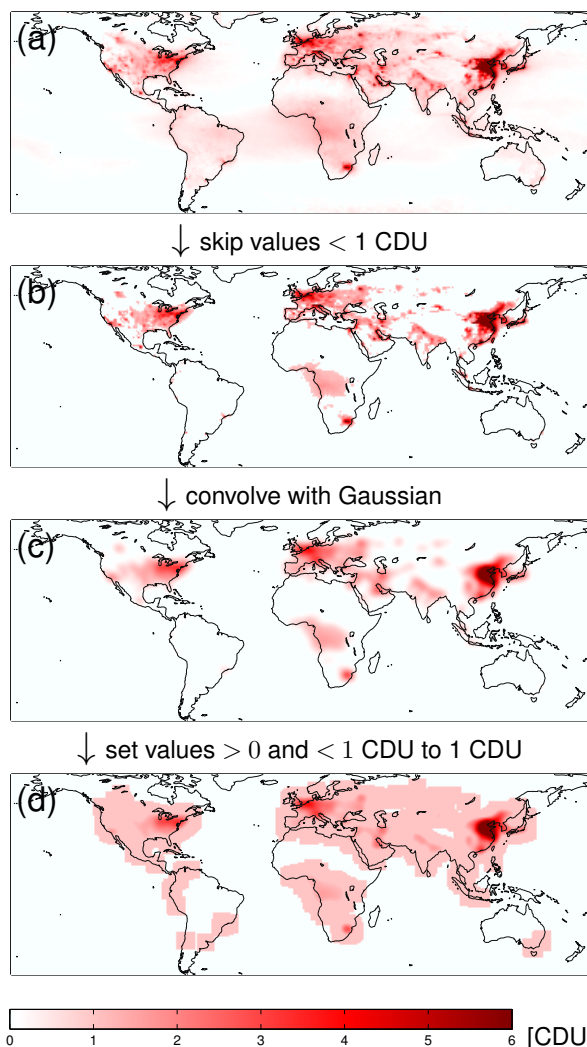


Fig. S 2. Stages of the calculation of the pollution proxy P : The tropospheric NO₂ climatology (a) is clipped to values >1 CDU (b), convolved with a Gaussian (c), and extended in space by setting values between 0 and 1 CDU to a minimum of 1 CDU (d).

Pollution weights are defined based on a pollution proxy which is derived from the NO₂ climatology by the following steps:

1. Grid pixels with a mean TVCD below 1 CDU are removed (Fig. S2b).
2. The resulting clipped climatology is smoothed by convolution with a 2D-Gaussian with $\sigma = 2^\circ$ (Fig. S2c).
3. For the pollution proxy P , values between 0 and 1 CDU are set to 1 CDU. By this operation, a “safety margin” of *potentially* polluted areas is created (Fig. S2d).

Note that due to steps 2&3, the initial spatial resolution of SCIAMACHY is fully sufficient for the definition of P (and thus w_{pol}) even for applications of STREAM to instruments with better spatially resolution.

S2.3 Weighted convolution

We illustrate the procedure of weighted convolution, as explained in Section 2.3 of the manuscript and described by eqs. (7)-(12), by a simple, constructed example on a 10×1 grid.

Table S 1. NO₂ VCDs and weighting factors for the constructed example for illustration of weighted convolution.

i	k	v_{ik}	w_{pol}	w_{clid}	w
1	1	1.1	1	1	1
2	1	1.15	1	1	1
	2	0.95	1	20	20
3	1	1.1	1	1	1
4					
5	1	1.5	0.15	1	0.15
6	1	2	0.05	1	0.05
	2	1.1	0.05	50	2.5
7	1	3.5	0.025	1	0.025
8	1	2	0.05	1	0.05
9	1	1.1	0.1	1	0.1
10	1	1.05	1	1	1

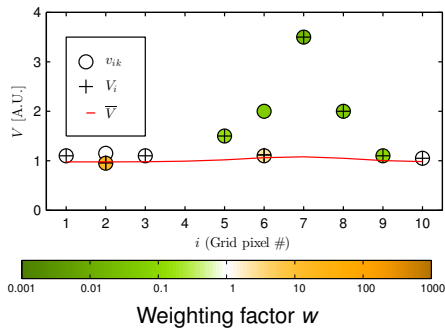


Fig. S 3. Illustration of weighted convolution for the constructed VCDs listed in Table 1. Weighting factors are color coded. Circles represent the individual V^* for each satellite pixel. The weighted mean VCD in each grid pixel (eq. 9) is indicated by a “+”. In cases of multiple satellite pixels per grid ($i=2,6$), the weighted mean is dominated by the clouded satellite pixel due to the high weighting factor. The finally resulting stratospheric pattern \bar{V} is shown in red.

Table S1 lists the values for V^* and their respective weights. Pixels 1-3 and 9-10 are free of tropospheric pollution, while pixels 5-8 are exposed to regular tropospheric pollution, causing low values for w_{pol} . Two observations were made under cloudy conditions, causing a cloud weight >1 . Figure S3 displays the respective individual VCDs v_{ik} (with their net weights shown by color) and the stratospheric estimate \bar{V} resulting from weighted convolution.

Two convolution kernels G^{pol} and G^{eq} , as defined in Eq. 15, are used in STREAM, matching the different needs for high versus low latitudes, respectively. G^{pol} and G^{eq} are displayed in Fig. S4.

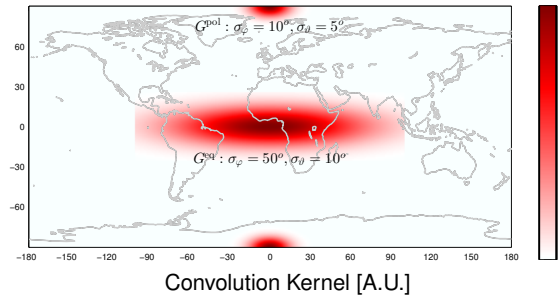


Fig. S 4. Illustration of the convolution kernels used for weighted convolution at the poles and at the equator, respectively. G^{eq} is clipped to $\pm 100^\circ$, i.e. $\pm 2\sigma_\varphi$, to keep computation time low. Global convolution results from the weighted mean of both kernels according to Eq. 15.

In STREAM default set-up, the overall latitudinal dependency of V^* is estimated over the Pacific, removed before the weighted convolution, and added again thereafter. This procedure avoids artefacts of latitudinal convolution in case of gradients on spatial scales of σ_ϑ or smaller. Figure S5 illustrates this effect; the impact of the latitude correction on the resulting TR will be shown in detail below (section S5.3.1).

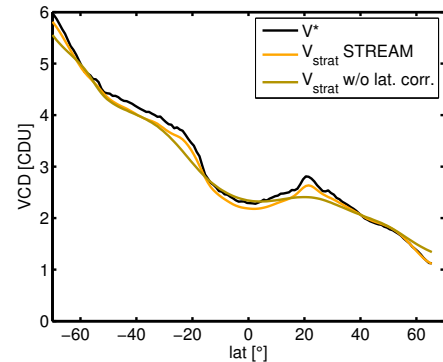


Fig. S 5. Mean total column V^* and stratospheric estimates as function of latitude from STREAM with and without initial latitude correction over the Pacific for OMI data on 1 January OMI.

S2.4 Data Processing

Diurnal variation of stratospheric NO₂

In case of orbital overlap, as for OMI, a grid pixel might contain satellite pixels with different local time. This effect is neglected in STREAM. We have estimated the magnitude of this effect by calculating the mean total NO₂ VCD separately for the different OMI viewing zenith angles, which are directly related to local time (LT) (see Fig. S6).

For low latitudes, the effect is negligible. Only for high latitudes (>50°), the effect can exceed ±0.2 CDU at the swath edges. Consequently, if individual orbits are considered, a small cross-track dependency of TR could be observed for high latitudes, which is actually caused by the LT dependency of stratospheric NO₂. For gridded data, however, where OMI orbits significantly overlap, the effect (and its impact on STREAM performance) is generally negligible.

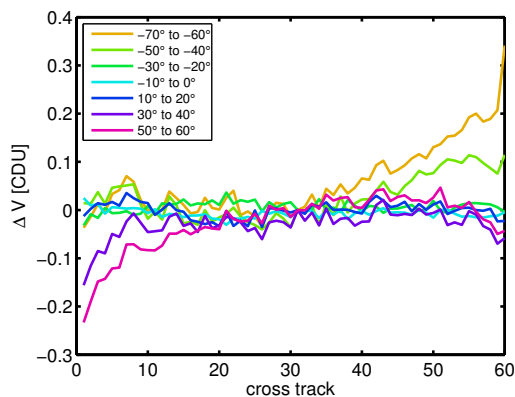


Fig. S 6. Dependency of OMI total VCD V^* on cross-track position (compared to nadir) at different latitudes in January 2005.

S3.3 Synthetic VCD

Figure S7 displays synthetic stratospheric, tropospheric, and total (V^*) column densities. See section 3.3 for details.

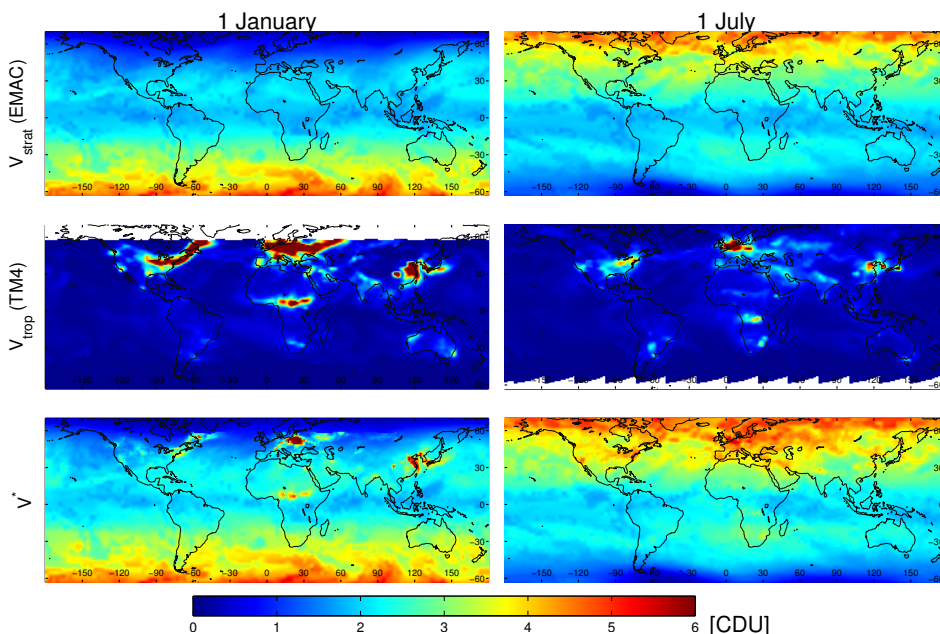


Fig. S 7. Synthetic NO₂ column densities of stratosphere (EMAC, top), troposphere (TM4, center) and total V^* (bottom) for 1 January (left) and 1 July (right) 2005. Note that EMAC stratospheric columns differ from those shown in Fig. 3 of the manuscript, as the latter were adjusted to OMI measurements over the Pacific.

S4 Algorithm performance

S4.1 STREAM versus RSM for OMI

Figure S8 provides information on the definition of percentile bars (left), and shows the definition of the regions (right) used for the regional statistical analysis in Figs. 6-8, 12, 14 and 16, and several diagrams in the supplement.

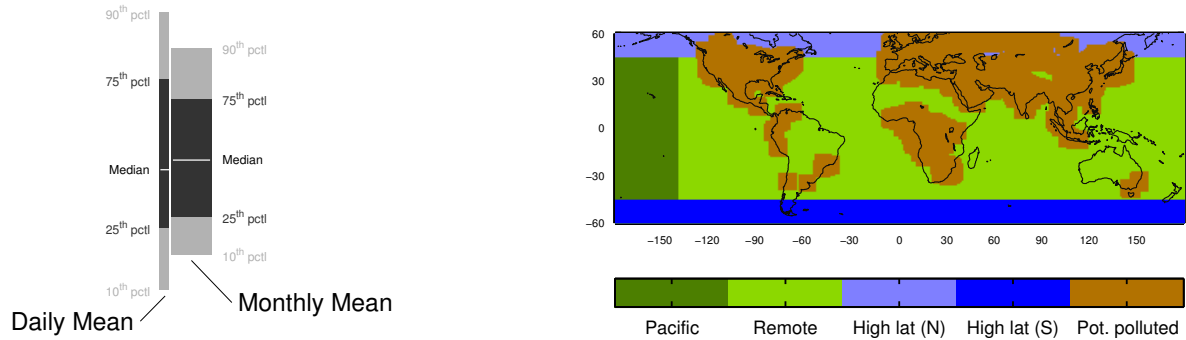


Fig. S 8. Left: Illustration of the meaning of percentile bars used in diagrams on regional statistics of T^* . Light and dark bars reflect the 10th-90th and 25th-75th percentiles, respectively. The median is indicated in white. The narrow and wide bars show the statistics for the first day of the month and the monthly mean, respectively.

Right: Definition of the regions used for the calculation of the statistics of T^* . Note that in the diagrams, “high latitudes” always refers to the respective winter hemisphere.

S4.2 Impact of a-priori settings

S4.2.1 Impact of cloud weight w_{cld}

Figures S9 and S10 display the TR resulting from STREAM for w_{cld} switched off and increased by a factor of 10 (for cloudy pixels, see text for details), respectively, for OMI in 2005. Figure S11 displays the respective TR if low clouds are also considered for the calculation of w_{TR} (by setting $w_{\text{P}} = 1$ for $p > p_{\text{ref}}$ in Eq. 6(c)). The respective regional statistics of T^* are shown in Fig. S12.

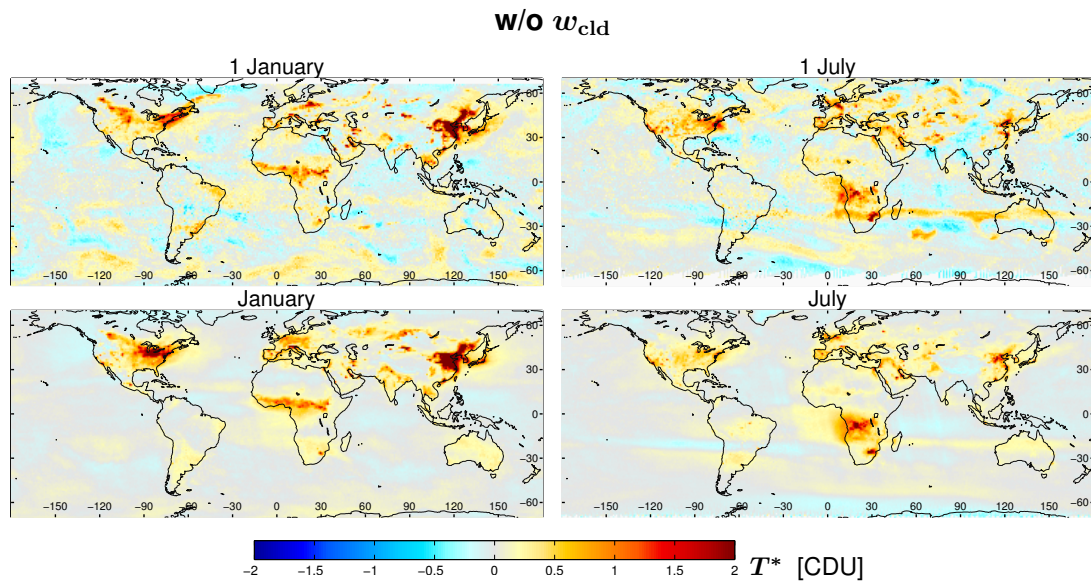


Fig. S 9. OMI tropospheric residues T^* based on STREAM for January (left) and July (right) 2005 for the first day of the month (top) and the monthly mean (bottom) without applying w_{cld} .

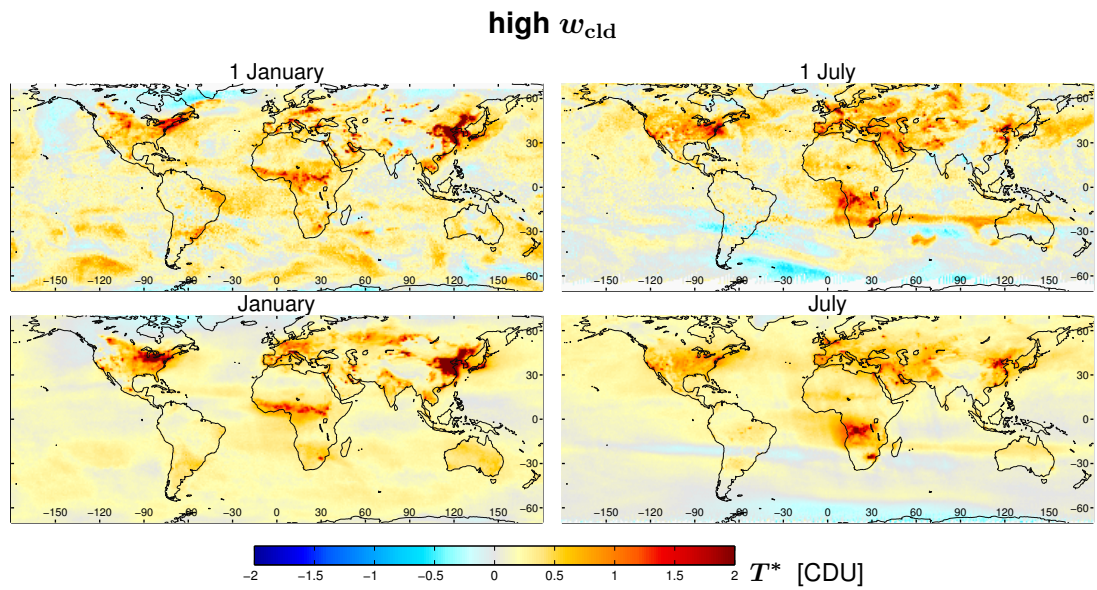


Fig. S 10. OMI tropospheric residues T^* based on STREAM for January (left) and July (right) 2005 for the first day of the month (top) and the monthly mean (bottom) for high w_{cld} ($\times 10$ compared to the baseline for clouded pixels).

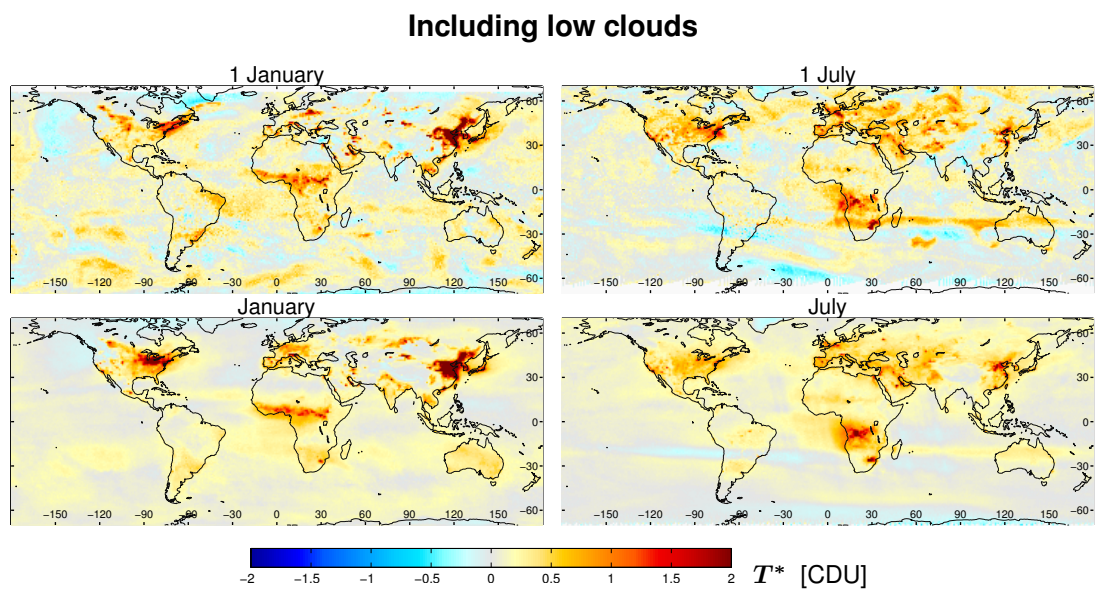


Fig. S 11. OMI tropospheric residues T^* based on STREAM for January (left) and July (right) 2005 for the first day of the month (top) and the monthly mean (bottom) for w_{cld} based on clouds of medium or low altitude.

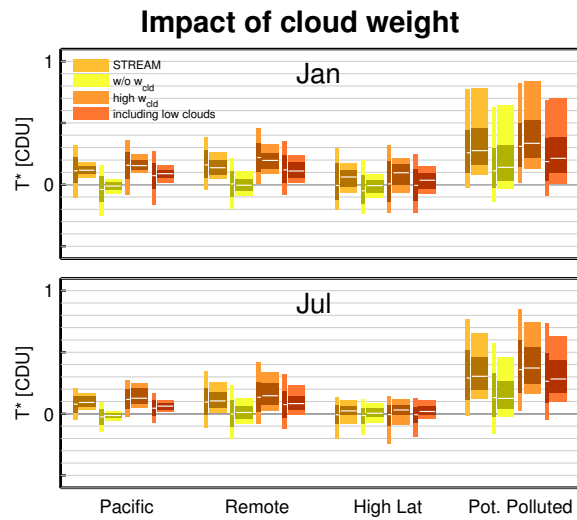


Fig. S 12. Regional statistics of OMI tropospheric residues T^* from STREAM for different settings of w_{cld} . Light and dark bars reflect the 10-90th and 25-75th percentiles, respectively. The median is indicated in white. Narrow bars show the statistics for the first day of the month, wide bars those of the monthly means (see also Fig. S8 (left) for illustration). The regions are defined in Fig. S8 (right). “High latitudes” refer to the respective hemispheric winter only.

S4.2.2 Impact of convolution kernel

Figures S13 and 14 display the TR resulting from STREAM for the convolution kernels G^{pol} and G^{eq} applied globally, respectively, for OMI in 2005.

The respective regional statistics of T^* are shown in Fig. S15.

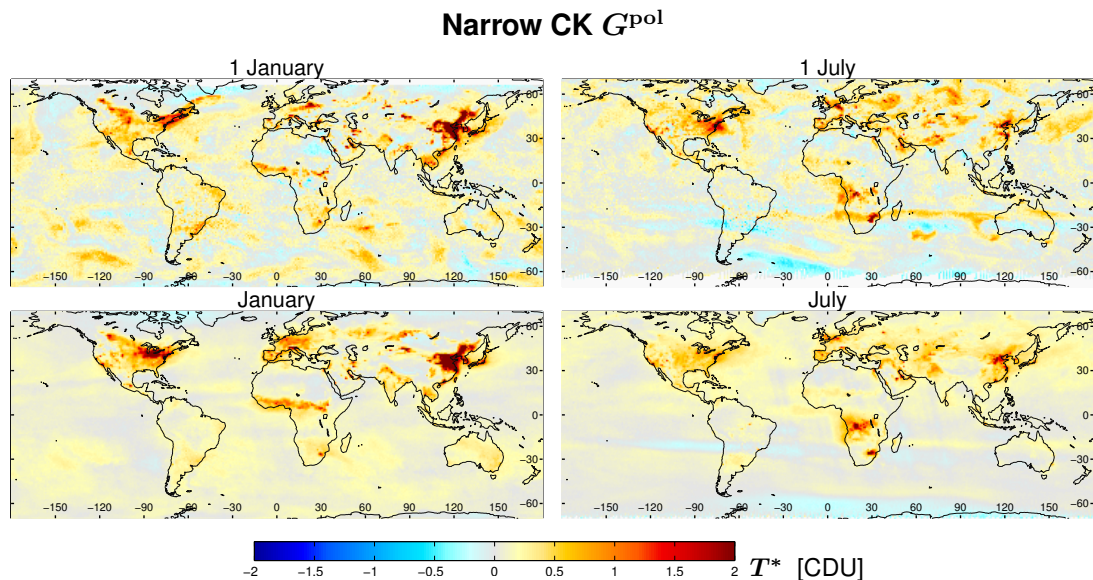


Fig. S 13. OMI tropospheric residues T^* based on STREAM for January (left) and July (right) 2005 for the first day of the month (top) and the monthly mean (bottom) resulting from weighted convolution using G^{pol} .

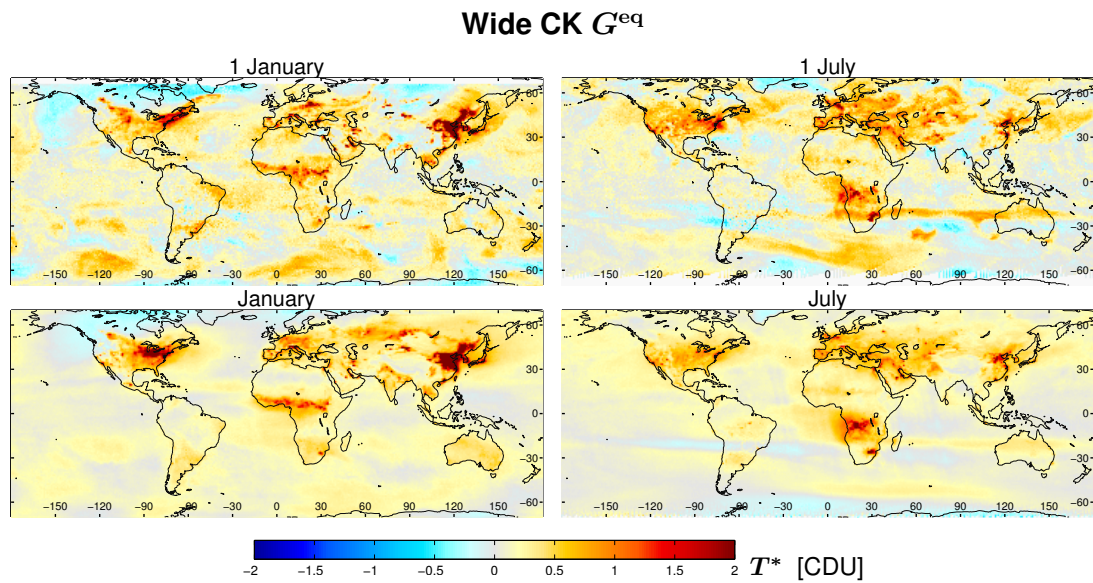


Fig. S 14. OMI tropospheric residues T^* based on STREAM for January (left) and July (right) 2005 for the first day of the month (top) and the monthly mean (bottom) resulting from weighted convolution using G^{eq} .

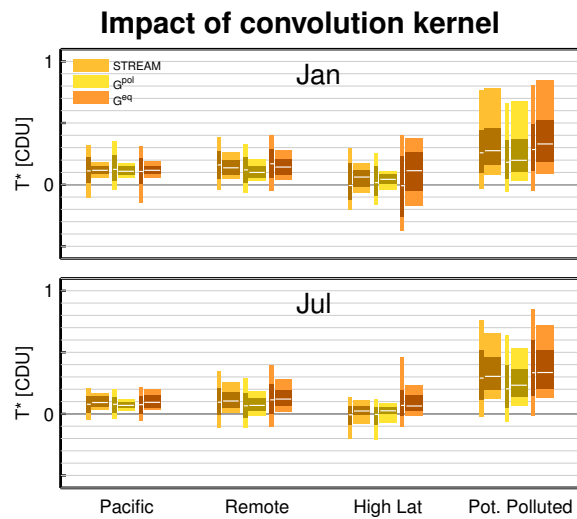


Fig. S 15. Regional statistics of tropospheric residues T^* from STREAM for different settings of the CK G (compare sect. 2.3). Conventions as in Fig. S12.

S4.2.3 Impact of latitude correction

Figure S16 displays the TR resulting from STREAM if the a-priori correction of latitudinal dependency before weighted convolution is switched off for OMI in 2005.

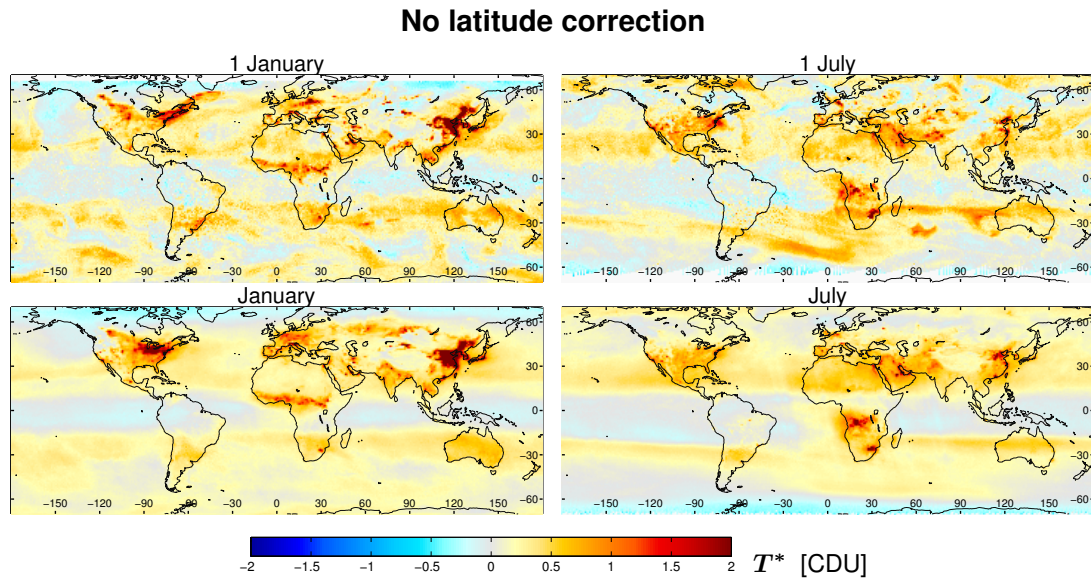


Fig. S 16. OMI tropospheric residues T^* based on STREAM for January (left) and July (right) 2005 for the first day of the month (top) and the monthly mean (bottom) for latitude correction switched off.

S4.2.4 Impact of the number of considered orbits

Figure S17 summarizes the statistics of TR for variations of the number of orbits included for the stratospheric estimate.

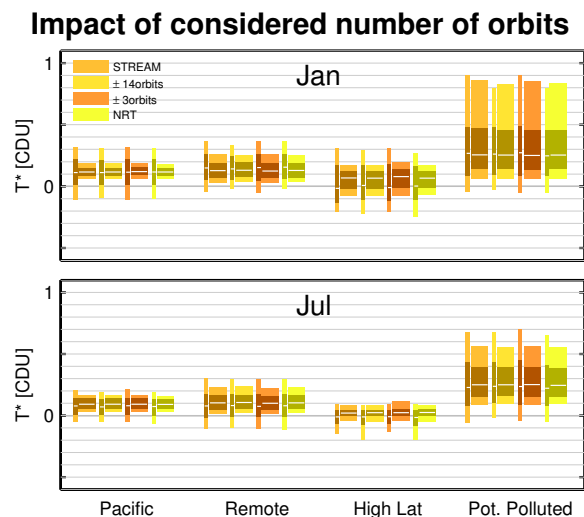


Fig. S 17. Regional statistics of OMI tropospheric residues T^* from STREAM for different number of orbits considered in weighted convolution for January (top) and July (bottom) 2005. Conventions as in Fig. S12.

S4.2.5 Impact of tropospheric residue weight

Figure S18 summarizes the statistics of TR for variations of the number of iterations with w_{TR} .

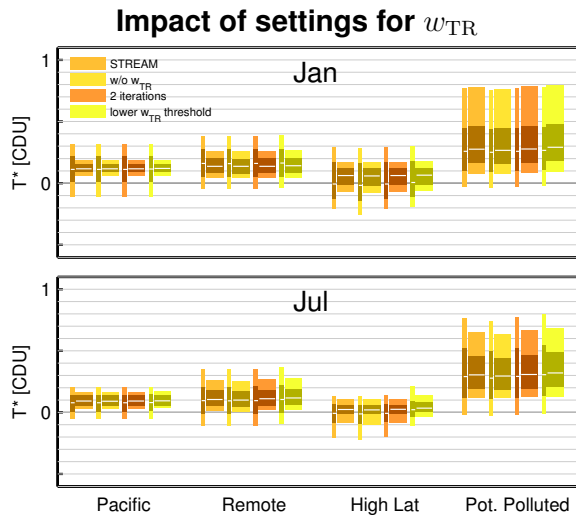


Fig. S 18. Regional statistics of OMI tropospheric residues T^* from STREAM for different settings for w_{TR} for January (top) and July (bottom) 2005. Conventions as in Fig. S12.

S4.2.6 Impact of pollution weight

Figure S19 summarizes the statistics of TR for variations of the pollution weight w_{pol} .

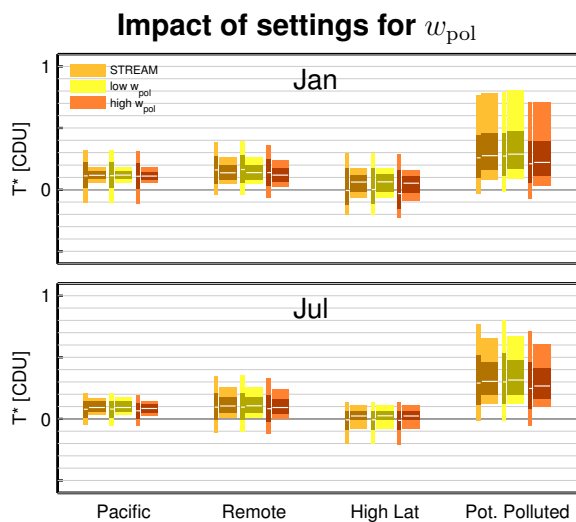


Fig. S 19. Regional statistics of OMI tropospheric residues T^* from STREAM for different settings for w_{pol} for January (top) and July (bottom) 2005. Conventions as in Fig. S12.

S4.3 Performance for synthetic data

Figure S20 displays the expected error of T^* , i.e. the difference of estimated and “true” a priori TR, based on synthetic total columns for OMI in 2005.

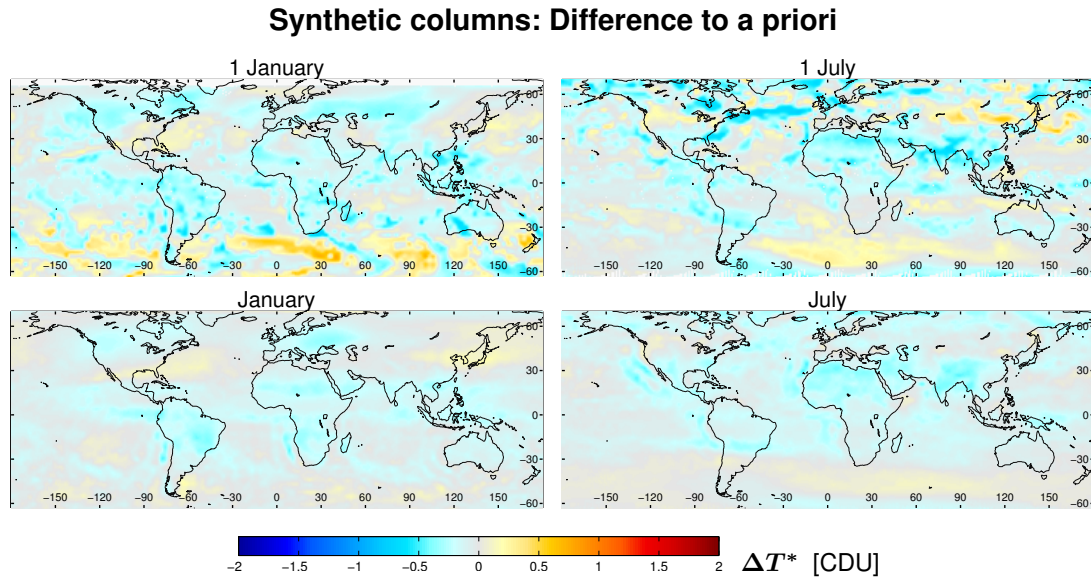


Fig. S 20. Expected error of T^* from STREAM based on synthetic total columns in January (left) and July (right) 2005 for the first day of the month (top) and the monthly mean (bottom).

S5 Discussion

S5.1 OMI

S5.1.1 Comparison to DOMINO

Figure S21 displays the TR resulting from data assimilation as provided in DOMINO for OMI in 2005.

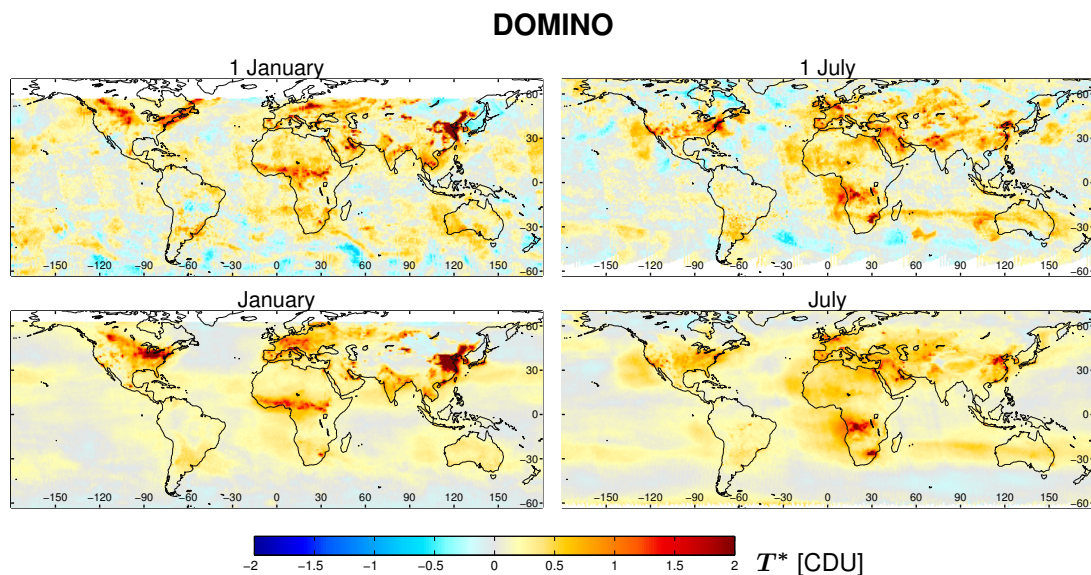


Fig. S 21. OMI tropospheric residues T^* from DOMINO for January (left) and July (right) 2005 for the first day of the month (top) and the monthly mean (bottom).

S5.1.2 Comparison to NASA

Figure S22 displays the TR resulting from NASA v3 for OMI in 2005.

Figure S23 provides additional case studies of features of the NASA stratospheric estimate (see main text for discussion).

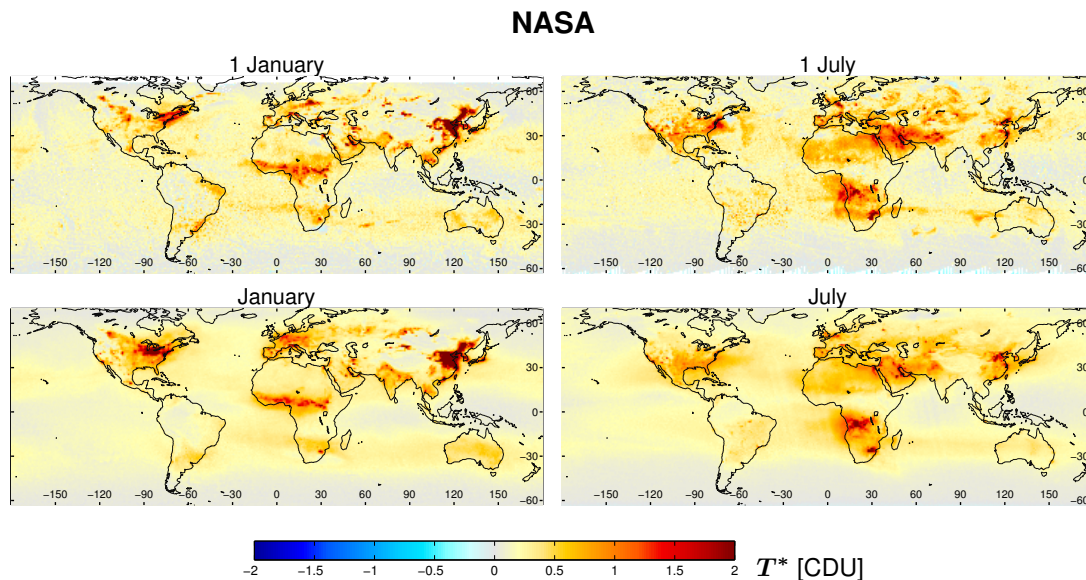


Fig. S 22. OMI tropospheric residues T^* from NASA for January (left) and July (right) 2005 for the first day of the month (top) and the monthly mean (bottom).

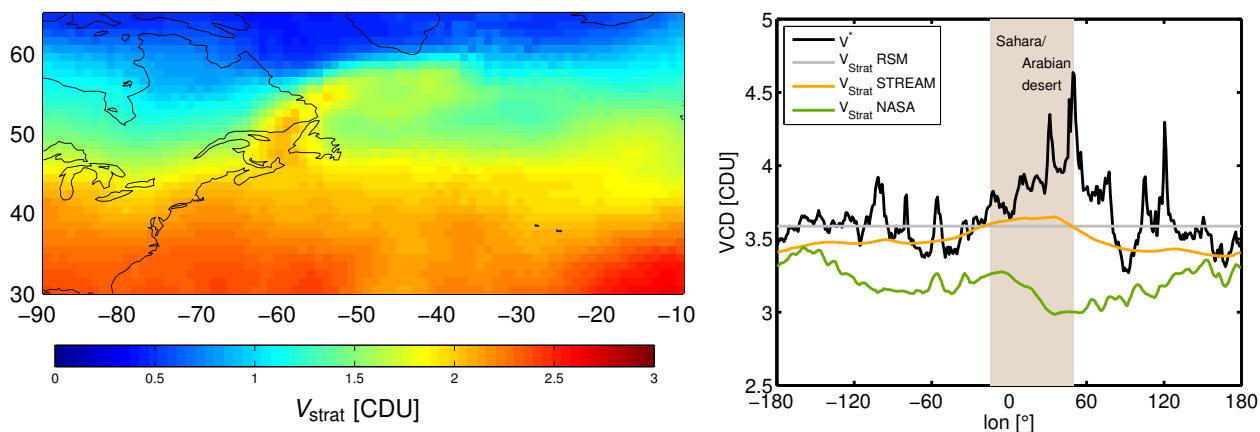


Fig. S 23. Left: Stratospheric VCD as provided by NASA for 1 January 2005. The outflow pattern of NO₂ east of Canada, which is also visible in the total column (Fig. 3 top left), is partly classified as stratospheric.

Right: Longitudinal dependency of total and stratospheric NO₂ column densities in July 2005 for 20°-30°N. Over the Sahara, V^* as well as V_{strat} from STREAM are maximal, while V_{strat} from NASA (which skips the Sahara for the stratospheric estimation) shows a local minimum.

S5.1.3 Comparison to STS EMAC

Figure S24 displays the TR resulting from STS_{EMAC} for OMI in 2005.

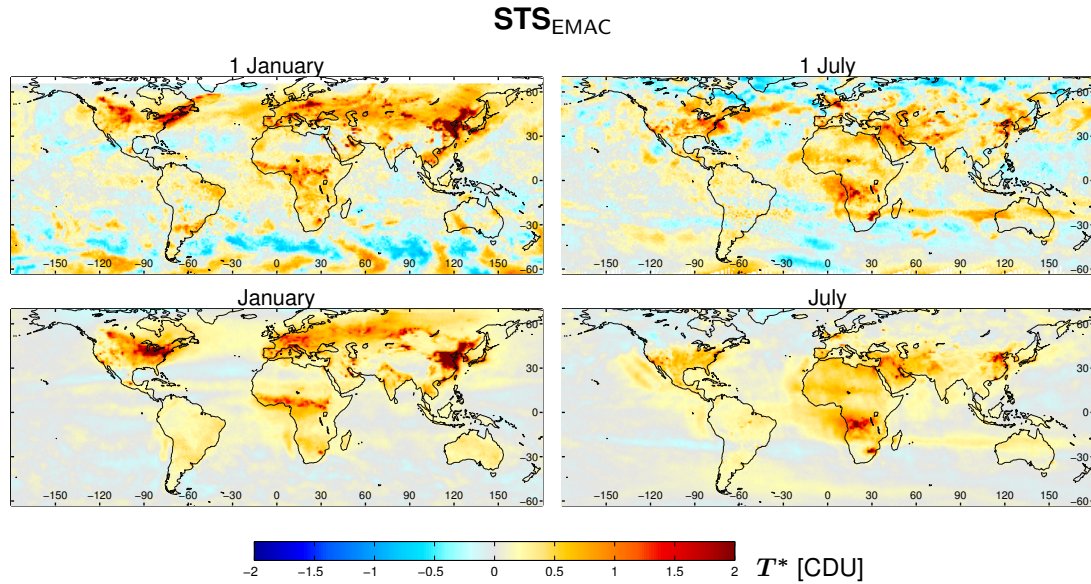


Fig. S 24. OMI tropospheric residues T^* from STS_{EMAC} for January (left) and July (right) 2005 for the first day of the month (top) and the monthly mean (bottom).

S5.1.4 OMI after row anomaly

Figure S25 displays the TR resulting from STREAM for OMI in 2010, analogue to Fig. 5. Due to the row anomaly, gaps occur in the daily maps. Regional statistics, however, are quite similar to those in 2005 (compare Fig. S26 and Fig. 8).

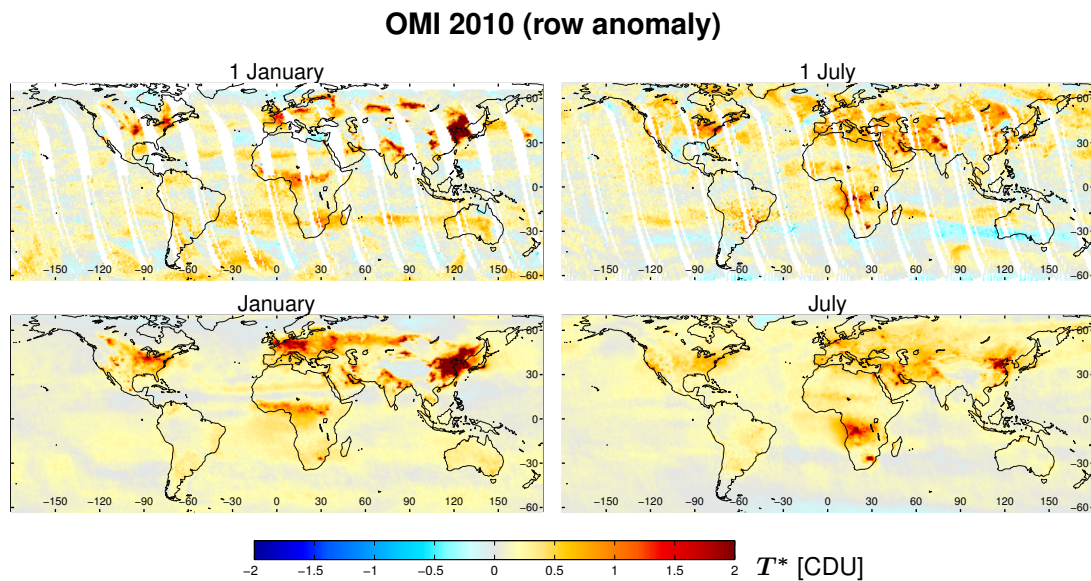


Fig. S 25. OMI tropospheric residues T^* based on STREAM for January (left) and July (right) 2010 for the first day of the month (top) and the monthly mean (bottom).

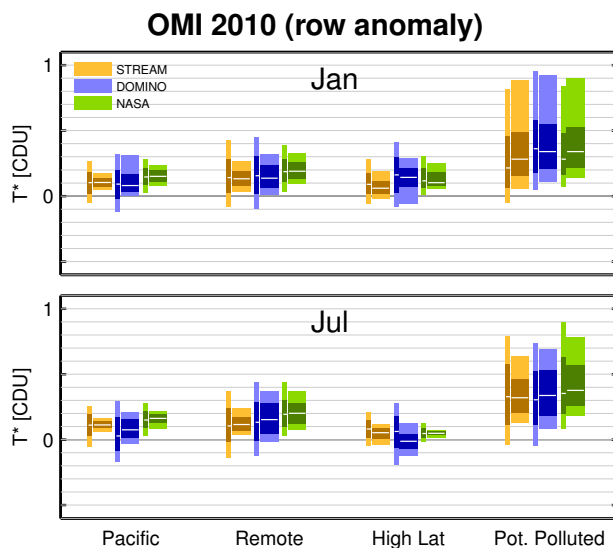


Fig. S 26. Statistics of OMI tropospheric residues T^* from different algorithms for different regions of the globe for January (top) and July (bottom) 2010. Conventions as in Fig. S12.

S5.2 GOME-2

Figure S27 displays the TR resulting from STREAM for GOME-2 in 2010. On 1 July 2010, measurements are performed in narrow swath mode.

Figure S28 shows the artefacts in total and stratospheric VCD caused by a solar eclipse on 15 January 2010. This event was removed from the monthly mean.

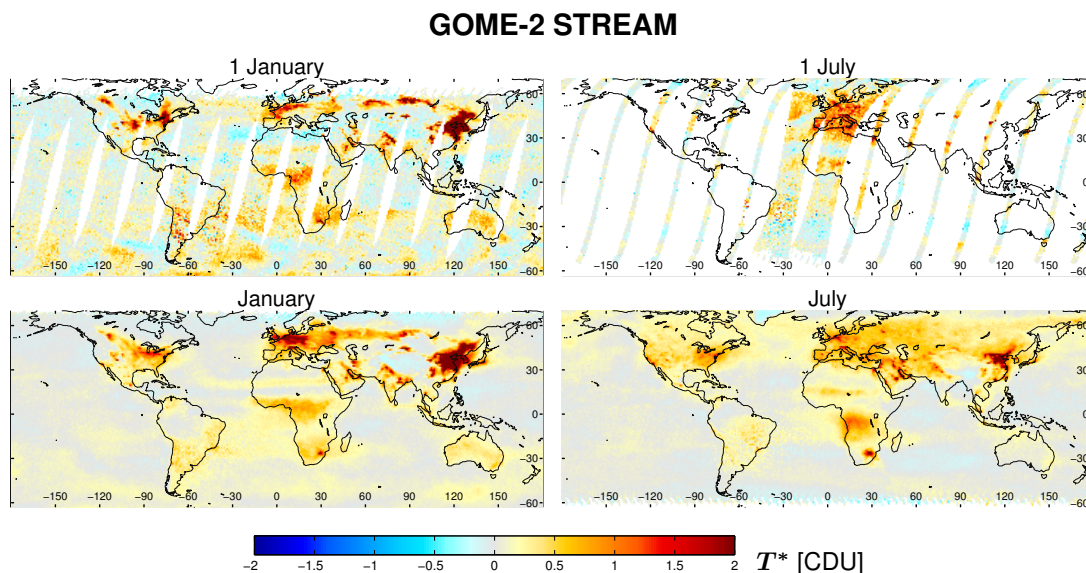


Fig. S 27. GOME-2 tropospheric residues T^* based on STREAM for January (left) and July (right) 2010 for the first day of the month (top) and the monthly mean (bottom).

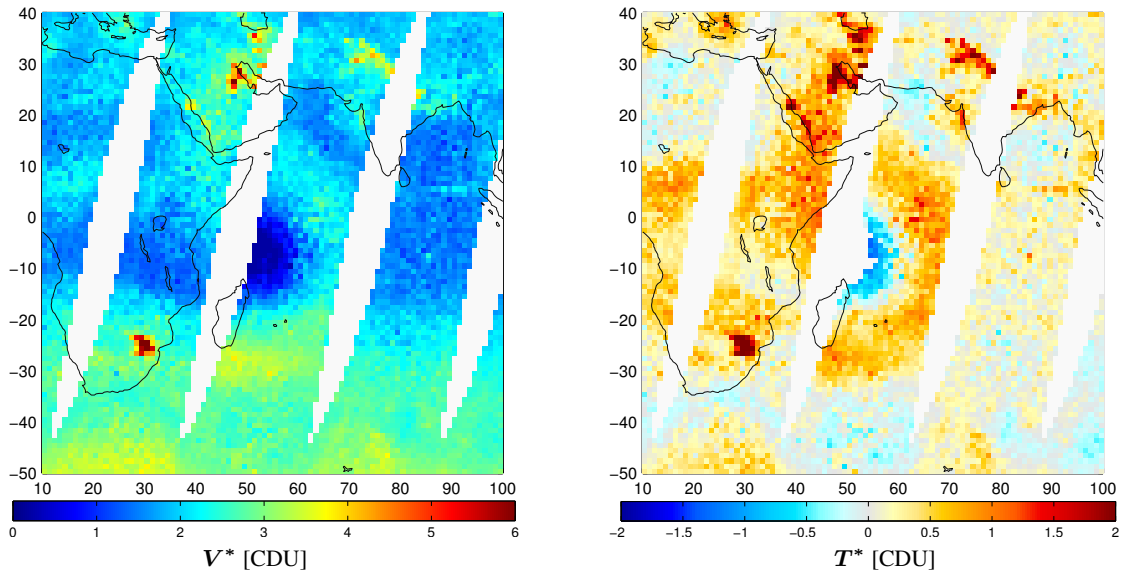


Fig. S 28. GOME-2 total VCD (left) and tropospheric residues T^* (right) on 15 January 2010. Negative VCDs are observed East from Africa caused by poor fit performance due to a solar eclipse. Thus, T^* shows large artificial patterns.

S5.2.1 Comparison to NRT

Figure S29 displays the TR resulting from STREAM in NRT mode for GOME-2 in 2010.

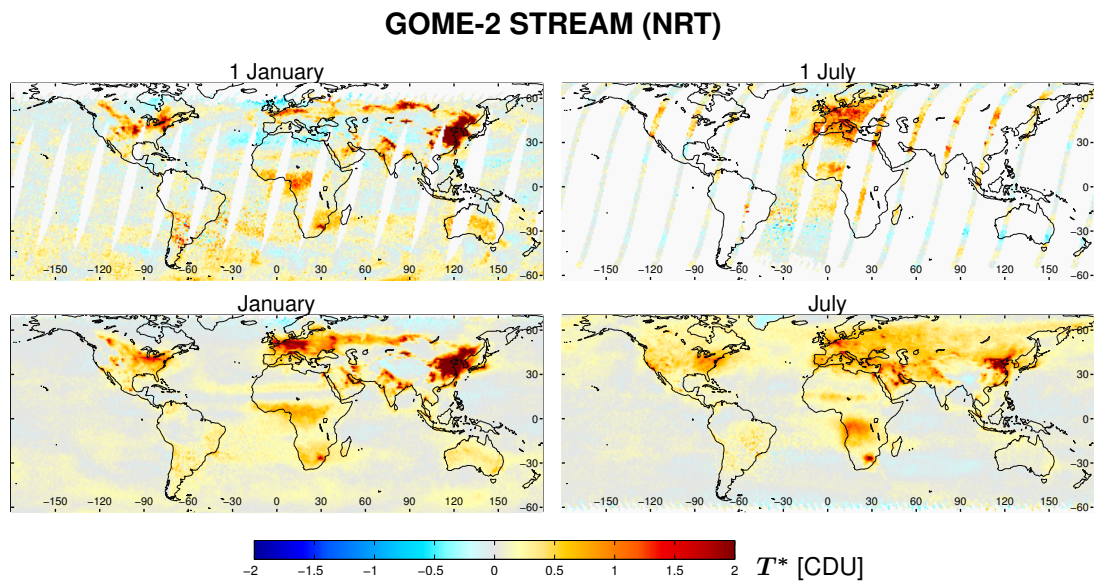


Fig. S 29. GOME-2 tropospheric residues T^* based on STREAM in NRT mode for January (left) and July (right) 2010 for the first day of the month (top) and the monthly mean (bottom).

S5.2.2 Comparison to GDP 4.7

Figure S30 displays the TR resulting from GDP 4.7 for GOME-2 in 2010.

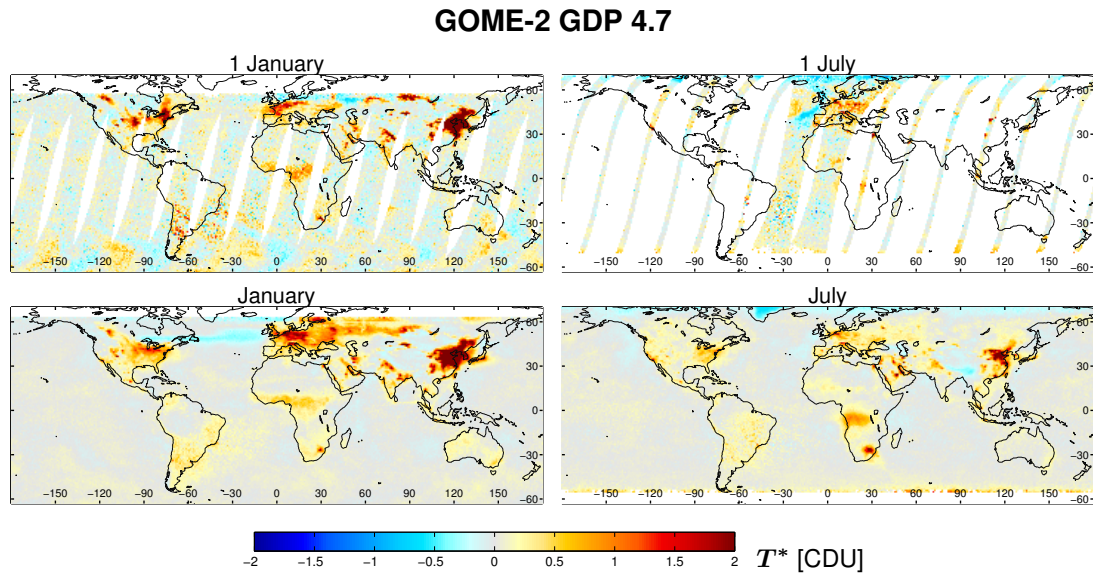


Fig. S 30. GOME-2 tropospheric residues T^* as provided by GDP 4.7 for January (left) and July (right) 2010 for the first day of the month (top) and the monthly mean (bottom).

S5.3 SCIAMACHY

Figure S31 displays the TR resulting from STREAM for SCIAMACHY in 2010.

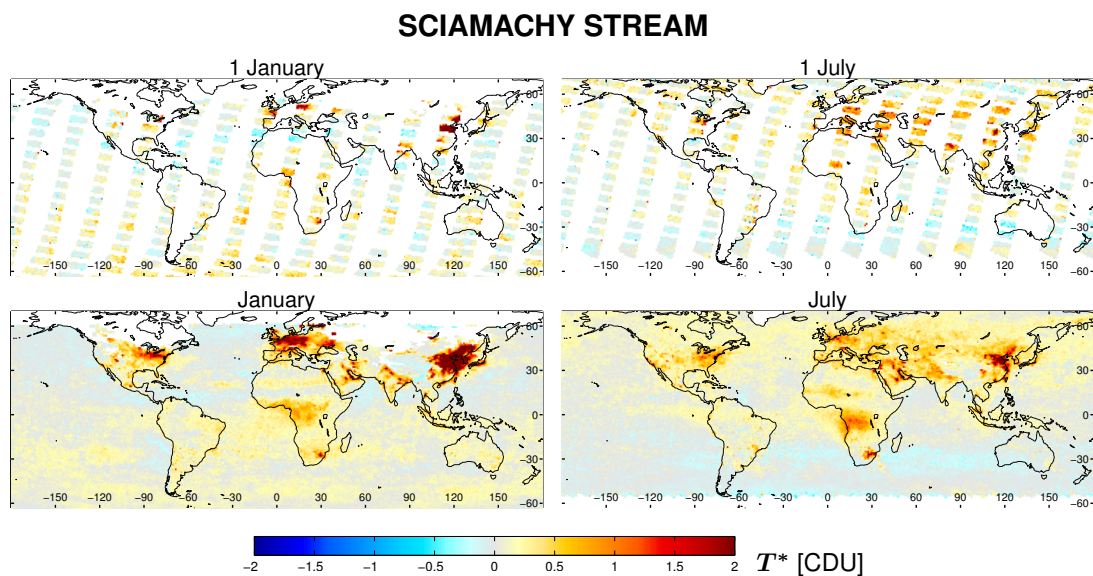


Fig. S 31. SCIAMACHY tropospheric residues T^* based on STREAM for January (left) and July (right) 2010 for the first day of the month (top) and the monthly mean (bottom).

S5.3.1 Comparison to LNM

Figure S32 displays the TR resulting from LNM for SCIAMACHY in 2010.

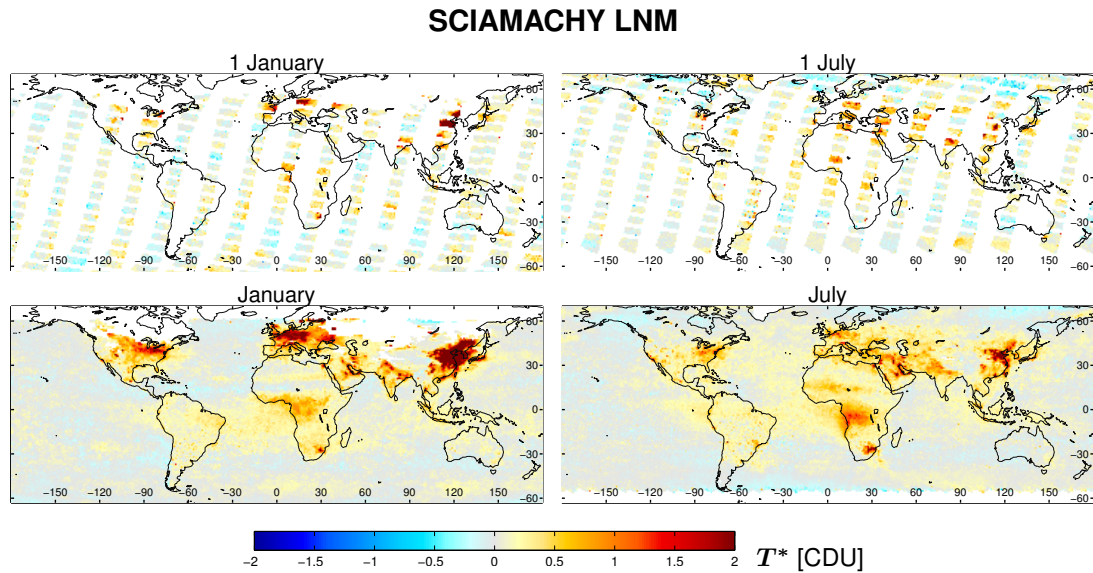


Fig. S 32. SCIAMACHY tropospheric residues T^* based on LNM for January (left) and July (right) 2010 for the first day of the month (top) and the monthly mean (bottom).

Figure S33 displays the mean total VCD V^* over the Pacific as function of latitude, separately for low and high cloud weight. On the summer hemisphere, V^* is lower over clouded pixels, as expected, as the tropospheric background is shielded. This is however not observed in the winter hemisphere, where clouded and cloud free pixels show no difference in V^* , for reasons not yet fully understood. This difference in latitudinal dependency of V^* for clouded vs. cloud free pixels causes the latitudinal dependent biases in the comparison to LNM (Fig. 15).

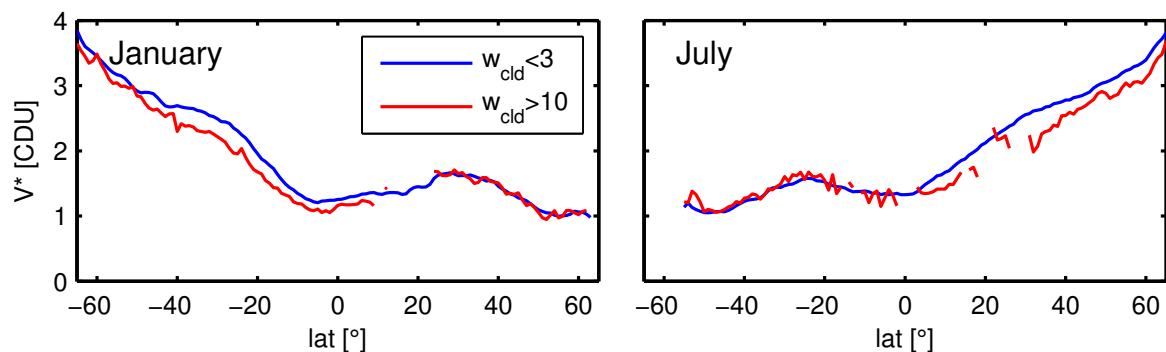


Fig. S 33. Mean V^* over the Pacific as function of latitude, separately for low and high cloud weight, for SCIAMACHY measurements on 1 January (left) and 1 July (right) 2010.

Appendix C

An improved total and tropospheric NO₂ column retrieval for GOME-2

Liu, S., Valks, P., Pinardi, G., De Smedt, I., Yu, H., Beirle, S., and Richter, A.: An Improved Total and Tropospheric NO₂ Column Retrieval for GOME-2, *Atmos. Meas. Tech.*, 12, 1029-1057, <https://doi.org/10.5194/amt-12-1029-2019>, 2019.



An improved total and tropospheric NO₂ column retrieval for GOME-2

Song Liu¹, Pieter Valks¹, Gaia Pinardi², Isabelle De Smedt², Huan Yu², Steffen Beirle³, and Andreas Richter⁴

¹Deutsches Zentrum für Luft- und Raumfahrt (DLR), Institut für Methodik der Fernerkundung (IMF), Oberpfaffenhofen, Germany

²Belgian Institute for Space Aeronomy (BIRA-IASB), Brussels, Belgium

³Max Planck Institute for Chemistry, Mainz, Germany

⁴Institute of Environmental Physics (IUP-UB), University of Bremen, Bremen, Germany

Correspondence: Song Liu (Song.Liu@dlr.de)

Received: 16 July 2018 – Discussion started: 6 August 2018

Revised: 14 January 2019 – Accepted: 17 January 2019 – Published: 18 February 2019

Abstract. An improved algorithm for the retrieval of total and tropospheric nitrogen dioxide (NO₂) columns from the Global Ozone Monitoring Experiment-2 (GOME-2) is presented. The refined retrieval will be implemented in a future version of the GOME Data Processor (GDP) as used by the EUMETSAT Satellite Application Facility on Atmospheric Composition and UV Radiation (AC-SAF). The first main improvement is the application of an extended 425–497 nm wavelength fitting window in the differential optical absorption spectroscopy (DOAS) retrieval of the NO₂ slant column density, based on which initial total NO₂ columns are computed using stratospheric air mass factors (AMFs). Updated absorption cross sections and a linear offset correction are used for the large fitting window. An improved slit function treatment is applied to compensate for both long-term and in-orbit drift of the GOME-2 slit function. Compared to the current operational (GDP 4.8) dataset, the use of these new features increases the NO₂ columns by $\sim 1\text{--}3 \times 10^{14}$ molec cm² and reduces the slant column error by $\sim 24\%$. In addition, the bias between GOME-2A and GOME-2B measurements is largely reduced by adopting a new level 1b data version in the DOAS retrieval. The retrieved NO₂ slant columns show good consistency with the Quality Assurance for Essential Climate Variables (QA4ECV) retrieval with a good overall quality. Second, the STRatospheric Estimation Algorithm from Mainz (STREAM), which was originally developed for the TROPOspheric Monitoring Instrument (TROPOMI) in-

strument, was optimised for GOME-2 measurements to determine the stratospheric NO₂ column density. Applied to synthetic GOME-2 data, the estimated stratospheric NO₂ columns from STREAM shows good agreement with the a priori truth. An improved latitudinal correction is introduced in STREAM to reduce the biases over the subtropics. Applied to GOME-2 measurements, STREAM largely reduces the overestimation of stratospheric NO₂ columns over polluted regions in the GDP 4.8 dataset. Third, the calculation of AMF applies an updated box-air-mass factor (box-AMF) look-up table (LUT) calculated using the latest version 2.7 of the Vector-Linearized Discrete Ordinate Radiative Transfer (VLIDORT) model with an increased number of reference points and vertical layers, a new GOME-2 surface albedo climatology, and improved a priori NO₂ profiles obtained from the TM5-MP chemistry transport model. A large effect (mainly enhancement in summer and reduction in winter) on the retrieved tropospheric NO₂ columns by more than 10% is found over polluted regions. To evaluate the GOME-2 tropospheric NO₂ columns, an end-to-end validation is performed using ground-based multiple-axis DOAS (MAXDOAS) measurements. The validation is illustrated for six stations covering urban, suburban, and background situations. Compared to the GDP 4.8 product, the new dataset presents improved agreement with the MAXDOAS measurements for all the stations.

1 Introduction

Nitrogen dioxide (NO₂) is an important trace gas in the Earth's atmosphere. In the stratosphere, NO₂ is strongly related to halogen compound reactions and ozone destruction (Solomon, 1999). In the troposphere, nitrogen oxides (NO_x = NO₂ + NO) serve as a precursor of ozone in the presence of volatile organic compounds (VOCs) and of secondary aerosol through gas-to-particle conversion (Seinfeld et al., 1998). As a prominent air pollutant affecting human health and ecosystems, large amounts of NO₂ are produced in the boundary layer by industrial processes, power generation, transportation, and biomass burning over polluted hot spots. For instance, a strong growth of NO₂ during the past 2 decades has caused severe air pollution problems for China, with the largest NO₂ columns in 2011; since then, cleaner techniques and stricter controlling have been applied to reduce the NO₂ pollution (Richter et al., 2005; van der A et al., 2017; Liu et al., 2017). An increase in NO₂ concentrations due to economic growth is also found over India, with a peak in 2012 (Hilboll et al., 2017). Despite the decrease in NO_x emissions in Europe, around half of European Union member states still exceed the air quality standards, mainly caused by diesel car emissions (European Commission, 2017).

NO₂ column measurements have been provided by satellite instruments, e.g. Global Ozone Monitoring Experiment (GOME) (Burrows et al., 1999), Scanning Imaging Absorption SpectroMeter for Atmospheric CHartographY (SCIAMACHY) (Bovensmann et al., 1999), Ozone Monitoring Instrument (OMI) (Levelt et al., 2006), and Global Ozone Monitoring Experiment-2 (GOME-2) (Callies et al., 2000; Munro et al., 2016). NO₂ observations will be continued by the new generation instruments with high spatial resolution such as Tropospheric Monitoring Instrument (TROPOMI) (launched in October 2017; Veefkind et al., 2012) and by geostationary missions such as Sentinel-4 (Ingmann et al., 2012). The GOME-2 instrument, which is the main focus of this study, is included on a series of MetOp satellites as part of the EUMETSAT Polar System (EPS). The first GOME-2 was launched in October 2006 aboard the MetOp-A satellite, and a second GOME-2 was launched in September 2012 aboard MetOp-B. The consistent long-term dataset will be further extended by the third GOME-2 on the upcoming MetOp-C platform (to be launched in September 2018). NO₂ measurements from GOME-2 have been widely used to characterise the distribution, evolution, or transport of NO₂ (e.g. Hilboll et al., 2013, 2017; Zien et al., 2014), to estimate the NO_x emission (e.g. Gu et al., 2014; Miyazaki et al., 2017; Ding et al., 2017), and to interpret VOC levels, ozone variation, or anthropogenic aerosol loading (e.g. Vrekoussis et al., 2010; Safieddine et al., 2013; Penning de Vries et al., 2015).

The GOME-2 total and tropospheric NO₂ products are generated using the GOME Data Processor (GDP) algorithm at the German Aerospace Center (DLR). The retrieval algorithm has been first described by Valks et al. (2011) as imple-

mented in the GDP version 4.4 and was later updated to the current operational version 4.8 (Valks et al., 2017). The NO₂ retrieval for GOME-2 follows a classical three-step scheme.

First, the total NO₂ slant columns (namely the concentration integrated along the effective light path from the sun through the atmosphere to the instrument) are derived using the differential optical absorption spectroscopy (DOAS) method (Platt and Stutz, 2008). The DOAS technique is a least-squares method fitting the molecular absorption cross sections to the measured GOME-2 sun-normalised radiances provided by the EUMETSAT's processing facility. The fit is applied on the data within a fitting window optimised for NO₂. As analysed by Richter et al. (2011) and in the Quality Assurance for Essential Climate Variables (QA4ECV; <http://www.qa4ecv.eu>) project, extension of the fitting window for GOME-2 increases the signal-to-noise ratio and hence improves the NO₂ slant column error. The total NO₂ slant columns depend on the viewing geometry and also on parameters such as surface albedo and the presence of clouds and aerosol loads. They are therefore converted to initial total NO₂ vertical columns through division by a stratospheric air mass factor.

Second, the stratospheric contribution is estimated and separated from the NO₂ slant columns (referred to as "stratosphere–troposphere separation"). The GDP 4.8 algorithm applies a modified reference sector method, which uses measurements over clean regions to estimate the stratospheric NO₂ columns based on the assumptions of longitudinally invariable stratospheric NO₂ layers and of negligible tropospheric NO₂ abundance over the clean areas. The modified reference sector method defines a global pollution mask to remove potentially polluted regions and applies an interpolation over the unmasked areas to derive the stratospheric NO₂ columns. As a result of using a fixed pollution mask, the modified reference sector method in GDP 4.8 has larger uncertainties over polluted areas, because limited amount of information over continents is used. To overcome the shortcomings, the STRatospheric Estimation Algorithm from Mainz (STREAM) method (Beirle et al., 2016) has been developed for the TROPOMI instrument and was also successfully applied on GOME, SCIAMACHY, OMI, and GOME-2 measurements. Also belonging to the modified reference sector method, STREAM defines not a fixed pollution mask but rather weighting factors for each observation to determine its contribution to the stratospheric estimation.

Third, the tropospheric NO₂ vertical columns are calculated from the tropospheric slant columns by an air mass factor (AMF) calculation, which contributes the largest uncertainty to the NO₂ retrieval, particularly over polluted regions (Boersma et al., 2004). The AMFs are determined with a radiative transfer model (RTM) and stored in a look-up table (LUT) requiring ancillary information such as surface albedo, vertical shape of the a priori NO₂ profile, clouds, and aerosols. Improvements in the RTM and LUT interpolation scheme, the ancillary parameters, and the cloud and

aerosol correction approach have been reported for the OMI instrument (e.g. Boersma et al., 2011; Lorente et al., 2017; Vasilkov et al., 2017; Krotkov et al., 2017; Veeffkind et al., 2016; Lin et al., 2014; Castellanos et al., 2015; Laughner et al., 2018), which in principle are beneficial for similar satellite instruments like GOME-2.

In this paper, a new algorithm to retrieve the total and tropospheric NO₂ for the GOME-2 instruments is described, which includes improvements in each of the three algorithm steps introduced above. The improved algorithm will be implemented in the next version of GDP (referred to as GDP 4.9 hereafter). We briefly introduce the GOME-2 instrument (Sect. 2) and the current operational (GDP 4.8) total and tropospheric NO₂ retrieval algorithm (Sect. 3). We present the improvements to the DOAS slant column retrieval (Sect. 4), the stratosphere–troposphere separation (Sect. 5), and the AMF calculation (Sect. 6). Finally, we show an end-to-end validation of the tropospheric NO₂ dataset using ground-based multiple-axis DOAS (MAXDOAS) datasets with different pollution conditions (Sect. 7).

2 Instrument and measurements

GOME-2 is a nadir-scanning UV–VIS spectrometer aboard the MetOp-A and MetOp-B satellites (referred to as GOME-2A and GOME-2B throughout this study) with a satellite repeating cycle of 29 days and an equator crossing time of 19:30 local time (LT) (descending node). The GOME-2 instrument measures the Earth's backscattered radiance and extraterrestrial solar irradiance in the spectral range between 240 and 790 nm. The morning measurements from GOME-2 provide a better understanding of the diurnal variations of the NO₂ columns in combination with afternoon observations from for example the OMI, and TROPOMI instruments (13:30 LT). The default swath width of GOME-2 is 1920 km, enabling a global coverage in ~ 1.5 days. The default ground pixel size is 80 km \times 40 km in the forward scan, which remains almost constant over the full swath width. In a tandem operation of MetOp-A and MetOp-B from July 2013 onwards, a decreased swath of 960 km and an increased spatial resolution of 40 km \times 40 km are employed by GOME-2A. See Munro et al. (2016) for more details on instrument design and performance.

The operational GOME-2 NO₂ product is provided by DLR in the framework of EUMETSAT's Satellite Application Facility on Atmospheric Composition Monitoring (AC-SAF). The product processing chain starts with the level 0 to 1b processing within the core ground segment at EUMETSAT in Darmstadt (Germany), where the raw instrument (level 0) data are converted into geolocated and calibrated (level 1b) (ir)radiances by the GOME-2 Product Processing Facility (PPF). The level 1b (ir)radiances are disseminated through the EUMETCast system to the AC-SAF processing facility at DLR in Oberpfaffenhofen (Germany) and

further processed using the Universal Processor for UV/VIS Atmospheric Spectrometers (UPAS) system. Broadcasted via EUMETCast, WMO GTS, and the Internet, the resulting level 2 near-real-time total column products including NO₂ columns can be received by user communities 2 h after sensing. Offline and reprocessed GOME-2 level 2 and consolidated products are also provided within 1 day by DLR, which can be ordered via FTP server and the EUMETSAT Data Centre (<https://acsaf.org/>, last access: 1 February 2019).

3 Total and tropospheric NO₂ retrieval for GDP 4.8

The first main step of the retrieval algorithm is the DOAS technique, which is applied to determine the total NO₂ slant columns from the (ir)radiance spectra measured by the instrument. Based on the Beer–Lambert law, the DOAS fit is a least-squares inversion to isolate the trace gas absorption from the background processes, e.g. extinction resulting from scattering on molecules and aerosols, with a background polynomial $P(\lambda)$ at wavelength λ :

$$\ln \left[\frac{I(\lambda) + \text{offset}(\lambda)}{I^0(\lambda)} \right] = - \sum_g S_g \sigma_g(\lambda) - \alpha_R R(\lambda) - P(\lambda). \quad (1)$$

The measurement-based term is defined as the natural logarithm of the measured earthshine radiance spectrum $I(\lambda)$ divided by the daily solar irradiance spectrum $I^0(\lambda)$. The intensity offset correction $\text{offset}(\lambda)$, which describes the additional contributions such as stray light in the spectrometer to the measured intensity, is modelled using a zero-order polynomial with the polynomial coefficient as the fitting parameter. The spectral effect from the absorption of species g is determined by the fitted slant column density S_g and associated absorption cross section $\sigma_g(\lambda)$. An additional term with the Ring scaling factor α_R and the Ring reference spectrum $R(\lambda)$ describes the filling-in effect of Fraunhofer lines by rotational Raman scattering (the so-called Ring effect). The GDP 4.8 algorithm adopts a wavelength range of 425–450 nm to ensure prominent NO₂ absorption structures and controllable interferences from other absorbing species, e.g. water vapour (H₂O^{vap}), ozone (O₃), and oxygen dimer (O₄). Table 1 gives an overview of the DOAS settings for the current operational GDP 4.8 algorithm, the improved version 4.9 algorithm (see Sect. 4), and the algorithm used in the QA4ECV product (see Sect. 4.5).

The second component in the retrieval is the calculation of initial total vertical column densities V_{init} using a stratospheric AMF (M_{strat}) conversion:

$$V_{\text{init}} = \frac{S}{M_{\text{strat}}}. \quad (2)$$

Given the small optical thickness of NO₂, M_{strat} can be determined as

$$M_{\text{strat}} = \frac{\sum_l m_l(\mathbf{b}) x_l c_l}{\sum_l x_l}, \quad (3)$$

Table 1. Main settings of GOME-2 DOAS retrieval of NO₂ slant columns discussed in this study.

	GDP 4.8, Valks et al. (2011, 2017)	GDP 4.9 (this work)	QA4ECV, Müller et al. (2016); Boersma et al. (2018)
Wavelength range	425–450 nm	425–497 nm	405–465 nm
Cross sections	NO ₂ 240 K, H ₂ O ^{vap} , O ₃ , O ₄ , Ring	NO ₂ 220 K, H ₂ O ^{vap} , O ₃ , O ₄ , Ring, H ₂ O ^{liq} , Eta, Zeta, resolution correction	NO ₂ 220 K, H ₂ O ^{vap} , O ₃ , O ₄ , Ring, H ₂ O ^{liq}
Polynomial degree	3	5	5
Intensity offset	Constant	Linear	Constant
Slit function	Preflight	Stretched preflight	Preflight

with m_l the box-air-mass factors (box-AMFs) in layer l , x_l the altitude-dependent sub-columns from a stratospheric a priori NO₂ profiles climatology (Lambert et al., 1999), and c_l a correction coefficient to account for the temperature dependency of NO₂ cross section (Boersma et al., 2004; Nüß et al., 2006). The calculation of V_{init} assumes negligible tropospheric NO₂ and hence uses only the stratospheric a priori NO₂ profiles to derive AMF. The box-AMFs m_l are derived using the multilayered multiple scattering LInearized Discrete Ordinate Radiative Transfer (LIDORT) RTM (Spurr et al., 2001) and stored in a LUT as a function of various model inputs \mathbf{b} , including GOME-2 viewing geometry, surface pressure, and surface albedo. The surface albedo is described by the Lambertian equivalent reflectivity (LER). The surface LER climatology used in the GDP 4.8 algorithm is derived from combined TOMS–GOME measurements (Boersma et al., 2004) for the years 1979–1993 with a spatial resolution of 1.25° long. × 1.0° lat.

In the presence of clouds, the calculation of M_{strat} adopts the independent pixel approximation based on GOME-2 cloud parameters:

$$M_{\text{strat}} = \omega M_{\text{strat}}^{\text{cloud}} + (1 - \omega) M_{\text{strat}}^{\text{clear}}, \quad (4)$$

with ω being the cloud radiance fraction, $M_{\text{strat}}^{\text{cloud}}$ the cloudy-sky stratospheric AMF, and $M_{\text{strat}}^{\text{clear}}$ the clear-sky stratospheric AMF. $M_{\text{strat}}^{\text{cloud}}$ and $M_{\text{strat}}^{\text{clear}}$ are derived with Eq. (3) with $M_{\text{strat}}^{\text{cloud}}$ mainly relying on the cloud pressure and the cloud albedo. The ω value is derived from the cloud fraction c_f :

$$\omega = \frac{c_f I^{\text{cloud}}}{(1 - c_f) I^{\text{clear}} + c_f I^{\text{cloud}}}, \quad (5)$$

where I^{cloud} is the radiance for a cloudy scene and I^{clear} for a clear scene. I^{cloud} and I^{clear} are calculated using LIDORT, depending mostly on the GOME-2 viewing geometry, surface albedo, and cloud albedo. From GOME-2, c_f is determined with the Optical Cloud Recognition Algorithm (OCRA) by separating a spectral scene into cloudy contribution and cloud-free background, and the cloud pressure and the cloud albedo are derived using the Retrieval Of Cloud Information using Neural Networks (ROCINN) algorithm by comparing simulated and measured radiance in and near the

O₂ A band (Loyola et al., 2007, 2011). Applied in the NO₂ retrieval in GDP 4.8, the latest version 3.0 of the OCRA (Lutz et al., 2016) applies a degradation correction on the GOME-2 level 1 measurements as well as corrections for viewing angle and latitudinal dependencies. A new cloud-free background is constructed from 6 years of GOME-2A measurements from the years 2008–2013. The updated OCRA also includes an improved detection and removal of sun glint that affects most of the GOME-2 orbits. Version 3.0 of ROCINN (Loyola et al., 2018) applies a forward RTM calculation using updated surface albedo climatology and spectroscopic data as well as a new inversion scheme based on Tikhonov regularisation (Tikhonov and Arsenin, 1977; Doicu et al., 2010). The computation time of ROCINN is optimised with a smart sampling method (Loyola et al., 2016).

The next retrieval step is the separation of stratospheric and tropospheric components from the initial vertical total columns, namely the stratosphere–troposphere separation. Since no direct stratospheric measurements are available for GOME-2, a spatial filtering algorithm is applied to estimate the stratospheric NO₂ columns in GDP 4.8. The spatial filtering algorithm belongs to the modified reference sector method, which uses total NO₂ columns over clean regions to approximate the stratospheric NO₂ columns based on the assumption of longitudinally invariable stratospheric NO₂ layers and of negligible tropospheric NO₂ abundance over the clean areas. The spatial filtering algorithm uses a pollution mask to filter the potentially polluted areas (tropospheric NO₂ columns larger than 1×10^{15} molec cm²), followed by a low-pass filtering (with a zonal 30° boxcar filter) on the initial total columns of the unmasked areas, and afterwards a removal of a tropospheric background NO₂ (1×10^{14} molec cm²) from the derived stratospheric columns.

Finally, the tropospheric NO₂ columns V_{trop} can be computed as

$$V_{\text{trop}} = \frac{M_{\text{strat}}}{M_{\text{trop}}} \times T, \quad (6)$$

where M_{strat} is the stratospheric AMF in Eq. (3), M_{trop} is the tropospheric AMF, and T is the tropospheric residues ($T = V_{\text{init}} - V_{\text{strat}}$). M_{trop} is determined using Eqs. (3) and (4) with tropospheric a priori NO₂ profiles. The calculation of M_{trop}

relies on the same model parameters as of M_{strat} , but the dependency on the parameters like surface albedo and cloud properties as well as on the a priori NO₂ profiles is much stronger. The GDP 4.8 adopts the tropospheric a priori NO₂ profiles from a run of the global chemistry transport model MOZART version 2 (Horowitz et al., 2003) with anthropogenic emissions from the EDGAR2.0 inventory (Olivier et al., 1996) for the early 1990s. The monthly average vertical profiles are calculated from MOZART-2 data from the year 1997 for the overpass time of GOME-2 (09:30 LT) with a resolution of 1.875° long × 1.875° lat.

4 Improved DOAS slant column retrieval

A larger 425–497 nm wavelength fitting window for the DOAS method (Richter et al., 2011) is implemented in the GDP 4.9 to retrieve the NO₂ slant columns, which improves the signal-to-noise ratio by including more NO₂ absorption structures. Compared to the extended 405–465 nm range, as employed by the QA4ECV GOME-2 NO₂ product and used in the NO₂ retrieval for OMI instrument (Boersma et al., 2002; van Geffen et al., 2015), the 425–497 nm fitting window has stronger sensitivity to NO₂ columns in the boundary layer because the importance of scattering decreases with wavelength (Richter and verification team, 2015). In this study, the slant columns are derived using QDOAS software developed at the Belgian Institute for Space Aeronomy (BIRA-IASB) (Danckaert et al., 2015)¹. Table 1 summarises the new settings of the GDP 4.9 algorithm.

4.1 Absorption cross sections

In the fitting window optimised for NO₂ retrieval, the DOAS fit includes species with strong and unique absorption structures and describes their spectral effect using absorption cross sections from literature. In our GDP 4.9 algorithm, the absorption cross sections of NO₂, H₂O^{vap}, O₃, and O₄ are updated mainly with newly released datasets as

- NO₂ absorption at 220 K from Vandaele et al. (2002);
- O₃ absorption at 228 K from Brion et al. (1998);
- H₂O^{vap} absorption at 293 K from HITEMP (Rothman et al., 2010), rescaled as in Lampel et al. (2015);
- O₄ absorption at 293 K from Thalman and Volkamer (2013).

In addition, to compensate for the larger spectral interference from liquid water (H₂O^{liq}), a H₂O^{liq} absorption (Pope and Fry, 1997) is included to reduce systematic errors above ocean for the wider wavelength range. Two additional GOME-2 polarisation key data (EUMETSAT, 2009)

¹Note that the derived slant columns are scaled by geometric AMFs to correct for the angular dependencies of GOME-2 measurements in this section.

are included to correct for remaining polarisation correction problems, particularly for GOME-2B:

- H₂O^{liq} absorption at 297 K from Pope and Fry (1997), smoothed as in Peters et al. (2014);
- Eta and Zeta from GOME-2 calibration key data (EUMETSAT, 2009).

It is worth noting that our improved DOAS retrieval in the GDP 4.9 adopts a decreased temperature of NO₂ cross section (220 instead of 240 K in GDP 4.8; Valks et al., 2017) for a consistency with other NO₂ retrievals from GOME-2, OMI, and TROPOMI (Müller et al., 2016; Boersma et al., 2002; van Geffen et al., 2015, 2016), with a minor effect on the fit quality (~ 0.02 %) from the two temperatures. Changing the temperature of the NO₂ cross section from 240 to 220 K reduces the NO₂ slant columns by ~ 6 %–9 %, but this temperature dependency is corrected in the AMF and vertical column calculation (see Eq. 3).

The spectral signature of sand absorption has been investigated by Richter et al. (2011) for GOME-2 data, but it is not applied here because of the potential interference with the broadband liquid water structure (Peters et al., 2014), which might lead to non-physical results over the ocean.

4.2 Intensity offset correction

Besides the radiances backscattered by the Earth's atmosphere, a number of both natural (i.e. the Ring effect) and instrumental (e.g. stray light in the spectrometer and change of detector's dark current) sources contribute to an additional "offset" to the scattering intensity. To correct for this drift, an intensity offset correction with a linear wavelength dependency (i.e. polynomial degree of 1) is applied for the large fitting window in this study. Figure 1 illustrates the effect of using a linear intensity offset correction for the large fitting window on 3 March 2008. The use of a linear offset correction increases the NO₂ columns by up to 3 × 10¹⁴ molec cm² (17 %) and decreases the fitting residues (retrieval root mean square, rms) by up to 30 %. Larger differences are found at the eastern scans (eastern part of GOME-2 swath), possibly suggesting instrumental issues specific to GOME-2. For the retrieval rms, stronger improvements are mainly located above ocean, arguably from the compensation of inelastic vibrational Raman scattering in water bodies (Vountas et al., 2003).

The intensity offset can also be fitted using only the constant term, as employed by the GDP 4.8 algorithm (with 425–450 nm wavelength window) and as recommended by the QA4ECV algorithm (with 405–465 nm). Compared to the use of the linear intensity offset correction, the application of a constant term on our retrieval shows a decrease in the NO₂ columns by up to 3.5 × 10¹⁴ molec cm² (17 %) and an increase in the retrieval rms by up to 14 %, which implies the necessity of using a linear intensity offset correction for the large 425–497 nm wavelength range.

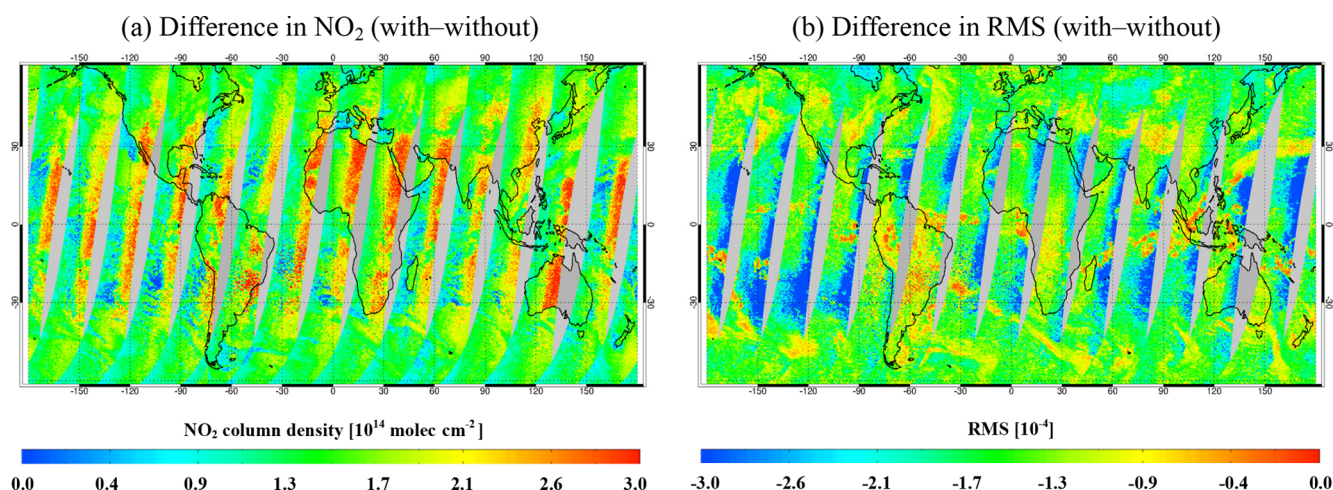


Figure 1. Difference in NO₂ columns (slant columns scaled by geometric AMFs) (a) and retrieval rms (b) estimated with and without a linear intensity offset correction for GOME-2A on 3 March 2008.

4.3 GOME-2 slit function treatment

An accurate treatment of the instrumental slit function is essential for the wavelength calibration and the convolution of high-resolution laboratory cross sections. In spite of a generally good spectral stability of GOME-2 in orbit, the width of GOME-2 slit function has been changing on both long and short timescales (Munro et al., 2016), which needs to be accounted for in the DOAS analysis. In this study, an improved treatment of GOME-2 slit function in the DOAS fit is achieved by calculating effective slit functions from GOME-2 irradiance measurements to correct for the long-term variations (see Sect. 4.3.1) and by including an additional cross section in the DOAS fit to correct for the short-term variations (see Sect. 4.3.2).

4.3.1 Long-term variations

To analyse the long-term variations of the GOME-2 instrumental slit function and the impact on our retrieval, effective slit functions are derived by convolving a high-resolution reference solar spectrum (Chance and Kurucz, 2010) with a stretched preflight GOME-2 slit function and aligning to the GOME-2 daily irradiance measurements with stretch factors as fit parameters. The effective slit functions are calculated in 13 sub-windows covering the full fitting window (425–497 nm). Figure 2 displays the long-term evolution of the fitted GOME-2 slit function width (full width at half maximum, FWHM) calculated from the stretch factors. The GOME-2 slit function has narrowed after the launch by $\sim 5\%$ for GOME-2A and $\sim 3.5\%$ for GOME-2B at 451 nm, in agreement with Dikty et al. (2011), Azam et al. (2015), and Munro et al. (2016). For GOME-2A, visible discontinuities of the slit function width are related to the in-orbit instrument operations, including an apparent anomaly in September 2009 when a major throughput test was performed (EUMETSAT,

2012). After the throughput test, the narrowing of the slit function slowed down. For GOME-2B, stronger seasonal fluctuations of the FWHM are found. The seasonal and long-term variations in the GOME-2 slit function are caused by changing temperatures of the optical bench due to the seasonal variation in solar heating and the lack of thermal stability of the optical bench, respectively (Munro et al., 2016). Although the variations are only a few percent, the effect on the DOAS retrieval is significant. Compared to the application of the preflight slit function, the use of a stretched slit function improves the calibration residuals by $\sim 40\%$ for both GOME-2A and GOME-2B (not shown).

In previous studies, slit functions have also been fitted using various Gaussian shapes. For instance, De Smedt et al. (2012) have derived effective GOME-2 slit functions for formaldehyde retrieval using an asymmetric Gaussian with its width and shape as fit parameters. For NO₂ retrieval, the use of effective slit functions with an asymmetric Gaussian leads to similar results as using a preflight slit function. In addition, Beirle et al. (2017) have proposed a slit function parameterisation using a super Gaussian, which is proved to quickly and robustly describe the slit function changes for satellite instrument OMI or TROPOMI. In the case of GOME-2, the super Gaussian obtains nearly identical results as the asymmetric Gaussian and is therefore not applied in here.

4.3.2 In-orbit variations

To correct for the in-orbit variations of GOME-2 slit function, a “resolution correction function” (Azam et al., 2015) is included as an additional cross section in the DOAS fit (see Table 1). The cross section is derived by dividing a high-resolution solar spectrum (Chance and Kurucz, 2010) convolved with a stretched preflight GOME-2 slit function (see

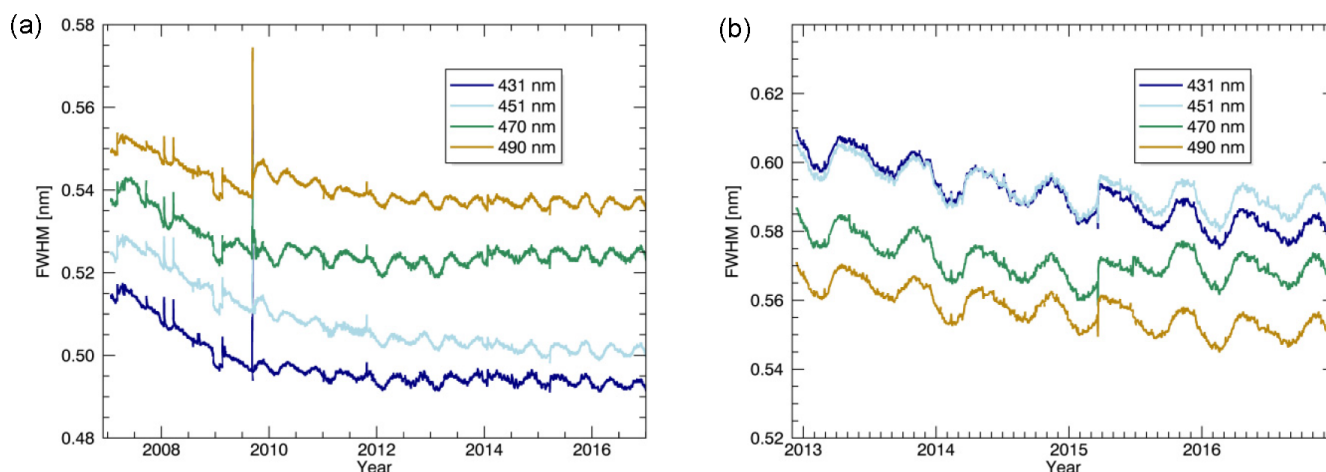


Figure 2. Temporal evolution of the fitted slit function FWHM for GOME-2A (a, January 2007–December 2016) and GOME-2B (b, December 2012–December 2016.)

Sect. 4.3.1) by itself but convolved with a slightly modified slit function. Figure 3 shows an example of the fit coefficients and the influence on our DOAS retrieval on 1 February 2013. As shown in the left panel, the slit function width increases along the orbit by $\sim 2 \times 10^{-3}$ nm ($\sim 0.4\%$) for GOME-2A (see Beirle et al., 2017, Fig. 8 therein) and $\sim 5.2 \times 10^{-3}$ nm ($\sim 1\%$) for GOME-2B (a fit coefficient of 1×10^{-2} corresponds to a change in the slit function width of $\sim 2.8 \times 10^{-3}$ nm). This in-orbit broadening of the slit function is caused by the increasing temperature of the instrument along the orbit. Taking into account the in-orbit broadening in the DOAS fit decreases the retrieval rms by up to 5% for GOME-2A and up to 12% for GOME-2B in Fig. 3b.

4.4 GOME-2 level 1b data

As described in Sect. 2, the level 0 to 1b processing by the PPF at EUMETSAT calculates the geolocation and calibration parameters and produces the calibrated level 1b (ir)radiance. Due to the incomplete removal of Xe-line contamination in the GOME-2B calibration key data (calibration key data are taken during the on-ground campaign and required as an input to the level 0 to 1b processing), artefacts at wavelengths larger than 460 nm have been reported by Azam et al. (2015) for GOME-2B irradiances. Mainly focusing on the cleaning of contamination in the GOME-2B calibration key data, a new 6.1 version of the GOME-2 level 0 to 1b processor has been activated from 25 June 2015 onwards (EUMETSAT, 2015). To study the impact of the new level 1b data on our GDP 4.9 algorithm using the 425–497 nm fitting window, the retrieval is analysed using both the new 6.1 version (testing dataset provided by EUMETSAT for March 2015) and the previous version 6.0 data for the same period. Figure 4 presents a comparison of the retrieved NO₂ columns over the Pacific for GOME-2A and GOME-2B. The application of the version 6.1 level 1b data slightly reduces the

NO₂ columns by $\sim 1\text{--}1.5 \times 10^{14}$ molec cm² ($\sim 6\%\text{--}11\%$) for GOME-2A. A larger effect is observed for GOME-2B with a decrease of NO₂ columns by $\sim 3\text{--}4 \times 10^{14}$ molec cm² ($\sim 15\%\text{--}23\%$) and a reduction of rms error by $\sim 27\%\text{--}33\%$ (not shown). The stronger decrease of GOME-2B NO₂ columns leads to a better consistency between the datasets from GOME-2A and GOME-2B with an overall bias reduced from $\sim 3 \times 10^{14}$ molec cm² to $\sim 1 \times 10^{14}$ molec cm².

4.5 Comparison to QA4ECV data

The quality of the GDP 4.9 retrieval is evaluated using the GOME-2 NO₂ dataset from QA4ECV, which is a project aiming at quality-assured satellite products using a retrieval algorithm harmonised for GOME, SCIAMACHY, OMI and GOME-2. The GOME-2A NO₂ columns from QA4ECV (version 1.1) for the years 2007–2015 have shown an improved quality over previous datasets (Zara et al., 2018). Table 1 gives an overview of the DOAS settings used in the QA4ECV project. Figure 5 shows a comparison of the NO₂ columns over the Pacific from the GDP 4.8 algorithm, the GDP 4.9 algorithm, and the QA4ECV data for February 2007. For comparison, only ground pixels with a solar zenith angle smaller than 80° are considered. The GDP 4.8 dataset has been adjusted using a 220 K (Vandaele et al., 2002) NO₂ cross section to remove the influence of temperature dependency of the NO₂ cross section (see discussion in Sect. 4.1). Compared to the GDP 4.8 dataset, the improved DOAS retrieval in GDP 4.9 increases the NO₂ columns by $\sim 1\text{--}3 \times 10^{14}$ molec cm² (up to 27%). Compared to the QA4ECV product, a good overall consistency is found with the GDP 4.9 dataset at all latitudes considering the different DOAS settings such as fitting window, offset correction, and slit function characterisation.

Figure 6 presents the time series of calculated slant column errors from the three datasets, following a statistical method

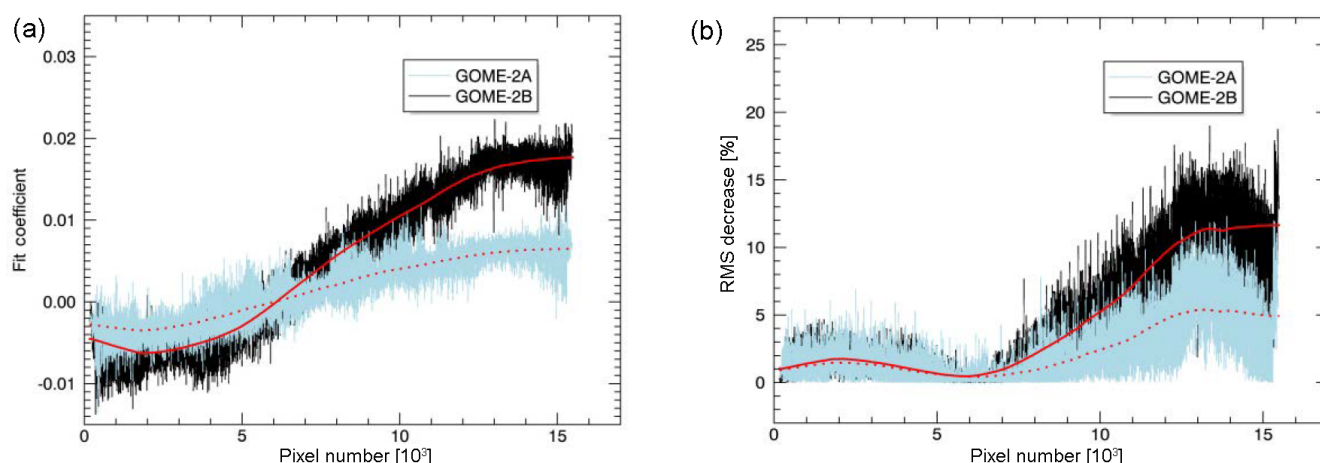


Figure 3. Changes of GOME-2 slit function width along orbit 32 636 on 1 February 2013 (a) and the impact on the retrieval rms error (b). Red lines provide the boxcar average for GOME-2A (dotted) and GOME-2B (solid). A fit coefficient of 1×10^{-2} corresponds to a change in the slit function width of $\sim 2.8 \times 10^{-3}$ nm (a).

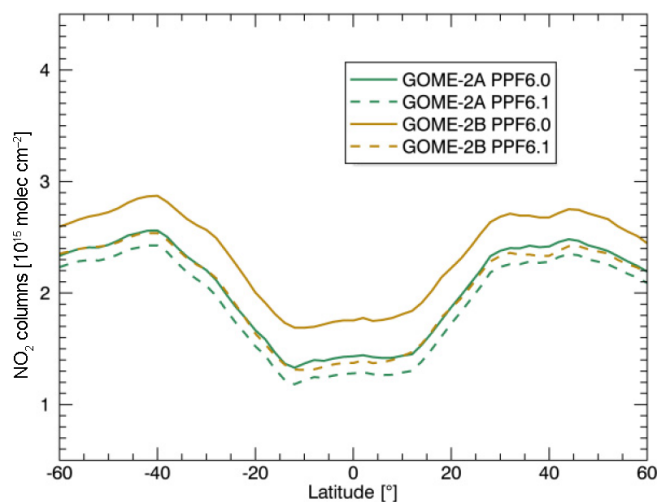


Figure 4. Monthly zonal average NO₂ columns (slant columns scaled by geometric AMFs) for GOME-2A (green) and GOME-2B (brown) using the new PPF 6.1 (dotted) and PPF 6.0 (solid) data in March 2015 over the Pacific (160–180° E).

to analyse the NO₂ slant column uncertainty for GOME-2 (Valks et al., 2011, Sect. 6.1 therein). The slant column errors, calculated as variations of NO₂ measurements within small boxes ($2^\circ \times 2^\circ$) over the tropical Pacific (20°S – 20°N , 160 – 180°E), increase for all the three datasets as a result of instrument degradation (Dikty et al., 2011; Munro et al., 2016) until the major throughput test in September 2009 (see Sect. 4.3.1) and stabilise afterwards. Mainly driven by the use of a wider fitting window with stronger absorptions, the smallest slant column errors are found by the GDP 4.9 algorithm, e.g. 23.8 % smaller than from the GDP 4.8 and 13.5 % smaller than from the QA4ECV dataset in February 2007,

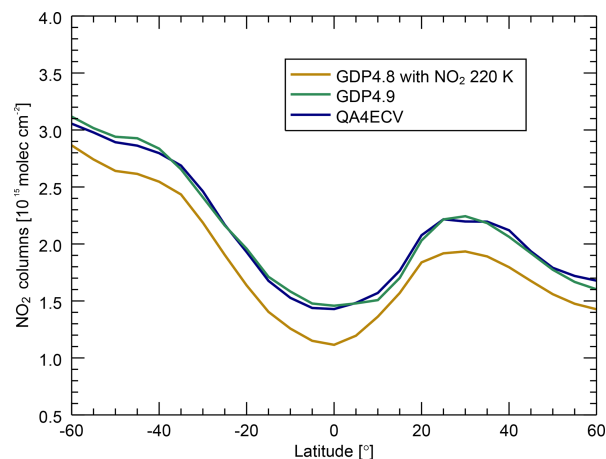


Figure 5. Comparisons of monthly zonal average NO₂ columns (slant columns scaled by geometric AMFs) from the operational GDP 4.8 product (but retrieved using a 220 K NO₂ cross section from Vandaele et al., 2002) (brown), the improved GDP 4.9 algorithm (green), and the QA4ECV dataset (blue) over the Pacific (160–180° E) in February 2007 for GOME-2A.

with an increasing difference with time for the QA4ECV dataset (27.9 % in December 2015).

5 New stratosphere–troposphere separation

The calculation of tropospheric NO₂ requires an estimation and removal of the stratospheric contribution to the initial total NO₂ columns. In our GDP 4.9 retrieval, the stratosphere–troposphere separation algorithm STREAM (Beirle et al., 2016) has been adapted to GOME-2 measurements. Belonging to the modified reference sector method, STREAM uses initial total NO₂ columns with negligible tropospheric

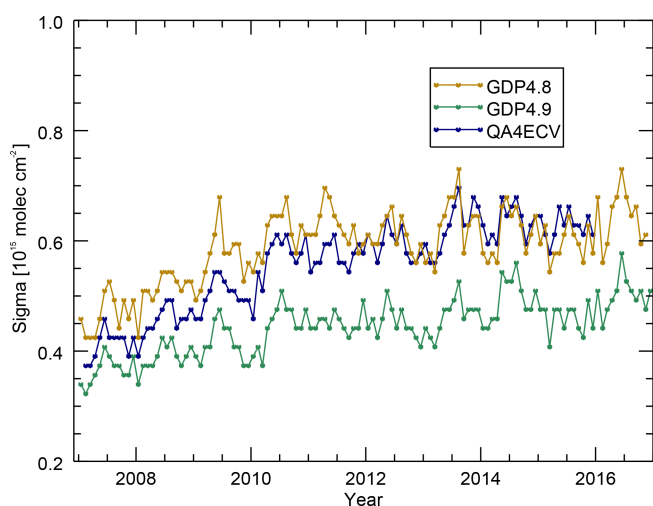


Figure 6. Temporal evolution of the NO₂ slant column errors from the operational GDP 4.8 product (brown, January 2007–December 2016), the improved GDP 4.9 algorithm (green, January 2007–December 2016), and the QA4ECV dataset (blue, February 2007–December 2015) for GOME-2A, using deviations of NO₂ slant columns from box ($2^\circ \times 2^\circ$) mean values over the tropical Pacific (20°S – 20°N , 160 – 180°E).

contribution, i.e. unpolluted measurements at remote areas and cloudy measurements at medium altitudes, to derive the stratospheric NO₂ columns. Based on a tropospheric NO₂ climatology and the GOME-2 cloud product, STREAM calculates weighting factors for each satellite pixel to define the contribution of initial total columns to the stratospheric estimation; potentially polluted pixels are weighted low instead of being totally masked out in the GDP 4.8 spatial filtering method, cloudy observations at medium altitudes are given higher weights because they directly provide the stratospheric information, and the weights are further adjusted in a second iteration if pixels suffer from large biases in the tropospheric residues. Depending on these weighting factors, stratospheric NO₂ fields are derived by weighted convolution on the daily initial total columns using convolution kernels. The convolution kernels are wider at lower latitudes due to the longitudinal homogeneity assumption of stratospheric NO₂ and narrower at higher latitudes to reflect the stronger natural variations. To remove the biases in the weighted convolution resulting from the large latitudinal gradients, a latitudinal correction is applied on the initial total columns: the latitudinal dependencies of initial total NO₂ are calculated over the clean Pacific, removed from the initial total NO₂ before weighted convolution, and added back to the estimated stratospheric columns afterwards. However, we found that longitudinal variations of NO₂ concentration resulted in biases in the latitudinal correction and hence in the stratospheric estimation. For the adaptation of STREAM to GOME-2 measurements, the performance of STREAM is analysed using synthetic GOME-2 NO₂ observations (see

Sect. 5.1), and an improved latitudinal correction is applied (see Sect. 5.2).

5.1 Performance of STREAM

To test the performance of STREAM for GOME-2, simulated NO₂ fields from the C-IFS-CB05-BASCOE (referred to as C-IFS throughout this work) experiment (Huijnen et al., 2016) are applied. The C-IFS model is a combination of tropospheric chemistry module in the Integrated Forecast System (IFS, with current version based on the Carbon Bond chemistry scheme, CB05) of the European Centre for Medium-Range Weather Forecasts (ECMWF) and stratospheric chemistry from the Belgian Assimilation System for Chemical Observations (BASCOE) system. Based on 1 year of C-IFS data (2009) at a resolution of $0.75^\circ \text{ long.} \times 0.75^\circ \text{ lat.}$, synthetic initial total columns V_{init} are calculated as

$$V_{\text{init}} = \frac{S}{M_{\text{strat}}} = \frac{V_{\text{total}} \times M_{\text{total}}}{M_{\text{strat}}} \quad (7)$$

(see Eq. 2). Modelled NO₂ slant columns S are based on the total vertical columns V_{total} from C-IFS with interpolation to match the GOME-2 centre pixel coordinate and measurement time. Total AMFs M_{total} and stratospheric AMFs M_{strat} are derived using Eqs. (3)–(5) with surface properties and cloud information from GOME-2 orbital data and with C-IFS a priori NO₂ profiles for the whole atmosphere and between the tropopause (defined by a latitude-dependent parameterisation with the tropopause height ranging from 270 hPa for arctic to 92 hPa for tropics) and the top of the atmosphere, respectively. The performance of STREAM is evaluated by applying the synthetic initial total NO₂ columns and comparing the estimated stratospheric NO₂ columns with the a priori truth (stratospheric fields from C-IFS integrated between the tropopause and the top of the atmosphere).

Figure 7 displays the synthetic initial total columns from C-IFS, the modelled stratospheric columns, and the estimated stratospheric columns from STREAM on 5 February and 5 August 2009. The result from STREAM presents an overall smooth stratospheric pattern with a strong latitudinal and seasonal dependency resulting from photochemical changes and dynamical variabilities. Because the stratospheric values over polluted regions are taken from the clean measurements at the same latitude, the stratospheric and tropospheric contribution over polluted regions is well separated by STREAM, especially in the Northern Hemisphere. Due to the latitude-dependent definition of convolution kernels, STREAM conserves the longitudinal gradients of stratospheric NO₂ at low latitudes and identifies certain strong stratospheric variations at high latitudes, e.g. in the polar vortex on 5 February. However, smaller structures in the synthetic initial total columns, for instance, resulting from the diurnal variation of NO₂ across an orbital swath,

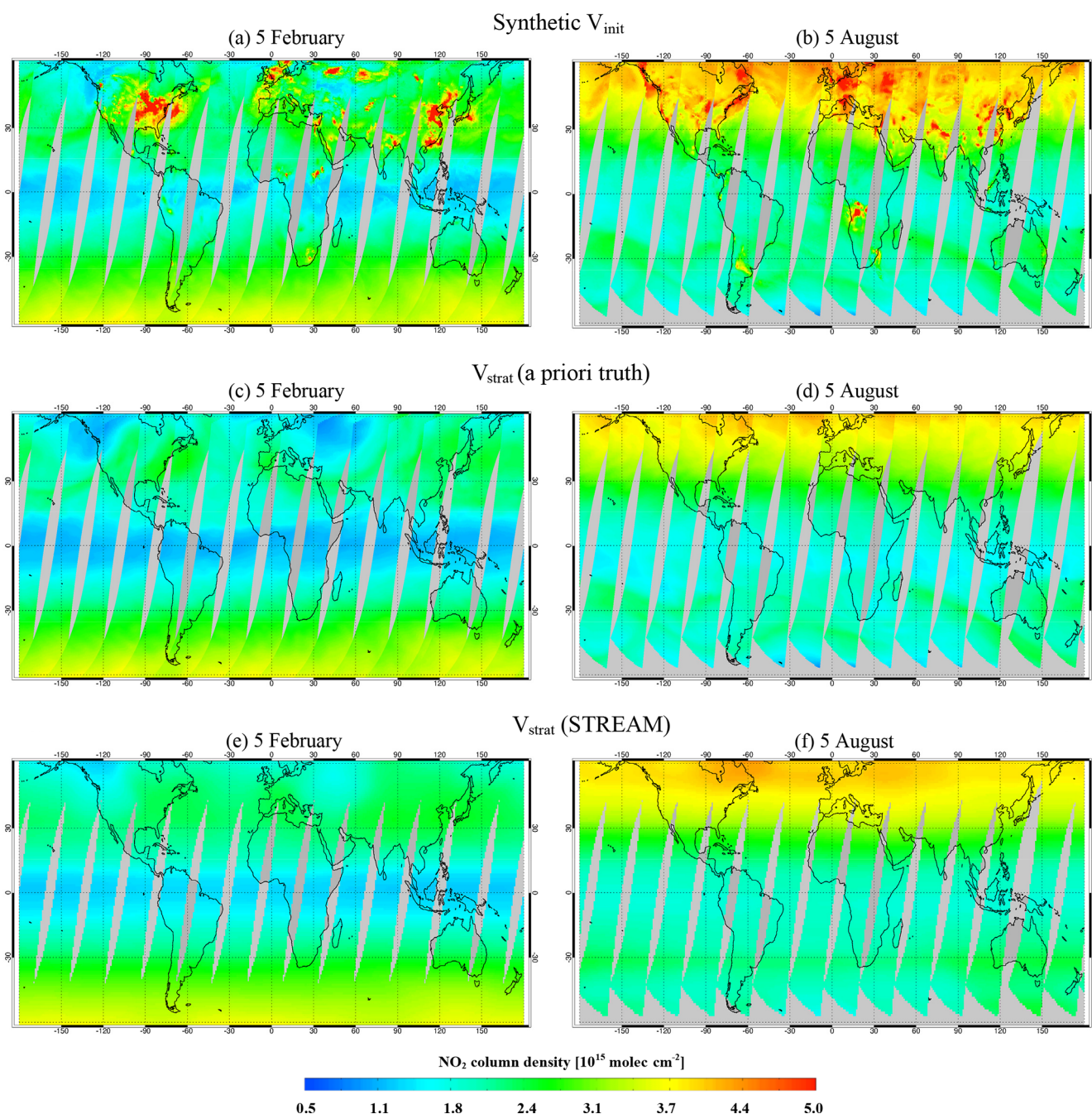


Figure 7. Synthetic initial total NO₂ columns (a, b), a priori stratospheric columns from C-IFS (c, d), and estimated stratospheric columns from STREAM (e, f) on 5 February (a, c, e) and 5 August (b, d, f) 2009.

are aliased into the troposphere by STREAM due to the use of convolution kernels.

Figure 8a, b shows the differences in estimated (Fig. 7e, f) and a priori (Fig. 7c, d) stratospheric NO₂. Overall, the stratospheric columns estimated from STREAM show good agreement with the modelled truth with a slight overestimation, e.g. by $\sim 1\text{--}2 \times 10^{14}$ molec cm⁻² over low latitudes for both days. Larger differences are found at higher latitudes,

especially in winter, e.g. by $\sim 5 \times 10^{14}$ molec cm⁻² over eastern Europe and over the North Pacific (west of Canada) on 5 February. The strong longitudinal variations of NO₂ over these regions in the a priori truth (Fig. 7c, d) can not be completely captured by STREAM (Fig. 7e, f), which is a general limitation of the modified reference sector method. Note that these larger differences are reduced to $\sim 2 \times 10^{14}$ molec cm⁻² in monthly averages (not shown). The found deviations are

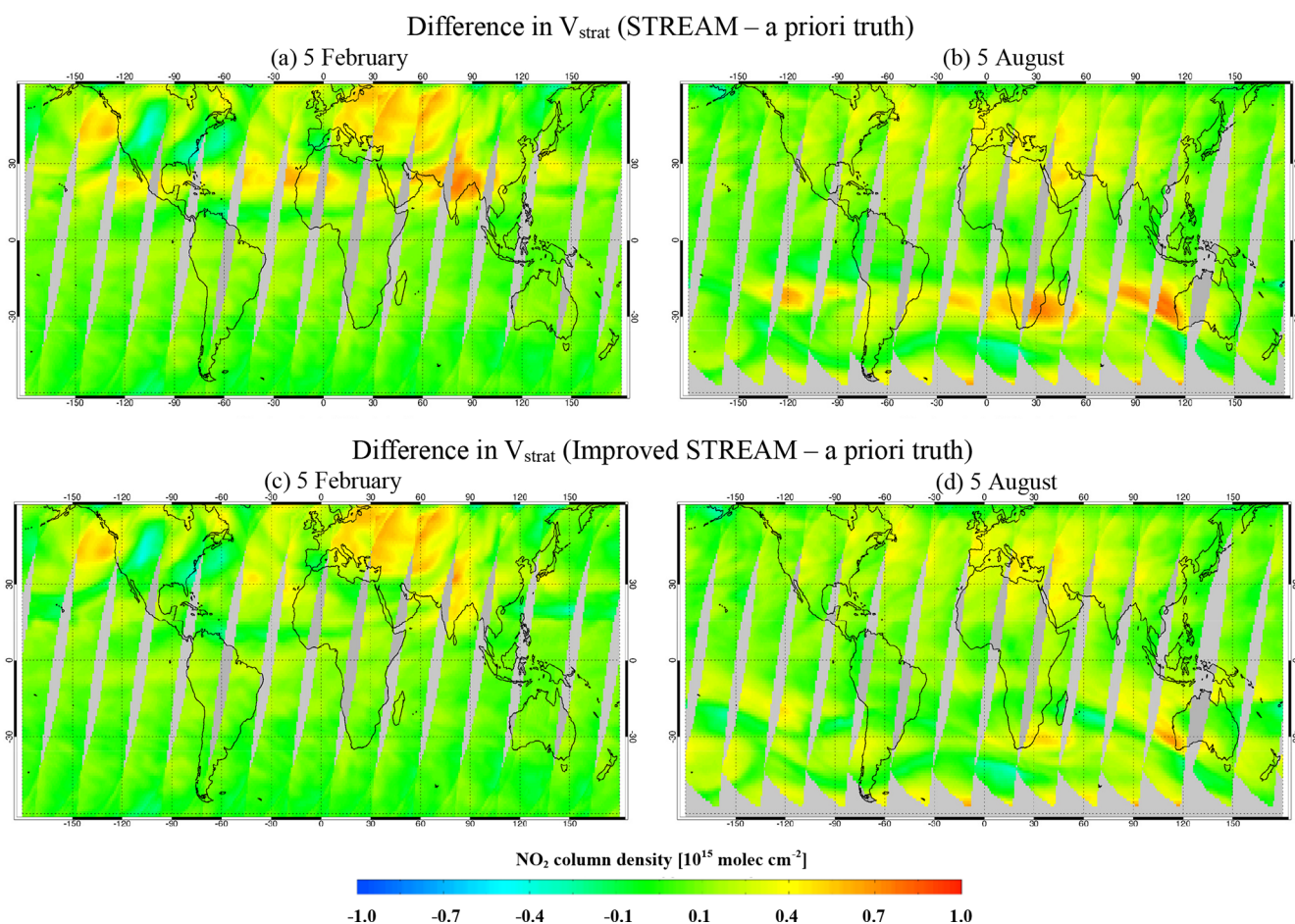


Figure 8. Difference in the stratospheric NO₂ columns estimated from STREAM and modelled by C-IFS on 5 February (a) and 5 August (b) 2009. Panels (c) and (d) show STREAM with improved latitudinal correction.

in agreement with the uncertainty estimates in Beirle et al. (2016).

5.2 Improved latitudinal correction

In Fig. 8a, b, larger differences are noticeable over the subtropical regions in winter for both days, primarily related to the latitudinal correction used in STREAM. As described in the previous Sect. 5, the latitudinal correction is applied by determining the latitudinal dependencies of total NO₂ over the clean Pacific, removing the latitudinal dependencies before convolution and adding it back to the estimated stratospheric columns. However, longitudinal variations of total NO₂, for instance, enhanced total NO₂ columns over the Pacific (compared to the Atlantic Ocean) at 15–30° N on 5 February 2009 (Fig. 7a), introduce biases in the stratospheric NO₂ columns. Therefore, an improved latitudinal correction is introduced to reduce the biases over the subtropics. The new latitudinal correction determines the latitudinal dependencies of total NO₂ based on clean measurements in the whole latitude band (the median of lowest NO₂ columns

for each 1° latitude band). Figure 8c, d shows the difference for the estimated stratospheric NO₂ using the improved latitudinal correction. For both days, the application of the new latitudinal correction in STREAM largely removes the biases over the subtropics in Fig. 8a, b.

Applying the improved STREAM on GOME-2 data, Fig. 9 presents the initial total columns from GOME-2 and the stratospheric NO₂ calculated with STREAM and with the spatial filtering method used in the GDP 4.8 algorithm (see Sect. 3) in February and August 2009. For both months, the results calculated with STREAM and with the spatial filtering method show similar global structures. Since the spatial filtering method applies a fixed pollution mask to remove the potentially polluted regions (tropospheric NO₂ larger than 1×10^{15} molec cm⁻²), moderately polluted pixels with tropospheric NO₂ up to 1×10^{15} molec cm⁻² still contribute to the stratospheric estimation. Therefore, enhanced stratospheric NO₂ by more than 5×10^{14} molec cm⁻² is found over polluted regions, e.g. the Middle East, China, central Africa, southern Africa, and Australia in Fig. 9e, f. This overestimation is largely removed by STREAM in Fig. 9c, d.

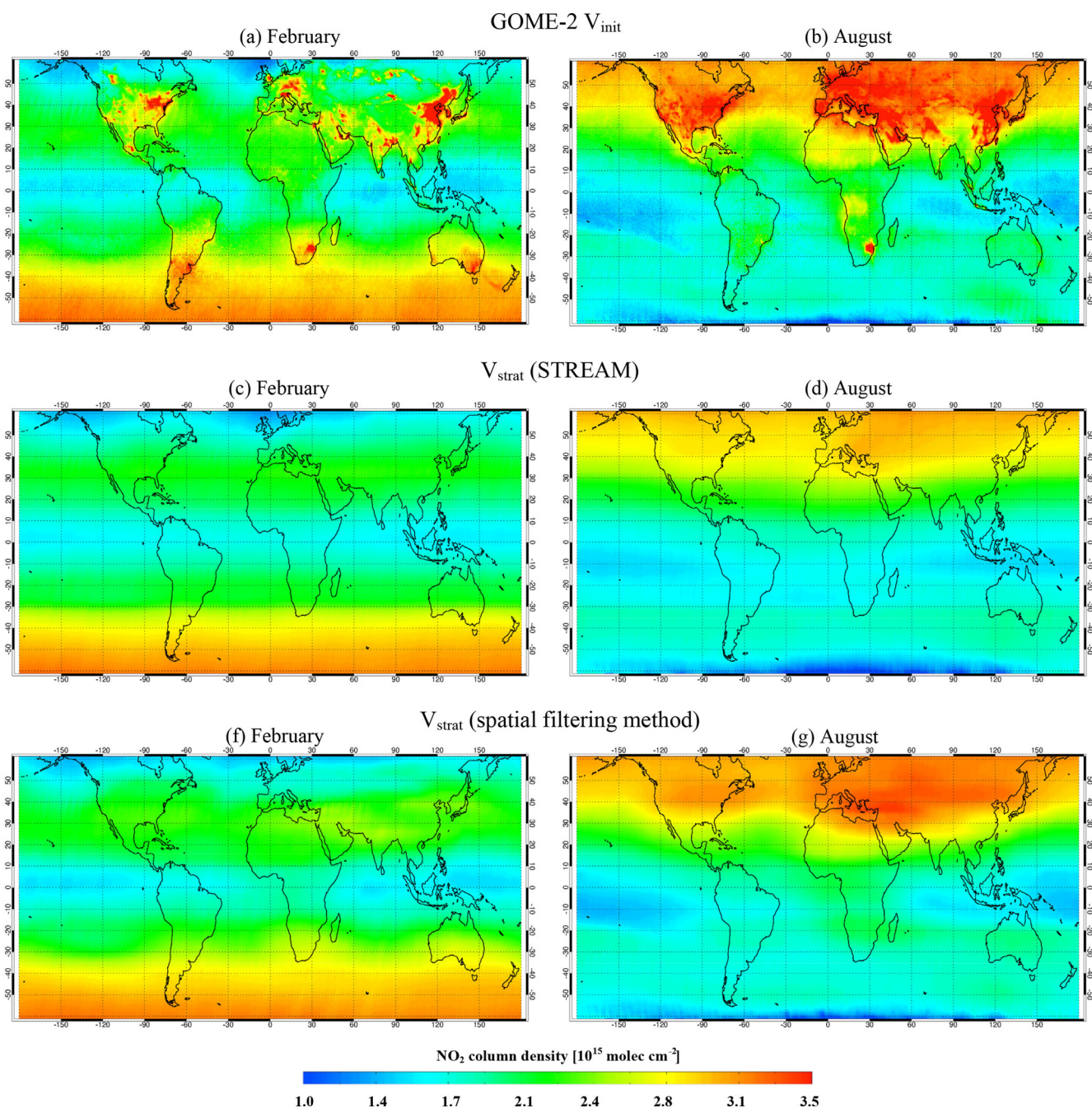


Figure 9. GOME-2 initial total NO₂ columns (a, b) and stratospheric NO₂ columns retrieved from the improved STREAM algorithm (c, d) and from the spatial filtering method used in GDP 4.8 (e, f), measured by GOME-2A in February (a, c, e) and August (b, d, f) 2009.

Table 2. Main settings of AMF calculation method and input data discussed in this study.

	GDP 4.8	GDP 4.9 (this work)
RTM	LIDORT v2.2+	VLIDORT v2.7
Surface albedo	TOMS–GOME LER, Boersma et al. (2004)	GOME-2 Min-LER v2.1, Tilstra et al. (2017b)
A priori profile	Monthly MOZART-2 (1.875° × 1.875°)	Daily TM5-MP (1° × 1°)

6 Improvements to NO₂ AMF calculation

6.1 RTM

As summarised in Table 2, updated box-AMFs are calculated using the linearised vector code VLIDORT (Spurr, 2006) version 2.7. VLIDORT applies the discrete ordinates method to generate simulated intensity and analytic intensity derivatives with respect to atmospheric and surface parameters (i.e. weighting functions). Box-AMFs m_l (see Eq. 3) are determined as

$$m_l = \frac{\partial \ln I}{\partial \tau_{\text{NO}_2,l}} = \frac{\frac{\partial I}{\partial \tau_{\text{NO}_2,l}} \cdot \tau_{\text{NO}_2,l}}{I \cdot \tau_{\text{NO}_2,l}}, \quad (8)$$

with I being the simulated top-of-atmosphere radiance, $\tau_{\text{NO}_2,l}$ the absorption optical thickness of NO₂ at layer l , and term $\frac{\partial I}{\partial \tau_{\text{NO}_2,l}} \cdot \tau_{\text{NO}_2,l}$ the NO₂ profile weighting function. Compared to the scalar (intensity-only) LIDORT code, VLIDORT provides more realistic modelling results with a treatment of light polarisation, which affects the tropospheric AMFs by up to 4 %.

The box-AMFs m_l for each layer are calculated for the midpoint wavelength of fitting window, i.e. 461 nm in our NO₂ retrieval, which is representative of the window-averaged box-AMFs. Compared to the tropospheric AMFs at 440 nm (midpoint wavelength in GDP 4.8), the ones calculated at 461 nm are higher by up to 10 % for polluted situations, due to the wavelength dependency of Rayleigh scattering, in agreement with Boersma et al. (2018) (see Fig. 7 therein). Note that the uncertainty related to the wavelength dependency of the AMF is much smaller than the uncertainties introduced by surface albedo, a priori NO₂ profile, cloud, and aerosol (see Sect. 6.4).

The m_l value is calculated with the RTM and stored in a LUT as a function of GOME-2 viewing geometry, surface pressure, and surface albedo. Compared to the LUT used in the GDP 4.8, a new LUT is calculated with an increased number of reference points, e.g. for surface pressure (from 10 to 16) and for surface albedo (from 10 to 14), as well as vertical layers (from 24 to 60) to reduce the interpolation error (Lorente et al., 2017), leading to differences in tropospheric AMFs by up to 2 %.

6.2 Surface albedo

Surface albedo is an important parameter for an accurate retrieval of NO₂ columns and cloud properties. The sensitivity of backscattered radiance to the boundary layer NO₂ is strongly related to the surface albedo, especially over polluted areas. In the GDP 4.9, the surface LER climatology based on TOMS–GOME data (Boersma et al., 2004) has been replaced by one based on GOME-2 observations (Tilstra et al., 2017b). Using the degradation-corrected GOME-2 level 1 measurements, the GOME-2 surface LER is derived by matching the measurements in a

pure Rayleigh scattering atmosphere without clouds. Compared to the TOMS–GOME LER climatology, the GOME-2 surface LER (version 2.1) dataset takes advantage of newer observations for 2007–2013, an increased spatial resolution of 1.0° long. × 1.0° lat. for standard grid cells and 0.25° long. × 0.25° lat. at coastlines (Tilstra et al., 2017a), and an improved treatment of cloud contaminated cells over the ocean.

Figure 10 shows the surface LER data from the GOME-2 and TOMS–GOME observations for 440 nm in February. A good overall consistency is found between the two LER datasets, particularly over the ocean. Larger differences are found over certain snow or ice areas, like Russia and southern Canada, which can be attributed to changes in snow or ice cover during the different measurement periods of the two LER datasets. Increased spatial resolution for the GOME-2 LER version 2.1 dataset enables a better representation of surface features for the land–sea boundaries, e.g. coasts around western Europe and eastern China. Improvements in the GOME-2 LER algorithm (Tilstra et al., 2017b) decreases the surface LER values over regions with persistent clouds, e.g. the North Atlantic Ocean and the North Pacific Ocean at middle latitudes. Systematic differences in the LER climatologies are also caused by the different overpass time, observing geometry, and radiometric calibration of the instruments.

Figure 11 illustrates the influence of the updated surface LER at 440 nm on the retrieved tropospheric NO₂ columns in February 2008. The difference over the ocean is very small. Larger effects are noticed primarily under polluted conditions with positive differences, e.g. over parts of central Europe, Russia, or USA, and negative values, e.g. over parts of South Africa, India, or China. The differences in the retrieved tropospheric NO₂ columns are consistent with the changes in the surface LER. For example, the GOME-2 surface LER over central Europe is ~ 0.012 smaller than TOMS–GOME data, and a lower sensitivity to tropospheric NO₂ is therefore assumed in the AMF calculation. This results in a decrease in the AMF and hence an increase in the retrieved tropospheric NO₂ column by ~ 7 × 10¹⁴ molec cm² (~ 12 %). Vice versa, an increase of the surface LER values by ~ 0.018 over the Yangtze River region in eastern China leads to a reduction of tropospheric NO₂ columns by ~ 4 × 10¹⁵ molec cm² (~ 15 %).

As described in Sect. 6.1, the AMFs are calculated for 461 nm in the GDP 4.9 (425–497 nm wavelength window) instead of 440 nm in the GDP 4.8 (with 425–450 nm wavelength window), and therefore the corresponding surface LER values of 463 nm are used. The surface LER values at 463 nm are higher by up to 0.02 over desert areas and lower by up to 0.02 over the ocean and the snow or ice areas, which result in differences of up to 5 % in the calculated AMFs.

The surface LER climatology from Kleipool et al. (2008) derived from OMI measurements for 2004–2007 has been widely used in satellite NO₂ retrievals (e.g. Boersma et al.,

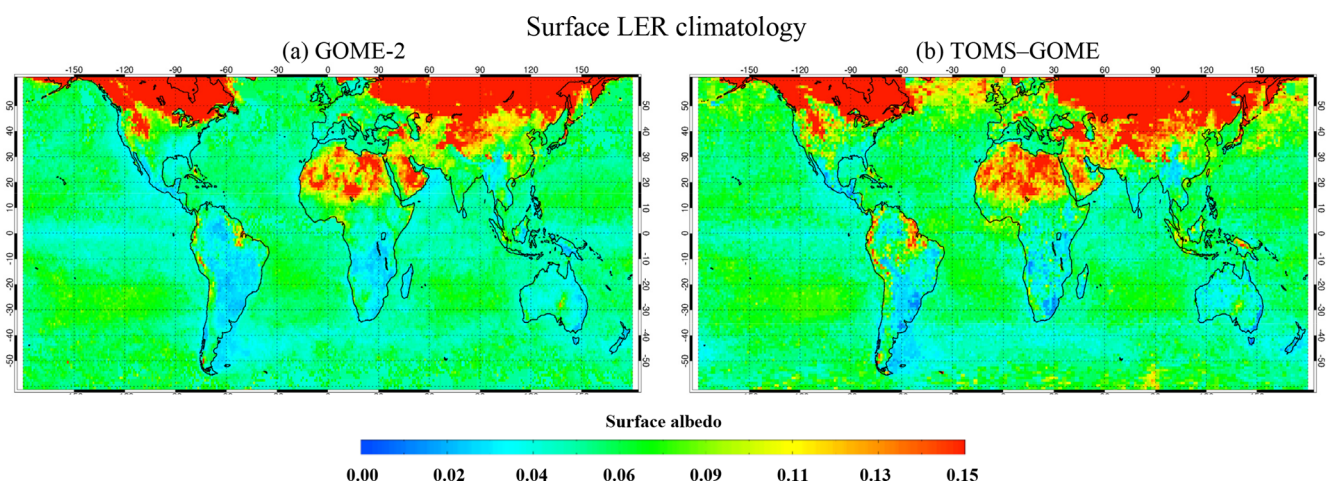


Figure 10. Map of surface LER data for 440 nm in February based on GOME-2 observations for 2007–2013 (Tilstra et al., 2017b) (a) and TOMS–GOME data for 1979–1993 (b).

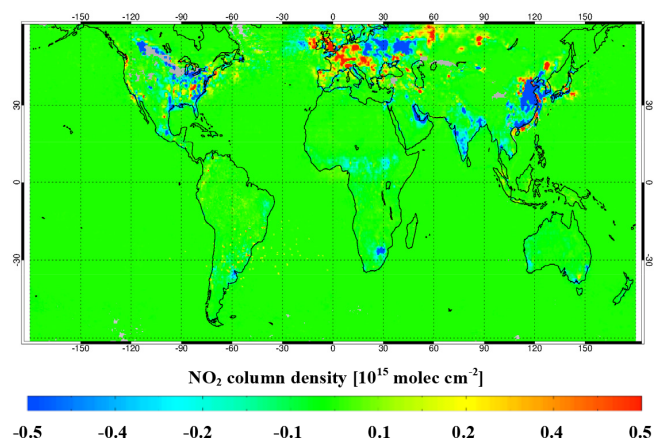


Figure 11. Difference in tropospheric NO₂ columns for clear-sky conditions (cloud radiance fraction smaller than 0.5) for February 2008 retrieved using the GOME-2 surface LER climatology version 2.1 and the LER climatology based on TOMS–GOME data at 440 nm.

2011; Barkley et al., 2013; Bucselo et al., 2013). An important advantage of using the GOME-2 LER climatology with respect to the OMI LER dataset in our retrieval is the consistency with the GOME-2 NO₂ observations, considering the illumination conditions, observation geometry, and instrumental characteristics. Another advantage of the GOME-2 LER climatology is the use of more recent observations to reduce the errors introduced by ignoring the interannual variability of surface albedo, which are possibly large for varying snow and ice situations. Possible corrections for the surface albedo from a climatology include the use of external information about the actual snow and ice conditions, e.g. from the Near-real-time Ice and Snow Extent (NISE) dataset (Nolin et al., 2005).

6.3 A priori vertical profiles

The retrieved tropospheric NO₂ columns are sensitive to changes in the relative vertical distribution of the a priori NO₂ concentrations (i.e. profile shape). Increasing the spatial and/or temporal resolution of the a priori profiles have shown to produce a more accurate NO₂ retrieval (e.g. Russell et al., 2011; Heckel et al., 2011; McLinden et al., 2014; Nüß et al., 2006; Laughner et al., 2016). To improve the tropospheric AMF calculation, daily a priori NO₂ profiles are obtained with a resolution of 1° long. × 1° lat. from the chemical transport model TM5-MP (Huijnen et al., 2010; Williams et al., 2017). The TM5-MP profiles have been used in several studies to derive AMFs and tropospheric NO₂ columns (e.g. van Geffen et al., 2016; Lorente et al., 2017; Boersma et al., 2018).

Figure 12 shows the TM5-MP and MOZART-2 a priori NO₂ profiles for two pollution hot spots located in Brussels (Belgium, lat. 50.9, long. 4.4) and Guangzhou (China; lat. 23.1, long. 113.3) on 1 day in February and August 2009 as examples. Monthly profiles are shown for MOZART-2, and profiles for the given days are shown for TM5-MP. Large differences between the a priori NO₂ profile shapes from TM5-MP and MOZART-2 are found for both cities. These differences are the result of the different chemical mechanism, transport scheme, and emission inventory employed by the model, the different spatial resolution, and the use of daily vs. monthly profiles. In TM5-MP, the use of an updated NO_x emissions from the MACCity inventory (Granier et al., 2011) produces more realistic profiles. Improvement in the spatial resolution gives a more accurate description of the NO₂ gradient and transport. The use of daily profiles provides a better description of the temporal NO₂ variation, especially for regions dominated by emission and transport like Brussels and Guangzhou.

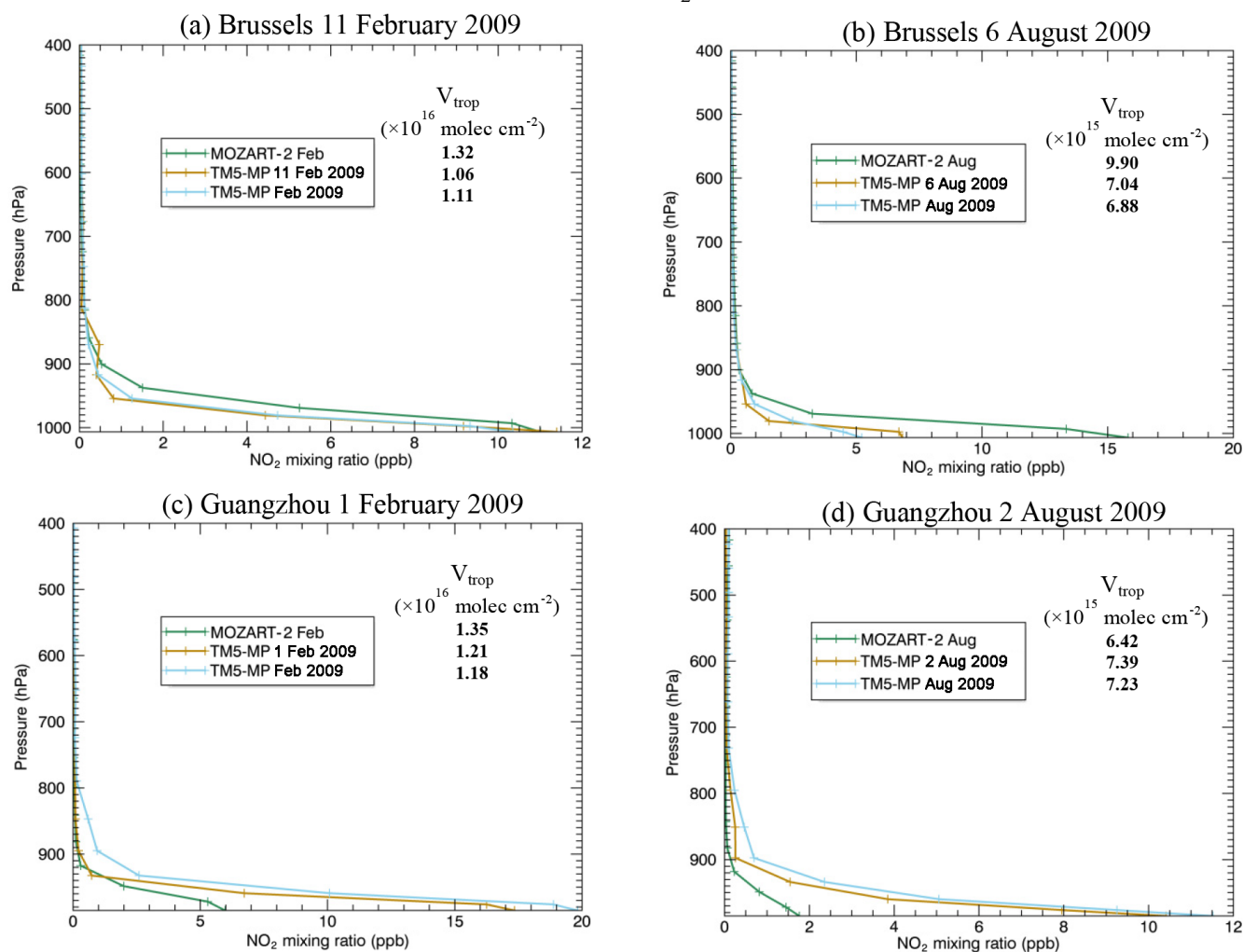
A priori NO₂ profile

Figure 12. Examples of a priori NO₂ profiles for Brussels (a, b) and Guangzhou (c, d) on a given day in February (a, c) and August (b, d) 2009. Monthly profiles are shown for MOZART-2 (green), and daily profiles on the given days are shown for TM5-MP (brown) together with the monthly average profiles calculated for TM5-MP (blue). The tropospheric NO₂ columns retrieved using each a priori NO₂ profile are also given.

In Fig. 12, the tropospheric NO₂ columns retrieved for the individual days using TM5-MP and MOZART-2 a priori NO₂ profiles are also reported. Taking Brussels on 11 February 2009 (Fig. 12a) as an example, the smaller boundary layer concentration modelled by TM5-MP (less steep profile shape) leads to an increase in the tropospheric AMF and hence a decrease in the retrieved tropospheric NO₂ columns by 2.6×10^{15} molec cm² (19.7%). Figure 13 presents a comparison of the monthly averaged tropospheric NO₂ columns retrieved using daily TM5-MP and monthly MOZART-2 a priori NO₂ profiles in February and August 2009. The application of the daily TM5-MP a priori NO₂ profiles affects the tropospheric NO₂ columns by more than 1×10^{15} molec cm² mostly over polluted regions with enhanced NO₂ in the boundary layer, e.g. with an increase of tropospheric NO₂

over parts of China, India, and South Africa and a decrease over parts of the eastern US, Europe, and Japan.

To analyse the effect of using daily vs. monthly profiles, the tropospheric NO₂ columns are also retrieved using the monthly average TM5-MP profiles, as shown in Fig. 12. Differences in the profile shape of daily and monthly profiles are mainly related to the variations in the meteorology. In agreement with Nüß et al. (2006) and Laughner et al. (2016), the use of monthly profiles changes the tropospheric NO₂ columns by up to 3×10^{15} molec cm² depending on the wind speed and wind direction, in particular for regions affected by transport (not shown). For the example of Brussels on 11 February 2009 (Fig. 12a), the use of monthly profiles increases the tropospheric NO₂ columns by 5×10^{14} molec cm² (4.7%). A comprehensive analysis of the effect of using a

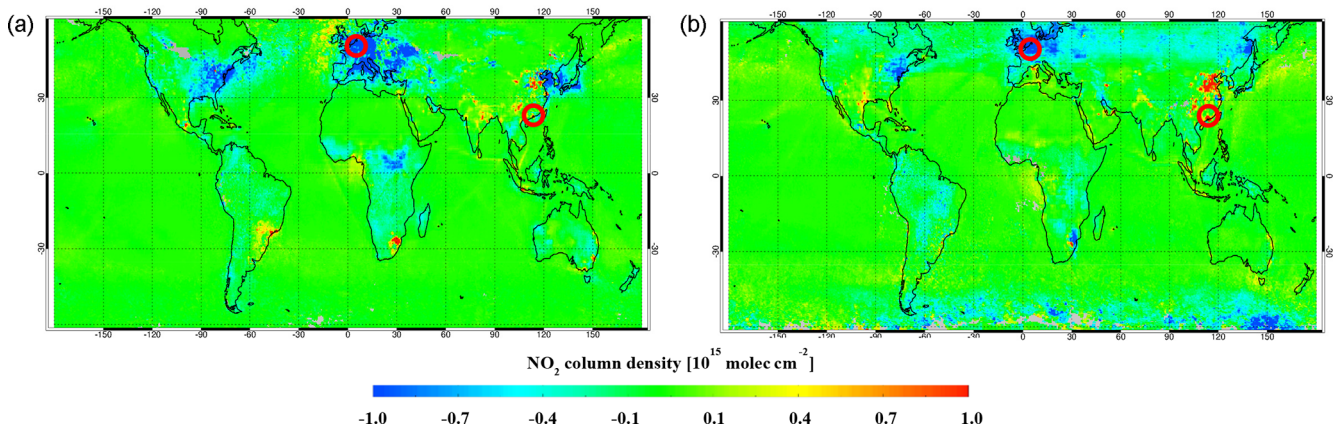


Figure 13. Difference in tropospheric NO₂ columns for clear-sky conditions (cloud radiance fraction smaller than 0.5) retrieved using daily TM5-MP and monthly MOZART-2 a priori NO₂ profiles for February (a) and August (b) 2009. Red circles indicate locations in Fig. 12.

priori NO₂ profiles from different chemistry transport models on the retrieved tropospheric NO₂ will be described in a subsequent paper.

6.4 Examples of GOME-2 tropospheric NO₂

Figure 14 shows the tropospheric NO₂ columns from the improved GDP 4.9 algorithm for February and August averaged for the year 2007–2016. Figure 15 shows the difference in tropospheric NO₂ columns from the GDP 4.9 and GDP 4.8 product. The tropospheric NO₂ columns increase globally by $\sim 1 \times 10^{14}$ molec cm² due to the improved DOAS slant column fitting and increase further by $\sim 3 \times 10^{14}$ molec cm² around moderately polluted regions benefiting from the use of new stratosphere–troposphere separation algorithm STREAM. A stronger change by more than 1×10^{15} molec cm² is found mainly over polluted continents as a result of the improvements to the AMF calculation, primarily the surface albedo (which also affects the snow or ice area, e.g. southern Canada and northeastern Europe) and/or the a priori NO₂ profiles (which also affect the polluted ocean, e.g. shipping lanes in southeastern Asia).

Over central northern Europe, the tropospheric NO₂ columns are reduced by $\sim 1 \times 10^{15}$ molec cm² for GDP 4.9 in winter and $\sim 3 \times 10^{14}$ molec cm² in summer. A larger number of negative values in GDP 4.8, possibly related to the overestimated stratospheric NO₂ around polar vortex areas, is largely corrected in GDP 4.9 by improving the stratosphere–troposphere separation algorithm. Over eastern China and eastern US, the seasonal variation is consistent between GDP 4.8 and 4.9, with reduced values in winter (by more than 1×10^{15} molec cm²) and enlarged values in summer (by more than 1×10^{15} molec cm² for eastern China and 5×10^{14} molec cm² for eastern US) for GDP 4.9 due to the combined impact of the algorithm changes, mainly the AMF calculation. Over India and its surrounding areas, a systematic increase in tropospheric NO₂ columns by

$\sim 7 \times 10^{14}$ molec cm² for GDP 4.9 benefits from the use of STREAM.

6.5 Uncertainty estimates for GOME-2 total and tropospheric NO₂

The uncertainty in our GDP 4.9 NO₂ slant columns is 4.4×10^{14} molec cm², calculated from the average slant column error using a statistical method described in Sect. 4.5. The uncertainty in the GOME-2 stratospheric columns is $\sim 4\text{--}5 \times 10^{14}$ molec cm² for polluted conditions based on the daily synthetic GOME-2 data and $\sim 1\text{--}2 \times 10^{14}$ molec cm² for monthly averages. The uncertainty in the GDP 4.9 AMF calculation is likely reduced, considering the improved surface albedo climatology and a priori NO₂ profiles, which are the main causes of AMF structural uncertainty (Lorente et al., 2017). In addition, the AMF uncertainty is substantially driven by the cloud parameters and the aerosol correction approach.

The largest cloud-related uncertainty in NO₂ retrieval is introduced by the surface albedo–cloud fraction error correlation, as analysed by Boersma et al. (2018) for OMI using the OMCLDO₂ cloud product, which requires a surface albedo climatology as input in the cloud fraction retrieval. But this uncertainty is likely smaller for OCRA and ROCINN cloud algorithms, since the surface albedo is treated differently in OCRA’s cloud fraction calculation. Retrieved by separating a spectral scene into cloudy contribution and cloud-free background, the cloud fraction from OCRA is affected by surface albedo through the cloud-free map construction with a larger impact over bright surfaces like snow or ice cover, particularly during snowfall (higher background) or melting (lower background), which has been corrected by interpolating towards a daily value between two monthly cloud-free maps in OCRA (Lutz et al., 2016).

The uncertainty introduced by aerosol in GDP 4.9 is $\sim 50\%$ for high aerosol loading, in agreement with Lorente

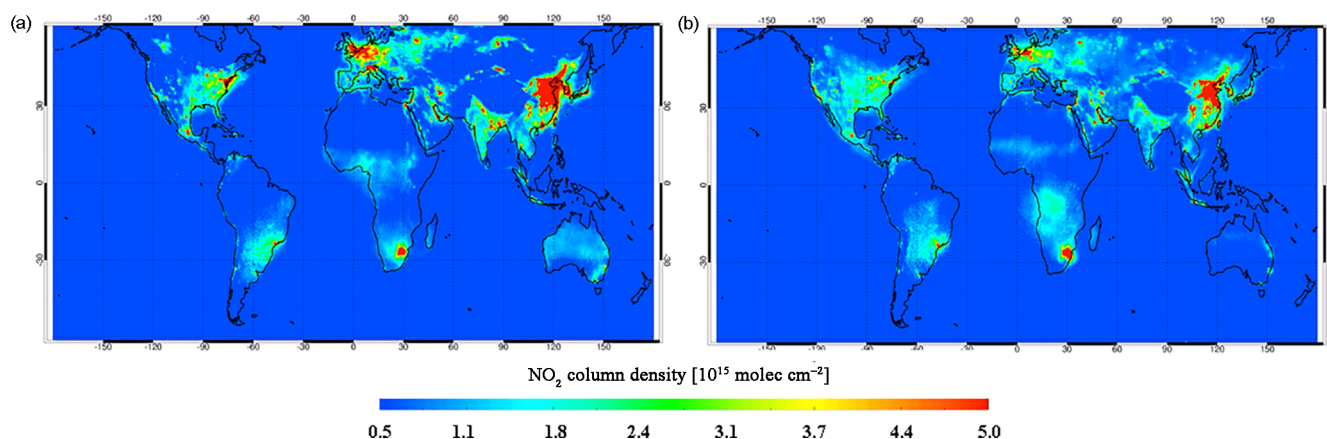


Figure 14. Monthly average tropospheric NO₂ columns from GDP 4.9 for clear-sky conditions (cloud radiance fraction smaller than 0.5), measured by GOME-2A in February (a) and August (b) 2007–2016.

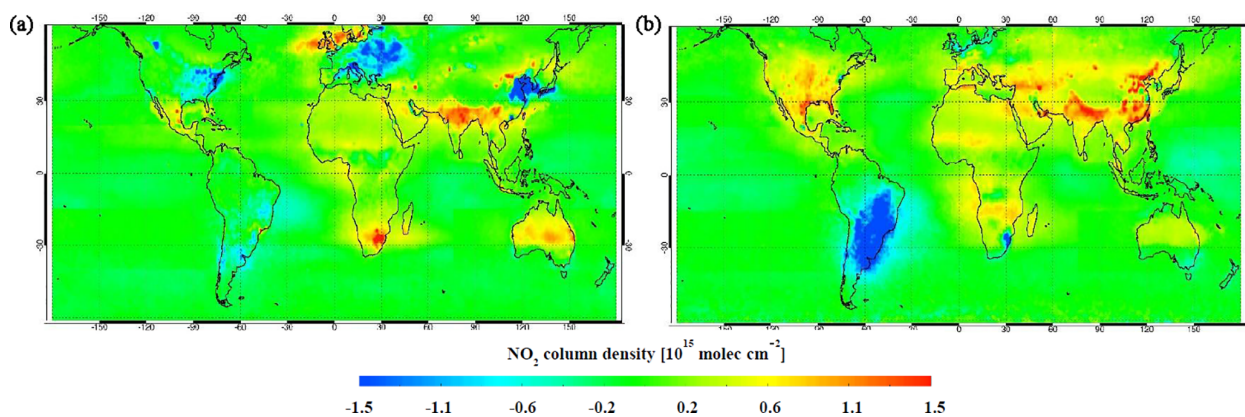


Figure 15. Difference in tropospheric NO₂ columns from GDP 4.9 and GDP 4.8 for clear-sky conditions (cloud radiance fraction smaller than 0.5) in February (a) and August (b) 2007–2016 for GOME-2A.

et al. (2017). With direct impact on NO₂ AMF calculation and indirect impact via cloud parameter retrieval, the aerosol effect has been considered for OMI implicitly through the cloud correction (Boersma et al., 2004, 2011) or explicitly with additional aerosol information for regional studies (Lin et al., 2014, 2015; Kuhlmann et al., 2015; Castellanos et al., 2015; Chimot et al., 2018), leading to an increase or decrease of NO₂ AMF by up to 40 % depending on NO₂ distribution and aerosol properties and distribution. Since aerosol is highly variable in space and time due to the dependency on emission sources, transports, and atmospheric processes (Holben et al., 1991), explicit aerosol correction will be applied in our AMF calculation when reliable observations or model outputs of aerosol optical properties and vertical distributions are available. To conclude, the uncertainty in the AMF calculation is estimated to be in the 10 %–45 % range for polluted conditions, leading to a total uncertainty in the tropospheric NO₂ columns likely in the range of 30 %–70 %.

7 End-to-end GOME-2 NO₂ validation

The validation of NO₂ data derived from the GOME-2 GDP algorithm is part of the validation activities done at BIRA-IASB in the AC-SAF context (Hassinen et al., 2016). An end-to-end validation approach is usually performed for each main release and summarised in validation reports that can be found on AC-SAF validation website (<http://cdop.aeronomie.be/validation/valid-reports>, last access: 1 February 2019). This includes several steps, such as

1. the DOAS analysis results, cloud property retrievals, and AMF evaluations by confrontation of GOME-2 retrievals to other established satellite retrievals and AMF evaluations;
2. the stratospheric reference evaluation by comparison with correlative observations from ground-based zenith-looking DOAS spectrometers and from other nadir-looking satellites; and

3. the tropospheric and total NO₂ column data evaluation by comparison with correlative observations from ground-based MAXDOAS and direct-sun spectrometers (Pinardi et al., 2014).

In this paper, we focus on the last point: the validation of tropospheric data with BIRA-IASB ground-based MAXDOAS data. The MAXDOAS instruments collect scattered sky light in a series of line-of-sight angular directions extending from the horizon to the zenith. High sensitivity towards absorbers near the surface is obtained for the smallest elevation angles, while measurements at higher elevations provide information on the rest of the column. This technique allows the determination of vertically resolved abundances of atmospheric trace species in lowermost troposphere (Hönninger et al., 2004; Wagner et al., 2004; Wittrock et al., 2004; Heckel et al., 2005). Here the bePRO retrieval code (Clémer et al., 2010; Hendrick et al., 2014; Vlemmix et al., 2015) is used to retrieve tropospheric columns and low tropospheric profiles (up to 3.5 km with about 2 to 3 degrees of freedom).

As summarised in Table 3, a set of MAXDOAS stations (Beijing, Bujumbura, Observatoire de Haute-Provence (OHP), Réunion, Uccle, and Xianghe) is providing interesting test cases for GOME-2 sensitivity to tropospheric NO₂. Indeed Beijing and Uccle are typical urban stations, Xianghe is a suburban station (~ 60 km from Beijing), Bujumbura and Réunion are small cities in remote regions, and OHP is largely rural but occasionally influenced by polluted air masses transported from neighbouring cities. These different station types are important in the validation context as it is generally expected that urban stations are underestimated by the satellite data, due to the averaging of a local source over a pixel size (80 km × 40 km and 40 km × 40 km for GOME-2) larger than the horizontal sensitivity of the ground-based measurements which is about a few to tens of kilometres (Irie et al., 2011; Wagner et al., 2011; Ortega et al., 2015). In this context, MAXDOAS data are already better than in situ measurements with an extended horizontal and vertical sensitivity, more similar to the satellite sensitivity, but differences in sampling and sensitivity still remain and explain part of the biases highlighted by validation exercises. Several validation studies show a significant underestimation of tropospheric trace gases, such as NO₂, from satellite observations over regions with strong spatial gradients in tropospheric pollution (e.g. Celarier et al., 2008; Kramer et al., 2008; Chen et al., 2009; Irie et al., 2012; Ma et al., 2013; Wu et al., 2013; Kanaya et al., 2014; Wang et al., 2017; Drosoglou et al., 2017, 2018). Other possible explanations include the uncertainties in the applied satellite retrieval assumptions, such as the choices of surface albedo, a priori NO₂ profiles, or cloud and aerosol treatment (Boersma et al., 2004, 2011; Leitão et al., 2010; Heckel et al., 2011; Lin et al., 2014, 2015). The best agreement is generally obtained in the case of suburban and remote stations, but difficulties may arise when small local sources are present in a remote location, such as Réu-

nion island or Bujumbura (Pinardi et al., 2015; Gielen et al., 2017).

The same methodology as in the GDP 4.8 validation report (Pinardi et al., 2015) is used for the validation of this improved GDP 4.9 tropospheric NO₂ dataset; the satellite data are filtered for clouds (cloud radiance fraction smaller than 0.5), and the mean value of all the valid pixels within 50 km of the stations is compared to the ground-based value. The original ground-based MAXDOAS data usually retrieve NO₂ columns all day long every 20 to 30 min, and these values are linearly interpolated to the GOME-2 overpass time (09:30 LT) if original data exist within ±1 h.

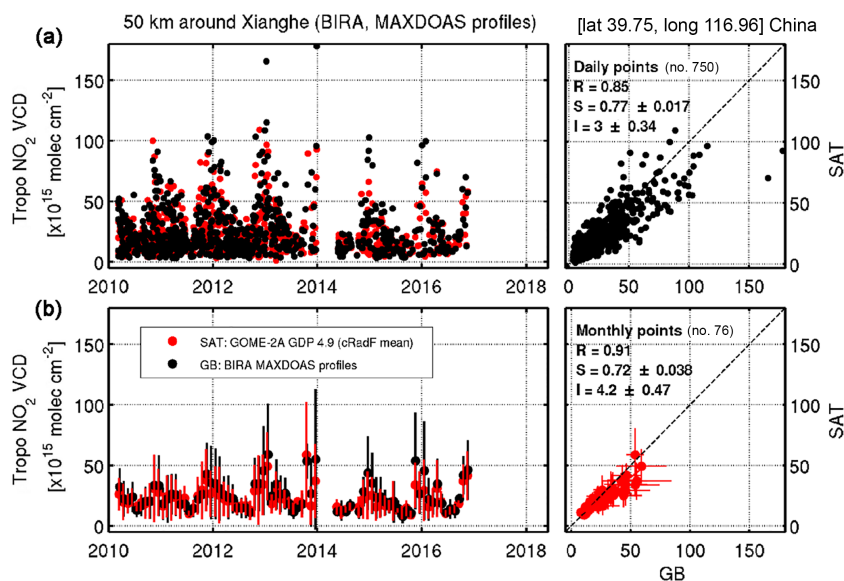
Figure 16 shows an example of the time series and scatter plot of the daily and monthly mean comparison between GDP 4.9 tropospheric NO₂ columns and ground-based MAXDOAS measurements in Xianghe, including the statistical information on the number of points, correlation coefficient, slope, and intercept of orthogonal regression analysis. Figure 17 presents the daily and monthly mean absolute and relative differences of GDP 4.9 and ground-based measurements. As can be seen in Figs. 16 and 17, the seasonal variation in the tropospheric NO₂ columns is similarly captured by both observation systems, with differences on average within $\pm 3 \times 10^{15}$ molec cm² (median difference of -1.2×10^{15} molec cm²). Larger differences are observed on some days and months, particularly in winter when NO₂ and aerosol loadings are large. A relatively compact scatter is found, with a correlation coefficient of 0.91 and a slope of 0.72 ± 0.04 for the orthogonal regression fit. These results are qualitatively similar to those obtained in previous validation exercises (Celarier et al., 2008; Kramer et al., 2008; Chen et al., 2009; Irie et al., 2012; Ma et al., 2013; Wu et al., 2013; Kanaya et al., 2014; Wang et al., 2017; Drosoglou et al., 2017, 2018). Similar figures for GDP 4.8 can be found on the AC-SAF validation website (<http://cdop.aeronomie.be/validation/valid-results>, last access: 1 February 2019).

Figure 18 reports the monthly mean absolute and relative differences for both GDP 4.8 and GDP 4.9 for Xianghe station. The daily differences are also reported through the histogram panel, where the reduction in the spread of the daily comparison points is clearly visible for GDP 4.9. The reduction of the bias, which is smaller and more stable in time, is seen in the absolute and relative monthly mean bias time series. A total of 3 years show a standard deviation of the monthly biases larger for GDP 4.9 than for GDP 4.8 ($\pm 12\%$ instead of $\pm 8\%$ in 2010, $\pm 12\%$ instead of $\pm 8\%$ in 2013, and $\pm 41\%$ instead of $\pm 27\%$ in 2014) but with a strongly reduced mean bias (-4% instead of -20% , -8% instead of -34% , and -1% instead of -44%).

Similar figures as Figs. 16 and 18 for all the stations are gathered in Figs. S1 to S4 in the Supplement, and all the statistics are summarised in Tables 4 and 5 for GOME-2A and GOME-2B, respectively. Figures S1 and S2 in the Supplement present the time series and scatter plots for GDP 4.9, while Figs. S3 and S4 in the Supplement present the differ-

Table 3. An overview of BIRA-IASB MAXDOAS datasets used in this study.

MAXDOAS station	Period	Position	Description
Beijing	6/2008–4/2009	Lat. 39.98, long. 116.38	urban polluted site in China
Bujumbura	12/2013–11/2016	Lat. −3.38, long. 29.38	urban site in Burundi
OHP	3/2007–11/2016	Lat. 43.94, long. 5.71	background site in southern France
Réunion	4/2016–11/2016	Lat. −21, long. 55.3	urban site in Réunion island
Uccle	4/2011–11/2016	Lat. 51, long. 4.36	urban polluted site in Belgium with a miniDOAS
Xianghe	3/2010–11/2016	Lat. 39.75, long. 116.96	suburban polluted site in China

**Figure 16.** Daily (a) and monthly mean (b) time series and scatter plots of GOME-2A and MAXDOAS tropospheric NO₂ columns (mean value of all the pixels within 50 km around Xianghe).

ences for both GDP 4.9 and GDP 4.8 comparisons. As discussed in Pinardi et al. (2015), for background stations (here Bujumbura, Réunion, and OHP), the mean bias is considered the best indicator of the validation results, due to the relatively small variability in the measured NO₂. In urban (Beijing and Uccle) and suburban (Xianghe) situations, the NO₂ variability is large enough and in this case, the correlation coefficient is a good indication of the linearity or coherence of the satellite and ground-based dataset, although a larger difference in terms of slope (closer to 0.5 than to 1 for urban cases) and mean bias can be expected because satellite measurements (and especially GOME-2 80 km × 40 km and 40 km × 40 km pixels) smooth out the local NO₂ hot spots. This can be seen, e.g. in the cases of Beijing and Xianghe for GOME-2A (see Fig. S1a in the Supplement and Fig. 16, respectively), where very high correlations ($R = 0.94$ and 0.91 , respectively) are obtained from GDP 4.9, showing the very consistent behaviour of both datasets for small and large NO₂ columns, while their slopes ($S = 0.4$ and 0.72 , respectively) show almost a factor of 2 difference, with a smaller slope in the Beijing case, where the MAXDOAS instrument is in the city centre and thus much more subject to local emis-

sion smeared out by the GOME-2 large pixel. This last effect is also seen through the bias values ($RD = -47\%$ and -5.8% , respectively) that are strongly reduced when moving the MAXDOAS outside the city in a suburban location like Xianghe. A slope of 0.47 (similar to the 0.4 of Beijing) is also obtained in Uccle, another urban site, where the MAXDOAS is affected by local emissions.

In remote cases such as OHP, Bujumbura, or Réunion island, as discussed above, the variation of the NO₂ columns is small and the statistical analysis on the regression is not very representative of the situation, with a cloud of points giving small slopes and low correlation coefficients (see e.g. Fig. S1b–d in the Supplement and Table 4 for GOME-2A). In those cases, GOME-2 is lower than the ground-based measurements, with sometimes almost no seasonal variation, e.g. Bujumbura and Réunion, and in other cases, like OHP, some of the daily peaks are captured by GOME-2 (as days in the winter of 2014 and 2015), and the seasonal patterns and the orders of magnitude of both datasets are similar. In these cases, it is best to look at the absolute biases (as relative biases are large due to the division with small ground-based columns), as presented in e.g. Fig. S3b–d and Table 4.

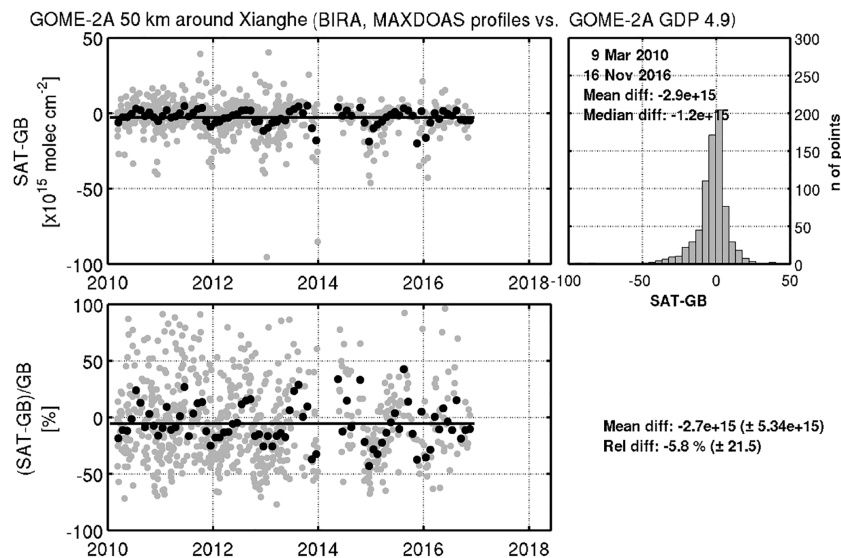


Figure 17. Daily (grey dots) and monthly mean (back dots) absolute and relative GOME-2A and MAXDOAS time series differences for the Xianghe station. The histogram of the daily differences is also given, with the mean and median difference, and the total time-series absolute and relative monthly differences are given outside the panels.

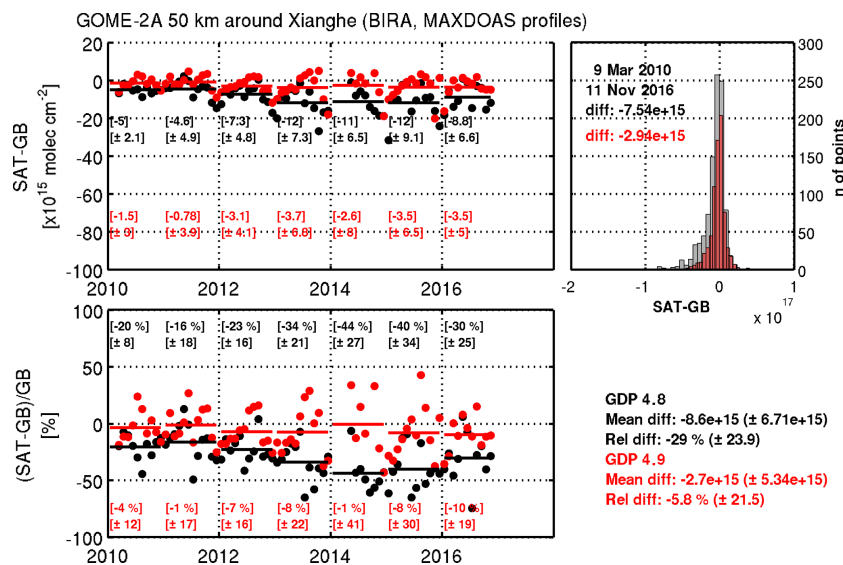


Figure 18. Absolute and relative differences of GOME-2A and MAXDOAS tropospheric NO₂ columns. The time series presents the monthly mean differences for GDP 4.8 (black) and GDP 4.9 (red). The total mean difference values and standard deviations are given, as well as the yearly values. The histogram presents the daily differences over the whole time series for the two products (grey for GDP 4.8 and red for GDP 4.9).

Mean absolute differences for GDP 4.9 are about -3.6×10^{15} molec cm² for Bujumbura, -8.5×10^{14} molec cm² for OHP, and -1.5×10^{15} molec cm² for Réunion, which are all smaller than their respective GDP 4.8 values. The daily differences presented in the histograms of those figures also show reduced spread of GDP 4.9 comparisons when superposed to the GDP 4.8 results. Similar differences are also found for GOME-2B.

To conclude, although the Xianghe case presented in Figs. 16 to 18 is the best case (due to its suburban location and its long time series), better seasonal agreement between GDP 4.9 and MAXDOAS data is found for urban and suburban cases like Beijing, Uccle, and Xianghe, compared to results with GDP 4.8. In remote locations such as OHP, which is occasionally influenced by polluted air masses transported from neighbouring cities, the comparison is also meaningful (e.g. with a mean bias reduced from -45% for GDP 4.8

to -25% for GDP 4.9 for GOME-2A), while cases such as Bujumbura and Réunion are quite challenging for satellite validation, with specific local conditions (Bujumbura is in a valley on the side of Lake Tanganyika, while the MAXDOAS at Réunion is in St-Denis, on the coast of the 65 km long and 50 km wide island in the Indian Ocean, containing a mountain massif with summits above 2740 m a.s.l.). In both cases the MAXDOAS instrument is located in small cities surrounded by specific orography, difficult for satellite retrievals and challenging for validation. The absolute and relative differences show, however, a clear improvement for all the stations when comparing to GDP 4.8 results for both daily and monthly mean biases. The daily biases and spreads are all reduced.

To summarise, the impact of the improvement of the algorithm (as seen in Tables 4 and 5 and in Figs. S3 and S4 in the Supplement) leads to a decrease of the relative differences in urban conditions such as in Beijing or Uccle from $[-52, -60]\%$ for GDP 4.8 to $[-43, -47]\%$ for GDP 4.9 for GOME-2A and from -54% to -40% for GOME-2B. In suburban conditions such as in Xianghe, the differences go from -30% to -6% for GOME-2A and from -26% to -2% for GOME-2B. In remote (difficult) cases such as in Bujumbura or Réunion, the differences go from $[-89, -90]\%$ to $[-64, -76]\%$ for GOME-2A and from $[-86, -87]\%$ to $[-47, -74]\%$ for GOME-2B, while in background cases such as in OHP, the differences decrease from -45% to -25% for GOME-2A and from -42% to -17% for GOME-2B. The differences in numbers for GOME-2A and GOME-2B are due to the different time-series lengths of both comparisons (e.g. March 2010–November 2016 for GOME-2A and December 2012–November 2016 for GOME-2B in Xianghe), the different sampling of the atmosphere by GOME-2A and GOME-2B (slight time delay between both overpasses and reduced swath pixels for GOME-2A since July 2013), and the impact of the decreasing quality of the satellite in time, i.e. the GOME-2A degradation (Dikty et al., 2011; Munro et al., 2016). This lead, e.g. for Xianghe, to -2% bias and 0.49 slope for GOME-2B compared to -6% and 0.72 for GOME-2A for GDP 4.9.

These comparisons results aim at showing how the final GDP 4.9 product is improved compared to its predecessor, and not to summarise the improvements of each of the changes discussed in previous sections. In addition, the specific validation method could be improved or at least better characterised (including results uncertainties), by, e.g. changing the collocation method (averaging the MAXDOAS within 1 h of the satellite overpass or selecting the closest satellite pixel, or only considering the pixels containing the station, etc.), but this is out of the scope of the present paper that wants to compare to standard validation results performed routinely on GDP 4.8 (and publicly available at <http://cdop.aeronomie.be/validation/valid-results>, last access: 1 February 2019).

For most stations, in addition of the tropospheric columns, MAXDOAS retrieved NO₂ profiles can also be exploited with satellite column averaging kernels (AKs) to further investigate the impact of the satellite a priori NO₂ profiles in the comparison differences (Eskes and Boersma, 2003). The satellite AK describes the vertical sensitivity of measurements to NO₂ concentrations and relates the MAXDOAS profiles to satellite column measurements by calculating the “smoothed MAXDOAS columns” as

$$V_{\text{MAXDOAS,smoothed}} = \sum_l \text{AK}_{\text{sat},l} \times x_{\text{MAXDOAS},l} \quad (9)$$

The smoothed MAXDOAS NO₂ columns $V_{\text{MAXDOAS,smoothed}}$ are derived for each day by convolving the layer (l)-dependent daily profile (interpolated to the satellite overpass time) x_{MAXDOAS} expressed in partial columns with the satellite column averaging kernel AK_{sat} .

The comparisons of satellite and smoothed MAXDOAS columns for the different stations are reported in the supplement (Figs. S5 and S6 in the Supplement) and Tables 4 and 5. The different impact of MAXDOAS smoothing on the 2 GDP products results from the different AKs as parameters like surface albedo or a priori NO₂ profiles used in both satellite retrievals are quite different (see Sect. 6). In general, the use of smoothing reduces the MAXDOAS columns and thus reduces both the daily and monthly differences of satellite and MAXDOAS columns. When the average kernels are used to remove the contribution of a priori NO₂ profile shape, as seen in Tables 4 and 5 and in Figs. S5 and S6 in the Supplement, the relative differences in urban conditions such as in Beijing or Uccle decrease from $[-52, -57]\%$ for GDP 4.8 to $[-34, -37]\%$ for GDP 4.9 for GOME-2A and from -56% to -29% for GOME-2B. The differences go from -32% to -13% for GOME-2A and from -27% to -11% for GOME-2B for suburban conditions such as in Xianghe and go from -77% to -31% for GOME-2A and from -64% to -7% for GOME-2B for remote conditions such as in Réunion.

The results obtained here are coherent with other validation exercises at different stations and with other satellite products, where the NO₂ levels are underestimated by the satellite sensors, e.g. with differences of 5% to 25% over China (Ma et al., 2013; Wu et al., 2013; Wang et al., 2017; Drosoglou et al., 2018), mostly explained by the relatively low sensitivity of space-borne measurements near the surface, the gradient-smoothing effect, and the aerosol shielding effect. These effects are often inherent to the different measurements types or the specific conditions of the validation sites (as seen for the different results for Beijing and Xianghe sites in this paper), but also to the remaining impact of structural uncertainties (Boersma et al., 2016), such as the impact of the choices of the a priori NO₂ profiles and/or the albedo database assumed for the satellite AMF calculations (see Sect. 6). Lorente et al. (2017) estimated, e.g. the AMF structural uncertainty to be on average 42% over polluted

Table 4. Averaged absolute differences (AD, SAT-GB in 10^{15} molec cm²), relative differences (RD, (SAT-GB)/GB in %), standard deviation (SD), correlation coefficient R , and regression parameters (slope S and intercept I) of the orthogonal regression for the monthly means GOME-2A tropospheric NO₂ product when comparing to MAXDOAS data. Values for GDP 4.9 (this study) are given and the values for GDP 4.8 are reported in brackets for comparison. Results for both the original comparisons and the smoothed comparisons (smo.) are reported.

	AD \pm SD ($\times 10^{15}$); RD (%)	R	Regression parameters
Beijing	-16 ± 7.3 ; -47% (-21 ± 4.5 ; -60%)	0.94 (0.95)	$S = 0.4 \pm 0.05$, $I = 3.4 \pm 0.6$ ($S = 0.58 \pm 0.06$, $I = -6.2 \pm 0.7$)
Beijing (smo.)	-11 ± 6.5 ; -37% (-16 ± 6.3 ; -52%)	0.94 (0.96)	$S = 0.43 \pm 0.05$, $I = 4.4 \pm 0.6$ ($S = 0.48 \pm 0.04$, $I = 0.11 \pm 0.5$)
Bujumbura	-3.6 ± 1.8 ; -76% (-3.7 ± 1.1 ; -89%)	n/a (0.29)	n/a ($S = 0.1 \pm 0.05$, $I = 0.012 \pm 0.12$)
Bujumbura (smo.)	-1.9 ± 1.2 ; -62% (-2.4 ± 0.8 ; -84%)	n/a (0.51)	n/a ($S = 0.22 \pm 0.06$, $I = -0.18 \pm 0.1$)
OHP	-0.85 ± 1 ; -25% (-1.2 ± 0.7 ; -45%)	0.4 (0.69)	$S = 0.25 \pm 0.06$, $I = 1.2 \pm 0.1$ ($S = 0.73 \pm 0.07$, $I = -0.5 \pm 0.1$)
Réunion	-1.5 ± 0.5 ; -64% (-1.9 ± 0.4 ; -90%)	0.14 (0.23)	$S = 0.05 \pm 0.12$, $I = 0.64 \pm 0.2$ ($S = 0.06 \pm 0.06$, $I = 0.12 \pm 0.08$)
Réunion (smo.)	-0.4 ± 0.4 ; -31% (-0.7 ± 0.2 ; -77%)	0.15 (0.28)	$S = 0.12 \pm 0.25$, $I = 0.06 \pm 0.09$ ($S = 0.32 \pm 0.25$, $I = -0.01 \pm 0.2$)
Uccle	-5 ± 2.7 ; -43% (-6.2 ± 3.7 ; -52%)	0.82 (0.49)	$S = 0.47 \pm 0.04$, $I = 0.83 \pm 0.2$ ($S = 0.35 \pm 0.08$, $I = 1.1 \pm 0.4$)
Uccle (smo.)	-3.8 ± 2.8 ; -34% (-7.6 ± 4.3 ; -57%)	0.75 (0.51)	$S = 0.45 \pm 0.05$, $I = 0.15 \pm 0.05$ ($S = 0.28 \pm 0.06$, $I = 1.5 \pm 0.3$)
Xianghe	-2.7 ± 5.3 ; -5.8% (-9.2 ± 7.1 ; -30%)	0.91 (0.86)	$S = 0.72 \pm 0.04$, $I = 4.2 \pm 0.5$ ($S = 0.63 \pm 0.04$, $I = 1.3 \pm 0.5$)
Xianghe (smo.)	-6.1 ± 8.8 ; -13% (-11 ± 9.6 ; -32%)	0.92 (0.9)	$S = 0.52 \pm 0.03$, $I = 7.4 \pm 0.4$ ($S = 0.48 \pm 0.03$, $I = 4.3 \pm 0.5$)

n/a denotes values that are not applicable.

Table 5. Same as Table 4 but for GOME-2B product.

	AD \pm SD ($\times 10^{15}$); RD (%)	R	Regression parameters
Bujumbura	-2.8 ± 0.9 ; -74% (-3.4 ± 1 ; -87%)	0.14 (0.09)	$S = 0.05 \pm 0.06$, $I = 0.76 \pm 0.12$ ($S = 0.03 \pm 0.06$, $I = 0.34 \pm 0.1$)
Bujumbura (smo.)	-1.3 ± 0.7 ; -57% (-2 ± 0.8 ; -81%)	0.28 (0.35)	$S = 0.14 \pm 0.06$, $I = 0.06 \pm 0.04$ ($S = 0.15 \pm 0.06$, $I = 0.08 \pm 0.1$)
OHP	-0.5 ± 0.7 ; -17% (-1 ± 0.6 ; -42%)	0.13 (0.52)	$S = 0.11 \pm 0.13$, $I = 1.5 \pm 0.2$ ($S = 0.82 \pm 0.2$, $I = -0.6 \pm 0.3$)
Réunion	-0.8 ± 0.3 ; -47% (-1.6 ± 0.3 ; -86%)	0.56 (0.26)	$S = 0.71 \pm 0.4$, $I = -0.36 \pm 0.52$ ($S = 0.08 \pm 0.06$, $I = 0.13 \pm 0.09$)
Réunion (smo.)	0.05 ± 0.2 ; 6.7% (-0.5 ± 0.2 ; -64%)	0.78 (0.14)	$S = -2.5 \pm 0.8$, $I = -0.12 \pm 0.22$ ($S = 0.38 \pm 0.6$, $I = 0.004 \pm 0.5$)
Uccle	-4.2 ± 2.4 ; -40% (-5.6 ± 3.1 ; -54%)	0.71 (0.71)	$S = 0.53 \pm 0.09$, $I = 0.47 \pm 0.4$ ($S = 0.64 \pm 0.1$, $I = -1.7 \pm 0.5$)
Uccle (smo.)	-2.8 ± 2.5 ; -29% (-6.8 ± 3.4 ; -56%)	0.69 (0.73)	$S = 0.53 \pm 0.09$, $I = 0.13 \pm 0.09$ ($S = 0.52 \pm 0.11$, $I = -1 \pm 0.4$)
Xianghe	-3 ± 9.4 ; -2.2% (-8.4 ± 8.7 ; -26%)	0.87 (0.84)	$S = 0.49 \pm 0.04$, $I = 9.6 \pm 0.66$ ($S = 0.6 \pm 0.05$, $I = 2.5 \pm 0.7$)
Xianghe (smo.)	-6.4 ± 13 ; -11% (-11 ± 12 ; -27%)	0.89 (0.89)	$S = 0.38 \pm 0.03$, $I = 11 \pm 0.6$ ($S = 0.46 \pm 0.03$, $I = 5.2 \pm 0.58$)

regions and 31 % over unpolluted regions, mostly driven by substantial differences in the a priori trace gas profiles, surface albedo and cloud parameters used to represent the state of the atmosphere. However, the differences in Bujumbura are still of -62% , because of the peculiar condition with the MAXDOAS being in a valley, close to Lake Tanganyika, which always leads to a higher surface pressure for the satellite pixels due to the information coming from the a priori model. This is leading to large representation errors and uncertainties in the comparisons (Boersma et al., 2016) that needs to be investigated in more details.

8 Conclusions

NO₂ columns retrieved from measurements of the GOME-2 aboard the MetOp-A and MetOp-B platforms have been successfully applied in many studies. The abundance of NO₂ is retrieved from the narrow band absorption structures of NO₂ in the backscattered and reflected radiation in the visible spectral region. The current operational retrieval algorithm (GDP 4.8) for total and tropospheric NO₂ from GOME-2 was first introduced by Valks et al. (2011), and an improved algorithm (GDP 4.9) is described in this paper.

To calculate the NO₂ slant columns, a larger 425–497 nm wavelength fitting window is used in the DOAS fit to increase the signal-to-noise ratio. Absorption cross sections are updated and a linear intensity offset correction is applied. The long-term and in-orbit variations of GOME-2 slit function are corrected by deriving effective slit functions with a stretched preflight GOME-2 slit function and by including a resolution correction function as a pseudo absorber cross section in the DOAS fit, respectively. Compared to the GDP 4.8 algorithm, the NO₂ columns from GDP 4.9 are higher by $\sim 1\text{--}3 \times 10^{14}$ molec cm² (up to 27 %) and the NO₂ slant column noise is lower by $\sim 24\%$. In addition, the effect of using a new version (6.1) of the GOME-2 level 1b data has been analysed in our NO₂ algorithm. The application of new GOME-2 level 1b data largely reduces the offset between GOME-2A and GOME-2B NO₂ columns by removing calibration artefacts in the GOME-2B irradiances (due to Xe-line contaminations in the calibration key data). Compared to the GOME-2 NO₂ product from the QA4ECV project, the NO₂ columns from GDP 4.9 show good consistency and the NO₂ slant column noise is $\sim 14\text{--}28\%$ smaller, indicating a good overall quality of the improved DOAS retrieval.

The stratosphere–troposphere separation algorithm STREAM, which was designed for TROPOMI, was optimised for GOME-2 instrument. Compared to the spatial filtering method used in the GDP 4.8, STREAM provides an improved treatment of polluted and cloudy pixels by defining weighting factors for each measurement depending on polluted situation and cloudy information. For the adaptation to GOME-2 measurements, the performance of STREAM is analysed by applying it to synthetic GOME-2 data and by comparing the difference between estimated and original stratospheric fields. Applied to synthetic GOME-2 data calculated by a RTM using C-IFS model data, the estimated stratospheric NO₂ columns from STREAM show good consistency with the a priori truth. A slight overestimation by $\sim 1\text{--}2 \times 10^{14}$ molec cm² is found over lower latitudes, and larger differences of up to $\sim 5 \times 10^{14}$ molec cm² are found at higher latitudes. To reduce the biases over the subtropical regions in winter, an improved latitudinal correction is used in STREAM. Applied to GOME-2 measurements, the updated STREAM successfully separates the stratospheric and tropospheric contribution over polluted regions, especially in the Northern Hemisphere. Compared to the current method in the GDP 4.8, the use of STREAM slightly decreases the stratospheric NO₂ columns by $\sim 1 \times 10^{14}$ molec cm² in general and largely reduces the overestimation over polluted areas.

To improve the calculation of NO₂ AMF, a new box-AMF LUT was generated using the latest version of the VLIDORT RTM with an increased number of reference points and vertical layers to reduce interpolation errors. The new GOME-2 surface LER climatology (Tilstra et al., 2017b) used in this study is derived with a high resolution of 1° long. $\times 1^\circ$ lat. (0.25° long. $\times 0.25^\circ$ lat. at coastlines) and an improved LER algorithm based on observations for 2007–2013. Daily a priori NO₂ profiles, obtained from the chemistry transport model TM5-MP, capture the short-term variability in the NO₂ fields with a resolution of 1° long. $\times 1^\circ$ lat. A large impact on the retrieved tropospheric NO₂ columns (more than 10 %) is found over polluted areas.

The uncertainty in our GDP 4.9 NO₂ slant columns is 4.4×10^{14} molec cm², calculated from the average slant column error using a statistical method described in Sect. 4.5. The uncertainty in the GOME-2 stratospheric columns is $\sim 4\text{--}5 \times 10^{14}$ molec cm² for polluted conditions based on the daily synthetic GOME-2 data and $\sim 1\text{--}2 \times 10^{14}$ molec cm² for monthly averages. The uncertainty in the tropospheric AMFs is estimated to be in the 10 %–45 % range, considering the use of updated box-AMF LUT and improved surface albedo climatology and a priori NO₂ profiles, resulting in a total uncertainty in the tropospheric NO₂ columns likely in the range of 30 %–70 % for polluted conditions.

An end-to-end validation of the improved GOME-2 GDP 4.9 dataset was performed by comparing the GOME-2 tropospheric NO₂ columns with BIRA-IASB ground-based MAXDOAS measurements. The validation was illustrated

for different MAXDOAS stations (Beijing, Bujumbura, OHP, Réunion, Uccle, and Xianghe) covering urban, suburban, and background situations. Taking Xianghe station as an example, the GDP 4.9 dataset shows a similar seasonal variation in the tropospheric NO₂ columns as the MAXDOAS measurements with a relative difference of -5.8% (i.e. -2.7×10^{15} molec cm² in absolute) and a correlation coefficient of 0.91 for GOME-2A, indicating good agreement. The Xianghe site, by its suburban nature, is the best site for validation. At the other sites, mean biases range from (-47% ; -16×10^{15} molec cm²) for Beijing, (-76% , -74% ; -3.6×10^{15} molec cm², -2.8×10^{15} molec cm²) for Bujumbura, (-25% , -17% ; -0.9×10^{15} molec cm², -0.5×10^{15} molec cm²) for OHP, (-64% , -47% ; -1.5×10^{15} molec cm², -0.8×10^{15} molec cm²) for Réunion, and (-43% , -40% ; -5×10^{15} molec cm², -4.2×10^{15} molec cm²) for Uccle. Réunion and Bujumbura are difficult sites for validation, due to their valley and mountain nature, while urban sites Beijing and Uccle show similar relative results. A smaller absolute bias is found at the rural OHP station. Compared to the current operational GDP 4.8 product, the GDP 4.9 dataset is a significant improvement. Although GOME-2 measurements are still underestimating the tropospheric NO₂ columns with respect to the ground data, the absolute and relative differences with the different MAXDOAS stations are smaller, both for the original comparisons and for the comparisons with the smoothed MAXDOAS columns.

In the future, the AMF calculation will be further improved, since uncertainty in AMF is one dominating source of errors in the tropospheric NO₂ retrieval, especially over polluted areas. The surface bidirectional reflectance distribution function (BRDF) effect will be included using a direction-dependent LER climatology from GOME-2 (L. Gijbert Tilstra, personal communication, 2018) to describe the angular distribution of the surface reflectance. Aerosol properties will be considered explicitly in the RTM calculation using ground-based aerosol observations from, e.g. MAXDOAS instruments, Mie scattering lidars, or sun photometers operated by the AEROSOL ROBOTIC NETWORK (AERONET). A priori NO₂ profiles from different global and regional models will help to analyse the effect of spatial resolution, temporal resolution, and emissions on the tropospheric NO₂ retrieval for GOME-2. Furthermore, the NO₂ algorithm will be adapted to measurements from the TROPOMI instrument with a spatial resolution as high as $7\text{ km} \times 3.5\text{ km}$.

Data availability. The current operational (GDP 4.8) NO₂ data from GOME-2 can be ordered via the FTP server and the EUMETSAT Data Centre (<https://acsaf.org/>, last access: 1 February 2019). The improved (GDP 4.9) dataset is currently available upon request.

Supplement. The supplement related to this article is available online at: <https://doi.org/10.5194/amt-12-1029-2019-supplement>.

Competing interests. The authors declare that they have no conflict of interest.

Acknowledgements. This work is funded by the DLR-DAAD Research Fellowships 2015 (57186656) programme with reference number 91585186 and is undertaken in the framework of the EUMETSAT AC-SAF project. We acknowledge the Belgian Science Policy Office (BELSPO) supporting part of this work through the PRODEX project B-ACSAF. We thank EUMETSAT for the ground segment interfacing work and for the provision of GOME-2 level 1 products. We thank the UPAS team for the development work on the UPAS system at DLR. We are thankful to Rüdiger Lang (EUMETSAT) for providing the GOME-2 level 1b testing data, Vincent Huijnen (KNMI) for providing the C-IFS model data, Gijbert Tilstra (KNMI) for discussions on surface albedo, and Henk Eskes (KNMI) for creating the TM5-MP a priori NO₂ profiles. We acknowledge the free use of GOME-2 NO₂ column data from the QA4ECV project available at <http://www.qa4ecv.eu>. We also acknowledge the free use of the GOME-2 surface LER database created by KNMI and provided through the AC-SAF of EUMETSAT.

The article processing charges for this open-access publication were covered by a Research Centre of the Helmholtz Association.

Edited by: Jun Wang

Reviewed by: Kai Yang and one anonymous referee

References

- Azam, F., Richter, A., Weber, M., Noë, S., and Burrows, J.: GOME-2 on MetOp-B Follow-on analysis of GOME2 in orbit degradation, Tech. rep., EUM/CO/09/4600000696/RM, Final Report, IUP University of Bremen, 2015.
- Barkley, M. P., Smedt, I. D., Van Roozendael, M., Kurosu, T. P., Chance, K., Arneeth, A., Hagberg, D., Guenther, A., Paulot, F., Marais, E., and Mao, J.: Top-down isoprene emissions over tropical South America inferred from SCIAMACHY and OMI formaldehyde columns, *J. Geophys. Res.-Atmos.*, 118, 6849–6868, 2013.
- Beirle, S., Hörmann, C., Jöckel, P., Liu, S., Penning de Vries, M., Pozzer, A., Sihler, H., Valks, P., and Wagner, T.: The STRatospheric Estimation Algorithm from Mainz (STREAM): estimating stratospheric NO₂ from nadir-viewing satellites by weighted convolution, *Atmos. Meas. Tech.*, 9, 2753–2779, <https://doi.org/10.5194/amt-9-2753-2016>, 2016.
- Beirle, S., Lampel, J., Lerot, C., Sihler, H., and Wagner, T.: Parameterizing the instrumental spectral response function and its changes by a super-Gaussian and its derivatives, *Atmos. Meas. Tech.*, 10, 581–598, <https://doi.org/10.5194/amt-10-581-2017>, 2017.
- Boersma, K., Bucsela, E., Brinksma, E., and Gleason, J.: OMI algorithm theoretical basis document: OMI trace gas algorithms, vol. 4, edited by: Chance, K., Rep. ATBD-OMI, p. 19, 2002.
- Boersma, K., Eskes, H., and Brinksma, E.: Error analysis for tropospheric NO₂ retrieval from space, *J. Geophys. Res.-Atmos.*, 109, <https://doi.org/10.1029/2003JD003962>, 2004.
- Boersma, K. F., Eskes, H. J., Richter, A., De Smedt, I., Lorente, A., Beirle, S., van Geffen, J. H. G. M., Zara, M., Peters, E., Van Roozendael, M., Wagner, T., Maasakkers, J. D., van der A, R. J., Nightingale, J., De Rudder, A., Irie, H., Pinardi, G., Lambert, J.-C., and Compernolle, S. C.: Improving algorithms and uncertainty estimates for satellite NO₂ retrievals: results from the quality assurance for the essential climate variables (QA4ECV) project, *Atmos. Meas. Tech.*, 11, 6651–6678, [doi:10.5194/amt-11-6651-2018](https://doi.org/10.5194/amt-11-6651-2018), 2018.
- Boersma, K. F., Eskes, H. J., Dirksen, R. J., van der A, R. J., Veefkind, J. P., Stammes, P., Huijnen, V., Kleipool, Q. L., Sneep, M., Claas, J., Leitão, J., Richter, A., Zhou, Y., and Brunner, D.: An improved tropospheric NO₂ column retrieval algorithm for the Ozone Monitoring Instrument, *Atmos. Meas. Tech.*, 4, 1905–1928, <https://doi.org/10.5194/amt-4-1905-2011>, 2011.
- Boersma, K. F., Vinken, G. C. M., and Eskes, H. J.: Representativeness errors in comparing chemistry transport and chemistry climate models with satellite UV-Vis tropospheric column retrievals, *Geosci. Model Dev.*, 9, 875–898, <https://doi.org/10.5194/gmd-9-875-2016>, 2016.
- Bovensmann, H., Burrows, J., Buchwitz, M., Frerick, J., Rozanov, V., Chance, K., and Goede, A.: SCIAMACHY: Mission objectives and measurement modes, *J. Atmos. Sci.*, 56, 127–150, 1999.
- Brion, J., Chakir, A., Charbonnier, J., Daumont, D., Parisse, C., and Malicet, J.: Absorption spectra measurements for the ozone molecule in the 350–830 nm region, *J. Atmos. Chem.*, 30, 291–299, 1998.
- Bucsela, E. J., Krotkov, N. A., Celarier, E. A., Lamsal, L. N., Swartz, W. H., Bhartia, P. K., Boersma, K. F., Veefkind, J. P., Gleason, J. F., and Pickering, K. E.: A new stratospheric and tropospheric NO₂ retrieval algorithm for nadir-viewing satellite instruments: applications to OMI, *Atmos. Meas. Tech.*, 6, 2607–2626, <https://doi.org/10.5194/amt-6-2607-2013>, 2013.
- Burrows, J. P., Weber, M., Buchwitz, M., Rozanov, V., Ladstätter-Weißenmayer, A., Richter, A., DeBeek, R., Hoogen, R., Bramstedt, K., Eichmann, K.-U., Eisinger, M., and Perner, D.: The global ozone monitoring experiment (GOME): Mission concept and first scientific results, *J. Atmos. Sci.*, 56, 151–175, 1999.
- Callies, J., Corpaccioli, E., Eisinger, M., Hahne, A., and Lefebvre, A.: GOME-2-Metop's second-generation sensor for operational ozone monitoring, *ESA bulletin*, 102, 28–36, 2000.
- Castellanos, P., Boersma, K. F., Torres, O., and de Haan, J. F.: OMI tropospheric NO₂ air mass factors over South America: effects of biomass burning aerosols, *Atmos. Meas. Tech.*, 8, 3831–3849, <https://doi.org/10.5194/amt-8-3831-2015>, 2015.
- Celarier, E. A., Brinksma, E. J., Gleason, J. F., Veefkind, J. P., Cede, A., Herman, J. R., Ionov, D., Goutail, F., Pommereau, J.-P., Lambert, J.-C., van Roozendael, M., Pinardi, G., Wittrock, F., Schönhardt, A., Richter, A., Ibrahim, O. W., Wagner, T., Bojkov, B., Mount, G., Spinei, E., Chen, C. M., Pongetti, T. J., Sander, S. P., Bucsela, E. J., Wenig, M. O., Swart, D. P. J., Volten, H., Kroon, M., and Levelt, P. F.: Validation of Ozone Monitoring Instru-

- ment nitrogen dioxide columns, *J. Geophys. Res. Atmos.*, 113, <https://doi.org/10.1029/2007JD008908>, 2008.
- Chance, K. and Kurucz, R.: An improved high-resolution solar reference spectrum for earth's atmosphere measurements in the ultraviolet, visible, and near infrared, *J. Quant. Spectrosc. Ra.*, 111, 1289–1295, 2010.
- Chen, D., Zhou, B., Beirle, S., Chen, L. M., and Wagner, T.: Tropospheric NO₂ column densities deduced from zenith-sky DOAS measurements in Shanghai, China, and their application to satellite validation, *Atmos. Chem. Phys.*, 9, 3641–3662, <https://doi.org/10.5194/acp-9-3641-2009>, 2009.
- Chimot, J., Veeffkind, J. P., de Haan, J. F., Stammes, P., and Levelt, P. F.: Minimizing aerosol effects on the OMI tropospheric NO₂ retrieval – An improved use of the 477 nm O₂–O₂ band and an estimation of the aerosol correction uncertainty, *Atmos. Meas. Tech. Discuss.*, <https://doi.org/10.5194/amt-2018-247>, in review, 2018.
- Clémer, K., Van Roozendaal, M., Fayt, C., Hendrick, F., Hermans, C., Pinardi, G., Spurr, R., Wang, P., and De Mazière, M.: Multiple wavelength retrieval of tropospheric aerosol optical properties from MAXDOAS measurements in Beijing, *Atmos. Meas. Tech.*, 3, 863–878, <https://doi.org/10.5194/amt-3-863-2010>, 2010.
- Danckaert, T., Fayt, C., Van Roozendaal, M., De Smedt, I., Letocart, V., Merlaud, A., and Pinardi, G.: QDOAS software user manual 2.109, IASB/BIRA, Uccle, Belgium, available at: <http://uvvis.aeronomie.be/software/QDOAS> (last access: 19 September 2015), 2015.
- De Smedt, I., Van Roozendaal, M., Stavrou, T., Müller, J.-F., Lerot, C., Theys, N., Valks, P., Hao, N., and van der A, R.: Improved retrieval of global tropospheric formaldehyde columns from GOME-2/MetOp-A addressing noise reduction and instrumental degradation issues, *Atmos. Meas. Tech.*, 5, 2933–2949, <https://doi.org/10.5194/amt-5-2933-2012>, 2012.
- Dikty, S., Richter, A., Weber, M., Noël, S., Bovensmann, H., Wittrock, F., and Burrows, J.: GOME-2 on MetOp-A Support for Analysis of GOME-2 In-Orbit Degradation and Impacts on Level 2 Data Products—Final Report, Tech. rep., ITT 09/10000262, IUP University of Bremen, 2011.
- Ding, J., Miyazaki, K., van der A, R. J., Mijling, B., Kurokawa, J.-I., Cho, S., Janssens-Maenhout, G., Zhang, Q., Liu, F., and Levelt, P. F.: Intercomparison of NO_x emission inventories over East Asia, *Atmos. Chem. Phys.*, 17, 10125–10141, <https://doi.org/10.5194/acp-17-10125-2017>, 2017.
- Doicu, A., Trautmann, T., and Schreier, F.: Numerical regularization for atmospheric inverse problems, Springer Science & Business Media, 2010.
- Drosoglou, T., Bais, A. F., Zyrichidou, I., Kouremeti, N., Poupkou, A., Liora, N., Giannaros, C., Koukouli, M. E., Balis, D., and Melas, D.: Comparisons of ground-based tropospheric NO₂ MAX-DOAS measurements to satellite observations with the aid of an air quality model over the Thessaloniki area, Greece, *Atmos. Chem. Phys.*, 17, 5829–5849, <https://doi.org/10.5194/acp-17-5829-2017>, 2017.
- Drosoglou, T., Koukouli, M. E., Kouremeti, N., Bais, A. F., Zyrichidou, I., Balis, D., van der A, R. J., Xu, J., and Li, A.: MAX-DOAS NO₂ observations over Guangzhou, China; ground-based and satellite comparisons, *Atmos. Meas. Tech.*, 11, 2239–2255, <https://doi.org/10.5194/amt-11-2239-2018>, 2018.
- Eskes, H. J. and Boersma, K. F.: Averaging kernels for DOAS total-column satellite retrievals, *Atmos. Chem. Phys.*, 3, 1285–1291, <https://doi.org/10.5194/acp-3-1285-2003>, 2003.
- EUMETSAT: GOME-2 Products Guide, Tech. rep., Ref.: EUM/OPSEPS/MAN/07/0445, Issue: v2D, 2009.
- EUMETSAT: GOME-2/Metop-A Level 1B Product Validation Report No. 5: Status at Reprocessing, Tech. rep., EUM/OPS/EPS/REP/09/0619, v1F, 2012.
- EUMETSAT: GOME-2 Newsletter Archive, Tech. rep., EUM/OPS-EPS/TEN/09/0552, 2015.
- European Commission: The EU Environmental Implementation Review: Common challenges and how to combine efforts to deliver better results, Tech. rep., Ref.: SWD(2017)33-60 fina, 2017.
- Gielen, C., Hendrick, F., Pinardi, G., De Smedt, I., Fayt, C., Hermans, C., Stavrou, T., Bauwens, M., Müller, J.-F., Ndenzako, E., Nzohabonayo, P., Akimana, R., Niyonzima, S., Van Roozendaal, M., and De Mazière, M.: Characterisation of Central-African aerosol and trace-gas emissions based on MAX-DOAS measurements and model simulations over Bujumbura, Burundi, *Atmos. Chem. Phys. Discuss.*, <https://doi.org/10.5194/acp-2016-1104>, in review, 2017.
- Granier, C., Bessagnet, B., Bond, T., D'Angiola, A., van Der Gon, H. D., Frost, G. J., Heil, A., Kaiser, J. W., Kinne, S., Klimont, Z., Kloster, S., Lamarque, J.-F., Liousse, C., Masui, T., Meleux, F., Mieville, A., Ohara, T., Raut, J.-C., Riahi, K., Schultz, M. G., Smith, S. J., Thompson, A., van Aardenne, J., van der Werf, G. R., and van Vuuren, D. P.: Evolution of anthropogenic and biomass burning emissions of air pollutants at global and regional scales during the 1980–2010 period, *Clim. Change*, 109, p. 163, 2011.
- Gu, D., Wang, Y., Smeltzer, C., and Boersma, K. F.: Anthropogenic emissions of NO_x over China: Reconciling the difference of inverse modeling results using GOME-2 and OMI measurements, *J. Geophys. Res.-Atmos.*, 119, 7732–7740, 2014.
- Hassinen, S., Balis, D., Bauer, H., Begoin, M., Delcloo, A., Eleftheratos, K., Gimeno Garcia, S., Granville, J., Grossi, M., Hao, N., Hedelt, P., Hendrick, F., Hess, M., Heue, K.-P., Hovila, J., Jönch-Sørensen, H., Kalakoski, N., Kauppi, A., Kiemle, S., Kins, L., Koukouli, M. E., Kujanpää, J., Lambert, J.-C., Lang, R., Lerot, C., Loyola, D., Pedernana, M., Pinardi, G., Romahn, F., van Roozendaal, M., Lutz, R., De Smedt, I., Stammes, P., Steinbrecht, W., Tamminen, J., Theys, N., Tilstra, L. G., Tuinder, O. N. E., Valks, P., Zerefos, C., Zimmer, W., and Zyrichidou, I.: Overview of the O3M SAF GOME-2 operational atmospheric composition and UV radiation data products and data availability, *Atmos. Meas. Tech.*, 9, 383–407, <https://doi.org/10.5194/amt-9-383-2016>, 2016.
- Heckel, A., Richter, A., Tarsu, T., Wittrock, F., Hak, C., Pundt, I., Junkermann, W., and Burrows, J. P.: MAX-DOAS measurements of formaldehyde in the Po-Valley, *Atmos. Chem. Phys.*, 5, 909–918, <https://doi.org/10.5194/acp-5-909-2005>, 2005.
- Heckel, A., Kim, S.-W., Frost, G. J., Richter, A., Trainer, M., and Burrows, J. P.: Influence of low spatial resolution a priori data on tropospheric NO₂ satellite retrievals, *Atmos. Meas. Tech.*, 4, 1805–1820, <https://doi.org/10.5194/amt-4-1805-2011>, 2011.
- Hendrick, F., Müller, J.-F., Clémer, K., Wang, P., De Mazière, M., Fayt, C., Gielen, C., Hermans, C., Ma, J. Z., Pinardi, G., Stavrou, T., Vlemmix, T., and Van Roozendaal, M.: Four years of ground-based MAX-DOAS observations of HONO and

- NO₂ in the Beijing area, *Atmos. Chem. Phys.*, 14, 765–781, <https://doi.org/10.5194/acp-14-765-2014>, 2014.
- Hilboll, A., Richter, A., and Burrows, J. P.: Long-term changes of tropospheric NO₂ over megacities derived from multiple satellite instruments, *Atmos. Chem. Phys.*, 13, 4145–4169, <https://doi.org/10.5194/acp-13-4145-2013>, 2013.
- Hilboll, A., Richter, A., and Burrows, J. P.: NO₂ pollution over India observed from space – the impact of rapid economic growth, and a recent decline, *Atmos. Chem. Phys. Discuss.*, <https://doi.org/10.5194/acp-2017-101>, in review, 2017.
- Holben, B., Eck, T., and Fraser, R.: Temporal and spatial variability of aerosol optical depth in the Sahel region in relation to vegetation remote sensing, *Int. J. Remote Sens.*, 12, 1147–1163, 1991.
- Hönninger, G., von Friedeburg, C., and Platt, U.: Multi axis differential optical absorption spectroscopy (MAX-DOAS), *Atmos. Chem. Phys.*, 4, 231–254, <https://doi.org/10.5194/acp-4-231-2004>, 2004.
- Horowitz, L. W., Walters, S., Mauzerall, D. L., Emmons, L. K., Rasch, P. J., Granier, C., Tie, X., Lamarque, J.-F., Schultz, M. G., Tyndall, G. S., Orlando, J. J., and Brasseur, G. P.: A global simulation of tropospheric ozone and related tracers: Description and evaluation of MOZART, version 2, *J. Geophys. Res. Atmos.*, 108, <https://doi.org/10.1029/2002JD002853>, 2003.
- Huijnen, V., Williams, J., van Weele, M., van Noije, T., Krol, M., Dentener, F., Segers, A., Houweling, S., Peters, W., de Laat, J., Boersma, F., Bergamaschi, P., van Velthoven, P., Le Sager, P., Eskes, H., Alkemade, F., Scheele, R., Nédélec, P., and Pätz, H.-W.: The global chemistry transport model TM5: description and evaluation of the tropospheric chemistry version 3.0, *Geosci. Model Dev.*, 3, 445–473, <https://doi.org/10.5194/gmd-3-445-2010>, 2010.
- Huijnen, V., Flemming, J., Chabrilat, S., Errera, Q., Christophe, Y., Blechschmidt, A.-M., Richter, A., and Eskes, H.: C-IFS-CB05-BASCOE: stratospheric chemistry in the Integrated Forecasting System of ECMWF, *Geosci. Model Dev.*, 9, 3071–3091, <https://doi.org/10.5194/gmd-9-3071-2016>, 2016.
- Ingmann, P., Veihelmann, B., Langen, J., Lamarre, D., Stark, H., and Courrèges-Lacoste, G. B.: Requirements for the GMES Atmosphere Service and ESA's implementation concept: Sentinels-4/-5 and -5p, *Remote Sens. Environ.*, 120, 58–69, 2012.
- Irie, H., Takashima, H., Kanaya, Y., Boersma, K. F., Gast, L., Wittrock, F., Brunner, D., Zhou, Y., and Van Roozendaal, M.: Eight-component retrievals from ground-based MAX-DOAS observations, *Atmos. Meas. Tech.*, 4, 1027–1044, <https://doi.org/10.5194/amt-4-1027-2011>, 2011.
- Irie, H., Boersma, K. F., Kanaya, Y., Takashima, H., Pan, X., and Wang, Z. F.: Quantitative bias estimates for tropospheric NO₂ columns retrieved from SCIAMACHY, OMI, and GOME-2 using a common standard for East Asia, *Atmos. Meas. Tech.*, 5, 2403–2411, <https://doi.org/10.5194/amt-5-2403-2012>, 2012.
- Kanaya, Y., Irie, H., Takashima, H., Iwabuchi, H., Akimoto, H., Sudo, K., Gu, M., Chong, J., Kim, Y. J., Lee, H., Li, A., Si, F., Xu, J., Xie, P.-H., Liu, W.-Q., Dzhola, A., Postlyakov, O., Ivanov, V., Grechko, E., Terpugova, S., and Panchenko, M.: Long-term MAX-DOAS network observations of NO₂ in Russia and Asia (MADRAS) during the period 2007–2012: instrumentation, elucidation of climatology, and comparisons with OMI satellite observations and global model simulations, *Atmos. Chem. Phys.*, 14, 7909–7927, <https://doi.org/10.5194/acp-14-7909-2014>, 2014.
- Kleipool, Q., Dobber, M., de Haan, J., and Levelt, P.: Earth surface reflectance climatology from 3 years of OMI data, *J. Geophys. Res.-Atmos.*, 113, <https://doi.org/10.1029/2008JD010290>, 2008.
- Kramer, L. J., Leigh, R. J., Remedios, J. J., and Monks, P. S.: Comparison of OMI and ground-based in situ and MAX-DOAS measurements of tropospheric nitrogen dioxide in an urban area, *J. Geophys. Res.-Atmos.*, 113, <https://doi.org/10.1029/2007JD009168>, 2008.
- Krotkov, N. A., Lamsal, L. N., Celarier, E. A., Swartz, W. H., Marchenko, S. V., Bucsela, E. J., Chan, K. L., Wenig, M., and Zara, M.: The version 3 OMI NO₂ standard product, *Atmos. Meas. Tech.*, 10, 3133–3149, <https://doi.org/10.5194/amt-10-3133-2017>, 2017.
- Kuhlmann, G., Lam, Y. F., Cheung, H. M., Hartl, A., Fung, J. C. H., Chan, P. W., and Wenig, M. O.: Development of a custom OMI NO₂ data product for evaluating biases in a regional chemistry transport model, *Atmos. Chem. Phys.*, 15, 5627–5644, <https://doi.org/10.5194/acp-15-5627-2015>, 2015.
- Lambert, J., Granville, J., Van Roozendaal, M., Sarkissian, A., Goutail, F., Müller, J., Pommereau, J., and Russell III, J.: A climatology of NO₂ profile for improved air mass factors for ground-based vertical column measurements, in: *Proceedings of the 5th European Symposium Strat. Ozone*, Saint Jean de Luz, p. 703, 1999.
- Lampel, J., Pöhler, D., Tschirner, J., Frieß, U., and Platt, U.: On the relative absorption strengths of water vapour in the blue wavelength range, *Atmos. Meas. Tech.*, 8, 4329–4346, <https://doi.org/10.5194/amt-8-4329-2015>, 2015.
- Laughner, J. L., Zare, A., and Cohen, R. C.: Effects of daily meteorology on the interpretation of space-based remote sensing of NO₂, *Atmos. Chem. Phys.*, 16, 15247–15264, <https://doi.org/10.5194/acp-16-15247-2016>, 2016.
- Laughner, J. L., Zhu, Q., and Cohen, R. C.: The Berkeley High Resolution Tropospheric NO₂ product, *Earth Syst. Sci. Data*, 10, 2069–2095, <https://doi.org/10.5194/essd-10-2069-2018>, 2018.
- Leitão, J., Richter, A., Vrekoussis, M., Kokhanovsky, A., Zhang, Q. J., Beekmann, M., and Burrows, J. P.: On the improvement of NO₂ satellite retrievals – aerosol impact on the airmass factors, *Atmos. Meas. Tech.*, 3, 475–493, <https://doi.org/10.5194/amt-3-475-2010>, 2010.
- Levelt, P., Van den Oord, G., Dobber, M., Malkki, A., Visser, H., de Vries, J., Stammes, P., Lundell, J., and Saari, H.: The Ozone Monitoring Instrument, *IEEE T. Geosci. Remote Sens.*, 44, 1093–1101, 2006.
- Lin, J.-T., Martin, R. V., Boersma, K. F., Sneep, M., Stammes, P., Spurr, R., Wang, P., Van Roozendaal, M., Clémer, K., and Irie, H.: Retrieving tropospheric nitrogen dioxide from the Ozone Monitoring Instrument: effects of aerosols, surface reflectance anisotropy, and vertical profile of nitrogen dioxide, *Atmos. Chem. Phys.*, 14, 1441–1461, <https://doi.org/10.5194/acp-14-1441-2014>, 2014.
- Lin, J.-T., Liu, M.-Y., Xin, J.-Y., Boersma, K. F., Spurr, R., Martin, R., and Zhang, Q.: Influence of aerosols and surface reflectance on satellite NO₂ retrieval: seasonal and spatial characteristics and implications for NO_x emission constraints, *Atmos. Chem. Phys.*, 15, 11217–11241, <https://doi.org/10.5194/acp-15-11217-2015>, 2015.

- Liu, F., Beirle, S., Zhang, Q., van der A, R. J., Zheng, B., Tong, D., and He, K.: NO_x emission trends over Chinese cities estimated from OMI observations during 2005 to 2015, *Atmos. Chem. Phys.*, 17, 9261–9275, <https://doi.org/10.5194/acp-17-9261-2017>, 2017.
- Lorente, A., Folkert Boersma, K., Yu, H., Dörner, S., Hilboll, A., Richter, A., Liu, M., Lamsal, L. N., Barkley, M., De Smedt, I., Van Roozendaal, M., Wang, Y., Wagner, T., Beirle, S., Lin, J.-T., Krotkov, N., Stammes, P., Wang, P., Eskes, H. J., and Krol, M.: Structural uncertainty in air mass factor calculation for NO₂ and HCHO satellite retrievals, *Atmos. Meas. Tech.*, 10, 759–782, <https://doi.org/10.5194/amt-10-759-2017>, 2017.
- Loyola, D., Thomas, W., Livschitz, Y., Ruppert, T., Albert, P., and Hollmann, R.: Cloud properties derived from GOME/ERS-2 backscatter data for trace gas retrieval, *IEEE T. Geosci. Remote Sens.*, 45, 2747–2758, 2007.
- Loyola, D., Koukouli, M., Valks, P., Balis, D., Hao, N., Van Roozendaal, M., Spurr, R., Zimmer, W., Kiemle, S., Lerot, C., et al.: The GOME-2 total column ozone product: Retrieval algorithm and ground-based validation, *J. Geophys. Res.-Atmos.*, 116, <https://doi.org/10.1029/2010JD014675>, 2011.
- Loyola, D. G., Pedernana, M., and García, S. G.: Smart sampling and incremental function learning for very large high dimensional data, *Neural Networks*, 78, 75–87, 2016.
- Loyola, D. G., Gimeno García, S., Lutz, R., Argyrouli, A., Romahn, F., Spurr, R. J. D., Pedernana, M., Doicu, A., Molina García, V., and Schüssler, O.: The operational cloud retrieval algorithms from TROPOMI on board Sentinel-5 Precursor, *Atmos. Meas. Tech.*, 11, 409–427, <https://doi.org/10.5194/amt-11-409-2018>, 2018.
- Lutz, R., Loyola, D., Gimeno García, S., and Romahn, F.: OCRA radiometric cloud fractions for GOME-2 on MetOp-A/B, *Atmos. Meas. Tech.*, 9, 2357–2379, <https://doi.org/10.5194/amt-9-2357-2016>, 2016.
- Ma, J. Z., Beirle, S., Jin, J. L., Shaiganfar, R., Yan, P., and Wagner, T.: Tropospheric NO₂ vertical column densities over Beijing: results of the first three years of ground-based MAX-DOAS measurements (2008–2011) and satellite validation, *Atmos. Chem. Phys.*, 13, 1547–1567, <https://doi.org/10.5194/acp-13-1547-2013>, 2013.
- McLinden, C. A., Fioletov, V., Boersma, K. F., Kharol, S. K., Krotkov, N., Lamsal, L., Makar, P. A., Martin, R. V., Veefkind, J. P., and Yang, K.: Improved satellite retrievals of NO₂ and SO₂ over the Canadian oil sands and comparisons with surface measurements, *Atmos. Chem. Phys.*, 14, 3637–3656, <https://doi.org/10.5194/acp-14-3637-2014>, 2014.
- Miyazaki, K., Eskes, H., Sudo, K., Boersma, K. F., Bowman, K., and Kanaya, Y.: Decadal changes in global surface NO_x emissions from multi-constituent satellite data assimilation, *Atmos. Chem. Phys.*, 17, 807–837, <https://doi.org/10.5194/acp-17-807-2017>, 2017.
- Müller, J.-P., Kharbouche, S., Gobron, N., Scanlon, T., Govaerts, Y., Danne, O., Schultz, J., Lattanzio, A., Peters, E., De Smedt, I., Beirle, S., Lorente, A., Coheur, P., George, M., Wagner, T., Hilboll, A., Richter, A., Van Roozendaal, M., and Boersma, K.: Recommendations (scientific) on best practices for retrievals for Land and Atmosphere ECVs, *Tech. rep.*, Deliverable 4.2 – version 1.0, 2016.
- Munro, R., Lang, R., Klaes, D., Poli, G., Retscher, C., Lindstrot, R., Huckle, R., Lacan, A., Grzegorski, M., Holdak, A., Kokhanovsky, A., Livschitz, J., and Eisinger, M.: The GOME-2 instrument on the Metop series of satellites: instrument design, calibration, and level 1 data processing – an overview, *Atmos. Meas. Tech.*, 9, 1279–1301, <https://doi.org/10.5194/amt-9-1279-2016>, 2016.
- Nolin, A., Armstrong, R., and Maslanik, J.: Near real-time SSM/I EASE-grid daily global ice concentration and snow extent, *Digital Media*, National Snow and Ice Data Center, Boulder, CO, USA, 2005.
- Nuß, H., Richter, A., Valks, P., and Burrows, J.: Improvement of the NO₂ total column retrieval for GOME-2, O3M SAF Visiting Scientist Activity, Final Report, IUP University of Bremen, 2006.
- Olivier, J. G., Bouwman, A., Berdowski, J., Veldt, C., Bloos, J., Visschedijk, A., Zandveld, P., and Haverlag, J.: Description of EDGAR Version 2.0: A set of global emission inventories of greenhouse gases and ozone-depleting substances for all anthropogenic and most natural sources on a per country basis and on 1 degree × 1 degree grid, RIVM report no. 771060 002/TNO-MEP report no. R96/119, <https://www.rivm.nl/bibliotheek/rapporten/771060002.pdf> (last access: 1 February 2019), 1996.
- Ortega, I., Koenig, T., Sinreich, R., Thomson, D., and Volkamer, R.: The CU 2-D-MAX-DOAS instrument – Part I: Retrieval of 3-D distributions of NO₂ and azimuth-dependent OVOC ratios, *Atmos. Meas. Tech.*, 8, 2371–2395, <https://doi.org/10.5194/amt-8-2371-2015>, 2015.
- Penning de Vries, M. J. M., Beirle, S., Hörmann, C., Kaiser, J. W., Stammes, P., Tilstra, L. G., Tuinder, O. N. E., and Wagner, T.: A global aerosol classification algorithm incorporating multiple satellite data sets of aerosol and trace gas abundances, *Atmos. Chem. Phys.*, 15, 10597–10618, <https://doi.org/10.5194/acp-15-10597-2015>, 2015.
- Peters, E., Wittrock, F., Richter, A., Alvarado, L. M. A., Rozanov, V. V., and Burrows, J. P.: Liquid water absorption and scattering effects in DOAS retrievals over oceans, *Atmos. Meas. Tech.*, 7, 4203–4221, <https://doi.org/10.5194/amt-7-4203-2014>, 2014.
- Pinardi, G., Van Roozendaal, M., Lambert, J.-C., Granville, J., Hendrick, F., Tack, F., Yu, H., Cede, A., Kanaya, Y., Irie, I., Goutail, F., Pommereau, J.-P., Pazmino, A., Wittrock, F., Richter, A., Wagner, T., Gu, M., Remmers, J., Friess, U., Vlemmix, T., PETERS, A., Hao, N., Tiefengraber, M., Herman, J., Abuhassan, N., Bais, A., Kouremeti, N., Hovila, J., Holla, R., Chong, J., Postylyakov, O., and Ma, J.: GOME-2 total and tropospheric NO₂ validation based on zenith-sky, direct-sun and multi-axis DOAS network observations, in: *Proc. of the 2014 EUMETSAT Meteorological Satellite Conference*, Geneva, Switzerland, 22–26 September 2014, EUMETSAT, 2014.
- Pinardi, G., Lambert, J.-C., Granville, J., Yu, H., De Smedt, I., van Roozendaal, M., and Valks, P.: O3M-SAF validation report, *Tech. rep.*, SAF/O3M/IASB/VR/NO₂/TN-IASB-GOME2-O3MSAF-NO₂-2015, 1/1, 2015.
- Platt, U. and Stutz, J.: *Differential Optical Absorption Spectroscopy*, Springer, 2008.
- Pope, R. M. and Fry, E. S.: Absorption spectrum (380–700 nm) of pure water. II. Integrating cavity measurements, *Appl. Opt.*, 36, 8710–8723, 1997.
- Richter, A. and verification team: S5P/TROPOMI Science Verification Report, *Tech. rep.*, S5P-IUP-L2-ScVR-RP issue 2.1, 2015.

- Richter, A., Burrows, J. P., Nüß, H., Granier, C., and Niemeier, U.: Increase in tropospheric nitrogen dioxide over China observed from space, *Nature*, 437, p. 129, 2005.
- Richter, A., Begoin, M., Hilboll, A., and Burrows, J. P.: An improved NO₂ retrieval for the GOME-2 satellite instrument, *Atmos. Meas. Tech.*, 4, 1147–1159, <https://doi.org/10.5194/amt-4-1147-2011>, 2011.
- Rothman, L., Gordon, I., Barber, R., Dothe, H., Gamache, R., Goldman, A., Perevalov, V., Tashkun, S., and Tennyson, J.: HITEMP, the high-temperature molecular spectroscopic database, *J. Quant. Spectrosc. Ra.*, 111, 2139–2150, 2010.
- Russell, A. R., Perring, A. E., Valin, L. C., Bucsela, E. J., Browne, E. C., Wooldridge, P. J., and Cohen, R. C.: A high spatial resolution retrieval of NO₂ column densities from OMI: method and evaluation, *Atmos. Chem. Phys.*, 11, 8543–8554, <https://doi.org/10.5194/acp-11-8543-2011>, 2011.
- Safieddine, S., Clerbaux, C., George, M., Hadji-Lazaro, J., Hurtmans, D., Coheur, P.-F., Wespes, C., Loyola, D., Valks, P., and Hao, N.: Tropospheric ozone and nitrogen dioxide measurements in urban and rural regions as seen by IASI and GOME-2, *J. Geophys. Res.-Atmos.*, 118, 10555–10566, <https://doi.org/10.1002/jgrd.50669>, 2013.
- Seinfeld, J. H., Pandis, S., and Noone, K.: *Atmospheric chemistry and physics: from air pollution to climate change*, Wiley, 1998.
- Solomon, S.: Stratospheric ozone depletion: A review of concepts and history, *Rev. Geophys.*, 37, 275–316, 1999.
- Spurr, R., Kurosu, T., and Chance, K.: A linearized discrete ordinate radiative transfer model for atmospheric remote-sensing retrieval, *J. Quant. Spectrosc. Ra.*, 68, 689–735, 2001.
- Spurr, R. J.: VLIDORT: A linearized pseudo-spherical vector discrete ordinate radiative transfer code for forward model and retrieval studies in multilayer multiple scattering media, *J. Quant. Spectrosc. Ra.*, 102, 316–342, 2006.
- Thalman, R. and Volkamer, R.: Temperature dependent absorption cross-sections of O₂–O₂ collision pairs between 340 and 630 nm and at atmospherically relevant pressure, *Phys. Chem. Chem. Phys.*, 15, 15371–15381, 2013.
- Tikhonov, A. and Arsenin, V.: *Solutions of ill-posed problems*, V. H. Winston & Sons, Washington, 1977.
- Tilstra, L., Tuinder, O., and Stammes, P.: GOME-2 surface LER product – Algorithm Theoretical Basis Document, Tech. rep., KNMI Report O3MSAF/KNMI/ATBD/003, Issue 2.2, 2017a.
- Tilstra, L., Wang, P., and Stammes, P.: Surface reflectivity climatologies from UV to NIR determined from Earth observations by GOME-2 and SCIAMACHY, *J. Geophys. Res.-Atmos.*, 122, 4084–4111, 2017b.
- Valks, P., Pinardi, G., Richter, A., Lambert, J.-C., Hao, N., Loyola, D., Van Roozendaal, M., and Emmadi, S.: Operational total and tropospheric NO₂ column retrieval for GOME-2, *Atmos. Meas. Tech.*, 4, 1491–1514, <https://doi.org/10.5194/amt-4-1491-2011>, 2011.
- Valks, P., Loyola, D., Hao, N., Hedelt, P., Slijkhuis, S., Grossi, M., Begoin, M., Gimeno Garcia, S., and Lutz, R.: Algorithm Theoretical Basis Document for GOME-2 Total Column Products of Ozone, NO₂, BrO, SO₂, H₂O, HCHO and Cloud Properties (GDP 4.8 for AC SAF OTO and NTO), Tech. rep., SAF/AC/DLR/ATBD/01, Iss./Rev.: 3/A/2, 2017.
- van Geffen, J. H. G. M., Boersma, K. F., Van Roozendaal, M., Hendrick, F., Mahieu, E., De Smedt, I., Sneepe, M., and Veefkind, J. P.: Improved spectral fitting of nitrogen dioxide from OMI in the 405–465 nm window, *Atmos. Meas. Tech.*, 8, 1685–1699, <https://doi.org/10.5194/amt-8-1685-2015>, 2015.
- van Geffen, J., Boersma, K., Eskes, H., Maasakkers, J., and Veefkind, J.: TROPOMI ATBD of the total and tropospheric NO₂ data products, Tech. rep., S5P-KNMI-L2-0005-RP issue 1.0.0. KNMI, De Bilt, the Netherlands, 2016.
- Vandaele, A. C., Hermans, C., Fally, S., Carleer, M., Colin, R., Merienne, M.-F., Jenouvrier, A., and Coquart, B.: High-resolution Fourier transform measurement of the NO₂ visible and near-infrared absorption cross sections: Temperature and pressure effects, *J. Geophys. Res.-Atmos.*, 107, <https://doi.org/10.1029/2001JD000971>, 2002.
- van der A, R. J., Mijling, B., Ding, J., Koukouli, M. E., Liu, F., Li, Q., Mao, H., and Theys, N.: Cleaning up the air: effectiveness of air quality policy for SO₂ and NO_x emissions in China, *Atmos. Chem. Phys.*, 17, 1775–1789, <https://doi.org/10.5194/acp-17-1775-2017>, 2017.
- Vasilkov, A., Qin, W., Krotkov, N., Lamsal, L., Spurr, R., Haffner, D., Joiner, J., Yang, E.-S., and Marchenko, S.: Accounting for the effects of surface BRDF on satellite cloud and trace-gas retrievals: a new approach based on geometry-dependent Lambertian equivalent reflectivity applied to OMI algorithms, *Atmos. Meas. Tech.*, 10, 333–349, <https://doi.org/10.5194/amt-10-333-2017>, 2017.
- Veefkind, J., Aben, I., McMullan, K., Förster, H., De Vries, J., Oter, G., Claas, J., Eskes, H., De Haan, J., Kleipool, Q., van Weele, M., Hasekamp, O., Hoogeveen, R., Landgraf, J., Snel, R., Tol, P., Ingmann, P., Voors, R., Kruizinga, B., Vink, R., Visser, H., and Levelt, P.: TROPOMI on the ESA Sentinel-5 Precursor: A GMES mission for global observations of the atmospheric composition for climate, air quality and ozone layer applications, *Remote Sens. Environ.*, 120, 70–83, 2012.
- Veefkind, J. P., de Haan, J. F., Sneepe, M., and Levelt, P. F.: Improvements to the OMI O₂–O₂ operational cloud algorithm and comparisons with ground-based radar–lidar observations, *Atmos. Meas. Tech.*, 9, 6035–6049, <https://doi.org/10.5194/amt-9-6035-2016>, 2016.
- Vlemmix, T., Hendrick, F., Pinardi, G., De Smedt, I., Fayt, C., Hermans, C., Pitters, A., Wang, P., Levelt, P., and Van Roozendaal, M.: MAX-DOAS observations of aerosols, formaldehyde and nitrogen dioxide in the Beijing area: comparison of two profile retrieval approaches, *Atmos. Meas. Tech.*, 8, 941–963, <https://doi.org/10.5194/amt-8-941-2015>, 2015.
- Vountas, M., Richter, A., Wittrock, F., and Burrows, J. P.: Inelastic scattering in ocean water and its impact on trace gas retrievals from satellite data, *Atmos. Chem. Phys.*, 3, 1365–1375, <https://doi.org/10.5194/acp-3-1365-2003>, 2003.
- Vrekoussis, M., Wittrock, F., Richter, A., and Burrows, J. P.: GOME-2 observations of oxygenated VOCs: what can we learn from the ratio glyoxal to formaldehyde on a global scale?, *Atmos. Chem. Phys.*, 10, 10145–10160, <https://doi.org/10.5194/acp-10-10145-2010>, 2010.
- Wagner, T., Dix, B. V., Friedeburg, C. V., Frieß, U., Sanghavi, S., Sinreich, R., and Platt, U.: MAX-DOAS O₄ measurements: A new technique to derive information on atmospheric aerosols – Principles and information content, *J. Geophys. Res.-Atmos.*, 109, <https://doi.org/10.1029/2004JD004904>, 2004.

- Wagner, T., Beirle, S., Brauers, T., Deutschmann, T., Frieß, U., Hak, C., Halla, J. D., Heue, K. P., Junkermann, W., Li, X., Platt, U., and Pundt-Gruber, I.: Inversion of tropospheric profiles of aerosol extinction and HCHO and NO₂ mixing ratios from MAX-DOAS observations in Milano during the summer of 2003 and comparison with independent data sets, *Atmos. Meas. Tech.*, 4, 2685–2715, <https://doi.org/10.5194/amt-4-2685-2011>, 2011.
- Wang, Y., Beirle, S., Lampel, J., Koukouli, M., De Smedt, I., Theys, N., Li, A., Wu, D., Xie, P., Liu, C., Van Roozendael, M., Stavrou, T., Müller, J.-F., and Wagner, T.: Validation of OMI, GOME-2A and GOME-2B tropospheric NO₂, SO₂ and HCHO products using MAX-DOAS observations from 2011 to 2014 in Wuxi, China: investigation of the effects of priori profiles and aerosols on the satellite products, *Atmos. Chem. Phys.*, 17, 5007–5033, <https://doi.org/10.5194/acp-17-5007-2017>, 2017.
- Williams, J. E., Boersma, K. F., Le Sager, P., and Verstraeten, W. W.: The high-resolution version of TM5-MP for optimized satellite retrievals: description and validation, *Geosci. Model Dev.*, 10, 721–750, <https://doi.org/10.5194/gmd-10-721-2017>, 2017.
- Wittrock, F., Oetjen, H., Richter, A., Fietkau, S., Medeke, T., Rozanov, A., and Burrows, J. P.: MAX-DOAS measurements of atmospheric trace gases in Ny-Ålesund – Radiative transfer studies and their application, *Atmos. Chem. Phys.*, 4, 955–966, <https://doi.org/10.5194/acp-4-955-2004>, 2004.
- Wu, F. C., Xie, P. H., Li, A., Chan, K. L., Hartl, A., Wang, Y., Si, F. Q., Zeng, Y., Qin, M., Xu, J., Liu, J. G., Liu, W. Q., and Wenig, M.: Observations of SO₂ and NO₂ by mobile DOAS in the Guangzhou eastern area during the Asian Games 2010, *Atmos. Meas. Tech.*, 6, 2277–2292, <https://doi.org/10.5194/amt-6-2277-2013>, 2013.
- Zara, M., Boersma, K. F., De Smedt, I., Richter, A., Peters, E., van Geffen, J. H. G. M., Beirle, S., Wagner, T., Van Roozendael, M., Marchenko, S., Lamsal, L. N., and Eskes, H. J.: Improved slant column density retrieval of nitrogen dioxide and formaldehyde for OMI and GOME-2A from QA4ECV: intercomparison, uncertainty characterisation, and trends, *Atmos. Meas. Tech.*, 11, 4033–4058, <https://doi.org/10.5194/amt-11-4033-2018>, 2018.
- Zien, A. W., Richter, A., Hilboll, A., Blechschmidt, A.-M., and Burrows, J. P.: Systematic analysis of tropospheric NO₂ long-range transport events detected in GOME-2 satellite data, *Atmos. Chem. Phys.*, 14, 7367–7396, <https://doi.org/10.5194/acp-14-7367-2014>, 2014.

Supplement of Atmos. Meas. Tech., 12, 1029–1057, 2019
<https://doi.org/10.5194/amt-12-1029-2019-supplement>
© Author(s) 2019. This work is distributed under
the Creative Commons Attribution 4.0 License.



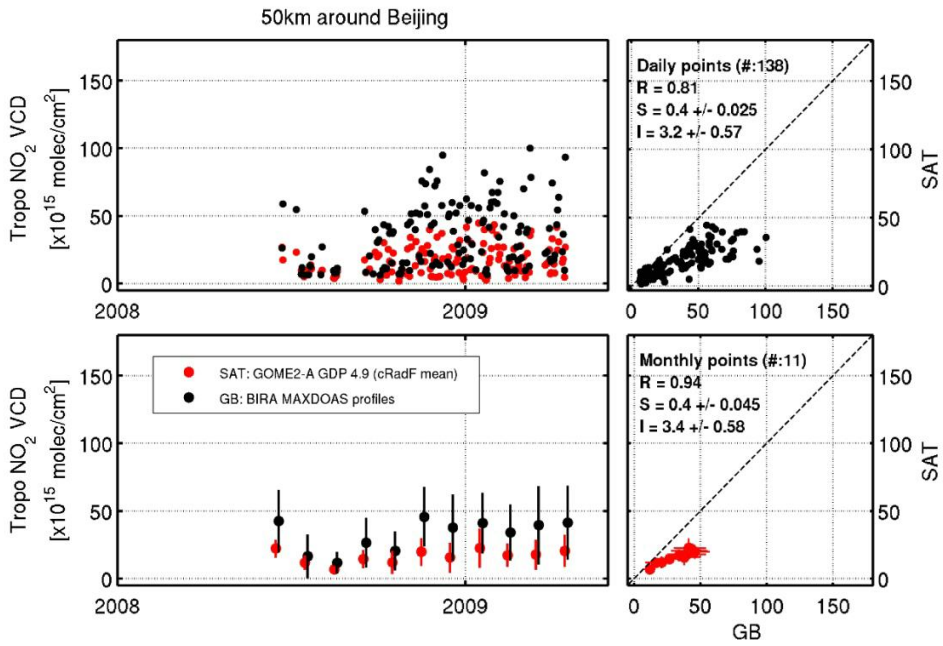
Supplement of

An improved total and tropospheric NO₂ column retrieval for GOME-2

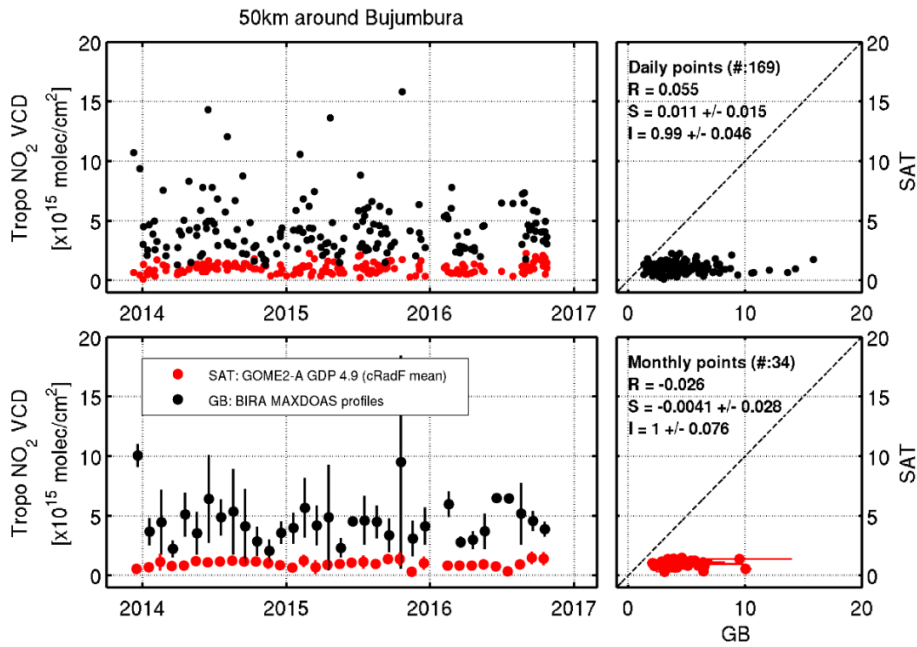
Song Liu et al.

Correspondence to: Song Liu (Song.Liu@dlr.de)

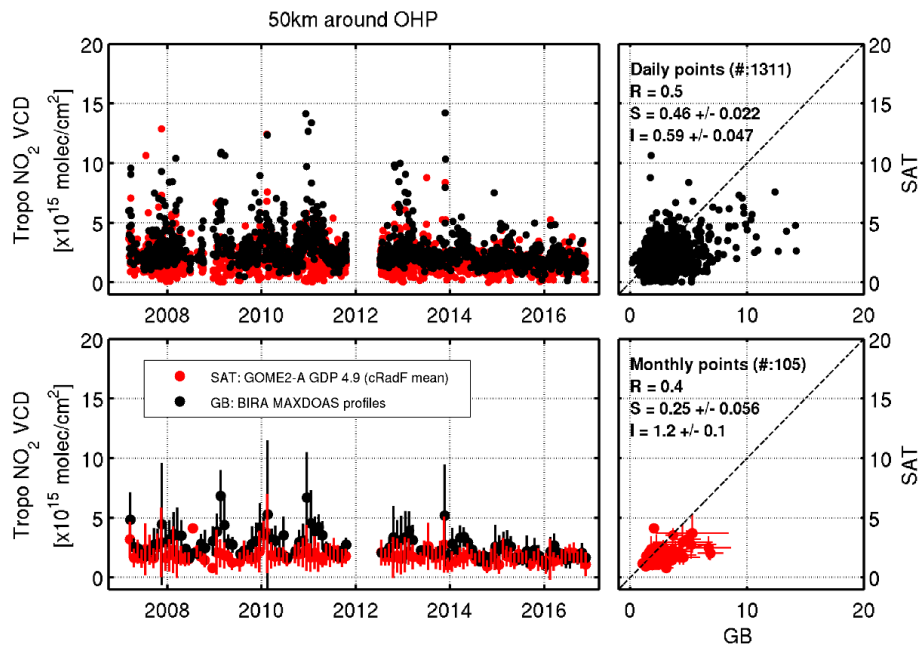
The copyright of individual parts of the supplement might differ from the CC BY 4.0 License.



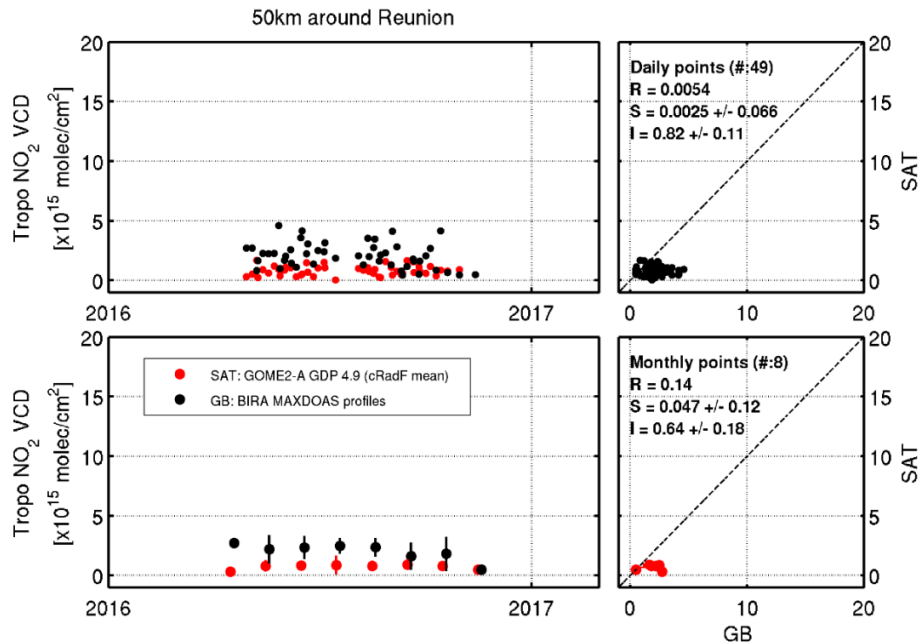
(a)



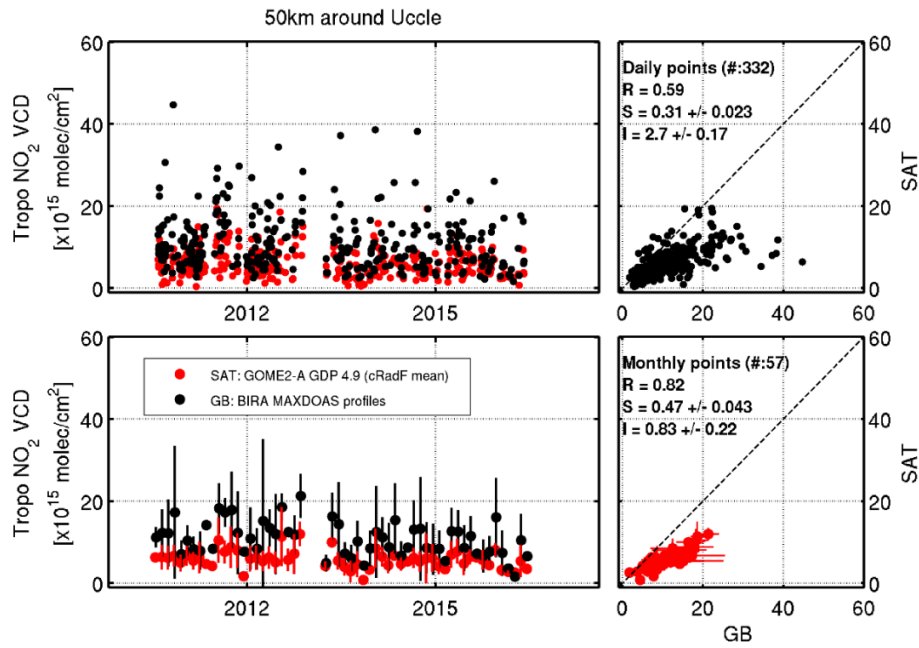
(b)



(c)

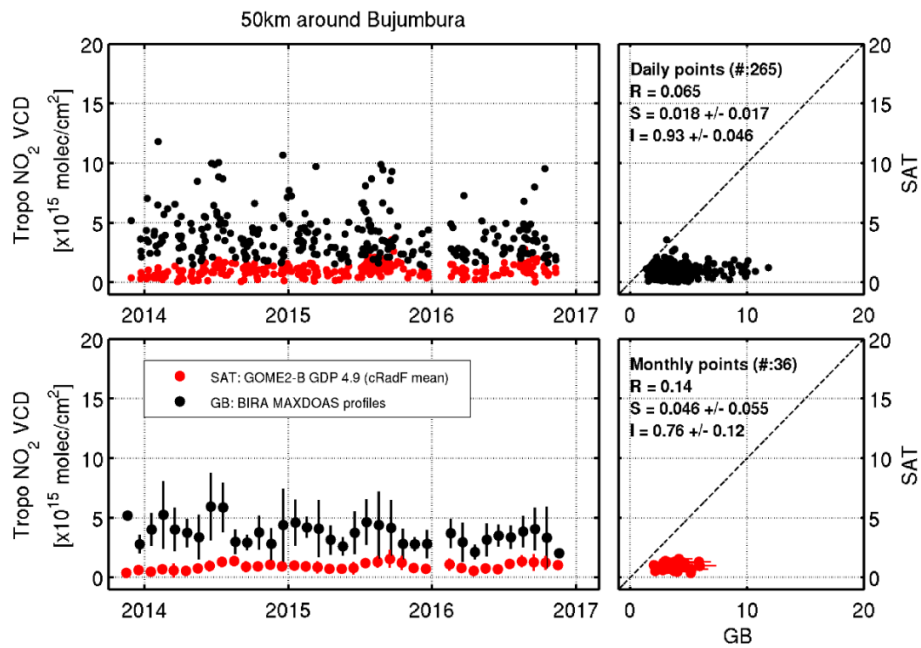


(d)

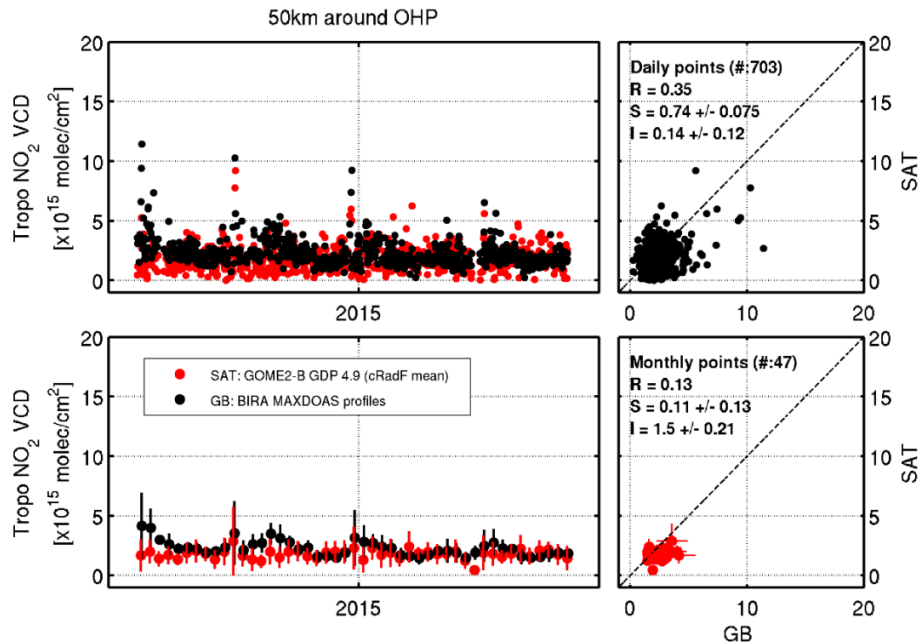


(e)

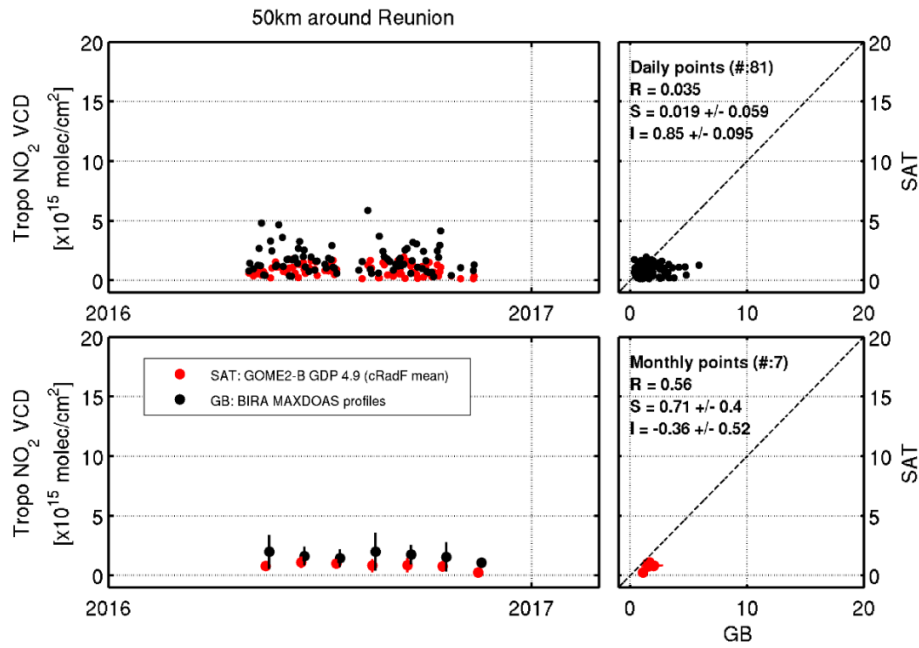
Figure S1. Daily (upper row) and monthly mean (lower row) time series and scatter plot of GOME-2A and MAXDOAS NO₂ tropospheric columns (mean value of all the pixels within 50km) around Beijing (a), Bujumbura (b), OHP (c), Reunion (d), and Uccle (e).



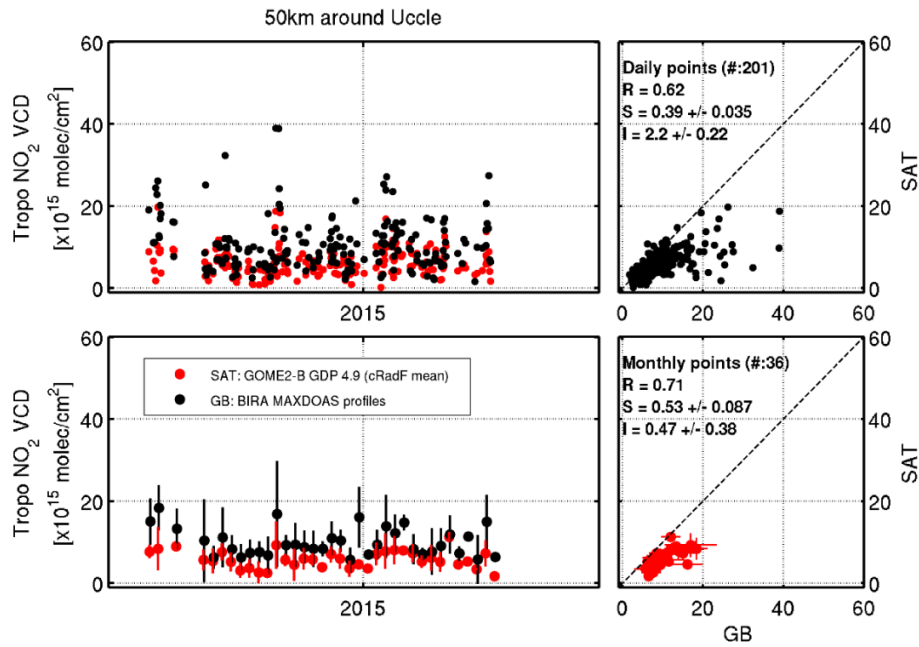
(a)



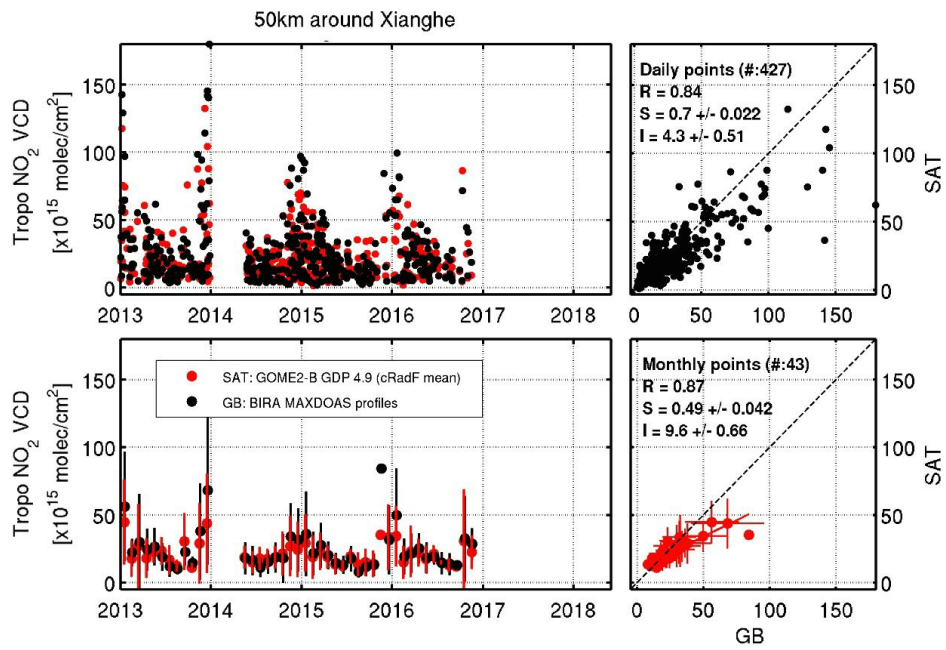
(b)



(c)



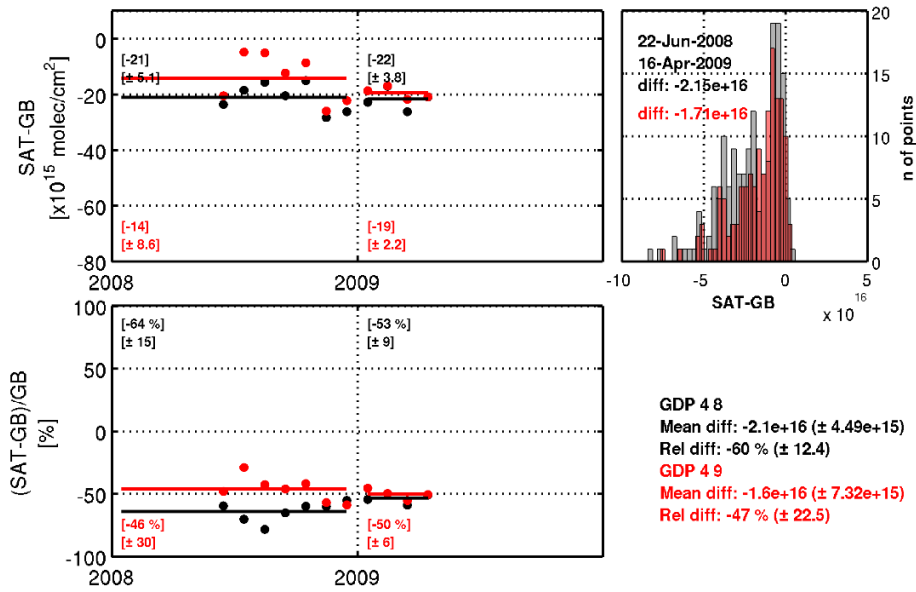
(d)



(e)

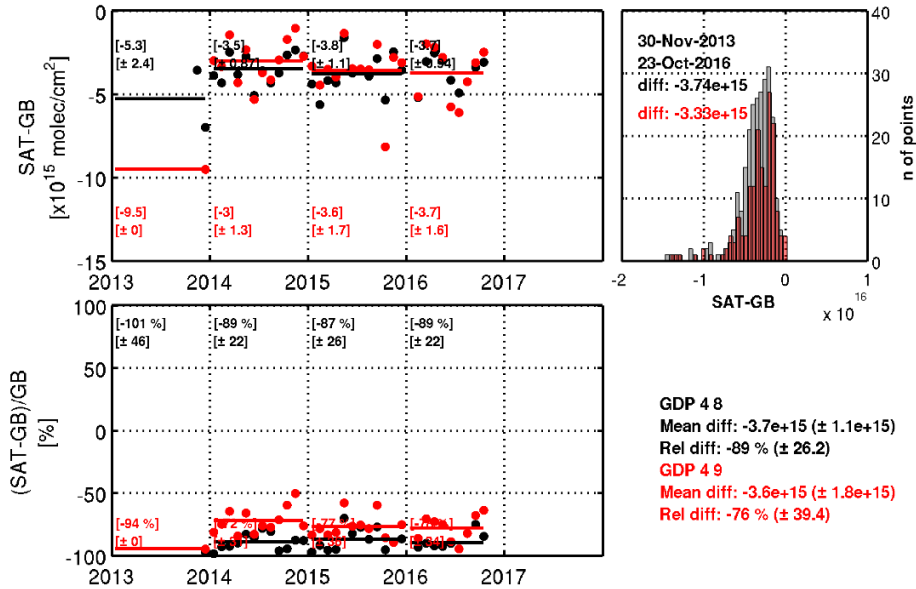
Figure S2. Same as Fig. S1 but for GOME-2B product around Bujumbura (a), OHP (b), Reunion (c), Uccle (d), and Xianghe (e).

GOME2-A 50km around Beijing (BIRA, MAXDOAS profiles)

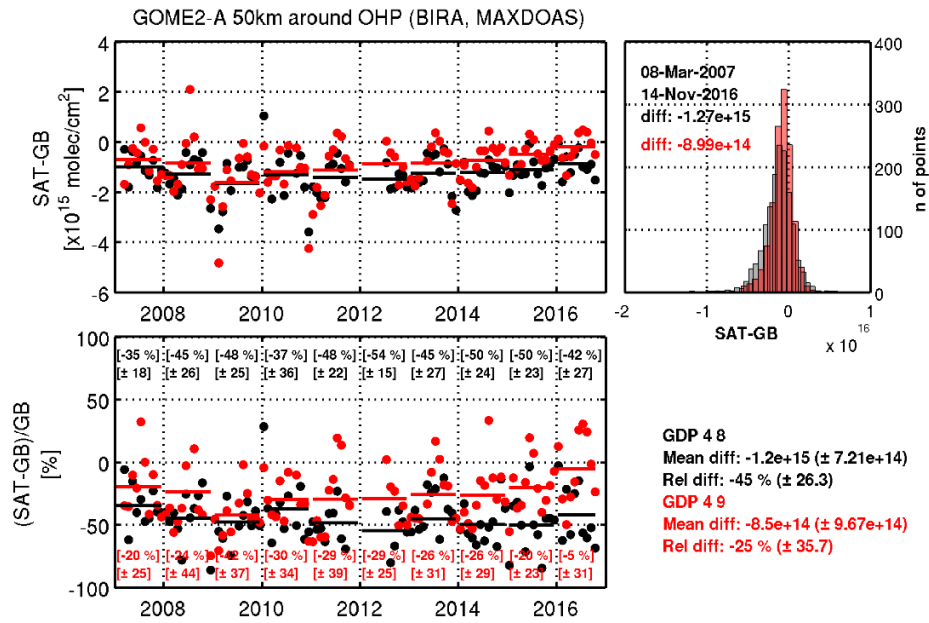


(a)

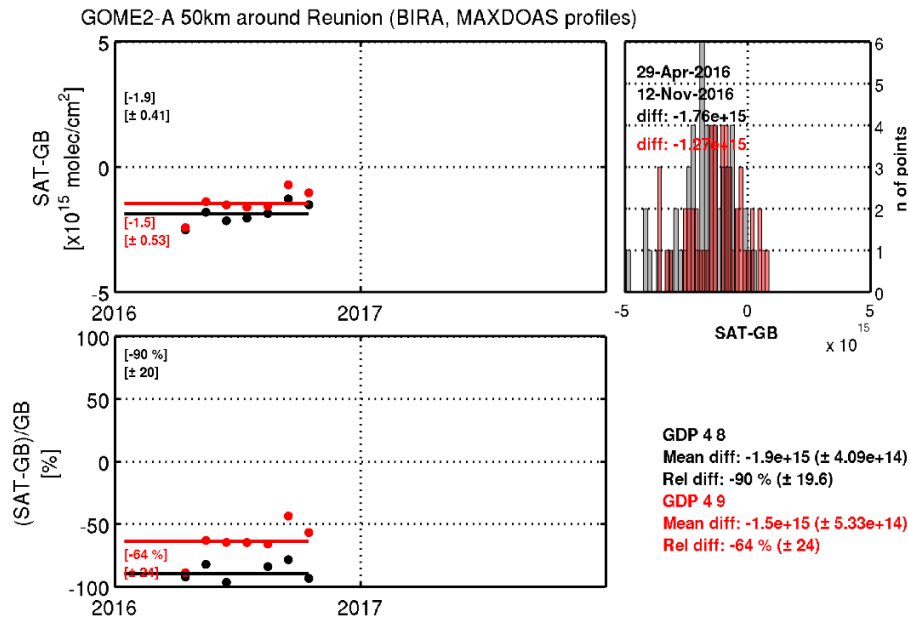
GOME2-A 50km around Bujumbura (BIRA, MAXDOAS profiles)



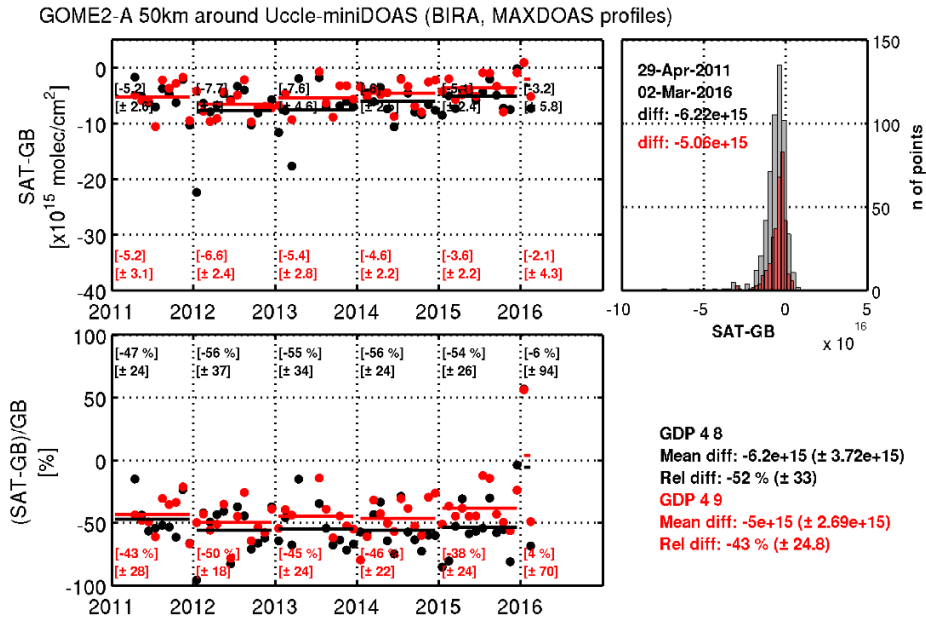
(b)



(c)



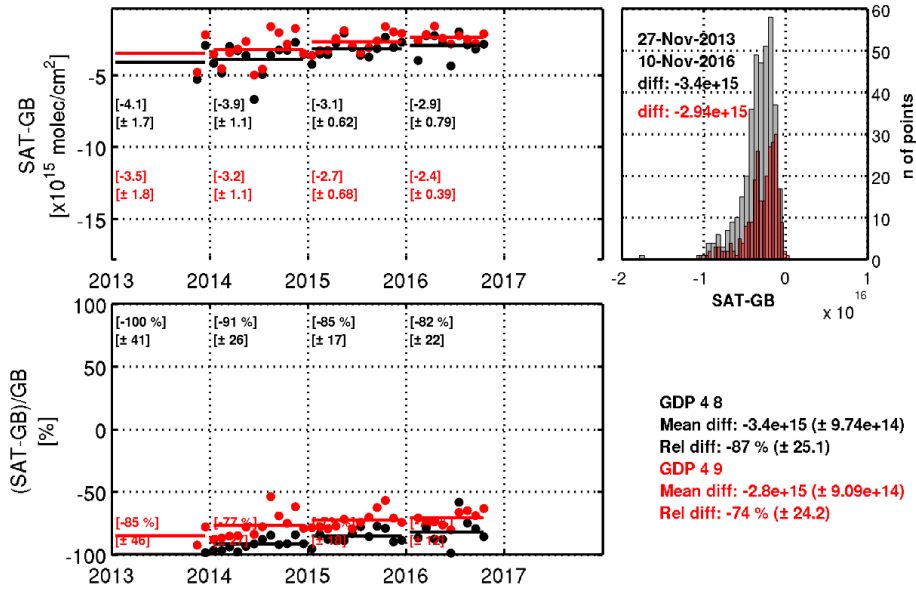
(d)



(e)

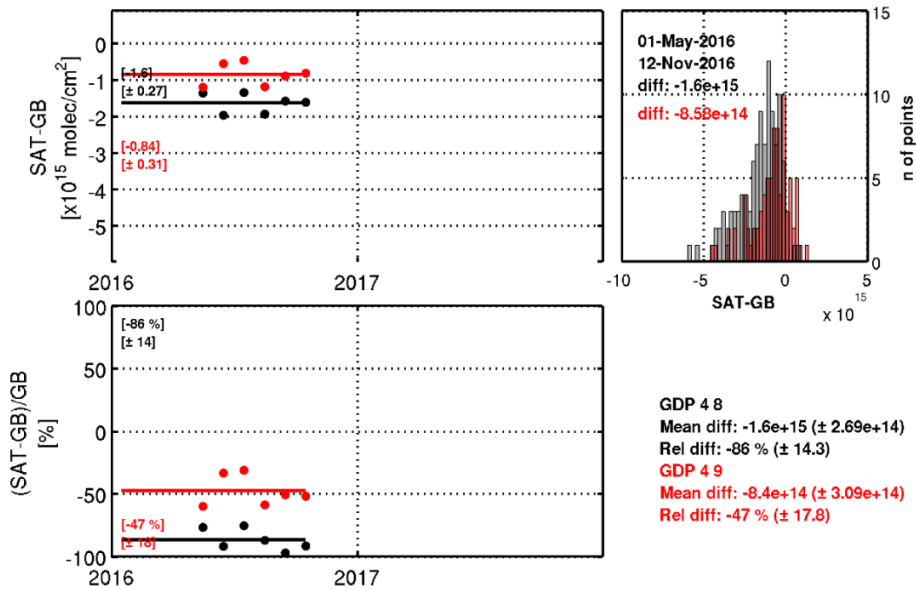
Figure S3. Absolute and relative differences of GOME-2A and MAXDOAS NO₂ tropospheric columns at Beijing (a), Bujumbura (b), OHP (c), Reunion (d), and Uccle (e). The time-series presents the monthly mean differences for GDP 4.8 (black) and GDP 4.9 (red). The total mean differences values and standard deviations are given, as well as the yearly values. The histogram presents the daily differences over the whole time-series for the two products (grey for GDP 4.8 and red for GDP 4.9).

GOME2-B 50km around Bujumbura (BIRA, MAXDOAS profiles)

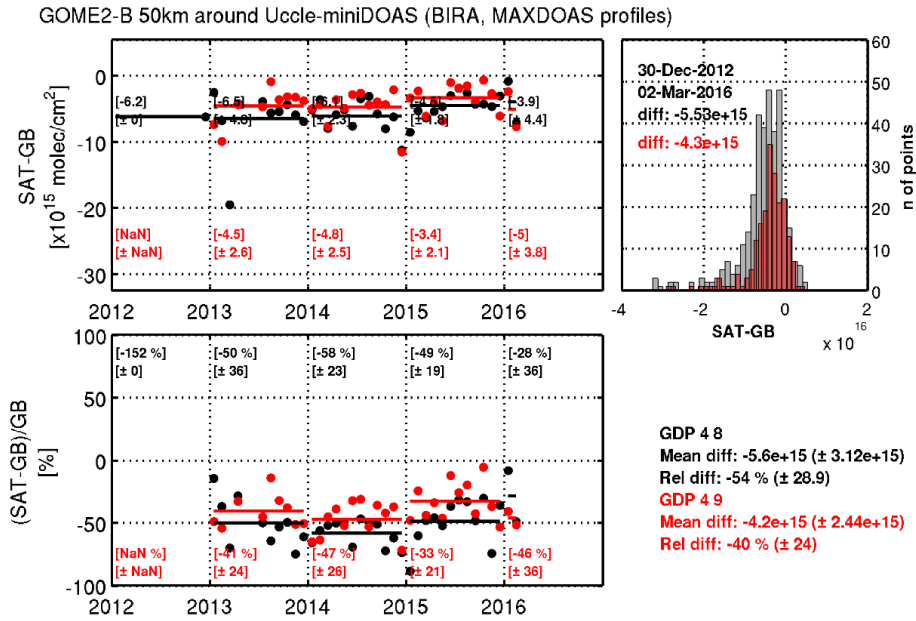


(a)

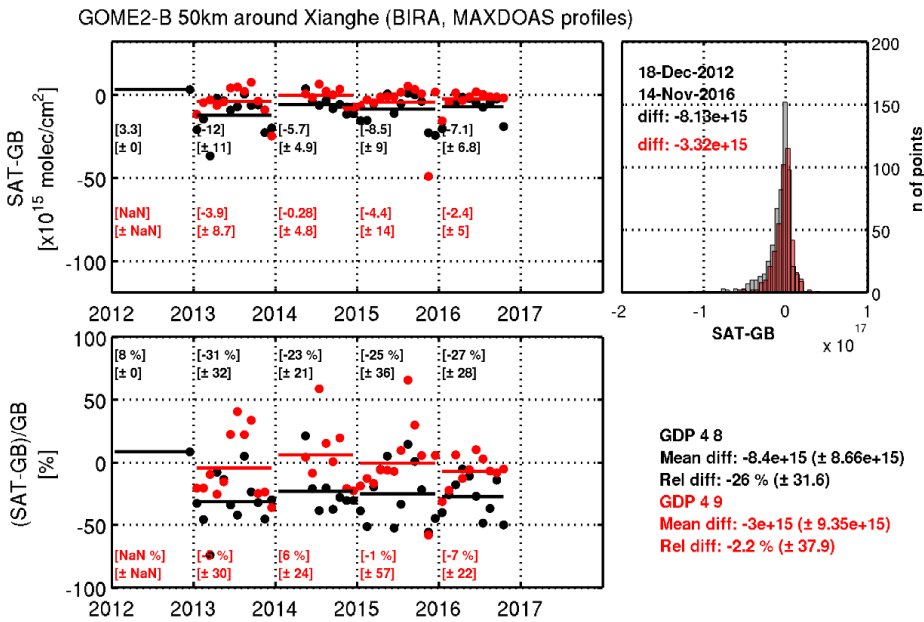
GOME2-B 50km around Reunion (BIRA, MAXDOAS profiles)



(b)



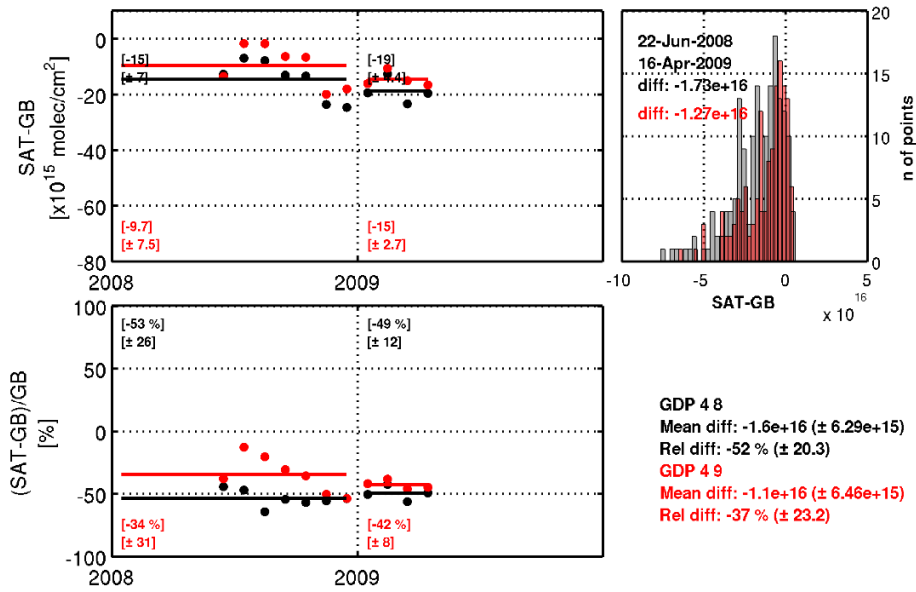
(c)



(d)

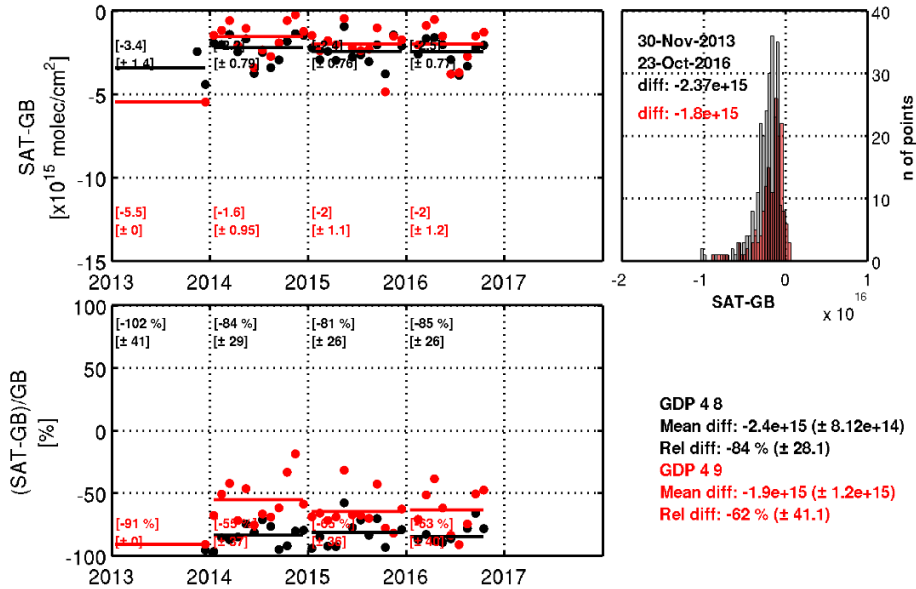
Figure S4. Same as Fig. S3 but for GOME-2B product around Bujumbura (a), Reunion (b), Uccle (c), and Xianghe (d).

GOME2-A 50km around Beijing (BIRA, MAXDOAS profiles smoothed)



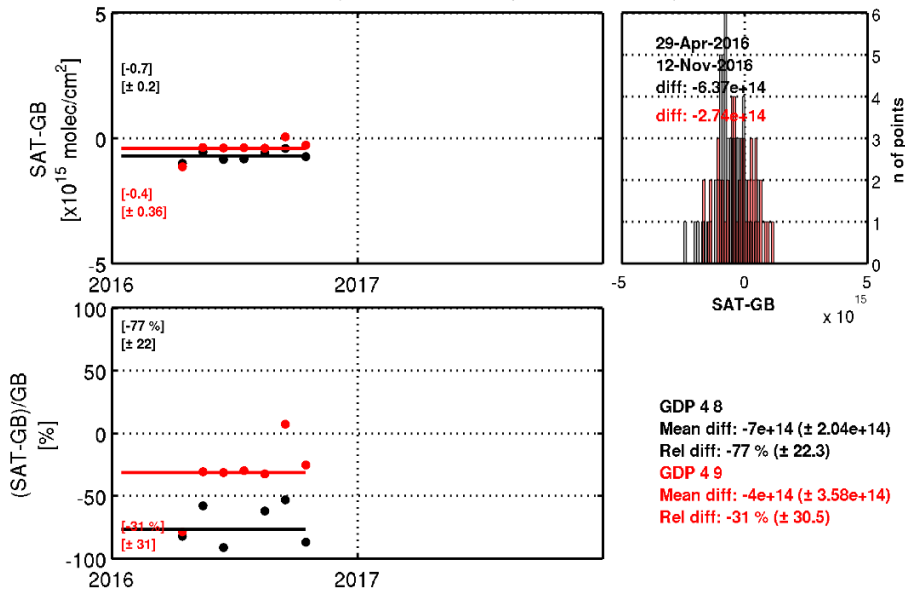
(a)

GOME2-A 50km around Bujumbura (BIRA, MAXDOAS profiles smoothed)



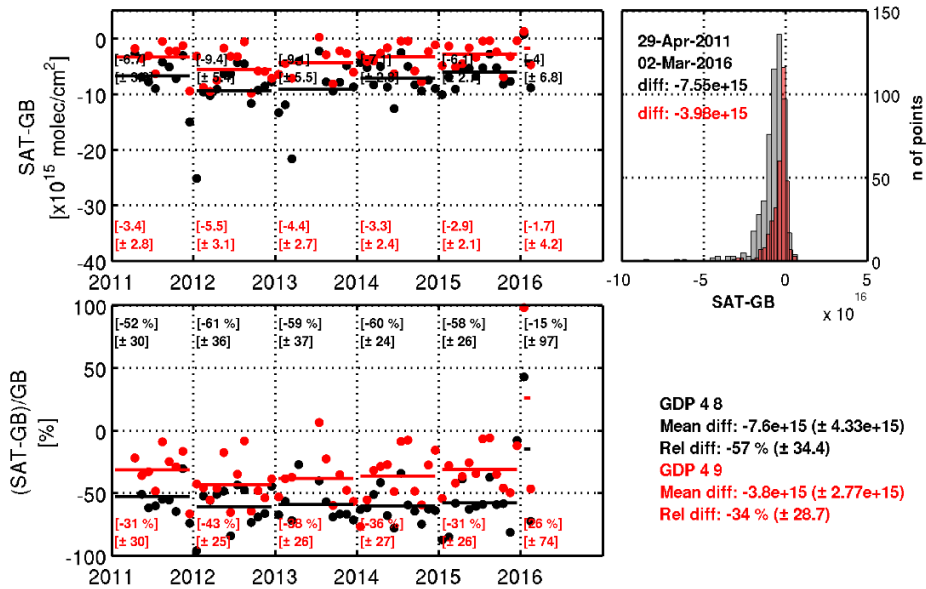
(b)

GOME2-A 50km around Reunion (BIRA, MAXDOAS profiles smoothed)

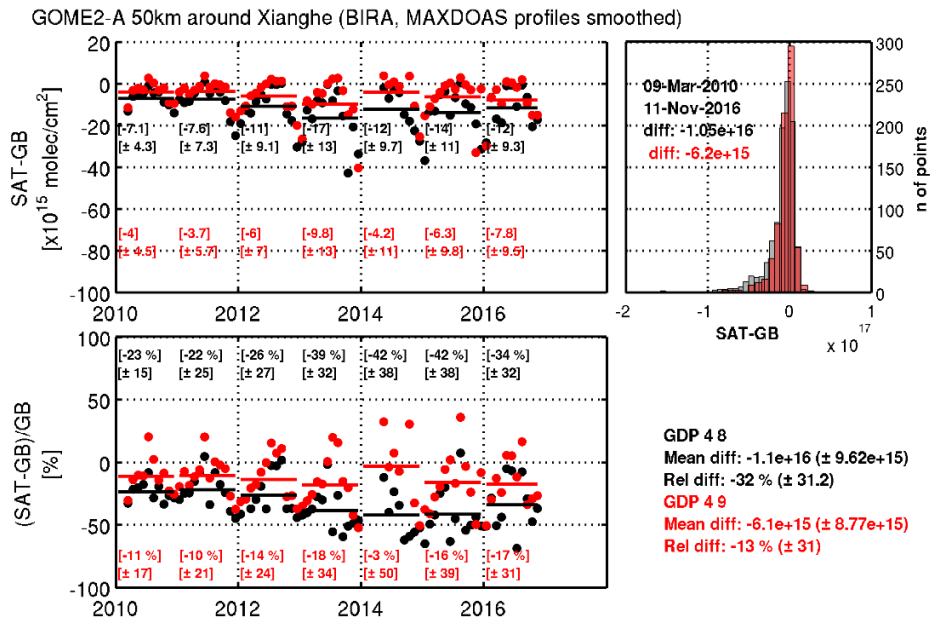


(c)

GOME2-A 50km around Uccle-miniDOAS (BIRA, MAXDOAS profiles smoothed)



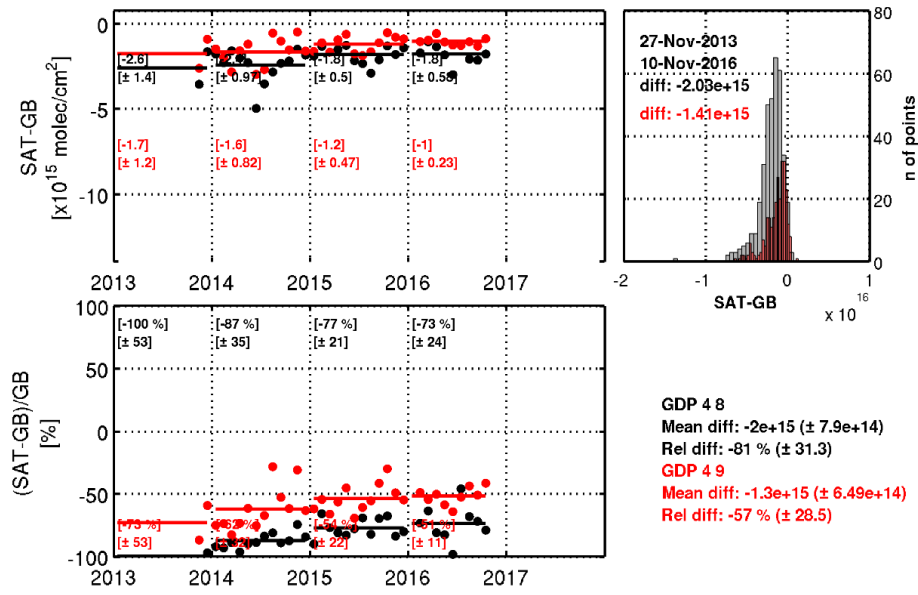
(d)



(e)

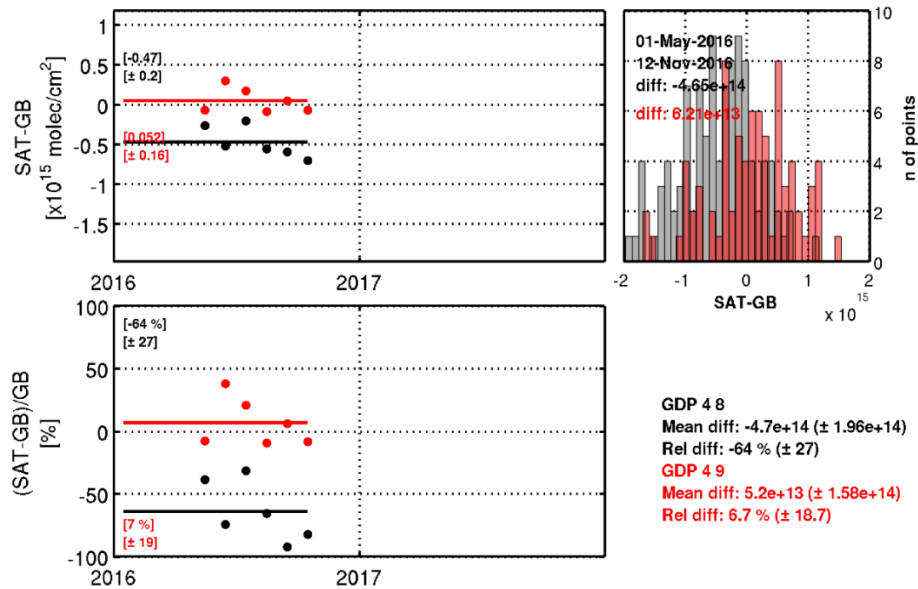
Figure S5. Same as Fig. S3 but with smoothed MAXDOAS columns around Beijing (a), Bujumbura (b), Reunion (c), Uccle (d), and Xianghe (e).

GOME2-B 50km around Bujumbura (BIRA, MAXDOAS profiles smoothed)



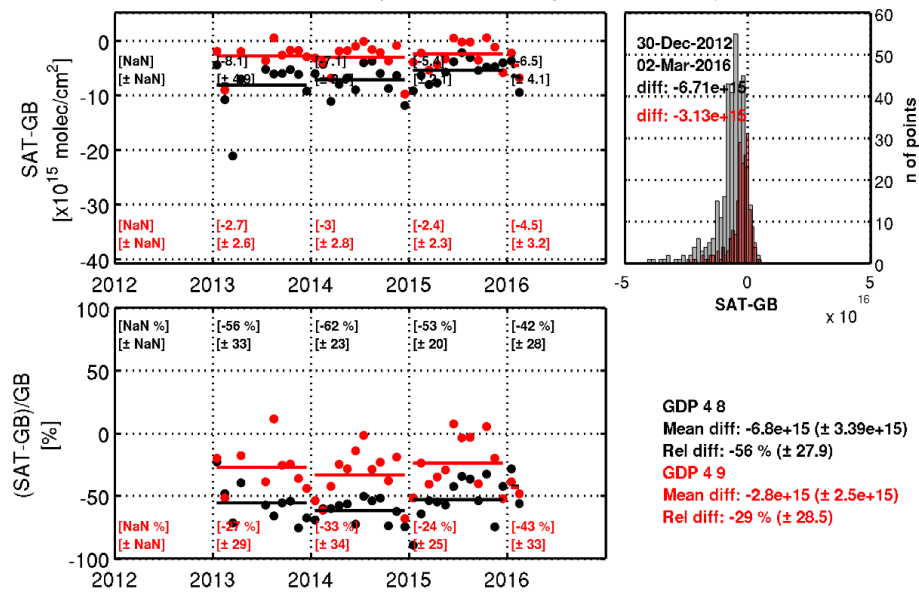
(a)

GOME2-B 50km around Reunion (BIRA, MAXDOAS profiles smoothed)



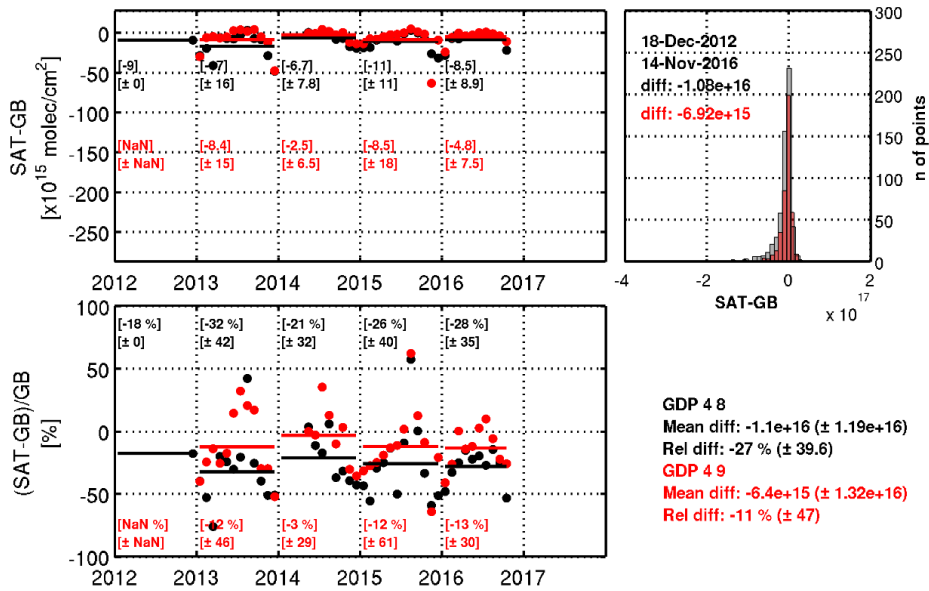
(b)

GOME2-B 50km around Uccle-miniDOAS (BIRA, MAXDOAS profiles smoothed)



(c)

GOME2-B 50km around Xianghe (BIRA, MAXDOAS profiles smoothed)



(d)

Figure S6. Same as Fig. S4 but with smoothed MAXDOAS columns around Bujumbura (a), Reunion (b), Uccle (c), and Xianghe (d).

Appendix D

An improved air mass factor calculation for NO₂ measurements from GOME-2

Liu, S., Valks, P., Pinardi, G., Xu, J., Argyrouli, A., Lutz, R., Tilstra, L. G., Huijnen, V., Hendrick, F., and Van Roozendael, M.: An Improved Air Mass Factor Calculation for NO₂ Measurements from GOME-2, *Atmos. Meas. Tech. Discuss.*, in review, <https://doi.org/10.5194/amt-2019-265>, 2019.



An improved air mass factor calculation for NO₂ measurements from GOME-2

Song Liu¹, Pieter Valks¹, Gaia Pinardi², Jian Xu¹, Athina Argyrouli^{4,1}, Ronny Lutz¹, L. Gijbert Tilstra³, Vincent Huijnen³, François Hendrick², and Michel Van Roozendael²

¹Deutsches Zentrum für Luft- und Raumfahrt (DLR), Institut für Methodik der Fernerkundung (IMF), Oberpfaffenhofen, Germany

²Belgian Institute for Space Aeronomy (BIRA-IASB), Brussels, Belgium

³Royal Netherlands Meteorological Institute (KNMI), De Bilt, the Netherlands

⁴Technical University of Munich (TUM), Department of Civil, Geo and Environmental Engineering, Chair of Remote Sensing Technology, Munich, Germany

Correspondence to: Song Liu (Song.Liu@dlr.de)

Abstract. An improved tropospheric nitrogen dioxide (NO₂) retrieval algorithm from the Global Ozone Monitoring Experiment-2 (GOME-2) instrument based on air mass factor (AMF) calculations performed with more realistic model parameters is presented. The viewing angle-dependency of surface albedo is taken into account by improving the GOME-2 Lambertian-equivalent reflectivity (LER) climatology with a directionally dependent LER (DLER) dataset over land and an ocean surface albedo parametrization over water. A priori NO₂ profiles with higher spatial and temporal resolutions are obtained from the IFS(CB05BASCOE) chemistry transport model based on recent emission inventories. A more realistic cloud treatment is provided by a Cloud-As-Layers (CAL) approach, which treats the clouds as uniform layers of water droplets, instead of the current Clouds-as-Reflecting-Boundaries (CRB) model, which assumes the clouds as Lambertian reflectors. Improvements in the AMF calculation affect the tropospheric NO₂ columns on average within $\pm 15\%$ in winter and $\pm 5\%$ in summer over largely polluted regions. In addition, the impact of aerosols on our tropospheric NO₂ retrieval is investigated by comparing the concurrent retrievals based on ground-based aerosol measurements (explicit aerosol correction) and aerosol-induced cloud parameters (implicit aerosol correction). Compared to the implicit aerosol correction through the CRB cloud parameters, the use of CAL reduces the AMF errors by more than 10%. Finally, to evaluate the improved GOME-2 tropospheric NO₂ columns, a validation is performed using ground-based Multi-AXis Differential Optical Absorption Spectroscopy (MAXDOAS) measurements at the BIRA-IASB Xianghe station. The improved tropospheric NO₂ dataset shows good agreement with coincident ground-based measurements with a correlation coefficient of 0.94 and a relative difference of -9.9% on average.

1 Introduction

Tropospheric nitrogen dioxide (NO₂) is an important air pollutant that harms the human respiratory system even with short exposures (Gamble et al., 1987; Kampa and Castanas, 2008) and contributes to the formation of tropospheric ozone, urban haze, and acid rain (Charlson and Ahlquist, 1969; Crutzen, 1970; McCormick, 2013). Besides the natural sources like soil emissions and lightning, the combustion-related emission sources from anthropogenic activities like fossil fuel consumption, car



traffic, and biomass burning produce substantial amounts of NO₂. Satellite measurements from the Global Ozone Monitoring Experiment (GOME) (Burrows et al., 1999), the SCanning Imaging Absorption SpectroMeter for Atmospheric CHartographY (SCIAMACHY) (Bovensmann et al., 1999), the Ozone Monitoring Instrument (OMI) (Levelt et al., 2006), and the Global Ozone Monitoring Experiment-2 (GOME-2) (Callies et al., 2000; Munro et al., 2016) have produced global NO₂ measurements on long-time scales. In the following years, new generation instruments like the TROPOspheric Monitoring Instrument (TROPOMI) (Veefkind et al., 2012) aboard the Sentinel-5 Precursor satellite and geostationary missions like the Sentinel-4 (Ingmann et al., 2012) will deliver NO₂ dataset with high spatial resolution and short revisit time.

The GOME-2 instruments, which are on the EUMETSAT's MetOp-A and MetOp-B satellites (referred to as GOME-2A and GOME-2B in this work), have provided a long-term NO₂ dataset started in the year 2007. This dataset will be extended with a third GOME-2 aboard the MetOp-C satellite, launched in December 2018. GOME-2 is a scanning spectrometer measuring the solar irradiance and Earth's backscattered radiance in the UV and VIS spectral ranges with a spectral resolution of 0.2-0.4 nm and a spatial resolution of 80 km×40 km (the spatial resolution has been increased to 40 km×40 km for GOME-2A from July 2013 onwards). GOME-2 provides morning observations of NO₂ at about 9:30 local time (LT), which complements early afternoon measurements e.g. from OMI or TROPOMI. The GOME-2 NO₂ measurements have been widely used in trend studies, satellite dataset intercomparisons, and NO₂ emission estimations (e.g. Mijling et al., 2013; Hilboll et al., 2013, 2017; Krotkov et al., 2017; Irie et al., 2012; Gu et al., 2014; Miyazaki et al., 2017; Ding et al., 2017).

The NO₂ retrieval algorithm for the GOME-2 instrument contains three steps: the spectral fitting of the slant column (concentration along the effective light path) with the differential optical absorption spectroscopy (DOAS) method (Platt and Stutz, 2008) from the measured GOME-2 (ir)radiances, the separation of stratospheric and tropospheric contributions with a modified reference sector method, and the conversion of the tropospheric slant column to a vertical column with a tropospheric air mass factor (AMF) calculation. The quality of GOME-2 NO₂ measurements is strongly related to the calculation of the AMF, determined with a radiative transfer model, depending on a set of model parameters, such as viewing geometry, surface albedo, vertical distribution of NO₂, cloud, and aerosol. The model parameters, generally taken from external databases, contribute substantially to the overall AMF uncertainty, estimated to be in the range of 30-40% (Lorente et al., 2017).

The surface is normally assumed to be Lambertian with an isotropic diffuse reflection independent of viewing and illumination geometry in NO₂ retrieval (e.g. Boersma et al., 2011; van Geffen et al., 2019; Liu et al., 2019b). However, due to the occurrences of retroreflection and shading effects (mainly over rough surfaces like vegetation) and specular reflection (mainly over smooth surfaces like water), the Lambertian assumption is not always fulfilled. To account for the geometry-dependent surface scattering characteristics, the surface bidirectional reflectance distribution function (BRDF) (Nicodemus et al., 1992) has been considered in previous studies (e.g. Zhou et al., 2010; Lin et al., 2014, 2015; Noguchi et al., 2014; Vasilkov et al., 2017; Lorente et al., 2018; Laughner et al., 2018; Qin et al., 2019), mainly based on measurements from MODerate resolution Imaging Spectroradiometer (MODIS) over land. However, due to the use of different instruments, biases are possibly introduced in the NO₂ retrieval. In addition, due to the generally unavailable full surface BRDF in all conditions and the complexity of accounting for BRDF, most of the current NO₂ and cloud retrievals still rely on Lambertian surface reflection (e.g., Boersma et al., 2018; van Geffen et al., 2019; Loyola et al., 2018; Desmons et al., 2019).



To account for the varying sensitivity of the satellite to NO₂ at different altitudes, a priori vertical profiles of NO₂ are required, generally prescribed using a chemistry transport model. The importance of the a priori NO₂ profiles used in the retrieval has been recognised earlier and motivated the use of model data with high spatial resolution and/or high temporal resolution (e.g. Valin et al., 2011; Heckel et al., 2011; Russell et al., 2011; McLinden et al., 2014; Yamaji et al., 2014; Kuhlmann et al., 2015; Lin et al., 2014; Boersma et al., 2016; Laughner et al., 2016). Within the Monitoring Atmospheric Composition and Climate (MACC) European project, a global data assimilation system for atmospheric composition forecasts and analyses has been developed and running operationally in Copernicus Atmosphere Monitoring Service (CAMS, <http://atmosphere.copernicus.eu>). The CAMS system relies on a combination of satellite observations with state-of-the-art atmospheric modelling (Flemming et al., 2017), for which purpose the European Centre for Medium Range Weather Forecasts (ECMWF) numerical weather prediction Integrated Forecast System (IFS) was extended with modules for describing atmospheric composition (Flemming et al., 2015; Inness et al., 2015; Morcrette et al., 2009; Benedetti et al., 2009; Engelen et al., 2009; Agustí-Panareda et al., 2016). Profile forecasts from CAMS are planned to be applied in the operational NO₂ retrieval algorithm for the Sentinel-4 (Sanders et al., 2018) and Sentinel-5 (van Geffen et al., 2018) missions with the advantage of operational implementation and high resolution. Lately, an advanced IFS system, referred to IFS(CB05BASCOE) (Huijnen et al., 2016, 2019) or IFS(CBA) for short, operates at high horizontal, vertical, and temporal resolutions based on recent emission inventories, providing an improved profile "representativeness".

Clouds influence the NO₂ retrieval through their increased reflectivity, their shielding effect on NO₂ column below the cloud, and multiple scattering that enhances absorption inside the cloud (Liu et al., 2004; Stammes et al., 2008; Kokhanovsky and Rozanov, 2008). The presence of clouds is taken into account in the NO₂ AMF calculation using cloud parameters based on the Optical Cloud Recognition Algorithm (OCRA) and the Retrieval Of Cloud Information using Neural Networks (ROCINN) algorithms (Loyola et al., 2007, 2011). OCRA/ROCINN has been applied in the operational retrieval of trace gases from GOME (Van Roozendaal et al., 2006), GOME-2 (Valks et al., 2011; Hao et al., 2014; Liu et al., 2019b), and TROPOMI (Heue et al., 2016; Theys et al., 2017; Loyola, in preparation). The latest version of OCRA/ROCINN (Lutz et al., 2016; Loyola et al., 2018) provides two sets of cloud products: one treats clouds as ideal Lambertian reflectors in a "Clouds-as-Reflecting-Boundaries" (CRB) model, and the second treats clouds as uniform layers of water droplets in a "Clouds-As-Layers" (CAL) model. The CAL model, which allows for the penetration of photons through the cloud, is more realistic than the CRB model, which screens the atmosphere below the cloud (Rozanov and Kokhanovsky, 2004; Richter et al., 2015).

Aerosol scattering and absorption influence the top-of-atmosphere radiances and the light path distribution. The radiative effect of scattering aerosols and clouds is comparable (i.e., the albedo effect, shielding effect, and multiple scattering), while the presence of absorbing aerosols generally reduces the sensitivity to NO₂ within and below the aerosol layer by decreasing the number of photons returning from this region to the satellite (Leitão et al., 2010). Because cloud retrieval does not distinguish between clouds and aerosols, the effect of aerosol on the AMF is normally corrected using an "implicit aerosol correction" by assuming that the effective clouds retrieved as Lambertian reflectors (i.e., using the CRB model) account for the effect of aerosols on the light path (Boersma et al., 2004, 2011). Previous works have also applied an "explicit aerosol correction" for OMI pixels considering additional aerosol parameters (e.g. Lin et al., 2014, 2015; Kuhlmann et al., 2015; Castellanos et al.,



2015; Liu et al., 2019a; Chimot et al., 2019) and have reported large biases related to the implicit aerosol correction for polluted cases, likely because the simple CRB model can not fully describe the effects inherent to aerosol particles (Chimot et al., 2019).

The operational GOME-2 NO₂ products are generated with the GOME Data Processor (GDP) algorithm and provided by DLR in the framework of EUMETSAT's Satellite Application Facility on Atmospheric Composition Monitoring (AC-SAF). The retrieval algorithm of total and tropospheric NO₂ from GOME-2 has been introduced by Valks et al. (2011, 2017) as implemented in the current operational GDP version 4.8. An updated slant column retrieval and stratosphere-troposphere separation have been presented by Liu et al. (2019b), and an improved AMF calculation is described in this paper, which will be implemented in the next version of GDP.

In the AC-SAF context (Hassinen et al., 2016), the NO₂ data derived from the GOME-2 GDP algorithm is being validated at BIRA-IASB by comparison with correlative observations from ground-based Multi-AXis Differential Optical Absorption Spectroscopy (MAXDOAS) (Pinaridi et al., 2014, 2015; Pinaridi, in preparation). The MAXDOAS instrument collects scattered sky light in a series of line-of-sight angular directions extending from the horizon to the zenith. High sensitivity towards absorbers near the surface is obtained for the smallest elevation angles, while measurements at higher elevations provide information on the rest of the column. This technique allows the determination of vertically resolved abundances of atmospheric trace species in the lowermost troposphere (Hönninger et al., 2004; Wagner et al., 2004; Wittrock et al., 2004; Heckel et al., 2005).

In this work, we briefly introduce in Sect. 2 the reference retrieval algorithm for GOME-2 NO₂ measurements, which was described in detail in Liu et al. (2019b). We improve the AMF calculation in the reference retrieval algorithm in Sect. 3 by accounting for the direction-dependency of surface albedo over land and over water, applying the advanced high-resolution IFS(CBA) a priori NO₂ profiles, and implementing the more realistic CAL cloud model. We investigate the properties of the implicit aerosol correction for aerosol-dominated scenes by comparing it to the explicit aerosol correction in Sect. 4. Finally, we show a validation of the GOME-2 tropospheric NO₂ columns using MAXDOAS datasets in Sect. 5.

2 Reference retrieval for GOME-2 NO₂ measurements

As described in Liu et al. (2019b), the NO₂ slant column retrieval applies an extended 425-497 nm wavelength fitting window (Richter et al., 2011) to include more NO₂ structures and an improved slit function treatment to compensate for the long-term and in-orbit drifts of the GOME-2 slit function. The uncertainty in the NO₂ slant columns is $\sim 4.4 \times 10^{14}$ molec/cm², calculated from the average slant column error using a statistical method (Valks et al., 2011, Sect. 6.1 therein). To determine the stratospheric NO₂ components, the STRatospheric Estimation Algorithm from Mainz (STREAM) method (Beirle et al., 2016) with an improved treatment of polluted and cloudy pixels is adopted. The uncertainty in the GOME-2 stratospheric columns is $\sim 4\text{-}5 \times 10^{14}$ for polluted conditions based on the daily synthetic GOME-2 data and $\sim 1\text{-}2 \times 10^{14}$ for monthly averages.

Mainly focusing on the third retrieval step, we apply the tropospheric AMF M conversion (Palmer et al., 2001; Boersma et al., 2004) to account for the average light path through the atmosphere:

$$M = \frac{\sum_l m_l(\mathbf{b}) x_l c_l}{\sum_l x_l} \quad (1)$$



Table 1. Ancillary parameters in deriving GOME-2 tropospheric NO₂ columns.

	reference retrieval (Liu et al., 2019b)	improved algorithm (this work)
surface albedo	GOME-2 LER climatology	GOME-2 direction-dependent LER
a priori NO ₂ profile	TM5-MP	IFS(CBA)
cloud parameter	OCRA/ROCINN_CRB	OCRA/ROCINN_CAL

with m_l the box-air mass factors (box-AMFs) in layer l , x_l the partial columns from the a priori NO₂ profiles, and c_l a correction coefficient to account for the temperature dependency of NO₂ cross-section (Boersma et al., 2004; Nüß et al., 2006).

5 The box-AMFs m_l are derived using the multi-layered multiple scattering LIDORT (Spurr et al., 2001) radiative transfer model and stored in a look-up table (LUT) as a function of several model inputs \mathbf{b} , including GOME-2 viewing geometry, surface pressure, and surface albedo. Table 1 summarises the ancillary parameters used in the AMF calculation.

The surface albedo is described by a monthly Lambertian-equivalent reflectivity (LER) database (Tilstra et al., 2017), derived from GOME-2 measurements for the years 2007-2013 with a spatial resolution of 1.0° long×1.0° lat for standard grid cells
 10 and 0.25° long×0.25° lat for coastlines (Tilstra et al., 2019). The LER is retrieved by matching the simulated reflectances to the Earth reflectance measurements for cloud-free scenes found with a statistic method (Koelemeijer et al., 2003; Kleipool et al., 2008; Tilstra et al., 2017).

The daily a priori NO₂ profiles are obtained from the three-dimensional chemistry transport model TM5-MP (Williams et al., 2017) with a horizontal resolution of 1° long×1° lat for 34 vertical layers, as summarised in Table 2. The model is driven by
 15 ECMWF ERA-Interim meteorological re-analysis (Dee et al., 2011) and updated every 3 h with interpolation of fields for the intermediate time periods. Compared to previous versions of TM model (e.g. Williams et al., 2009; Huijnen et al., 2010), which have been commonly used in tropospheric NO₂ retrieval studies (e.g. Boersma et al., 2011; Chimot et al., 2016; Lorente et al., 2017), the main advantages of TM5-MP is the better spatial resolution (1° long×1° lat), updated NO_x emissions (year-specific MACCity emission inventory, Granier et al. (2011)), and improved chemistry scheme (an expanded version of the modified
 20 CB05 chemistry scheme, Williams et al. (2013)).

In the presence of clouds, the AMF is derived based on the independent pixel approximation (Cahalan et al., 1994), which assumes the AMF as a linear combination of a cloudy-sky AMF M_{cl} and a clear-sky AMF M_{cr} :

$$M = \omega M_{cl} + (1 - \omega)M_{cr}, \quad (2)$$

where ω is the cloud radiance fraction. M_{cl} is determined using Eq. (1) with the cloud surface regarded as a Lambertian reflector and with $m_l=0$ for layers below the cloud top pressure c_p . ω is derived from the GOME-2 cloud fraction c_f :

$$\omega = \frac{c_f I_{cl}}{(1 - c_f)I_{cr} + c_f I_{cl}} \quad (3)$$

with I_{cr} the backscattered radiance for a clear scene derived using LIDORT and I_{cl} for a cloudy scene. Note that the cloud fraction c_f is a radiometric or effective cloud fraction instead of a geometric one.



Table 2. Summary of chemistry transport model specifications.

	TM5-MP (Huijnen et al., 2010) (Williams et al., 2017)	IFS(CBA) (Flemming et al., 2015) (Huijnen et al., 2016)
horizontal resolution	1° (long/lat)	~80 km (T255) or ~0.7° (long/lat)
vertical resolution	34 layers (~6 layers below 1.5 km)	137 ¹ layers (~12 layers below 1.5 km)
temporal resolution	2 h archiving	1 h archiving
meteorological fields	ECMWF 3 h	ECMWF online (initialized with ERA-5)
tropospheric chemistry	modified CB05 (Williams et al., 2013)	modified CB05 (Williams et al., 2013)
anthropogenic emission	MACCity (Granier et al., 2011)	CAMS_GLOB_ANT v2.1 (Granier et al., 2019)
advection	slopes scheme (Russell and Lerner, 1981)	semi-Lagrangian scheme as described in Temperton et al. (2001) and Hortal (2002)
convection	ECMWF	Bechtold et al. (2014)
diffusion	Holtslag and Boville (1993)	Beljaars and Viterbo (1998)

¹ 69 layers are employed in this study.

5 The GOME-2 cloud properties are derived by the OCRA and the ROCINN algorithms (Loyola et al., 2007, 2011; Lutz et al., 2016; Loyola et al., 2018). Since clouds generally have a higher reflectivity than the ground, OCRA calculates the radiometric cloud fractions by comparing the measured reflectances in 3 broadband wavelength regions across the UV-VIS-NIR region with corresponding cloud-free background composite maps using a RGB color space approach. The monthly cloud-free background map is calculated from GOME-2A measurements for the years 2008-2013, accounting for instrumental
 10 degradation and dependencies on viewing zenith angle (VZA), latitude, and season. With the radiometric cloud fractions from OCRA as input, ROCINN retrieves the cloud top pressures (cloud top heights) and cloud albedo (cloud optical depth) by comparing the simulated and measured satellite radiances in the O₂ A band around 760 nm using regularization theory. Based on the independent pixel approximation and the CRB cloud model, the ROCINN algorithm treats the clouds as Lambertian surfaces.

15 3 Improved AMF calculation

3.1 Surface albedo

The dependency of surface reflection on incoming and outgoing directions is mathematically described by the BRDF (Nicodemus et al., 1992), which shows a "hot spot" of increased reflectivity in backward scattering directions over rough surfaces like vegetation and a strong forward scattering peak near "sun glint" geometries over smooth surfaces like water. In this study, we
 5 account for the direction-dependency of surface albedo for the GOME-2 LER climatology by applying a directionally depen-



dent LER (DLER) dataset over land surfaces (see Sect. 3.1.1) and by implementing an ocean surface albedo parametrization over water surfaces (see Sect. 3.1.2).

3.1.1 Over land

To account for the surface BRDF in our NO₂ AMF calculation over land, the surface reflectivity is described by a GOME-2 DLER dataset (Tilstra et al., 2019) that captures the VZA-dependency. Compared to the traditional GOME-2 LER climatology (Tilstra et al., 2017), derived from a range of viewing angles ($\sim 115^\circ$ for GOME-2 measurements covering the directions from east to west), the GOME-2 DLER dataset is derived by dividing the range of viewing angles into five segments and applying the same retrieval method as in the traditional GOME-2 LER determination for each segment with a parabolic fit to parametrize the VZA-dependency. The main idea of this VZA-dependency parametrization is to use the VZA as a proxy of observation geometry over land, since solar zenith angle (SZA) and relative azimuth angle (RAA) are nearly constant at a given latitude and thus have been captured in the original GOME-2 LER dataset.

For each GOME-2 measurement, the surface DLER α_{DLER} is calculated as:

$$\alpha_{DLER} = \alpha_{LER} + c_0 + c_1 \times \theta + c_2 \times \theta^2 \quad (4)$$

with VZA θ positive on the west side of the orbit swath and negative on the east side of the orbit swath. c_0 , c_1 , and c_2 are parabolic fitting coefficients depending on latitude, longitude, month, and wavelength. The non-directional LER α_{LER} is taken from the traditional GOME-2 LER climatology. Note that no directionality is provided by the DLER dataset over water (without sea ice cover), mainly due to the dependency on parameters such as wind speed and chlorophyll concentration, which can not be cast into climatology easily. Additionally, due to the strong solar and viewing angles-dependency of specular reflection, changes of the solar position during a month influence the albedo over water bodies much more than for land, and this influence is modelled and described in Sect. 3.1.2.

Figure 1a-c shows the traditional GOME-2 LER climatology, the GOME-2 DLER dataset over land, and their differences on 3 February and 5 August 2010. The DLER data shows a stronger increase for western viewing direction by ~ 0.02 over vegetation, ~ 0.05 over desert, and ~ 0.2 over snow and ice, due to the increasing BRDF in the backward scattering direction. A slight change by up to 0.01 is found over vegetation and desert with enhancement for the central part of the orbit swath and reduction for the east side of the orbit swath, and this effect is larger over snow and ice, resulted from the forward scattering peak or double scattering peak in the BRDF pattern for snow (Dumont et al., 2010). The difference in surface albedo is generally larger in winter, due to the change of surface condition and/or sun elevation, at the exception of desert.

Figure 2 compares the surface LER and DLER as a function of VZA and presents the impact on the clear-sky AMFs over western Europe (44° N- 53° N, 0° E- 7° E) and eastern China (21° N- 41° N, 110° E- 122° E) in February 2010. The surface albedo on the west side of the orbit swath (backward scattering direction) is higher for both regions by up to 0.024, which reduces the calculated clear-sky AMFs by 9-14%. Smaller differences are found for the central and eastern viewing direction by up to 0.006 for surface albedo and up to 4% for clear-sky AMFs.

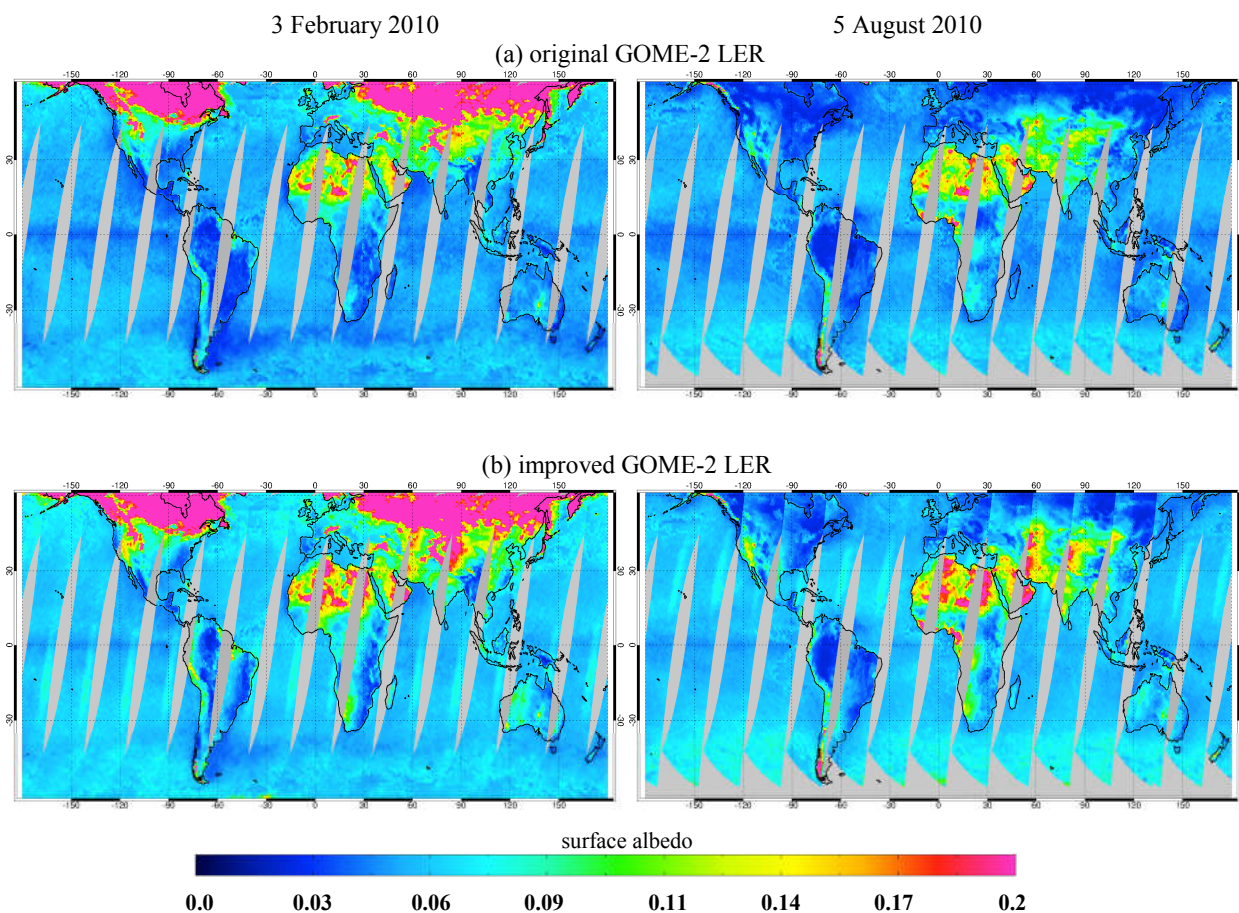


Figure 1. Map of GOME-2 surface LER climatology (Tilstra et al., 2017) version 3.1 in February and August (a), improved GOME-2 surface LER data taking into account the direction-dependency on 3 February and 5 August 2010 (b), and their differences over land (c) and over water (d) (figure continued on next page). The improvements are described in Sect. 3.1.1 for land and in Sect. 3.1.2 for water.

Figure 3 shows the differences in tropospheric NO_2 columns retrieved using surface LER and DLER dataset for a given day and for the monthly average in February and August 2010. The daily differences in tropospheric NO_2 columns are consistent with Fig. 1c, with a larger impact found over polluted regions. Taking Spain on 3 February 2010 as an example, the smaller surface DLER on the central part of the orbit swath by ~ 0.005 results in a lower sensitivity to tropospheric NO_2 columns in the AMF calculation, and therefore the AMF decreases and the tropospheric NO_2 columns increases by $\sim 1 \times 10^{14}$ molec/cm² (3%). Vice versa, the surface DLER is higher by ~ 0.02 on the west side of the orbit swath over eastern China at the same day, and thus the tropospheric NO_2 column is lower by $\sim 3 \times 10^{15}$ molec/cm² (11%). The monthly differences in tropospheric NO_2 columns show a larger reduction in winter by more than 5×10^{14} molec/cm² over e.g. central Europe, South Africa, India, and eastern China, and by $\sim 1 \times 10^{14}$ molec/cm² over e.g. the eastern US, Southeast Asia, and Mexico.

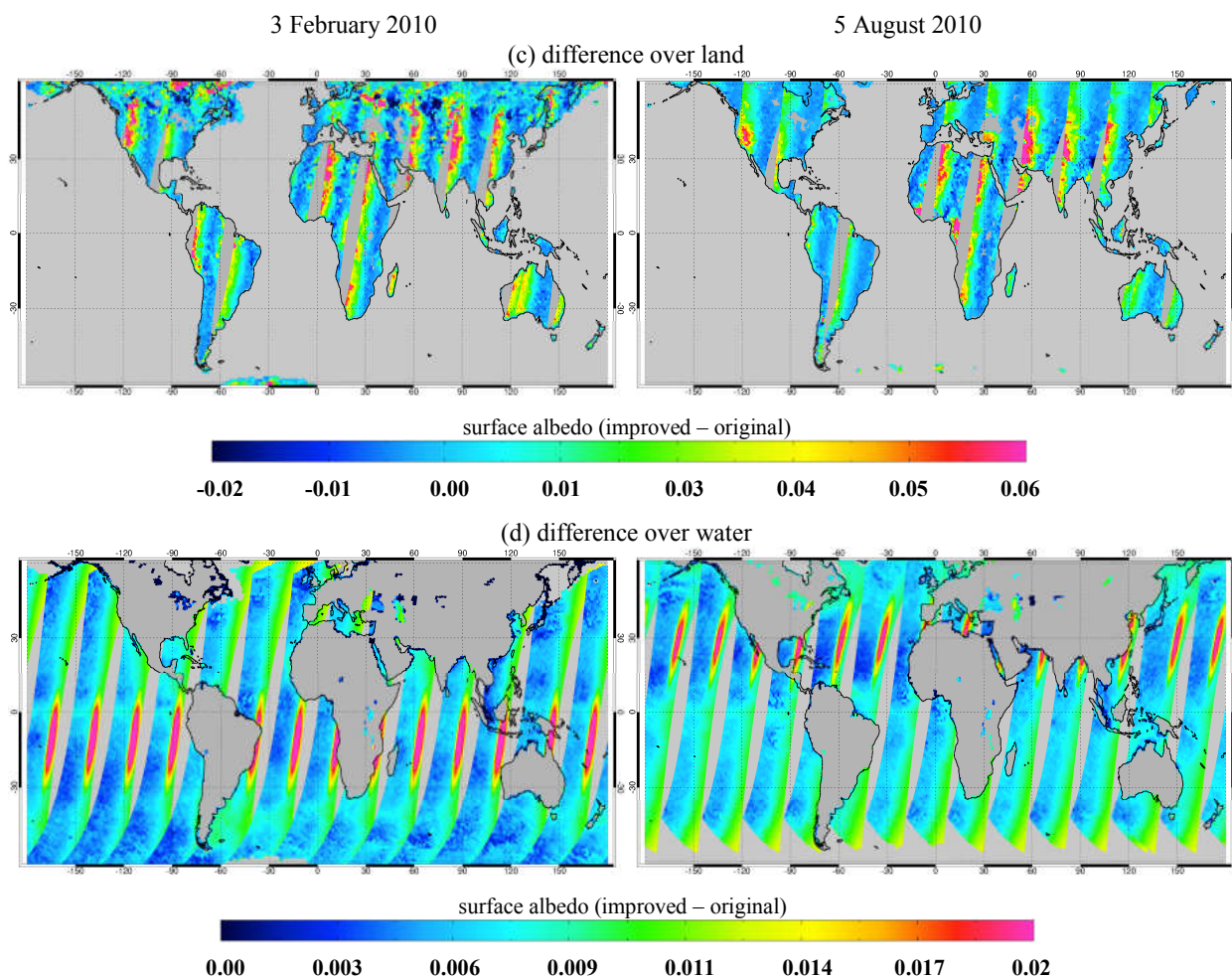


Figure 1. (figure continued from previous page)

The above results are in agreement with studies applying the BRDF product from MODIS to describe the dependency of land surface reflectance on illumination and viewing geometry (e.g. Zhou et al., 2010; Noguchi et al., 2014; Vasilkov et al., 2017; Lorente et al., 2018; Laughner et al., 2018; Qin et al., 2019). With a good agreement with the established MODIS BRDF product (Tilstra et al., 2019), the GOME-2 DLER dataset is derived from measurements of the instrument itself, consistent with the
10 GOME-2 NO₂ observations, considering the illumination conditions, observation geometry, and instrumental characteristics, and therefore the use of GOME-2 DLER introduces no additional bias caused by the instrumental differences.

3.1.2 Over water

The surface reflectivity over water is described with an improved GOME-2 LER data using an ocean surface albedo parametrization (Jin et al., 2004, 2011) to account for the direction-dependency. Based on atmospheric radiation measurements

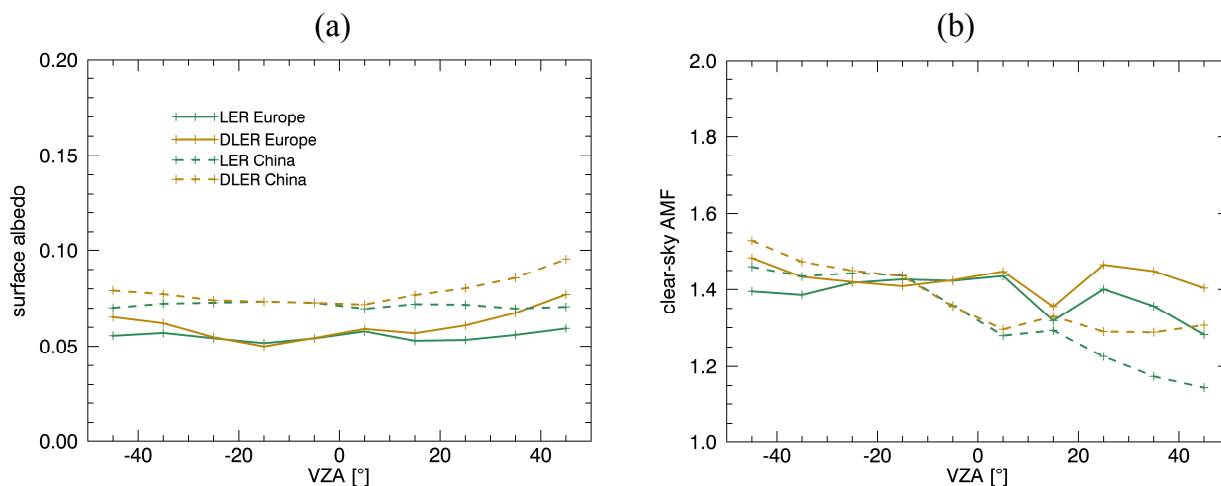


Figure 2. Comparison of GOME-2 LER climatology (Tilstra et al., 2017) and GOME-2 DLER data (a) and the impact on the clear-sky AMFs (b) over western Europe (44° N-53° N, 0° E-7° E) and eastern China (21° N-41° N, 110° E-122° E) as a function of VZA in February 2010 (VZAs are negative for observations on the east side of the orbit swath).

5 and the Coupled Ocean-Atmosphere Radiative Transfer (COART) model (Jin et al., 2006), the parametrization developed by Jin et al. (2011) derives the surface reflectivity for the direct and diffuse incident radiation separately and further divides each of them into contributions from surface and water, respectively. This parametrization has been used to derive ocean surface albedo (e.g. Séférian et al., 2018) and to generate satellite NO₂ product (e.g. Laughner et al., 2018).

Following Jin et al. (2011), the ocean surface albedo α_{total} is defined as:

$$10 \quad \alpha_{total} = f_{dir}(\alpha_{dir}^s + \alpha_{dir}^w) + f_{dif}(\alpha_{dif}^s + \alpha_{dif}^w) \quad (5)$$

with α_{dir}^s and α_{dif}^s the direct and diffuse contribution of the surface reflection and α_{dir}^w and α_{dif}^w the direct and diffuse contribution of the volume scattering of water below the surface, respectively. The direct and diffuse fraction of downward surface flux f_{dir} and f_{dif} ($f_{dif} = 1 - f_{dir}$) are calculated using the online COART (<https://satcorps.larc.nasa.gov/jin/coart.html>). The direct surface albedo α_{dir}^s , which is one main component of the total ocean surface albedo, describes the contribution of Fresnel reflection depending on the incident angle, refractive index of seawater (1.343 at 460 nm), and slope distribution of the ocean surface (defined by Cox and Munk (1954) and related to wind speed (5 m/s from the climatological mean)). The diffuse surface albedo α_{dif}^s is difficult to formulate analytically due to its variation with atmospheric conditions and thus parametrized practically to be 0.06 for an assumed 5 m/s wind speed. The direct water volume albedo α_{dir}^w is considered for the case 1 waters (consist 99% of the ocean) and primarily affected by the chlorophyll concentration (0.2 mg/m³ from the global ocean average). The diffuse water volume albedo α_{dif}^w is defined by the α_{dir}^w at an effective incident direction (i.e. $\arccos(0.676)$) and calculated to be 0.0145. The direct fraction of downward surface flux f_{dir} is calculated with radiative

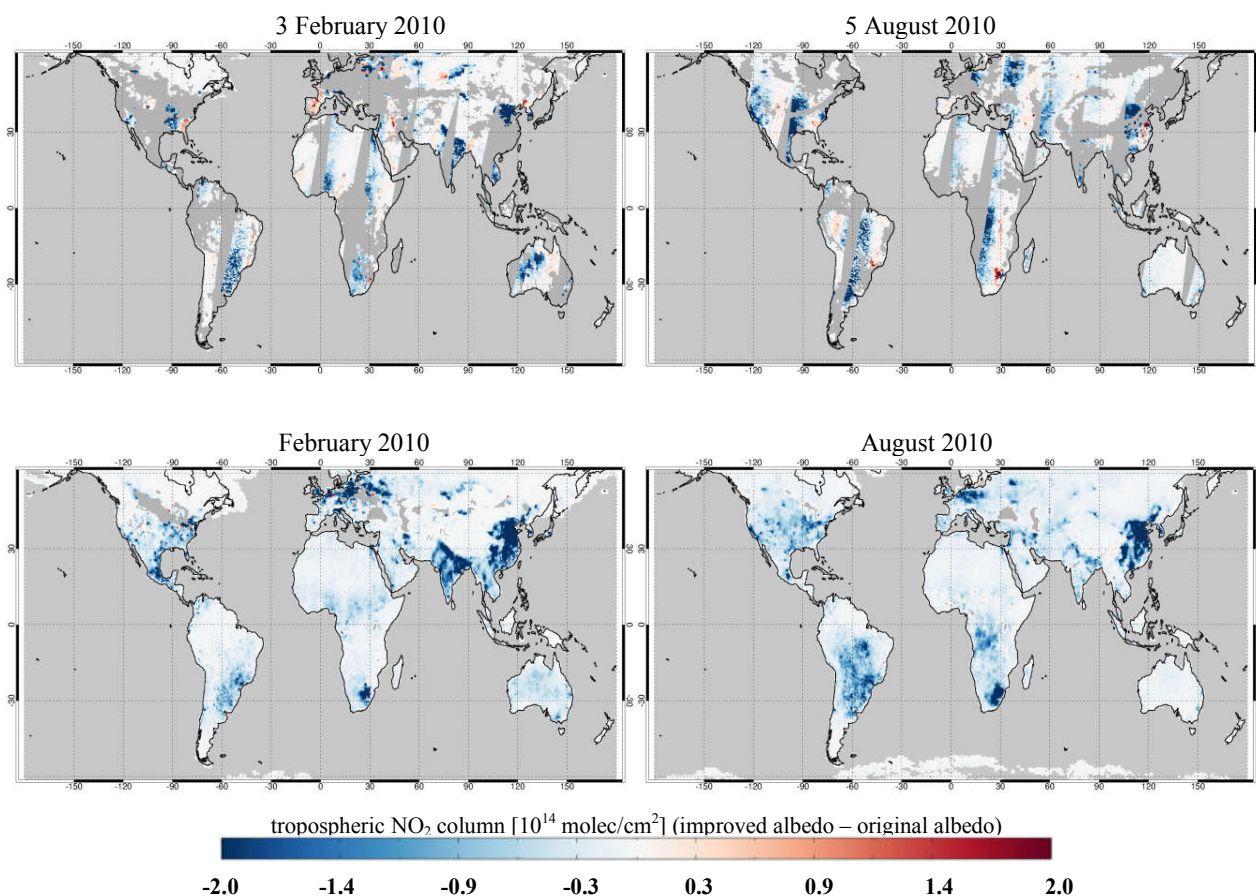


Figure 3. Differences in GOME-2 tropospheric NO₂ columns retrieved using GOME-2 LER and DLER dataset for a given day and for the monthly average in February and August 2010. Only measurements with cloud radiance fraction < 0.5 are included.

5 transfer simulation using a mid-latitude summer atmosphere with a marine aerosol optical depth of 1 (at 550 nm) and using a 100 m depth ocean with the average Petzold phase function for ocean particle scattering.

Figure 4 shows the parametrized ocean surface albedo for a non-glint situation and its four albedo components as a function of incident angle. The overall shape of the total ocean surface albedo α_{total} is dependent on incident angle with a peak near 70°, similar with Jin et al. (2004) and Laughner et al. (2018). The surface component ($\alpha_{dir}^s + \alpha_{dif}^s$) is larger than the water volume component ($\alpha_{dir}^w + \alpha_{dif}^w$), particularly for larger incident angles. The direct component ($\alpha_{dir}^s + \alpha_{dir}^w$) increases with incident angle with lower values than the diffuse component ($\alpha_{dif}^s + \alpha_{dif}^w$) for smaller incident angles (below 55°) and higher values for larger incident angles. The relative contribution of diffuse component to the total ocean surface albedo f_{dif} increases from ~0.65 to ~1 with incident angle. It is worth noting that the four albedo components are independent of each other and thus flexible to update or replace.

10

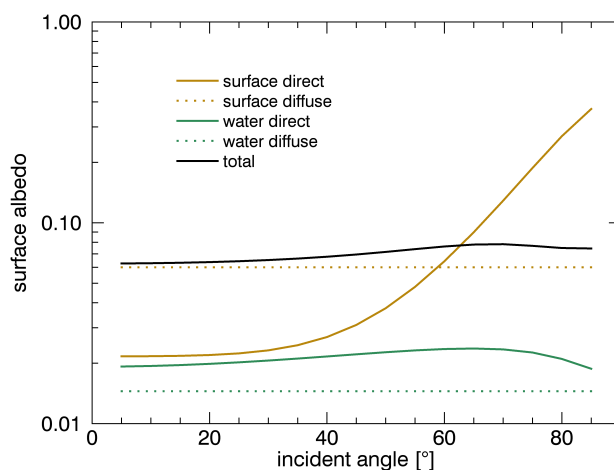


Figure 4. Parametrized ocean surface albedo for a non-glint condition and its albedo components due to direct and diffuse surface reflection and direct and diffuse water volume scattering as a function of incident angle.

Based on measurements over a long period (2007-2018 for version 3.1), the GOME-2 LER climatology provides mainly
5 the diffuse component ($\alpha_{dif}^s + \alpha_{dif}^w$) over water bodies with minimized impact of direct contribution. Therefore, we replace
the simplified expression of $\alpha_{dif}^s + \alpha_{dif}^w$ in Jin et al. (2011) with values taken from the GOME-2 LER climatology. This
scheme enables the consideration of the direction-dependency for the GOME-2 LER climatology over water with minimal
bias introduced. In addition, most of the ocean surface albedo studies (e.g. Ohlmann, 2003; Jin et al., 2004; Li et al., 2006; Jin
et al., 2011; Laughner et al., 2018) employ a straightforward assumption that SZA is the only directional parameter involved
10 in the parametrization, namely the incident angle is assumed to be equivalent to the SZA in the Fresnel reflection calculation.
In this work, we apply the full equation to derive the local incident angle with dependencies on VZA and RAA also taken into
account, and we additionally implement the Cox-Munk sun glitter model over glint-contaminated regions. See Cox and Munk
(1954) and Gordon (1997) for more details on configuration and derivation.

Figure 1b,d presents the calculated ocean surface albedo and the differences with values taken from GOME-2 LER climatol-
15 ogy on 3 February and 5 August 2010. Consistent with Vasilkov et al. (2017), the improved ocean surface albedo shows higher
values by up to 0.015 at larger SZAs and VZAs, where the higher incident angles result in stronger Fresnel reflections, and by
up to 0.025 over areas affected by sun glint, typically the eastern swath of GOME-2 orbits.

Figure 5 shows the impact of using updated ocean surface albedo on our GOME-2 NO_2 retrieval for a given day and for the
monthly average in February and August 2010. The tropospheric NO_2 columns are reduced mainly over the polluted coastal
regions with large NO_2 concentrations and with large SZAs and VZAs. For instance, the ocean surface albedo around Spain
increases by ~ 0.01 on 3 February 2010, leading to a decrease of tropospheric NO_2 columns by up to 8×10^{14} molec/cm² (9%).
The monthly average of tropospheric NO_2 columns decreases in winter by more than 3×10^{14} molec/cm² near the coastal

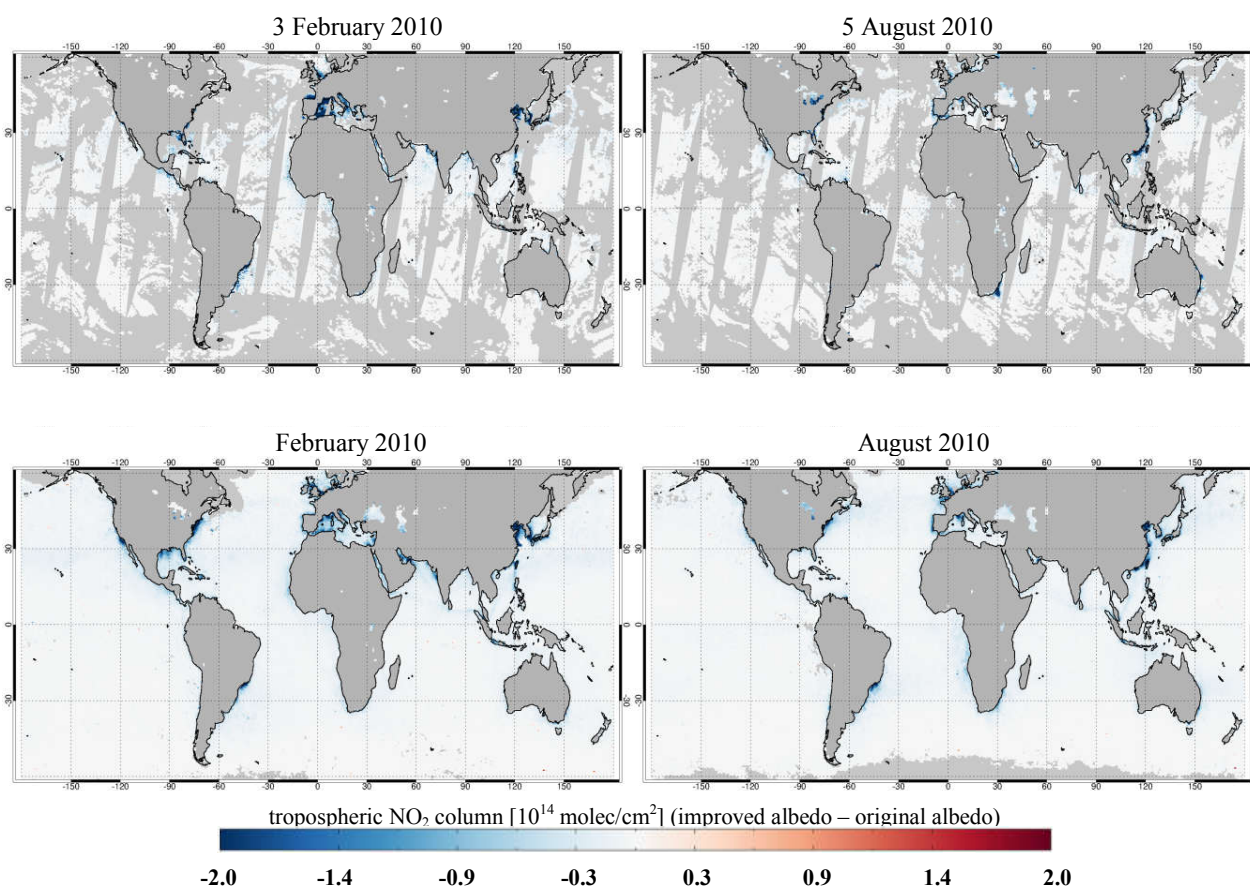


Figure 5. Differences in GOME-2 tropospheric NO₂ columns retrieved using the original GOME-2 LER climatology and the GOME-2 LER data improved with the ocean surface albedo parametrization for a given day and for the monthly average in February and August 2010. Only measurements with cloud radiance fraction < 0.5 are included.

5 area, e.g. around the US, eastern China, and Brazil, and by up to 1×10^{14} molec/cm² along the shipping lanes, e.g. in the Mediterranean Sea, the Red Sea, and the maritime Southeast Asia.

3.2 A priori NO₂ profile

In regions with strong gradients in NO_x emission in space and time, the significant variation of surface NO₂ can only be captured in a model with sufficient horizontal, vertical, and temporal resolutions. The advanced IFS(CBA) (Huijnen et al., 2016, 2019) global chemistry forecast and analysis system combines the stratospheric chemistry scheme developed for the Belgian Assimilation System for Chemical Observations (BASCOE, Skachko et al. (2016)) and the modified CB05 tropospheric chemistry scheme (Williams et al., 2013). As summarized in Table 2, the spatial resolution of IFS(CBA) is a reduced Gaussian grid at a spectral truncation of T255, which is equivalent to a grid spacing of ~ 80 km globally ($\sim 0.7^\circ$). The model

5

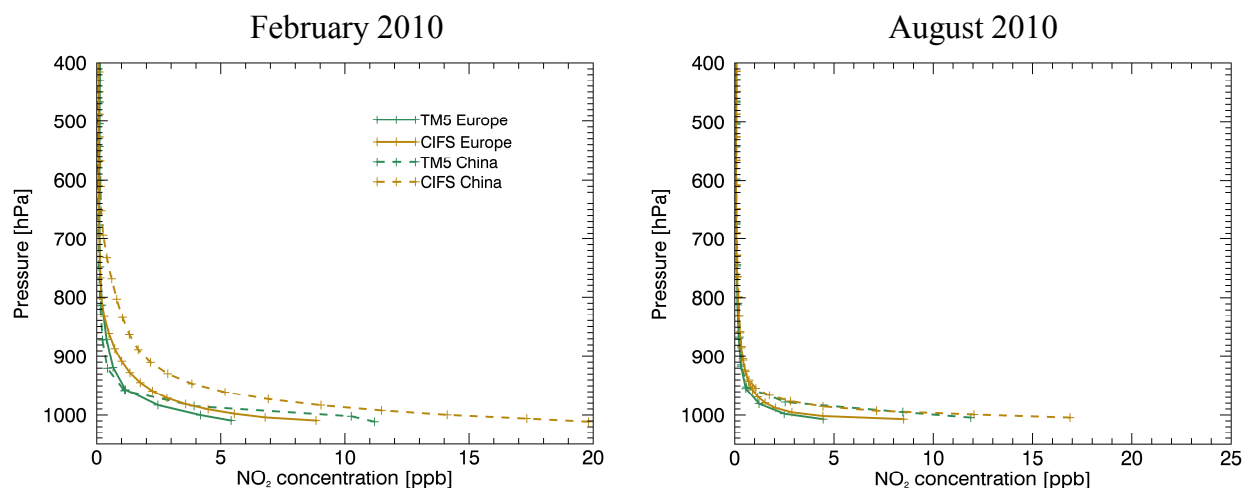


Figure 6. Area-averaged and monthly-averaged profiles from TM5-MP and IFS(CBA) at GOME-2 overpass time (9:30 LT) over western Europe (44° N- 53° N, 0° E- 7° E) and eastern China (21° N- 41° N, 110° E- 122° E) in February and August 2010.

is run with the standard 137 hybrid sigma-pressure layers as also used operationally in the ECMWF⁷ forecast and reanalysis model. From this we select a vertical discretisation based on 69 vertical levels up to 0.1 hPa with ~ 12 layers in the boundary layer for further processing. An essential difference compared to TM5-MP is that in IFS(CBA) the chemistry is an integral part of the meteorological forecast model. Here we use the forecast model from cycle 45r2, which is daily initialized using ERA5 meteorology. Additionally, anthropogenic emissions are based on the recently prepared CAMS_GLOB_ANT v2.1 emission inventory (Granier et al., 2019), while day-specific biomass burning emissions are taken from GFASv2.1 (Kaiser et al., 2012). The NO_2 data is available on hourly basis, based on which the profiles at the satellite measurement time can be obtained with a linear interpolation.

Figure 6 shows an intercomparison of area-averaged and monthly-averaged profiles from TM5-MP and IFS(CBA) at GOME-2 overpass time (9:30 LT) over western Europe (44° N- 53° N, 0° E- 7° E) and eastern China (21° N- 41° N, 110° E- 122° E) in February and August 2010. Generally, TM5-MP and IFS(CBA) show similar mean profile shapes over the two regions. In February, IFS(CBA) shows a larger boundary layer concentration and a sharper transition to the free troposphere over western Europe and a larger NO_2 gradients in the free troposphere over eastern China. In August, the NO_2 concentrations in the free troposphere are lower than in February for both models due to the reduced emissions and the reduced lifetime of NO_2 , and a larger surface layer NO_2 gradient is found for the IFS(CBA) model for both regions.

Figure 7 shows the daily TM5-MP and IFS(CBA) a priori NO_2 profiles over the Netherlands (52.8° N, 4.7° E) and China (39.1° N, 118.0° E) on 3 February 2010 as examples. IFS(CBA) shows a higher surface layer NO_2 concentration (more steep profile shape) and yields a tropospheric AMF reduced by 0.21 over the Netherlands, which will enhance the retrieved tropospheric NO_2 column. In contrast, the tropospheric AMF increases by 0.06 over China due to the larger NO_2 gradients in the free troposphere (less steep profile shape) modelled by IFS(CBA).

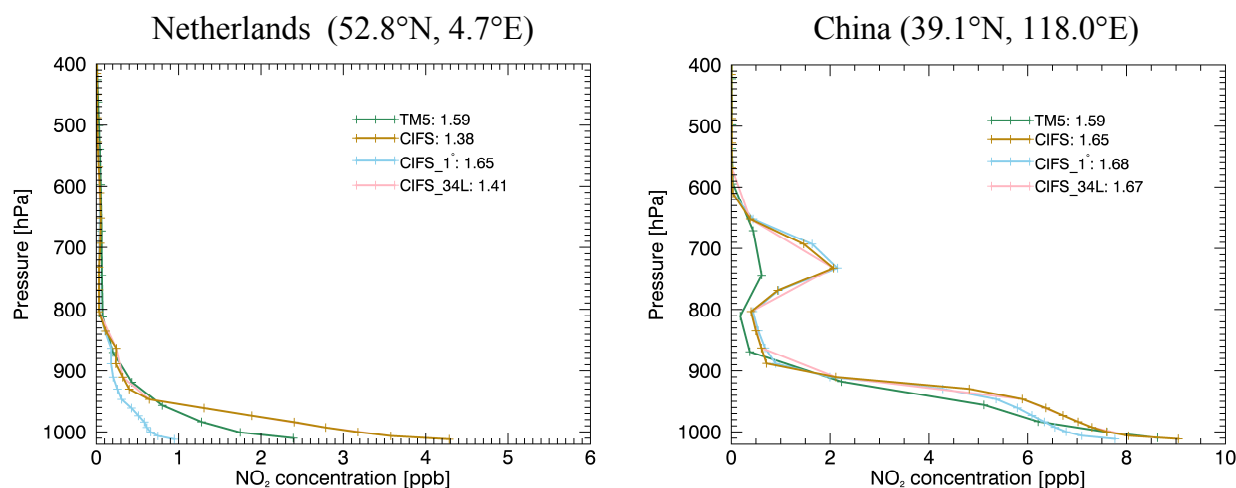


Figure 7. A priori NO_2 profiles from TM5-MP, IFS(CBA) (original resolution), and IFS(CBA) with different model resolutions over the Netherlands (52.8°N , 4.7°E) and China (39.1°N , 118.0°E) on 3 February 2010. The IFS(CBA) profiles are compared for 1° grid and for 34 layers. The calculated clear-sky tropospheric AMF is given next to each label.

Figure 8 shows the differences in tropospheric NO_2 columns retrieved using TM5-MP and IFS(CBA) a priori NO_2 profiles for a given day and for the monthly average in February and August 2010. The differences are consistent with the changes in the profile shapes in Fig. 6 and 7. The use of IFS(CBA) generally increases the tropospheric NO_2 columns over polluted regions by up to $2 \times 10^{15} \text{ molec/cm}^2$, e.g. over western Europe, eastern US, and Argentina, and decreases the values by up to $1 \times 10^{15} \text{ molec/cm}^2$, e.g. over central Africa, South Africa, and Brazil. In February, however, a strong enhancement by $\sim 7 \times 10^{15} \text{ molec/cm}^2$ is found over northern Germany and Poland, and a strong reduction by $\sim 4 \times 10^{15} \text{ molec/cm}^2$ is found over the North China Plain. The differences in Fig. 8 are likely related to the different chemical mechanism, transport scheme, and emission inventories employed by the model as well as the different model resolutions.

To quantify the effect of model resolutions, a more detailed analysis for IFS(CBA) is implemented with 1° grids for horizontal resolution, with 34 layers for vertical resolution, and with 2-hours time steps for temporal resolution, respectively. These values are of the same order of magnitude as the model resolutions of TM5-MP and other chemistry transport models currently employed in the satellite retrieval of NO_2 (e.g. van Geffen et al., 2019; Lorente et al., 2017; Boersma et al., 2018; Liu et al., 2019b). Figure 7 compares the IFS(CBA) a priori NO_2 profiles with original and different model resolutions over the Netherlands (52.8°N , 4.7°E) and China (39.1°N , 118.0°E) on 3 February 2010. Both examples are located at polluted coastal regions, which typically have a large heterogeneity and variability in the NO_2 distribution. The AMFs differ by more than 0.02 for both examples due to differences in horizontal and vertical resolutions. The current 2-hours temporal sampling and subsequent linear interpolation between the sampling points is sufficient for the retrieval of tropospheric NO_2 columns (not shown). When a coarser spatial resolution is used, the "domain-averaged" profiles generally show an increased surface NO_2 concentration for unpolluted domain and the opposite for emission source. Consequently, the AMF is underestimated

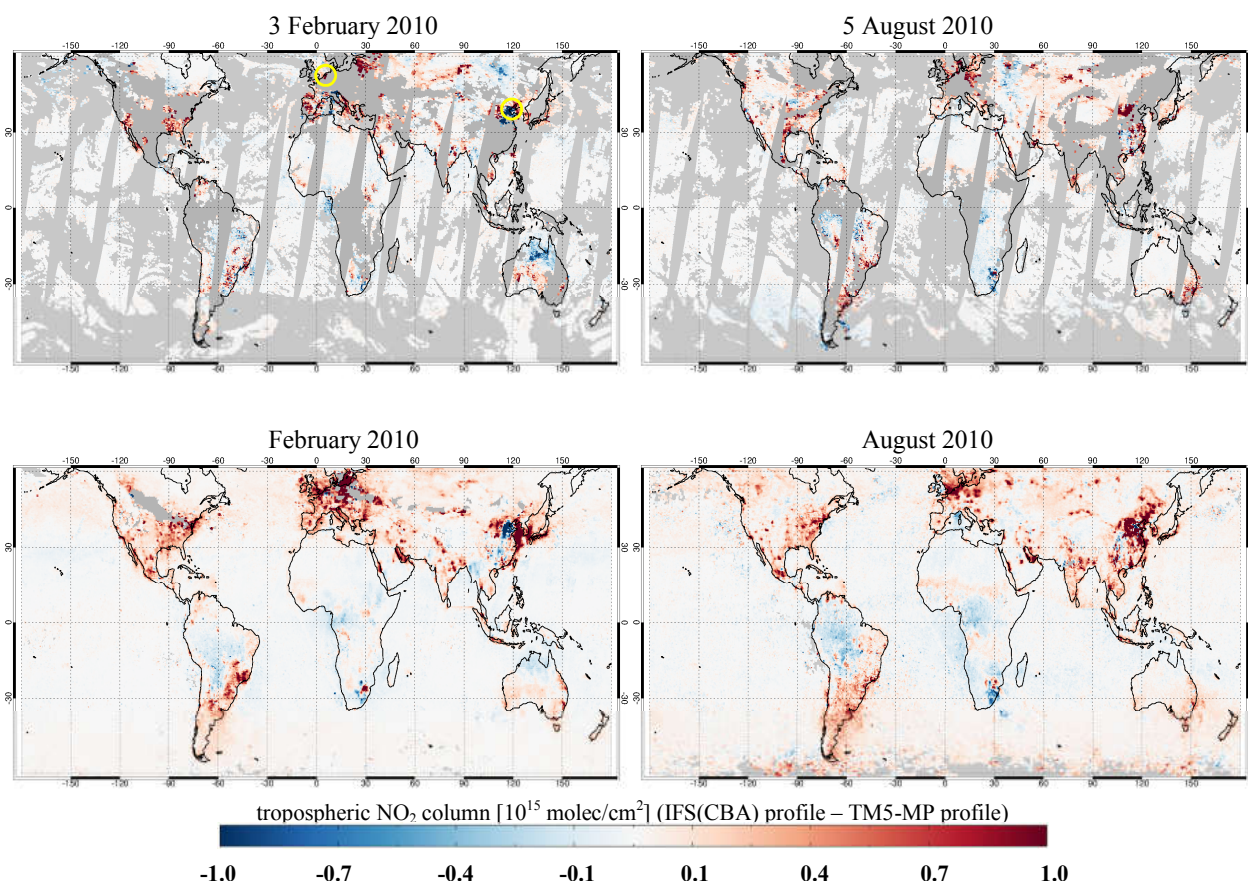


Figure 8. Differences in tropospheric NO_2 columns retrieved using TM5-MP and IFS(CBA) a priori NO_2 profiles for a given day and for the monthly average in February and August 2010. Yellow circles on 3 February 2010 indicate locations in Fig. 7. Only measurements with cloud radiance fraction < 0.5 are included.

for unpolluted areas and overestimated for polluted areas. When the number of layers is reduced, the coarser sampling points can not capture accurately the large NO_2 gradients at low altitudes, particularly for polluted regions where the measurement sensitivity of the satellite decreases significantly towards the surface.

- 5 Figure 9 shows the absolute and relative differences in tropospheric NO_2 columns retrieved by altering the model resolutions for IFS(CBA) a priori NO_2 profiles in February 2010. In Fig. 9a, the increase of the spatial resolution (1° vs. 0.7° grid) changes the tropospheric NO_2 columns by up to 7×10^{14} molec/cm² or 20% for polluted regions, in agreement with previous case studies or regional retrievals (Heckel et al., 2011; Lin et al., 2014; Kuhlmann et al., 2015). Larger relative differences are observed over cities surrounded by rural areas, coastal regions, isolated islands, and shipping lanes, where the use of high
- 10 spatial resolutions captures more accurately the NO_2 emission and chemistry for a priori profiles. In Fig. 9b, the improvement in the vertical resolution (34 vs. 69 layers) enhances the tropospheric NO_2 columns by up to 5×10^{14} molec/cm² or 15%. Increasing the number of layers generally better resolves the NO_2 vertical variation, especially for the lowest model layers

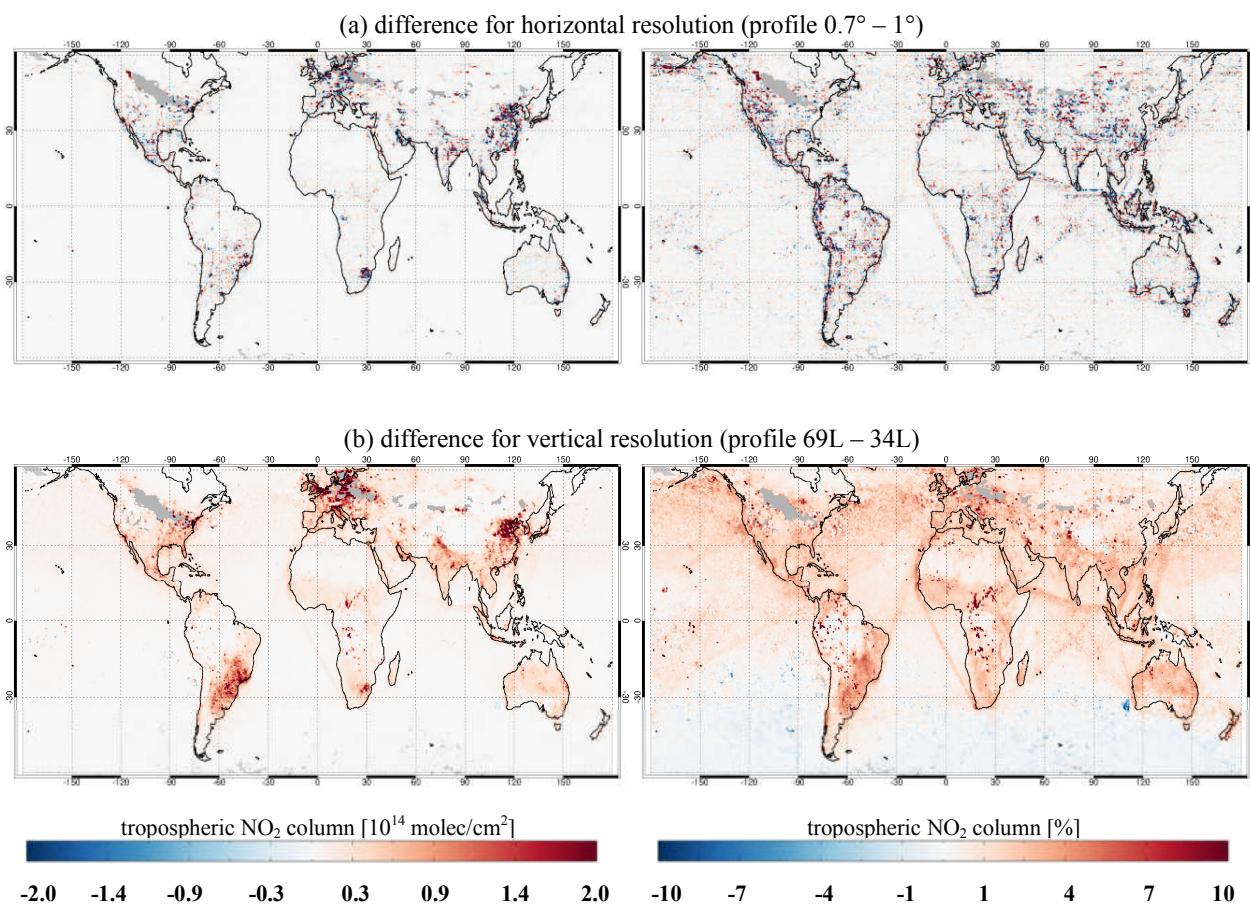


Figure 9. Absolute and relative differences in tropospheric NO₂ columns retrieved by altering the model resolutions for IFS(CBA) a priori NO₂ profiles in February 2010. The tropospheric NO₂ columns are compared for 1° and 0.7° grid (a) and for 34 and 69 layers (b). Only measurements with cloud radiance fraction < 0.5 are included.

where the box-AMF decreases significantly in the polluted cases. Consequently, the tropospheric AMFs are lower and the tropospheric NO₂ columns are higher for polluted regions. For unpolluted regions, the differences are generally small (within $\pm 2 \times 10^{14}$ molec/cm² or $\pm 3\%$). In addition, the use of different temporal resolution (2-hours vs. 1-hour time step) generally has a negligible impact on the tropospheric NO₂ columns (less than 2×10^{14} molec/cm² or 3%, not shown).

3.3 Cloud correction

For cloudy scenarios, the retrieval of tropospheric NO₂ is affected by the cloud parameters due to the variation of scene albedo and the photon path redistribution in the troposphere. As described in Sect. 2, the cloudy-sky AMFs are calculated with the independent pixel approximation using GOME-2 cloud parameters: radiometric cloud fraction from OCRA and cloud top pressure (cloud top height) and cloud albedo (cloud optical depth) from ROCINN. To improve the cloud correction in

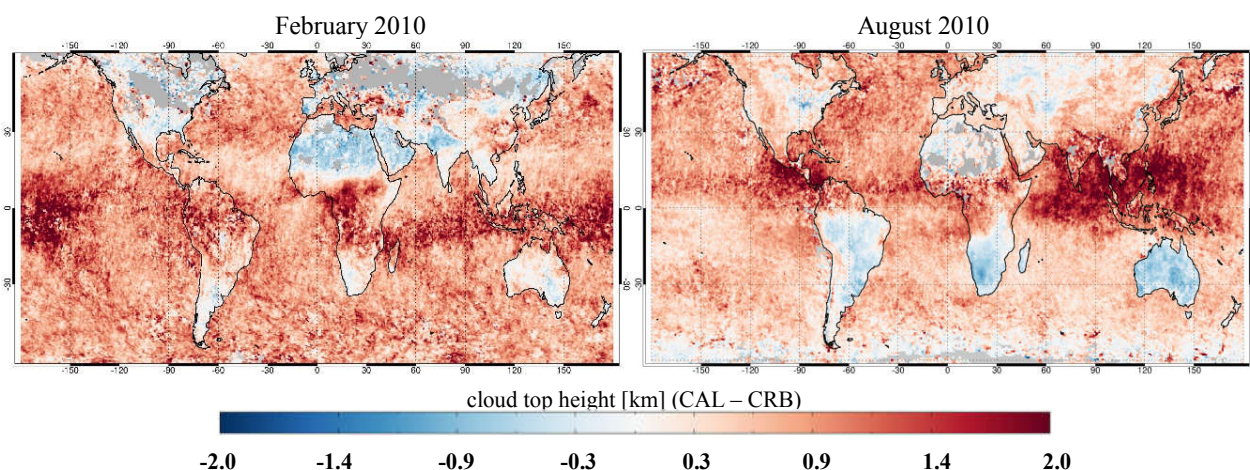


Figure 10. Differences in cloud top heights retrieved using ROCINN_CAL and ROCINN_CRB cloud model in February and August 2010. Only measurements with cloud fraction < 0.3 are included. Observations with fitting RMS $> 1 \times 10^{-4}$ or number of iterations > 20 are filtered out.

our NO_2 retrieval, the CAL model from ROCINN cloud algorithm (Loyola et al., 2018), with the clouds treated as optically uniform layers of light-scattering water droplets, is applied. The CAL model is more representative of the real situation than the CRB model (with the clouds idealized as Lambertian reflectors with zero transmittance) by allowing the penetration of photons through the cloud layer. This treatment takes the multiple scattering of light inside the cloud and the contribution of the atmospheric layer between the cloud bottom and the ground into account.

Figure 10 shows the differences in cloud top heights obtained with the CRB and CAL model from GOME-2 measurements in February and August 2010. Consistent with Loyola et al. (2018) (see Fig 3 and 13 therein), the cloud top heights from CAL are generally higher by on average ~ 0.9 km. Stronger increases (up to 2 km) are found over regions with thick and high clouds, such as the Intertropical Convergence Zone and the Western Hemisphere Warm Pool, very similar to Lelli et al. (2012) (see Fig. 12 therein). In general, the CRB-based cloud retrieval underestimates the cloud top height due to the neglect of oxygen absorption throughout a cloud layer (Vasilkov et al., 2008) and thus the misinterpretation of the smaller top-of-atmosphere reflectance as a lower cloud layer (Saiedy et al., 1967). Additionally, since the enhanced multiple scattering is not fully taken into account in the CRB-based cloud retrieval, the retrieved cloud height is normally close to the middle, i.e., the optical centroid of clouds (Ferlay et al., 2010; Richter et al., 2015).

In Fig. 10, higher cloud top heights are found using CRB mainly over land surfaces characterised by the presence of a large amount of absorbing aerosols, for instance, over regions with strong desert dust emissions, such as the Sahara, the Arabian Desert, and the deserts in Australia, as well as regions with strong biomass burning emissions, such as South America, South Africa, and Southeast Asia. Over these areas, ROCINN likely retrieves an effective aerosol height close to the top of aerosol layer, depending on the type of absorbing aerosols and on aerosol optical depth. The presence of strongly absorbing aerosols, which typically have large aerosol optical depth and/or locate at high altitudes (up to ~ 8 km), reduces the fraction of photons

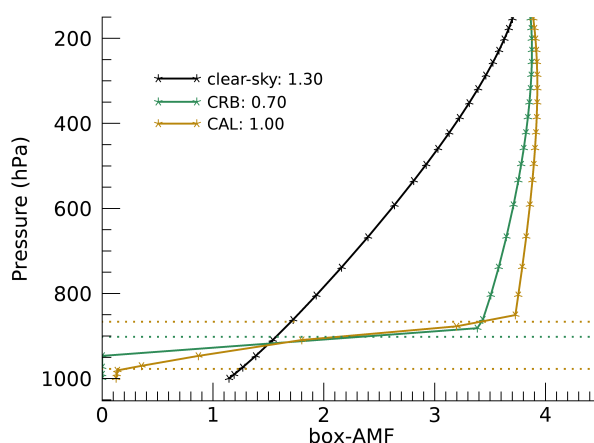


Figure 11. The box-AMFs for clear and cloudy sky using ROCINN_CAL and ROCINN_CRB cloud model over Italy (45.3° N, 11.2° E) on 1 February 2010. The tropospheric AMF is given next to each label. The ROCINN_CRB cloud top pressure is shown as a horizontal green line, and the ROCINN_CAL cloud top and base pressure are shown as horizontal brown lines. Cloud radiance fraction = 0.47, cloud optical depth = 6.85, SZA = 69° , VZA = 3° , RAA = 42° .

reaching the lowest part of the atmosphere. In order to approximate this shortened light path, the CRB-based cloud retrieval has to put the Lambertian reflector at a higher altitude (Wang et al., 2012; Chimot et al., 2016). This effect is larger for aerosol
10 layers at higher altitudes and dependent also on geometry parameters like SZA, on surface properties like surface albedo, and on the accuracy of radiometric cloud fractions from OCRA.

To apply the CAL cloud model in our NO_2 AMF calculation, a single scattering albedo of 1 and an asymmetry parameter of 0.85 for water clouds are assumed for the radiative transfer calculation, consistent with the values used in the cloud retrieval (Loyola et al., 2018). Cloud observations with fitting root mean square (RMS) $> 1 \times 10^{-4}$ or number of iterations > 20 are
5 filtered out. The NO_2 box-AMFs are derived through the pixel-specific radiative transfer calculation instead of the interpolation from a LUT with fixed reference points, which requires no projection from the layer coordinate of NO_2 profile to the coordinate assumed in the LUT and requires no linear interpolation based on the model parameters.

Figure 11 shows an example of the derived box-AMFs for clear and cloudy sky using the CRB and CAL model over Italy (45.3° N, 11.2° E) on 1 February 2010. The cloud information and the calculated tropospheric AMFs are also reported.
10 Compared to the clear-sky box-AMFs, the CAL-based cloudy-sky box-AMFs increase above the cloud layer (albedo effect) and decrease below the cloud layer (shielding effect). Compared to the CRB model, the use of CAL model takes account of the sensitivities inside and below the cloud layer and increases the cloudy-sky AMF by 0.3, which consequently decreases the retrieved tropospheric NO_2 column by 2.5×10^{15} molec/cm² (12%), based on the polluted NO_2 profile with most of the NO_2 concentration located near the surface.

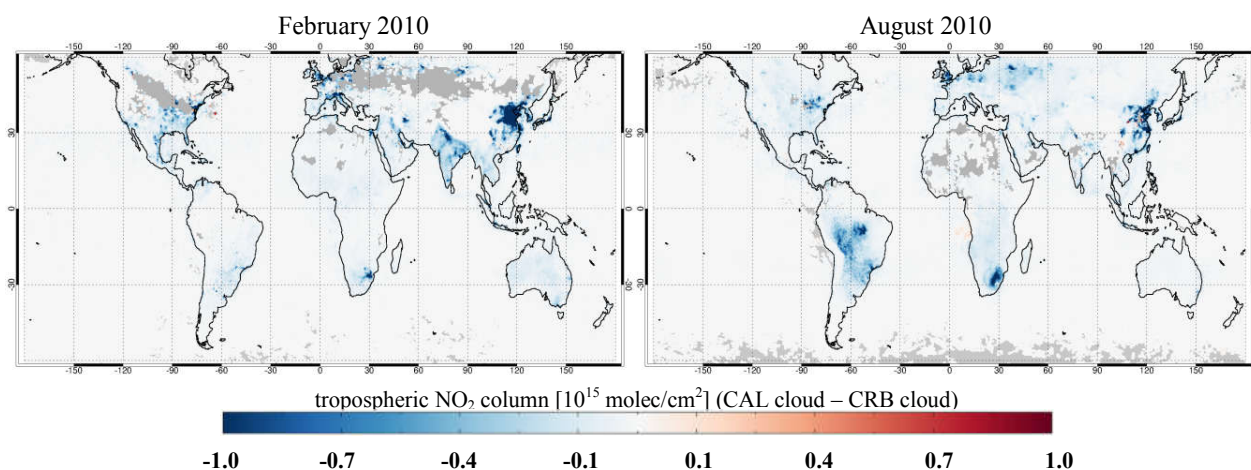


Figure 12. Differences in GOME-2 tropospheric NO₂ columns retrieved using ROCINN_CRB and ROCINN_CAL cloud model in February and August 2010. Only measurements with cloud radiance fraction < 0.5 are included. Cloud observations with fitting RMS > 1×10^{-4} or number of iterations > 20 are filtered out.

15 Figure 12 shows the differences in tropospheric NO₂ columns retrieved using CRB and CAL model in February and August 2010. The use of CAL model decreases the tropospheric NO₂ columns by more than 1×10^{14} molec/cm² over polluted regions. Larger values are found in winter (up to 3×10^{15} molec/cm²), when most of the NO₂ concentrations are located at the surface and the cloud fractions are generally larger due to the seasonal variation of clouds.

3.4 Combined impact

Figure 13 shows the tropospheric NO₂ columns retrieved using the improved AMF calculation and the differences with the reference data in February and August 2010. Larger differences are found in winter over the polluted regions. For instance, the tropospheric NO₂ columns are reduced by more than 1×10^{15} molec/cm² over China and India in February and Brazil and South Africa in August. Increased values are found e.g. over Mexico, Argentina, and Russia.

5 Table 3 summarizes the individual changes and combined effect of our improved AMF calculation on the retrieved tropospheric NO₂ columns over western Europe, eastern China, eastern US, and central Africa. Increases in GOME-2 surface albedo reduce the tropospheric NO₂ columns by 2-6%. The use of IFS(CBA) a priori NO₂ profiles affects (mostly increases) the tropospheric NO₂ columns by up to 21%, and the use of CAL cloud parameters decreases the values by up to 14%. The combined effect of individual improvements yields to a change of tropospheric NO₂ columns on average within $\pm 15\%$ in winter and
10 $\pm 5\%$ in summer over polluted regions.

The uncertainty in the improved AMF calculation is likely reduced comparing to the reference retrieval, considering the improved surface albedo dataset, a priori NO₂ profiles, and cloud parameters, which are the main causes of AMF uncertainty (Lorente et al., 2017). The uncertainty in the AMF calculation for polluted conditions is estimated to improve from 10-45% for the reference retrieval to the 10-35% range for this work.

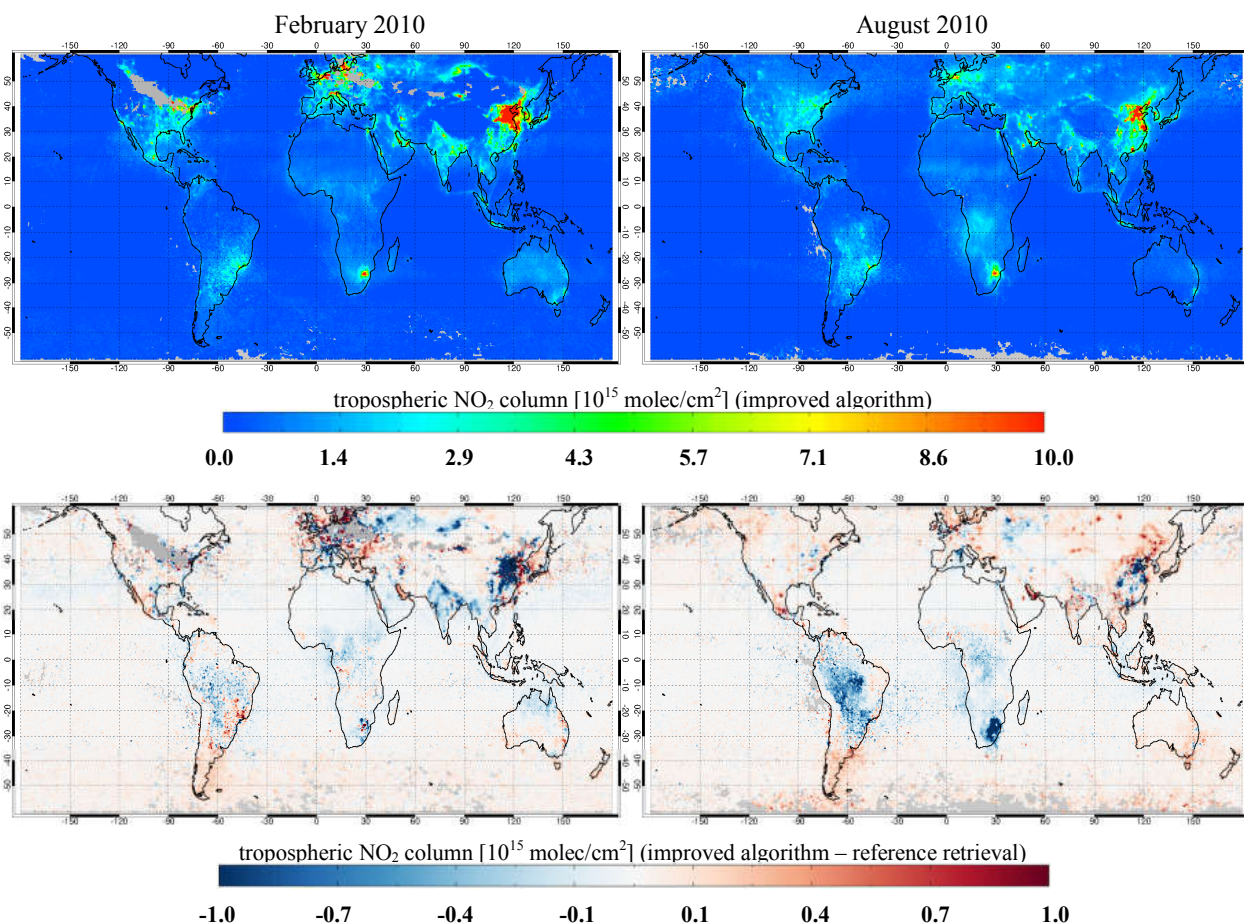


Figure 13. GOME-2 tropospheric NO_2 columns retrieved using the improved algorithm and the differences with the reference data in February and August 2010. Only measurements with cloud radiance fraction < 0.5 are included. Cloud observations with fitting RMS $> 1 \times 10^{-4}$ or number of iterations > 20 are filtered out.

15 4 Implicit aerosol correction

Aerosols can increase or decrease the sensitivity to tropospheric NO_2 , depending on the NO_2 and aerosol vertical distribution, and the optical and physical properties of the particles (Martin et al., 2003; Leitão et al., 2010). Since the OCRA/ROCINN cloud retrieval does not distinguish between clouds and aerosols, the aerosol effect is assumed to be corrected implicitly in the AMF calculation via the effective cloud parameters (i.e., aerosols are treated as clouds).

Figure 14 and 15 show the land surface RGB image with active fire locations from the Moderate Resolution Imaging Spectroradiometer (MODIS) on board the Terra (10:30 LT) and OCRA/ROCINN cloud products measured by GOME-2 (9:30 LT) over eastern China and central Africa on a given day, respectively. The MODIS dataset (<https://worldview.earthdata.nasa.gov/>) describes the cloud or aerosol amount and fire locations (for central Africa). For both regions, a large amount of aerosol



Table 3. Individual changes and combined effect in tropospheric NO₂ columns relative to reference retrievals for western Europe (44° N-53° N, 0° E-7° E), eastern China (21° N-41° N, 110° E-122° E), eastern US (30° N-45° N, 70° W-90° W), and central Africa (5° S-15° S, 10° E-30° E).

	surface albedo	a priori NO ₂ profile	cloud correction	combined effect
Europe (February 2010)	-2.2%	+19.6%	-9.3%	+2.0%
China	-5.9%	+0.7%	-12.1%	-13.3%
US	-4.6%	+15.6%	-12.2%	+8.9%
Africa	-2.1%	-1.2%	-3.3%	-5.8%
Europe (August 2010)	-3.6%	+20.5%	-9.4%	+1.1%
China	-5.6%	+15.9%	-14.0%	-2.3%
US	-4.3%	+10.1%	-9.7%	+1.1%
Africa	-3.8%	-0.6%	-5.4%	-4.8%

loads are found in the RGB image for cloud-free areas, e.g. Beijing-Tianjin-Hebei economic region in eastern China and burning regions across central Africa, where the aerosol loads are identified as thin clouds (cloud optical depth of ~ 5) near the surface (cloud top height of ~ 3 km) with cloud fractions up to 0.18.

Therefore, we assume that the thin clouds near the surface from the OCRA/ROCINN cloud products are attributed to aerosol loads for measurements with cloud radiance fraction < 0.5 or cloud fraction < 0.2 , and we evaluate the accuracy of implicit aerosol correction by comparing it with explicit aerosol correction. For that purpose, the explicit correction for aerosols is implemented using ground-based aerosol observations in Xianghe (39.75° N, 116.96° E), which is a suburban site surrounded by heavily industrialized areas in northeastern China (Cl mer et al., 2010; Hendrick et al., 2014; Vlemmix et al., 2015), and in Bujumbura (3.38° S, 29.3° E), which is located in the Central African country of Burundi with intensive biomass burning activities in the surroundings (Gielen et al., 2017), as indicated in Fig. 14 and 15, respectively. Our analysis is further limited to satellite measurements with cloud optical depth < 5 and cloud top height < 3 km to reduce the cloud contamination. With this selection, the aerosol concentrations are generally low or moderate (aerosol optical depth < 1).

The explicit modelling of aerosol scattering and absorption for the AMF calculation is implemented by introducing the aerosol optical properties (i.e., single scattering albedo and phase function) and vertical distributions (i.e., extinction vertical profiles) in the radiative transfer calculation. The single scattering albedo describes the fraction of the aerosol light scattering over the extinction, and the phase function describes the angular distribution of scattered light intensity. In this study, we apply the Henyey-Greenstein phase function with an asymmetry parameter (the first moment of phase function) describing the asymmetry between forward and backward scattering. A long-term statistics of single scattering albedo and asymmetry parameter at 440 nm is derived for Xianghe and Bujumbura using the version 3 level 2.0 inversion products from the sun photometer radiance measurements at AERONET (Holben et al., 1998; Giles et al., 2019) (<http://aeronet.gsfc.nasa.gov/>). Monthly mean

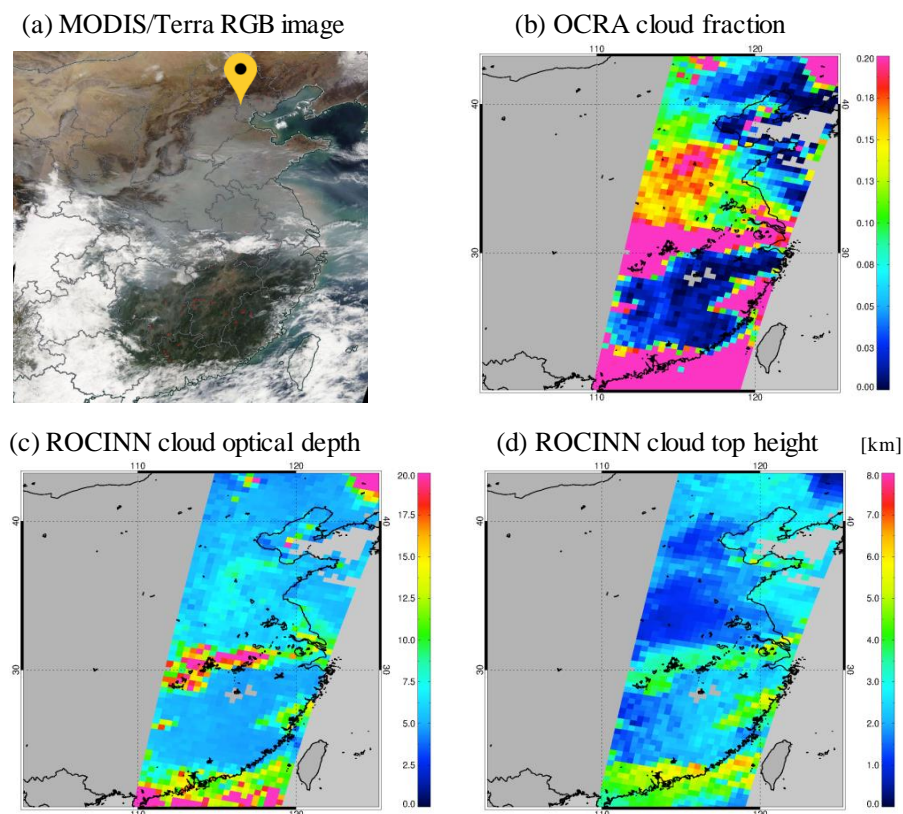


Figure 14. MODIS/Terra RGB image (a), GOME-2 OCRA cloud fraction (b), GOME-2 ROCINN_CAL cloud optical depth (c), and GOME-2 ROCINN_CAL cloud top height (d) over eastern China on 21 November 2013. Cloud observations with fitting RMS $> 1 \times 10^{-4}$ or number of iterations > 20 are filtered out. The yellow location symbol in MODIS image indicates the Xianghe station (39.75° N, 116.96° E), and the red dots indicate fires.

parameters are calculated based on up to seven years of observations (2010-2016 for Xianghe and 2013-2016 for Bujumbura) available within ± 1 h of the GOME-2 overpass time (9:30 LT) for each month.

- 10 Xianghe is located ~ 60 km south-east of Beijing, belonging to the highly urbanized Beijing-Tianjin-Hebei economic region on the North China Plain with heavy anthropogenic aerosol emissions, especially in winter due to the enhanced domestic heating. Mixtures of desert dust with the urban-industrial aerosols affect the regions mainly in spring (March-May). Based on the monthly climatology of AERONET measurements, the single scattering albedo in Xianghe is on average 0.91 with a maximum in July (0.96) and low values in winter (~ 0.87), which are mostly related to the black carbon emissions (Yang et al., 2011). The asymmetry parameter ranges between 0.7 and 0.75, consistent with the values from the urban aerosol models in East Asia (Lee and Kim, 2010).

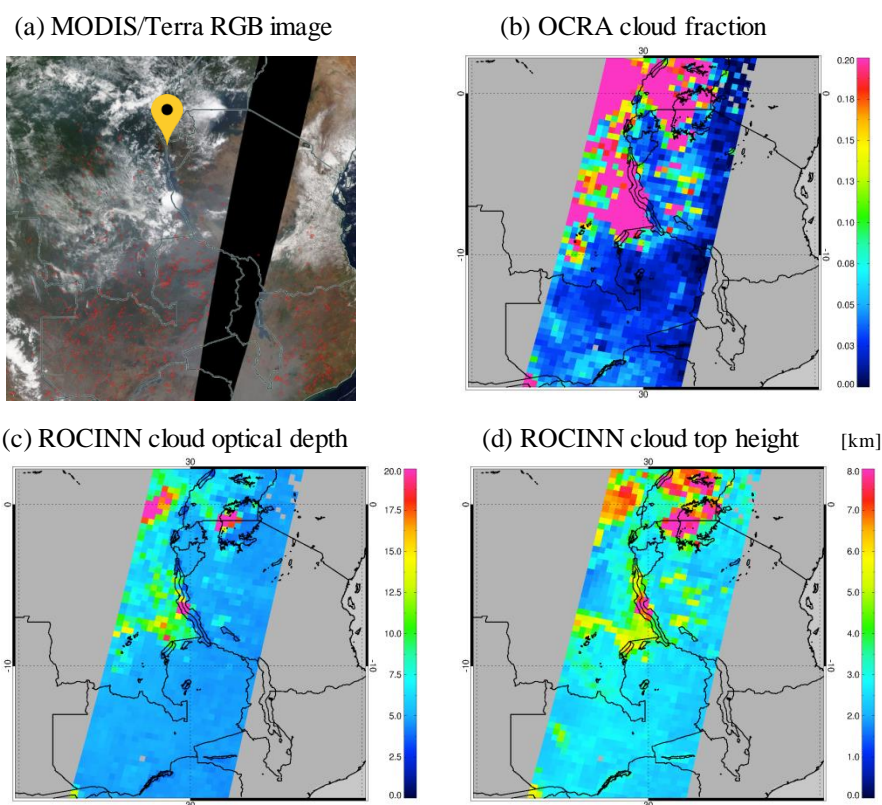


Figure 15. Similar as Fig. 14 but for central Africa on 9 September 2015. The yellow location symbol in MODIS image indicates the Bujumbura station (3.38° S, 29.3° E).

5 Bujumbura is located in tropical Africa that is typically affected by the biomass burning emissions, mainly during the local dry seasons (June-August and January-February), and to a lesser extend, by the anthropogenic emissions, throughout the year with negligible seasonal variations. The single scattering albedo in Bujumbura is higher in March-May (~ 0.9), related to the major rain season, and lower in July-August and December-January (0.83-0.87), coinciding with the intensive agricultural activities and transport of forest fire emissions in the surrounding regions (Gielen et al., 2017). The asymmetry parameter is on
10 average 0.69, in agreement with values in biomass burning aerosol models (Torres et al., 2013).

The collocated aerosol extinction vertical profiles at 477 nm are taken from the MAXDOAS measurements in Xianghe from March 2010 to December 2016 (Clémer et al., 2010) and in Bujumbura from December 2013 to December 2015 (Gielen et al., 2017). The MAXDOAS data is used to derive aerosol information based on the oxygen collision complexes (O_4) absorption, since the O_4 vertical profile is generally constant and thus capable of describing the influence of aerosol scattering and absorp-
15 tion on photon path (Wagner et al., 2004; Frieß et al., 2006). The MAXDOAS technique can reliably determine the aerosol extinction profiles in the lower troposphere (Frieß et al., 2016), where most aerosols are located over Xianghe and Bujum-

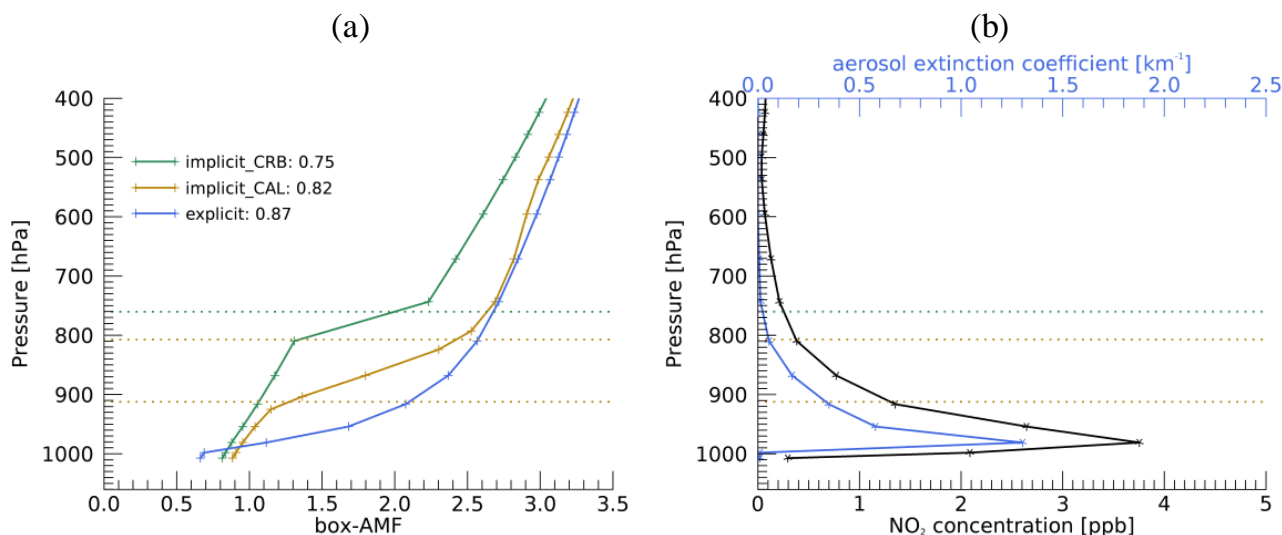


Figure 16. The NO₂ box-AMFs from the explicit aerosol correction and implicit correction using ROCINN_CRB and ROCINN_CAL cloud model (a) and the TM5-MP NO₂ profiles and the MAXDOAS aerosol extinction profiles used in the retrievals (b) at the Xianghe station on 21 November 2013. The tropospheric AMF is given next to each label. The ROCINN_CRB cloud top pressure is shown as a horizontal green line, and the ROCINN_CAL cloud top and base pressure are shown as horizontal brown lines. Cloud radiance fraction = 0.28, cloud optical depth = 4.96, aerosol optical depth = 0.66, SZA = 66°, VZA = 17°, RAA = 133°.

bura. We collocate the space- and ground-based measurements by selecting GOME-2 pixels within 50 km of the stations and averaging the MAXDOAS aerosol profiles within ± 1 h of the GOME-2 overpass time (9:30 LT).

Figure 16 shows typical NO₂ box-AMFs, simulated TM5-MP NO₂ profile, and MAXDOAS aerosol extinction profile for Xianghe on 21 November 2013. The MAXDOAS aerosol profile follows an exponentially decreasing shape with a peak of aerosol loads close to the ground (950 hPa or 0.4 km). The NO₂ follows the same profile shape and is well mixed with aerosol. Depending on seasonal variation, local emission, and transport process, aerosol profiles with peak at elevated heights (up to 900 hPa or 1 km) are also observed (not shown) due to the long residence time. The discontinuity of box-AMFs corrected using the CRB cloud model is introduced by the effective clouds (see Eq. (2)), below which the cloudy box-AMFs are zero. Due to the overestimated cloud altitudes from the CRB-based cloud retrieval (see Sect. 3.3), the CRB-based implicit aerosol correction underestimates the tropospheric AMF by 14%, and this bias is largely reduced by applying the CAL cloud model (6%), which brings a gradual reduction in box-AMFs towards the surface, agreeing reasonably better with the shape from explicit aerosol correction. Figure 17 shows the same data as Fig. 16 but for Bujumbura on 9 September 2015. Compared to the data in Xianghe, the aerosol profile in Bujumbura shows a smaller amount but an uplifted layer of aerosol loads (820 hPa or 1.8 km), while NO₂ continues to peak at the surface. The difference in AMF between implicit and explicit aerosol correction decreases from 15% using CRB to 5% using CAL.

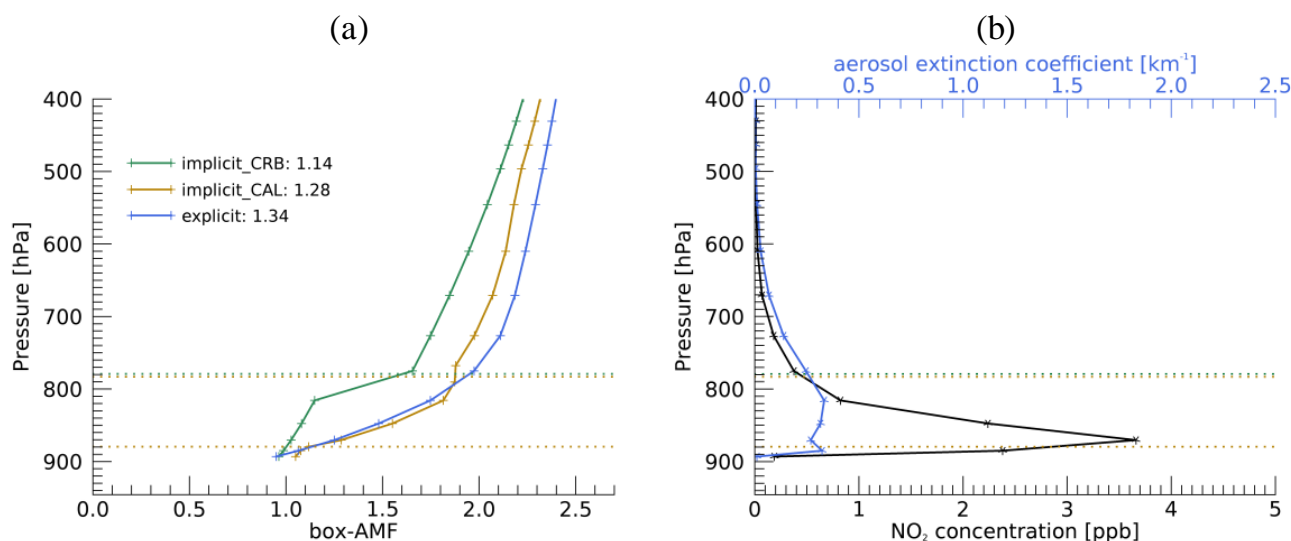


Figure 17. Similar as Fig. 16 but for the Bujumbura station on 9 September 2015. Cloud radiance fraction = 0.18, cloud optical depth = 4.83, aerosol optical depth = 0.58, SZA = 40°, VZA = 14°, RAA = 155°.

Figure 18 presents the relative biases in tropospheric NO₂ columns retrieved assuming no aerosol correction and assuming implicit aerosol correction via the CRB and CAL cloud model for Xianghe from March 2010 to December 2016. Only measurements with cloud radiance fraction < 0.5, cloud optical depth < 5, and cloud top height < 3 km are included. The relative biases introduced by assuming no aerosol correction vary between -30% to 31% with an average of 7% for GOME-2 pixels, in agreement with previous studies focusing on the industrialized part of eastern China (Ma et al., 2013; Lin et al., 2014, 2015; Kuhlmann et al., 2015; Chimot et al., 2016; Wang et al., 2017). Resulted from the overestimated shielding effect, the tropospheric NO₂ columns retrieved using CRB-based implicit aerosol correction are on average 33% larger than using explicit aerosol correction, and the differences are largely reduced by applying the CAL cloud model (9%). Enhanced differences are found for larger cloud radiance fraction, probably due to the increased pollution level (NO₂ columns) comparing to the clear sky (Richter et al., 2017), as the cloud (radiance) fraction is highly correlated with the MAXDOAS aerosol optical depth (correlation coefficient of 0.7 and regression slope of 0.17, not shown). Figure 19 shows the same data but for Bujumbura from December 2013 to December 2015. The explicit aerosol correction yields tropospheric NO₂ columns on average 6% smaller than the clear-sky tropospheric NO₂ columns, consistent with Martin et al. (2003); Castellanos et al. (2015). The average difference between the tropospheric NO₂ columns from the implicit and explicit aerosol correction decreases from 15% using CRB model to 5% using CAL model.

In Fig. 18 and 19, the relative biases introduced by the CAL-based implicit aerosol correction are close to the values assuming no aerosol correction, addressing the complexities related to the tropospheric NO₂ measurements in the presence of aerosols. In combination with the cloud model error, errors related to the implicit aerosol correlation can result from the different radiative

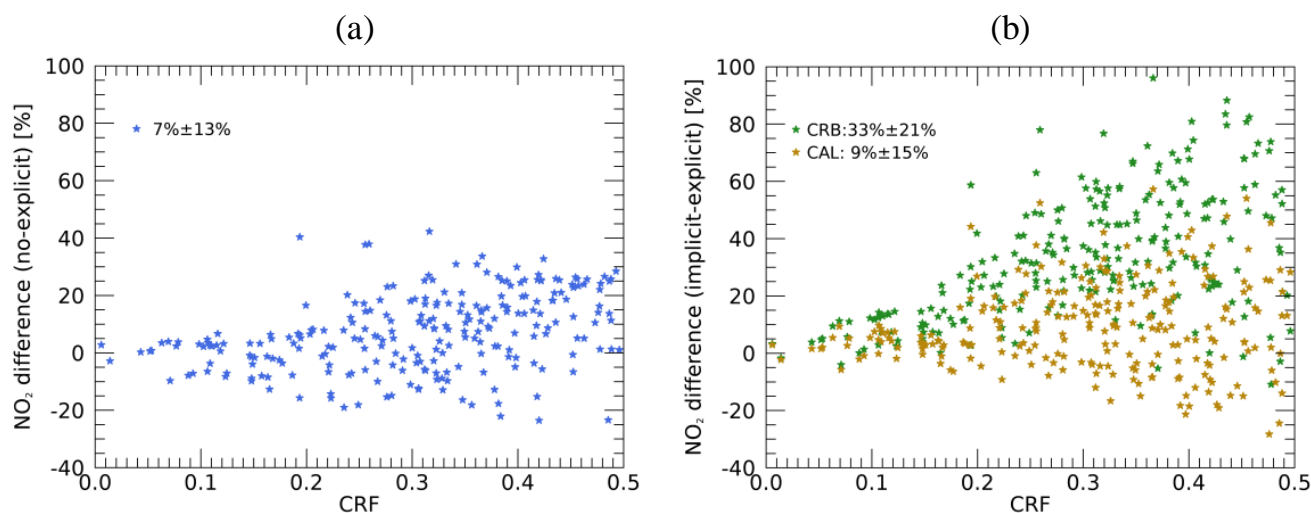


Figure 18. Scatter plot for relative biases in GOME-2 tropospheric NO₂ columns assuming no aerosol correction (a) and assuming implicit aerosol correction through ROCINN_CRB and ROCINN_CAL cloud model (b) with respect to the cloud radiance fraction at the Xianghe station from March 2010 to December 2016. Only measurements with cloud radiance fraction < 0.5, cloud optical depth < 5, and cloud top height < 3 km are included. Cloud observations with fitting RMS > 1×10^{-4} or number of iterations > 20 are filtered out. The mean value and standard deviation are given next to each label.

- 15 effect of scattering clouds and absorbing aerosols and the different characteristic sizes and phase functions of clouds and aerosols in general. The errors may be additionally enhanced in the presence of actual clouds. Therefore, future works include the further quantitative interpretation of OCRA/ROCINN cloud parameters for aerosol-dominated scenes and the impact on NO₂ retrieval algorithm.

5 Tropospheric NO₂ validation

- 20 A validation of our improved GOME-2 tropospheric NO₂ columns is performed with BIRA-IASB ground-based MAXDOAS measurements at the Xianghe station from March 2010 to December 2016. For the validation of GOME-2 measurements, the satellite data is filtered for clouds (cloud radiance fraction < 0.5), and the closest valid pixel within 50 km of the stations is compared to the ground-based MAXDOAS data, which is linearly interpolated to the GOME-2 overpass time (9:30 LT), if original data exists within ± 1 hour. As introduced in Sect. 4, Xianghe is a typical suburban station adequate for GOME-2
25 tropospheric NO₂ validation (Liu et al., 2019b). Urban stations are generally underestimated by GOME-2 data due to the averaging of a local source over a pixel size (Pinardi et al., 2015; Pinardi, in preparation).

Figure 20 shows the time series and scatter plot of the daily and monthly means comparison between the improved GOME-2 tropospheric NO₂ columns and the ground-based MAXDOAS measurements in Xianghe, including the statistical information

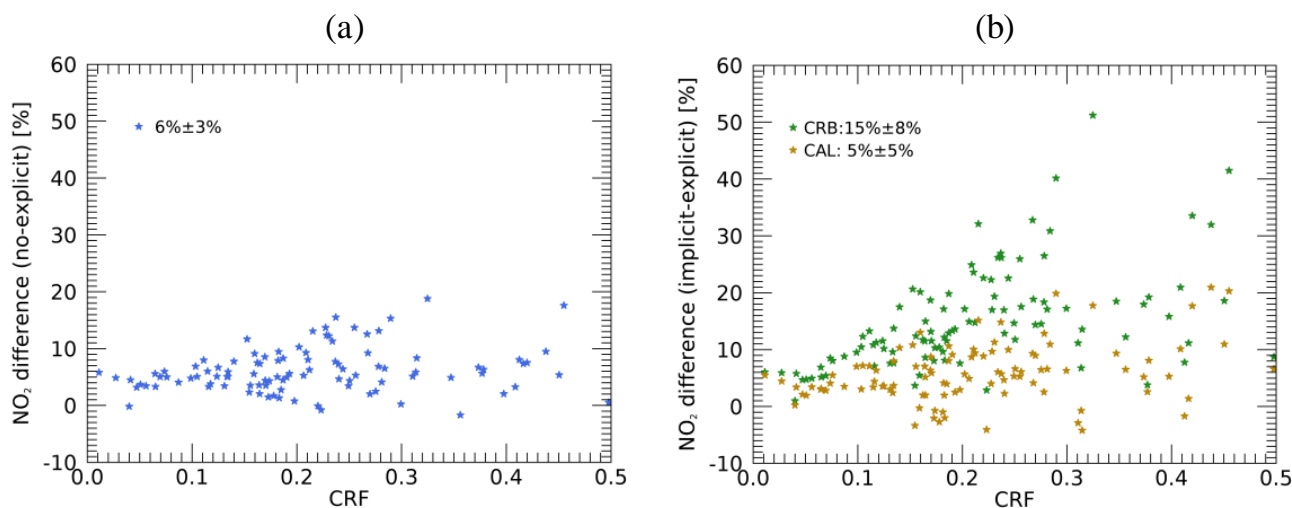


Figure 19. Similar as Fig. 18 but for the Bujumbura station from December 2013 to December 2015.

on the correlation coefficient, slope, and intercept of orthogonal regression analysis. The monthly mean values from the GOME-2 and MAXDOAS measurements indicate good agreement with similar seasonal variations in tropospheric NO₂ column. A correlation coefficient of 0.94, a regression slope of 0.69 (± 0.03) and an intercept of $0.41 (\pm 0.06) \times 10^{15}$ molec/cm² are derived when comparing the monthly mean values. These results are qualitatively similar to previous validation exercises at other sites, other satellites, and other NO₂ products (Celarier et al., 2008; Kramer et al., 2008; Chen et al., 2009; Irie et al., 2012; Ma et al., 2013; Wu et al., 2013; Kanaya et al., 2014; Wang et al., 2017; Drosoglou et al., 2017, 2018). Similar figures for previous GDP products can be found in Liu et al. (2019b) and AC-SAF validation website (<http://cdop.aeronomie.be/validation/valid-results>).

Figure 21 presents the daily and monthly mean absolute and relative differences of GOME-2 and MAXDOAS measurements. The differences are on average within $\pm 1 \times 10^{16}$ molec/cm² with a mean difference of -3.7×10^{15} molec/cm². The NO₂ levels are underestimated by 9.9% by GOME-2 with a standard deviation of $\pm 21\%$, mostly explained by the relatively low sensitivity of space-borne measurements near the surface, the gradient-smoothing effect, and the aerosol shielding effect. These effects are often inherent to the different measurements types or the specific conditions of the validation sites and also to the remaining impact of structural uncertainties (Boersma et al., 2016), such as the impact of the choices of the a priori NO₂ profiles and/or the albedo database assumed for the satellite AMF calculations.

To summarise the improvements of each of the changes discussed in previous sections, Table 4 reports the statistical results including the biases and regression analysis for the use of different surface albedo and a priori NO₂ profiles at the Xianghe station for completely clear sky (cloud radiance fraction = 0). Compared to the reference retrieval (based on GOME-2 surface LER climatology and TM5-MP a priori profile), better results are obtained with the improved algorithm (based on surface DLER dataset and IFS(CBA) a priori profile) with a median difference of -1.0×10^{15} molec/cm², which will be used to further test for aerosol correction type below.

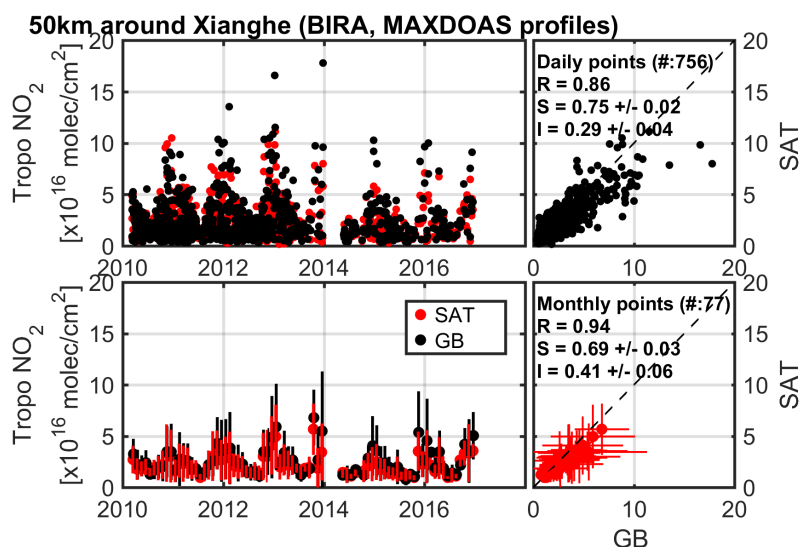


Figure 20. Daily and monthly mean time series and scatter plot of GOME-2 and MAXDOAS tropospheric NO₂ columns (mean value of all the pixels within 50km around Xianghe).

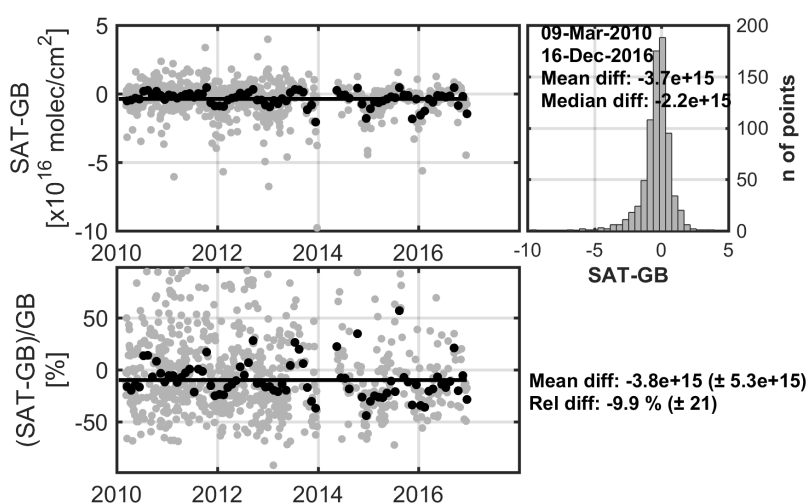


Figure 21. Daily and monthly mean absolute and relative GOME-2 and MAXDOAS time series differences for the Xianghe station. The histogram of the daily differences is also given, with the mean and median difference. The total time series absolute and relative monthly differences are given outside the panels.



Table 4. Mean difference (MD), median difference (AD) (SAT-GB in 10^{15} molec/cm²), standard deviation (STDEV), and correlation coefficient R and regression parameters (slope S and intercept I) of the orthogonal regression for the daily GOME-2 tropospheric NO₂ product when comparing to MAXDOAS data at Xianghe. Intermediate results for different surface albedo and a priori NO₂ profiles are reported for completely clear sky (cloud radiance fraction = 0) for a total of 73 GOME-2 pixels.

surface albedo	LER	DLER	DLER
a priori NO ₂ profile	TM5-MP	TM5-MP	IFS(CBA)
MD±STDEV ($\times 10^{15}$)	-2.5±7.2	-2.6±7.1	-1.9±7.2
AD ($\times 10^{15}$)	-1.9	-1.7	-1.0
R	0.63	0.64	0.63
S	0.60±0.09	0.60±0.08	0.63±0.09
I	0.30±0.12	0.29±0.12	0.31±0.12

Table 5. Similar as Table 4 but for different aerosol corrections for aerosol-dominated conditions (cloud radiance fraction < 0.5, cloud optical depth < 5, and cloud top height < 3 km) for a total of 146 GOME-2 pixels. Results are calculated using DLER surface albedo and IFS(CBA) a priori profiles.

aerosol correction	no	implicit_CAL
MD±STDEV ($\times 10^{15}$)	-4.0±10.0	-2.7±9.4
AD ($\times 10^{15}$)	-2.8	-2.3
R	0.83	0.86
S	0.72±0.04	0.91±0.05
I	0.34±0.09	-0.05±0.10

Table 5 presents the statistical results for the retrievals with no aerosol correction and CAL-based implicit aerosol correction at the Xianghe station for aerosol-dominated cases (cloud radiance fraction < 0.5, cloud optical depth < 5, and cloud top height < 3 km). Consistent with Fig. 18, the GOME-2 NO₂ columns retrieved using the CAL-based implicit aerosol correction are higher than the results assuming no aerosol correction, which improve the biases relative to the MAXDOAS measurements, as well as the standard deviation, correlation coefficient, and regression parameters. We note here that all the validation results in this work show a significant improvement compared to the current operational GDP 4.8 product (Pinardi et al., 2015; Pinardi, in preparation; Liu et al., 2019b) in the AC-SAF context (Hassinen et al., 2016).

6 Conclusion

The operational GOME-2 NO₂ dataset, generated with the GDP algorithm at DLR, has been introduced in detail by Valks et al. (2011, 2017) and successfully applied in many studies. An improved AMF calculation with more accurate knowledge



of surface albedo, a priori NO₂ profile, as well as cloud and aerosol correction is described in this paper and expected to be implemented in an upcoming version of GDP in combination with Liu et al. (2019b).

The viewing angle-dependency of surface albedo is taken into account by improving the currently used GOME-2 surface LER climatology (Tilstra et al., 2017). Over land, the surface albedo is described by a GOME-2 DLER dataset (Tilstra et al., 2019), determined by dividing the GOME-2 orbit swath into five segments and retrieving the traditional surface LER for each segment based on the data from the respective part of orbit swath. Compared to the non-directional GOME-2 LER climatology, the use of the DLER dataset improves the underestimation of the surface albedo at the west side of the GOME-2 orbit (backscattering geometry) and increases the AMFs by up to 15% for polluted regions. Over water, the surface albedo is improved with an ocean surface albedo parametrization (Jin et al., 2011), in which the albedo is parametrized for the direct and diffuse incident radiation separately. We update the simplified expression of diffuse contribution with more realistic values taken from the GOME-2 LER data, and we improve the description of the dependency on viewing direction for the parametrization. The resulting surface albedo increases over sun glint areas and polluted coastal regions with large SZAs and VZAs, for which the tropospheric NO₂ columns are reduced by up to 10%.

High-resolution a priori profiles, obtained from the chemistry transport model IFS(CBA) with recent emission inventories, provide a better description of the spatial and temporal variability in the NO₂ fields. Compared to the currently used TM5-MP profiles, the application of IFS(CBA) profiles affects the tropospheric NO₂ columns by up to 7×10^{15} molec/cm² for polluted regions, mainly due to the differences in the model specifications and model resolutions. To quantify the influence of model resolutions, we implement an analysis by altering the horizontal, vertical, and temporal resolutions for IFS(CBA). Changing the horizontal resolution from 1° to 0.7° affects the tropospheric NO₂ columns by up to 20%, with enhanced values for emission sources and the opposite for their unpolluted surroundings. When the vertical resolution changes from 34 layers to 69 layers, the tropospheric NO₂ columns increase by up to 15% due to the capture of small box-AMFs at low altitudes. Small differences (< 3%) are found for a temporal resolution of 2-hours and 1-hour time step.

The CAL model from the ROCINN cloud algorithm, with the clouds treated as uniform layers of water droplets, allows the penetration of photons through the clouds and provides more realistic cloud parameters than the current CRB model, with the clouds idealised as Lambertian reflectors. The application of CAL cloud parameters in the AMF calculation takes the sensitivities inside and below the cloud layers into account and reduces the tropospheric NO₂ columns by up to 3×10^{15} molec/cm² for polluted regions.

As the cloud retrieval does not distinguish between clouds and aerosols, the aerosol correction is implicitly implemented in the AMF calculation using the cloud parameters. To evaluate the accuracy of the implicit aerosol correction through a cloud model, we explicitly account for the aerosol effect using ground-based aerosol measurements for aerosol-dominated conditions. For Xianghe, a suburban site in China with primarily anthropogenic aerosol emissions, and Bujumbura, a remote site in tropical Africa typically affected by biomass burning aerosols, aerosol optical properties from AERONET measurements and extinction vertical profiles from correlative MAXDOAS measurements are applied. Assuming the explicit aerosol correction as reference, the use of implicit aerosol correction through the CAL cloud model yields a bias 24% smaller than the CRB cloud model for Xianghe and 10% smaller for Bujumbura.



A validation of the improved NO₂ measurements is performed by comparing the GOME-2 tropospheric NO₂ dataset with
20 ground-based MAXDOAS measurements at the Xianghe station. The GOME-2 NO₂ measurements show similar seasonal
variation as the MAXDOAS dataset with a monthly averaged difference of -9.9% (-3.8×10^{15} molec/cm² in absolute) and a
correlation coefficient of 0.94, indicating good agreement. The application of the new surface albedo, a priori NO₂ profile, and
cloud correction in the AMF calculation improves the biases, correlation coefficients, and regression parameters for Xianghe.

In the future, further studies focusing on the cloud correction will be implemented due to its importance in the AMF cal-
25 culation. The BRDF effect on cloud parameters will be considered by implementing the GOME-2 DLER dataset in the cloud
retrieval from ROCINN, providing a consistent treatment of surface albedo for both NO₂ and cloud retrieval. Note that the
BRDF effect is not discussed for OCRA, because no surface albedo climatology is directly needed, and the correction for
VZA-dependency has been applied in the cloud fraction retrieval as a proxy of BRDF constellation (see Lutz et al., 2016, Sect.
2.2.2 therein). In addition, the interpretation of the OCRA/ROCINN cloud product for aerosol-dominated scenes and the im-
30 pact on NO₂ retrieval algorithm will be further investigated in future studies. Furthermore, the NO₂ algorithm will be adapted
to measurements from the TROPOMI instrument with a spatial resolution as high as 7 km × 3.5 km.

Acknowledgements. This work is funded by the DLR-DAAD Research Fellowships 2015 (57186656) programme with reference number
91585186 and is undertaken in the framework of the EUMETSAT AC-SAF project. We acknowledge the Belgian Science Policy Office
(BELSPO) supporting part of this work through the PRODEX project B-ACSAF. We thank EUMETSAT for the GOME-2 ground segment
interfacing work and for the provision of GOME-2 level 1 products. We thank the UPAS team for the development work on the Universal
Processor for UV/VIS Atmospheric Spectrometers (UPAS) system at DLR. We are thankful to Henk Eskes (KNMI) for creating the TM5-
MP a priori NO₂ profiles. We acknowledge the free use of the GOME-2 surface LER database created by KNMI and provided through the
AC-SAF of EUMETSAT. We also acknowledge the free use of the online COART radiative transfer model established at NASA Langley
5 Research Center. We thank the use of imagery from the NASA Worldview application (<https://worldview.earthdata.nasa.gov/>) as part of the
NASA Earth Observing System Data and Information System (EOSDIS). We also thank the PIs of the AERONET sites used in this study
for maintaining their instruments and providing their data to the community.



References

- Agustí-Panareda, A., Massart, S., Chevallier, F., Balsamo, G., Boussetta, S., Dutra, E., and Beljaars, A.: A biogenic CO₂ flux adjustment scheme for the mitigation of large-scale biases in global atmospheric CO₂ analyses and forecasts, *Atmos. Chem. Phys.*, 16, 10 399–10 418, 2016.
- Bechtold, P., Semane, N., Lopez, P., Chaboureau, J.-P., Beljaars, A., and Bormann, N.: Representing equilibrium and nonequilibrium convection in large-scale models, *J. Atmos. Sci.*, 71, 734–753, 2014.
- 5 Beirle, S., Hörmann, C., Jöckel, P., Liu, S., Penning de Vries, M., Pozzer, A., Sihler, H., Valks, P., and Wagner, T.: The STRatospheric Estimation Algorithm from Mainz (STREAM): estimating stratospheric NO₂ from nadir-viewing satellites by weighted convolution, *Atmos. Meas. Tech.*, 9, 2753–2779, 2016.
- Beljaars, A. and Viterbo, P.: Role of the boundary layer in a numerical weather prediction model, *Clear and cloudy boundary layers*, pp. 10 287–304, 1998.
- Benedetti, A., Morcrette, J.-J., Boucher, O., Dethof, A., Engelen, R. J., Fisher, M., Flentje, H., Huneeus, N., Jones, L., Kaiser, J. W., Kinne, S., Mangold, A., Razinger, M., Simmons, A. J., and Suttie, M.: Aerosol analysis and forecast in the European centre for medium-range weather forecasts integrated forecast system: 2. Data assimilation, *J. Geophys. Res. Atmos.*, 114, 2009.
- Boersma, K., Eskes, H., and Brinkma, E.: Error analysis for tropospheric NO₂ retrieval from space, *J. Geophys. Res. Atmos.*, 109, 2004.
- 15 Boersma, K., Vinken, G., and Eskes, H.: Representativeness errors in comparing chemistry transport and chemistry climate models with satellite UV–Vis tropospheric column retrievals, *Geosci. Model Dev.*, 9, 875, 2016.
- Boersma, K. F., Eskes, H. J., Dirksen, R. J., van der A, R. J., Veefkind, J. P., Stammes, P., Huijnen, V., Kleipool, Q. L., Sneep, M., Claas, J., Leitão, J., Richter, A., Zhou, Y., and Brunner, D.: An improved tropospheric NO₂ column retrieval algorithm for the Ozone Monitoring Instrument, *Atmos. Meas. Tech.*, 4, 1905, 2011.
- 20 Boersma, K. F., Eskes, H. J., Richter, A., De Smedt, I., Lorente, A., Beirle, S., van Geffen, J. H. G. M., Zara, M., Peters, E., Van Roozendaal, M., Wagner, T., Maasakkers, J. D., van der A, R. J., Nightingale, J., De Rudder, A., Irie, H., Pinardi, G., Lambert, J.-C., and Compornolle, S. C.: Improving algorithms and uncertainty estimates for satellite NO₂ retrievals: results from the quality assurance for the essential climate variables (QA4ECV) project, *Atmos. Meas. Tech.*, 11, 6651–6678, 2018.
- Bovensmann, H., Burrows, J., Buchwitz, M., Frerick, J., Rozanov, V., Chance, K., and Goede, A.: SCIAMACHY: Mission objectives and 25 measurement modes, *J. Atmos. Sci.*, 56, 1999.
- Burrows, J. P., Weber, M., Buchwitz, M., Rozanov, V., Ladstätter-Weissenmayer, A., Richter, A., DeBeek, R., Hoogen, R., Bramstedt, K., Eichmann, K.-U., Eisinger, M., and Perner, D.: The global ozone monitoring experiment (GOME): Mission concept and first scientific results, *J. Atmos. Sci.*, 56, 151–175, 1999.
- Cahalan, R. F., Ridgway, W., Wiscombe, W. J., Bell, T. L., and Snider, J. B.: The albedo of fractal stratocumulus clouds, *J. Atmos. Sci.*, 51, 30 2434–2455, 1994.
- Callies, J., Corpaccioli, E., Eisinger, M., Hahne, A., and Lefebvre, A.: GOME-2-Metop’s second-generation sensor for operational ozone monitoring, *ESA bulletin*, 102, 28–36, 2000.
- Castellanos, P., Boersma, K., Torres, O., and De Haan, J.: OMI tropospheric NO₂ air mass factors over South America: effects of biomass burning aerosols, *Atmos. Meas. Tech.*, 8, 3831–3849, 2015.
- 35 Celarier, E. A., Brinkma, E. J., Gleason, J. F., Veefkind, J. P., Cede, A., Herman, J. R., Ionov, D., Goutail, F., Pommereau, J.-P., Lambert, J.-C., van Roozendaal, M., Pinardi, G., Wittrock, F., Schönhardt, A., Richter, A., Ibrahim, O. W., Wagner, T., Bojkov, B., Mount, G.,



- Spinei, E., Chen, C. M., Pongetti, T. J., Sander, S. P., Bucsela, E. J., Wenig, M. O., Swart, D. P. J., Volten, H., Kroon, M., and Levelt, P. F.: Validation of Ozone Monitoring Instrument nitrogen dioxide columns, *J. Geophys. Res. Atmos.*, 113, 2008.
- Charlson, R. and Ahlquist, N.: Brown haze: NO₂ or aerosol?, *Atmos. Environ.*, 3, 653–656, 1969.
- Chen, D., Zhou, B., Beirle, S., Chen, L., and Wagner, T.: Tropospheric NO₂ column densities deduced from zenith-sky DOAS measurements in Shanghai, China, and their application to satellite validation, *Atmos. Chem. Phys.*, 9, 3641–3662, 2009.
- 5 Chimot, J., Vlemmix, T., Veefkind, J., de Haan, J., and Levelt, P.: Impact of aerosols on the OMI tropospheric NO₂ retrievals over industrialized regions: how accurate is the aerosol correction of cloud-free scenes via a simple cloud model?, *Atmos. Meas. Tech.*, 9, 359, 2016.
- Chimot, J., Veefkind, J. P., Haan, J. F. d., Stammes, P., and Levelt, P. F.: Minimizing aerosol effects on the OMI tropospheric NO₂ retrieval—An improved use of the 477 nm O₂-O₂ band and an estimation of the aerosol correction uncertainty, *Atmos. Meas. Tech.*, 12, 491–516, 2019.
- 10 Clémer, K., Van Roozendaal, M., Fayt, C., Hendrick, F., Hermans, C., Pinardi, G., Spurr, R., Wang, P., and De Mazière, M.: Multiple wavelength retrieval of tropospheric aerosol optical properties from MAXDOAS measurements in Beijing, *Atmos. Meas. Tech.*, 3, 863, 2010.
- Cox, C. and Munk, W.: Measurement of the roughness of the sea surface from photographs of the sun's glitter, *Josa*, 44, 838–850, 1954.
- 15 Crutzen, P. J.: The influence of nitrogen oxides on the atmospheric ozone content, *Q. J. R. Meteorol. Soc.*, 96, 320–325, 1970.
- Dee, D. P., Uppala, S. M., Simmons, A. J., Berrisford, P., Poli, P., Kobayashi, S., Andrae, U., Balmaseda, M. A., Balsamo, G., Bauer, P., Bechtold, P., Beljaars, A. C. M., van de Berg, L., Bidlot, J., Bormann, N., Delsol, C., Dragani, R., Fuentes, M., Geer, A. J., Haimberger, L., Healy, S. B., Hersbach, H., Hólm, E. V., Isaksen, I., Kållberg, P., Köhler, M., Matricardi, M., McNally, A. P., Monge-Sanz, B. M., Morcrette, J.-J., Park, B.-K., Peubey, C., de Rosnay, P., Tavolato, C., Thépaut, J.-N., and Vitart, F.: The ERA-Interim reanalysis: Configuration and performance of the data assimilation system, *Q. J. R. Meteorol. Soc.*, 137, 553–597, 2011.
- 20 Desmons, M., Wang, P., Stammes, P., and Tilstra, L. G.: FRESCO-B: a fast cloud retrieval algorithm using oxygen B-band measurements from GOME-2, *Atmos. Meas. Tech.*, 12, 2485–2498, 2019.
- Ding, J., Miyazaki, K., van der A, R. J., Mijling, B., Kurokawa, J.-I., Cho, S., Janssens-Maenhout, G., Zhang, Q., Liu, F., and Levelt, P. F.: Intercomparison of NO_x emission inventories over East Asia, *Atmos. Chem. Phys.*, 17, 10125, 2017.
- 25 Drosoglou, T., Bais, A. F., Zyrichidou, I., Kouremeti, N., Poupkou, A., Liora, N., Giannaros, C., Koukouli, M. E., Balis, D., and Melas, D.: Comparisons of ground-based tropospheric NO₂ MAX-DOAS measurements to satellite observations with the aid of an air quality model over the Thessaloniki area, Greece, *Atmos. Chem. Phys.*, 17, 5829–5849, 2017.
- Drosoglou, T., Koukouli, M. E., Kouremeti, N., Bais, A. F., Zyrichidou, I., Balis, D., van der A, R. J., Xu, J., and Li, A.: MAX-DOAS NO₂ observations over Guangzhou, China; ground-based and satellite comparisons, *Atmos. Meas. Tech.*, 11, 2239–2255, 2018.
- 30 Dumont, M., Brissaud, O., Picard, G., Schmitt, B., Gallet, J.-C., and Arnaud, Y.: High-accuracy measurements of snow Bidirectional Reflectance Distribution Function at visible and NIR wavelengths—comparison with modelling results, *Atmos. Chem. Phys.*, 10, 2507–2520, 2010.
- Engelen, R. J., Serrar, S., and Chevallier, F.: Four-dimensional data assimilation of atmospheric CO₂ using AIRS observations, *J. Geophys. Res. Atmos.*, 114, 2009.
- 35 Ferlay, N., Thieuleux, F., Cornet, C., Davis, A. B., Dubuisson, P., Ducos, F., Parol, F., Riédi, J., and Vanbauce, C.: Toward new inferences about cloud structures from multidirectional measurements in the oxygen A band: Middle-of-cloud pressure and cloud geometrical thickness from POLDER-3/PARASOL, *J. Appl. Meteorol. Climatol.*, 49, 2492–2507, 2010.



- Flemming, J., Huijnen, V., Arteta, J., Bechtold, P., Beljaars, A., Blechschmidt, A.-M., Diamantakis, M., Engelen, R. J., Gaudel, A., Inness, A., Jones, L., Josse, B., Katragkou, E., Marecal, V., Peuch, V.-H., Richter, A., Schultz, M. G., Stein, O., and Tsikerdekis, A.: Tropospheric chemistry in the Integrated Forecasting System of ECMWF, *Geosci. Model Dev.*, 8, 975–1003, 2015.
- Flemming, J., Benedetti, A., Inness, A., Engelen, R. J., Jones, L., Huijnen, V., Remy, S., Parrington, M., Suttie, M., Bozzo, A., Peuch, V.-H., Akritidis, D., and Katragkou, E.: The CAMS interim reanalysis of carbon monoxide, ozone and aerosol for 2003–2015, *Atmos. Chem. Phys.*, 17, 1945–1983, 2017.
- 5 Frieß, U., Monks, P., Remedios, J., Rozanov, A., Sinreich, R., Wagner, T., and Platt, U.: MAX-DOAS O₄ measurements: A new technique to derive information on atmospheric aerosols: 2. Modeling studies, *J. Geophys. Res. Atmos.*, 111, 2006.
- Frieß, U., Klein Baltink, H., Beirle, S., Clémer, K., Hendrick, F., Henzing, B., Irie, H., de Leeuw, G., Li, A., Moerman, M. M., van Roozendaal, M., Shaiganfar, R., Wagner, T., Wang, Y., Xie, P., Yilmaz, S., and Zieger, P.: Intercomparison of aerosol extinction profiles retrieved from MAX-DOAS measurements, *Atmos. Meas. Tech.*, 9, 3205–3222, 2016.
- 10 Gamble, J., Jones, W., and Minshall, S.: Epidemiological-environmental study of diesel bus garage workers: acute effects of NO₂ and respirable particulate on the respiratory system, *Environ. Res.* 42, 201–214, 1987.
- Gielen, C., Hendrick, F., Pinardi, G., De Smedt, I., Fayt, C., Hermans, C., Stavrakou, T., Bauwens, M., Müller, J.-F., Ndenzako, E., Nzo-habonayo, P., Akimana, R., Niyonzima, S., Van Roozendaal, M., and De Mazière, M.: Characterisation of Central-African aerosol and trace-gas emissions based on MAX-DOAS measurements and model simulations over Bujumbura, Burundi., *Atmospheric Chemistry and Physics Discussions*, pp. 1–41, 2017.
- 15 Giles, D. M., Sinyuk, A., Sorokin, M. G., Schafer, J. S., Smirnov, A., Slutsker, I., Eck, T. F., Holben, B. N., Lewis, J. R., Campbell, J. R., Welton, E. J., Korkin, S. V., and Lyapustin, A. I.: Advancements in the Aerosol Robotic Network (AERONET) Version 3 database—automated near-real-time quality control algorithm with improved cloud screening for Sun photometer aerosol optical depth (AOD) measurements, *Atmos. Meas. Tech.*, 12, 169–209, 2019.
- 20 Gordon, H. R.: Atmospheric correction of ocean color imagery in the Earth Observing System era, *J. Geophys. Res. Atmos.*, 102, 17 081–17 106, 1997.
- Granier, C., Bessagnet, B., Bond, T., D’Angiola, A., van Der Gon, H. D., Frost, G. J., Heil, A., Kaiser, J. W., Kinne, S., Klimont, Z., Kloster, S., Lamarque, J.-F., Liousse, C., Masui, T., Meleux, F., Mieville, A., Ohara, T., Raut, J.-C., Riahi, K., Schultz, M. G., Smith, S. J., Thompson, A., van Aardenne, J., van der Werf, G. R., and van Vuuren, D. P.: Evolution of anthropogenic and biomass burning emissions of air pollutants at global and regional scales during the 1980–2010 period, *Climatic Change*, 109, 163, 2011.
- 25 Granier, C., Darras, S., Denier van der Gon, H., Doubalova, J., Elguindi, N., Galle, B., Gauss, M., Guevara, M., Jalkanen, J.-P., Kuenen, J., Liousse, C., Quack, B., Simpson, D., and Sindelarova, K.: The Copernicus Atmosphere Monitoring Service global and regional emissions (April 2019 version), Tech. rep., Copernicus Atmosphere Monitoring Service (CAMS) report, 2019.
- 30 Gu, D., Wang, Y., Smeltzer, C., and Boersma, K. F.: Anthropogenic emissions of NO_x over China: Reconciling the difference of inverse modeling results using GOME-2 and OMI measurements, *J. Geophys. Res. Atmos.*, 119, 7732–7740, 2014.
- Hao, N., Koukouli, M. E., Inness, A., Valks, P., Loyola, D. G., Zimmer, W., Balis, D. S., Zyrichidou, I., Van Roozendaal, M., Lerot, C., and Spurr, R. J. D.: GOME-2 total ozone columns from MetOp-A/MetOp-B and assimilation in the MACC system, *Atmos. Meas. Tech.*, 7, 2937–2951, 2014.
- 35 Hassinen, S., Balis, D., Bauer, H., Begoin, M., Delcloo, A., Eleftheratos, K., Gimeno Garcia, S., Granville, J., Grossi, M., Hao, N., Hedelt, P., Hendrick, F., Hess, M., Heue, K.-P., Hovila, J., Jönch-Sørensen, H., Kalakoski, N., Kauppi, A., Kiemle, S., Kins, L., Koukouli, M. E., Kujanpää, J., Lambert, J.-C., Lang, R., Lerot, C., Loyola, D., Pedergnana, M., Pinardi, G., Romahn, F., van Roozendaal, M., Lutz, R.,



- De Smedt, I., Stammes, P., Steinbrecht, W., Tamminen, J., Theys, N., Tilstra, L. G., Tuinder, O. N. E., Valks, P., Zerefos, C., Zimmer, W., and Zyrichidou, I.: Overview of the O3M SAF GOME-2 operational atmospheric composition and UV radiation data products and data availability, *Atmos. Meas. Tech.*, 9, 383, 2016.
- Heckel, A., Richter, A., Tarsu, T., Wittrock, F., Hak, C., Pundt, I., Junkermann, W., and Burrows, J.: MAX-DOAS measurements of formaldehyde in the Po-Valley, *Atmos. Chem. Phys.*, 5, 909–918, 2005.
- 5 Heckel, A., Kim, S.-W., Frost, G., Richter, A., Trainer, M., and Burrows, J.: Influence of low spatial resolution a priori data on tropospheric NO₂ satellite retrievals, *Atmos. Meas. Tech.*, 4, 1805, 2011.
- Hendrick, F., Müller, J.-F., Clémer, K., Wang, P., De Mazière, M., Fayt, C., Gielen, C., Hermans, C., Ma, J. Z., Pinardi, G., Stavrou, T., Vlemmix, T., and Van Roozendaal, M.: Four years of ground-based MAX-DOAS observations of HONO and NO₂ in the Beijing area, *Atmos. Chem. Phys.*, 14, 765–781, 2014.
- 10 Heue, K.-P., Coldewey-Egbers, M., Delcloo, A., Lerot, C., Loyola, D., Valks, P., and Roozendaal, M. v.: Trends of tropical tropospheric ozone from 20 years of European satellite measurements and perspectives for the Sentinel-5 Precursor, *Atmos. Meas. Tech.*, 9, 5037–5051, 2016.
- Hilboll, A., Richter, A., and Burrows, J.: Long-term changes of tropospheric NO₂ over megacities derived from multiple satellite instruments, *Atmos. Chem. Phys.*, 13, 4145–4169, 2013.
- Hilboll, A., Richter, A., and Burrows, J. P.: NO₂ pollution over India observed from space—The impact of rapid economic growth, and a
15 recent decline, *Atmospheric Chemistry and Physics Discussions*, 2017.
- Holben, B. N., Eck, T. F., Slutsker, I., Tanre, D., Buis, J. P., Setzer, A., Vermote, E., Reagan, J. A., Kaufman, Y. J., Nakajima, T., Lavenu, F., Jankowiak, I., and Smirnov, A.: AERONET—A federated instrument network and data archive for aerosol characterization, *Remote Sens. Environ.*, 66, 1–16, 1998.
- Holtlag, A. and Boville, B.: Local versus nonlocal boundary-layer diffusion in a global climate model, *J. Clim.*, 6, 1825–1842, 1993.
- 20 Hönninger, G., Friedeburg, C. v., and Platt, U.: Multi axis differential optical absorption spectroscopy (MAX-DOAS), *Atmos. Chem. Phys.*, 4, 231–254, 2004.
- Hortal, M.: The development and testing of a new two-time-level semi-Lagrangian scheme (SETTLES) in the ECMWF forecast model, *Q. J. R. Meteorol. Soc.*, 128, 1671–1687, 2002.
- Huijnen, V., Williams, J., van Weele, M., van Noije, T., Krol, M., Dentener, F., Segers, A., Houweling, S., Peters, W., de Laat, J., Boersma, F.,
25 Bergamaschi, P., van Velthoven, P., Le Sager, P., Eskes, H., Alkemade, F., Scheele, R., Nédélec, P., and Pätz, H.-W.: The global chemistry transport model TM5: description and evaluation of the tropospheric chemistry version 3.0, *Geosci. Model Dev.*, 3, 445–473, 2010.
- Huijnen, V., Flemming, J., Chabrillat, S., Errera, Q., Christophe, Y., Blechschmidt, A.-M., Richter, A., and Eskes, H.: C-IFS-CB05-BASCOE: stratospheric chemistry in the Integrated Forecasting System of ECMWF, *Geosci. Model Dev.*, 9, 3071–3091, 2016.
- Huijnen, V., Pozzer, A., Arteta, J., Brasseur, G., Bouarar, I., Chabrillat, S., Christophe, Y., Doumbia, T., Flemming, J., Guth, J., Josse, B.,
30 Karydis, V. A., Marécal, V., and Pelletier, S.: Quantifying uncertainties due to chemistry modelling: Evaluation of tropospheric composition simulations in the CAMS model (cycle 43R1), *Geosci. Model Dev.*, 12, 1725–1752, 2019.
- Ingmann, P., Veihelmann, B., Langen, J., Lamarre, D., Stark, H., and Courrèges-Lacoste, G. B.: Requirements for the GMES Atmosphere Service and ESA's implementation concept: Sentinels-4/-5 and-5p, *Remote Sens. Environ.*, 120, 58–69, 2012.
- Inness, A., Blechschmidt, A.-M., Bouarar, I., Chabrillat, S., Crepulja, M., Engelen, R. J., Eskes, H., Flemming, J., Gaudel, A., Hendrick, F.,
35 Huijnen, V., Jones, L., Kapsomenakis, J., Katragkou, E., Keppens, A., Langerock, B., de Mazière, M., Melas, D., Parrington, M., Peuch, V. H., Razinger, M., Richter, A., Schultz, M. G., Suttie, M., Thouret, V., Vrekoussis, M., Wagner, A., and Zerefos, C.: Data assimilation of



- satellite-retrieved ozone, carbon monoxide and nitrogen dioxide with ECMWF's Composition-IFS, *Atmos. Chem. Phys.*, 15, 5275–5303, 2015.
- Irie, H., Boersma, K., Kanaya, Y., Takashima, H., Pan, X., and Wang, Z.: Quantitative bias estimates for tropospheric NO₂ columns retrieved from SCIAMACHY, OMI, and GOME-2 using a common standard for East Asia, *Atmos. Meas. Tech.*, 5, 2403–2411, 2012.
- Jin, Z., Charlock, T. P., Smith Jr, W. L., and Rutledge, K.: A parameterization of ocean surface albedo, *Geophys. Res. Lett.*, 31, 2004.
- 5 Jin, Z., Charlock, T. P., Rutledge, K., Stamnes, K., and Wang, Y.: Analytical solution of radiative transfer in the coupled atmosphere-ocean system with a rough surface, *Appl. Opt.*, 45, 7443–7455, 2006.
- Jin, Z., Qiao, Y., Wang, Y., Fang, Y., and Yi, W.: A new parameterization of spectral and broadband ocean surface albedo, *Opt. Express*, 19, 26429–26443, 2011.
- Kaiser, J. W., Heil, A., Andreae, M. O., Benedetti, A., Chubarova, N., Jones, L., Morcrette, J.-J., Razinger, M., Schultz, M. G., Suttie, M.,
10 and van der Werf, G. R.: Biomass burning emissions estimated with a global fire assimilation system based on observed fire radiative power, *Biogeosciences*, 9, 527–554, 2012.
- Kampa, M. and Castanas, E.: Human health effects of air pollution, *Environ. Pollut.* 151, 362–367, 2008.
- Kanaya, Y., Irie, H., Takashima, H., Iwabuchi, H., Akimoto, H., Sudo, K., Gu, M., Chong, J., Kim, Y. J., Lee, H., Li, A., Si, F., Xu, J., Xie, P.-H., Liu, W.-Q., Dzhola, A., Postlyakov, O., Ivanov, V., Grechko, E., Terpigova, S., and Panchenko, M.: Long-term MAX-DOAS
15 network observations of NO₂ in Russia and Asia (MADRAS) during the period 2007–2012: instrumentation, elucidation of climatology, and comparisons with OMI satellite observations and global model simulations., *Atmos. Chem. Phys.*, 14, 7909–7927, 2014.
- Kleipool, Q., Dobber, M., de Haan, J., and Levelt, P.: Earth surface reflectance climatology from 3 years of OMI data, *J. Geophys. Res. Atmos.*, 113, 2008.
- Koelemeijer, R., De Haan, J., and Stammes, P.: A database of spectral surface reflectivity in the range 335–772 nm derived from 5.5 years of
20 GOME observations, *J. Geophys. Res. Atmos.*, 108, 2003.
- Kokhanovsky, A. and Rozanov, V.: The uncertainties of satellite DOAS total ozone retrieval for a cloudy sky, *Atmos. Environ.*, 87, 27–36, 2008.
- Kramer, L. J., Leigh, R. J., Remedios, J. J., and Monks, P. S.: Comparison of OMI and ground-based in situ and MAX-DOAS measurements of tropospheric nitrogen dioxide in an urban area, *J. Geophys. Res. Atmos.*, 113, 2008.
- 25 Krotkov, N. A., Lamsal, L. N., Celarier, E. A., Swartz, W. H., Marchenko, S. V., Bucsela, E. J., Chan, K. L., Wenig, M., and Zara, M.: The version 3 OMI NO₂ standard product, *Atmos. Meas. Tech.*, 10, 3133–3149, 2017.
- Kuhlmann, G., Lam, Y., Cheung, H., Hartl, A., Fung, J. C. H., Chan, P., and Wenig, M. O.: Development of a custom OMI NO₂ data product for evaluating biases in a regional chemistry transport model, *Atmos. Chem. Phys.*, 15, 5627–5644, 2015.
- Laughner, J. L., Zare, A., and Cohen, R. C.: Effects of daily meteorology on the interpretation of space-based remote sensing of NO₂, *Atmos. Chem. Phys.*, 16, 15247–15264, 2016.
- 30 Laughner, J. L., Zhu, Q., and Cohen, R. C.: The Berkeley High Resolution Tropospheric NO₂ product, *Earth Syst. Sci. Data*, 10, 2069–2095, 2018.
- Lee, K. and Kim, Y.: Satellite remote sensing of Asian aerosols: a case study of clean, polluted, and Asian dust storm days, *Atmos. Meas. Tech.*, 3, 1771–1784, 2010.
- 35 Leitão, J., Richter, A., Vrekoussis, M., Kokhanovsky, A., Zhang, Q., Beekmann, M., and Burrows, J.: On the improvement of NO₂ satellite retrievals–aerosol impact on the airmass factors, *Atmos. Meas. Tech.*, 3, 475–493, 2010.



- Lelli, L., Kokhanovsky, A., Rozanov, V., Vountas, M., Sayer, A., and Burrows, J.: Seven years of global retrieval of cloud properties using space-borne data of GOME, *Atmos. Meas. Tech.*, 5, 1551, 2012.
- Levelt, P., Van den Oord, G., Dobber, M., Malkki, A., Visser, H., de Vries, J., Stammes, P., Lundell, J., and Saari, H.: The Ozone Monitoring Instrument, *IEEE T. Geosci. Remote Sens.*, 44, 1093–1101, 2006.
- Li, J., Scinocca, J., Lazare, M., McFarlane, N., Von Salzen, K., and Solheim, L.: Ocean surface albedo and its impact on radiation balance in climate models, *J. Clim.*, 19, 6314–6333, 2006.
- Lin, J., Martin, R., Boersma, K., Sneep, M., Stammes, P., Spurr, R., Wang, P., Van Roozendael, M., Clémer, K., and Irie, H.: Retrieving tropospheric nitrogen dioxide from the Ozone Monitoring Instrument: effects of aerosols, surface reflectance anisotropy, and vertical profile of nitrogen dioxide, *Atmos. Chem. Phys.*, 14, 1441–1461, 2014.
- Lin, J., Liu, M., Xin, J., Boersma, K., Spurr, R., Martin, R., and Zhang, Q.: Influence of aerosols and surface reflectance on satellite NO₂ retrieval: seasonal and spatial characteristics and implications for NO_x emission constraints, *Atmos. Chem. Phys.*, 15, 11 217, 2015.
- Liu, M., Lin, J., Boersma, K. F., Pinardi, G., Wang, Y., Chimot, J., Wagner, T., Xie, P., Eskes, H., Van Roozendael, M., Hendrick, F., Wang, P., Wang, T., Yan, Y., Chen, L., and Ni, R.: Improved aerosol correction for OMI tropospheric NO₂ retrieval over East Asia: constraint from CALIOP aerosol vertical profile, *Atmos. Meas. Tech.*, 12, 1–21, 2019a.
- Liu, S., Valks, P., Pinardi, G., De Smedt, I., Yu, H., Beirle, S., and Richter, A.: An Improved Total and Tropospheric NO₂ Column Retrieval for GOME-2, *Atmos. Meas. Tech.*, 12, 1029–1057, 2019b.
- Liu, X., Newchurch, M., Loughman, R., and Bhartia, P.: Errors resulting from assuming opaque Lambertian clouds in TOMS ozone retrieval, *J. Quant. Spectrosc. Radiat. Transf.*, 85, 337–365, 2004.
- Lorente, A., Folkert Boersma, K., Yu, H., Dörner, S., Hilboll, A., Richter, A., Liu, M., Lamsal, L. N., Barkley, M., De Smedt, I., Van Roozendael, M., Wang, Y., Wagner, T., Beirle, S., Lin, J.-T., Krotkov, N., Stammes, P., Wang, P., Eskes, H. J., and Krol, M.: Structural uncertainty in air mass factor calculation for NO₂ and HCHO satellite retrievals, *Atmos. Meas. Tech.*, 10, 759, 2017.
- Lorente, A., Boersma, K. F., Stammes, P., Tilstra, L. G., Richter, A., Yu, H., Kharbouche, S., and Muller, J.-P.: The importance of surface reflectance anisotropy for cloud and NO₂ retrievals from GOME-2 and OMI, *Atmos. Meas. Tech.*, 11, 4509–4529, 2018.
- Loyola, D.: The near-real-time total ozone retrieval algorithm from TROPOMI onboard Sentinel-5 Precursor, in preparation.
- Loyola, D., Thomas, W., Livschitz, Y., Ruppert, T., Albert, P., and Hollmann, R.: Cloud properties derived from GOME/ERS-2 backscatter data for trace gas retrieval, *IEEE Trans. Geosci. Remote Sens.*, 45, 2747–2758, 2007.
- Loyola, D., García, S. G., Lutz, R., Argyrouli, A., Romahn, F., Spurr, R. J., Pedernana, M., Doicu, A., García, V. M., and Schüssler, O.: The operational cloud retrieval algorithms from TROPOMI on board Sentinel-5 Precursor, *Atmos. Meas. Tech.*, 11, 409, 2018.
- Loyola, D. G., Koukouli, M. E., Valks, P., Balis, D. S., Hao, N., Van Roozendael, M., Spurr, R. J. D., Zimmer, W., Kiemle, S., Lerot, C., and Lambert, J.-C.: The GOME-2 total column ozone product: Retrieval algorithm and ground-based validation, *J. Geophys. Res. Atmos.*, 116, 2011.
- Lutz, R., Loyola, D., Gimeno García, S., and Romahn, F.: OCRA radiometric cloud fractions for GOME-2 on MetOp-A/B, *Atmos. Meas. Tech.*, 9, 2357–2379, 2016.
- Ma, J., Beirle, S., Jin, J., Shaiganfar, R., Yan, P., and Wagner, T.: Tropospheric NO₂ vertical column densities over Beijing: results of the first three years of ground-based MAX-DOAS measurements (2008–2011) and satellite validation, *Atmos. Chem. Phys.*, 13, 1547–1567, 2013.
- Martin, R. V., Jacob, D. J., Chance, K., Kurosu, T. P., Palmer, P. I., and Evans, M. J.: Global inventory of nitrogen oxide emissions constrained by space-based observations of NO₂ columns, *J. Geophys. Res. Atmos.*, 108, 2003.



- McCormick, J.: Acid Earth: the global threat of acid pollution, Routledge, 2013.
- McLinden, C. A., Fioletov, V., Boersma, K. F., Kharol, S. K., Krotkov, N., Lamsal, L., Makar, P. A., Martin, R. V., Veefkind, J. P., and Yang, K.: Improved satellite retrievals of NO₂ and SO₂ over the Canadian oil sands and comparisons with surface measurements, *Atmos. Chem. Phys.*, 14, 3637–3656, 2014.
- Mijling, B., van der A, R., and Zhang, Q.: Regional nitrogen oxides emission trends in East Asia observed from space, *Atmos. Chem. Phys.*, 13, 12 003–12 012, 2013.
- Miyazaki, K., Eskes, H., Sudo, K., Boersma, K. F., Bowman, K., and Kanaya, Y.: Decadal changes in global surface NO_x emissions from multi-constituent satellite data assimilation, *Atmos. Chem. Phys.*, 17, 807–837, 2017.
- Morcrette, J.-J., Boucher, O., Jones, L., Salmond, D., Bechtold, P., Beljaars, A., Benedetti, A., Bonet, A., Kaiser, J. W., Razinger, M., Schulz, M., Serrar, S., Simmons, A. J., Sofiev, M., Suttie, M., Tompkins, A. M., and Untch, A.: Aerosol analysis and forecast in the European Centre for medium-range weather forecasts integrated forecast system: Forward modeling, *J. Geophys. Res. Atmos.*, 114, 2009.
- Munro, R., Lang, R., Klaes, D., Poli, G., Retscher, C., Lindstrot, R., Huckle, R., Lacan, A., Grzegorski, M., Holdak, A., Kokhanovsky, A., Livschitz, J., and Eisinger, M.: The GOME-2 instrument on the Metop series of satellites: instrument design, calibration, and level 1 data processing—an overview, *Atmos. Meas. Tech.*, 9, 1279–1301, 2016.
- Nicodemus, F. E., Richmond, J., Hsia, J., Ginsberg, I., and Limperis, T.: Geometrical considerations and nomenclature for reflectance, in: *Radiometry*, pp. 94–145, Jones and Bartlett Publishers, Inc., 1992.
- Noguchi, K., Richter, A., Rozanov, V., Rozanov, A., Burrows, J., Irie, H., and Kita, K.: Effect of surface BRDF of various land cover types on geostationary observations of tropospheric NO₂, *Atmos. Meas. Tech.*, 7, 3497–3508, 2014.
- Nüß, H., Richter, A., Valks, P., and Burrows, J.: Improvement of the NO₂ total column retrieval for GOME-2, O3M SAF Visiting Scientist Activity, Final Report, IUP University of Bremen, 2006.
- Ohlmann, J. C.: Ocean radiant heating in climate models, *J. Clim.*, 16, 1337–1351, 2003.
- Palmer, P. I., Jacob, D. J., Chance, K., Martin, R. V., Spurr, R. J., Kurosu, T. P., Bey, I., Yantosca, R., Fiore, A., and Li, Q.: Air mass factor formulation for spectroscopic measurements from satellites: Application to formaldehyde retrievals from the Global Ozone Monitoring Experiment, *J. Geophys. Res. Atmos.*, 106, 14 539–14 550, 2001.
- Pinardi, G.: in preparation.
- Pinardi, G., Van Roozendaal, M., Lambert, J.-C., Granville, J., Hendrick, F., Tack, F., Yu, H., Cede, A., Kanaya, Y., Irie, I., Goutail, F., Pommereau, J.-P., Pazmino, A., Wittrock, F., Richter, A., Wagner, T., Gu, M., Remmers, J., Friess, U., Vlemmix, T., Pitters, A., Hao, N., Tiefengraber, M., Herman, J., Abuhassan, N., Bais, A., Kouremeti, N., Hovila, J., Holla, R., Chong, J., Postlyakov, O., and Ma, J.: GOME-2 total and tropospheric NO₂ validation based on zenith-sky, direct-sun and multi-axis DOAS network observations, in: *Proc. of the 2014 EUMETSAT Meteorological Satellite Conference*, Geneva, Switzerland, EUMETSAT, 2014.
- Pinardi, G., Lambert, J.-C., Granville, J., Yu, H., De Smedt, I., van Roozendaal, M., and Valks, P.: O3M-SAF validation report, *Tech. rep.*, SAF/O3M/IASB/VR/NO₂/TN-IASB-GOME2-O3MSAF-NO₂-2015, Issue 1/1, 2015.
- Platt, U. and Stutz, J.: *Differential Optical Absorption Spectroscopy*, Springer, 2008.
- Qin, W., Fasnacht, Z., Haffner, D., Vasilkov, A., Joiner, J., Krotkov, N., Fisher, B., and Spurr, R.: A geometry-dependent surface Lambertian-equivalent reflectivity product at 466 nm for UV/Vis retrievals: Part I. Evaluation over land surfaces using measurements from OMI, *Atmospheric Measurement Techniques Discussions*, pp. 1–31, doi:10.5194/amt-2018-327, 2019.
- Richter, A., Begoin, M., Hilboll, A., and Burrows, J.: An improved NO₂ retrieval for the GOME-2 satellite instrument, *Atmos. Meas. Tech.*, 4, 1147–1159, 2011.



- Richter, A., Behrens, L. K., Hilboll, A., Munassar, S., Burrows, J. P., Pinardi, G., and Van Roozendael, M.: cloud effects on satellite retrievals of tropospheric NO₂ over China, in: 8th International DOAS Workshop, Yokohama, Japan, 2017.
- Richter, A. et al.: S5P/TROPOMI Science Verification Report, Tech. rep., S5P-IUP-L2-ScVR-RP issue 2.1, 2015.
- Rozanov, V. V. and Kokhanovsky, A. A.: Semianalytical cloud retrieval algorithm as applied to the cloud top altitude and the cloud geometrical thickness determination from top-of-atmosphere reflectance measurements in the oxygen A band, *J. Geophys. Res. Atmos.*, 109, 5 2004.
- Russell, A., Perring, A., Valin, L., Bucseles, E., Browne, E., Wooldridge, P., and Cohen, R.: A high spatial resolution retrieval of NO₂ column densities from OMI: method and evaluation, *Atmos. Chem. Phys.*, 11, 8543–8554, 2011.
- Russell, G. L. and Lerner, J. A.: A new finite-differencing scheme for the tracer transport equation, *J. Appl. Meteorol.*, 20, 1483–1498, 1981.
- Saiedy, F., Jacobowitz, H., and Wark, D.: On cloud-top determination from Gemini-5, *J. Atmos. Sci.*, 24, 63–69, 1967.
- 10 Sanders, A., Richter, A., and Eskes, H.: Sentinel-4 Level-2 ATBD Total and Tropospheric NO₂, Tech. rep., S4-L2-IUP_KNMI-ATBD-2004 issue 2.0, 2018.
- Séférian, R., Baek, S., Boucher, O., Dufresne, J.-L., Decharme, B., Saint-Martin, D., and Roehrig, R.: An interactive ocean surface albedo scheme (OSAv1. 0): formulation and evaluation in ARPEGE-Climat (V6. 1) and LMDZ (V5A), *Geosci. Model Dev.*, 11, 321–338, 2018.
- Skachko, S., Ménard, R., Errera, Q., Christophe, Y., and Chabrilat, S.: EnKF and 4D-Var data assimilation with chemical transport model 15 BASCOE (version 05.06), *Geosci. Model Dev.*, 9, 2893–2908, 2016.
- Spurr, R., Kurosu, T., and Chance, K.: A linearized discrete ordinate radiative transfer model for atmospheric remote-sensing retrieval, *J. Quant. Spectrosc. Radiat. Transf.*, 68, 689–735, 2001.
- Stammes, P., Sneep, M., De Haan, J., Veefkind, J., Wang, P., and Levelt, P.: Effective cloud fractions from the Ozone Monitoring Instrument: Theoretical framework and validation, *J. Geophys. Res. Atmos.*, 113, 2008.
- 20 Temperton, C., Hortal, M., and Simmons, A.: A two-time-level semi-Lagrangian global spectral model, *Q. J. R. Meteorol. Soc.*, 127, 111–127, 2001.
- Theys, N., De Smedt, I., Yu, H., Danckaert, T., van Gent, J., Hörmann, C., Wagner, T., Hedelt, P., Bauer, H., Romahn, F., Pedergnana, M., Loyola, D., and Van Roozendael, M.: Sulfur dioxide retrievals from TROPOMI onboard Sentinel-5 Precursor: algorithm theoretical basis., *Atmos. Meas. Tech.*, 10, 2017.
- 25 Tilstra, L., Tuinder, O., Wang, P., and Stammes, P.: Surface reflectivity climatologies from UV to NIR determined from Earth observations by GOME-2 and SCIAMACHY, *J. Geophys. Res. Atmos.*, 122, 4084–4111, 2017.
- Tilstra, L., Tuinder, O., and Stammes, P.: GOME-2 surface LER product - Algorithm Theoretical Basis Document, Tech. rep., KNMI Report SAF/AC/KNMI/ATBD/003, Issue 3.1, 2019.
- Torres, O., Ahn, C., and Chen, Z.: Improvements to the OMI near-UV aerosol algorithm using A-train CALIOP and AIRS observations, 30 *Atmos. Meas. Tech.*, 6, 3257–3270, 2013.
- Valin, L., Russell, A., Hudman, R., and Cohen, R.: Effects of model resolution on the interpretation of satellite NO₂ observations, *Atmos. Chem. Phys.*, 11, 11 647–11 655, 2011.
- Valks, P., Pinardi, G., Richter, A., Lambert, J.-C., Hao, N., Loyola, D., Van Roozendael, M., and Emmadi, S.: Operational total and tropospheric NO₂ column retrieval for GOME-2, *Atmos. Meas. Tech.*, 4, 1491, 2011.
- 35 Valks, P., Loyola, D., Hao, N., Hedelt, P., Slijkhuis, S., Grossi, M., Begoin, M., Gimeno Garcia, S., and Lutz, R.: Algorithm Theoretical Basis Document for GOME-2 Total Column Products of Ozone, NO₂, BrO, SO₂, H₂O, HCHO and Cloud Properties (GDP 4.8 for AC SAF OTO and NTO), Tech. rep., SAF/AC/DLR/ATBD/01, Iss./Rev.: 3/A/2, 2017.



- van Geffen, J., Boersma, K., Eskes, H., Maasakkers, J., and Veefkind, J.: TROPOMI ATBD of the total and tropospheric NO₂ data products, Tech. rep., S5P-KNMI-L2-0005-RP issue 1.4.0., 2019.
- van Geffen, J. H. G. M., Eskes, H. J., Boersma, K. F., and Veefkind, J. P.: ATBD for NO₂ in Sentinel-5 L2 Prototype Processors, Tech. rep., KNMI-ESA-S5L2PP-ATBD-001 version 3.0., 2018.
- Van Roozendael, M., Spurr, R., Loyola, D., Lerot, C., Balis, D., Lambert, J.-C., Zimmer, W., van Gent, J., van Geffen, J., Koukouli, M., Granville, J., Doicu, A., Fayt, C., and Zehner, C.: Ten years of GOME/ERS-2 total ozone data—The new GOME data processor (GDP) version 4: 1. Algorithm description, *J. Geophys. Res. Atmos.*, 111, 2006.
- 5 Vasilkov, A., Joiner, J., Spurr, R., Bhartia, P. K., Levelt, P., and Stephens, G.: Evaluation of the OMI cloud pressures derived from rotational Raman scattering by comparisons with other satellite data and radiative transfer simulations, *J. Geophys. Res. Atmos.*, 113, 2008.
- Vasilkov, A., Qin, W., Krotkov, N., Lamsal, L., Spurr, R., Haffner, D., Joiner, J., Eun-Su, Y., and Marchenko, S.: Accounting for the effects of surface BRDF on satellite cloud and trace-gas retrievals: a new approach based on geometry-dependent Lambertian equivalent reflectivity applied to OMI algorithms, *Atmos. Meas. Tech.*, 10, 333, 2017.
- 10 Veefkind, J., Aben, I., McMullan, K., Förster, H., De Vries, J., Otter, G., Claas, J., Eskes, H., De Haan, J., Kleipool, Q., van Weele, M., Hasekamp, O., Hoogeveen, R., Landgraf, J., Snel, R., Tol, P., Ingmann, P., Voors, R., Kruizinga, B., Vink, R., Visser, H., and Levelt, P.: TROPOMI on the ESA Sentinel-5 Precursor: A GMES mission for global observations of the atmospheric composition for climate, air quality and ozone layer applications, *Remote Sens. Environ.*, 120, 70–83, 2012.
- 15 Vlemmix, T., Hendrick, F., Pinardi, G., De Smedt, I., Fayt, C., Hermans, C., Piters, A., Wang, P., Levelt, P., and Van Roozendael, M.: MAX-DOAS observations of aerosols, formaldehyde and nitrogen dioxide in the Beijing area: comparison of two profile retrieval approaches, *Atmos. Meas. Tech.*, 8, 941, 2015.
- Wagner, T., Dix, B. v., Friedeburg, C. v., Frieß, U., Sanghavi, S., Sinreich, R., and Platt, U.: MAX-DOAS O₄ measurements: A new technique to derive information on atmospheric aerosols—Principles and information content, *J. Geophys. Res. Atmos.*, 109, 2004.
- 20 Wang, P., Tilstra, L., de Graaf, M., and Stammes, P.: Interpretation of FRESCO cloud retrievals in case of absorbing aerosol events., *Atmos. Chem. Phys.*, 12, 2012.
- Wang, Y., Beirle, S., Lampel, J., Koukouli, M., De Smedt, I., Theys, N., Li, A., Wu, D., Xie, P., Liu, C., Van Roozendael, M., Stavrou, T., Müller, J.-F., and Wagner, T.: Validation of OMI, GOME-2A and GOME-2B tropospheric NO₂, SO₂ and HCHO products using MAX-DOAS observations from 2011 to 2014 in Wuxi, China: investigation of the effects of priori profiles and aerosols on the satellite products, *Atmos. Chem. Phys.*, 17, 5007–5033, 2017.
- 25 Williams, J., Scheele, M., van Velthoven, P., Cammas, J.-P., Thouret, V., Galy-Lacaux, C., and Volz-Thomas, A.: The influence of biogenic emissions from Africa on tropical tropospheric ozone during 2006: a global modeling study, *Atmos. Chem. Phys.*, 9, 5729–5749, 2009.
- Williams, J., Van Velthoven, P., and Brenninkmeijer, C.: Quantifying the uncertainty in simulating global tropospheric composition due to the variability in global emission estimates of Biogenic Volatile Organic Compounds, *Atmos. Chem. Phys.*, 13, 2857–2891, 2013.
- 30 Williams, J. E., Boersma, K. F., Le Sager, P., and Verstraeten, W. W.: The high-resolution version of TM5-MP for optimized satellite retrievals: description and validation, *Geosci. Model Dev.*, 10, 721, 2017.
- Wittrock, F., Oetjen, H., Richter, A., Fietkau, S., Medeke, T., Rozanov, A., and Burrows, J.: MAX-DOAS measurements of atmospheric trace gases in Ny-Ålesund-Radiative transfer studies and their application, *Atmos. Chem. Phys.*, 4, 955–966, 2004.
- 35 Wu, F. C., Xie, P. H., Li, A., Chan, K. L., Hartl, A., Wang, Y., Si, F. Q., Zeng, Y., Qin, M., Xu, J., Liu, J. G., Liu, W. Q., and Wenig, M.: Observations of SO₂ and NO₂ by mobile DOAS in the Guangzhou eastern area during the Asian Games 2010, *Atmos. Meas. Tech.*, 6, 2277–2292, 2013.



- Yamaji, K., Ikeda, K., Irie, H., Kurokawa, J.-i., and Ohara, T.: Influence of model grid resolution on NO₂ vertical column densities over East Asia, *J. Air Waste Manage.*, 64, 436–444, 2014.
- Yang, F., Tan, J., Zhao, Q., Du, Z., He, K., Ma, Y., Duan, F., and Chen, G.: Characteristics of PM 2.5 speciation in representative megacities and across China, *Atmos. Chem. Phys.*, 11, 5207–5219, 2011.
- Zhou, Y., Brunner, D., Spurr, R., Boersma, K., Sneep, M., Popp, C., and Buchmann, B.: Accounting for surface reflectance anisotropy in
5 satellite retrievals of tropospheric NO₂, *Atmos. Meas. Tech.*, 3, 1185–1203, 2010.

Lebenslauf

Bildungsweg

- 09/2007 - Fernerkundung Wissenschaft und Technologie (B.Eng.)**
06/2011 an der Wuhan Universität (WHU) in China
mit dem Bachelorarbeitsthema “The application of Genetic Algorithm in solving for SIR model parameters”
- 09/2011 - Kartographie und Geographisches Informationssystem (M.Sc.)**
10/2014 an der Wuhan Universität (WHU) in China
- 10/2012 - Earth Oriented Space Science and Technology (M.Sc.)**
10/2014 an der Technischen Universität München (TUM) in Deutschland
mit dem Masterarbeitsthema “Retrieval and validation of aerosol and NO₂ profiles over Nanjing using Mini-MAX-DOAS instrument”

Praxiserfahrung

- 07/2013 - Praktikum im Bereich Atmosphärenprozessoren**
03/2014 im Deutschen Zentrum für Luft- und Raumfahrt (DLR) in Deutschland

Auslandserfahrung

- 03/2018 - Forschungsaufenthalt im Bereich UV-sichtbare DOAS**
04/2018 am Belgischen Institut für Weltraum-Aeronomie (BIRA-IASB) in Belgien

